博士論文

# Quantum Measurement of Itinerant Microwave Photons Using Superconducting Circuits

（超伝導回路を用いた伝搬マイクロ波光子の量子測定）

河野信吾

Dissertation

# Quantum Measurement of Itinerant Microwave Photons Using Superconducting Circuits

Supervisor: Prof. Yasunobu Nakamura

Department of Applied Physics
School of Engineering
The University of Tokyo

Shingo Kono

Submitted in February 2019

# Abstract

Microwave photons are indispensable for realizing a quantum information carrier or a coupling bus between superconducting qubits. While microwave photons confined in a resonator have been characterized in the quantum limit with a superconducting qubit strongly coupled, it remains challenging to measure itinerant microwave photons due to the lack of high-efficiency photodetectors in the microwave domain, in contrast to the optical frequency domain. In this thesis, we demonstrate quantum measurements of itinerant microwave photons by using a circuit quantum electrodynamical system, where a microwave cavity plays a crucial role in facilitating the interaction between itinerant photons and a superconducting qubit. First, we characterize the photon-number distribution of a microwave squeezed vacuum by measuring the photon-number-resolved excitation spectrum of the qubit in a cavity that is driven externally and continuously with the squeezed vacuum. We confirm that the photon-number distribution reveals an even-odd photon number oscillation and quantitatively constitutes the nonclassicality. Second, we perform Wigner quantum state tomography of itinerant microwave photons by measuring the quadratures which are efficiently amplified by a Josephson parametric amplifier. The quantum state is reconstructed via the maximum likelihood method with corrected measurement inefficiency, which is reliably calibrated based on the qubit dephasing induced by itinerant microwave photons. Last, we implement a deterministic entangling gate between a superconducting qubit and an itinerant microwave photon reflected by a cavity containing the qubit. Using entanglement and high-fidelity qubit readout, we demonstrate a quantum non-demolition detection of a single photon. The existence of the detected microwave photon is confirmed by using Wigner quantum state tomography. These results on the fundamental characterizations of itinerant microwave photons have promising applications for quantum sensing and metrology in the microwave regime. Furthermore, the efficient entangling gate between itinerant photons and a superconducting qubit can be a building block for quantum networks connecting distant qubit modules as well as for a microwave photon counting device for multiple-photon signals.

# Acknowledgments

I acknowledge the support of all the people who are related to my research life. The following is an incomplete list.

First, thanks to the members of my thesis committee, Profs. Yasunobu Nakamura, Akira Furusawa, Masato Koashi, Masahito Ueda, Koji Usami, for their time, feedback, and support.

I would like to thank my supervisor, Prof. Yasunobu Nakamura. He gave me a great opportunity to do my best in this interesting field. I really enjoyed my research with his continued support and encouragement throughout my bachelor's, master's, and PhD. life. I will never forget what he always says, "Beauty is in the details." He not only pays attention to the details in papers and presentations, but also he never misses small things in experimental results, which always improves my research up to the best that it can possibly be. I feel delighted to have worked with him from the starting point of my research.

I also would like to thank Prof. Koji Usami. It is a pity that I have not directly collaborated on a specific theme with him. Nevertheless, I believe in his sense of values in physics, which always improves my presentations and papers. I will continue my research with his inspirational quote, "Physics changes the world by orders of magnitude."

The theoretical support of Prof. Kazuki Koshino from the Tokyo Medical and Dental University was immensely important to me. I learned the basic concepts of quantum optics from him. With the aid of his support, I was able to feel free to challenge various experiments without feeling fear about an encounter with exotic experimental results.

The assistance of Dr. Yutaka Tabuchi has been invaluable for the conducting of my experiments. He always leads me to a correct direction based on his deep understanding of physics and engineering. I have succeeded in saving my time thanks to his help throughout my research. His outspoken remarks sometimes may discourage me. However, this is because he always captures the essence of the problem and makes me consider things more deeply.

I deeply treasure the practical discussions that I held with Dr. Shuhei Tamate. I can truly sympathize with his intention to learn things by himself. Therefore, I could always have down-to-earth discussions with him.

Dr. Takanori Sugiyama helped me to understand more deeply the theoretical side of quantum information. I learned many things by considering the difference in quantum information between the experimental and theoretical points of view.

I would like to thank Dr. Koichi Kusuyama and Dr. Koichi Nittoh in RIKEN for their sample fabrications. Thanks to their irreplaceable experience, my samples were successfully fabricated.

I can recall uncountable fruitful discussions with Prof. Atsushi Noguchi, for which I am thankful to him. I was always surprised at his speedy logical thinking. I had many chances to discuss with him, as he is seated next to me. Our discussions often proceeded in various directions and made my research broaden.

I would like to thank Dr. Dany Lachance-Quirion. I was always impressed with his

experiments which goes to the goal without hesitation. Moreover, I feel happy to see that the experiments in the dilution refrigerator 'Kirin' are proceeding ceaselessly with his help when I was busy writing the thesis.

Dr. Rekishu Yamazaki always inspired and encouraged me to try to achieve the biggest goals. What I can say with confidence is that the hardest time in my laboratory life was going to the Sea of Japan from Tokyo by bicycle with him in two days. I have obtained confidence in my underlying strength.

I would like to thank Dr. Hiroki Takahashi, Dr. Maria Fuwa, Dr. Yosuke Nakata, Dr. Arnaud Gloppe, and Dr. Nicolas Gheeraert for fruitful discussions. I was so happy to work with these experts in many different fields.

I would like to thank Jacob Koenig, Akhil Pratap Singh, and Samuel Piotr Wolski for reading and improving my thesis. I was super-surprised that Jacob could read through my long thesis fast and give me many nice feedbacks.

My experience would not have been the same without my colleagues, Ryusuke Hisatomi and Ayato Okada. I have shared the laboratory life's joys and sorrows with them. I'm really looking forward to drinking after our defenses.

I would like to thank Yutaka Takeda, Amarsanaa Davaasuren, Kentaro Heya, Akihiro Fujiwara, and Yoshiki Sunada. I was so happy to work with the talented younger players. Especially, I can graduate from the group without any worry, because Sunada-kun is really interested in what I have done and is proactively advancing the quantum optics project in our group.

Finally, I would like to thank Mrs. Kimiko Soda, Mrs. Megumi Mikami, Mrs. Yukiko Watanabe Collins and Dr. Shinichiro Fujii for their administrative support. I have been able to concentrate on my research without any stress.

# Contents

# Chapter 1

# Introduction

A technological breakthrough in quantum measurement always opens up a new possibility to explore a fundamental aspect in the quantum nature. Seeing the quantum world from the new point of view brings us an improvement in quantum technology. The quantum control and measurement with high fidelity offer various applications in a broad range of fields, such as quantum computation, communication, and sensing.

For realizing these quantum applications by utilizing their own advantages, many physical systems have been investigated, including trapped ions, ultracold atoms, nuclear spins, electron spins in quantum dots, optical photons, and superconducting circuits [1]. Here, the important point is how to attack the trade-off between accessibility and quantum coherence since quantum channels for control and measurement inevitably cause relaxation and decoherence. Particularly, in the context of quantum computation, superconducting circuits are one of the leading candidates thanks to their design flexibility, readily enabling the optimization of the trade-off. Moreover, taking full advantage of the conventional technologies in integrated circuits and microwave engineering, the number of individually controllable and measurable superconducting qubits have been dramatically increased together with the improvements in their coherence.

A superconducting qubit was first controlled and measured in a quantum mechanical manner [2], following the controversial discussions on the possibility of observing macroscopic quantum coherence [3, 4]. Although the coherence time in the first device was about 1 ns, there have been several improvements in circuit design and fabrication process, which have increased their coherence times up to 10 - 100 $\mu$s [5, 6, 7, 8]. The invention of a transmon qubit is one of the notable breakthroughs, which brings a charge-noise insensitivity, a way of design based on microwave engineering, and a simple fabrication process [9, 10].

The family of superconducting qubits is considered microwave circuits with the nonlinearity brought by Josephson junctions and mimics the energy levels in an atom, in the microwave frequency domain. The usefulness of this analogy is supported by the concept of cavity quantum electrodynamics (QED), where an atom is strongly coupled to a cavity mode [11]. In other words, a superconducting qubit can be considered an artificial atom which coupled to a microwave photon in a resonator, which is called a circuit QED [12, 13]. By asking for the help of atomic physics, the building blocks for a quantum computer have been established [14, 15].

In addition to the application to quantum computing, the circuit QED system is a powerful platform for exploring a light-matter interaction. Because of the strong coupling of the superconducting qubit and the microwave photons [16], the circuit QED system can easily achieve the strong dispersive regime, where the state-dependent frequency shifts exceed their dephasing rates [17, 18]. With the high-fidelity control and measurement of superconducting qubits, microwave quantum states have been generated and characterized

with the comparable high fidelity. For example, the microwave state has been deterministically prepared in an arbitrary superposition state of a few photon-number states [19, 20] or a Schrödinger cat state with large-amplitude coherent states [21]. Furthermore, a quantum non-demolition detection of a microwave photon was also demonstrated [22]. The longer lifetime of microwave photons in a three-dimensional cavity, due to the simple structure and the large mode volume [23, 24], triggered the idea of utilizing the cavity mode as a carrier of quantum information, giving rise to another architecture of quantum computer [25, 26].

Thanks to the continuous efforts in the world, the number of integrated superconducting qubits has been increasing to several tens [27, 28]. In other words, small and noisy quantum computers are now available. Today, one of the hottest topics in this field is how we apply the baby quantum computers to industry and scientific research [29]. However, to implement a fault-tolerant quantum computer, we need to push up the number of the qubits by orders of magnitude.

It is not certain if it is sufficient to just scale up the existing superconducting circuit technologies in order to achieve the number of qubits around $10^7$ to $10^8$ [30]. One of the solutions may be to utilize a quantum network, where modules containing several qubits are connected to each other via flying microwave photons [31]. The generation and characterization of itinerant photons have been demonstrated [32, 33, 34]. More recently, quantum state transfers are demonstrated between two localized circuit QED systems [35, 36, 37]. For realizing a well-defined communication channel as a key component of the large-scale quantum computer, quantum technologies on itinerant microwave photons need to be more matured. While the microwave photons confined in a cavity have successfully been used as quantum information carriers, it remains challenging to improve the fidelity of the manipulations on the itinerant microwave photons. One of the bottlenecks is the imperfect quantum measurement of itinerant microwave photons due to the lack of a high-efficient photodetector [38, 39, 40], in contrast to the case of the optical-frequency domain [41].

In this thesis, we demonstrate quantum measurements of itinerant microwave photons by using a three-dimensional circuit QED system, where a microwave cavity assists the coupling between the itinerant microwave photons and a superconducting qubit. First, we characterize the photon-number distribution in a microwave squeezed vacuum by measuring the photon-number-resolved excitation spectrum of the qubit in the cavity that is driven externally and continuously with the squeezed vacuum [42]. Second, we perform a Wigner quantum state tomography of itinerant microwave photons by measuring the quadratures which are efficiently amplified by a Josephson parametric amplifier (JPA) [43]. Finally, using an entanglement between an itinerant photon and a superconducting qubit through a cavity mode, we demonstrate a quantum non-demolition (QND) detection of a single photon [43].

## 1.1 Thesis overview

This thesis consists of the following parts.

Chapter 2 introduces the quantization of superconducting circuits. The basic circuit models necessary for designing the circuit QED system and explaining the experimental results are presented. Chapter 3 describes the representation of quantum states in a superconducting qubit and a harmonic oscillator. As a preparation for the Wigner quantum state tomography of the microwave photons, we discuss the quantum measurement of the quadratures through photon loss, amplification, and heterodyne detection. Chapter 4 introduces the design of the three-dimensional circuit QED system using a

classical electromagnetic simulator. We discuss the validity of the design methodology by comparing the simulation results with the experimental data. Chapter 5 shows the experimental setup. We discuss the required conditions for the setup based on the theoretical perspective on the circuit QED model in the dispersive regime. Chapter 6 describes the experimental characterization of the circuit QED system. This chapter describes the optimization methods of the control and readout of the superconducting qubit which is dispersively coupled to the cavity.

Chapters 7, 8, and 9 shows the experimental results on the quantum measurements of the itinerant microwave photons. Chapter 7 shows the results of the measurement of the nonclassical photon-number distribution in the cavity driven by the microwave squeezed vacuum. We discuss the determination of the actual photon number distribution from the excitation spectrum of the superconducting qubit. Chapter 8 describes the Wigner quantum state tomography of the itinerant microwave photons using the JPA as a phase-sensitive amplifier. We introduce the iterative maximum likelihood reconstruction without or with the correction of the inefficiency of the quadrature measurements. This chapter describes the calibration of the measurement efficiency based on the microwave-induced dephasing of the superconducting qubit. Chapter 9 describes the QND detection of itinerant microwave photons using a entangling gate with the superconducting qubit in the cavity. We characterize the QND detection with quantum efficiency and dark-count probability. Finally, we discuss the quantum state of the itinerant mode after the QND detection, which is reconstructed by the Wigner quantum state tomography.

Finally, we summarize the results discussed in this thesis and offer prospects. We discuss the applications of our quantum measurement scheme of itinerant microwave photons.

# Chapter 2

# Superconducting quantum circuits

Here, we explain the quantization of superconducting circuits. In this thesis, we use a transmon qubit, which can be considered as an anharmonic oscillator. Therefore, we introduce its Hamiltonian from an LC resonator by treating a nonlinear term from a Josephson junction perturbatively. Then, we derive the Hamiltonian of a circuit quantum electrodynamical (QED) system, where a transmon qubit is coupled to an LC resonator. Furthermore, we introduce the Hamiltonian of a Josephson parametric amplifier (JPA). We also introduce coupling to a waveguide for each system. The basic procedure of the quantization is explained in Appendix. A, where the description of the quantization follows [44].

## 2.1 LC resonator

An LC resonator is known as a fundamental microwave circuit. It is often used for readout, coupling, and filtering for superconducting qubits. By tightly confining electromagnetic fields, it allows to readily reach the strong coupling regime. In the context of quantum mechanics, an LC resonator is a harmonic oscillator with uniform energy level spacing. An energy quantum in the LC circuit is conventionally called a photon.

As shown in Fig. 2.1, an LC resonator is formed by an inductor and a capacitor. The Lagrangian of the circuit is written as

$$\mathcal{L} = \frac{C}{2}\dot{\Phi}^2 - \frac{\Phi^2}{2L}, \tag{2.1}$$

where $L$ is the inductance, $C$ is the capacitance and $\Phi$ is the magnetic flux in the inductor.

The conjugate momentum $Q$ is calculated by

$$Q = \frac{\partial \mathcal{L}}{\partial \dot{\Phi}} = C\dot{\Phi}, \tag{2.2}$$

where $Q$ is understood as the electric charge in the capacitor, since $\dot{\Phi}$ gives the voltage across the capacitance. Through a Legendre transformation, we obtain the Hamiltonian

$$\mathcal{H} = \frac{Q^2}{2C} + \frac{\Phi^2}{2L}. \tag{2.3}$$

By replacing the classical variables $\Phi$ and $Q$ with their corresponding operators $\hat{\Phi}$ and $\hat{Q}$ and imposing the canonical commutation relation $[\hat{\Phi}, \hat{Q}] = i\hbar$, we obtain the quantum-mechanical Hamiltonian

$$\hat{\mathcal{H}} = \frac{\hat{Q}^2}{2C} + \frac{\hat{\Phi}^2}{2L}. \tag{2.4}$$

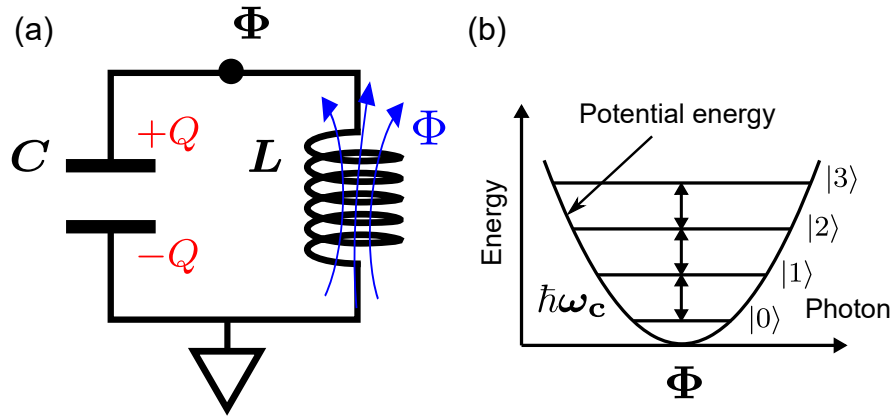


Figure 2.1: LC resonator. (a) Circuit diagram. (b) Energy levels.

To diagonalize it, we define the annihilation and creation operators as

$$\hat{a} = \frac{\left(\frac{C}{\hbar^2 L}\right)^{\frac{1}{4}} \hat{\Phi} + i \left(\frac{L}{\hbar^2 C}\right)^{\frac{1}{4}} \hat{Q}}{\sqrt{2}}, \quad \hat{a}^\dagger = \frac{\left(\frac{C}{\hbar^2 L}\right)^{\frac{1}{4}} \hat{\Phi} - i \left(\frac{L}{\hbar^2 C}\right)^{\frac{1}{4}} \hat{Q}}{\sqrt{2}}, \tag{2.5}$$

which satisfy the bosonic commutation relation, $[\hat{a}, \hat{a}^\dagger] = 1$. Then, the conjugate operators $\hat{\Phi}$ and $\hat{Q}$ are described in terms of the annihilation and creation operators by

$$\hat{\Phi} = \left(\frac{\hbar^2 L}{C}\right)^{\frac{1}{4}} \frac{\hat{a} + \hat{a}^\dagger}{\sqrt{2}}, \quad \hat{Q} = \left(\frac{\hbar^2 C}{L}\right)^{\frac{1}{4}} \frac{\hat{a} - \hat{a}^\dagger}{\sqrt{2}i}. \tag{2.6}$$

By substituting Eq. (2.6) in the Hamiltonian of Eq. (2.4), we can diagonalize the Hamiltonian as

$$\hat{\mathcal{H}} = \hbar\omega_{\mathrm{c}} \left(\hat{a}^\dagger \hat{a} + \frac{1}{2}\right), \tag{2.7}$$

where $\omega_{\mathrm{c}} = 1/\sqrt{LC}$ is the resonance frequency of the LC resonator. The eignestates are the photon number state or the Fock states, as shown in Fig. 2.1(b).

### 2.1.1 Dimensionless parameters

It is useful to analyze the system with dimensionless parameters. Here, we define the dimensionless magnetic flux and electric charge as

$$\hat{\varphi} = \frac{\hat{\Phi}}{\phi_0}, \quad \hat{n} = \frac{\hat{Q}}{2e}, \tag{2.8}$$

where $\phi_0 = \frac{\hbar}{2e}$ is the reduced magnetic flux quantum and $e$ is the elementary electric charge. Note that the magnetic flux quantum is given by $\Phi_0 = 2\pi\phi_0 = \frac{h}{2e}$. The phase $\hat{\varphi}$ can be understood as the magnetic flux normalized with the reduced magnetic flux quantum, which is consistent with the definition of the phase difference in a Josephson junction. The number $\hat{n}$ can be understood as the electric charge normalized with the electric charge of a Cooper pair. Here, the new commutation relation is given by

$$[\hat{\varphi}, \hat{n}] = i. \tag{2.9}$$

The Hamiltonian of Eq. (2.3) is rewritten as

$$\hat{\mathcal{H}} = \hbar\left(\frac{\omega_{\rm C}}{2}\,\hat{n}^2 + \frac{\omega_{\rm L}}{2}\,\hat{\varphi}^2\right), \tag{2.10}$$

where $\hbar\omega_{\rm C} = \frac{(2e)^2}{C} = \hbar\frac{Z_0}{C}$ is the capacitive energy quantum, and $\hbar\omega_{\rm L} = \frac{\phi_0^2}{L} = \hbar\frac{1}{Z_0 L}$ is the inductive energy quantum. Here, we also define the quantum impedance $Z_0 = \frac{\phi_0}{2e} = \hbar/(2e)^2$, the ratio of the reduced magnetic flux quantum to the electric charge of a Cooper pair. The annihilation and creation operators $\hat{a}$, $\hat{a}^\dagger$ are now described by

$$\hat{a} = \frac{\left(\frac{\omega_{\rm L}}{\omega_{\rm C}}\right)^{\frac{1}{4}}\hat{\varphi} + i\left(\frac{\omega_{\rm C}}{\omega_{\rm L}}\right)^{\frac{1}{4}}\hat{n}}{\sqrt{2}}, \quad \hat{a}^\dagger = \frac{\left(\frac{\omega_{\rm L}}{\omega_{\rm C}}\right)^{\frac{1}{4}}\hat{\varphi} - i\left(\frac{\omega_{\rm C}}{\omega_{\rm L}}\right)^{\frac{1}{4}}\hat{n}}{\sqrt{2}}. \tag{2.11}$$

On the other hand, the pair of conjugate operators are now represented as

$$\hat{\varphi} = \left(\frac{\omega_{\rm C}}{\omega_{\rm L}}\right)^{\frac{1}{4}}\frac{\hat{a}+\hat{a}^\dagger}{\sqrt{2}}, \quad \hat{n} = \left(\frac{\omega_{\rm L}}{\omega_{\rm C}}\right)^{\frac{1}{4}}\frac{\hat{a}-\hat{a}^\dagger}{\sqrt{2}i}. \tag{2.12}$$

We find that the zero-point fluctuations of the conjugate variables are described by the ratio of the energy quanta. In additoin, the resonance frequency $\omega_{\rm c}$ is described by the geometric mean of the frequencies of the capacitive and inductive energy quanta:

$$\omega_{\rm c} = \sqrt{\omega_{\rm L}\omega_{\rm C}}. \tag{2.13}$$

An LC resonator is sometimes characterized by the characteristic impedance $Z = \sqrt{L/C}$. From this definition, we find the characteristic impedance divided by the quantum impedance corresponds to the ratio of the energy quanta: $\omega_{\rm C}/\omega_{\rm L} = (Z/Z_0)^2$.

## 2.2 Capacitively coupled LC resonators

A coupled system is an indispensable tool for quantum information processing since a coupling interaction between two or more quantum systems enables us to entangle the systems together or to transfer quantum information. Here, we will study capacitively coupled LC resonators as a basic coupled system. As shown in Fig. 2.2(a), two independent magnetic fluxes $\Phi_1$ and $\Phi_2$ are defined as the degrees of freedom of the two LC resonators. Using these variables, we derive the Lagrangian as

$$\mathcal{L} = \frac{C_1}{2}\dot{\Phi}_1^2 - \frac{\Phi_1^2}{2L_1} + \frac{C_2}{2}\dot{\Phi}_2^2 - \frac{\Phi_2^2}{2L_2} + \frac{C_g}{2}\left(\dot{\Phi}_1 - \dot{\Phi}_2\right)^2, \tag{2.14}$$

where the last term gives us the coupling between the two LC resonators. Using the magnetic flux vector $\boldsymbol{\Phi}$ and the capacitance matrix $\boldsymbol{C}$, the Lagrangian can be represented as

$$\mathcal{L} = \frac{1}{2}\dot{\boldsymbol{\Phi}}^{\rm T}\boldsymbol{C}\dot{\boldsymbol{\Phi}} - \frac{\Phi_1^2}{2L_1} - \frac{\Phi_2^2}{2L_2}, \tag{2.15}$$

where

$$\boldsymbol{\Phi} = \begin{pmatrix}\Phi_1\\ \Phi_2\end{pmatrix}, \quad \boldsymbol{C} = \begin{pmatrix}C_1+C_g & -C_g\\ -C_g & C_2+C_g\end{pmatrix}. \tag{2.16}$$

Then, we obtain the conjugate momentum vector

$$\boldsymbol{Q} = \begin{pmatrix}Q_0\\ Q_1\end{pmatrix} = \boldsymbol{C}\dot{\boldsymbol{\Phi}} = \begin{pmatrix}(C_1+C_g)\Phi_1 - C_g\Phi_2\\ -C_g\Phi_1 + (C_2+C_g)\Phi_2\end{pmatrix}. \tag{2.17}$$

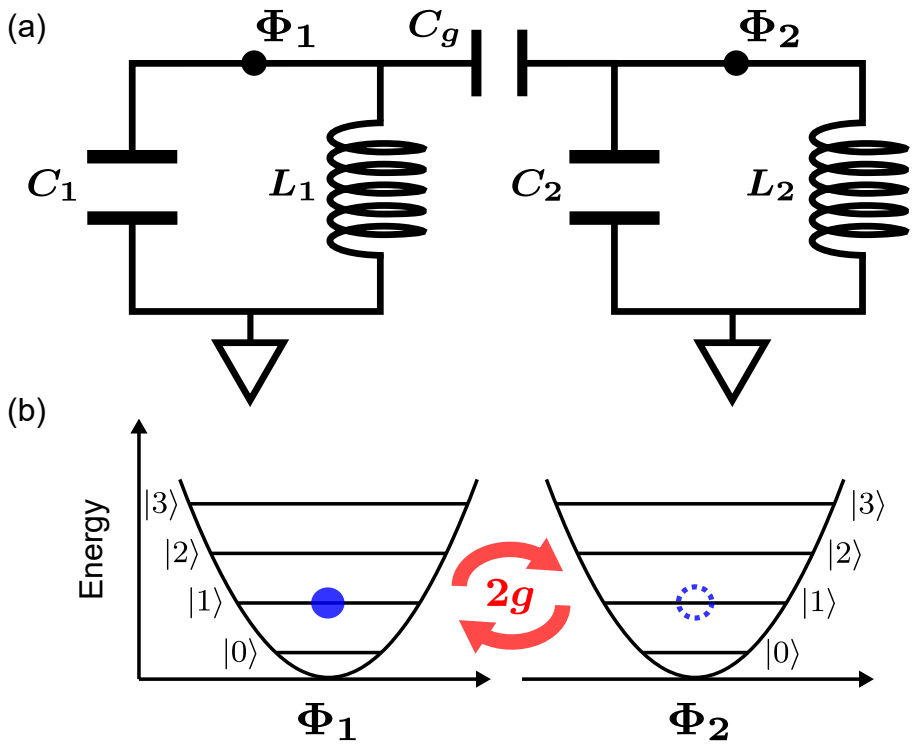


Figure 2.2: Capacitively coupled LC resonators. (a) Circuit diagram. (b) Oscillation of a single photon between the two resonators at the frequency of $2g$.

and the inverse of the capacitance matrix

$$\boldsymbol{C}^{-1} = \frac{1}{{C_*}^2} \begin{pmatrix} C_2 + C_g & C_g \\ C_g & C_1 + C_g \end{pmatrix}, \tag{2.18}$$

where ${C_*}^2 = (C_1 + C_g)(C_2 + C_g) - C_g^2$. For simplicity, ${C_*}^2 = (C_1 + C_g)(C_2 + C_g)(1 - \epsilon)$, where $\epsilon = \frac{C_g^2}{(C_1+C_g)(C_2+C_g)}$. Using Eq. (A.44), we obtain the Hamiltonian

$$\begin{aligned} \mathcal{H} &= \frac{1}{2}\boldsymbol{Q}^{\mathrm{T}}\boldsymbol{C}^{-1}\boldsymbol{Q} + \frac{\Phi_1^2}{2L_1} + \frac{\Phi_2^2}{2L_2} \\ &= \frac{Q_1^2}{2\bar{C}_1} + \frac{\Phi_1^2}{2L_1} + \frac{Q_2^2}{2\bar{C}_2} + \frac{\Phi_2^2}{2L_2} + (1-\epsilon)\frac{C_g}{\bar{C}_1\bar{C}_2}Q_1Q_2, \end{aligned} \tag{2.19}$$

where $\bar{C}_n = (C_n + C_g)(1 - \epsilon)$ are the renormalized capacitances for $n = 1, 2$. We can find that the first and the second terms describe one of the renormalized resonator, that the third and the forth terms describe the other renormalized resonator, and that the last term describes the coupling between the resonators.

We can then obtain the quantum-mechanical Hamiltonian by replacing the conjugate variables with their corresponding operators:

$$\hat{\mathcal{H}} = \frac{\hat{Q}_1^2}{2\bar{C}_1} + \frac{\hat{\Phi}_1^2}{2L_1} + \frac{\hat{Q}_2^2}{2\bar{C}_2} + \frac{\hat{\Phi}_2^2}{2L_2} + (1-\epsilon)\frac{C_g}{\bar{C}_1\bar{C}_2}\hat{Q}_1\hat{Q}_2, \tag{2.20}$$

where the pairs of conjugate operators have the commutation relation $[\hat{\Phi}_n, \hat{Q}_n] = i\hbar$, for $n = 1, 2$.

Using the annihilation and creation operators for each mode which are defined as in Eq. (2.5), the Hamiltonian can be represented as

$$\hat{\mathcal{H}} = \hbar \left[ \omega_{\mathrm{c}_1}\, \hat{a}_1^\dagger \hat{a}_1 + \omega_{\mathrm{c}_2}\, \hat{a}_2^\dagger \hat{a}_2 - g(\hat{a}_1 - \hat{a}_1^\dagger)(\hat{a}_2 - \hat{a}_2^\dagger) \right], \tag{2.21}$$

where $\omega_{\mathrm{r}_n} = 1/\sqrt{L_n \bar{C}_n}$ is the resonance frequency of the LC resonator for $n = 1,\ 2$ and $g = \frac{1}{2}\sqrt{\frac{\omega_{\mathrm{c}_1}\omega_{\mathrm{c}_2} C_g^2}{(C_1+C_g)(C_2+C_g)}}$ is the coupling strength.

The ratio of the coupling strength to the resonance frequency (the geometric mean of both resonant frequencies) is important to characterize how strong the coupling strength is. It is given by

$$\frac{g}{\sqrt{\omega_{\mathrm{c}_1}\omega_{\mathrm{c}_2}}} = \frac{1}{2}\sqrt{\frac{C_g}{C_1 + C_g}\frac{C_g}{C_2 + C_g}}. \tag{2.22}$$

We find the ratio of the coupling strength to the geometric mean of the resonator frequencies is determined by the geometric mean of the ratios of the coupling capacitance $C_g$ to the total capacitance $C_n + C_g$, for $n = 1,\ 2$. The ratio of $C_g/(C_n + C_g)$ is sometimes called the participation ratio, which is useful for the characterization of the coupling strength and the energy loss rate of the LC resonator.

In this thesis, we do not consider the ultra- or deep-strong coupling regime where the coupling strength is comparable to the resonance frequencies of the system. We only consider the regime $\frac{g}{\sqrt{\omega_{\mathrm{c}_1}\omega_{\mathrm{c}_2}}} \ll 1$. In that limit, we can neglect $\epsilon = \frac{C_g^2}{(C_1+C_g)(C_2+C_g)}$ since the condition of $\frac{g}{\sqrt{\omega_{\mathrm{c}_1}\omega_{\mathrm{c}_2}}} \ll 1$ exactly corresponds to $\epsilon = \frac{C_g^2}{(C_1+C_g)(C_2+C_g)} \ll 1$. Then, we simply approximate the renormalized capacitance as $\bar{C}_n = (C_n + C_g)$ and the resonance frequency as $\omega_{\mathrm{r}_n} = 1/\sqrt{L_n(C_n + C_g)} = 1/\sqrt{L_n \bar{C}_n}$, for $n = 1,\ 2$ hereinafter.

In the coupling Hamiltonian in Eq. (2.21), we have the terms of $\hat{a}_1^\dagger \hat{a}_2^\dagger$ and $\hat{a}_1 \hat{a}_2$, which are called the counter rotating terms. The frequency detuning between the interacting states is described as $\omega_{\mathrm{c}_1} + \omega_{\mathrm{c}_2}$ and it is much larger than the coupling strength $g$ as long as the system is in the normal coupling regime. Therefore, the interactions are adiabatically suppressed and the counter rotating terms can be safely neglected. This approximation is called the Rotating Wave Approximation (RWA). Using this approximation, the Hamiltonian is represented as

$$\hat{\mathcal{H}} = \hbar \left[ \omega_{\mathrm{c}_1}\, \hat{a}_1^\dagger \hat{a}_1 + \omega_{\mathrm{c}_2}\, \hat{a}_2^\dagger \hat{a}_2 + g(\hat{a}_1^\dagger \hat{a}_2 + \hat{a}_2^\dagger \hat{a}_1) \right]. \tag{2.23}$$

### 2.2.1 Diagonalization

In the Hamiltonian of the capacitively coupled LC resonators, the two harmonic oscillator modes exchange energy in a coupled oscillation. Here, it is useful to represent the Hamiltonian using diagonalized modes, which are defined as superpositions of the two harmonic oscillator modes.

To proceed with the diagonalization, we write the Hamiltonian as

$$\begin{aligned} \hat{\mathcal{H}} &= \hbar \left[ \left( \bar{\omega}_{\mathrm{c}} + \frac{\Delta}{2} \right) \hat{a}_1^\dagger \hat{a}_1 + \left( \bar{\omega}_{\mathrm{c}} - \frac{\Delta}{2} \right) \hat{a}_2^\dagger \hat{a}_2 + g(\hat{a}_1^\dagger \hat{a}_2 + \hat{a}_2^\dagger \hat{a}_1) \right] \\ &= \hbar\, \hat{\boldsymbol{a}}^\dagger\, \hat{\boldsymbol{H}}\, \hat{\boldsymbol{a}}, \end{aligned} \tag{2.24}$$

where $\bar{\omega}_{\mathrm{c}} = (\omega_{\mathrm{c}_1} + \omega_{\mathrm{c}_2})/2$ is the mean of the two resonance frequencies and $\Delta = \omega_{\mathrm{c}_1} - \omega_{\mathrm{c}_2}$ is the detuning between them. The one-dimensional column vector $\hat{\boldsymbol{a}}$ and the two-dimensional matrix $\hat{\boldsymbol{H}}$ are defined as

$$\hat{\boldsymbol{a}} = \begin{pmatrix} \hat{a}_1 \\ \hat{a}_2 \end{pmatrix}, \quad \hat{\boldsymbol{H}} = \begin{pmatrix} \bar{\omega}_{\mathrm{c}} + \frac{\Delta}{2} & g \\ g & \bar{\omega}_{\mathrm{c}} - \frac{\Delta}{2} \end{pmatrix}. \tag{2.25}$$

Using the unitary operator $\hat{\boldsymbol{U}}$, the matrix $\hat{\boldsymbol{H}}$ can be diagonalized as

$$\hat{\boldsymbol{H}} = \hat{\boldsymbol{U}}^{\dagger} \begin{pmatrix} \bar{\omega}_{\mathrm{c}} + \frac{\Delta'}{2} & 0 \\ 0 & \bar{\omega}_{\mathrm{c}} - \frac{\Delta'}{2} \end{pmatrix} \hat{\boldsymbol{U}}, \tag{2.26}$$

where $\Delta' = \sqrt{\Delta^2 + (2g)^2}$ is the frequency splitting of the two resonator modes. Here, the unitary operator can be determined as

$$\hat{\boldsymbol{U}} = \begin{pmatrix} \cos\Theta & \sin\Theta \\ -\sin\Theta & \cos\Theta \end{pmatrix}, \tag{2.27}$$

where $\Theta = \frac{1}{2}\arctan\left(\frac{2g}{\Delta}\right)$ is the mixing angle.

Then, we can define the diagonalizing annihilation operators as

$$\begin{aligned} \hat{\mathfrak{a}} &= \hat{\boldsymbol{U}}\hat{\boldsymbol{a}} \\ \begin{pmatrix} \hat{\mathfrak{a}}_1 \\ \hat{\mathfrak{a}}_2 \end{pmatrix} &= \begin{pmatrix} \cos\Theta\, \hat{a}_1 + \sin\Theta\, \hat{a}_2 \\ -\sin\Theta\, \hat{a}_1 + \cos\Theta\, \hat{a}_2 \end{pmatrix}, \end{aligned} \tag{2.28}$$

where the diagonalizing annihilation and creation operators satisfy the commutation relation as $[\hat{\mathfrak{a}}_n, \hat{\mathfrak{a}}_m^{\dagger}] = \delta_{nm}$, for $n,\ m = 1,\ 2$. The original annihilation operators are rewritten as

$$\begin{aligned} \hat{\boldsymbol{a}} &= \hat{\boldsymbol{U}}^{\dagger}\hat{\mathfrak{a}} \\ \begin{pmatrix} \hat{a}_1 \\ \hat{a}_2 \end{pmatrix} &= \begin{pmatrix} \cos\Theta\, \hat{\mathfrak{a}}_1 - \sin\Theta\, \hat{\mathfrak{a}}_2 \\ \sin\Theta\, \hat{\mathfrak{a}}_1 + \cos\Theta\, \hat{\mathfrak{a}}_2 \end{pmatrix}. \end{aligned} \tag{2.29}$$

Finally, we rewrite the Hamiltonian with the diagonalizing annihilation and creation operators:

$$\hat{\mathcal{H}} = \hbar \left[ \left( \bar{\omega}_{\mathrm{c}} + \frac{\Delta'}{2} \right) \hat{\mathfrak{a}}_1^{\dagger}\hat{\mathfrak{a}}_1 + \left( \bar{\omega}_{\mathrm{c}} - \frac{\Delta'}{2} \right) \hat{\mathfrak{a}}_2^{\dagger}\hat{\mathfrak{a}}_2 \right]. \tag{2.30}$$

After the diagonalization, we can consider the coupled LC resonator to be two independent LC resonators with a splitting of $\Delta' = \sqrt{\Delta^2 + (2g)^2}$.

The minimum of the frequency splitting can be obtained with the resonance condition of $\Delta \ll g$ as $\min\ \Delta' = 2g$. In this condition, the diagonalized modes is given by

$$\begin{pmatrix} \hat{\mathfrak{a}}_1 \\ \hat{\mathfrak{a}}_2 \end{pmatrix} = \begin{pmatrix} \frac{1}{\sqrt{2}}(\hat{a}_1 + \hat{a}_2) \\ \frac{1}{\sqrt{2}}(-\hat{a}_1 + \hat{a}_2) \end{pmatrix}. \tag{2.31}$$

It shows that a single photon oscillates between the two resonator modes of $\hat{a}_1$ and $\hat{a}_2$ at the frequency of $2g$, as shown in Fig. 2.2(b).

### 2.2.2 Dispersive regime

The dispersive regime is defined as the space in which the coupling strength is much smaller than the detuning, $g \ll |\Delta| = |\omega_{\mathrm{c}_1} - \omega_{\mathrm{c}_2}|$. In this regime, we can approximate the frequency splitting $\Delta' = \sqrt{\Delta^2 + (2g)^2}$ in the leading order of $g/\Delta$ as

$$\Delta' = \Delta + 2\,\frac{g^2}{\Delta}. \tag{2.32}$$

Therefore, the Hamiltonian can be rewritten as

$$\hat{\mathcal{H}} = \hbar \left[ \left( \omega_{\mathrm{c}_1} + \frac{g^2}{\Delta} \right) \hat{\mathfrak{a}}_1^{\dagger}\hat{\mathfrak{a}}_1 + \left( \omega_{\mathrm{c}_2} - \frac{g^2}{\Delta} \right) \hat{\mathfrak{a}}_2^{\dagger}\hat{\mathfrak{a}}_2 \right]. \tag{2.33}$$

The above equation shows that the resonator modes obtain a frequency shift of $\frac{g^2}{\Delta}$, which is called the Lamb shift.

Furthermore, the diagonalized basis is approximated with $\Theta = \frac{1}{2}\arctan\left(\frac{2g}{\Delta}\right) \approx \frac{g}{\Delta}$

$$\begin{pmatrix} \hat{\mathfrak{a}}_1 \\ \hat{\mathfrak{a}}_2 \end{pmatrix} \approx \begin{pmatrix} \cos\left(\frac{g}{\Delta}\right)\hat{a}_1 + \sin\left(\frac{g}{\Delta}\right)\hat{a}_2 \\ -\sin\left(\frac{g}{\Delta}\right)\hat{a}_1 + \cos\left(\frac{g}{\Delta}\right)\hat{a}_2 \end{pmatrix} \approx \begin{pmatrix} \hat{a}_1 + \left(\frac{g}{\Delta}\right)\hat{a}_2 \\ -\left(\frac{g}{\Delta}\right)\hat{a}_1 + \hat{a}_2 \end{pmatrix}, \tag{2.34}$$

where we neglect those terms with higher orders of $\frac{g}{\Delta}$. From these calculations, we find the diagonalized modes can be roughly considered to be the original modes.

## 2.3 Waveguide

Waveguides, which enable us to transmit microwave signals, are indispensable tools for readout and control of superconducting circuits.

A waveguide is modeled by a ladder-type circuit as shown in Fig. 2.3(a). The total length $D$ is divided into $2n+1$ nodes and the unit length of the ladder is described by $d = D/(2n+1)$. Suppose that the inductance and capacitance per unit length are $l$ and $c$, then the inductance and capacitance in the ladder-type circuit are $ld$ and $cd$, respectively. Considering the circuit diagram around the node $j$ shown in Fig. 2.3(b), the Lagrangian of the circuit is described by

$$\mathcal{L} = \sum_{j=-n}^{n-1}\left[\frac{cd}{2}\dot{\phi}_j^2 - \frac{1}{2ld}\left(\phi_{j+1}-\phi_j\right)^2\right], \tag{2.35}$$

where $\phi_j$ is the magnetic flux at node $j$. With the conjugate momentum

$$Q_j = \frac{\partial \mathcal{L}}{\partial \dot{\phi}_j} = cd\dot{\phi}_j, \tag{2.36}$$

we obtain the Hamiltonian:

$$\mathcal{H} = \sum_{j=-n}^{n-1}\left[\frac{1}{2cd}Q_j^2 + \frac{1}{2ld}\left(\phi_{j+1}-\phi_j\right)^2\right], \tag{2.37}$$

where $Q_j$ is understood as the electric charge stored in the capacitor of capacitance $cd$ at node $j$. By replacing the conjugate variables $\phi_j$ and $Q_j$ with the operators $\hat{\phi}_j$ and $\hat{Q}_j$ and imposing the canonical commutation relations $[\hat{\phi}_j, \hat{Q}_k] = i\hbar\delta_{jk}$, $[\hat{\phi}_j, \hat{\phi}_k] = 0$, and $[\hat{Q}_j, \hat{Q}_k] = 0$, we obtain the quantum-mechanical Hamiltonian of the waveguide:

$$\hat{\mathcal{H}} = \sum_{j=-n}^{n-1}\left[\frac{1}{2cd}\hat{Q}_j^2 + \frac{1}{2ld}\left(\hat{\phi}_{j+1}-\hat{\phi}_j\right)^2\right]. \tag{2.38}$$

Note that $\delta_{jk}$ is the Kronecker delta.

In a realistic situation, the waveguide is not a ladder-type circuit but a distributed circuit. Therefore, it is useful to take the limit of $n \to \infty$ ($d \to 0$). However, from Eq. (2.36), the conjugate momentum $Q_j$ vanishes in this limit. Then, we define the new conjugate momentum

$$q_j \equiv \frac{Q_j}{d} = c\dot{\phi}_j. \tag{2.39}$$

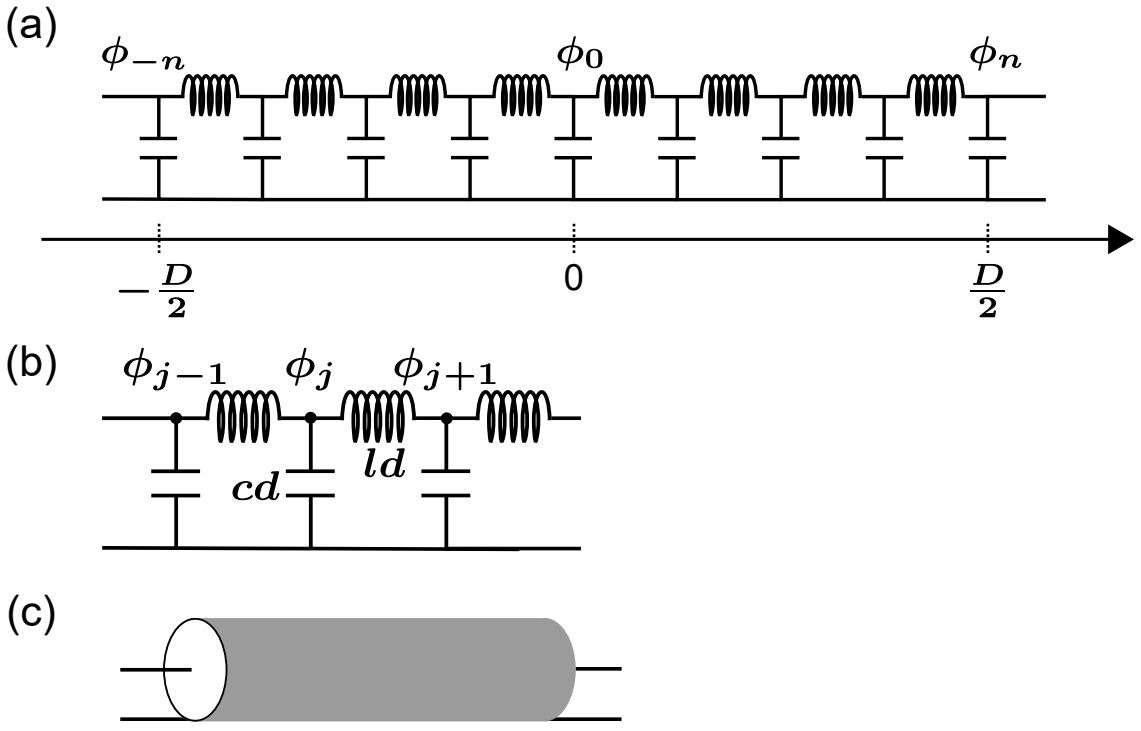


Figure 2.3: Circuit diagram of a waveguide. (a) Entire circuit diagram. The total length of the waveguide is $D$. (b) Magnified circuit diagram around node $j$. (c) Simplified circuit diagram.

From this definition, $q_j$ is found to be the electric charge density at node $j$. In the same way, the operator is defined as $\hat{q}_j \equiv \frac{\hat{Q}_j}{d}$. Thus, the Hamiltonian is modified as

$$\hat{\mathcal{H}} = \sum_{j=-n}^{n-1} d \left[ \frac{1}{2c}\hat{q}_j^2 + \frac{1}{2l}\left( \frac{\hat{\phi}_{j+1} - \hat{\phi}_j}{d} \right)^2 \right], \tag{2.40}$$

where $[\hat{\phi}_j,\, \hat{q}_k] = \frac{i\hbar\delta_{jk}}{d}$.

Taking the limit of $n \to \infty$, we obtain the Hamiltonian of the waveguide in the continuum limit as

$$\hat{\mathcal{H}} = \int_{-D/2}^{D/2} dx \left[ \frac{1}{2c}\hat{q}_x^2 + \frac{1}{2l}\left( \frac{\partial\hat{\phi}_x}{\partial x} \right)^2 \right], \tag{2.41}$$

where $[\hat{\phi}_x,\, \hat{q}_{x'}] = i\hbar\delta(x - x')$. Here, we use $\frac{jd}{2n+1} \to x$, $\sum_{j=-n}^{n-1} d \to \int_{-D/2}^{D/2} dx$, $\hat{\phi}_j \to \hat{\phi}_x$, $\hat{q}_j \to \hat{q}_x$, $\frac{\hat{\phi}_{j+1} - \hat{\phi}_j}{d} \to \frac{\partial\hat{\phi}_x}{\partial x}$, and $\frac{\delta_{jk}}{d} \to \delta(x - x')$. Note that $\delta(x - x')$ is the Dirac delta function.

### 2.3.1 Diagonalization

To diagonalize the Hamiltonian, the Fourier transformation of $\hat{\phi}_x, \hat{q}_x$ is defined with the periodic condition as

$$\hat{\phi}_{k_n} = \frac{1}{\sqrt{2\pi}} \int_{-D/2}^{D/2} dx\ \hat{\phi}_x e^{-ik_n x}, \quad \hat{q}_{k_n} = \frac{1}{\sqrt{2\pi}} \int_{-D/2}^{D/2} dx\ \hat{q}_x e^{-ik_n x}, \tag{2.42}$$

where $k_n = 2\pi n/D$ ($n = 0, \pm1, \pm2, \cdots$). Note that $\hat{\phi}^\dagger_{k_n} = \hat{\phi}_{-k_n}$ and $\hat{q}^\dagger_{k_n} = \hat{q}_{-k_n}$, since $\hat{\phi}_x$ and $\hat{q}_x$ are Hermite operators. Then, the inverse Fourier transformation is given by

$$\hat{\phi}_x = \frac{\sqrt{2\pi}}{D}\sum_{k_n}\hat{\phi}_{k_n}e^{ik_nx}, \quad \hat{q}_x = \frac{\sqrt{2\pi}}{D}\sum_{k_n}\hat{q}_{k_n}e^{ik_nx}. \tag{2.43}$$

Here, we use $\frac{1}{D}\int_{-D/2}^{D/2}dx\ e^{ik_nx} = \delta_{k_n,0}$ and $\frac{1}{D}\sum_{k_n}e^{ik_nx} = \delta(x)$. Then, the Hamiltonian is represented as

$$\hat{\mathcal{H}} = \frac{2\pi}{D}\sum_{k_n}\left\{\frac{1}{2c}\hat{q}^\dagger_{k_n}\hat{q}_{k_n} + \frac{k_n^2}{2l}\hat{\phi}^\dagger_{k_n}\hat{\phi}_{k_n}\right\}, \tag{2.44}$$

where $[\hat{\phi}^\dagger_{k_n}, \hat{q}_{k_{n'}}] = [\hat{\phi}_{k_n}, \hat{q}^\dagger_{k_{n'}}] = \frac{i\hbar D}{2\pi}\delta_{k_n,k_{n'}}$. Using their corresponding annihilation and creation operators, which are defined as

$$\hat{a}_{k_n} = \frac{\left(\frac{k_n^2c}{\hbar^2l}\right)^{\frac{1}{4}}\hat{\phi}_{k_n} + i\left(\frac{l}{\hbar^2k_n^2c}\right)^{\frac{1}{4}}\hat{q}_{k_n}}{\sqrt{2}}, \quad \hat{a}^\dagger_{k_n} = \frac{\left(\frac{k_n^2c}{\hbar^2l}\right)^{\frac{1}{4}}\hat{\phi}^\dagger_{k_n} - i\left(\frac{l}{\hbar^2k_n^2c}\right)^{\frac{1}{4}}\hat{q}^\dagger_{k_n}}{\sqrt{2}}, \tag{2.45}$$

the Hamiltonian can be diagonalized as

$$\hat{\mathcal{H}} = \frac{2\pi}{D}\sum_{k_n}\hbar\omega_{k_n}\hat{a}^\dagger_{k_n}\hat{a}_{k_n}, \tag{2.46}$$

where $[\hat{a}_{k_n}, \hat{a}^\dagger_{k_{n'}}] = \frac{L}{2\pi}\delta_{k_n,k_{n'}}$ and constants are neglected.

### 2.3.2 Infinite-length limit

Here, we consider the infinite-length limit of $D \to \infty$, then $\frac{2\pi}{D}\sum_{k_n} \to \int_{-\infty}^{\infty}dk$ and $k_n \to k$. From Eqs. (2.42) and (2.43), we obtain the Fourier transformation in this limit as

$$\begin{aligned}
\hat{\phi}_k &= \frac{1}{\sqrt{2\pi}}\int_{-\infty}^{\infty}dx\ \hat{\phi}_x e^{-ikx}, \quad \hat{q}_k = \frac{1}{\sqrt{2\pi}}\int_{-\infty}^{\infty}dx\ \hat{q}_x e^{-ikx}, \\
\hat{\phi}_x &= \frac{1}{\sqrt{2\pi}}\int_{-\infty}^{\infty}dk\ \hat{\phi}_k e^{ikx}, \quad \hat{q}_x = \frac{1}{\sqrt{2\pi}}\int_{-\infty}^{\infty}dk\ \hat{q}_k e^{ikx},
\end{aligned} \tag{2.47}$$

where $[\hat{\phi}^\dagger_k, \hat{q}_{k'}] = [\hat{\phi}_k, \hat{q}^\dagger_{k'}] = i\hbar\delta(k-k')$. Note that we use $\int_{-\infty}^{\infty}dk\ e^{ikx} = 2\pi\delta(x)$ and $\int_{-\infty}^{\infty}dx\ e^{ikx} = 2\pi\delta(k)$. Then, the diagonalized annihilation and creation operators can be described as

$$\hat{a}_k = \frac{\left(\frac{l}{\hbar^2k^2c}\right)^{\frac{1}{4}}\hat{q}_k - i\left(\frac{k^2c}{\hbar^2l}\right)^{\frac{1}{4}}\hat{\phi}_k}{\sqrt{2}}, \quad \hat{a}^\dagger_k = \frac{\left(\frac{l}{\hbar^2k^2c}\right)^{\frac{1}{4}}\hat{q}^\dagger_k + i\left(\frac{k^2c}{\hbar^2l}\right)^{\frac{1}{4}}\hat{\phi}^\dagger_k}{\sqrt{2}}, \tag{2.48}$$

where $[\hat{a}_k, \hat{a}^\dagger_{k'}] = \delta(k-k')$. In addition, the Hamiltonian can be represented as

$$\hat{\mathcal{H}} = \int_{-\infty}^{\infty}dk\ \hbar\omega_k\ \hat{a}^\dagger_k\hat{a}_k, \tag{2.49}$$

where $\omega_k = |k|/\sqrt{cl}$.

The magnetic flux and electric charge in real space can be represented as

$$\begin{aligned}\hat{\phi}_x &= \frac{1}{\sqrt{2\pi}}\int_{-\infty}^{\infty} dk\ \sqrt{\frac{\hbar}{c\omega_k}}\frac{\hat{a}_k e^{ikx}+\hat{a}_k^\dagger e^{-ikx}}{\sqrt{2}},\\ \hat{q}_x &= \frac{1}{\sqrt{2\pi}}\int_{-\infty}^{\infty} dk\ \sqrt{c\hbar\omega_k}\frac{\hat{a}_k e^{ikx}-\hat{a}_k^\dagger e^{-ikx}}{\sqrt{2}i}.\end{aligned} \tag{2.50}$$

Here, we calculate the time-evolution of these operators in the Heisenberg picture as

$$\begin{aligned}\hat{\phi}_x(t) &= \frac{1}{\sqrt{2\pi}}\int_{-\infty}^{\infty} dk\ \sqrt{\frac{\hbar}{c\omega_k}}\frac{\hat{a}_k e^{i(kx-\omega_k t)}+\hat{a}_k^\dagger e^{-i(kx-\omega_k t)}}{\sqrt{2}},\\ \hat{q}_x(t) &= \frac{1}{\sqrt{2\pi}}\int_{-\infty}^{\infty} dk\ \sqrt{c\hbar\omega_k}\frac{\hat{a}_k e^{i(kx-\omega_k t)}-\hat{a}_k^\dagger e^{-i(kx-\omega_k t)}}{\sqrt{2}i}.\end{aligned} \tag{2.51}$$

We find the left- and right-going waves are orthogonal. Then, a phase velocity is found to be $v = \omega_k/|k| = 1/\sqrt{cl}$.

### 2.3.3 One directional propagating mode

In the waveguide Hamiltonian, the right- and left- going modes are orthogonal. Thus, we consider only one directional propagating mode, or a right-going propagating mode, here. The Hamiltonian of the right-going propagating mode is described as

$$\hat{\mathcal{H}} = \int_0^\infty dk\ \hbar\omega_k\ \hat{a}_k^\dagger\hat{a}_k, \tag{2.52}$$

where $[\hat{a}_k, \hat{a}_{k'}^\dagger] = \delta(k-k')$.

In experiments, a right-going microwave in a waveguide is measured and controlled in the frequency or time domains. Therefore, it is useful to represent the propagating mode in terms of frequency as

$$\hat{a}_\omega = \frac{1}{\sqrt{v}}\hat{a}_k, \tag{2.53}$$

where $v$ is the phase velocity of the waveguide and $\hat{a}_\omega$ is the frequency mode, which satisfies $[\hat{a}_\omega, \hat{a}_{\omega'}^\dagger] = \delta(\omega-\omega')$. Note that the frequency $\omega$ labels the wavenumber mode uniquely, since we consider only the right-going mode.

Then, the Hamiltonian can be represented as

$$\hat{\mathcal{H}} = \hbar\int_0^\infty d\omega\ \omega\ \hat{a}_\omega^\dagger\hat{a}_\omega \tag{2.54}$$

where $\omega = \omega_k$ is the resonance frequency of the frequency mode, and we use the variable transformation of $k \to \omega = vk$.

Suppose the right-going mode is weakly coupled to a localized mode with a resonance frequency $\omega_0$. Only the frequency modes whose resonance frequency is close to $\omega_0$ are involved with the dynamics. Therefore, we can add the virtual negative frequency modes without affecting the dynamics as

$$\hat{\mathcal{H}} = \hbar\int_{-\infty}^\infty d\omega\ \omega\ \hat{a}_\omega^\dagger\hat{a}_\omega. \tag{2.55}$$

Furthermore, the time mode $\hat{a}_t$ is defined as the Fourier transform of the frequency mode:

$$\hat{a}_t = \frac{1}{\sqrt{2\pi}}\int_{-\infty}^\infty d\omega\ \hat{a}_\omega e^{-i\omega t}, \tag{2.56}$$

where $[\hat{a}_t, \hat{a}_{t'}^\dagger] = \delta(t-t')$. The field operator in time corresponds to the field operator in real space.

### 2.3.4 Pulse mode

In many experiments, only a few pulse modes may be concerned with the dynamics of generations, interactions, and measurements. Therefore, it is useful to represent a quantum state of the right-going mode with a finite number of pulse modes. The description on pulse mode can be seen in [45].

Using a mode function described by $m(\omega)$ or $m(t)$, the pulse mode is defined as

$$\begin{aligned}\hat{a} &= \int_{-\infty}^{\infty} d\omega\, m(\omega)\hat{a}_\omega \\ &= \int_{-\infty}^{\infty} dt\, m(t)\hat{a}_t.\end{aligned} \tag{2.57}$$

Then, the pulse mode can be understood as the superposition of the frequency-domain modes $\hat{a}_\omega$ or of the time-domain modes $\hat{a}_t$ with the coeeficients defined by the mode functions. From the definition of Eq. (2.56), we obtain the relation of the Fourier transformation between the mode functions as

$$\begin{aligned}m(\omega) &= \frac{1}{\sqrt{2\pi}}\int_{-\infty}^{\infty} dt\, m(t)e^{-i\omega t} \\ m(t) &= \frac{1}{\sqrt{2\pi}}\int_{-\infty}^{\infty} d\omega\, m(\omega)e^{i\omega t}.\end{aligned} \tag{2.58}$$

Furthermore, the annihilation and creation operators of the pulse mode have a bosonic commutation relation

$$\begin{aligned}[\hat{a},\hat{a}^\dagger] &= \iint_{-\infty}^{\infty} d\omega d\omega'\, m^*(\omega')m(\omega)[\hat{a}_\omega,\hat{a}_{\omega'}] \\ &= \iint_{-\infty}^{\infty} d\omega d\omega'\, m^*(\omega')m(\omega)\delta(\omega-\omega') \\ &= \int_{-\infty}^{\infty} d\omega\, m^*(\omega)m(\omega) = \int_{-\infty}^{\infty} d\omega\, |m(\omega)|^2 = 1, \\ [\hat{a},\hat{a}^\dagger] &= \int_{-\infty}^{\infty} dt\, m^*(t)m(t) = \int_{-\infty}^{\infty} dt\, |m(t)|^2 = 1,\end{aligned} \tag{2.59}$$

where we impose the normalization conditions on the mode functions as

$$\begin{aligned}\int_{-\infty}^{\infty} d\omega\, m^*(\omega)m(\omega) = 1, \\ \int_{-\infty}^{\infty} dt\, m^*(t)m(t) = 1.\end{aligned} \tag{2.60}$$

Note that when one of the normalization conditions is satisfied, the other condition is automatically satisfied by Parseval's theorem. As the annihilation and creation operators of the pulse mode have the same commutation relation as that of a harmonic oscillator mode, we can consider the pulse mode as a single harmonic oscillator mode.

Examples of the quantum states of the pulse mode are shown in the following. Here, the vacuum state of all the continuous modes is defined as $|0\rangle$.

The single photon state of the pulse mode can be described as

$$\begin{aligned}|1\rangle &= \hat{a}^\dagger|0\rangle \\ &= \int_{-\infty}^{\infty} d\omega\, m^*(\omega)\hat{a}_\omega^\dagger|0\rangle = \int_{-\infty}^{\infty} d\omega\, m^*(\omega)|1\rangle_\omega \\ &= \int_{-\infty}^{\infty} dt\, m^*(t)\hat{a}_t^\dagger|0\rangle = \int_{-\infty}^{\infty} dt\, m^*(t)|1\rangle_t.\end{aligned} \tag{2.61}$$

The single photon state can be understand as the superposition of the single photon states in the frequency-domain modes ($|1\rangle_\omega = \hat{b}^\dagger_\omega|0\rangle$) or in the time-domain modes ($|1\rangle_t = \hat{b}^\dagger_t|0\rangle$).

The coherent state of the pulse mode can be described as

$$\begin{aligned} |\beta\rangle &= e^{\beta\hat{b}^\dagger - \beta^*\hat{b}}|0\rangle \\ &= \exp\left[\int_{-\infty}^{\infty} d\omega \ \left(\beta(\omega)\hat{b}^\dagger_\omega - \beta^*(\omega)\hat{b}_\omega\right)\right]|0\rangle \\ &= \exp\left[\int_{-\infty}^{\infty} dt \ \left(\beta(t)\hat{b}^\dagger_t - \beta^*(t)\hat{b}_t\right)\right]|0\rangle, \end{aligned} \tag{2.62}$$

where $\beta(\omega) = \beta m^*(\omega)$ and $\beta(t) = \beta m^*(t)$. From this calculation, the coherent state in the pulse mode can be described as the tensor product state of the coherent states in the frequency-domain modes $|\beta(\omega)\rangle_\omega = e^{\beta m^*(\omega)\hat{b}^\dagger_\omega - \beta^* m(\omega)\hat{b}_\omega}|0\rangle$ or in the time-domain modes $|\beta(t)\rangle_t = e^{\beta m^*(t)\hat{b}^\dagger_t - \beta^* m(t)\hat{b}_t}|0\rangle$.

Here, we define another pulse mode $\hat{a}'$ using a new mode function $n(\omega)$ or $n(t)$ as

$$\begin{aligned} \hat{a}' &= \int_{-\infty}^{\infty} d\omega \, n(\omega)\hat{a}_\omega \\ &= \int_{-\infty}^{\infty} d\omega \, n(t)\hat{a}_t, \end{aligned} \tag{2.63}$$

where the normalization conditions are satisfied for the mode functions. Then, the pulse mode also has the same bosonic commutation relation as $[\hat{a}', \hat{a}'^\dagger] = 1$. Suppose the new mode functions $n(\omega)$ and $n(t)$ are orthogonal to the previous mode functions $m(\omega)$ and $m(t)$, respectively, as

$$\begin{aligned} \int_{-\infty}^{\infty} d\omega \, n^*(\omega)m(\omega) = 0, \\ \int_{-\infty}^{\infty} dt \, n^*(t)m(t) = 0. \end{aligned} \tag{2.64}$$

The commutation relation between $\hat{a}$ and $\hat{a}'^\dagger$ can be calculated as

$$\begin{aligned} [\hat{a}, \hat{a}'^\dagger] &= \int_{-\infty}^{\infty} d\omega \, n^*(\omega)m(\omega) = 0 \\ &= \int_{-\infty}^{\infty} dt \, n^*(t)m(t) = 0. \end{aligned} \tag{2.65}$$

It shows that the pulse modes $\hat{a}$ and $\hat{a}'$, which have mode functions which are orthogonal to each other, are themselves orthogonal modes which can be controlled and measured separately in principle.

### 2.3.5 Replacement of pulse modes

A replacement of pulse modes is useful when we consider the mode matching between the pulse modes. Here, we will replace a pulse mode $\hat{a}_1$ with a new pulse mode $\hat{a}'_1$. These modes are defined as

$$\hat{a}_1 = \int_{-\infty}^{\infty} d\omega \, m_1(\omega)\hat{a}_\omega \tag{2.66}$$

$$\hat{a}'_1 = \int_{-\infty}^{\infty} d\omega \, m'_1(\omega)\hat{a}_\omega. \tag{2.67}$$

Note that although we represent the mode functions only with the frequency domain in the following, we can consider the same treatment also with the time domain.

We describe the new mode function $m_1'(\omega)$ with $m_1(\omega)$ and $m_2(\omega)$, where $m_2(\omega)$ is an indispensable mode function which is orthogonal to $m_1(\omega)$, as

$$m_1'(\omega) = \sqrt{\eta}\, m_1(\omega) + \sqrt{1-\eta}\, m_2(\omega), \tag{2.68}$$

which is a general form to satisfy the normalization condition of $m_1'(\omega)$. Since there is arbitrariness in the global phases of mode functions, $\sqrt{\eta}$ and $\sqrt{1-\eta}$ can be defined to be real numbers without loss of generality. Using the annihilation operators, this can be represented as

$$\hat{a}_1' = \sqrt{\eta}\, \hat{a}_1 + \sqrt{1-\eta}\, \hat{a}_2, \tag{2.69}$$

where $\hat{a}_2 = \int_{-\infty}^{\infty} d\omega\, m_2(\omega)\hat{a}_\omega$. From this, we find the replacement of the pulse modes corresponds to a beam splitter transformation, as discussed in Sec. 3.4.4. To be consistent with the unitary transformation, or the beam splitter transformation, the replacement is fully characterized with introducing another pulse mode $\hat{a}_2' = \int_{-\infty}^{\infty} d\omega\, m_2'(\omega)\hat{a}_\omega$ which is orthogonal to $\hat{a}_1'$, as

$$\begin{pmatrix} \hat{a}_1' \\ \hat{a}_2' \end{pmatrix} = \begin{pmatrix} \sqrt{\eta} & \sqrt{1-\eta} \\ -\sqrt{1-\eta} & \sqrt{\eta} \end{pmatrix} \begin{pmatrix} \hat{a}_1 \\ \hat{a}_2 \end{pmatrix}. \tag{2.70}$$

From Eq. (2.68), the transmittance can be calculated as the overlap between the mode functions:

$$\begin{aligned} &\int_{-\infty}^{\infty} d\omega\, m_1'^*(\omega) m_1(\omega) \\ =&\sqrt{\eta} \int_{-\infty}^{\infty} d\omega\, m_1^*(\omega) m_1(\omega) + \sqrt{1-\eta} \int_{-\infty}^{\infty} d\omega\, m_1^*(\omega) m_2(\omega) \\ =&\sqrt{\eta} \end{aligned} \tag{2.71}$$

Furthermore, using the transmittance $\eta$, the mode function $m_2(\omega)$ is obtained as

$$m_2(\omega) = \frac{1}{\sqrt{1-\eta}}\, m_1'(\omega) - \sqrt{\frac{\eta}{1-\eta}}\, m_1(\omega). \tag{2.72}$$

Finally, the mode function $m_2'(\omega)$ is obtained as

$$m_2'(\omega) = -\sqrt{1-\eta}\, m_1(\omega) - \sqrt{\eta}\, m_2(\omega). \tag{2.73}$$

Thus, we can fully characterize the replacement of the pulse modes by using the beam splitter transformation.

In summary, when we determine a new mode function $m_1'(\omega)$ which replaces an initial mode function $m_1(\omega)$, the replacement corresponds to a beam splitter transformation with the transmittance, calculated as $\sqrt{\eta} = \int_{-\infty}^{\infty} d\omega\, m_1'^*(\omega) m_1(\omega)$. The mode function $m_2(\omega)$ which participates in $m_1'(\omega)$ can be calculated as $m_2(\omega) = \frac{1}{\sqrt{1-\eta}}\, m_1'(\omega) - \sqrt{\frac{\eta}{1-\eta}}\, m_1(\omega)$.

## 2.4 LC resonator connected to waveguide

Coupling between a system and a waveguide is indispensable to control and measure the system.

Here, we consider a semi-infinite waveguide which is coupled to an LC resonator, as shown in Fig. 2.4(a). As explained in Sec. 2.3, an infinite waveguide has independent

right- and left-going waves. However, in the semi-infinite waveguide, a right-going wave is converted to a left-going wave at the edge. Therefore, we can effectively consider the actual system as a system in which only a right-going mode in an infinite waveguide is coupled to an LC resonator, as shown in Fig. 2.4(b). Actually, the assumption is reasonable since we can control and measure the right- and left-going waves in the semi-infinite waveguide separately using a non-reciprocal device, such as a circulator.

According to the coupling terms in Eq. (2.23), the Hamiltonian of the LC resonator coupled to the right-going mode can be described as

$$\hat{\mathcal{H}} = \hbar\omega_{\mathrm{c}}\,\hat{a}^{\dagger}\hat{a} + \hbar\int_{-\infty}^{\infty} d\omega \left[\omega\,\hat{a}_{\omega}^{\dagger}\hat{a}_{\omega} + \sqrt{\frac{\kappa}{2\pi}}(\hat{a}^{\dagger}\hat{a}_{\omega} + \hat{a}_{\omega}^{\dagger}\hat{a})\right], \tag{2.74}$$

where $\kappa$ is the coupling constant. Here, the frequency dependence in the coupling strength is approximately neglected. The Hamiltonian can be used to derive a Lindblad master equation and an input-output formalism [46]. Note that the coupling mechanism is not crucial to derive these formalisms.

Practically, the LC resonator has a finite energy relaxation, even when it is made of superconductors. Regardless of the coupling mechanism with relaxation channels, the energy relaxation can be modeled by coupling with a waveguide. The number of relaxation channels is not necessarily unity. Nevertheless, the relaxation can be modeled by coupling with a single waveguide with an effective coupling rate. Therefore, the full Hamiltonian of the LC resonator coupled to a waveguide with a finite internal relaxation can be written as

$$\begin{aligned}\hat{\mathcal{H}} = \hbar\omega_{\mathrm{c}}\,\hat{a}^{\dagger}\hat{a} &+ \hbar\int_{-\infty}^{\infty} d\omega \left[\omega\,\hat{a}_{\omega}^{\dagger}\hat{a}_{\omega} + \sqrt{\frac{\kappa_{\mathrm{ex}}}{2\pi}}(\hat{a}^{\dagger}\hat{a}_{\omega} + \hat{a}_{\omega}^{\dagger}\hat{a})\right] \\ &+ \hbar\int_{-\infty}^{\infty} d\omega \left[\omega\,\hat{c}_{\omega}^{\dagger}\hat{c}_{\omega} + \sqrt{\frac{\kappa_{\mathrm{in}}}{2\pi}}(\hat{a}^{\dagger}\hat{c}_{\omega} + \hat{c}_{\omega}^{\dagger}\hat{a})\right],\end{aligned} \tag{2.75}$$

where $\kappa_{\mathrm{ex}}$ and $\kappa_{\mathrm{in}}$ are the external coupling rate and internal loss rate of the LC resonator, and $\hat{c}_{\omega}$ is a waveguide mode modeling the relaxation.

### 2.4.1 Lindblad master equation

According to the reference [46], the Lindblad master equation can be obtained from the Hamiltonian in Eq. (2.75) as

$$\begin{aligned}\frac{d\hat{\rho}}{dt} = \frac{1}{i\hbar}\left[\hat{\mathcal{H}}_{\mathrm{sys}}, \hat{\rho}\right] &+ \mathcal{D}\left[\sqrt{\kappa_{\mathrm{ex}}(n_{\mathrm{th,ex}}+1)}\,\hat{a}\right]\hat{\rho} + \mathcal{D}\left[\sqrt{\kappa_{\mathrm{ex}}\,n_{\mathrm{th,ex}}}\,\hat{a}^{\dagger}\right]\hat{\rho} \\ &+ \mathcal{D}\left[\sqrt{\kappa_{\mathrm{in}}(n_{\mathrm{th,in}}+1)}\,\hat{a}\right]\hat{\rho} + \mathcal{D}\left[\sqrt{\kappa_{\mathrm{in}}\,n_{\mathrm{th,in}}}\,\hat{a}^{\dagger}\right]\hat{\rho}\end{aligned} \tag{2.76}$$

where $\hat{\rho}$ is a density matrix of the LC resonator, $\hat{\mathcal{H}}_{\mathrm{sys}} = \hbar\omega_{\mathrm{c}}\,\hat{a}^{\dagger}\hat{a}$ is the system Hamiltonian of the LC resonator, $n_{\mathrm{th,ex}}$ and $n_{\mathrm{th,in}}$ are the thermal photon numbers in the corresponding waveguides, and $\mathcal{D}[\hat{O}]\hat{\rho} = \hat{O}\hat{\rho}\hat{O}^{\dagger} - \frac{1}{2}(\hat{O}^{\dagger}\hat{O}\hat{\rho} + \hat{\rho}\hat{O}^{\dagger}\hat{O})$ is the Lindblad superoperator. Then, the master equation can be simply rewritten as

$$\frac{d\hat{\rho}}{dt} = \frac{1}{i\hbar}\left[\hat{\mathcal{H}}_{\mathrm{sys}}, \hat{\rho}\right] + \mathcal{D}\left[\sqrt{\kappa(n_{\mathrm{th}}+1)}\,\hat{a}\right]\hat{\rho} + \mathcal{D}\left[\sqrt{\kappa\,n_{\mathrm{th}}}\,\hat{a}^{\dagger}\right]\hat{\rho}, \tag{2.77}$$

where $\kappa = \kappa_{\mathrm{ex}} + \kappa_{\mathrm{in}}$ is the total relaxation rate of the cavity and $n_{\mathrm{th}} = \frac{\kappa_{\mathrm{ex}} n_{\mathrm{th,ex}} + \kappa_{\mathrm{in}} n_{\mathrm{th,in}}}{\kappa_{\mathrm{ex}} + \kappa_{\mathrm{in}}}$ is the effective thermal photon number.

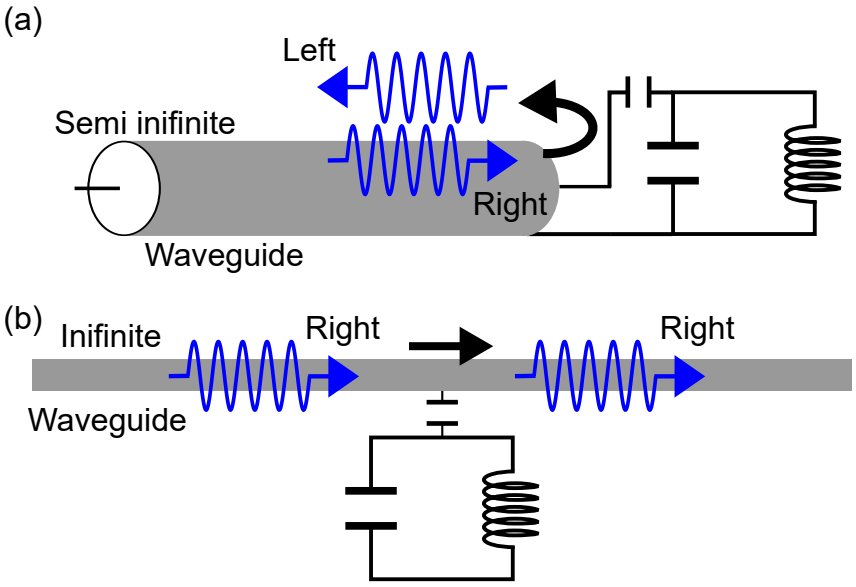


Figure 2.4: Schematic of LC resonator coupled to a waveguide. (a) LC resonator coupled to a semi-infinite waveguide. (b) LC resonator coupled to the only right-going wave mode in an infinite waveguide.

When the LC resonator is coherently driven by a microwave, the system Hamiltonian is replaced by

$$\hat{\mathcal{H}}_{\rm sys} = \hbar \left[ \omega_{\rm c}\, \hat{a}^\dagger \hat{a} + \left( \frac{\Omega_{\rm d}}{2}\, \hat{a}^\dagger e^{-i\omega_{\rm d} t} + \frac{\Omega_{\rm d}^*}{2}\, \hat{a} e^{i\omega_{\rm d} t} \right) \right], \tag{2.78}$$

where $\Omega_{\rm d} = 2\sqrt{\kappa_{\rm ex} \dot{n}_{\rm d}}$ is the coherent amplitude of the drive, and $\dot{n}_{\rm d}$ is the photon flux per unit time, reaching the LC resonator. In the rotating flame at $\omega_{\rm d}$, the Hamiltonian can be described as

$$\hat{\mathcal{H}}_{\rm sys} = \hbar \left[ (\omega_{\rm c} - \omega_{\rm d})\, \hat{a}^\dagger \hat{a} + \left( \frac{\Omega_{\rm d}}{2}\, \hat{a}^\dagger + \frac{\Omega_{\rm d}^*}{2}\, \hat{a} \right) \right]. \tag{2.79}$$

Note that the Lindblad terms in Eq. (2.76) are the same in the rotating frame.

### 2.4.2 Input-output formalism

The dynamics of input and output field operators can be described, as well as system operators in input-output formalism. Then, the Fourier transform of the frequency modes is defined as the input modes:

$$\begin{aligned} \hat{a}_i(t) &= \frac{1}{\sqrt{2\pi}} \int_{-\infty}^{\infty} d\omega\, \hat{a}_\omega e^{-i\omega t} \\ \hat{c}_i(t) &= \frac{1}{\sqrt{2\pi}} \int_{-\infty}^{\infty} d\omega\, \hat{a}_\omega e^{-i\omega t} \end{aligned} \tag{2.80}$$

where $[\hat{a}_t, \hat{a}_{t'}^\dagger] = \delta(t - t')$ and $[\hat{c}_t, \hat{c}_{t'}^\dagger] = \delta(t - t')$. Note that these definitions are consistent with Eq. (2.56). Furthermore, an input quantum state in the temporal mode $\hat{a}_{\rm i}(t)$ can be controlled in experiments.

According to the reference [46, 47], the time evolution of the annihilation operator $\hat{a}$ in the LC resonator can be described in the Heisenberg picture as

$$\begin{aligned}\frac{d\hat{a}(t)}{dt} &= \frac{1}{i\hbar}\left[\hat{a}(t), \hat{\mathcal{H}}_{\rm sys}\right] - \frac{\kappa_{\rm ex}+\kappa_{\rm in}}{2}\,\hat{a}(t) - i\sqrt{\kappa_{\rm ex}}\,\hat{a}_{\rm i}(t) - i\sqrt{\kappa_{\rm in}}\,\hat{c}_{\rm i}(t) \\ &= -i\omega_{\rm c}\,\hat{a}(t) - \frac{\kappa_{\rm ex}+\kappa_{\rm in}}{2}\,\hat{a}(t) - i\sqrt{\kappa_{\rm ex}}\,\hat{a}_{\rm i}(t) - i\sqrt{\kappa_{\rm in}}\,\hat{c}_{\rm i}(t)\end{aligned} \tag{2.81}$$

where we assume $\hat{\mathcal{H}}_{\rm sys} = \hbar\omega_{\rm c}\,\hat{a}^\dagger\hat{a}$.

Then, we also define the output mode after the interaction as

$$\begin{aligned}\hat{a}_{\rm o}(t) &= \int_{-\infty}^{\infty} d\omega\,\hat{a}'_\omega e^{-i\omega t} \\ \hat{c}_{\rm o}(t) &= \int_{-\infty}^{\infty} d\omega\,\hat{c}'_\omega e^{-i\omega t},\end{aligned} \tag{2.82}$$

where $\hat{a}'_\omega$ and $\hat{c}'_\omega$ are the frequency modes after the interaction with the LC resonator in the Heisenberg picture. The quantum state in the temporal mode $\hat{a}_{\rm o}(t)$ can be measured in experiments. Finally, the input-output relation is given by

$$\hat{a}_{\rm o}(t) = \hat{a}_{\rm i}(t) - i\sqrt{\kappa_{\rm ex}}\hat{a}(t). \tag{2.83}$$

Using the Fourier transformation, Eqs. (2.81) and (2.83) can be transformed into

$$\begin{aligned}\hat{a}(\omega) &= -i\frac{\sqrt{\kappa_{\rm ex}}\,\hat{a}_{\rm i}(\omega) + \sqrt{\kappa_{\rm in}}\,\hat{c}_{\rm i}(\omega)}{\frac{\kappa_{\rm ex}+\kappa_{\rm in}}{2} - i(\omega-\omega_{\rm c})} \\ \hat{a}_{\rm o}(\omega) &= \hat{a}_{\rm i}(\omega) - i\sqrt{\kappa_{\rm ex}}\,\hat{a}(\omega) \\ &= -\frac{\frac{\kappa_{\rm ex}-\kappa_{\rm in}}{2} + i(\omega-\omega_{\rm c})}{\frac{\kappa_{\rm ex}+\kappa_{\rm in}}{2} - i(\omega-\omega_{\rm c})}\hat{a}_{\rm i}(\omega) - \frac{\sqrt{\kappa_{\rm ex}\kappa_{\rm in}}}{\frac{\kappa_{\rm ex}+\kappa_{\rm in}}{2} - i(\omega-\omega_{\rm c})}\hat{c}_{\rm i}(\omega).\end{aligned} \tag{2.84}$$

Supposing that the input state is a coherent state, we obtain the reflection coefficient $S_{11}(\omega)$ of the LC resonator as a function of the frequency as

$$S_{11}(\omega) = \frac{\langle\hat{a}_{\rm o}(\omega)\rangle}{\langle\hat{a}_{\rm i}(\omega)\rangle} = -\frac{\frac{\kappa_{\rm ex}-\kappa_{\rm in}}{2} + i(\omega-\omega_{\rm c})}{\frac{\kappa_{\rm ex}+\kappa_{\rm in}}{2} - i(\omega-\omega_{\rm c})}, \tag{2.85}$$

where we assume that the input state of the internal loss mode is in a vacuum or a thermal state, i.e., $\langle\hat{c}_{\rm i}(\omega)\rangle = 0$. Generally speaking, the solution of the reflection coefficient holds for a general harmonic oscillator. Therefore, it is used to characterize the harmonic oscillator with obtaining system parameters such as a resonance frequency, an external coupling rate, and an internal loss rate.

In addition, using the inverse Fourier transformation, the average photon number in the LC resonator can be calculated as

$$\langle\hat{a}(t)^\dagger\hat{a}(t)\rangle = \frac{\kappa_{\rm ex}}{\frac{(\kappa_{\rm ex}+\kappa_{\rm in})^2}{4} + (\omega-\omega_{\rm c})^2}\langle\hat{a}_{\rm i}(t)^\dagger\hat{a}_{\rm i}(t)\rangle, \tag{2.86}$$

where $\langle\hat{a}_{\rm i}(t)^\dagger\hat{a}_{\rm i}(t)\rangle = P/\hbar\omega$ is the flux of the average photon number in the coherent drive per unit time, and $P$ is the coherent drive power.

## 2.5 Superconducting qubit

Nonlinearity is the key ingredient which allows us to reach the realm of quantum state engineering by enabling us to excite a single energy quantum. More concretely, we need a non-dissipative element which gives a nonlinearity strong enough at the single energy quantum level. In superconducting circuits, Josephson junctions play this role. A Josephson junction is an element which is made by a thin insulator sandwiched between two superconductors, as shown in Fig. 2.5. In the Josephson junction, a Cooper pair can tunnel quantum-mechanically, introducing a strong nonlinearity. An sufficiently anharmonic microwave resonator with one or more Josephson junctions is called a superconducting qubit since it can be operated as a qubit, or an effective two-level system, as shown in Fig. 2.5(c). Here, we will focus on the transmon qubit, one of the simplest superconducting qubits.

The circuit diagram of the transmon qubit is shown in Fig. 2.6(a). It can be understood as an LC resonator whose inductor is replaced with a Josephson junction. Since the potential energy does not affect the quantization procedure in the node flux representation, we can easily obtain the quantum-mechanical Hamiltonian just by replacing the inductive energy with the Josephson energy:

$$\hat{\mathcal{H}} = \frac{\hat{Q}^2}{2C} - E_{\mathrm{J}} \cos\left(\frac{\hat{\Phi}}{\phi_0}\right), \tag{2.87}$$

where $C$ is the total capacitance including the capacitance associated with the Josephson junction, $E_{\mathrm{J}}$ is the tunneling energy of the Josephson junction, $\hat{\Phi}$ is the operator of the generalized magnetic flux in the Josephson junction, and $\hat{Q}$ is the operator of the conjugate momentum of the magnetic flux, or the electric charge on the capacitance. The canonical commutation relation is $[\hat{\Phi}, \hat{Q}] = i\hbar$.

In the analysis of the nonlinear potential energy of the Josephson junction, it is useful to use dimensionless parameters as discussed in Sec. 2.1.1. Then, the Hamiltonian is represented with $\hat{\varphi}$ and $\hat{n}$ whose commutation relation is $[\hat{\varphi}, \hat{n}] = i$:

$$\hat{\mathcal{H}} = \hbar\left(\frac{\omega_{\mathrm{C}}}{2}\,\hat{n}^2 - \omega_{\mathrm{J}} \cos\hat{\varphi}\right), \tag{2.88}$$

where $\omega_{\mathrm{C}} = \frac{(2e)^2}{C}$ and $\omega_{\mathrm{J}} = E_{\mathrm{J}}/\hbar$.

In the so-called transmon regime, the ratio of the capacitive to inductive energy quantum is much smaller than unity: $\omega_{\mathrm{C}}/\omega_{\mathrm{J}} \ll 1$. Since the trapping potential energy (magnetic flux energy) is much larger than the conjugate momentum energy (capacitive energy), the dynamic range of $\hat{\varphi}$ is smaller than the period of $2\pi$. The localization of $\varphi$, which corresponds to the delocalization of the charge $n$, gives rise to the robustness against the charge noise which causes the dephasing of the charge qubit.

Then, thanks to the localization of $\varphi$, we can rewrite the Hamiltonian using the Taylor expansion with respect to $\hat{\varphi}$:

$$\hat{\mathcal{H}} = \hbar\left(\frac{\omega_{\mathrm{C}}}{2}\,\hat{n}^2 + \frac{\omega_{\mathrm{J}}}{2}\,\hat{\varphi}^2 - \frac{\omega_{\mathrm{J}}}{24}\,\hat{\varphi}^4\right), \tag{2.89}$$

where we consider up to the forth order terms of $\hat{\varphi}$ and neglect the constant term. Now, we can consider the first two terms as the Hamiltonian of a harmonic oscillator, where the Josephson energy $\hbar\omega_{\mathrm{J}}$ exactly corresponds to the inductive energy quantum $\hbar\omega_{\mathrm{L_J}} = \phi_0^2/L_{\mathrm{J}}$. From the relation, the Josephson inductance can be defined as

$$L_{\mathrm{J}} = \frac{\phi_0^2}{E_{\mathrm{J}}} = \frac{\phi_0^2}{\hbar\omega_{\mathrm{J}}}. \tag{2.90}$$

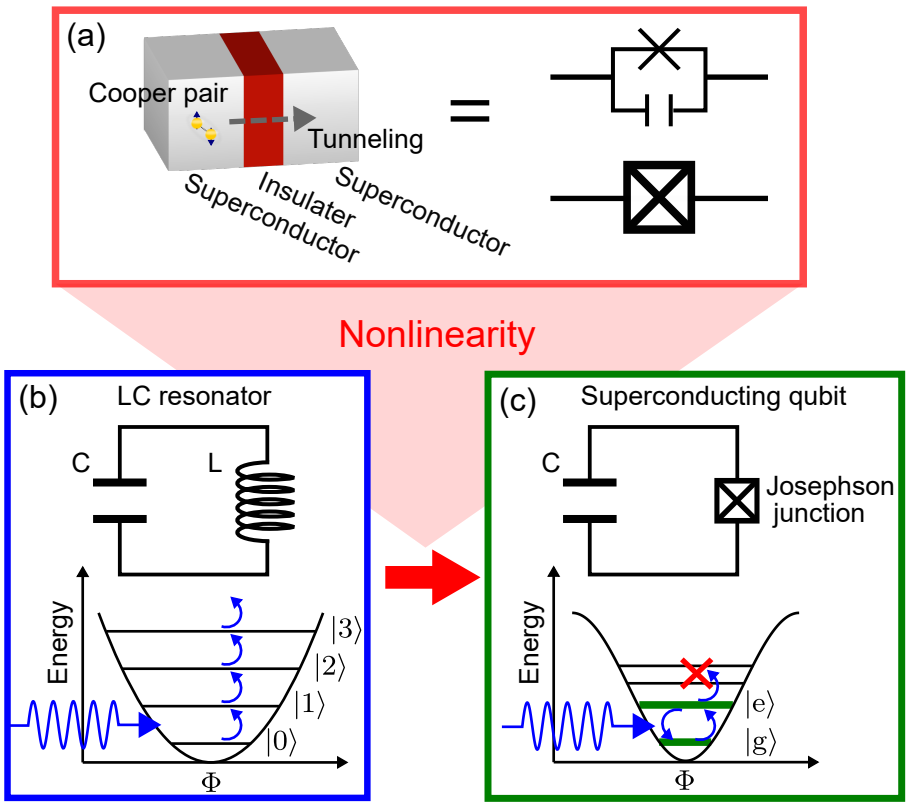


Figure 2.5: Josephson junction and superconducting qubit. (a) Josephson junction and its circuit symbol. (b) Harmonic oscillator and its energy levels. (c) Anharmonic oscilator with a Josephson junction and its energy levels.

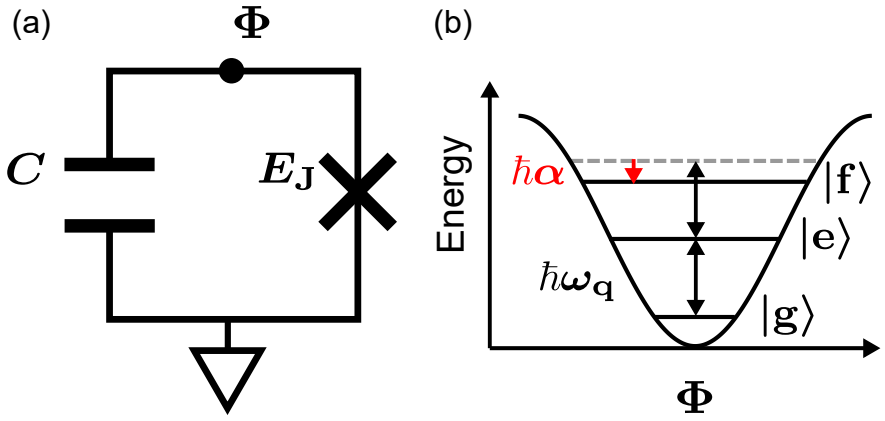


Figure 2.6: Transmon qubit. (a) Circuit diagram. (b) Energy levels.

Then, the annihilation and creation operators, $\hat{b}$ and $\hat{b}^\dagger$, are defined as

$$\hat{b} = \frac{\left(\frac{\omega_J}{\omega_C}\right)^{\frac{1}{4}} \hat{\varphi} + i \left(\frac{\omega_C}{\omega_J}\right)^{\frac{1}{4}} \hat{n}}{\sqrt{2}}, \quad \hat{b}^\dagger = \frac{\left(\frac{\omega_J}{\omega_C}\right)^{\frac{1}{4}} \hat{\varphi} - i \left(\frac{\omega_C}{\omega_J}\right)^{\frac{1}{4}} \hat{n}}{\sqrt{2}}, \tag{2.91}$$

which can diagonalize the first two terms in the Hamiltonian:

$$\hat{\mathcal{H}} = \hbar \left( \omega_q^l \, \hat{b}^\dagger \hat{b} - \frac{\omega_J}{24} \hat{\varphi}^4 \right), \tag{2.92}$$

where $\omega_{\mathrm{q}}^{l} = \sqrt{\omega_{\mathrm{J}}\omega_{\mathrm{C}}}$ is the resonance frequency of the harmonic oscillator.

Next, we approximate the nonlinear term in the Hamiltonian. Since $\hat{\varphi}$ is represented by

$$\hat{\varphi} = \left(\frac{\omega_{\mathrm{C}}}{\omega_{\mathrm{J}}}\right)^{\frac{1}{4}} \frac{\hat{b} + \hat{b}^{\dagger}}{\sqrt{2}}, \tag{2.93}$$

the nonlinear term is rewritten as

$$-\frac{\omega_{\mathrm{J}}}{24}\,\hat{\varphi}^{4} = -\frac{\omega_{\mathrm{C}}}{96}\left(\hat{b} + \hat{b}^{\dagger}\right)^{4}. \tag{2.94}$$

When we expand the fourth order term, we find off-diagonal terms, such as $\hat{b}^{4}$ and $\hat{b}^{3}\hat{b}^{\dagger}$. Here, the frequency of the off-diagonal terms is on the order of $\omega_{\mathrm{C}}$. The frequency detuning between the qubit states which interact with each other through the off-diagonal terms is on the order of the resonance frequency $\omega_{\mathrm{q}}^{l}$. When the off-diagonal frequencies are much smaller than the frequency detuning between the interacting states, the off-diagonal elements can be neglected with the rotating wave approximation. The condition is described by $\frac{\omega_{\mathrm{C}}}{\omega_{\mathrm{q}}^{l}} = \sqrt{\frac{\omega_{\mathrm{C}}}{\omega_{\mathrm{J}}}} \ll 1$, which is well satisfied in the transmon regime $\frac{\omega_{\mathrm{C}}}{\omega_{\mathrm{J}}} \ll 1$. By neglecting the off-diagonal terms with the rotating wave approximation, we obtain the fourth order nonlinear terms as

$$\begin{aligned} -\frac{\omega_{\mathrm{J}}}{24}\,\hat{\varphi}^{4} &\approx -\frac{\omega_{\mathrm{C}}}{96}\left(6\,\hat{b}^{\dagger 2}\hat{b}^{2} + 12\,\hat{b}^{\dagger}\hat{b} + 3\right) \\ &\approx -\frac{\omega_{\mathrm{C}}}{16}\,\hat{b}^{\dagger 2}\hat{b}^{2} - \frac{\omega_{\mathrm{C}}}{8}\,\hat{b}^{\dagger}\hat{b}, \end{aligned} \tag{2.95}$$

where the annihilation and creation operators are arranged in the normal order with the commutation relation $[\hat{b}, \hat{b}^{\dagger}] = 1$. Note that we neglect the constant energy term in this calculation. Then, we obtain the approximated Hamiltonian

$$\begin{aligned} \hat{\mathcal{H}} &\approx \hbar\left(\omega_{\mathrm{q}}^{l}\,\hat{b}^{\dagger}\hat{b} - \frac{\omega_{\mathrm{C}}}{16}\,\hat{b}^{\dagger 2}\hat{b}^{2} - \frac{\omega_{\mathrm{C}}}{8}\,\hat{b}^{\dagger}\hat{b}\right) \\ &= \hbar\left[\left(\omega_{\mathrm{q}}^{l} - \frac{\omega_{\mathrm{C}}}{8}\right)\hat{b}^{\dagger}\hat{b} - \frac{\omega_{\mathrm{C}}}{16}\,\hat{b}^{\dagger 2}\hat{b}^{2}\right] \\ &= \hbar\left(\omega_{\mathrm{q}}\,\hat{b}^{\dagger}\hat{b} - \frac{\omega_{\mathrm{C}}}{16}\,\hat{b}^{\dagger 2}\hat{b}^{2}\right), \end{aligned} \tag{2.96}$$

where $\omega_{\mathrm{q}} = \sqrt{\omega_{\mathrm{J}}\omega_{\mathrm{C}}} - \frac{\omega_{\mathrm{C}}}{8} = \omega_{\mathrm{q}}^{l} - \frac{\omega_{\mathrm{C}}}{8}$ is the resonance frequency of the first excitation of the transmon qubit. Note that the frequency is shifted from the resonance frequency of the harmonic oscillator due to the presence of the nonlinear terms.

In this thesis, we denote the states of the transmon qubit as the ground state $|\mathrm{g}\rangle$, the first excited state $|\mathrm{e}\rangle$, the second excited state $|\mathrm{f}\rangle$, and the third excited state $|\mathrm{h}\rangle$. The excitation frequencies of these states are given by:

$$\begin{aligned} \omega_{\mathrm{eg}} &= \omega_{\mathrm{q}} \\ \omega_{\mathrm{fe}} &= \omega_{\mathrm{q}} - \frac{\omega_{\mathrm{C}}}{8} = \omega_{\mathrm{q}} + \alpha \\ \omega_{\mathrm{hf}} &= \omega_{\mathrm{q}} - \frac{\omega_{\mathrm{C}}}{4} = \omega_{\mathrm{q}} + 2\alpha, \end{aligned} \tag{2.97}$$

where we define the anharmonicity of the transmon qubit as

$$\begin{aligned} \alpha &= \omega_{\mathrm{fe}} - \omega_{\mathrm{eg}} \\ &= -\frac{\omega_{\mathrm{C}}}{8}. \end{aligned} \tag{2.98}$$

Note that the anharmonicity is always negative for the transmon qubit. The energy levels of the transmon qubit are shown in Fig. 2.6.

Furthermore, the relative anharmonicity, which is used to characterize the transmon qubit, is defined as

$$\alpha_r = \frac{\alpha}{\omega_{\rm q}} = -\frac{\frac{\omega_{\rm C}}{8}}{\sqrt{\omega_{\rm J}\omega_{\rm C}} - \frac{\omega_{\rm C}}{8}} \approx -\frac{1}{8}\sqrt{\frac{\omega_{\rm C}}{\omega_{\rm J}}}. \tag{2.99}$$

The anharmonicity vanishes in the small limit of $\omega_{\rm C}/\omega_{\rm J}$. In other words, the transmon qubit approaches a harmonic oscillator. A large relative anharmonicity is needed for the operation of the transmon qubit as an ideal qubit. On the other hand, it is the necessary condition of the transmon qubit that the ratio of $\omega_{\rm C}/\omega_{\rm J}$ is much smaller than unity. Typically the ratio of $\omega_{\rm C}/\omega_{\rm J}$ is set to about 0.1.

The anharmonicity $\alpha$ can be experimentally determined and is often used to characterize the transmon qubit together with the first excitation frequency $\omega_{\rm q}$. Using the anharmonicity $\alpha$, we write the Hamiltonian as

$$\hat{\mathcal{H}} = \hbar\left(\omega_{\rm q}\,\hat{b}^\dagger\hat{b} + \frac{\alpha}{2}\,\hat{b}^{\dagger 2}\hat{b}^2\right). \tag{2.100}$$

### 2.5.1 Superconducting qubit connected to waveguide

A superconducting qubit is modeled by a harmonic oscillator with a perturbatively-added nonlinear term. Therefore, we can simply obtain the Hamiltonian of a qubit connected to a waveguide by replacing the system Hamiltonian in Eq. (2.75) by that of the qubit as

$$\begin{aligned}\hat{\mathcal{H}} = {}& \hbar\left(\omega_{\rm q}\,\hat{b}^\dagger\hat{b} + \frac{\alpha}{2}\,\hat{b}^{\dagger 2}\hat{b}^2\right) + \hbar\int_{-\infty}^{\infty} d\omega\left[\omega\,\hat{a}_\omega^\dagger\hat{a}_\omega + \sqrt{\frac{\gamma_{\rm ex}}{2\pi}}(\hat{b}^\dagger\hat{a}_\omega + \hat{a}_\omega^\dagger\hat{b})\right] \\ & + \hbar\int_{-\infty}^{\infty} d\omega\left[\omega\,\hat{c}_\omega^\dagger\hat{c}_\omega + \sqrt{\frac{\gamma_{\rm in}}{2\pi}}(\hat{b}^\dagger\hat{c}_\omega + \hat{c}_\omega^\dagger\hat{b})\right] + \hbar\int_{-\infty}^{\infty} d\omega\left[\omega\,\hat{d}_\omega^\dagger\hat{d}_\omega + \sqrt{\frac{2\gamma_{\phi,{\rm n}}}{2\pi}}\,\hat{b}^\dagger\hat{b}(\hat{d}_\omega + \hat{d}_\omega^\dagger)\right],\end{aligned} \tag{2.101}$$

where $\gamma_{\rm ex}$ and $\gamma_{\rm in}$ are the external coupling rate and internal loss rate of the qubit, and $\gamma_{\phi,{\rm n}}$ is the natural dephasing rate of the qubit. Note that we add another channel describing the natural dephasing of the qubit, since the qubit dephasing rate may not be limited by the energy relaxation.

Then, we obtain the Lindblad master equation of the qubit as

$$\frac{d\hat{\rho}}{dt} = \frac{1}{i\hbar}\left[\hat{\mathcal{H}}_{\rm sys}, \hat{\rho}\right] + \mathcal{D}\left[\sqrt{\gamma(n_{\rm th}+1)}\,\hat{b}\right]\hat{\rho} + \mathcal{D}\left[\sqrt{\gamma\,n_{\rm th}}\,\hat{b}^\dagger\right]\hat{\rho} + \mathcal{D}\left[\sqrt{2\gamma_{\phi,{\rm n}}}\,\hat{b}^\dagger\hat{b}\right]\hat{\rho}, \tag{2.102}$$

where $\hat{\rho}$ is a density matrix of the transmon qubit, $\hat{\mathcal{H}}_{\rm sys} = \hbar\left(\omega_{\rm q}\,\hat{b}^\dagger\hat{b} + \frac{\alpha}{2}\,\hat{b}^{\dagger 2}\hat{b}^2\right)$ is the system Hamiltonian of the qubit in the free evolution, $\gamma = \gamma_{\rm ex} + \gamma_{\rm in}$ is the total relaxation rate of the qubit, and $n_{\rm th}$ is the effective thermal photon number of the relaxation channels.

Furthermore, the system Hamiltonian of the coherently driven qubit in the rotating frame at the drive frequency $\omega_{\rm d}$ can be described as

$$\hat{\mathcal{H}}_{\rm sys} = \hbar\left[(\omega_{\rm q} - \omega_{\rm d})\,\hat{b}^\dagger\hat{b} + \frac{\alpha}{2}\,\hat{b}^{\dagger 2}\hat{b}^2 + \left(\frac{\Omega_{\rm d}}{2}\,\hat{b}^\dagger + \frac{\Omega_{\rm d}^*}{2}\,\hat{b}\right)\right]. \tag{2.103}$$

where $\Omega_{\rm d} = 2\sqrt{\gamma_{\rm ex}\dot{n}_{\rm d}}$ is the coherent amplitude of the drive, and $\dot{n}_{\rm d}$ is the photon flux per unit time, reaching the qubit.

### 2.5.2 Truncation to qubit subspace

While the transmon qubit is a multi-level system, it can be considered as a qubit because of the anharmonicity. Here, we explain the truncation in terms of the Hamiltonian of the driven transmon qubit. The Hamiltonian in Eq. (2.103) can be represented in the subspace spanned by $\{|\mathrm{g}\rangle, |\mathrm{e}\rangle, |\mathrm{f}\rangle\}$ as

$$\hat{\mathcal{H}}_{\mathrm{sys}} = \begin{pmatrix} 0 & \frac{\Omega_{\mathrm{d}}}{2} & 0 \\ \frac{\Omega_{\mathrm{d}}}{2} & \delta & \frac{\sqrt{2}\Omega_{\mathrm{d}}}{2} \\ 0 & \frac{\sqrt{2}\Omega_{\mathrm{d}}}{2} & 2\delta+\alpha \end{pmatrix}, \tag{2.104}$$

where $\delta = \omega_{\mathrm{q}} - \omega_{\mathrm{d}}$ is the detuning between the qubit frequency and the drive frequency. Note that the higher energy eigenstates are omitted since they do not affect the qubit subspace. Here, the drive frequency is set to be the qubit frequency, i.e., $\delta \approx 0$. Then, for the transition element between $|\mathrm{e}\rangle$ and $|\mathrm{f}\rangle$ much smaller than the corresponding detuning, i.e., $\sqrt{2}\Omega_{\mathrm{d}} \ll \alpha$, the Hamiltonian regarding the subspace of $|\mathrm{e}\rangle$ and $|\mathrm{f}\rangle$ can be diagonalized approximately as

$$\hat{\mathcal{H}}_{\mathrm{sys}} = \begin{pmatrix} 0 & \frac{\Omega_{\mathrm{d}}}{2} & 0 \\ \frac{\Omega_{\mathrm{d}}}{2} & \delta - \frac{|\Omega_{\mathrm{d}}|^2}{2\alpha} & 0 \\ 0 & 0 & 2\delta+\alpha+\frac{|\Omega_{\mathrm{d}}|^2}{2\alpha} \end{pmatrix}, \tag{2.105}$$

where we use the results of the dispersive Hamiltonian in Eq. (2.32). Moreover, we assume $\delta/\alpha \approx 0$, for simplicity. We find that the transition between $|\mathrm{e}\rangle$ and $|\mathrm{f}\rangle$ is adiabatically suppressed and the eigenfrequency of $|\mathrm{e}\rangle$ obtains an ac Stark shift from $|\mathrm{f}\rangle$. Therefore, we can consider the Hamiltonian of the driven transmon qubit as a driven qubit with the ac Stark shift as

$$\hat{\mathcal{H}}_{\mathrm{sys}} = \hbar \left[ \frac{\left(\omega_{\mathrm{q}} - \frac{|\Omega_{\mathrm{d}}|^2}{2\alpha}\right) - \omega_{\mathrm{d}}}{2} \hat{\sigma}_z + \left( \frac{\Omega_{\mathrm{d}}}{2} \hat{\sigma}_+ + \frac{\Omega_{\mathrm{d}}^*}{2} \hat{\sigma}_- \right) \right], \tag{2.106}$$

where $\hat{\sigma}_z$ is the Pauli $z$ operator, $\hat{\sigma}_-$ and $\hat{\sigma}_+$ are the annihilation and creation operators in the qubit subspace. The schematic of the energy levels with thre qubit drive is shown in Fig. 2.7(a). Note that the frequency shift can be neglected in the weak drive amplitude limit ($\sqrt{2}\Omega_{\mathrm{d}} \ll \alpha$). Furthermore, when the ac Stark shift is not negligible, it can be canceled by using a Derivative Reduction by Adiabatic Gate (DRAG) pulse [48, 49].

Using the truncation, the Hamiltonian including the waveguides can be represented as

$$\begin{aligned} \hat{\mathcal{H}} = \hat{\mathcal{H}}_{\mathrm{sys}} &+ \hbar \int_{-\infty}^{\infty} d\omega \left[ \omega\, \hat{a}_\omega^\dagger \hat{a}_\omega + \sqrt{\frac{\gamma_{\mathrm{ex}}}{2\pi}} (\hat{a}_\omega \hat{\sigma}_+ + \hat{a}_\omega^\dagger \hat{\sigma}_-) \right] \\ &+ \hbar \int_{-\infty}^{\infty} d\omega \left[ \omega\, \hat{c}_\omega^\dagger \hat{c}_\omega + \sqrt{\frac{\gamma_{\mathrm{in}}}{2\pi}} (\hat{c}_\omega \hat{\sigma}_+ + \hat{c}_\omega^\dagger \hat{\sigma}_-) \right] + \hbar \int_{-\infty}^{\infty} d\omega \left[ \omega\, \hat{d}_\omega^\dagger \hat{d}_\omega + \sqrt{\frac{2\gamma_{\phi,\mathrm{n}}}{2\pi}} \frac{\hat{\sigma}_z}{2} (\hat{d}_\omega + \hat{d}_\omega^\dagger) \right]. \end{aligned} \tag{2.107}$$

Then, the Lindblad master equation can be described as

$$\frac{d\hat{\rho}}{dt} = \frac{1}{i\hbar} \left[ \hat{\mathcal{H}}_{\mathrm{sys}}, \hat{\rho} \right] + \mathcal{D} \left[ \sqrt{\gamma(n_{\mathrm{th}}+1)}\, \hat{\sigma}_- \right] \hat{\rho} + \mathcal{D} \left[ \sqrt{\gamma\, n_{\mathrm{th}}}\, \hat{\sigma}_+ \right] \hat{\rho} + \mathcal{D} \left[ \sqrt{2\gamma_{\phi,\mathrm{n}}} \frac{\hat{\sigma}_z}{2} \right] \hat{\rho}. \tag{2.108}$$

From the master equation without the drive ($\Omega_{\mathrm{d}} = 0$), the energy-relaxation and dephasing times of the qubit are given by $1/T_1 = (2n_{\mathrm{th}}+1)\gamma$ and $1/T_2^* = (2n_{\mathrm{th}}+1)\gamma/2 + \gamma_{\phi,\mathrm{n}}$, respectively.

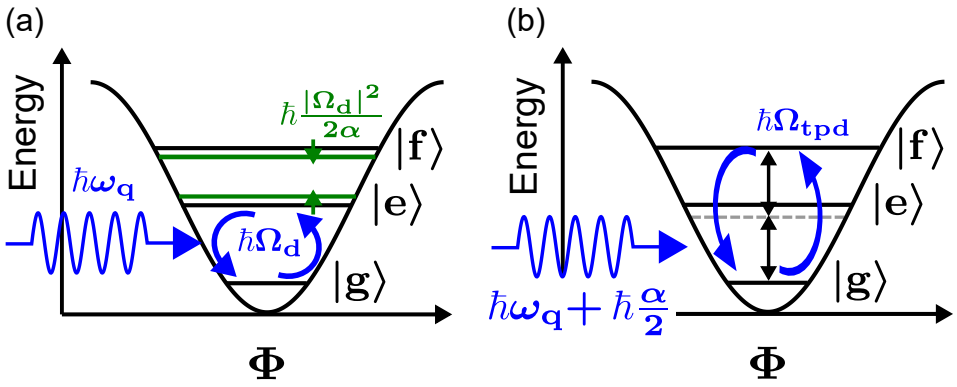


Figure 2.7: Control of transmon qubit. (a) Truncation to qubit subspace. (b) Transition to second excited state with two photon drive.

### 2.5.3 Transition to second excited state

Anharmonicity of $\alpha$ is one of the characteristic parameters for the transmon qubit. To obtain the anharmonicity in experiments, the qubit is excited to the second excited state with a two-photon drive. Here, we derive the Hamiltonian of the transmon qubit with a two-photon drive. The Hamiltonian of the driven transmon qubit is described as

$$\hat{\mathcal{H}}_{\rm sys} = \hbar\left[\delta\,\hat{b}^\dagger\hat{b} + \frac{\alpha}{2}\,\hat{b}^{\dagger 2}\hat{b}^2 + \left(\frac{\Omega_{\rm d}}{2}\,\hat{b}^\dagger + \frac{\Omega_{\rm d}^*}{2}\,\hat{b}\right)\right], \tag{2.109}$$

where $\delta = \omega_{\rm q} - \omega_{\rm d}$ is the detuning. Now, the drive frequency is set to be about half of the transition frequency between the ground and second excited state, and then $\delta \approx \alpha/2$. When the drive amplitude is much smaller than the detuning, i.e., $\Omega_{\rm d} \ll \delta \approx \alpha/2$, the driven terms of the Hamiltonian can be diagonalized using the displacement operator of $\hat{D}(-\Omega_{\rm d}/2\delta)$. In other words, the Hamiltonian can be approximated as

$$\begin{aligned}\hat{\mathcal{H}}_{\rm sys} &\approx \hat{D}^\dagger\left(-\frac{\Omega_{\rm d}}{2\delta}\right)\hat{\mathcal{H}}_{\rm sys}\,\hat{D}\left(-\frac{\Omega_{\rm d}}{2\delta}\right)\\ &= \hbar\left[\left(\delta + \frac{2|\Omega_{\rm d}|^2}{\alpha}\right)\hat{b}^\dagger\hat{b} + \frac{\alpha}{2}\,\hat{b}^{\dagger 2}\hat{b}^2 + \left(\frac{\Omega_{\rm tpd}}{2}\,\frac{\hat{b}^{\dagger 2}}{\sqrt{2}} + \frac{\Omega_{\rm tpd}^*}{2}\,\frac{\hat{b}^2}{\sqrt{2}}\right)\right],\end{aligned} \tag{2.110}$$

where $\Omega_{\rm tpd} = \sqrt{2}\Omega_{\rm d}^2/\alpha$ is the amplitude of the two-photon drive, and we neglect the constant terms and the far-off-resonant drive terms. Moreover, we use

$$\hat{D}^\dagger\left(-\frac{\Omega_{\rm d}}{2\delta}\right)\hat{b}\,\hat{D}\left(-\frac{\Omega_{\rm d}}{2\delta}\right) = \hat{b} - \frac{\Omega_{\rm d}}{2\delta}. \tag{2.111}$$

From the effective Hamiltonian, we find that the transmon qubit can be resonantly excited to the second excited state with a two-photon drive at the frequency of $\omega_{\rm d} = \omega_{\rm q} + \alpha/2 + 2|\Omega_{\rm d}|^2/\alpha$, as shown in Fig. 2.7(b). Note that the transition frequency is shifted by the order of the magnitude of the linewidth of the Rabi broadening. Nevertheless, as long as the drive amplitude is much smaller than the anharmonicity, we obtain the anharmonicity by measuring the transition frequency.

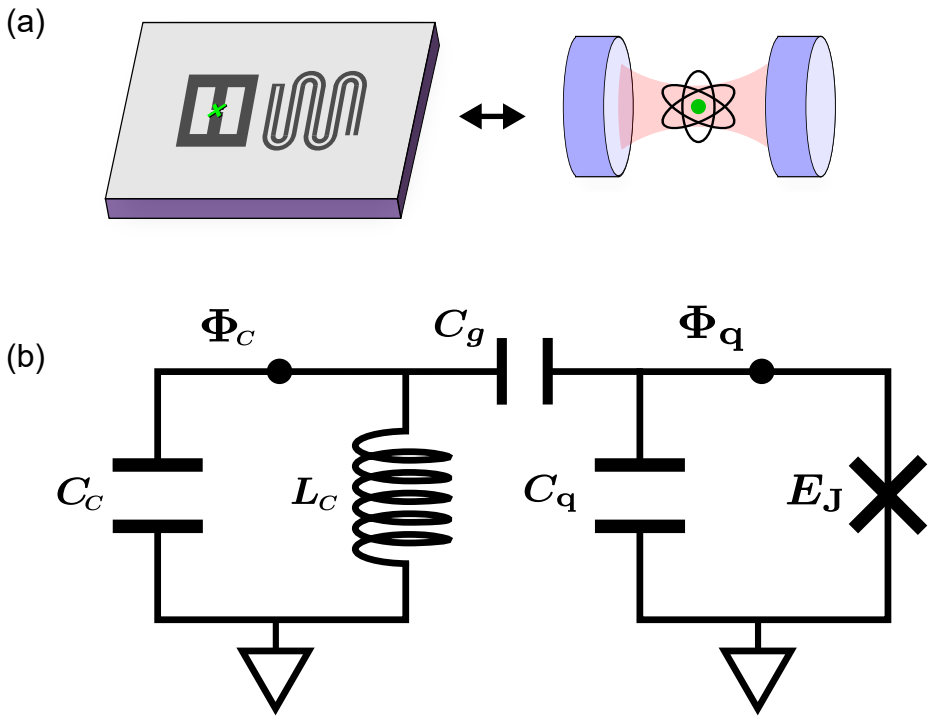


Figure 2.8: (a) Circuit QED and Cavity QED. (b) Circuit diagram of a circuit QED system.

## 2.6 Circuit quantum electrodynamics

Cavity quantum electrodynamics (QED) is a powerful tool for studying light-matter interactions, where a cavity mode is coupled to an atom strongly. Then, a concept of circuit QED is derived from the cavity QED [12], as shown in Fig. 2.8(a). So far, control and measurement of superconducting qubits and photons in a circuit QED system have been dramatically developed by applying the technologies which have been implemented in a cavity QED system.

A typical circuit diagram of a circuit QED system consists of an LC resonator capacitively coupled to a transmon qubit, as shown in Fig. 2.8(b). As discussed in the quantization of a transmon qubit, the nonlinear term in the Josephson potential energies does not affect the quantization of the circuit. Therefore, we derive the quantum-mechanical Hamiltonian of the circuit QED system by replacing one of the inductive energy in the Hamiltonian of the capacitively coupled LC resonators Eq. (2.20) with a Josephson energy as

$$\hat{\mathcal{H}} = \frac{\hat{Q}_{\rm c}^2}{2\bar{C}_{\rm c}} + \frac{\hat{\Phi}_{\rm c}^2}{2L_{\rm c}} + \frac{\hat{Q}_{\rm q}^2}{2\bar{C}_{\rm q}} - E_{\rm J}\cos\left(\frac{\hat{\Phi}_{\rm q}}{\phi_0}\right) + \frac{C_g}{\bar{C}_{\rm c}\bar{C}_{\rm q}}\hat{Q}_{\rm c}\hat{Q}_{\rm q}, \tag{2.112}$$

where $\hat{\Phi}_n$ and $\hat{Q}_n$ are the conjugate operators whose commutation relation is $[\hat{\Phi}_n, \hat{Q}_n] = i\hbar$ (for $n = {\rm c},\ {\rm q}$), $C_{\rm g}$ is the coupling capacitance, $\bar{C}_{\rm c} = C_{\rm c}+C_{\rm g}$ is the renormalized capacitance of the LC resonator, $L_{\rm c}$ is the inductance of the LC resonator, $\bar{C}_{\rm q} = C_{\rm q} + C_{\rm g}$ is the normalized capacitance of the transmon qubit, and $E_{\rm J}$ is the Josephson energy of the Josephson junction. Note that the capacitance of the transmon qubit $C_{\rm q}$ includes that of the Josephson junction and that we assume $\epsilon = \frac{C_g^2}{(C_1+C_g)(C_2+C_g)} \approx 0$ for simplicity. Here, taking into account up to the second order of the conjugate operators, the Hamiltonian exactly corresponds to that of the coupled LC resonators in Eq. (2.20).

According to Sec. 2.2 and Sec. 2.5, the Hamiltonian therefore is described using the corresponding annihilation and creation operators as

$$\hat{\mathcal{H}} = \hbar \left[ \omega_{\mathrm{c}}^{l}\, \hat{a}^{\dagger}\hat{a} + \omega_{\mathrm{q}}^{l}\, \hat{b}^{\dagger}\hat{b} - \frac{\omega_{\bar{\mathrm{C}}_{\mathrm{q}}}}{96} \left( \hat{b} + \hat{b}^{\dagger} \right)^{4} - g(\hat{a} - \hat{a}^{\dagger})(\hat{b} - \hat{b}^{\dagger}) \right], \tag{2.113}$$

where $\hat{a}$ ($\hat{a}^{\dagger}$) is the annihilation (creation) operator of the LC resonator, $\hat{b}$ ($\hat{b}^{\dagger}$) is the annihilation (creation) operator of the transmon qubit, $\omega_{\mathrm{c}}^{l} = \sqrt{\omega_{\bar{\mathrm{C}}_{\mathrm{c}}}\omega_{\mathrm{L_c}}}$ and $\omega_{\mathrm{q}}^{l} = \sqrt{\omega_{\bar{\mathrm{C}}_{\mathrm{q}}}\omega_{\mathrm{J}}}$ are the linearized resonance frequency of the LC resonator and the transmon qubit, and $g = \frac{1}{2}\sqrt{\frac{\omega_{\mathrm{c}}^{l}\omega_{\mathrm{q}}^{l}C_g^2}{(C_{\mathrm{c}}+C_g)(C_{\mathrm{q}}+C_g)}}$ is the coupling strength. Note that $\hbar\omega_{\bar{\mathrm{C}}_{\mathrm{n}}} = \frac{(2e)^2}{\bar{C}_n}$ ($n = \mathrm{c},\, \mathrm{q}$) are the capacitive energy quanta, and $\hbar\omega_{\mathrm{L_c}} = \frac{\phi_0^2}{L_{\mathrm{c}}}$ is the inductive energy quantum.

By using the rotating wave approximation, valid under the conditions $g \ll \omega_{\mathrm{c}} + \omega_{\mathrm{q}}^{l}$ and $\omega_{\bar{\mathrm{C}}_{\mathrm{q}}} \ll \sqrt{\omega_{\mathrm{J}}\omega_{\bar{\mathrm{C}}_{\mathrm{q}}}}$ (corresponding to the transmon qubit limit $\frac{\omega_{\bar{\mathrm{C}}_{\mathrm{q}}}}{\omega_{\mathrm{J}}} \ll 1$), we obtain the approximate Hamiltonian,

$$\hat{\mathcal{H}} = \hbar \left[ \omega_{\mathrm{c}}\, \hat{a}^{\dagger}\hat{a} + \omega_{\mathrm{q}}\, \hat{b}^{\dagger}\hat{b} + \frac{\alpha}{2}\hat{b}^{\dagger 2}\hat{b}^{2} + g(\hat{a}^{\dagger}\hat{b} + \hat{a}\hat{b}^{\dagger}) \right], \tag{2.114}$$

where $\omega_{\mathrm{c}} = \omega_{\mathrm{c}}^{l}$ and $\omega_{\mathrm{q}} = \omega_{\mathrm{q}}^{l} - \frac{\omega_{\mathrm{C}}}{8}$ is the resonance frequencies of the LC resonator and the transmon qubit, and $\alpha = -\frac{\omega_{\bar{\mathrm{C}}_{\mathrm{q}}}}{8}$ is the anharmonicity of the transmon qubit. Note that the LC resonance frequency is not affected by the nonlinear term of the Josephson junction, here. This is the Hamiltonian of the typical circuit QED system, which is called the generalized Jaynes-Cummings Hamiltonian.

### 2.6.1 Dispersive regime

As discussed in Sec. 2.2.1, except for the nonlinear term, we can diagonalize and approximate the Hamiltonian in the dispersive regime $g \ll |\Delta| = |\omega_{\mathrm{c}}^{l} - \omega_{\mathrm{q}}^{l}|$ as

$$\begin{aligned} \hat{\mathcal{H}} &= \hbar \left[ \left( \omega_{\mathrm{c}}^{l} + \frac{g^2}{\Delta} \right) \hat{\mathfrak{a}}^{\dagger}\hat{\mathfrak{a}} + \left( \omega_{\mathrm{q}}^{l} - \frac{g^2}{\Delta} \right) \hat{\mathfrak{b}}^{\dagger}\hat{\mathfrak{b}} - \frac{\omega_{\bar{\mathrm{C}}_{\mathrm{q}}}}{96} \left( \hat{b} + \hat{b}^{\dagger} \right)^{4} \right] \\ &= \hbar \left[ \omega_{\mathrm{c}}^{l\prime}\, \hat{\mathfrak{a}}^{\dagger}\hat{\mathfrak{a}} + \omega_{\mathrm{q}}^{l\prime}\, \hat{\mathfrak{b}}^{\dagger}\hat{\mathfrak{b}} - \frac{\omega_{\bar{\mathrm{C}}_{\mathrm{q}}}}{96} \left( \hat{b} + \hat{b}^{\dagger} \right)^{4} \right], \end{aligned} \tag{2.115}$$

where $\omega_{\mathrm{c}}^{l\prime} = \omega_{\mathrm{c}}^{l} + \frac{g^2}{\Delta}$ and $\omega_{\mathrm{q}}^{l\prime} = \omega_{\mathrm{q}}^{l} - \frac{g^2}{\Delta}$ are the Lamb-shifted linearized resonance frequencies of the LC resonator and the transmon qubit, respectively. Here, we need to represent the nonlinear terms $\frac{\omega_{\bar{\mathrm{C}}_{\mathrm{q}}}}{96} \left( \hat{b} + \hat{b}^{\dagger} \right)^{4}$ by diagonalizing annihilation operators $\hat{\mathfrak{a}}$ and $\hat{\mathfrak{b}}$. Since the original annihilation operators are approximated in the leading order of $\frac{g}{\Delta}$ as

$$\begin{pmatrix} \hat{a} \\ \hat{b} \end{pmatrix} \approx \begin{pmatrix} \hat{\mathfrak{a}} - \frac{g}{\Delta}\, \hat{\mathfrak{b}} \\ \frac{g}{\Delta}\, \hat{\mathfrak{a}} + \hat{\mathfrak{b}} \end{pmatrix}, \tag{2.116}$$

the nonlinear term is represented by

$$\begin{aligned} &- \frac{\omega_{\bar{\mathrm{C}}_{\mathrm{q}}}}{96} \left( \hat{b} + \hat{b}^{\dagger} \right)^{4} \\ &\approx - \frac{\omega_{\bar{\mathrm{C}}_{\mathrm{q}}}}{96} \left( \frac{g}{\Delta}\, \hat{\mathfrak{a}} + \hat{\mathfrak{b}} + \frac{g}{\Delta}\, \hat{\mathfrak{a}}^{\dagger} + \hat{\mathfrak{b}}^{\dagger} \right)^{4} \\ &\approx - \frac{\omega_{\bar{\mathrm{C}}_{\mathrm{q}}}}{96} \left[ 6 \left( \frac{g}{\Delta} \right)^{4} \hat{\mathfrak{a}}^{\dagger 2}\hat{\mathfrak{a}}^{2} + 24 \left( \frac{g}{\Delta} \right)^{2} \hat{\mathfrak{a}}^{\dagger}\hat{\mathfrak{a}}\hat{\mathfrak{b}}^{\dagger}\hat{\mathfrak{b}} + 6\, \hat{\mathfrak{b}}^{\dagger 2}\hat{\mathfrak{b}}^{2} + 12 \left( \frac{g}{\Delta} \right)^{2} \hat{\mathfrak{a}}^{\dagger}\hat{\mathfrak{a}} + 12\, \hat{\mathfrak{b}}^{\dagger}\hat{\mathfrak{b}} + 3 \right] \\ &\approx - \frac{\omega_{\bar{\mathrm{C}}_{\mathrm{q}}}}{16} \left( \frac{g}{\Delta} \right)^{4} \hat{\mathfrak{a}}^{\dagger 2}\hat{\mathfrak{a}}^{2} - \frac{\omega_{\bar{\mathrm{C}}_{\mathrm{q}}}}{4} \left( \frac{g}{\Delta} \right)^{2} \hat{\mathfrak{a}}^{\dagger}\hat{\mathfrak{a}}\hat{\mathfrak{b}}^{\dagger}\hat{\mathfrak{b}} - \frac{\omega_{\bar{\mathrm{C}}_{\mathrm{q}}}}{16}\, \hat{\mathfrak{b}}^{\dagger 2}\hat{\mathfrak{b}}^{2} - \frac{\omega_{\bar{\mathrm{C}}_{\mathrm{q}}}}{8} \left( \frac{g}{\Delta} \right)^{2} \hat{\mathfrak{a}}^{\dagger}\hat{\mathfrak{a}} - \frac{\omega_{\bar{\mathrm{C}}_{\mathrm{q}}}}{8}\, \hat{\mathfrak{b}}^{\dagger}\hat{\mathfrak{b}}, \end{aligned} \tag{2.117}$$

where we have used the rotating wave approximation under the condition $\frac{\omega_{\bar{C}_q}}{\omega_q^l} = \sqrt{\frac{\omega_{\bar{C}_q}}{\omega_J}} \ll 1$, $\frac{\omega_{\bar{C}_q}}{\omega_c} \ll 1$ and neglected the constant terms. From these calculations, the dispersive Hamiltonian is therefore written as

$$\hat{\mathcal{H}} = \hbar \left[ \omega_c' \, \hat{\mathfrak{a}}^\dagger \hat{\mathfrak{a}} - \frac{\omega_{\bar{C}_q}}{16} \left(\frac{g}{\Delta}\right)^4 \hat{\mathfrak{a}}^{\dagger 2} \hat{\mathfrak{a}}^2 + \omega_q' \, \hat{\mathfrak{b}}^\dagger \hat{\mathfrak{b}} - \frac{\omega_{\bar{C}_q}}{16} \, \hat{\mathfrak{b}}^{\dagger 2} \hat{\mathfrak{b}}^2 - \frac{\omega_{\bar{C}_q}}{4} \left(\frac{g}{\Delta}\right)^2 \hat{\mathfrak{a}}^\dagger \hat{\mathfrak{a}} \hat{\mathfrak{b}}^\dagger \hat{\mathfrak{b}} \right], \quad (2.118)$$

where $\omega_c' = \omega_c^{l\prime} - \frac{\omega_{\bar{C}_q}}{8} \left(\frac{g}{\Delta}\right)^2$ and $\omega_q' = \omega_q^{l\prime} - \frac{\omega_{\bar{C}_q}}{8}$ are the resonance frequencies of the LC resonator and the transmon qubit with the shift due to the nonlinear terms.

For simplicity, we define the anharmonicity and the dispersive interaction parameter as in the Hamiltonian

$$\hat{\mathcal{H}} = \hbar \left[ \omega_c' \, \hat{\mathfrak{a}}^\dagger \hat{\mathfrak{a}} + \frac{K}{2} \hat{\mathfrak{a}}^{\dagger 2} \hat{\mathfrak{a}}^2 + \omega_q' \, \hat{\mathfrak{b}}^\dagger \hat{\mathfrak{b}} + \frac{\alpha}{2} \, \hat{\mathfrak{b}}^{\dagger 2} \hat{\mathfrak{b}}^2 + 2\chi \, \hat{\mathfrak{a}}^\dagger \hat{\mathfrak{a}} \hat{\mathfrak{b}}^\dagger \hat{\mathfrak{b}} \right], \quad (2.119)$$

where $K = -\frac{\omega_{\bar{C}_q}}{8} \left(\frac{g}{\Delta}\right)^4$ is the self-Kerr frequency shift (anharmonicity) of the LC resonator, $\alpha = -\frac{\omega_{\bar{C}_q}}{8}$ is the anharmonicity of the transmon qubit, and $\chi = -\frac{\omega_{\bar{C}_q}}{8} \left(\frac{g}{\Delta}\right)^2 = \alpha \left(\frac{g}{\Delta}\right)^2$ is the dispersive interaction strength. The interaction strength is described by the geometric mean of the two anharmonicities, i.e., $\chi = -\sqrt{K\alpha}$. From the interaction Hamiltonian, the dispersive interaction can be understood as the strength of the state-dependent frequency shifts. Normally, the anharmonicity of the LC resonator is neglected since it is on the order of $(g/\Delta)^4$.

With the larger photon number in the cavity, the coupling strength between the qubit and the resonator mode are increased. For example, the coupling strength between $|\mathrm{g}, n\rangle$ and $|\mathrm{e}, n-1\rangle$ is calculated as $\langle \mathrm{e}, n-1 | (g(\hat{a}^\dagger \hat{b} + \hat{a}\hat{b}^\dagger)) | \mathrm{g}, n\rangle = g\sqrt{n}$. Here, the detuning is unchanged as $\Delta$. Therefore, when twice the coupling strength matches the detuning, the approximation of the dispersive regime completely collapses. Then, the critical photon number [12] is defined as

$$n_{\mathrm{crit}} = \frac{\Delta^2}{4g^2}. \quad (2.120)$$

The power of a cavity probe or a qubit readout should be set to be so weak to excite the average photon number much below the critical photon number.

As explained in Sec. 2.5.2, the Hamiltonian of the transmon qubit can be truncated to the qubit subspace as $\hat{\mathfrak{b}}^\dagger \hat{\mathfrak{b}} \to \hat{\sigma}_z/2$ and $\hat{\mathfrak{b}} \to \hat{\sigma}_-$. Thus, the Hamiltonian can be written as

$$\hat{\mathcal{H}} = \hbar \left[ \omega_c \, \hat{a}^\dagger \hat{a} + \frac{\omega_q}{2} \hat{\sigma}_z + \chi \, \hat{a}^\dagger \hat{a} \hat{\sigma}_z \right], \quad (2.121)$$

where we replace the resonance frequencies and the operators as $\omega_c' \to \omega_c$, $\omega_q' \to \omega_q$, and $\hat{\mathfrak{a}} \to \hat{a}$ for simplicity. Furthermore, we neglect the anharmonicity of the LC resonator. A schematic of the resonance frequencies in the dispersive circuit QED system are shown in Fig. 2.9.

### 2.6.2 Dispersive circuit QED system connected to waveguide

Here, we consider a dispersive circuit QED system where only an LC resonator is coupled to a waveguide, as shown in Fig. 2.10(a). Therefore, by adding the external coupling to the LC resonator, the Hamitonian in Eq. (2.115) can be described as

$$\begin{aligned} \hat{\mathcal{H}} = \hbar & \left[ \left( \omega_c^l + \frac{g^2}{\Delta} \right) \hat{\mathfrak{a}}^\dagger \hat{\mathfrak{a}} + \left( \omega_q^l - \frac{g^2}{\Delta} \right) \hat{\mathfrak{b}}^\dagger \hat{\mathfrak{b}} - \frac{\omega_{\bar{C}_q}}{96} \left( \hat{b} + \hat{b}^\dagger \right)^4 \right] \\ & + \hbar \int_{-\infty}^{\infty} d\omega \left[ \omega \, \hat{a}_\omega^\dagger \hat{a}_\omega + \sqrt{\frac{\kappa_{\mathrm{ex}}}{2\pi}} (\hat{a}^\dagger \hat{a}_\omega + \hat{a}_\omega^\dagger \hat{a}) \right], \end{aligned} \quad (2.122)$$

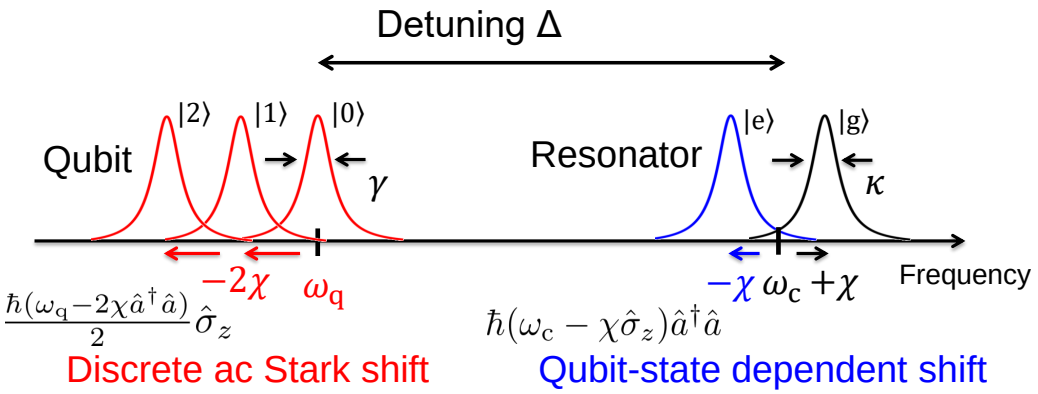


Figure 2.9: Resonance frequencies of a circuit QED system in the dispersive regime. The qubit obtains the photon-number dependent shift (discrete as Stark shift). The resonator obtains the qubit-state dependent shift.

where $\kappa_{\rm ex}$ is the external coupling rate of the LC resonator. As the nonlinear terms are represented in terms of the diagonalized modes in Sec. 2.6.1, the external coupling term can be also represented in terms of the diagonalized modes. Using the relation

$$\begin{pmatrix} \hat{a} \\ \hat{b} \end{pmatrix} \approx \begin{pmatrix} \hat{\mathfrak{a}} - \frac{g}{\Delta}\hat{\mathfrak{b}} \\ \frac{g}{\Delta}\hat{\mathfrak{a}} + \hat{\mathfrak{b}} \end{pmatrix}, \tag{2.123}$$

the Hamiltonian can be described as

$$\begin{aligned} \hat{\mathcal{H}} &= \hbar\left[\omega_{\rm c}'\,\hat{\mathfrak{a}}^\dagger\hat{\mathfrak{a}} + \frac{K}{2}\hat{\mathfrak{a}}^{\dagger 2}\hat{\mathfrak{a}}^2 + \omega_{\rm q}'\,\hat{\mathfrak{b}}^\dagger\hat{\mathfrak{b}} + \frac{\alpha}{2}\,\hat{\mathfrak{b}}^{\dagger 2}\hat{\mathfrak{b}}^2 + 2\chi\,\hat{\mathfrak{a}}^\dagger\hat{\mathfrak{a}}\hat{\mathfrak{b}}^\dagger\hat{\mathfrak{b}}\right] \\ &\quad + \hbar\int_{-\infty}^{\infty} d\omega\left[\omega\,\hat{a}_\omega^\dagger\hat{a}_\omega + \sqrt{\frac{\kappa_{\rm ex}}{2\pi}}(\hat{\mathfrak{a}}^\dagger\hat{a}_\omega + \hat{a}_\omega^\dagger\hat{\mathfrak{a}}) - \frac{g}{\Delta}\sqrt{\frac{\kappa_{\rm ex}}{2\pi}}(\hat{\mathfrak{b}}^\dagger\hat{a}_\omega + \hat{a}_\omega^\dagger\hat{\mathfrak{b}})\right], \end{aligned} \tag{2.124}$$

where the frequency parameters are defined as in Eq. (2.119). As shown in Fig. 2.10(b), we find that the qubit mode is coupled to the waveguide through the resonator mode with the external coupling rate of $\gamma_{\rm ex} = (g/\Delta)^2\kappa_{\rm ex}$, via the Purcell effect [12]. Note that the qubit and resonator modes are coupled to an identical waveguide. Nevertheless, due to the large detuning between the qubit and the resonator, these modes can be considered to be coupled to independent waveguides.

Again, the transmon qubit mode can be truncated to the qubit subspace as $\hat{\mathfrak{b}}^\dagger\hat{\mathfrak{b}} \to \hat{\sigma}_z/2$ and $\hat{\mathfrak{b}} \to \hat{\sigma}_-$. Thus, the Hamiltonian can be represented as

$$\begin{aligned} \hat{\mathcal{H}} &= \hbar\left[\omega_{\rm c}\,\hat{a}^\dagger\hat{a} + \frac{\omega_{\rm q}}{2}\hat{\sigma}_z + \chi\,\hat{a}^\dagger\hat{a}\hat{\sigma}_z\right] \\ &\quad + \hbar\int_{-\infty}^{\infty} d\omega\left[\omega\,\hat{a}_\omega^\dagger\hat{a}_\omega + \sqrt{\frac{\kappa_{\rm ex}}{2\pi}}(\hat{a}^\dagger\hat{a}_\omega + \hat{a}_\omega^\dagger\hat{a}) - \sqrt{\frac{\gamma_{\rm ex}}{2\pi}}(\hat{a}_\omega\hat{\sigma}_+ + \hat{a}_\omega^\dagger\hat{\sigma}_-)\right]. \end{aligned} \tag{2.125}$$

where we replace the resonance frequencies and the operators as $\omega_{\rm c}' \to \omega_{\rm c}$, $\omega_{\rm q}' \to \omega_{\rm q}$, and $\hat{\mathfrak{a}} \to \hat{a}$ for simplicity. Here, the internal loss and dephasing terms are not included. However, these terms can be easily added as discussed in Sec. 2.5.1 and Sec. 2.4.

## 2.7 Josephson parametric amplifier (JPA)

A Josephson parametric amplifier (JPA) is a useful tool for implementing a single-shot readout of a superconducting qubit. Furthermore, it is used for the characterization of

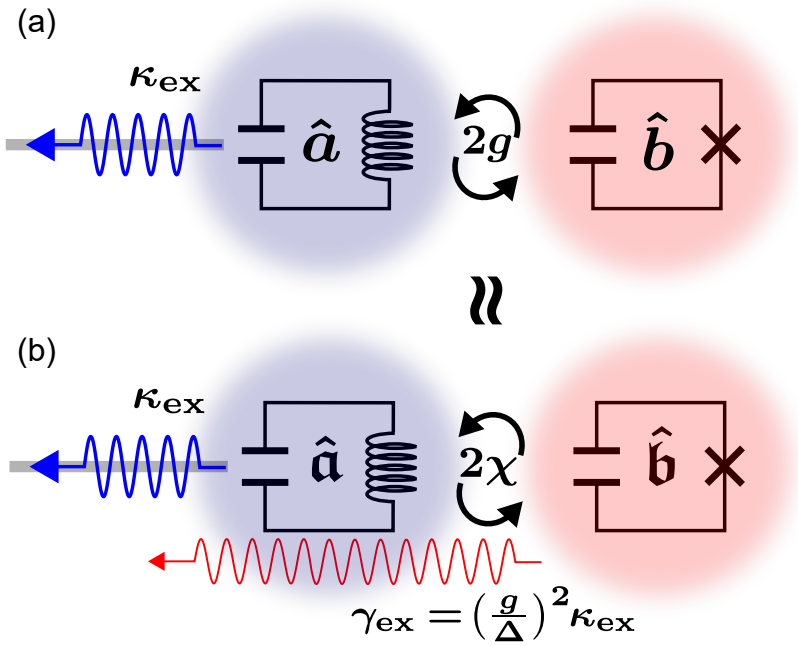


Figure 2.10: (a) Circuit QED system in the dispersive regime, where a resonator mode is coupled to a waveguide. (b) Approximate circuit QED system in the dispersive regime. These diagonalized modes are coupled via the state-dependent dispersive shift. The qubit mode obtains the external coupling to the waveguide through the resonator mode.

quantum states in propagating modes. There are several types of microwave amplifiers based on Josephson junctions [50, 51, 52, 53]. Here, we focus on a flux-driven JPA, which is used in this thesis. For the circuit diagram shown in Fig. 2.11, the JPA is a parallel circuit consisting of a capacitor and a SQUID (Superconducting QUantum Interference Device) which is formed by two parallel Josephson junctions. The Hamiltonian of the JPA is written as

$$\hat{\mathcal{H}} = \frac{\hat{Q}^2}{2C} - E_{\mathrm{J}}(\Phi_{\mathrm{ex}}) \cos\left(\frac{\hat{\Phi}}{\phi_0}\right), \tag{2.126}$$

where $C$ is the total capacitance including the one from the SQUID, $\Phi_{\mathrm{ex}}$ is the external magnetic flux penetrating the loop of the SQUID, $E_{\mathrm{J}}(\Phi_{\mathrm{ex}}) = \phi_0 I_{\mathrm{c}}(\Phi_{\mathrm{ex}})$ is the tunneling energy of the SQUID, and $I_{\mathrm{c}}(\Phi_{\mathrm{ex}}) = 2I_{\mathrm{c0}} \cos\left(\frac{\Phi_{\mathrm{ex}}}{2\phi_0}\right)$ is the critical current depending on the external magnetic flux $\Phi_{\mathrm{ex}}$, $I_{\mathrm{c0}}$ is the critical current of a single Josephson junction forming the SQUID. The canonical commutation relation of the pair of the conjugate operators is $[\hat{\Phi}, \hat{Q}] = i\hbar$, where we approximate the operator of the generalized magnetic field by neglecting the periodic condition since the Josephson energy is much larger than that of the capacitance. Thus, we consider the SQUID as a nonlinear inductor with tunability provided by an applied external magnetic flux.

When we operate the JPA as an amplifier, we bias the SQUID with the dc magnetic flux $\Phi_{\mathrm{dc}}$ to tune the resonance frequency of the JPA and pump the SQUID with the ac magnetic flux $\Phi_{\mathrm{ac}}$ to obtain the gain, i.e., $\Phi_{\mathrm{ex}} = \Phi_{\mathrm{dc}} + \Phi_{\mathrm{ac}}$. Considering that the ac magnetic flux is much smaller than the magnetic flux quantum, $\Phi_{\mathrm{ac}} \ll \Phi_0$ $(2\pi\phi_0)$, we can

linearize the ac magnetic dependence of the tunneling energy of the SQUID

$$\begin{aligned} E_{\mathrm{J}}(\Phi_{\mathrm{ex}}) &= E_{\mathrm{J}} \cos\left(\frac{\Phi_{\mathrm{dc}}+\Phi_{\mathrm{ac}}}{2\phi_0}\right) \\ &= E_{\mathrm{J}}\left[\cos\left(\frac{\Phi_{\mathrm{dc}}}{2\phi_0}\right)\cos\left(\frac{\Phi_{\mathrm{ac}}}{2\phi_0}\right) - \sin\left(\frac{\Phi_{\mathrm{dc}}}{2\phi_0}\right)\sin\left(\frac{\Phi_{\mathrm{ac}}}{2\phi_0}\right)\right] \\ &\approx E_{\mathrm{J}}\cos\left(\frac{\Phi_{\mathrm{dc}}}{2\phi_0}\right) - E_{\mathrm{J}}\sin\left(\frac{\Phi_{\mathrm{dc}}}{2\phi_0}\right)\frac{\Phi_{\mathrm{ac}}}{2\phi_0} \\ &= \left[1-\tan\left(\frac{\varphi_{\mathrm{dc}}}{2}\right)\ \frac{\varphi_{\mathrm{ac}}}{2}\right] E_{\mathrm{J}}\cos\left(\frac{\varphi_{\mathrm{dc}}}{2}\right) \end{aligned} \tag{2.127}$$

where $E_{\mathrm{J}} = 2\phi_0 I_{\mathrm{c0}}$ is the maximum tunneling energy of the SQUID or the sum of the two tunneling energies of the single Josephson junctions, $\varphi_{\mathrm{dc}} = \frac{\Phi_{\mathrm{dc}}}{\phi_0}$ is the dimensionless dc magnetic flux, and $\varphi_{\mathrm{ac}} = \frac{\Phi_{\mathrm{ac}}}{\phi_0}$ is the dimensionless ac magnetic flux. Then, the Hamiltonian is given by

$$\hat{\mathcal{H}} = \frac{\hat{Q}^2}{2C} - \left[1-\tan\left(\frac{\varphi_{\mathrm{dc}}}{2}\right)\ \frac{\varphi_{\mathrm{ac}}}{2}\right] E_{\mathrm{J}}\cos\left(\frac{\varphi_{\mathrm{dc}}}{2}\right)\cos\left(\frac{\hat{\Phi}}{\phi_0}\right). \tag{2.128}$$

To obtain a large dynamic range of the amplification or to reduce the nonlinearity of the JPA, the tunneling energy of the SQUID should be much larger than the capacitive energy. In this regime, the nonlinear potential of the SQUID can be expanded as

$$\begin{aligned} \hat{\mathcal{H}} &\approx \frac{\hat{Q}^2}{2C} + \left[1-\tan\left(\frac{\varphi_{\mathrm{dc}}}{2}\right)\ \frac{\varphi_{\mathrm{ac}}}{2}\right] E_{\mathrm{J}}\cos\left(\frac{\varphi_{\mathrm{dc}}}{2}\right)\frac{1}{2}\left(\frac{\hat{\Phi}}{\phi_0}\right)^2 \\ &= \frac{\hat{Q}^2}{2C} + \left[1-\tan\left(\frac{\varphi_{\mathrm{dc}}}{2}\right)\ \frac{\varphi_{\mathrm{ac}}}{2}\right] \frac{E_{\mathrm{J}}\cos\left(\frac{\varphi_{\mathrm{dc}}}{2}\right)}{\phi_0^2}\ \frac{\hat{\Phi}^2}{2} \\ &= \frac{\hat{Q}^2}{2C} + \frac{\hat{\Phi}^2}{2L_{\mathrm{J}}} - \frac{1}{4}\tan\left(\frac{\varphi_{\mathrm{dc}}}{2}\right)\varphi_{\mathrm{ac}}\,\frac{\hat{\Phi}^2}{L_{\mathrm{J}}}, \end{aligned} \tag{2.129}$$

where $L_{\mathrm{J}} = \frac{\phi_0^2}{E_{\mathrm{J}}\cos\left(\frac{\varphi_{\mathrm{dc}}}{2}\right)} = \frac{\phi_0}{2I_{\mathrm{c0}}\cos\left(\pi\frac{\Phi_{\mathrm{dc}}}{\Phi_0}\right)}$ is the inductance of the SQUID. Note that unlike a transmon qubit, we neglect forth-order terms of $\hat{\Phi}$ since the anharmonicity of a conventional JPA is much smaller than that of a transmon qubit. The first two terms describe the Hamiltonian of the harmonic oscillator and the last term corresponds to a driving term with $\varphi_{\mathrm{ac}}$.

By using the annihilation and creation operators, which are defined as in Eq. (2.5), we can diagonalize the harmonic terms as

$$\hat{\mathcal{H}} = \hbar\left[\omega_{\mathrm{r}}\,\hat{a}^\dagger\hat{a} - \frac{\omega_{\mathrm{c}}}{8}\tan\left(\frac{\varphi_{\mathrm{dc}}}{2}\right)\varphi_{\mathrm{ac}}\ \left(\hat{a}+\hat{a}^\dagger\right)^2\right], \tag{2.130}$$

where $\omega_{\mathrm{r}}$ is the resonance frequency of the JPA. Now, we describe the Hamiltonian with $\varphi_{\mathrm{ac}} = \varphi_{\mathrm{p}}\cos\left(\omega_{\mathrm{p}}t+\phi_{\mathrm{p}}\right)$, where $\varphi_{\mathrm{p}}$ is the dimensionless pump amplitude, $\omega_{\mathrm{p}}$ is the pump frequency, and $\phi_{\mathrm{p}}$ is the pump phase. When the JPA is operated as an amplifier, the pump frequency is twice the resonance frequency of the JPA: $\omega_{\mathrm{p}} \sim 2\omega_{\mathrm{c}}$. In that case, the Hamiltonian can be described, in the rotating wave approximation, as

$$\begin{aligned} \hat{\mathcal{H}} &= \hbar\left[\omega_{\mathrm{r}}\,\hat{a}^\dagger\hat{a} - \frac{\omega_{\mathrm{r}}}{8}\tan\left(\frac{\varphi_{\mathrm{dc}}}{2}\right)\varphi_{\mathrm{p}}\cos\left(\omega_{\mathrm{p}}t+\phi_{\mathrm{p}}\right)\ \left(\hat{a}+\hat{a}^\dagger\right)^2\right] \\ &\approx \hbar\left[\omega_{\mathrm{r}}\,\hat{a}^\dagger\hat{a} - \frac{\Omega_{\mathrm{p}}}{2}\ \left(\hat{a}^2 e^{i(\omega_{\mathrm{p}}t+\phi_{\mathrm{p}})} + \hat{a}^{\dagger 2} e^{-i(\omega_{\mathrm{p}}t+\phi_{\mathrm{p}})}\right)\right], \end{aligned} \tag{2.131}$$

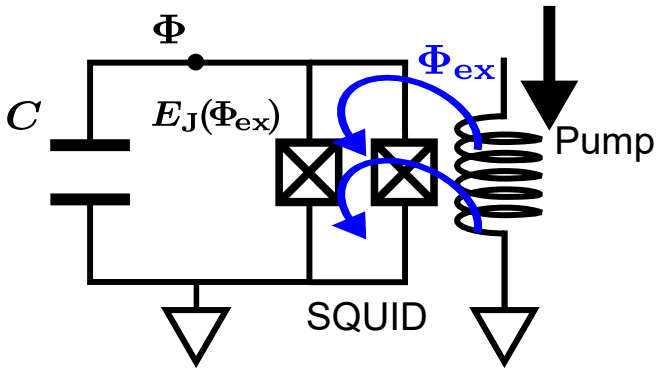


Figure 2.11: Circuit diagram of Josephson parametric amplifier (JPA).

where $\Omega_{\rm p} = \frac{\omega_{\rm r}}{4}\tan\left(\frac{\varphi_{\rm dc}}{2}\right)\varphi_{\rm p} = \frac{\omega_{\rm r}}{4}\tan\left(\frac{\Phi_{\rm dc}}{\phi_0}\right)\frac{\Phi_{\rm p}}{\phi_0}$ is the pump amplitude, and $\Phi_{\rm p}$ is the pump magnetic flux penetrating the loop of the SQUID. Note that we neglect the modulation terms of the resonance frequency of the JPA. From the Hamiltonian, we find the flux-driven JPA is a harmonic oscillator with a two-photon drive.

### 2.7.1 JPA connected to waveguide

Here, we study the JPA coupled to a waveguide. As in the case for the LC resonator, the Hamiltonian can be represented as

$$\hat{\mathcal{H}} = \hbar\left[\omega_{\rm r}\,\hat{a}^\dagger\hat{a} - \frac{\Omega_{\rm p}}{2}\left(\hat{a}^2 e^{i(\omega_{\rm p}t+\phi_{\rm p})} + \hat{a}^{\dagger 2}e^{-i(\omega_{\rm p}t+\phi_{\rm p})}\right)\right] + \hbar\int_{-\infty}^{\infty}d\omega\left[\omega\,\hat{a}_\omega^\dagger\hat{a}_\omega + \sqrt{\frac{\kappa_{\rm ex}}{2\pi}}(\hat{a}^\dagger\hat{a}_\omega + \hat{a}_\omega^\dagger\hat{a})\right] + \hbar\int_{-\infty}^{\infty}d\omega\left[\omega\,\hat{c}_\omega^\dagger\hat{c}_\omega + \sqrt{\frac{\kappa_{\rm in}}{2\pi}}(\hat{a}^\dagger\hat{c}_\omega + \hat{c}_\omega^\dagger\hat{a})\right], \tag{2.132}$$

where $\kappa_{\rm ex}$ and $\kappa_{\rm in}$ are the external coupling rate and internal loss rates of the JPA.

The time evolution of $\hat{a}$ is described in the Heisenberg picture as

$$\frac{d\hat{a}(t)}{dt} = \left(-i\omega_{\rm r} - \frac{\kappa}{2}\right)\hat{a}(t) + i\Omega_{\rm p}e^{-i\omega_p t - i\phi_{\rm p}}\hat{a}^\dagger - i\sqrt{\kappa_{\rm ex}}\hat{a}_{\rm i}(t) - i\sqrt{\kappa_{\rm in}}\hat{c}_{\rm i}(t), \tag{2.133}$$

where $\hat{a}_{\rm i}(t)$ and $\hat{c}_{\rm i}(t)$ are the input modes in the waveguide and the loss channel, and $\kappa = \kappa_{\rm ex} + \kappa_{\rm in}$ is the total relaxation rate of the JPA. The Fourier transform of Eq. (2.133) can be described as

$$-i\omega\hat{a}(\omega) = \left(-i\omega_{\rm r} - \frac{\kappa}{2}\right)\hat{a}(\omega) + i\Omega_{\rm p}e^{-i\phi_{\rm p}}\hat{a}^\dagger(\omega_{\rm p} - \omega) - i\sqrt{\kappa_{\rm ex}}\hat{a}_{\rm i}(\omega) - i\sqrt{\kappa_{\rm in}}\hat{c}_{\rm i}(\omega). \tag{2.134}$$

Here, the pump frequency is set to be twice the JPA frequency, i.e., $\omega_{\rm p} = 2\omega_{\rm r}$. The frequency $\omega$ is represented by the detuning between the input signal and the JPA frequency, i.e., $\omega = \omega_{\rm r} + \delta$. Then, $\hat{a}(\omega)$, $\hat{a}_{\rm i}(\omega)$ and $\hat{c}_{\rm i}(\omega)$ are denoted as $\hat{a}(\delta)$, $\hat{a}_{\rm i}(\delta)$ and $\hat{c}_{\rm i}(\delta)$, respectively. Then, Eq. (2.134) can be represented as

$$-i\delta\hat{a}(\delta) = -\frac{\kappa}{2}\hat{a}(\delta) + i\Omega_{\rm p}e^{-i\phi_{\rm p}}\hat{a}^\dagger(-\delta) - i\sqrt{\kappa_{\rm ex}}\hat{a}_{\rm i}(\delta) - i\sqrt{\kappa_{\rm in}}\hat{c}_{\rm i}(\delta). \tag{2.135}$$

Using the conjugate relation, Eq. (2.135) can be simply represented as

$$\begin{pmatrix} \frac{\kappa}{2} - i\delta & -i\Omega_{\rm p}e^{-i\phi_{\rm p}} \\ i\Omega_{\rm p}e^{i\phi_{\rm p}} & \frac{\kappa}{2} - i\delta \end{pmatrix}\begin{pmatrix} \hat{a}(\delta) \\ \hat{a}^\dagger(-\delta) \end{pmatrix} = i\sqrt{\kappa_{\rm ex}}\begin{pmatrix} -\hat{a}_{\rm i}(\delta) \\ \hat{a}_{\rm i}^\dagger(-\delta) \end{pmatrix} + i\sqrt{\kappa_{\rm in}}\begin{pmatrix} -\hat{c}_{\rm i}(\delta) \\ \hat{c}_{\rm i}^\dagger(-\delta) \end{pmatrix}. \tag{2.136}$$

Then, we have

$$\begin{pmatrix} \hat{a}(\delta) \\ \hat{a}^\dagger(-\delta) \end{pmatrix} = \frac{i}{\left(\frac{\kappa}{2} - i\delta\right)^2 - \Omega_\mathrm{p}^2} \begin{pmatrix} \frac{\kappa}{2} - i\delta & i\Omega_\mathrm{p} e^{-i\phi_\mathrm{p}} \\ -i\Omega_\mathrm{p} e^{i\phi_\mathrm{p}} & \frac{\kappa}{2} - i\delta \end{pmatrix} \left[ \sqrt{\kappa_\mathrm{ex}} \begin{pmatrix} -\hat{a}_\mathrm{i}(\delta) \\ \hat{a}_\mathrm{i}^\dagger(-\delta) \end{pmatrix} + \sqrt{\kappa_\mathrm{in}} \begin{pmatrix} -\hat{c}_\mathrm{i}(\delta) \\ \hat{c}_\mathrm{in}^\dagger(-\delta) \end{pmatrix} \right]. \tag{2.137}$$

Using the input-output relation as $\hat{a}_\mathrm{o}(\delta) = \hat{a}_\mathrm{i}(\delta) - i\sqrt{\kappa_\mathrm{ex}}\hat{a}(\delta)$, we obtain

$$\begin{aligned} \hat{a}_\mathrm{o}(\delta) = {} & \frac{1}{\left(\frac{\kappa}{2} - i\delta\right)^2 - \Omega_\mathrm{p}^2} \left[ \left( - \left( \frac{\kappa_\mathrm{ex} - \kappa_\mathrm{in}}{2} + i\delta \right) \left( \frac{\kappa}{2} - i\delta \right) - \Omega_\mathrm{p}^2 \right) \hat{a}_\mathrm{i}(\delta) + i\kappa_\mathrm{ex}\Omega_\mathrm{p} e^{-i\phi_\mathrm{p}} \hat{a}_\mathrm{i}^\dagger(-\delta) \right] \\ & + \frac{\sqrt{\kappa_\mathrm{in}\kappa_\mathrm{ex}}}{\left(\frac{\kappa}{2} - i\delta\right)^2 - \Omega_\mathrm{p}^2} \left[ - \left( \frac{\kappa}{2} - i\delta \right) \hat{c}_\mathrm{i}(\delta) + i\Omega_\mathrm{p} e^{-i\phi_\mathrm{p}} \hat{c}_\mathrm{i}^\dagger(-\delta) \right]. \end{aligned} \tag{2.138}$$

We find that the output mode state is the input mode state multiplied with a squeezing operator with a finite photon loss. In this thesis, the JPA is used for a squeezed source or a phase-sensitive amplifier.

# Chapter 3

# State representation and transformation

Here, we explain the representations of a quantum state in a qubit and a harmonic oscillator (photonic mode). The basic concepts in this chapter can be seen in [54, 55, 56, 1].

## 3.1 Qubit

A qubit, a quantum system with two eigenstates, is known as the fundamental component of in a quantum information processor. Although the superconducting qubit is a multi-level system, it is well approximated as a two-level system due to its strong anharmonicity (see Sec. 2.5.2). The Hamiltonian of the qubit is written as

$$\hat{\mathcal{H}} = \frac{\hbar\omega_{\mathrm{q}}}{2}\hat{\sigma}_z, \tag{3.1}$$

where $\omega_{\mathrm{q}}$ is the resonance frequency of the qubit and $\hat{\sigma}_z$ is the Pauli $z$ operator. The lower and higher eigenstates are called the ground state $|\mathrm{g}\rangle$ and the excited state $|\mathrm{e}\rangle$, respectively.

### 3.1.1 Bloch sphere

An arbitrary quantum state of the qubit, including a classical mixed state, is represented as

$$\rho = \frac{1}{2}(\hat{1} + r_x\hat{\sigma}_x + r_y\hat{\sigma}_y + r_z\hat{\sigma}_z), \tag{3.2}$$

where $\hat{\sigma}_x$, $\hat{\sigma}_y$, and $\hat{\sigma}_z$ are the Puali matrices, and $r_x^2 + r_y^2 + r_z^2 \leq 1$ is satisfied. Therefore, the quantum state is visually represented by the coordinate of a point $(r_x, r_y, r_z)$ in the Bloch sphere, as shown in Fig. 3.1. The Bloch sphere is a three-dimensional sphere with the radius equal to unity. The pure state $|\Psi\rangle$ is represented by the point on the surface $(r_x, r_y, r_z) = (\sin\theta\cos\theta, \sin\theta\sin\theta, \cos\theta)$, which satisfies $r_x^2 + r_y^2 + r_z^2 = 1$. The pure states located at the antipodes on the Bloch sphere are the states orthogonal to each other. While the pure state is located on the surface, the mixed state is located inside the Bloch sphere. The projection onto one axis corresponds to the occupation probability of the eigenstate defined by the axis.

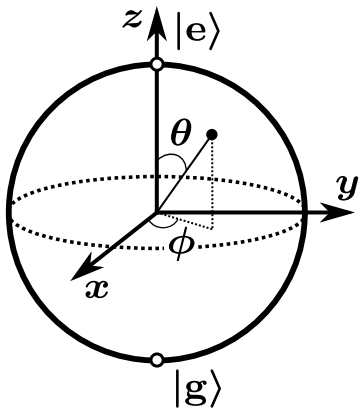


Figure 3.1: Bloch sphere.

### 3.1.2 Unitary operation

A generator or Hamiltonian of an unitary operator for the qubit system is described in the basis of the Pauli matrix as

$$\hat{\mathcal{H}} \propto n_x\hat{\sigma}_x + n_y\hat{\sigma}_y + n_z\hat{\sigma}_z, \tag{3.3}$$

where $n_x^2 + n_y^2 + n_z^2 = 1$ can be satisfied without loss of generality. Then, the unitary operator with the Hamiltonian is described as

$$\begin{aligned}\hat{U} &= \exp\left[-i\frac{\Theta}{2}(n_x\hat{\sigma}_x + n_y\hat{\sigma}_y + n_z\hat{\sigma}_z)\right] \\ &= \cos\frac{\Theta}{2}\,\hat{1} - i\sin\frac{\Theta}{2}(n_x\hat{\sigma}_x + n_y\hat{\sigma}_y + n_z\hat{\sigma}_z).\end{aligned} \tag{3.4}$$

In the Bloch sphere, the unitary operation corresponds to the rotation by $+\Theta$ about the axis of $\overrightarrow{n} = (n_x,\, n_y,\, n_z)$.

### 3.1.3 Rabi oscillation

As explained in Sec. 2.5.2, a superconducting qubit is controlled by applying an on-resonant microwave pulse. As schematically shown in Fig. 3.2(a), the driven qubit state goes back and forth between the ground state and the excited state without being excited to the higher energy levels.

From Sec. 2.5.2, the Hamiltonian of the driven qubit is represented in the rotating frame at the drive frequency $\omega_\mathrm{d}$ as

$$\begin{aligned}\hat{\mathcal{H}} &= \hbar\left[\frac{\omega_\mathrm{q} - \omega_\mathrm{d}}{2}\hat{\sigma}_z + \left(\frac{|\Omega_\mathrm{d}|}{2}e^{-i\phi_\mathrm{d}}\hat{\sigma}_+ + \frac{|\Omega_\mathrm{d}|}{2}e^{i\phi_\mathrm{d}}\hat{\sigma}_-\right)\right] \\ &= \frac{\hbar}{2}\begin{pmatrix}\delta & |\Omega_\mathrm{d}|e^{-i\phi_\mathrm{d}} \\ |\Omega_\mathrm{d}|e^{i\phi_\mathrm{d}} & -\delta\end{pmatrix},\end{aligned} \tag{3.5}$$

where $|\Omega_\mathrm{d}|$ is the drive amplitude, $\phi_\mathrm{d}$ is the drive phase, and $\delta = \omega_\mathrm{q} - \omega_\mathrm{d}$ is the detuning between the qubit frequency and the drive frequency. Note that the as Stark shift from the second higher excited state is neglected for simplicity. When the detuning is much

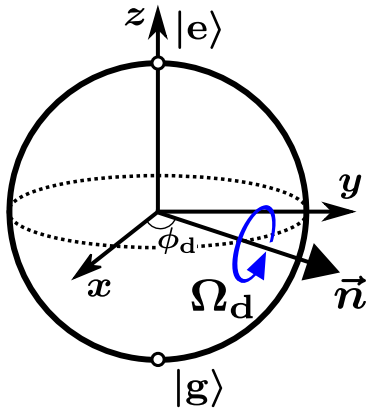


Figure 3.2: Unitary operation of the Rabi oscillation.

less than the Rabi frequency, $\delta \ll |\Omega_{\mathrm{d}}|$, the Hamiltonian is rewritten as

$$\begin{aligned}\hat{\mathcal{H}} &= \frac{\hbar|\Omega_{\mathrm{d}}|}{2}\begin{pmatrix} 0 & e^{-i\phi_{\mathrm{d}}} \\ e^{i\phi_{\mathrm{d}}} & 0 \end{pmatrix} \\ &= \frac{\hbar|\Omega_{\mathrm{d}}|}{2}(\cos\phi_{\mathrm{d}}\,\hat{\sigma}_x + \sin\phi_{\mathrm{d}}\,\hat{\sigma}_y).\end{aligned} \tag{3.6}$$

As shown in Fig. 3.2(b), the rotation axis with this Hamiltonian is $\vec{n} = (\cos\theta, \sin\theta, 0)$ or the $x$-axis rotated by $\phi_{\mathrm{d}}$ on the $xy$-plane in the Bloch sphere. The unitary operator describing the evolution from time $t_i$ to $t_f$ is given by

$$\begin{aligned}\hat{U} &= \exp\left(\int_{t_i}^{t_f} dt\,\frac{|\Omega_{\mathrm{d}}|}{2}(\cos\phi_{\mathrm{d}}\,\hat{\sigma}_x + \sin\phi_{\mathrm{d}}\,\hat{\sigma}_y)\right) \\ &= \exp\left(\frac{\Theta}{2}(\cos\phi_{\mathrm{d}}\,\hat{\sigma}_x + \sin\phi_{\mathrm{d}}\,\hat{\sigma}_y)\right),\end{aligned} \tag{3.7}$$

where $\Theta = \int_{t_i}^{t_f} dt\,|\Omega_{\mathrm{d}}|$ is the rotation angle in the Bloch sphere. From this, the Rabi frequency is found to be the angular velocity of the rotation due to the unitary operation.

By using the two different drive phases, we can realize the rotations about the two different rotation axes on the $xy$ plane. Therefore, the unitary operation with the Rabi oscillation enables us to perform an arbitrary unitary operation on the qubit.

### 3.1.4 Gates

Here, we introduce Pauli operations on the qubit, which are often used for characterization of the qubit itself and for implementing various algorithms.

By setting the rotation angle to $\pi/2$ and $\pi$ with a drive phase of $\phi_{\mathrm{d}} = 0$, the $\hat{X}/2$ gate and the $\hat{X}$ gate can be implemented as

$$\hat{X/2} = \frac{1}{\sqrt{2}}\begin{pmatrix} 1 & -i \\ -i & 1 \end{pmatrix}, \quad \hat{X} = \begin{pmatrix} 0 & -i \\ -i & 0 \end{pmatrix}. \tag{3.8}$$

A operation with a drive phase of $\phi_{\mathrm{d}} = \pi$ corresponds to the inverse operation of that of $\phi_{\mathrm{d}} = 0$. Therefore, we have

$$-\hat{X/2} = \hat{X/2}^{\dagger} = \frac{1}{\sqrt{2}}\begin{pmatrix} 1 & i \\ i & 1 \end{pmatrix}, \quad -\hat{X} = \hat{X}^{\dagger} = \begin{pmatrix} 0 & i \\ i & 0 \end{pmatrix}. \tag{3.9}$$

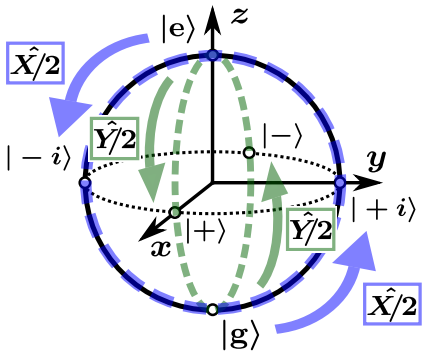


Figure 3.3: Schematic of the Pauli operation of the qubit. The superposition states are denoted as $|\pm\rangle = \frac{1}{\sqrt{2}}(|\mathrm{g}\rangle \pm |\mathrm{e}\rangle)$ and $|\pm i\rangle = \frac{1}{\sqrt{2}}(|\mathrm{g}\rangle \pm i|\mathrm{e}\rangle)$.

Furthermore, by setting the rotation angle to $\pi/2$ and $\pi$ with a drive phase of $\phi_\mathrm{d} = \pi/2$, the $\hat{Y}/2$ gate and the $\hat{Y}$ gate can be implemented as

$$\hat{Y/2} = \frac{1}{\sqrt{2}} \begin{pmatrix} 1 & -1 \\ 1 & 1 \end{pmatrix}, \quad \hat{Y} = \begin{pmatrix} 0 & -1 \\ 1 & 0 \end{pmatrix}. \tag{3.10}$$

The inverse operations of the $\hat{Y/2}$ and $\hat{Y}$ gates are realized by using a drive phase of $3\pi/2$ as

$$-\hat{Y/2} = \hat{Y/2}^\dagger = \frac{1}{\sqrt{2}} \begin{pmatrix} 1 & 1 \\ -1 & 1 \end{pmatrix}, \quad -\hat{Y} = \hat{Y}^\dagger = \begin{pmatrix} 0 & 1 \\ -1 & 0 \end{pmatrix}. \tag{3.11}$$

A schematic showing examples of the Pauli operations is shown in Fig. 3.3.

### 3.1.5 Quantum state tomography

In order to perform quantum state tomography of the qubit, we must determine $(r_x, r_y, r_z)$ in the Bloch sphere.

By measuring the qubit in the basis of $\hat{\sigma}_x$, we can obtain the expectation value of $\langle\hat{\sigma}_x\rangle$, which is calculated as

$$\begin{aligned} \langle\hat{\sigma}_x\rangle &= \mathrm{Tr}\left[\rho\,\hat{\sigma}_x\right] \\ &= \frac{1}{2}\mathrm{Tr}\left[(\hat{1} + r_x\hat{\sigma}_x + r_y\hat{\sigma}_y + r_z\hat{\sigma}_z)\hat{\sigma}_x\right] \\ &= \frac{r_x}{2}\mathrm{Tr}\left[\hat{1}\right] \\ &= r_x, \end{aligned} \tag{3.12}$$

where we use $\hat{\sigma}_x^2 = \hat{1}$, $\hat{\sigma}_y\hat{\sigma}_x = -i\hat{\sigma}_z$, $\hat{\sigma}_z\hat{\sigma}_x = i\hat{\sigma}_y$. From this calculation, we find that a measurement of the expectation value of $\hat{\sigma}_x$ enables us to determine $r_x$ of the density matrix. In the same way, we can determine $r_y$ and $r_z$ by measuring the qubit in the basis of $\hat{\sigma}_y$ and $\hat{\sigma}_z$, respectively:

$$\begin{aligned} \langle\hat{\sigma}_y\rangle &= \mathrm{Tr}\left[\rho\,\hat{\sigma}_y\right] = r_y \\ \langle\hat{\sigma}_z\rangle &= \mathrm{Tr}\left[\rho\,\hat{\sigma}_z\right] = r_z. \end{aligned} \tag{3.13}$$

Thus, we realize quantum state tomography of the qubit by measuring the qubit in the three orthogonal bases $\hat{\sigma}_x$, $\hat{\sigma}_y$, and $\hat{\sigma}_z$.

In usual experiments, a superconducting qubit can be measured only in the basis of $\hat{\sigma}_z$ or in an energy eigenstates. However, we can measure the qubit in an arbitrary basis by a measurement of $\hat{\sigma}_z$ with a qubit control.

For example, we can measure the qubit in the $\hat{\sigma}_x$ basis by performing the $-\hat{Y}/2$ gate and then measuring $\hat{\sigma}_z$:

$$\begin{aligned} &\mathrm{Tr}\left[-\hat{Y}/2\,\rho\,-\hat{Y}/2^{\dagger}\,\hat{\sigma}_z\right] \\ &= \mathrm{Tr}\left[\rho\,-\hat{Y}/2^{\dagger}\,\hat{\sigma}_z\,-\hat{Y}/2\right] \\ &= \mathrm{Tr}\left[\rho\,\hat{\sigma}_x\right] \\ &= \langle\hat{\sigma}_x\rangle \\ &= r_x. \end{aligned} \tag{3.14}$$

In the same way, we can measure the qubit in the $\hat{\sigma}_y$ basis with the $\hat{X/2}$ gate:

$$\begin{aligned} &\mathrm{Tr}\left[\hat{X/2}\,\rho\,\hat{X/2}^{\dagger}\,\hat{\sigma}_z\right] \\ &= r_y. \end{aligned} \tag{3.15}$$

Therefore, by using the expectation value of these measurements, we can perform quantum state tomography of the superconducting qubit.

## 3.2 Harmonic oscillator

Here, we study how to describe a quantum state in a harmonic oscillator. The Hamiltonian is written as

$$\hat{\mathcal{H}} = \hbar\omega_{\mathrm{c}}\,\hat{a}^{\dagger}\hat{a}, \tag{3.16}$$

where $\omega_{\mathrm{c}}$ is the resonance frequency and $\hat{a}$ and $\hat{a}^{\dagger}$ are the annihilation and creation operators, respectively. The bosonic commutation relation is imposed on the operators as $[\hat{a}, \hat{a}^{\dagger}] = 1$.

We also define the dimensionless quadrature operators as

$$\hat{x} = \frac{\hat{a} + \hat{a}^{\dagger}}{\sqrt{2}}, \quad \hat{p} \;= \frac{\hat{a} - \hat{a}^{\dagger}}{\sqrt{2}i}. \tag{3.17}$$

The operators $\hat{x}$ and $\hat{p}$ correspond to the real and imaginary parts of $\hat{a}$, respectively. The commutation relation is $[\hat{x}, \hat{p}] = i$. From the definition, the annihilation and creation operators are represented as

$$\hat{a} = \frac{\hat{x} + i\hat{p}}{\sqrt{2}}, \quad \hat{a}^{\dagger} \;= \frac{\hat{x} - i\hat{p}}{\sqrt{2}}. \tag{3.18}$$

By using the quadrature operators, the Hamiltonian is rewritten as

$$\mathcal{H} = \frac{\hbar\omega_{\mathrm{c}}}{2}\left(\hat{x}^2 + \hat{p}^2\right). \tag{3.19}$$

### 3.2.1 Fock basis

A photon number $\hat{a}^{\dagger}\hat{a}$ can be measured with a quantum-limited energy detector for the electromagnetic field, which is called a photon detector.

The eigenstates of the photon number operator $\hat{a}^\dagger\hat{a}$ are called Fock states, which satisfy

$$\hat{a}^\dagger\hat{a}|n\rangle = n|n\rangle, \tag{3.20}$$

where $n$ is a non-negative integer of the photon number. The Fock states are schematically shown in Fig. 3.4.

The annihilation and creation operators literally decrease and increase the photon number of the Fock state as

$$|n-1\rangle = \frac{1}{\sqrt{n}}\hat{a}|n\rangle, \quad |n+1\rangle \ = \frac{1}{\sqrt{n+1}}\hat{a}^\dagger|n\rangle. \tag{3.21}$$

The ground state with a photon number of zero is called the vacuum state, which satisfies $\hat{a}|0\rangle = 0$. An arbitrary Fock state can be generated from the vacuum state with repeated application of the creation operator as

$$|n\rangle = \frac{\hat{a}^{\dagger n}}{\sqrt{n!}}|0\rangle. \tag{3.22}$$

The set of eigenstates $|n\rangle$ is the complete orthogonal basis, which satisfies

$$\langle n|n'\rangle = \delta_{n,n'}, \quad \sum_{n=0}^{\infty}|n\rangle\langle n| = \hat{1}, \tag{3.23}$$

where $\hat{1}$ is the identity operator. In other words, an arbitrary quantum state $|\Psi\rangle$ in the single harmonic oscillator is represented in the Fock basis as

$$|\Psi\rangle = \sum_{n=0}^{\infty}\langle n|\Psi\rangle|n\rangle = \sum_{n=0}^{\infty}\Psi_n|n\rangle, \tag{3.24}$$

$\Psi_n = \langle n|\Psi\rangle$ is a complex value, which contains complete information about the pure quantum state. From the normalization condition, $\Psi_n$ ensures that

$$\sum_{n=0}^{\infty}|\Psi_n|^2 = 1. \tag{3.25}$$

The occupation probability in the Fock basis is described as

$$P_n = |\Psi_n|^2, \tag{3.26}$$

which is called the photon-number distribution. Although it does not contain phase information in the quantum state, the photon-number distribution is sometimes used for characterization of the quantum nature of the state in the harmonic oscillator.

### 3.2.2 Quadrature basis

The amplitude associated with quadrature operators of $\hat{x}$ and $\hat{p}$ can be measured by a quantum-limited electromagnetic field detector, which is realized by the homodyne or heterodyne scheme in quantum optics [54, 57].

By using the rotation operator $\hat{R}(\theta) = e^{-i\theta\hat{a}^\dagger\hat{a}}$, we can generalize the quadrature operators $\hat{x}$ and $\hat{p}$ as

$$\begin{aligned}\hat{x}_\theta &= \hat{R}^\dagger(\theta)\,\hat{x}\,\hat{R}(\theta) = \hat{x}\cos\theta + \hat{p}\sin\theta = \frac{\hat{a}e^{-i\theta} + \hat{a}^\dagger e^{i\theta}}{\sqrt{2}} \\ \hat{p}_\theta &= \hat{R}^\dagger(\theta)\,\hat{p}\,\hat{R}(\theta) = -\hat{x}\sin\theta + \hat{p}\cos\theta = \frac{\hat{a}e^{-i\theta} - \hat{a}^\dagger e^{i\theta}}{\sqrt{2}i},\end{aligned} \tag{3.27}$$

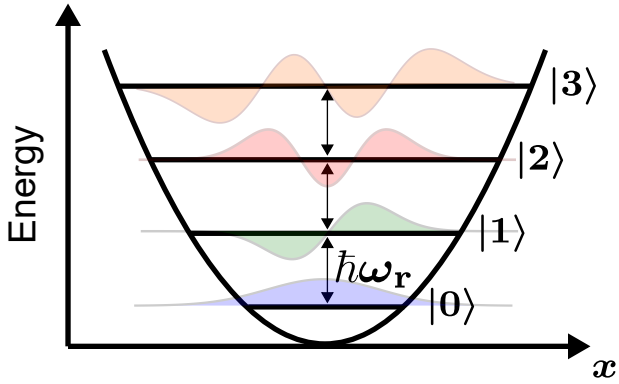


Figure 3.4: Energy levels and energy eigenstates (Fock states) of the single harmonic oscillator. The eigenstates are depicted by the wave functions plotted on the corresponding energy levels.

where $[\hat{x}_\theta, \hat{p}_\theta] = i$. From this definition, we find that these operators can be understood as the real and imaginary part of $\hat{a}e^{-i\theta} = \hat{R}^\dagger(\theta)\,\hat{a}\,\hat{R}(\theta)$:

$$\hat{a}e^{-i\theta} = \frac{\hat{x}_\theta + i\hat{p}_\theta}{\sqrt{2}}. \tag{3.28}$$

The eigenstates of the quadrature operators $\hat{x}_\theta$ satisfies

$$\hat{x}_\theta|x,\theta\rangle = x|x,\theta\rangle, \tag{3.29}$$

where $x$ is the eigenvalue. The set of these eigenstates is the complete orthogonal basis, which satisfies

$$\langle x,\theta|x',\theta\rangle = \delta(x-x'), \quad \int_{-\infty}^{\infty} dx\, |x,\theta\rangle\langle x,\theta| = \hat{1} \tag{3.30}$$

Therefore, we can represent an arbitrary quantum state as

$$|\Psi\rangle = \int_{-\infty}^{\infty} dx\, \langle x,\theta|\Psi\rangle|x,\theta\rangle = \int_{-\infty}^{\infty} dx_\theta\, \Psi_\theta(x)|x,\theta\rangle \tag{3.31}$$

where $\Psi_\theta(x) = \langle x,\theta|\Psi\rangle$ is called wave function. Note that the wave function satisfies the normalization condition

$$\int_{-\infty}^{\infty} dx\, |\Psi_\theta(x)|^2 = 1. \tag{3.32}$$

Thus, the probability density of the measurement outcome of the quadrature with $\theta$ is described as

$$P_\theta(x) = |\Psi_\theta(x)|^2. \tag{3.33}$$

The quadrature distribution is observed to reconstruct a quantum state in the harmonic oscillator via Wigner quantum state tomography.

Here, we consider the eigenstate of $\hat{x}_\theta$. First, the eigenstate of the original quadrature operator of $\hat{x}$ is given by

$$\hat{x}|x\rangle = x|x\rangle. \tag{3.34}$$

Using the unitary rotation operator, the equation is deformed as

$$\begin{aligned} \hat{R}^\dagger(\theta)\hat{x}\hat{R}(\theta)\hat{R}^\dagger(\theta)|x\rangle &= x\hat{R}^\dagger(\theta)|x\rangle \\ \hat{x}_\theta\hat{R}^\dagger(\theta)|x\rangle &= x\hat{R}^\dagger(\theta)|x\rangle. \end{aligned} \tag{3.35}$$

Then, we find $\hat{R}^\dagger(\theta)|x\rangle$ is the eigenstate of $\hat{x}_\theta$ with the eigenvalue of $x$. Therefore, we have

$$|x,\theta\rangle = \hat{R}^\dagger(\theta)|x\rangle. \tag{3.36}$$

This relation is used for the maximum likelihood reconstruction of a quantum state in the harmonic oscillator.

## 3.3 Wigner function

From the quadrature measurement of $\hat{x}_\theta$, we can obtain a quadrature distribution $P_\theta(x)$. As we will see later, the set of the distributions $P_\theta(x)$ in the various phases contains the complete information about a quantum state of a single harmonic oscillator. In other words, the set of distributions has one-to-one correspondence to the density matrix of the quantum state. However, the set of the distributions is not representable easily and not understandable intuitively. Then, we define a quasi-probability distribution $W(x,\, p)$ on the two-dimensional plane, which is called a Wigner function. One of the important properties is that the marginal distribution of $x_\theta$ (the distribution obtained by the integral of $W(x,\, p)$ with respect to the orthogonal quadrature $p_\theta$) corresponds to the distribution $P_\theta(x)$. Therefore, the Wigner function is well associated with the quadrature measurements and is easy to use in order to imagine how the quantum state is represented.

### 3.3.1 Definition and properties

A Wigner function $W(x,p)$ is a quasi-probability distribution in phase space (quadrature space). First, we define the characteristic function for a density matrix $\hat{\rho}$ as

$$\mathcal{W}(u,v) = \frac{1}{2\pi}\mathrm{Tr}\left[\hat{\rho}\, e^{-iu\hat{x}-iv\hat{p}}\right]. \tag{3.37}$$

The definition can be understood intuitively as a kind of Fourier transform of the density matrix $\hat{\rho}$ with the quadrature operators $\hat{x}$ and $\hat{p}$.

Then, the Wigner function is defined as the inverse Fourier transform of the characteristic function:

$$W(x,p) = \frac{1}{2\pi}\iint_{-\infty}^{\infty} dudv\, \mathcal{W}(u,v)e^{iux+ivp}, \tag{3.38}$$

or

$$W(x,p) = \frac{1}{4\pi^2}\iint_{-\infty}^{\infty} dudv\, \mathrm{Tr}\left[\hat{\rho}\, e^{-iu\hat{x}-iv\hat{p}}\right] e^{iux+ivp}. \tag{3.39}$$

The characteristic function is also obtained from a Fourier transform of the Wigner function as

$$\mathcal{W}(u,v) = \frac{1}{2\pi}\iint_{-\infty}^{\infty} dxdp\, W(x,p)e^{-iux-ivp}. \tag{3.40}$$

#### Coordinate transformation

We consider the coordinate transformation of the Wigner function $W(x,p)$. Here, we represent $W(x,p)$ with a new coordinate system $(\bar{x},\, \bar{p})$ which is described as

$$\begin{aligned} \bar{\boldsymbol{x}} &= \boldsymbol{A}\boldsymbol{x} + \boldsymbol{b} \\ \boldsymbol{x} &= \boldsymbol{A}^{-1}(\bar{\boldsymbol{x}} - \boldsymbol{b}), \end{aligned} \tag{3.41}$$

where $\boldsymbol{x}^{\mathrm{T}} = (x\ \ p)$, $\bar{\boldsymbol{x}}^{\mathrm{T}} = (\bar{x}\ \ \bar{p})$, $\boldsymbol{A}$ is the $2 \times 2$ real matrix describing the scaling and rotation, and $\boldsymbol{b}$ is the real column vector describing the displacement. The coordinate

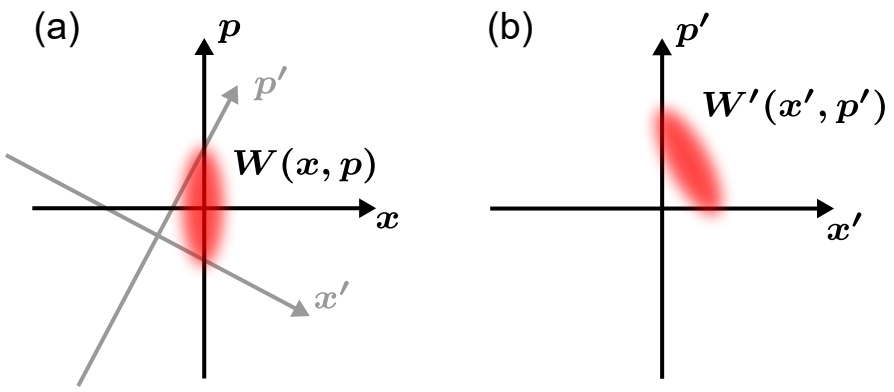


Figure 3.5: Coordinate transformation of Wigner function. (a) Wigner function represented in the coordinate system $(x,\, p)$. The coordinate system $(\bar{x},\, \bar{p})$ is shown at the same time. (b) Wigner function represented in the coordinate system $(\bar{x},\, \bar{p})$.

transformation given by the matrix $\boldsymbol{A}$ and the vector $\boldsymbol{b}$ is called an Affine transformation. Here, we assume that the coordinate transformation is consistent with the unitary operation in the Heisenberg picture:

$$\begin{aligned} \hat{\bar{\boldsymbol{x}}} &= \hat{U}^\dagger \hat{\boldsymbol{x}} \hat{U} = \boldsymbol{A}\hat{\boldsymbol{x}} + \boldsymbol{b} \\ \hat{\boldsymbol{x}} &= \hat{U} \hat{\bar{\boldsymbol{x}}} \hat{U}^\dagger = \boldsymbol{A}^{-1}(\hat{\bar{\boldsymbol{x}}} - \boldsymbol{b}), \end{aligned} \tag{3.42}$$

where $\hat{\boldsymbol{x}}^{\mathrm{T}} = (\hat{x}\ \hat{p})$, $\hat{\bar{\boldsymbol{x}}}^{\mathrm{T}} = (\hat{\bar{x}}\ \hat{\bar{p}})$, and $\hat{U}$ is the unitary operator. Note that the Affine transformation corresponds to the unitary operation whose generator (Hamiltonian) is composed of up to the second order of the annihilation and creation operators. As schematically shown in Figs. 3.5(a) and (b), the Wigner function in the coordinate system $(\bar{x},\, \bar{p})$ is represented by

$$\bar{W}(\bar{x}, \bar{p}) = W(x, p). \tag{3.43}$$

Note that the coordinate system $(x,\, p)$ is represented as a function of $\bar{x}$ and $\bar{p}$ from Eq. (3.41).

Here, we will derive the Wigner function $\bar{W}(\bar{x}, \bar{p})$ from the density matrix $\hat{\rho}$ using the transformed quadrature operators $\hat{\bar{x}}$, $\hat{\bar{p}}$. First of all, the Wigner function in the coordinate system $(x,\, p)$ can be written as

$$\begin{aligned} W(x,p) &= \frac{1}{4\pi^2} \iint_{-\infty}^{\infty} du dv\ \mathrm{Tr}\left[\hat{\rho}\, e^{-i\boldsymbol{u}^{\mathrm{T}}\hat{\boldsymbol{x}}}\right] e^{i\boldsymbol{u}^{\mathrm{T}}\boldsymbol{x}} \\ &= \frac{1}{4\pi^2} \iint_{-\infty}^{\infty} du dv\ \mathrm{Tr}\left[\hat{\rho}\, e^{-i\boldsymbol{u}^{\mathrm{T}}\hat{\boldsymbol{x}}}\right] e^{i\boldsymbol{u}^{\mathrm{T}}\boldsymbol{A}^{-1}(\bar{\boldsymbol{x}}-\boldsymbol{b})} \\ &= \frac{1}{4\pi^2} \iint_{-\infty}^{\infty} d\bar{u} d\bar{v}\ \det(\mathcal{J})\ \mathrm{Tr}\left[\hat{\rho}\, e^{-i\bar{\boldsymbol{u}}^{\mathrm{T}}(\boldsymbol{A}\hat{\boldsymbol{x}}+\boldsymbol{b})}\right] e^{i\bar{\boldsymbol{u}}^{\mathrm{T}}\bar{\boldsymbol{x}}} \\ &= \frac{1}{4\pi^2} \iint_{-\infty}^{\infty} d\bar{u} d\bar{v}\ \mathrm{Tr}\left[\hat{\rho}\, e^{-i\bar{\boldsymbol{u}}^{\mathrm{T}}\hat{\bar{\boldsymbol{x}}}}\right] e^{i\bar{\boldsymbol{u}}^{\mathrm{T}}\bar{\boldsymbol{x}}}, \end{aligned} \tag{3.44}$$

where $\boldsymbol{u}^{\mathrm{T}} = (u\ \ v)$ and $\bar{\boldsymbol{u}}^{\mathrm{T}} = (\bar{u}\ \ \bar{v})$. Here, we define $\bar{\boldsymbol{u}} = (\boldsymbol{A}^{-1})^{\mathrm{T}}\boldsymbol{u}$. Note that the determinant of the Jacobian matrix from $(u,\, v)$ to $(\bar{u},\, \bar{v})$ is unity $\det(\mathcal{J}) = 1$, as long as the coordinate transformation is consistent with the unitary operation of the quadrature operators. From the Eqs. (3.43) and (3.44), we find the Wigner function $\bar{W}(\bar{x}, \bar{p})$ can be

derived from the density matrix $\hat{\rho}$ using the corresponding quadrature operators $\hat{\bar{x}}$ and $\hat{\bar{p}}$ as

$$\bar{W}(\bar{x},\bar{p}) = \frac{1}{4\pi^2}\iint_{-\infty}^{\infty} d\bar{u}d\bar{v}\,\mathrm{Tr}\left[\hat{\rho}\,e^{-i\bar{\boldsymbol{u}}^{\mathrm{T}}\hat{\bar{\boldsymbol{x}}}}\right]e^{i\bar{\boldsymbol{u}}^{\mathrm{T}}\bar{\boldsymbol{x}}}. \tag{3.45}$$

Note that the Wigner function $\bar{W}(\bar{x},\bar{p})$ is obtained in the same way as in Eq. (3.39).

Finally, we will study the effect of the coordinate transformation of the Wigner function on the corresponding characteristic function. The characteristic function $\bar{\mathcal{W}}(\bar{u},\bar{v})$ is obtained by the Fourier transformation of the Wigner function $\bar{W}(\bar{x},\bar{p})$ as

$$\bar{\mathcal{W}}(\bar{u},\bar{v}) = \frac{1}{2\pi}\iint_{-\infty}^{\infty} d\bar{x}d\bar{p}\,\bar{W}(\bar{x},\bar{p})e^{-i\bar{u}\bar{x}-i\bar{v}\bar{p}}. \tag{3.46}$$

It is also given by

$$\bar{\mathcal{W}}(\bar{u},\bar{v}) = \frac{1}{2\pi}\,\mathrm{Tr}\left[\hat{\rho}\,e^{-i\bar{\boldsymbol{u}}^{\mathrm{T}}\hat{\bar{\boldsymbol{x}}}}\right]. \tag{3.47}$$

Using the transformation relation in Eq. (3.42), this is deformed as

$$\begin{aligned}
\bar{\mathcal{W}}(\bar{u},\bar{v}) &= \frac{1}{2\pi}\,\mathrm{Tr}\left[\hat{\rho}\,e^{-i\bar{\boldsymbol{u}}^{\mathrm{T}}\hat{\bar{\boldsymbol{x}}}}\right] \\
&= \frac{1}{2\pi}\,\mathrm{Tr}\left[\hat{\rho}\,e^{-i\bar{\boldsymbol{u}}^{\mathrm{T}}(\boldsymbol{A}\hat{\boldsymbol{x}}+\boldsymbol{b})}\right] \\
&= e^{-i\boldsymbol{u}^{\mathrm{T}}\boldsymbol{b}}\,\frac{1}{2\pi}\,\mathrm{Tr}\left[\hat{\rho}\,e^{-i\boldsymbol{u}^{\mathrm{T}}\hat{\boldsymbol{x}}}\right] \\
&= e^{-i\boldsymbol{u}^{\mathrm{T}}\boldsymbol{b}}\,\mathcal{W}(u,v).
\end{aligned} \tag{3.48}$$

Therefore, we find the coordinate transformation of the Wigner function results in the coordinate transformation and the sinusoidal modulations of the characteristic function.

### Integral representation

We will obtain another representation of the Wigner function. Here, the Wigner function is represented by the coordinate system ($\bar{x}$, $\bar{p}$) for generality. The characteristic function $\bar{\mathcal{W}}(\bar{u},\bar{v})$ in Eq. (3.47) is transformed as

$$\begin{aligned}
\bar{\mathcal{W}}(\bar{u},\bar{v}) &= \frac{1}{2\pi}\,\mathrm{Tr}\left[\hat{\rho}\,e^{-i\bar{u}\hat{\bar{x}}-i\bar{v}\hat{\bar{p}}}\right] \\
&= \frac{1}{2\pi}e^{\frac{-i\bar{u}\bar{v}}{2}}\,\mathrm{Tr}\left[\hat{\rho}\,e^{-i\bar{u}\hat{\bar{x}}}e^{-i\bar{v}\hat{\bar{p}}}\right]\ (\because \text{CBH Lemma}) \\
&= \frac{1}{2\pi}e^{\frac{-i\bar{u}\bar{v}}{2}}\,\mathrm{Tr}\left[e^{-i\frac{\bar{v}\hat{\bar{p}}}{2}}\hat{\rho}\,e^{-i\bar{u}\hat{\bar{x}}}e^{-i\frac{\bar{v}\hat{\bar{p}}}{2}}\right] \\
&= \frac{1}{2\pi}e^{\frac{-i\bar{u}\bar{v}}{2}}\int d\bar{\xi}\,\langle\bar{\xi}|e^{-i\frac{\bar{v}\hat{\bar{p}}}{2}}\hat{\rho}\,e^{-i\bar{u}\hat{\bar{x}}}e^{-i\frac{\bar{v}\hat{\bar{p}}}{2}}|\bar{\xi}\rangle \\
&= \frac{1}{2\pi}e^{\frac{-i\bar{u}\bar{v}}{2}}\int d\bar{\xi}\,\langle\bar{\xi}-\bar{v}/2|\hat{\rho}\,e^{-i\bar{u}\hat{\bar{x}}}|\bar{\xi}+\bar{v}/2\rangle\ (\because \text{Displacement}) \\
&= \frac{1}{2\pi}\int d\bar{\xi}\,e^{-i\bar{u}\bar{\xi}}\langle\bar{\xi}-\bar{v}/2|\hat{\rho}|\bar{\xi}+\bar{v}/2\rangle,
\end{aligned} \tag{3.49}$$

where $|\bar{\xi}\rangle$ is the eigenstate of the quadrature operator $\hat{\bar{x}}$. Then, the Wigner function in the coordinate system $(\bar{x},\, \bar{p})$ is obtained through the inverse Fourier transformation as

$$\begin{aligned}\bar{W}(\bar{x},\bar{p}) &= \frac{1}{2\pi}\iint_{-\infty}^{\infty} d\bar{u}d\bar{v}\,\bar{\mathcal{W}}(\bar{u},\bar{v})e^{i\bar{u}\bar{x}+i\bar{v}\bar{p}} \\ &= \frac{1}{4\pi^2}\iint_{-\infty}^{\infty} d\bar{u}d\bar{v}\int_{-\infty}^{\infty} d\bar{\xi}\, e^{i\bar{u}(\bar{x}-\bar{\xi})+i\bar{v}\bar{p}}\langle\bar{\xi}-\bar{v}/2|\rho|\bar{\xi}+\bar{v}/2\rangle \\ &= \frac{1}{4\pi^2}\iint_{-\infty}^{\infty} d\bar{v}d\bar{\xi}\, 2\pi\delta(\bar{x}-\bar{\xi})e^{i\bar{v}\bar{p}}\langle\bar{\xi}-\bar{v}/2|\rho|\bar{\xi}+\bar{v}/2\rangle \\ &= \frac{1}{2\pi}\int_{-\infty}^{\infty} d\bar{v}\, e^{i\bar{v}\bar{p}}\langle\bar{x}-\bar{v}/2|\rho|\bar{x}+\bar{v}/2\rangle.\end{aligned} \tag{3.50}$$

This is the integral representation of the Wigner function.

**Radon transformation (Marginal distribution)**

The integral transformation of a function with respect to one axis on a two-dimensional plane is called Radon transformation. Therefore, the marginal distribution of a Wigner function corresponds to the Radon transformation of the Wigner function. Then, one of the important properties of the Wigner function is that the marginal distribution of a Wigner function corresponds to the distribution of the outcomes from quadrature measurements.

Suppose that the coordinate system $(x_\theta,\, p_\theta)$ is rotated by $\phi$ with respect to the coordinate system $(x,\, p)$. The corresponding quadrature operators $\hat{x}_\theta$ and $\hat{p}_\theta$ are described by the rotation operation of the original quadrature operators $\hat{x}$ and $\hat{p}$:

$$\begin{pmatrix}\hat{x}_\theta \\ \hat{p}_\theta\end{pmatrix} = \begin{pmatrix}\hat{R}^\dagger(\theta)\,\hat{x}\,\hat{R}(\theta) \\ \hat{R}^\dagger(\theta)\,\hat{p}\,\hat{R}(\theta)\end{pmatrix} = \begin{pmatrix}\cos\theta & \sin\theta \\ -\sin\theta & \cos\theta\end{pmatrix}\begin{pmatrix}\hat{x} \\ \hat{p}\end{pmatrix}. \tag{3.51}$$

As schematically shown in Fig. 3.6(a), from Eq. (3.45), the Wigner function in the coordinate system $(x_\theta,\, p_\theta)$, or the Wigner function $W(x,p)$ which is rotated by $-\theta$, is written as

$$W_{-\theta}(x_\theta,p_\theta) = \frac{1}{4\pi^2}\iint_{-\infty}^{\infty} du_\theta dv_\theta\,\mathrm{Tr}\left[\hat{\rho}\, e^{-iu_\theta\hat{x}_\theta - v_\theta\hat{p}_\theta}\right] e^{iu_\theta x_\theta + iv_\theta p_\theta}, \tag{3.52}$$

where

$$\begin{pmatrix}x_\theta \\ p_\theta\end{pmatrix} = \begin{pmatrix}\cos\theta & \sin\theta \\ -\sin\theta & \cos\theta\end{pmatrix}\begin{pmatrix}x \\ p\end{pmatrix}. \tag{3.53}$$

As shown in Eq. (3.50), the integral representation writes

$$W_{-\theta}(x_\theta,p_\theta) = \frac{1}{2\pi}\int_{-\infty}^{\infty} dv_\theta\, e^{iv_\theta p_\theta}\langle x_\theta - v_\theta/2,\theta|\rho|x_\theta + v_\theta/2,\theta\rangle, \tag{3.54}$$

where $|x,\theta\rangle$ is an eigenstate of $\hat{x}_\theta$ with a eigenvalue of $x$. Then, we can easily calculate the integral of the Wigner function with respect to $p_\theta$ as

$$\begin{aligned}\int dp_\theta\, W_{-\theta}(x_\theta,p_\theta) &= \frac{1}{2\pi}\iint_{-\infty}^{\infty} dv_\theta dp_\theta\, e^{iv_\theta p_\theta}\langle x_\theta - v_\theta/2,\theta|\rho|x_\theta + v_\theta/2,\theta\rangle \\ &= \frac{1}{2\pi}\int_{-\infty}^{\infty} dv_\theta\, 2\pi\delta(v_\theta)\langle x_\theta - v_\theta/2,\theta|\rho|x_\theta + v_\theta/2,\theta\rangle \\ &= \langle x_\theta,\theta|\rho|x_\theta,\theta\rangle \\ &= P_\theta(x_\theta).\end{aligned} \tag{3.55}$$

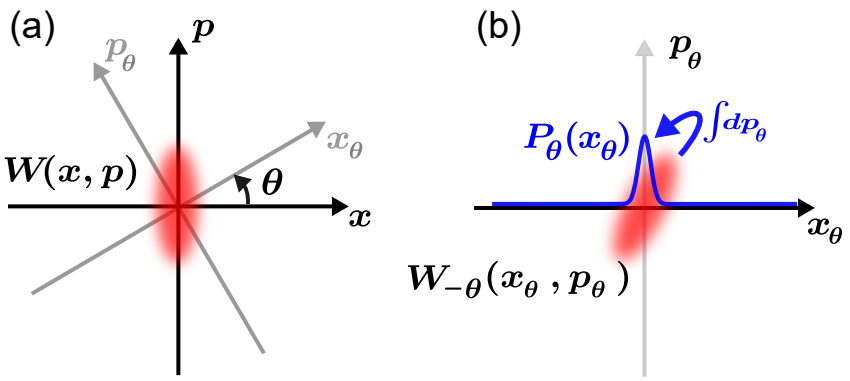


Figure 3.6: Wigner function $W(x,p)$ and quadrature distribution $P_\theta(x)$. (a) Wigner function represented in the coordinate system $(x,p)$. The coordinate system $(x_\theta, p_\theta)$ rotated by $-\theta$ is shown on the same plot. (b) Wigner function represented in the coordinate system $(x_\theta,\ p_\theta)$. The blue line is the quadrature distribution $P_\theta(x)$ or the marginal distribution obtained by the integral of the Wigner function $W_{-\theta}(x_\theta, p_\theta)$ with respect to $p_\theta$.

As schematically shown in Fig. 3.6(b), from this calculation, we confirm that the marginal distribution of the Wigner function corresponds to the quadrature distribution $P_\theta(x_\theta)$. This property of the Wigner function gives us the intuitive understanding of the density matrix $\rho$ from the viewpoint of the quadrature measurements.

### Inverse Radon transformation

As discussed in the previous section, we can obtain the quadrature distribution by the Radon transformation of the Wigner function. On the other hand, we will find the Wigner function can be reconstructed from the set of the quadrature distributions at various phases, which is called inverse Radon transformation. Since the Wigner function exactly corresponds to the density matrix of a single harmonic oscillator, we can perform quantum state tomography by measuring the quadratures at various phases.

From the definition in Eq. (3.40), the characteristic function can be represented as

$$\begin{aligned} W(x,p) &= \frac{1}{2\pi}\iint_{-\infty}^{\infty} du dv\, \mathcal{W}(u,v) e^{iux+ivp} \\ &= \int_0^\infty dk \int_0^{2\pi} d\theta\, k\mathcal{W}(k\cos\theta, k\sin\theta) e^{ik(x\cos\theta + p\sin\theta)}, \end{aligned} \tag{3.56}$$

where the integral is represented with the polar coordinate system ($u = k\cos\theta$, $v = k\sin\theta$). Note that $dudv = 2\pi k\, dkd\theta$. From Eq. (3.48), the characteristic function can be represented in the coordinate system $(u_\theta,\ v_\theta)$ as

$$\mathcal{W}(u,v) = \mathcal{W}_{-\theta}(u_\theta, v_\theta), \tag{3.57}$$

where

$$\begin{pmatrix} u_\theta \\ v_\theta \end{pmatrix} = \begin{pmatrix} \cos\theta & \sin\theta \\ -\sin\theta & \cos\theta \end{pmatrix} \begin{pmatrix} u \\ v \end{pmatrix}. \tag{3.58}$$

Note that the coordinate transformation between $(u,\ v)$ and $(u_\theta,\ v_\theta)$ corresponds to that between $(x,\ p)$ and $(x_\theta,\ p_\theta)$ in the case of the rotation operation. Using the coordinate

transformation, the Wigner function in Eq. (3.56) can be written as

$$W(x,p) = \int_0^\infty dk \int_0^{2\pi} d\theta \; k\mathcal{W}_{-\theta}(k,0)e^{ik(x\cos\theta + p\sin\theta)}. \tag{3.59}$$

By changing the integration interval, the Wigner function can be represented as

$$W(x,p) = \int_{-\infty}^\infty dk \int_0^{\pi} d\theta \; |k|\mathcal{W}_{-\theta}(k,0)e^{ik(x\cos\theta + p\sin\theta)}, \tag{3.60}$$

where we use that $\mathcal{W}_{-\theta+\pi}(-k,0) = \mathcal{W}_{-\theta}(k,0)$.

Using Eq. (3.55), the Fourier transform of the quadrature distribution of $P_\theta(x)$ can be calculated as

$$\begin{aligned}\mathcal{P}_\theta(k) &= \frac{1}{\sqrt{2\pi}} \int_{-\infty}^\infty dx_\theta \; P_\theta(x)e^{-ikx_\theta} \\ &= \frac{1}{\sqrt{2\pi}} \iint dx_\theta dp_\theta \; W_{-\theta}(x_\theta, p_\theta)e^{-ikx_\theta} \\ &= \sqrt{2\pi}\mathcal{W}_{-\theta}(k,0),\end{aligned} \tag{3.61}$$

where we use the fact that the characteristic function in the coordinate system $(u_\theta,\, v_\theta)$ is defined by

$$\mathcal{W}_{-\theta}(u_\theta, v_\theta) = \frac{1}{2\pi} \iint_{-\infty}^\infty dx_\theta dv_\theta \; W_{-\theta}(x_\theta, p_\theta)e^{-iu_\theta x_\theta - iv_\theta p_\theta}. \tag{3.62}$$

From Eqs. (3.60) and (3.61), the Wigner function can be represented with $\mathcal{P}_\theta(k)$ as

$$\begin{aligned}W(x,p) &= \frac{1}{\sqrt{2\pi}} \int_{-\infty}^\infty dk \int_0^{\pi} d\theta \; |k|\mathcal{P}_\theta(k)e^{ik(x\cos\theta + p\sin\theta)} \\ &= \int_0^{\pi} d\theta \left[\frac{1}{\sqrt{2\pi}} \int_{-\infty}^\infty dk \; |k|\mathcal{P}_\theta(k)e^{ik(x\cos\theta + p\sin\theta)}\right] \\ &= \int_0^{\pi} d\theta \; H_\theta(x\cos\theta + p\sin\theta),\end{aligned} \tag{3.63}$$

where we define the high-pass filtered quadrature distribution as

$$H_\theta(x) = \frac{1}{\sqrt{2\pi}} \int_{-\infty}^\infty dk \; |k|\mathcal{P}_\theta(k)e^{ikx}. \tag{3.64}$$

This is the inverse transform of the quadrature distribution with the high-pass filter function of $|k|$. Using a convolution integral, $H_\theta(x)$ can also be described in terms of the observable quadrature distribution as

$$H_\theta(x) = \int_{-\infty}^\infty dx' \; P_\theta(x')K(x\_x'), \tag{3.65}$$

where $K(x') = \frac{1}{\sqrt{2\pi}} \int_{-\infty}^\infty dk \; |k|e^{-ikx'}$ is the inverse transformation of the filter function.

From these calculations, we find the Wigner function can be calculated by integrating the high-pass filtered quadrature distributions with respect to the various phases. The quantum state tomography of a single harmonic oscillator from the set of the quadrature distributions is called Wigner tomography.

### Notable properties

#### Real function

The Wigner function is a real function, which is confirmed by the definition:

$$\begin{aligned} W^*(x,p) &= \frac{1}{2\pi}\int_{-\infty}^{\infty} dv\, e^{-ivp}\langle x+v/2|\rho|x-v/2\rangle \\ &= \frac{1}{2\pi}\int_{-\infty}^{\infty} dv\, e^{ivp}\langle x-v/2|\rho|x+v/2\rangle \\ &= W(x,p), \end{aligned} \tag{3.66}$$

where we use the variable transformation of $v \to -v$ in the second row.

#### Normalization condition

From the integral representation of Eq. (3.50), we can easily confirm that the Wigner function of the density matrix is normalized in the two-dimensional plane:

$$\iint dxdp\, W(x,p) = \mathrm{Tr}\,[\hat{\rho}] = 1. \tag{3.67}$$

#### Product

We can define the Wigner function of any operator, rather than a density matrix. For example, we consider the Wigner functions $W_1(x,p)$ and $W_2(x,p)$ which are derived from the operators $\hat{O}_1$ and $\hat{O}_2$, respectively.

Then, the trace of the product of these operators can be calculated with the product of Wigner functions as

$$\begin{aligned} &\mathrm{Tr}[\hat{O}_1\,\hat{O}_2] \\ &= \iint dx'\,\langle x'|\hat{O}_1\,\hat{O}_2|x'\rangle \\ &= \iint dxdv\,\langle x-v/2|\hat{O}_1|x+v/2\rangle\langle x+v/2|\hat{O}_2|x-v/2\rangle \\ &= \frac{1}{2\pi}\iint dxdp \iint dvdv'\, e^{ip(v+v')}\langle x-v/2|\hat{O}_1|x+v/2\rangle\langle x-v'/2|\hat{O}_2|x+v'/2\rangle \\ &= 2\pi\iint_{-\infty}^{\infty} dxdp\, W_1(x,p)W_2(x,p). \end{aligned} \tag{3.68}$$

Therefore, we can calculate the expectation value of an operator $\hat{O}$ for the density matrix $\hat{\rho}$, i.e., $\mathrm{Tr}\left[\hat{\rho}\,\hat{O}\right]$. We also calculate the state fidelity of the density matrix $\hat{\rho}$ to a pure state $|\Psi\rangle$, i.e., $\mathrm{Tr}\,[\hat{\rho}|\Psi\rangle\langle\Psi|]$.

#### Completeness

We will confirm that the Wigner function has one-to-one correspondence to the density matrix $\hat{\rho}$. Using the Fock basis, the density matrix is described by $\hat{\rho} = \sum_{n,m}\rho_{nm}|n\rangle\langle m|$. We can define the Wigner function $W_{nm}(x,p)$ from the operator $|n\rangle\langle m|$. Then, $\rho_{nm}$ is calculated from the product integral of the Wigner functions:

$$\begin{aligned} \rho_{nm} &= \langle n|\hat{\rho}|m\rangle \\ &= \mathrm{Tr}\,[\hat{\rho}|m\rangle\langle n|] \\ &= 2\pi\iint_{-\infty}^{\infty} dxdp\, W(x,p)W_{mn}(x,p). \end{aligned} \tag{3.69}$$

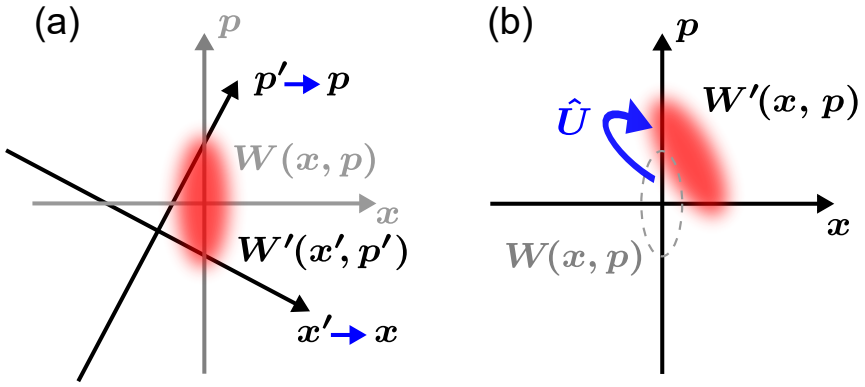


Figure 3.7: Effect of unitary operation on Wigner function. (a) Wigner function represented in the coordinate systems $(x,\ p)$ and $(x',\ p')$. The Wigner function transformed by the unitary operation $\hat{U}$ is obtained by replacing $x'$and $p'$ with $x$ and $p$ in the Wigner function represented in the coordinate system $(x',\ p')$. (b) Wigner function transformed by the unitary operator $\hat{U}$.

This means that we can reconstruct the density matrix $\hat{\rho}$ from the Wigner function $W(x,p)$ and that the Wigner function has complete information about the density matrix $\hat{\rho}$.

### Unitary operation

Here, we discuss how the Wigner function is transformed by the unitary operator $\hat{U}$, or how the Wigner function acts on the density matrix $\hat{\rho}' = \hat{U}\hat{\rho}\hat{U}^\dagger$.

Suppose that the generator of the unitary operator $\hat{U}$ is composed of up to the second order of $\hat{a}$ and $\hat{a}^\dagger$. Then, the quadrature operators transformed in the Heisenberg picture correspond to the Affine transformation [58] as

$$\begin{aligned} \hat{\boldsymbol{x}}' &= \hat{U}^\dagger \hat{x} \hat{U} = \boldsymbol{A}\hat{\boldsymbol{x}} + \boldsymbol{b} \\ \hat{\boldsymbol{x}} &= \hat{U}\hat{x}'\hat{U}^\dagger = \boldsymbol{A}^{-1}(\hat{\boldsymbol{x}} - \boldsymbol{b}), \end{aligned} \tag{3.70}$$

where $\hat{\boldsymbol{x}}'^{\mathrm{T}} = (\hat{x}'\ \ \hat{p}')$, $\hat{\boldsymbol{x}}^{\mathrm{T}} = (\hat{x}\ \ \hat{p})$, $\boldsymbol{A}$ is a $2\times 2$ real matrix, and $\boldsymbol{b}$ is a real vertical vector. From its definition, the transformed Wigner function $W'(x,p)$ can be described as

$$\begin{aligned} W'(x,p) &= \frac{1}{4\pi^2}\iint_{-\infty}^{\infty} du dv\ \mathrm{Tr}\left[\hat{\rho}'\, e^{-i\boldsymbol{u}^{\mathrm{T}}\hat{\boldsymbol{x}}}\right] e^{i\boldsymbol{u}^{\mathrm{T}}\boldsymbol{x}} \\ &= \frac{1}{4\pi^2}\iint_{-\infty}^{\infty} du dv\ \mathrm{Tr}\left[\hat{U}\hat{\rho}\hat{U}^\dagger\, e^{-i\boldsymbol{u}^{\mathrm{T}}\hat{\boldsymbol{x}}}\right] e^{i\boldsymbol{u}^{\mathrm{T}}\boldsymbol{x}} \\ &= \frac{1}{4\pi^2}\iint_{-\infty}^{\infty} du dv\ \mathrm{Tr}\left[\hat{\rho}\, e^{-i\boldsymbol{u}^{\mathrm{T}}\hat{U}^\dagger\hat{\boldsymbol{x}}\hat{U}}\right] e^{i\boldsymbol{u}^{\mathrm{T}}\boldsymbol{x}} \\ &= \frac{1}{4\pi^2}\iint_{-\infty}^{\infty} du dv\ \mathrm{Tr}\left[\hat{\rho}\, e^{-i\boldsymbol{u}^{\mathrm{T}}\hat{\boldsymbol{x}}'}\right] e^{i\boldsymbol{u}^{\mathrm{T}}\boldsymbol{x}}. \end{aligned} \tag{3.71}$$

As discussed in Sec. 3.3.1, the Wigner function $W(x,p)$ can be represented in the coordinate system $(x',\ p')$ as

$$W(x,p) = W'(x',p') = \frac{1}{4\pi^2}\iint_{-\infty}^{\infty} du dv\ \mathrm{Tr}\left[\hat{\rho}\, e^{-i\boldsymbol{u}^{\mathrm{T}}\hat{\boldsymbol{x}}'}\right] e^{i\boldsymbol{u}^{\mathrm{T}}\boldsymbol{x}'}. \tag{3.72}$$

From Eqs. (3.71) and (3.72), we find that the Wigner function transformed by the unitary operator $\hat{U}$ is obtained by replacing $x'$and $p'$ with $x$ and $p$ in the initial Wigner function in the coordinate system ($x'$, $p'$). In other words, the unitary transformation of the Wigner function corresponds to the coordinate transformation, as schematically shown in Figs. 3.7(a) and (b). Mathematically, the Wigner function $W(x,p)$ transformed by the unitary operator $\hat{U}$ is described as

$$W'(x,p) = W(x',p'), \tag{3.73}$$

where the coordinate transformation is obtained from Eq. (3.70) as

$$\boldsymbol{x}' = \boldsymbol{A}^{-1}(\boldsymbol{x} - \boldsymbol{b}). \tag{3.74}$$

Note that the coordinate transformation between $\boldsymbol{x}$ and $\boldsymbol{x}'$ is the inverse transformation between the quadrature operators $\hat{\boldsymbol{x}}$ and $\hat{\boldsymbol{x}}'$, since we replace $x'$and $p'$ with $x$ and $p$ in the transformation.

## 3.4 Transformation of Wigner function

### 3.4.1 Rotation operation

As explained before, the rotation operator is defined as

$$\hat{R}(\theta) = \exp\left(-i\theta\, \hat{a}^\dagger \hat{a}\right), \tag{3.75}$$

which can be implemented by shifting a resonance frequency of a harmonic oscillator or changing the rotating frame.

In the Heisenberg picture, the annihilation operator transformed by the rotation operator is described as

$$\hat{a}' = \hat{R}^\dagger(\theta)\hat{a}\hat{R}(\theta) = \hat{a}e^{-i\theta}. \tag{3.76}$$

Therefore, the quadrature operators are transformed as

$$\begin{pmatrix} \hat{x}' \\ \hat{p}' \end{pmatrix} = \begin{pmatrix} \cos\theta & \sin\theta \\ -\sin\theta & \cos\theta \end{pmatrix} \begin{pmatrix} \hat{x} \\ \hat{p} \end{pmatrix}. \tag{3.77}$$

From the transformation of the quadrature operators, the transformed Wigner function can be calculated from Eqs. (3.73) and (3.74). Using the coordinate transformation given by

$$\begin{pmatrix} x' \\ p' \end{pmatrix} = \begin{pmatrix} \cos\theta & -\sin\theta \\ \sin\theta & \cos\theta \end{pmatrix} \begin{pmatrix} x \\ p \end{pmatrix}, \tag{3.78}$$

the Wigner function transformed by the rotation operator is described as

$$W'(x,p) = W(x',p') = W(x\cos\theta - p\sin\theta, x\sin\theta + p\cos\theta). \tag{3.79}$$

As schematically shown in Fig. (3.8), the rotation operation with $\hat{R}(\theta)$ corresponds to rotation of the Wigner function about the origin by $-\theta$ in quadrature space.

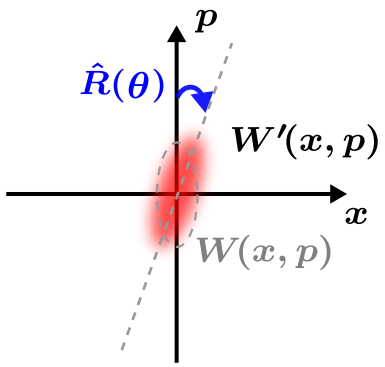


Figure 3.8: Rotation operation of Wigner function. The Wigner function is rotated about the origin by the rotation angle $-\theta$.

### 3.4.2 Displacement operation

A displacement operator is defined as

$$\hat{D}(\alpha) = \exp\left(\alpha\,\hat{a}^\dagger - \alpha^*\,\hat{a}\right), \tag{3.80}$$

which can be implemented by applying a resonant drive to a harmonic oscillator. Note that the rotating frame is set to be at the drive frequency.

In the Heisenberg picture, the annihilation operator transformed by the displacement operator is written as

$$\hat{a}' = \hat{D}^\dagger(\alpha)\hat{a}\hat{D}(\alpha) = \hat{a} + \alpha. \tag{3.81}$$

The transformed quadrature operators are calculated as

$$\begin{pmatrix} \hat{x}' \\ \hat{p}' \end{pmatrix} = \begin{pmatrix} \hat{x} + x_\alpha \\ \hat{p} + p_\alpha \end{pmatrix}, \tag{3.82}$$

where $x_\alpha$ and $p_\alpha$ are the real and imaginary parts of the complex amplitude, which are defined as

$$\alpha = \frac{x_\alpha + ip_\alpha}{\sqrt{2}}. \tag{3.83}$$

From the transformation of the quadrature operators, the transformed Wigner function can be calculated from Eqs. (3.73) and (3.74). Using the coordinate transformation given by

$$\begin{pmatrix} x' \\ p' \end{pmatrix} = \begin{pmatrix} x - x_\alpha \\ p - p_\alpha \end{pmatrix}, \tag{3.84}$$

the Wigner function transformed by the displacement operator is represented as

$$W'(x,p) = W(x',p') = W(x - x_\alpha, p - p_\alpha). \tag{3.85}$$

As schematically shown in Fig. (3.9), we can observe the displaced Wigner function in quadrature space.

### 3.4.3 Squeezing operation (Phase-sensitive amplification)

A squeezing operator is defined as

$$\hat{S}(r,\theta) = \exp\left[\frac{r}{2}\left(\hat{a}^{\dagger 2}e^{i2\theta} - \hat{a}^2 e^{-i2\theta}\right)\right], \tag{3.86}$$

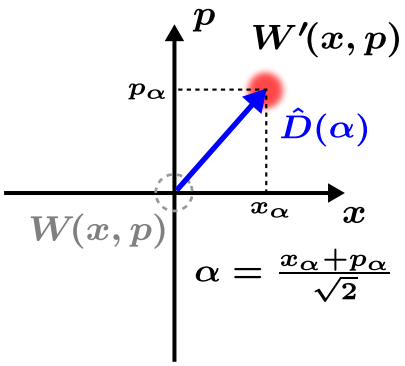


Figure 3.9: Displacement operation of Wigner function.

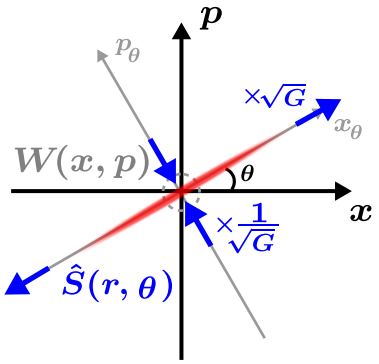


Figure 3.10: Squeezing operation of Wigner function. The Wigner function is squeezed and anti-squeezed in the $p_\theta$ and $x_\theta$ axis, respectively.

which can be implemented by driving a harmonic oscillator with a two-photon process. Note that the rotating frame is set to be at half the drive frequency.

In the Heisenberg picture, the annihilation and creation operators are transformed as

$$\begin{aligned}\hat{a}' e^{-i\theta} &= \hat{S}(r,\theta)^\dagger\, \hat{a}\, e^{-i\theta} \hat{S}(r,\theta) = \hat{a} e^{-i\theta} \cosh(r) + \hat{a}^\dagger e^{i\theta} \sinh(r) \\ \hat{a}'^\dagger e^{i\theta} &= \hat{S}(r,\theta)^\dagger\, \hat{a}^\dagger\, e^{i\theta} \hat{S}(r,\theta) = \hat{a}^\dagger e^{i\theta} \cosh(r) + \hat{a}^\dagger e^{-i\theta} \sinh(r),\end{aligned} \tag{3.87}$$

where we use the Campbell-Baker-Hausdorff formula. This transformation is called the Bogoliubov transformation. Then, the quadrature operators rotated by $\theta$ are transformed as

$$\begin{aligned}\hat{x}'_\theta &= \hat{S}^\dagger(r,\theta)\, \hat{x}_\theta\, \hat{S}(r,\theta) = [\cosh(r) + \sinh(r)]\, \hat{x}_\theta = e^r \hat{x}_\theta \\ \hat{p}'_\theta &= \hat{S}^\dagger(r,\theta)\, \hat{p}_\theta\, \hat{S}(r,\theta) = [\cosh(r) - \sinh(r)]\, \hat{p}_\theta = e^{-r} \hat{p}_\theta.\end{aligned} \tag{3.88}$$

From the transformation of quadrature operators Eqs. (3.73) and (3.74), the Wigner function transformed by the squeezing operator can be calculated. By using the coordinate transformation given by

$$\begin{pmatrix} x'_\theta \\ p'_\theta \end{pmatrix} = \begin{pmatrix} \frac{x_\theta}{e^r} \\ \frac{p_\theta}{e^{-r}} \end{pmatrix}, \tag{3.89}$$

the transformed Wigner functions is written as

$$W'_{-\theta}(x_\theta, p_\theta) = W_{-\theta}\left(\frac{x_\theta}{e^r}, \frac{p_\theta}{e^{-r}}\right) = W_{-\theta}\left(\frac{x_\theta}{\sqrt{G}}, \frac{p_\theta}{1/\sqrt{G}}\right), \tag{3.90}$$

where $W_{-\theta}(x_\theta, p_\theta)$ is the initial Wigner function in the coordinate system ($x_\theta$, $p_\theta$) or the Wigner function $W(x, p)$ rotated by $-\theta$.

In this thesis, we use a squeezing operation for phase-sensitive amplification. Thus, we define the phase-sensitive gain as $G = e^{2r}$ in Eq. (3.90). The phase-sensitive amplifier can amplify a single quadrature without adding any noise, while de-amplifying the orthogonal quadrature.

As schematically shown in Fig. 3.10, the Wigner function is squeezed and anti-squeezed along the axes of $p_\theta$ and $x_\theta$, respectively.

### 3.4.4 Non-unitary operation

So far, we have explained the unitary operations on Wigner function. However, we need to consider a non-unitary operation to describe photon loss, phase-insensitive amplification, and heterodyne detection. Here, these non-unitary operations are modeled by a harmonic oscillator which is coupled to an ancilla one.

#### Wigner function of dual harmonic oscillators

First of all, Wigner function of dual harmonic oscillators is defined straightforwardly. The characteristic function of the dual modes are defined as

$$\mathcal{W}(u_1, v_1, u_2, v_2) = \frac{1}{4\pi^2}\mathrm{Tr}\left[\hat{\rho}\, e^{-iu_1\hat{x}_1 - iv_1\hat{p}_1 - iu_2\hat{x}_2 - iv_2\hat{p}_2}\right], \tag{3.91}$$

where $\rho$ is the density matrix of the dual harmonic oscillators, $\hat{x}_n$ and $\hat{p}_n$ are the quadrature operators of each mode, for $n = 1$ and 2. Then, the Wigner function is defined as the inverse Fourier transform of the characteristic function

$$\begin{aligned} &W(x_1, p_1, x_2, p_2) \\ =&\frac{1}{4\pi^2}\iint_{-\infty}^{\infty} du_1 dv_1 du_2 dv_2\, \mathcal{W}(u_1, v_1, u_2, v_2) e^{iu_1x_1 + iv_1p_1 + iu_2x_2 + iv_2x_2} \\ =&\frac{1}{16\pi^4}\iint_{-\infty}^{\infty} du_1 dv_1 du_2 dv_2\, \mathrm{Tr}\left[\hat{\rho}\, e^{-iu_1\hat{x}_1 - iv_1\hat{p}_1 - iu_2\hat{x}_2 - iv_2\hat{p}_2}\right] e^{iu_1x_1 + iv_1p_1 + iu_2x_2 + iv_2x_2}. \end{aligned} \tag{3.92}$$

Basically, the properties of the Wigner function are also satisfied in the case of the dual harmonic oscillators.

The partial trace is described as the integral with respect to the corresponding quadratures. For instance, when the mode $n = 2$ is traced out, the Wigner function of the mode $n = 1$ is described as

$$W(x_1, p_1) = \iint dx_2 dp_2\, W(x_1, p_1, x_2, p_2). \tag{3.93}$$

#### Beam splitter transformation

A beam splitter is an object used in conventional optical physics experiments which divides a single beam of light into two separate beams, or combines two separate beams into one single beam.

A unitary operator of a beam splitter on dual harmonic oscillators is defined as

$$\hat{B}(\Theta) = \exp\left[\Theta(\hat{a}_1^\dagger \hat{a}_2 - \hat{a}_1\hat{a}_2^\dagger)\right], \tag{3.94}$$

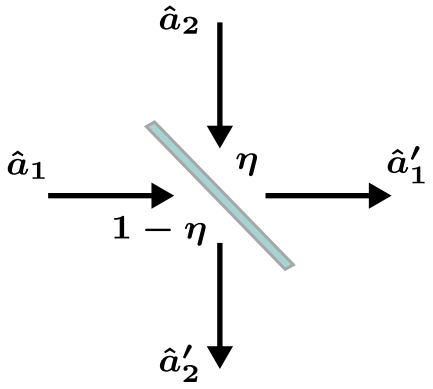


Figure 3.11: Schematic of beam splitter transformation.

which can be implemented by a resonant coupled dual harmonic oscillator. In the Heisenberg picture, the annihilation operator is transformed as

$$\begin{aligned}\begin{pmatrix}\hat{a}_1'\\ \hat{a}_2'\end{pmatrix} &= \begin{pmatrix}\hat{B}^\dagger(\Theta)\hat{a}_1\hat{B}(\Theta)\\ \hat{B}^\dagger(\Theta)\hat{a}_2\hat{B}(\Theta)\end{pmatrix}\\ &= \begin{pmatrix}\cos\Theta & \sin\Theta\\ -\sin\Theta & \cos\Theta\end{pmatrix}\begin{pmatrix}\hat{a}_1\\ \hat{a}_2\end{pmatrix}\\ &= \begin{pmatrix}\sqrt{\eta} & \sqrt{1-\eta}\\ -\sqrt{1-\eta} & \sqrt{\eta}\end{pmatrix}\begin{pmatrix}\hat{a}_1\\ \hat{a}_2\end{pmatrix},\end{aligned} \tag{3.95}$$

where $\sqrt{\eta} = \cos\Theta$, $\sqrt{1-\eta} = \sin\Theta$ and $\eta$ is the transmittance of the beam splitter. Hereinafter, we characterize the beam splitter transformation using the transmittance $\eta$ as schematically shown in Fig. (3.11).

Then, the quadrature operators are transformed as

$$\begin{pmatrix}\hat{x}_1'\\ \hat{x}_2'\end{pmatrix} = \begin{pmatrix}\sqrt{\eta} & \sqrt{1-\eta}\\ -\sqrt{1-\eta} & \sqrt{\eta}\end{pmatrix}\begin{pmatrix}\hat{x}_1\\ \hat{x}_2\end{pmatrix}, \begin{pmatrix}\hat{p}_1'\\ \hat{p}_2'\end{pmatrix} = \begin{pmatrix}\sqrt{\eta} & \sqrt{1-\eta}\\ -\sqrt{1-\eta} & \sqrt{\eta}\end{pmatrix}\begin{pmatrix}\hat{p}_1\\ \hat{p}_2\end{pmatrix} \tag{3.96}$$

Suppose that the initial state of the dual harmonic oscillators is a product state, i.e., $\rho = \hat{\rho}_1 \otimes \hat{\rho}_2$. Then the Wigner function is described as the product of each of the harmonic oscillators:

$$\begin{aligned}W(x_1,p_1,x_2,p_2) &= \frac{1}{4\pi^2}\iint_{-\infty}^{\infty} du_1 dv_1 \,\mathrm{Tr}\left[\hat{\rho}_1\, e^{-iu_1\hat{x}_1 - iv_1\hat{p}_1}\right] e^{iu_1x_1+iv_1p_1}\\ &\quad\times \frac{1}{4\pi^2}\iint_{-\infty}^{\infty} du_2 dv_2 \,\mathrm{Tr}\left[\hat{\rho}_2\, e^{-iu_2\hat{x}_2 - iv_2\hat{p}_2}\right] e^{iu_2x_2+iv_2p_2}\\ &= W_1(x_1,p_1)\,W_2(x_2,p_2),\end{aligned} \tag{3.97}$$

where $W_n(x_n,p_n)$ is the Wigner function of each oscillator, for $n = 1$ and 2. Then, the Wigner function transformed by the beam splitter operator is described as

$$W'(x_1,p_1,x_2,p_2) = W_1(x_1',p_1')\,W_2(x_2',p_2'), \tag{3.98}$$

where

$$\begin{pmatrix}x_1'\\ x_2'\end{pmatrix} = \begin{pmatrix}\sqrt{\eta} & -\sqrt{1-\eta}\\ \sqrt{1-\eta} & \sqrt{\eta}\end{pmatrix}\begin{pmatrix}x_1\\ x_2\end{pmatrix}, \begin{pmatrix}p_1'\\ p_2'\end{pmatrix} = \begin{pmatrix}\sqrt{\eta} & -\sqrt{1-\eta}\\ \sqrt{1-\eta} & \sqrt{\eta}\end{pmatrix}\begin{pmatrix}p_1\\ p_2\end{pmatrix}. \tag{3.99}$$

Therefore, we have

$$\begin{aligned} &W'(x_1, p_1, x_2, p_2) \\ =&W_1(\sqrt{\eta}x_1 - \sqrt{1-\eta}\, x_2, \sqrt{\eta}p_1 - \sqrt{1-\eta}\, p_2)\, W_2(\sqrt{1-\eta}\, x_1 + \sqrt{\eta}x_2, \sqrt{1-\eta}\, p_1 + \sqrt{\eta}p_2). \end{aligned} \tag{3.100}$$

**Noise function**

As we will see later, photon loss, phase-insensitive amplification, and heterodyne detection can be modeled by a rescaled Wigner function with an added noise.

To mathematically treat the added noise, we define a Gaussian noise function with an isotropic quadrature variances of $n$ as

$$N(x, p, n) = \frac{1}{2\pi n}\, \exp\left(-\frac{1}{2}\frac{x^2}{n} - \frac{1}{2}\frac{p^2}{n}\right). \tag{3.101}$$

Note that the noise function satisfies the normalization condition and that it describes the amount of noise added to a signal mode, though it does not describe a physical quantum state.

Furthermore, we define the convolution integral of an initial Wigner function $W(x, p)$ with the noise function as

$$W_{*N}(x, p, n) = (W * N)(x, p) = \iint dx_{\rm a} dp_{\rm a}\, W(x_{\rm a}, p_{\rm a})\; N(x - x_{\rm a}, p - p_{\rm a}, n), \tag{3.102}$$

where $x_{\rm a}$ and $p_{\rm a}$ are the quadratures of the ancilla mode, and the transformed distribution satisfies the normalization condition. We find the convolution integral with the Gaussian function describes the Wigner function with the adding noise. Note that the Wigner function with the added noise is consistent with a s-parameterized quasi-probability distribution, which is defined in [54].

Moreover, the convolution integral with $n = 0$ is the identity operation on the input Wigner function as

$$W_{*N}(x, p, n = 0) = W(x, p). \tag{3.103}$$

### 3.4.5 Photon loss

One of the main decoherence sources of a harmonic oscillator is photon loss. We can model photon loss by a harmonic oscillator which has undergone a beam splitter transformation with a vacuum state in an ancilla mode. Then, the ancilla mode is traced out.

From Eq. (3.100), the initial Wigner function $W(x, p)$ after the photon loss with the transmittance of $\eta$ is described as

$$\begin{aligned} &W'(x, p) \\ &= \iint dx_{\rm a} dp_{\rm a}\, W(\sqrt{\eta}x - \sqrt{1-\eta}x_{\rm a}, \sqrt{\eta}p - \sqrt{1-\eta}p_{\rm a})\, W_0(\sqrt{1-\eta}x + \sqrt{\eta}x_{\rm a}, \sqrt{1-\eta}p + \sqrt{\eta}p_{\rm a}) \\ &= \iint dx_{\rm a} dp_{\rm a}\, \frac{1}{\eta} W\left(\frac{x_{\rm a}}{\sqrt{\eta}}, \frac{p_{\rm a}}{\sqrt{\eta}}\right)\; \frac{1}{1-\eta} W_0\left(\frac{x - x_{\rm a}}{\sqrt{1-\eta}}, \frac{p - p_{\rm a}}{\sqrt{1-\eta}}\right), \end{aligned} \tag{3.104}$$

where $W_0(x, p) = \frac{1}{\pi}\, e^{-x^2 - p^2}$ is a Wigner function of a vacuum, which is defined in Sec. 3.6. Here, we use the variable transformation of $x_{\rm a} \to \sqrt{\frac{\eta}{1-\eta}}x - \frac{1}{\sqrt{\eta(1-\eta)}}x_{\rm a}$ and $p_{\rm a} \to \sqrt{\frac{\eta}{1-\eta}}p - \frac{1}{\sqrt{\eta(1-\eta)}}p_{\rm a}$ in the second row. We find that the obtained Wigner function is obtained by

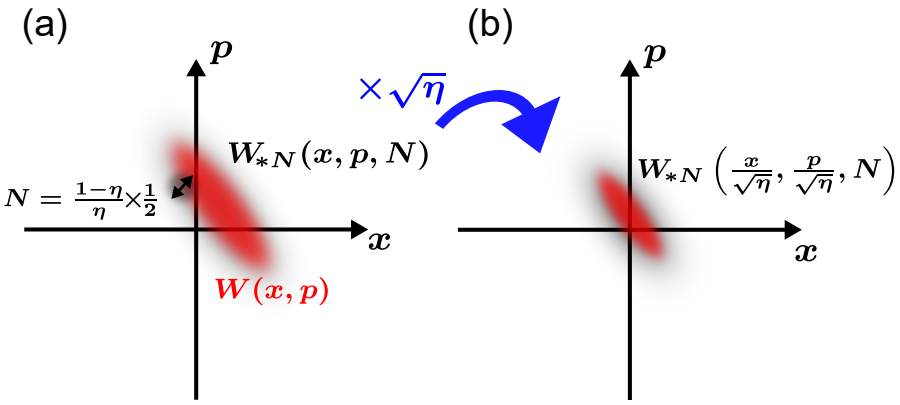


Figure 3.12: Effect of photon loss on Wigner function.

taking the convolution integral between the initial Wigner function scaled by $\sqrt{\eta}$ and the Wigner function of the vacuum state scaled by $\sqrt{1-\eta}$.

From the viewpoint of the input referred noise, it is useful to rescale the initial Wigner function as

$$\begin{aligned} W'(x,p) &= \frac{1}{\eta}\iint dx_{\rm a}dp_{\rm a}\, W\left(x_{\rm a},p_{\rm a}\right)\ \frac{\eta}{1-\eta}W_0\left(\frac{\frac{x}{\sqrt{\eta}}-x_{\rm a}}{\sqrt{\frac{1-\eta}{\eta}}},\frac{\frac{p}{\sqrt{\eta}}-p_{\rm a}}{\sqrt{\frac{1-\eta}{\eta}}}\right) \\ &= \frac{1}{\eta}\iint dx_{\rm a}dp_{\rm a}\, W\left(x_{\rm a},p_{\rm a}\right)\ N\left(\frac{x}{\sqrt{\eta}}-x_{\rm a},\frac{p}{\sqrt{\eta}}-p_{\rm a},n=\frac{1-\eta}{\eta}\times\frac{1}{2}\right) \\ &= \frac{1}{\eta}W_{*N}\left(\frac{x}{\sqrt{\eta}},\frac{p}{\sqrt{\eta}},n=\frac{1-\eta}{\eta}\times\frac{1}{2}\right), \end{aligned} \tag{3.105}$$

where we use the variable transformation of $\frac{x_{\rm a}}{\sqrt{\eta}}\to x_{\rm a}$ and $\frac{p_{\rm a}}{\sqrt{\eta}}\to p_{\rm a}$ in the first row. Here, the Wigner function of the vacuum state is represented by the noise function as $W_0\left(\frac{x}{\sqrt{\frac{1-\eta}{\eta}}},\frac{p}{\sqrt{\frac{1-\eta}{\eta}}}\right)=N\left(x,p,n=\frac{1-\eta}{\eta}\times\frac{1}{2}\right)$. The transformation of the Wigner function by the photon loss is schematically shown in Fig. 3.12.

Generally speaking, when the ancilla mode is not well cooled down, the ancilla mode is in the thermal state, which is defined in Sec. 3.6 as

$$W_{n_{\rm th}}(x,p)=\frac{1}{\pi(2n_{\rm th}+1)}\ \exp\left(-\frac{1}{2}\frac{x^2}{n_{\rm th}+\frac{1}{2}}-\frac{1}{2}\frac{p^2}{n_{\rm th}+\frac{1}{2}}\right), \tag{3.106}$$

where $n_{\rm th}$ is the average photon number. Thus, the Wigner function acted on by the photon loss with the thermal state can be described as

$$W'(x,p)=\frac{1}{\eta}W_{*N}\left(\frac{x}{\sqrt{\eta}},\frac{p}{\sqrt{\eta}},n=\frac{1-\eta}{\eta}\times\left(n_{\rm th}+\frac{1}{2}\right)\right). \tag{3.107}$$

### 3.4.6 Phase-insensitive amplification

A phase-insensitive amplification is used to amplify both of the quadratures $\hat{x}$ and $\hat{p}$ simultaneously or can also be used to magnify the Wigner function of the signal mode isotropically. However, this process does not satisfy the commutation relation as $[\sqrt{G}\hat{x},\sqrt{G}\hat{p}]=$

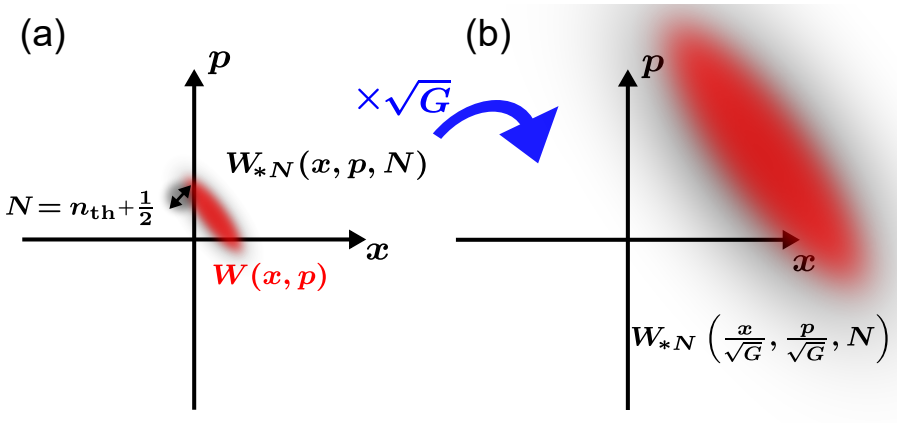


Figure 3.13: Phase-insensitive amplification of Wigner function.

$iG \neq i$. Therefore, there is no unitary operation to perform the phase-insensitive amplification without adding amplifier noise. As we will see, a phase sensitive amplifier is realized by adding the noise of the ancilla mode.

Here, we model a phase-insensitive amplification with two-mode squeezing operation. A unitary operator of a two-mode squeezing is defined as

$$\hat{S}(r) = \exp\left[\frac{r}{2}(\hat{a}^\dagger \hat{a}_{\rm a}^\dagger - \hat{a}\hat{a}_{\rm a})\right]. \tag{3.108}$$

In the Heisenberg picture, the annihilation operator is transformed as

$$\begin{pmatrix} \hat{a}' \\ \hat{a}_{\rm a}'^\dagger \end{pmatrix} = \begin{pmatrix} \cosh(r) & \sinh(r) \\ \sinh(r) & \cosh(r) \end{pmatrix} \begin{pmatrix} \hat{a} \\ \hat{a}_{\rm a}^\dagger \end{pmatrix} = \begin{pmatrix} \sqrt{G} & \sqrt{G-1} \\ \sqrt{G-1} & \sqrt{G} \end{pmatrix} \begin{pmatrix} \hat{a} \\ \hat{a}_{\rm a}^\dagger \end{pmatrix}, \tag{3.109}$$

where $G$ is the gain of the amplifier, $\sqrt{G} = \cosh(r)$ and $\sqrt{G-1} = \sinh(r)$.

Then, the quadrature operators in the Heisenberg picture are described by

$$\begin{aligned} \begin{pmatrix} \hat{x}' \\ \hat{x}_{\rm a}' \end{pmatrix} &= \begin{pmatrix} \sqrt{G} & \sqrt{G-1} \\ \sqrt{G-1} & \sqrt{G} \end{pmatrix} \begin{pmatrix} \hat{x} \\ \hat{x}_{\rm a} \end{pmatrix} \\ \begin{pmatrix} \hat{p}' \\ \hat{p}_{\rm a}' \end{pmatrix} &= \begin{pmatrix} \sqrt{G} & -\sqrt{G-1} \\ \sqrt{G-1} & -\sqrt{G} \end{pmatrix} \begin{pmatrix} \hat{p} \\ \hat{p}_{\rm a} \end{pmatrix} \end{aligned} \tag{3.110}$$

Generally speaking, the ancilla mode is in a thermal state with an average photon number of $n_{\rm th}$. From the coordinate transformation, we therefore obtain the Wigner function acted on by the two mode squeezing operation as

$$W'(x,p,x_{\rm a},p_{\rm a}) = W(x',p')\, W_{n_{\rm th}}(x_{\rm a}',p_{\rm a}'), \tag{3.111}$$

where

$$\begin{aligned} \begin{pmatrix} x' \\ x_{\rm a}' \end{pmatrix} &= \begin{pmatrix} \sqrt{G} & -\sqrt{G-1} \\ -\sqrt{G-1} & \sqrt{G} \end{pmatrix} \begin{pmatrix} x \\ x_{\rm a} \end{pmatrix} \\ \begin{pmatrix} p' \\ p_{\rm a}' \end{pmatrix} &= \begin{pmatrix} \sqrt{G} & -\sqrt{G-1} \\ \sqrt{G-1} & -\sqrt{G} \end{pmatrix} \begin{pmatrix} p \\ p_{\rm a} \end{pmatrix}. \end{aligned} \tag{3.112}$$

Then, we obtain the Wigner function of the signal mode after the phase-insensitive am-

plification by tracing out the ancilla mode as

$$\begin{aligned} W'(x,p) &= \iint dx_{\rm a}dp_{\rm a}\, W(\sqrt{G}x - \sqrt{G-1}x_{\rm a}, \sqrt{G}p - \sqrt{G-1}p_{\rm a}) \\ &\quad \times W_{n_{\rm th}}(-\sqrt{G-1}x + \sqrt{G}x_{\rm a}, \sqrt{G-1}p - \sqrt{G}p_{\rm a}) \\ &= \frac{1}{G}\iint dx_{\rm a}dp_{\rm a}\, W(x_{\rm a},p_{\rm a})\, \frac{G}{G-1} W_T\left(\frac{\frac{x}{\sqrt{G}} - x_{\rm a}}{\sqrt{\frac{G-1}{G}}}, \frac{\frac{p}{\sqrt{G}} - p_{\rm a}}{\sqrt{\frac{G-1}{G}}}\right) \\ &= \frac{1}{G}\iint dx_{\rm a}dp_{\rm a}\, W\left(x_{\rm a},p_{\rm a}\right)\, N\left(\frac{x}{\sqrt{G}} - x_{\rm a}, \frac{p}{\sqrt{G}} - p_{\rm a}, n = \frac{G-1}{G}\left(n_{\rm th} + \frac{1}{2}\right)\right) \\ &= \frac{1}{G} W_{*N}\left(\frac{x}{\sqrt{G}}, \frac{p}{\sqrt{G}}, n = \frac{G-1}{G}\left(n_{\rm th} + \frac{1}{2}\right)\right), \end{aligned} \tag{3.113}$$

where we use the variable transformation of $x_{\rm a} \to \sqrt{\frac{G}{G-1}}x - \frac{1}{\sqrt{G-1}}x_{\rm a}$ and $p_{\rm a} \to \sqrt{\frac{G}{G-1}}p - \frac{1}{\sqrt{G-1}}p_{\rm a}$ in the second row. Furthermore, we use the property that the Wigner function of the thermal state is symmetric with respect to the $x$-axis, i.e., $W_{n_{\rm th}}(x,-p) = W_{n_{\rm th}}(x,p)$. As discussed in Sec. 3.4.5, similarly to the case with the photon loss, the phase-insensitive amplification can be understood as the addition of noise and scaling.

When the gain is much larger than unity: $G \gg 1$, the Wigner function is well approximated as

$$W'(x,p) = \frac{1}{G} W_{*N}\left(\frac{x}{\sqrt{G}}, \frac{p}{\sqrt{G}}, n = \left(n_{\rm th} + \frac{1}{2}\right)\right). \tag{3.114}$$

In other words, the amplified Wigner function is the Wigner function with the amplifier noise $n_{\rm th} + \frac{1}{2}$ added and scaled by the amplifier gain $G$. Note that the noise corresponds to the input referred noise of the amplifier. The transformation of the Wigner function by the phase-insensitive amplification is schematically shown in Fig. 3.13

### 3.4.7 Heterodyne detection

With a heterodyne detection, information of two conjugate quadratures can be obtained simultaneously. Generally, however, conjugate operators not commuting with each other cannot be measured in the quantum limit simultaneously. Thus, in the heterodyne detection, we measure a composite complex amplitude operator, which is defined as

$$\hat{a}' = \hat{a} + \hat{h}^\dagger, \tag{3.115}$$

where $\hat{a}$ and $\hat{h}$ are the annihilation operators of the signal mode and the ancilla mode, respectively. The real and imaginary parts of the complex amplitude operator, which are defined as $\hat{x}' = (\hat{a}' + \hat{a}'^\dagger)/\sqrt{2}$ and $\hat{p}' = (\hat{a}' - \hat{a}'^\dagger)/\sqrt{2}i$, can commute with each other as $[\hat{x}', \hat{p}'] = 0$. Compared with Eq. (3.109), Eq. (3.115) corresponds to the phase-insensitive amplification in the large gain limit without the scaling. Then, the transformation of the Wigner function $W(x,p)$ is described as

$$W'(x,p) = W_{*N}\left(x, p, n = \left(n_{\rm th} + \frac{1}{2}\right)\right), \tag{3.116}$$

where $n_{\rm th}$ is the thermal average photon number in the ancilla mode. The transformed Wigner function can be directly measured as the probabilistic distribution of the measurement outcomes of the real and imaginary parts of the complex amplitude operator $\hat{a}'$. Adding the noise larger than half a vacuum noise enables us to obtain both of the

conjugate quadratures simultaneously. While the vacuum-noise-limited heterodyne detection can be realized in the optical frequency domain [54, 57], the heterodyne detection, which is realized with a demodulator and a digitizer, in the microwave domain is normally limited by thermal noise [32, 59].

## 3.5 Transformation of quadrature distribution

As explained in Sec. 3.3, a Wigner function can be reconstructed from a set of the observable quadrature distributions. It is useful to consider how the quadrature distribution is transformed in each process, such as amplification, photon loss, and detection. From Eq. (3.55), the quadrature distribution is obtained from the Wigner function as

$$P_\theta(x_\theta) = \int_{-\infty}^{\infty} dp\, W_{-\theta}(x_\theta, p_\theta), \tag{3.117}$$

where $x_\theta$ is a outcome of the measurement of $\hat{x}_\theta$.

First of all, the quadrature distribution from the noisy Wigner function $W_{-\theta *N}(x_\theta, p_\theta, n)$ in Eq. (3.102) can be calculated as

$$\begin{aligned} P_{\theta *N}(x_\theta, n) &= \int_{-\infty}^{\infty} dp_\theta\, W_{-\theta *N}(x_\theta, p_\theta, n) \\ &= \int_{-\infty}^{\infty} dp_\theta \iint dx_{\rm a} dp_{\rm a}\, W_{-\theta}\left(x_{\rm a}, p_{\rm a}\right)\, N\left(x - x_{\rm a}, p - p_{\rm a}, n\right) \\ &= \int_{-\infty}^{\infty} dx_{\rm a}\, P_\theta\left(x_{\rm a}\right)\, N\left(x_\theta - x_{\rm a}, n\right), \end{aligned} \tag{3.118}$$

where $W_{-\theta *N}(x_\theta, p_\theta, n)$ is the noisy Wigner function of $W_{*N}(x, p, n)$ in the coordinates $(x_\theta,\ p_\theta)$. Here, we define the normalized noise distribution as

$$N(x, n) = \frac{1}{\sqrt{2\pi n}}\, \exp\left(-\frac{1}{2}\frac{x^2}{n}\right). \tag{3.119}$$

Thus, the noisy quadrature distribution can be described by the convolution integral between the original quadrature distribution $P_\theta(x)$ and the noise distribution $N(x, n)$ as

$$P_{\theta *N}(x, n) = \int_{-\infty}^{\infty} dx_{\rm a}\, P_\theta\left(x_{\rm a}\right)\, N\left(x - x_{\rm a}, n\right). \tag{3.120}$$

Using the noisy quadrature distribution with the corresponding scaling, we can obtain the quadrature distribution transformed by each process, as follows.

From Eq. (3.90), the quadrature distribution amplified in the phase-sensitive manner can be written as

$$P'_\theta(x) = \frac{1}{\sqrt{G}} P\left(\frac{x}{\sqrt{G}}\right) = \frac{1}{\sqrt{G}} P_{\theta *N}\left(\frac{x}{\sqrt{G}}, n = 0\right), \tag{3.121}$$

From Eq. (3.107), the quadrature distribution with the photon loss can be written as

$$P'_\theta(x) = \frac{1}{\sqrt{\eta}} P_{\theta *N}\left(\frac{x}{\sqrt{\eta}}, n = \frac{1-\eta}{\eta} \times \left(n_{\rm th} + \frac{1}{2}\right)\right). \tag{3.122}$$

From Eq. (3.114), the quadrature distribution amplified by the phase-insensitive amplifier can be described as

$$P'_\theta(x) = \frac{1}{\sqrt{G}} P_{\theta *N}\left(\frac{x}{\sqrt{G}}, n = n_{\rm th} + \frac{1}{2}\right). \tag{3.123}$$

Finally, from Eq. (3.116), the quadrature distribution measured by the heterodyne detection is given by

$$P'_\theta(x) = P_{\theta * N}\left(x, n = n_{\rm th} + \frac{1}{2}\right). \tag{3.124}$$

To sum up, these transformations are characterized by the scaling and the added noise. The added noise amounts and scalings in each process are listed in Table 3.1.

### 3.5.1 Cascade transformation

Practically, microwave photons are measured through many processes in a measurement chain. Therefore, it is useful to consider a cascade transformation of the quadrature distribution.

Here, we suppose that the quadrature distribution of $P_\theta(x)$ will be measured after the cascade transformation in the quadrature measurement chain. Without loss of generality, using $P_\theta(x)$, the input quadrature distribution $P_{\theta,\rm i}(x)$ to a process in the measurement chain can be described as

$$\begin{aligned} P_{\theta,\rm i}(x) &= \frac{1}{\sqrt{c_\rm i}} P_{\theta * N}\left(\frac{x}{\sqrt{c_\rm i}}, n = n_\rm i\right) \\ &= \frac{1}{\sqrt{c_\rm i}} \int_{-\infty}^{\infty} dx_\rm a\, P\left(x_\rm a\right)\; N\left(\frac{x}{\sqrt{c_\rm i}} - x_\rm a, n = n_\rm i\right), \end{aligned} \tag{3.125}$$

where $c_\rm i$ and $n_\rm i$ is the input quadrature distribution, respectively. Then, the quadrature distribution is transformed by the process with the scaling $c_k$ and the added noise $n_k$ as

$$\begin{aligned} P_{\theta,\rm o}(x) =& \frac{1}{\sqrt{c_k}} \int_{-\infty}^{\infty} dx'_\rm a\, P_{\theta,\rm i}\left(x'_\rm a\right)\; N\left(\frac{x}{\sqrt{c_k}} - x'_\rm a, n = n_k\right) \\ =& \frac{1}{\sqrt{c_\rm i c_k}} \iint_{-\infty}^{\infty} dx_\rm a dx'_\rm a\, P_\theta\left(x_\rm a\right)\; N\left(\frac{x'_\rm a}{\sqrt{c_\rm i}} - x_\rm a, n = n_\rm i\right) N\left(\frac{x}{\sqrt{c_k}} - x'_\rm a, n = n_k\right) \\ =& \frac{1}{\sqrt{c_\rm i c_k}} \iint_{-\infty}^{\infty} dx_\rm a dx'_\rm a\, P_\theta\left(x_\rm a\right)\; N\left(x'_\rm a, n = n_\rm i\right) N\left(\left(\frac{x}{\sqrt{c_\rm i c_k}} - x_\rm a\right) - x'_\rm a, n = \frac{n_k}{c_\rm i}\right) \\ =& \frac{1}{\sqrt{c_\rm i c_k}} \iint_{-\infty}^{\infty} dx_\rm a\, P_\theta\left(x_\rm a\right)\; N\left(\frac{x}{\sqrt{c_\rm i c_k}} - x_\rm a, n = n_\rm i + \frac{n_k}{c_\rm i}\right) \\ =& \frac{1}{\sqrt{c_\rm i c_k}} P_{\theta * N}\left(\frac{x}{\sqrt{c_\rm i c_k}}, n = n_\rm i + \frac{n_k}{c_\rm i}\right), \end{aligned} \tag{3.126}$$

Table 3.1: Transformations of quadrature distribution.

| Process | Scaling | Added noise |
|---|---|---|
| Photon loss | $\sqrt{\eta}$ | $\frac{1-\eta}{\eta} \times (n_{\rm th} + \frac{1}{2})$ |
| Phase-sensitive amplification | $\sqrt{G}$ | $n_{\rm th} + \frac{1}{2}$ |
| Phase-insensitive amplification | $\sqrt{G}$ | 0 |
| Heterodyne detection | 1 | $n_{\rm th} + \frac{1}{2}$ |

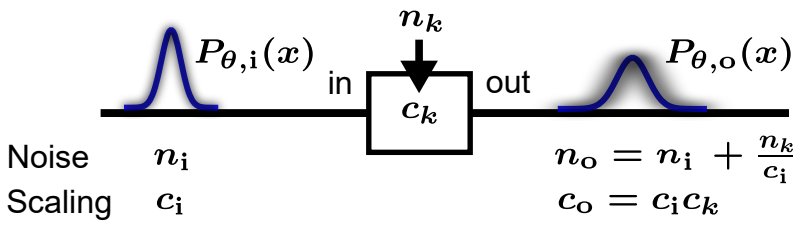


Figure 3.14: Transformation of quadrature distribution.

where, we use the variable transformation of $\frac{x'_\mathrm{a}}{\sqrt{c_\mathrm{i}}} - x_\mathrm{a} \to x'_\mathrm{a}$ and

$$\begin{aligned} &N\left(\frac{x}{\sqrt{c}}, n\right) = \sqrt{c} N(x, cn), \\ &\int_{-\infty}^{\infty} dx_\mathrm{a}\, N\left(x, n_1\right)\ N\left(x - x_\mathrm{a}, n_2\right) = N(x, n_1 + n_2). \end{aligned} \tag{3.127}$$

From these calculations, we find that the input scaling $c_\mathrm{i}$ and added noise $n_\mathrm{i}$ are modified by the transformation with $c_k$, $n_k$ as

$$\begin{aligned} c_\mathrm{i} &\to c_\mathrm{o} = c_\mathrm{i} c_k \\ n_\mathrm{i} &\to n_\mathrm{o} = n_\mathrm{i} + \frac{n_k}{c_\mathrm{i}}. \end{aligned} \tag{3.128}$$

The transformation of the quadrature distribution schematically shown in Fig. 3.14.

Therefore, $P_\theta(x)$, which is transformed in a step-by-step manner with the scalings of $c_1, c_2, c_3 \cdots$ and the added noise of $n_1, n_2, n_3, \cdots$, can be described as

$$\begin{aligned} P_{\theta,\mathrm{tot}}(x_\theta) &= \frac{1}{\sqrt{c_\mathrm{tot}}} P_{\theta * N}\left(\frac{x}{\sqrt{c_\mathrm{tot}}}, n = n_\mathrm{tot}\right) \\ &= \frac{1}{\sqrt{c_\mathrm{tot}}} \int_{-\infty}^{\infty} dx_\mathrm{a}\, P\left(x_\mathrm{a}\right)\ N\left(\frac{x}{\sqrt{c_\mathrm{tot}}} - x_\mathrm{a}, n = n_\mathrm{tot}\right), \end{aligned} \tag{3.129}$$

where

$$\begin{aligned} c_\mathrm{tot} &= c_1 c_2 c_3 \cdots \\ n_\mathrm{tot} &= n_1 + \frac{n_2}{c_1} + \frac{n_3}{c_1 c_2} + \cdots. \end{aligned} \tag{3.130}$$

We find that the added noise at a certain stage is divided by the scaling until then. In other words, the gain of a preamplifier can suppress the noises in the latter stages. Therefore, when a quantum-limited amplifier is used as the preamplifier, the quantum measurement of the quadrature can be achieved even with a classical measurement device.

## 3.6 Examples of quantum states

Here, we show examples of quantum states in a harmonic oscillator.

### 3.6.1 Fock states

A Fock state is an eigenstate of the photon number operator $\hat{a}^\dagger \hat{a}$ or the Hamiltonian of the single harmonic oscillator.

First, we can obtain the wave function of the vacuum state by solving the differential equation:

$$\hat{a}|0\rangle = \frac{\hat{x} + i\hat{p}}{\sqrt{2}}|0\rangle = 0. \tag{3.131}$$

The equation is represented in the quadrature basis $|x\rangle$ as

$$\left(x + \frac{\partial}{\partial x}\right)\Psi_0(x) = 0, \tag{3.132}$$

where $\Psi_0(x) = \langle x|0\rangle$ is the wave function of the vacuum state. With the normalization condition, we obtain the wave function of the vacuum state

$$\Psi_0(x) = \langle x|0\rangle = \left(\frac{1}{\pi}\right)^{\frac{1}{4}} e^{-\frac{x^2}{2}}. \tag{3.133}$$

Here, the expectation value and the variance of the quadrature are calculated as

$$\begin{aligned} \langle x\rangle &= \langle 0|\hat{x}|0\rangle = \langle 0|\frac{\hat{a} + \hat{a}^\dagger}{\sqrt{2}}|0\rangle = 0 \\ \langle p\rangle &= \langle 0|\hat{p}|0\rangle = \langle 0|\frac{\hat{a} - \hat{a}^\dagger}{\sqrt{2}i}|0\rangle = 0 \end{aligned} \tag{3.134}$$

and

$$\begin{aligned} \langle 0|(\hat{x} - \langle x\rangle)^2|0\rangle &= \langle 0|\hat{x}^2|0\rangle = \frac{1}{2}\langle 0|(\hat{a}^2 + \hat{a}^\dagger\hat{a} + \hat{a}\hat{a}^\dagger + \hat{a}^{\dagger 2})|0\rangle = \frac{1}{2} \\ \langle 0|(\hat{p} - \langle p\rangle)^2|0\rangle &= \langle 0|\hat{p}^2|0\rangle = \frac{1}{2}\langle 0|(-\hat{a}^2 + \hat{a}^\dagger\hat{a} + \hat{a}\hat{a}^\dagger - \hat{a}^{\dagger 2})|0\rangle = \frac{1}{2}. \end{aligned} \tag{3.135}$$

We find that the expectation of the quadrature is zero and that the variance of the quadrature is $\frac{1}{2}$, which is called the vacuum fluctuation or the vacuum noise.

Fock states with an arbitrary photon numbers are derived from Eq. (3.22) as

$$\Psi_m(x) = \langle x|m\rangle = \left(\frac{1}{\pi}\right)^{\frac{1}{4}} \frac{1}{\sqrt{n!}} \left(x + \frac{\partial}{\partial x}\right)^m e^{-\frac{x^2}{2}}. \tag{3.136}$$

With the Hermite polynomial $H_n(x)$, the Fock state is represented as

$$\Psi_m(x) = \left(\frac{1}{\pi}\right)^{\frac{1}{4}} \frac{1}{\sqrt{2^m m!}} H_m(x) e^{-\frac{x^2}{2}}. \tag{3.137}$$

The photon-number distribution of the Fock state $|m\rangle$ is obviously described by

$$P(n) = \delta_{n,m}. \tag{3.138}$$

Here, we show the examples of the Hermite polynomial for $m = 0, 1, 2$

$$\begin{aligned} H_0(x) &= 1 \\ H_1(x) &= 2x \\ H_2(x) &= 4x^2 - 2 \end{aligned} \tag{3.139}$$

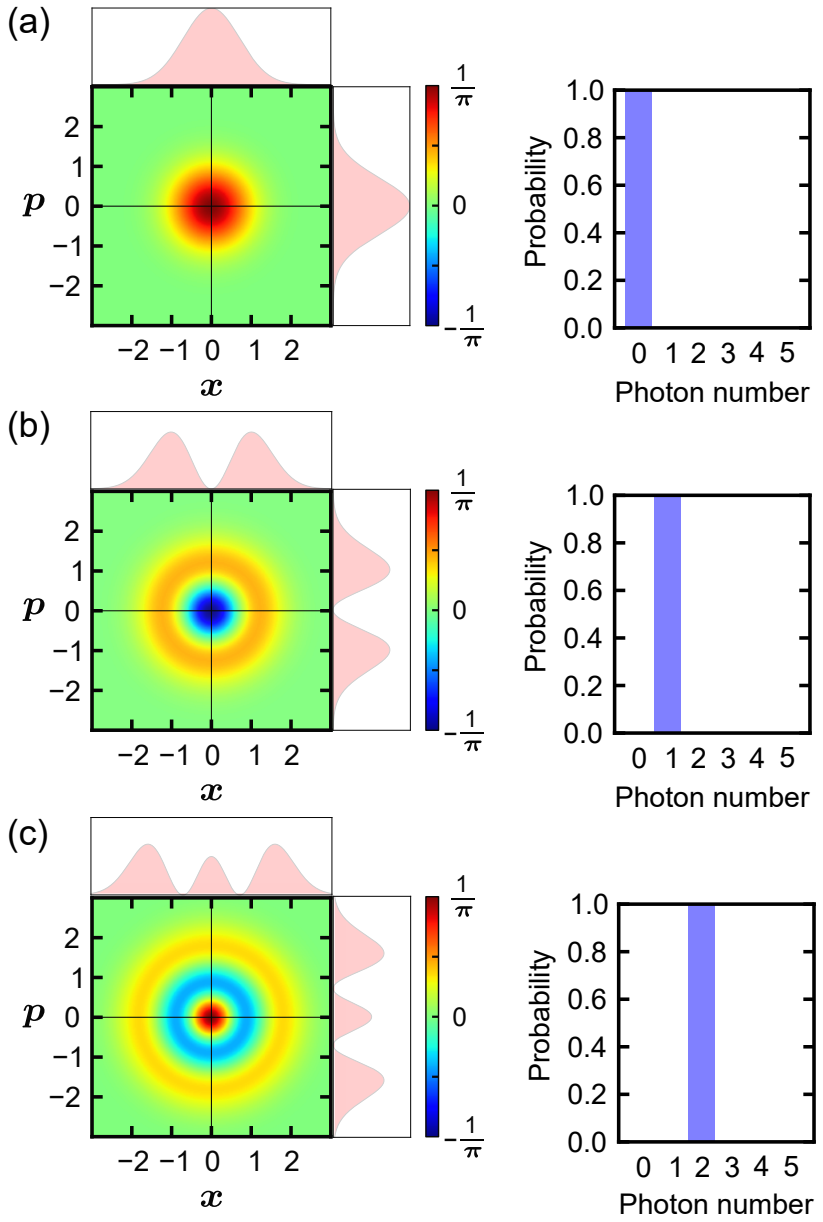


Figure 3.15: Wigner functions and photon-number distributions of Fock states of (a) the vacuum state $|0\rangle$, (b) the single photon state $|1\rangle$, and (c) the two photon state $|2\rangle$.

and the corresponding wave functions

$$\begin{aligned}\Psi_0(x) &= \left(\frac{1}{\pi}\right)^{\frac{1}{4}} e^{-\frac{x^2}{2}} \\ \Psi_1(x) &= \left(\frac{1}{\pi}\right)^{\frac{1}{4}} \sqrt{2}x\, e^{-\frac{x^2}{2}} \\ \Psi_2(x) &= \left(\frac{1}{\pi}\right)^{\frac{1}{4}} \frac{2x^2-1}{\sqrt{2}}\, e^{-\frac{x^2}{2}}.\end{aligned} \tag{3.140}$$

The Wigner functions are calculated in the coordinate system $(x,\, p)$ from Eq. (3.50)

as

$$\begin{aligned} W_m(x,p) &= \frac{e^{-x^2-p^2}}{\pi^{\frac{3}{2}} 2^m m!} \int_{-\infty}^{\infty} dv\, e^{i(v-ip)^2} H_m(x-v) H_m(x+v) \\ &= \frac{(-1)^m}{\pi} L_m\left(2(x^2+p^2)\right)\, e^{-x^2-p^2}, \end{aligned} \tag{3.141}$$

where $L_n(x)$ are the Laguerre polynomials. Here, we show examples of the Laguerre polynomials for $m = 0, 1, 2$:

$$\begin{aligned} L_0(x) &= 1 \\ L_1(x) &= 1 - x \\ L_2(x) &= 1 - 2x + \frac{1}{2}x^2 \end{aligned} \tag{3.142}$$

and the corresponding Wigner functions

$$\begin{aligned} W_0(x,p) &= \frac{1}{\pi}\, e^{-x^2-p^2} \\ W_1(x,p) &= \frac{-1}{\pi}\left(1-(x^2+p^2)\right)\, e^{-x^2-p^2} \\ W_2(x,p) &= \frac{1}{\pi}\left(1-2(x^2+p^2)+\frac{1}{2}(x^2+p^2)^2\right)\, e^{-x^2-p^2}. \end{aligned} \tag{3.143}$$

Here, we rewrite the Wigner function of the vacuum state to show the quadrature variances of $\frac{1}{2}$ more clearly as

$$W_0(x,p) = \frac{1}{\pi}\, \exp\left(-\frac{1}{2}\frac{x^2}{\frac{1}{2}} - \frac{1}{2}\frac{p^2}{\frac{1}{2}}\right). \tag{3.144}$$

The examples of the Wigner functions and the photon-number distributions of Fock states are shown in Fig. 3.15.

### 3.6.2 Coherent states

A coherent state $|\alpha\rangle$ is defined as the vacuum state acted on by a displacement operation:

$$|\alpha\rangle = \hat{D}(\alpha)|0\rangle. \tag{3.145}$$

The coherent state can also be defined as the eigenstate of the annihilation operator:

$$\hat{a}|\alpha\rangle = \alpha|\alpha\rangle. \tag{3.146}$$

Note that the annihilation operator $\hat{a}$ is not Hermitian and that the eigenvalues are not real, but rather a complex numbers. Using Eq. (3.146), we can easily calculate the average photon number as

$$\langle n\rangle = \langle\alpha|\hat{a}^\dagger\hat{a}|\alpha\rangle = |\alpha|^2. \tag{3.147}$$

Furthermore, the coherent state is represented in the Fock basis as

$$\begin{aligned} |\alpha\rangle &= \exp\left(\alpha\,\hat{a}^\dagger - \alpha^*\,\hat{a}\right)|0\rangle \\ &= e^{-|\alpha|^2/2} e^{\alpha\hat{a}^\dagger} e^{-\alpha^*\hat{a}}|0\rangle \\ &= e^{-|\alpha|^2/2} \sum_{n=0}^{\infty} \frac{\alpha^n}{\sqrt{n!}}|n\rangle. \end{aligned} \tag{3.148}$$

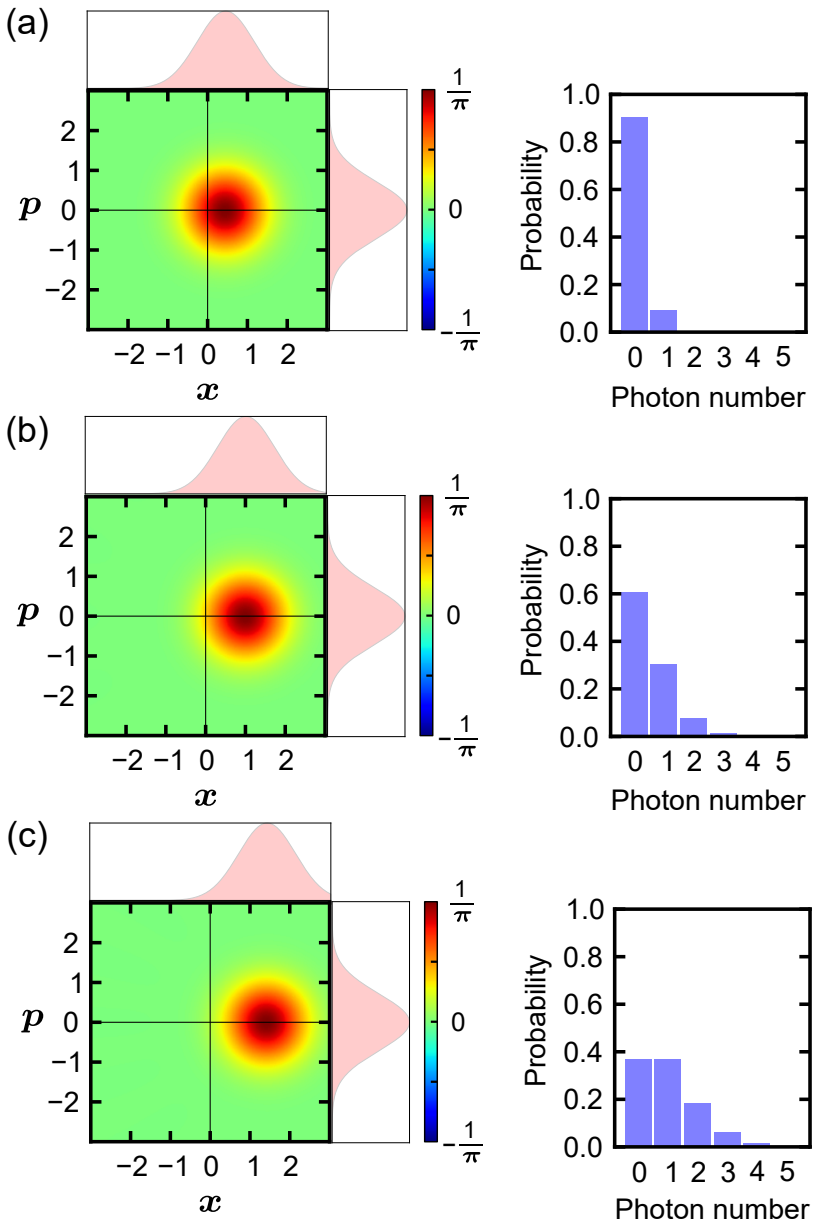


Figure 3.16: Wigner functions and the photon-number distributions of the coherent states with the average photon numbers of (a) $\langle n \rangle = 0.1$ ($\alpha = 0.32$), (b) $\langle n \rangle = 0.5$ ($\alpha = 0.71$), and (c) $\langle n \rangle = 1$ ($\alpha = 1$).

Therefore, the photon-number distribution is

$$\begin{aligned} P_\alpha(n) &= e^{-|\alpha|^2} \frac{|\alpha|^{2n}}{n!} \\ &= e^{-\langle n \rangle} \frac{\langle n \rangle^n}{n!}, \end{aligned} \tag{3.149}$$

where $\langle n \rangle = |\alpha|^2$ is the average photon number of the coherent state. We find the photon-number distribution corresponds to the Poisson distribution.

In the Heisenberg picture, the quadrature operators are transformed with the displacement operation as

$$\begin{pmatrix} \hat{x}' \\ \hat{p}' \end{pmatrix} = \begin{pmatrix} \hat{x} + x_\alpha \\ \hat{p} + p_\alpha \end{pmatrix}, \tag{3.150}$$

where

$$\alpha = \frac{x_\alpha + ip_\alpha}{\sqrt{2}}. \tag{3.151}$$

The expectation values and the variances of the quadratures are calculated as

$$\begin{aligned} \langle x \rangle &= \langle \alpha | \hat{x} | \alpha \rangle = \langle 0 | \hat{D}^\dagger(\alpha) \hat{x} \hat{D}(\alpha) | 0 \rangle = \langle 0 | (\hat{x} + x_\alpha) | 0 \rangle = x_\alpha \\ \langle p \rangle &= \langle \alpha | \hat{p} | \alpha \rangle = \langle 0 | \hat{D}^\dagger(\alpha) \hat{x} \hat{D}(\alpha) | 0 \rangle = \langle 0 | (\hat{p} + p_\alpha) | 0 \rangle = p_\alpha \end{aligned} \tag{3.152}$$

and

$$\begin{aligned} \langle \alpha | (\hat{x} - \langle x \rangle)^2 | \alpha \rangle &= \langle 0 | \hat{x}^2 | 0 \rangle = \frac{1}{2} \\ \langle \alpha | (\hat{p} - \langle p \rangle)^2 | \alpha \rangle &= \langle 0 | \hat{p}^2 | 0 \rangle = \frac{1}{2}. \end{aligned} \tag{3.153}$$

We find that the coherent state is the state whose expectation values of the quadratures are displaced but variances are the same as that of the vacuum state.

Using Eq. (3.85), the Wigner function of the coherent state $W_\alpha(x, p)$ is described as the coordinate transformation of the vacuum state $W_0(x, p)$:

$$\begin{aligned} W_\alpha(x, p) &= W_0(x - x_\alpha, p - p_\alpha) \\ &= \frac{1}{\pi} \exp\left( -\frac{1}{2} \frac{(x - x_\alpha)^2}{\frac{1}{2}} - \frac{1}{2} \frac{(p - p_\alpha)^2}{\frac{1}{2}} \right). \end{aligned} \tag{3.154}$$

Examples of these Wigner functions and photon-number distributions of coherent states are shown in Fig. 3.16.

### 3.6.3 Squeezed vacuum states

A squeezed vacuum state is defined as the vacuum state acted upon by a squeezing operation:

$$|S(r, \theta)\rangle = \hat{S}(r, \theta) |0\rangle. \tag{3.155}$$

Using the Campbell-Baker-Hausdorff formula, it is represented in the Fock basis as

$$\begin{aligned} |S(r, \theta)\rangle &= e^{-\frac{1}{2}\hat{a}^{\dagger 2} e^{i2\theta} \tanh(r)} e^{-\left(\hat{a}^\dagger \hat{a} + \frac{1}{2}\right) \ln[\cosh(r)]} e^{\frac{1}{2}\hat{a}^2 e^{i2\theta} \tanh(r)} |0\rangle \\ &= \frac{1}{\sqrt{\cosh(r)}} e^{-\frac{e^{2i\theta} \tanh(r)}{2} \hat{a}^{\dagger 2}} |0\rangle \\ &= \sum_{k=0}^{\infty} \frac{\sqrt{(2k)!}}{\sqrt{\cosh(r)} 2^k k!} \left[ -\tanh(r) e^{i2\theta} \right]^k |2k\rangle. \end{aligned} \tag{3.156}$$

Then, the photon-number distribution of the squeezed vacuum state is calculated as

$$P(2k) = \frac{(2k)!}{(k!)^2 2^{2k} \cosh(r)} \tanh^{2k}(r). \tag{3.157}$$

We find that the squeezed vacuum state contains only even photon numbers. The average photon number is also calculated as

$$\langle n \rangle = \sinh^2(r). \tag{3.158}$$

In the Heisenberg picture, the quadrature operators are transformed under the squeezing operation as

$$\begin{aligned} \hat{x}'_\theta &= \hat{S}^\dagger(r, \theta)\, \hat{x}_\theta\, \hat{S}(r, \theta) = [\cosh(r) + \sinh(r)]\, \hat{x}_\theta = e^r \hat{x}_\theta \\ \hat{p}'_\theta &= \hat{S}^\dagger(r, \theta)\, \hat{p}_\theta\, \hat{S}(r, \theta) = [\cosh(r) - \sinh(r)]\, \hat{p}_\theta = e^{-r} \hat{p}_\theta, \end{aligned} \tag{3.159}$$

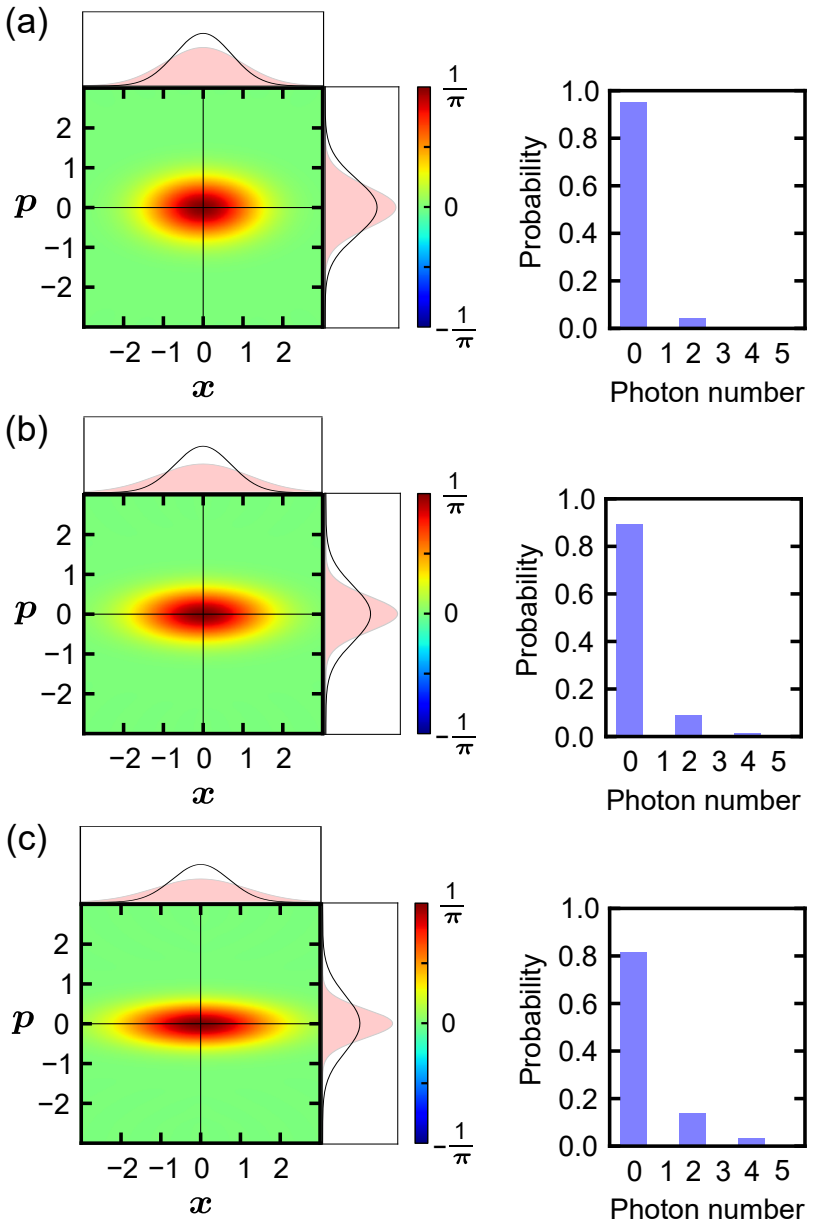


Figure 3.17: Wigner functions and photon-number distributions of the squeezed vacuum states with the average photon numbers of (a) $\langle n\rangle = 0.1$ ($r = 0.31$, $\theta = 0$), (b) $\langle n\rangle = 0.5$ ($r = 0.66$, $\theta = 0$), and (c) $\langle n\rangle = 1$ ($r = 0.88$, $\theta = 0$).

where we use $\sinh(r) = \frac{e^r - e^{-r}}{2}$ and $\cosh(r) = \frac{e^r + e^{-r}}{2}$. The expectation values and the variances of the quadratures of the squeezed vacuum state are calculated as

$$\begin{aligned}\langle x_\theta\rangle &= \langle S(r,\theta)|\hat{x}_\theta|S(r,\theta)\rangle = \langle 0|\hat{S}^\dagger(r,\theta)\,\hat{x}_\theta\,\hat{S}^\dagger(r,\theta)|0\rangle = \langle 0|e^r\hat{x}_\theta|0\rangle = 0\\ \langle p_\theta\rangle &= \langle S(r,\theta)|\hat{p}_\theta|S(r,\theta)\rangle = \langle 0|\hat{S}^\dagger(r,\theta)\,\hat{p}_\theta\,\hat{S}^\dagger(r,\theta)|0\rangle = \langle 0|e^{-r}\hat{p}_\theta|0\rangle = 0\end{aligned} \tag{3.160}$$

and

$$\begin{aligned}\langle(\hat{x}_\theta - \langle x_\theta\rangle)^2\rangle &= \langle S(r,\theta)|(\hat{x}_\theta - \langle x_\theta\rangle)^2|S(r,\theta)\rangle = \langle 0|e^{2r}\hat{x}_\theta^2|0\rangle = \frac{e^{2r}}{2}\\ \langle(\hat{p}_\theta - \langle p_\theta\rangle)^2\rangle &= \langle S(r,\theta)|(\hat{p}_\theta - \langle p_\theta\rangle)^2|S(r,\theta)\rangle = \langle 0|e^{-2r}\hat{p}^2|0\rangle = \frac{e^{-2r}}{2}.\end{aligned} \tag{3.161}$$

We find that the expectation values of the quadratures are zero as in the vacuum state and that the variance of one quadrature is squeezed while that of the orthogonal quadrature is anti-squeezed.

From Eq. (3.90), the Wigner function of the squeezed vacuum state in the coordinate system ($x_\theta$, $p_\theta$) is calculated from the coordinate transformation of the vacuum state $W_0(x_\theta, p_\theta)$:

$$\begin{aligned} W_{-\theta\, S}(x_\theta, p_\theta) &= W_0\left(\frac{x_\theta}{e^r}, \frac{p_\theta}{e^{-r}}\right) \\ &= \frac{1}{\pi}\, \exp\left(-\frac{1}{2}\,\frac{x_\theta^2}{\frac{e^{2r}}{2}} - \frac{1}{2}\,\frac{p_\theta^2}{\frac{e^{-2r}}{2}}\right). \end{aligned} \tag{3.162}$$

The Wigner function is represented in the coordinate system ($x$, $p$) as

$$\begin{aligned} W_S(x,p) &= W_0\left(e^{-r}(x\cos\theta + p\sin\theta), e^r(-x\sin\theta + p\cos\theta)\right) \\ &= \frac{1}{\pi}\, \exp\left(-\frac{1}{2}\,\frac{(x\cos\theta + p\sin\theta)^2}{\frac{e^{2r}}{2}} - \frac{1}{2}\,\frac{(-x\sin\theta + p\cos\theta)^2}{\frac{e^{-2r}}{2}}\right), \end{aligned} \tag{3.163}$$

which is derived from the rotation transformation of $W_{-\theta\, S}(x_\theta, p_\theta)$ by $\theta$.

Examples of these Wigner functions and the photon-number distributions of squeezed vacuum states are shown in Fig. 3.17.

### 3.6.4 Thermal states

A thermal state is a state which is in equilibrium with a thermal bath. The state is no longer a pure state but a classical mixed state of Fock states. The energy distribution or the photon-number distribution is the Boltzmann distribution. Then, we have the density matrix of the thermal state as

$$\hat{\rho}_{n_{\rm th}} = (1 - e^{-\beta}) \sum_{n=0}^{\infty} e^{-n\beta} |n\rangle\langle n|, \tag{3.164}$$

where $\beta = \hbar\omega_{\rm c}/k_{\rm B}T$ is the energy quantum normalized by $k_{\rm B}T$, $\omega_{\rm c}$ is the resonance frequency of the oscillator, $T$ is the bath temperature, and $k_{\rm B}$ is the Boltzmann constant. The thermal state taking the zero-temperature limit corresponds to the vacuum state.

The photon-number distribution is described by

$$P(n) = (1 - e^{-\beta}) e^{-n\beta}. \tag{3.165}$$

The average photon number is calculated by

$$\begin{aligned} \langle n \rangle &= (1 - e^{-\beta}) \sum_{n=0}^{\infty} n e^{-n\beta} \\ &= \frac{1}{e^\beta - 1}. \end{aligned} \tag{3.166}$$

Taking the high temperature limit of $\beta = \hbar\omega_{\rm c}/k_{\rm B}T \to 0$, the average photon number is approximated by $\langle n \rangle \approx k_{\rm B}T/\hbar\omega_{\rm c}$.

We find a thermal state can be characterized as an average photon number of $\langle n \rangle = n_{\rm th}$. Thus, the density matrix and the photon-number distribution can be described as

$$\begin{aligned} \hat{\rho}_{n_{\rm th}} &= \frac{1}{n_{\rm th} + 1} \sum_{n=0}^{\infty} \left(\frac{n_{\rm th}}{n_{\rm th} + 1}\right)^n |n\rangle\langle n| \\ P(n) &= \frac{1}{n_{\rm th} + 1} \left(\frac{n_{\rm th}}{n_{\rm th} + 1}\right)^n. \end{aligned} \tag{3.167}$$

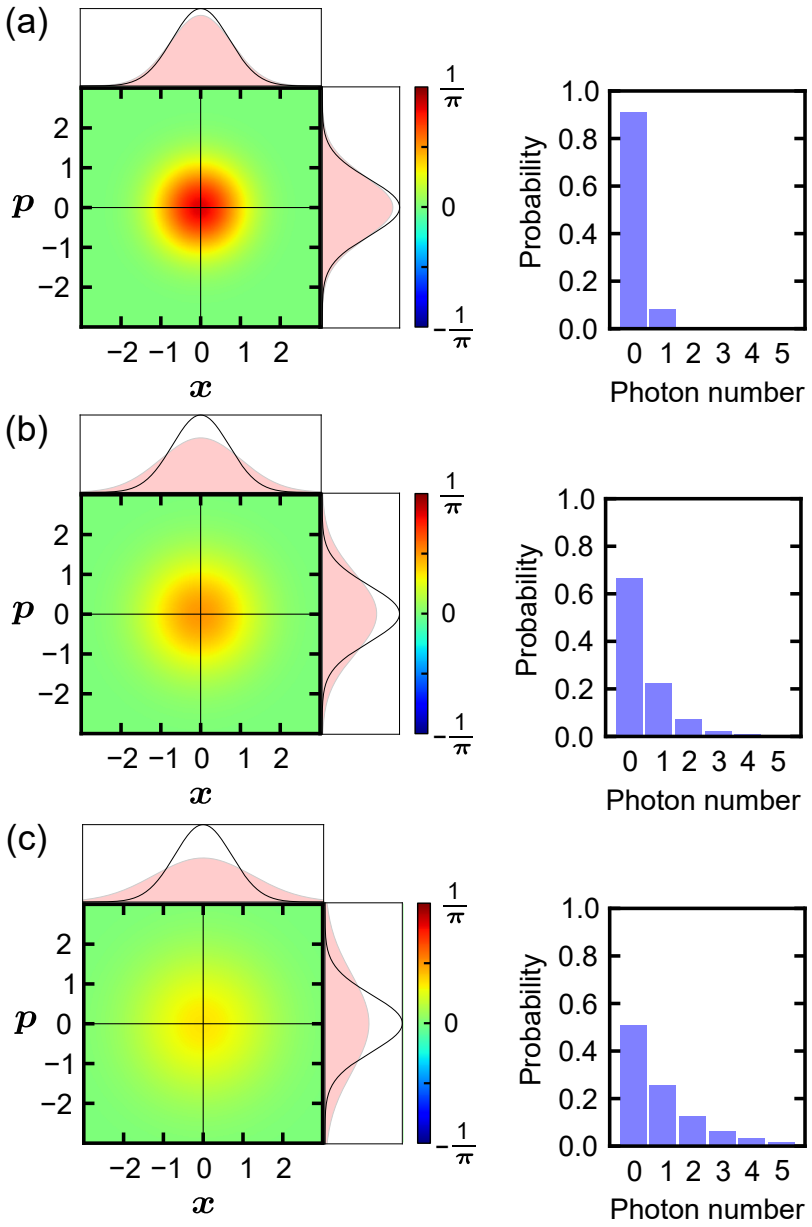


Figure 3.18: Wigner function and photon-numbers distributions of thermal states with the average photon number of (a) $\langle n \rangle = 0.1$, (b) $\langle n \rangle = 0.5$, and (c) $\langle n \rangle = 1$.

The Wigner function of the thermal state is described by

$$\begin{aligned} W_{n_{\rm th}}(x,p) &= \frac{1}{2n_{\rm th}+1} W_0\left(\frac{x}{\sqrt{2n_{\rm th}+1}}, \frac{p}{\sqrt{2n_{\rm th}+1}}\right) \\ &= \frac{1}{\pi(2n_{\rm th}+1)} \exp\left(-\frac{1}{2}\frac{x^2}{n_{\rm th}+\frac{1}{2}} - \frac{1}{2}\frac{p^2}{n_{\rm th}+\frac{1}{2}}\right). \end{aligned} \tag{3.168}$$

The variances of the quadratures are calculated as

$$\langle \hat{x}^2 \rangle = \langle \hat{p}^2 \rangle = n_{\rm th} + \frac{1}{2}. \tag{3.169}$$

Examples of these Wigner functions and the photon-number distributions of thermal states are shown in Fig. 3.18.

# Chapter 4

# Design

In this section, we explain how to design superconducting circuits. We focus on a three-dimensional (3D) circuit QED system, where a transmon qubit [9, 10] on a sapphire substrate is coupled to a 3D microwave cavity [23]. Since the transmon qubit can be modeled as an anharmonic LC resonator, we can simulate the system and extract its parameters, such as the resonance frequency, using a classical electromagnetic field simulator. We use the "Eigenfrequency Analysis" tool in the "RF module" of the COMSOL Multiphysics® software [60].

To design a 3D circuit QED system, it is known to use the Black Box Quantization, which is introduced by [61]. However, we design the system based on a circuit model to understand the system more concretely.

## 4.1 Three-dimensional (3D) microwave cavity

The reasons why we use the 3D cavity in this thesis are as following. First, the Q factor of the 3D cavity is known to be higher than that of a two-dimensional resonator, since its mode volume is larger and its electromagnetic field at the possibly lossy surface is diluted [24, 62]. Second, the external coupling rate of the 3D cavity is tunable by controlling the position of a coupling pin. Last, the transmon qubit on the substrate is separable from the 3D cavity, which enables us to choose the best samples from among transmon qubits and insert the selected qubit into 3D cavities after characterizations. The drawbacks of the 3D cavity when compared to the 2D resonator are that 3D cavities are too bulky for scaling up, vulnerable to crosstalk, and hard to implement functionality introduced by other elements common in 2D systems such as Purcell filters [63, 64].

We use a rectangular 3D cavity as shown in Fig. 4.1(a). A microwave field is confined in the 3D cavity with fixed-end conditions for the electric field, and thus a mode forms with the standing wave. The resonance frequencies of the $\mathrm{TE}_{n0m}$ mode of the rectangular 3D cavity can be calculated analytically as

$$\omega_\mathrm{c}/2\pi = \frac{c}{2D}\sqrt{\left(\frac{m}{\cos\theta_\mathrm{c}}\right)^2 + \left(\frac{n}{\sin\theta_\mathrm{c}}\right)^2}, \tag{4.1}$$

where $c$ is the speed of light, $D = \sqrt{D_x^2 + D_y^2}$ is the length of the hypotenuse, $D_x = D\cos\theta_\mathrm{c}$, and $D_y = D\sin\theta_\mathrm{c}$ are the length of the width ($x$) and height ($y$), and $n$ and $m$ are the mode numbers of the x and y components, respectively. The TE mode stands for a transverse electric mode, where the electric field is orthogonal to the direction of the propagation on the $xy$-plane.

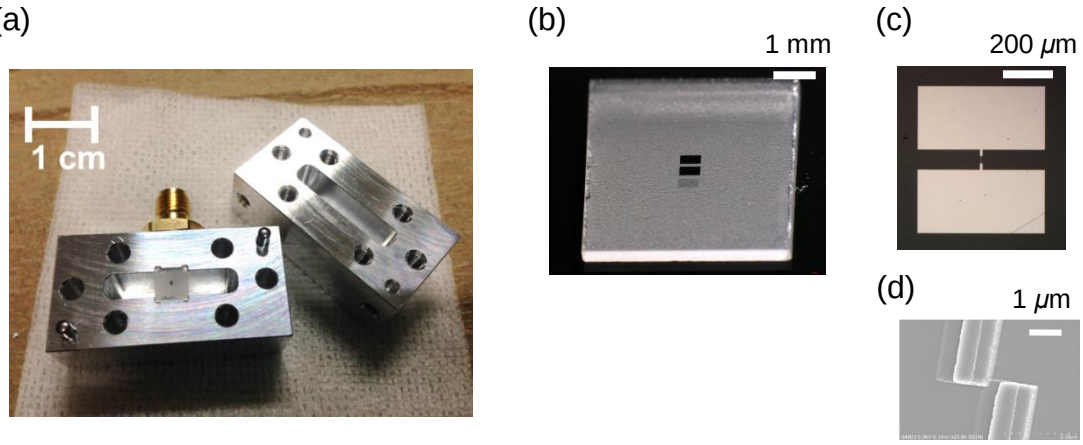


Figure 4.1: 3D circuit QED system. (a) 3D cavity. The connector with a coupling pin is installed on the top of the cavity. (b) Transmon qubit on a sapphire substrate. (c) Picture of a transmon qubit. (d) SEM image of a Josephson junction.

For the circuit QED system, we use the fundamental mode of the 3D rectangular cavity with $\theta_c = \pi/4$ and $n = m = 1$. The resonance frequency of the fundamental mode can be calculated as

$$\omega_c/2\pi = \frac{c}{D}. \tag{4.2}$$

Thus, the resonance frequency of the fundamental mode can be easily calculated with chosen design parameters as

$$10 \text{ GHz} \approx \frac{c}{30 \text{ mm}}. \tag{4.3}$$

We can roughly estimate the length of the cavity with the resonance frequency of 10 GHz as $D = 30$ mm and $D_x = D_y = 21$ mm.

The electric field distribution in the 3D cavity is useful to design the coupling strength of the 3D cavity with the transmon qubit, which can be roughly determined by the inner product between the normalized electric field of the 3D cavity and the dipole moment of the transmon qubit. The electric distribution of each $\mathrm{TE}_{n0m}$ mode of the rectangular cavity can be calculated analytically as

$$E_z(x, y) = E_0 \sin\left(\frac{n\pi x}{D_x}\right) \sin\left(\frac{m\pi y}{D_y}\right), \tag{4.4}$$

where $E_0$ is the normalized electric field. Note that the $x$ and $y$ components of the electric field are zero in the $\mathrm{TE}_{n0m}$ mode.

Some examples of the resonance frequencies and the electric field distributions of the 3D rectangular cavity modes are shown in Fig 4.2.

The aluminum-made cavity, as shown in Fig. 4.1(a), is machined by Ono Denki. We use the aluminum of "A1050" (Al: $\geq 99.5\%$) for the 3D cavity. The cavity is composed of two parts, whose joint surface is machined to be as flat as possible to suppress the seam loss. Six screws are used to close the cavity tightly. Two alignment pins are installed within the accuracy of 0.01 mm. The 3D cavity can be coupled to a waveguide through a pin connector. We use the pin connector model "PE4530", which is manufactured by Pasternack. The female-SMA connector with the coupling pin is made of beryllium copper to reduce magnetic noises.

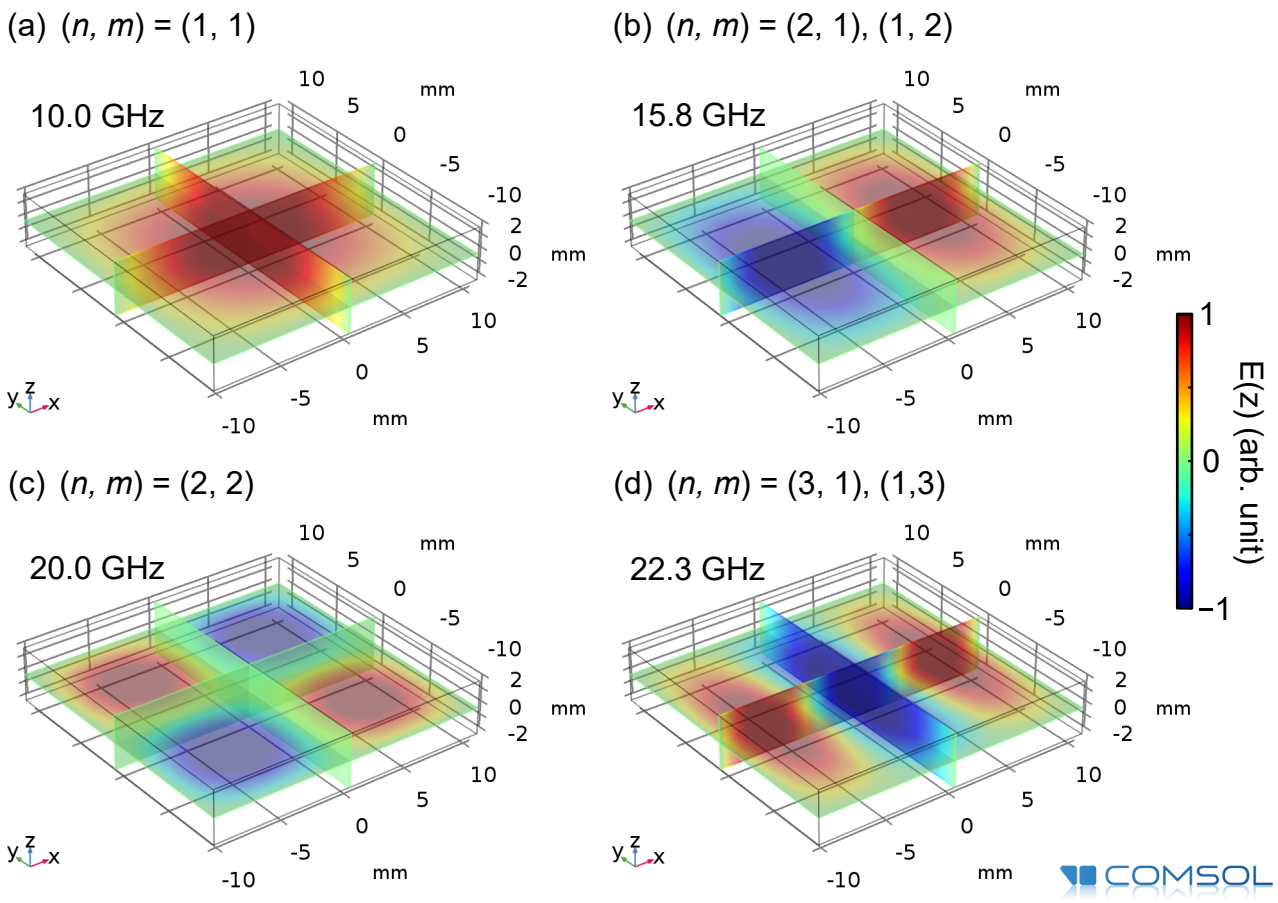


Figure 4.2: Resonance frequencies and electric field distributions of the rectangular 3D cavity. The lower cavity modes are shown in (a) $(n, m) = (1, 1)$, (b) $(n, m) = (2, 1), (1, 2)$, (c) $(n, m) = (2, 2)$, and (d) $(n, m) = (3, 1), (1, 3)$. The distributions of the normalized electric fields along the $z$-axis are plotted. Here, we set $D = 30$ mm and $\theta_c = \pi/4$ so that the resonance frequency of the fundamental mode is around 10 GHz.

### 4.1.1 Resonance frequency

The shape of the rectangular cavity, shown in Fig. 4.1(a), is not precisely rectangular due to the convenience for the machining. Furthermore, the sapphire substrate, on which the transmon qubit is fabricated, is placed at the center of the 3D cavity. Nevertheless, we can calculate its resonance frequency and its electric and magnetic field distributions using an electromagnetic field simulator. Here, we use the eigenfrequency analysis tool in COMSOL Multiphysics. We model the inner wall of the cavity including the coupling pin

Table 4.1: Resonance frequencies of the 3D cavities without the sapphire substrate. In the simulation, the cavity frequency is calculated from the design. The external coupling rates of the cavity at room temperature and at the base temperature are set individually.

| Configuration | $\omega_c/2\pi$ (GHz) | $\kappa_{ex}/2\pi$ (MHz) | $\kappa_{in}/2\pi$ (kHz) |
|---|---|---|---|
| Simulation | 11.6650988 | - | - |
| Room temperature | 11.69451 | 39.4 | 3420 |
| Base temperature | 11.7504721 | 4.7 | 2.0 |

and the substrate as shown in Fig. 4.3. The boundary condition of the wall is set to be a perfect electric conductor (PEC), since the 3D cavity becomes a superconductor at the base temperature of a dilution refrigerator. Therefore, we can design a 3D cavity with the target resonant frequency.

The accuracy of the resonance frequency is limited by the machining error. From Eq. (4.1), we can roughly estimate the effect of the machining error on the resonance frequency as

$$\frac{\Delta\omega_{\rm c}}{\omega_{\rm c}} = -\frac{\Delta D}{D}, \tag{4.5}$$

where $\Delta\omega_{\rm c}$ and $\Delta D$ are the errors of the resonance frequency and length of the 3D cavity. Suppose the typical machining error is 0.1 mm, then the relative frequency error at 10 GHz ($D$ =30 mm) can be calculated as $\Delta\omega_{\rm c}/\omega_{\rm c} = 0.003$, which corresponds to a frequency shift of 30 MHz at 10 GHz. We compare the resonance frequency of the 3D cavity between the simulation and the actual device without loading a sapphire substrate. The cavity frequencies of the simulation and the actual device at room temperature are shown in Table 4.1. The relative frequency error can be calculated to be about 0.0025, which is within the expectations.

For the cavity frequency at the base temperature of the dilution refrigerator, we may consider the effect of thermal expansion. By comparing the cavity frequencies between room temperature and the base temperature, shown in Table 4.1, we obtain a frequency shift of about 56.0 MHz at 11.75 GHz, which corresponds to $\Delta\omega_{\rm c}/\omega_{\rm c} = -\Delta D/D = 0.00476$. From Eq. (4.5), the thermal-expansion length from the base to room temperature can be calculated to be about 0.15 mm with the cavity length of 30 mm. Since the thermal-expansion length is comparable to the machining error, we may not dismiss the effect. Note that the thermal expansion coefficient obtained from the frequency shift is about $(\Delta D/D)/\Delta T = 17\ \mu{\rm K}^{-1}$, where $\Delta T$ is the difference between room temperature and the base temperature. This is consistent with the literature data of 23 $\mu{\rm K}^{-1}$ within an error of a few tens of percents.

As explained later, the transmon qubit is fabricated on a sapphire substrate and is placed in the 3D cavity. Then, the relative permittivity of the substrate is also needed for the simulation. We obtain the relative permittivity by measuring the cavity frequency shift at the base temperature. The cavity frequency with the sapphire substrate at the base temperature is listed in Table 4.2. Then, the frequency shift is found to be about 0.75 MHz. By fitting the cavity frequency in the simulation, we obtain the relative permittivity of the sapphire at the base temperature as $\varepsilon_{\rm r} = 7.96$. Here, the machining error and the thermal expansion effect are considered in the simulation. However, the anisotropy of the permittivity of sapphire is not considered, since the direction of the electric field of the cavity mode can be uniform in the substrate.

Table 4.2: Resonance frequencies of the 3D cavities with the sapphire substrate. In the simulation, the machining error and the heat expansion effect are considered. The position of the coupling pin is set to be the same as the bare cavity in the base temperature, shown in Table 4.1.

| Configuration | $\omega_{\rm c}/2\pi$ (GHz) | $\kappa_{\rm ex}/2\pi$ (MHz) | $\kappa_{\rm in}/2\pi$ (kHz) |
|---|---|---|---|
| Simulation ($\varepsilon_{\rm r} = 7.96$) | 11.0034030 | - | - |
| Base temperature | 11.0034484 | 2.92 | 29 |

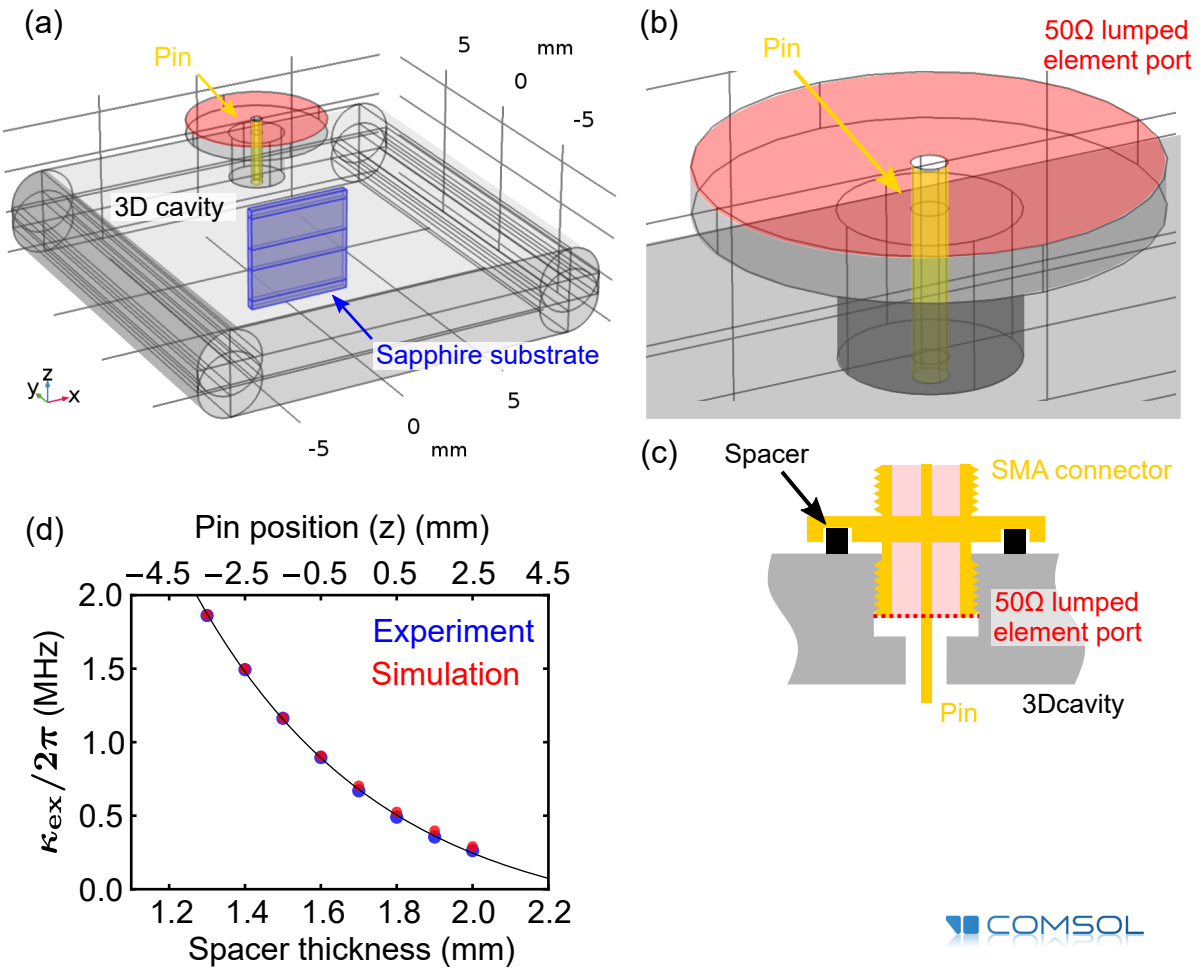


Figure 4.3: 3D cavity modeled in the simulation. (a) 3D cavity with the sapphire substrate and the coupling pin. The outer box and the blue box depict the cavity and the sapphire substrate, respectively. The yellow rod is the coupling pin. The red part is the lumped element port. (b) Coupling pin and 50 Ω lumped element port. The lumped port is defined at the part between the root of the pin and the external ground electrode. (c) Side view of the SMA connector and the cavity. (d) External coupling rate as a function of the pin position in the $z$-axis. The horizontal axis on the bottom is the spacer thickness, as shown in (c). The horizontal axis on the top is the position of the pin tip from the inner wall of the upper side of the 3D cavity. The blue and red dots are the experimental and simulated results, respectively. The black line is the exponential curve fit.

### 4.1.2 External coupling rate

The external coupling rate of the 3D cavity is set depending on a specific purpose. For instance, for the readout of the transmon qubit, it should be set to be on the same order of magnitude as the state-dependent dispersive shift, which is typically around 1 MHz. For the evaluation of the internal loss of the 3D cavity, it should be set to the order of magnitude of the internal loss, which is typically from 1 kHz to 100 kHz. Therefore, the 3D cavity is designed to have a tunable external coupling rate from 1 kHz to 10 MHz. As shown in Fig. 4.1, the pin connector is used for external coupling to the waveguide.

In the eigenfrequency analysis in COMSOL Multiphysics, the external coupling rate of the 3D cavity is characterized as the energy relaxation of the 3D cavity into the waveguide.

While the resonance frequency corresponds to the real part of the eigenfrequency, the total energy-relaxation rate corresponds to twice the imaginary part of the eigenfrequency as

$$\text{Eigenfrequency} = \omega_c/2\pi + i\frac{\kappa}{2}/2\pi, \tag{4.6}$$

where $\kappa$ is the total energy-relaxation rate of the cavity mode. The reason why twice the imaginary part corresponds to the energy-relaxation rate is that the simulator calculates the eigenfrequency of the electromagnetic field, or the square root of the energy. The semi-infinite waveguide whose end is coupled to the 3D cavity can be modeled with a resistive termination matched with the characteristic impedance of the waveguide. As shown in Figs. 4.3(b) and (c), we simulate the 3D cavity from the root of the pin, since the part of the connector is designed to have the characteristic impedance of 50 Ω. The 50 Ω lumped-element port is defined at the part between the root of the pin and the external ground electrode, the red part in Fig. 4.3(b). Then, the external coupling rate of the cavity can be obtained as the imaginary part of the eigenfrequency as $\kappa_{ex} = \kappa$, since there is no energy-relaxation channel except for the external coupling to the waveguide.

As shown in Fig. 4.3(c), we can control the pin position in the $z$-axis by interposing the spacer with 0.1 mm increments of thickness. The external coupling rate of the fundamental mode of the 3D cavity as a function of the total spacer thickness is shown in Fig. 4.3(d). Here, we measure the 3D cavity with the sapphire substrate at room temperature. The experimental results agree well with the simulation results. The data can also be fitted with an exponential curve [62].

Practically, the external coupling rate of the cavity is fine-tuned at room temperature. The important point is that the external coupling rate of the 3D cavity is determined only by the relative position between the pin and the 3D cavity. Therefore, the external coupling rate which is tuned at room temperature is supposed not to change at the base temperature of the dilution refrigerator. Here, the external coupling rates of the 3D cavity at room and base temperatures are shown in Table 4.3.We confirm that the external coupling rate does not change within ten percent.

## 4.2 Transmon qubit

The transmon qubit, which is used in this thesis, is shown in Fig. 4.1. The capacitor of the electrodes and the Josephson junction are deposited on the sapphire substrate. The Josephson junction is fabricated by the doube The transmon qubit can be considered as an anharmonic LC resonator. More precisely, the Josephson junction can be modeled as a lumped-element inductor. Then, the resonance frequency and the electromagnetic mode of the linearized transmon qubit can be obtained. By treating the nonlinearity of the Josephson junction perturbatively, the resonance frequency and the anharmonicity of the transmon qubit can be determined.

Table 4.3: External coupling rates of the 3D cavities with the sapphire substrate.

| Configuration | $\omega_c/2\pi$ (GHz) | $\kappa_{ex}/2\pi$ (MHz) | $\kappa_{in}/2\pi$ (kHz) |
|---|---|---|---|
| Room temperature | 10.56061 | 3.075 | 4000 |
| Base temperature | 10.62524 | 3.32 | 250 |

### 4.2.1 Josephson junction

The Josephson junction can be replaced with a corresponding lumped-element inductor in the model. The Josephson junction is characterized by the critical current $I_c$ and the tunneling energy $E_J = \hbar\omega_J$, where $\omega_J$ is the energy in frequency units. The relation between them can be described as

$$\hbar\omega_J = I_c\phi_0, \tag{4.7}$$

where $\phi_0 = \hbar/2e$ is the reduced magnetic flux quantum. Remember that the tunneling energy in the trasmon qubit corresponds to the inductive energy quantum in the LC resonator as $\hbar\omega_J = \phi_0^2/L_J$. Therefore, the Josephson inductance can be obtained as

$$L_J = \frac{\phi_0^2}{\hbar\omega_J}. \tag{4.8}$$

The Josephson inductance will be used in the electromagnetic field simulator.

It is useful to estimate the tunneling energy of the Josephson junction before cryogenic measurement of the transmon qubit. Here, we estimate the tunneling energy indirectly by measuring the normal-state resistance of the Josephson junction at room temperature. Following the Ambegoakar-Baratoff relation [65], the tunneling energy can be described as

$$\hbar\omega_J = \pi\left(\frac{Z_0}{R_n}\right)\Delta_s, \tag{4.9}$$

where $R_n$ is the normal-state resistance of the Josephson junction, $Z_0 = \hbar/(2e)^2 \approx 1.03\,\mathrm{k\Omega}$ is the reduced impedance quantum, and $\Delta_s$ is the superconducting gap energy. By measuring the normal-state resistance and assuming the superconducting gap, the tunneling energy of the Josephson junction can be estimated before the cryogenic measurement.

In this thesis, the Josephson junction is fabricated with $Al/AlO_x/Al$, as shown in Fig 4.1. The superconducting gap of thin-film aluminum is known in frequency units to be about $2\Delta_s/h = 84$ GHz [66]. Then, the tunneling energy of the aluminum-made Josephson junction can be determined in terms of the normal-state resistance as

$$\omega_J/2\pi = \left(\frac{Z_0}{R_n}\right) \times 132\ \mathrm{GHz}. \tag{4.10}$$

For the simulation, it is also useful to show the direct relation between the Josephson inductance and the normal-state resistance as

$$\begin{aligned} L_J &= \left(\frac{R_n}{Z_0}\right) \times 1.24\ \mathrm{nH} \\ R_n &= \left(\frac{L_J}{1.24\ \mathrm{nH}}\right) \times 1.03\ \mathrm{k\Omega}. \end{aligned} \tag{4.11}$$

### 4.2.2 Resonance frequency and anharmonicity

To design the transmon qubit is to determine the ratio of $\omega_C/\omega_J$ and the resonance frequency $\omega_q$, where the capacitive energy quantum is defined as $\hbar\omega_C = (2e)^2/C$. First, the ratio should be much smaller than unity to realize the transmon qubit. However, decreasing the ratio of $\omega_C/\omega_J$ also decreases the anharmonicity of the qubit. Empirically, $\omega_C/\omega_J$ is set to about 0.1. Second, the resonance frequency of the transmon qubit is described as $\omega_q = \omega_q^l - \omega_C/8 \approx \omega_q^l$, where $\omega_q^l = \sqrt{\omega_J\omega_C}$ is the linearized qubit frequency.

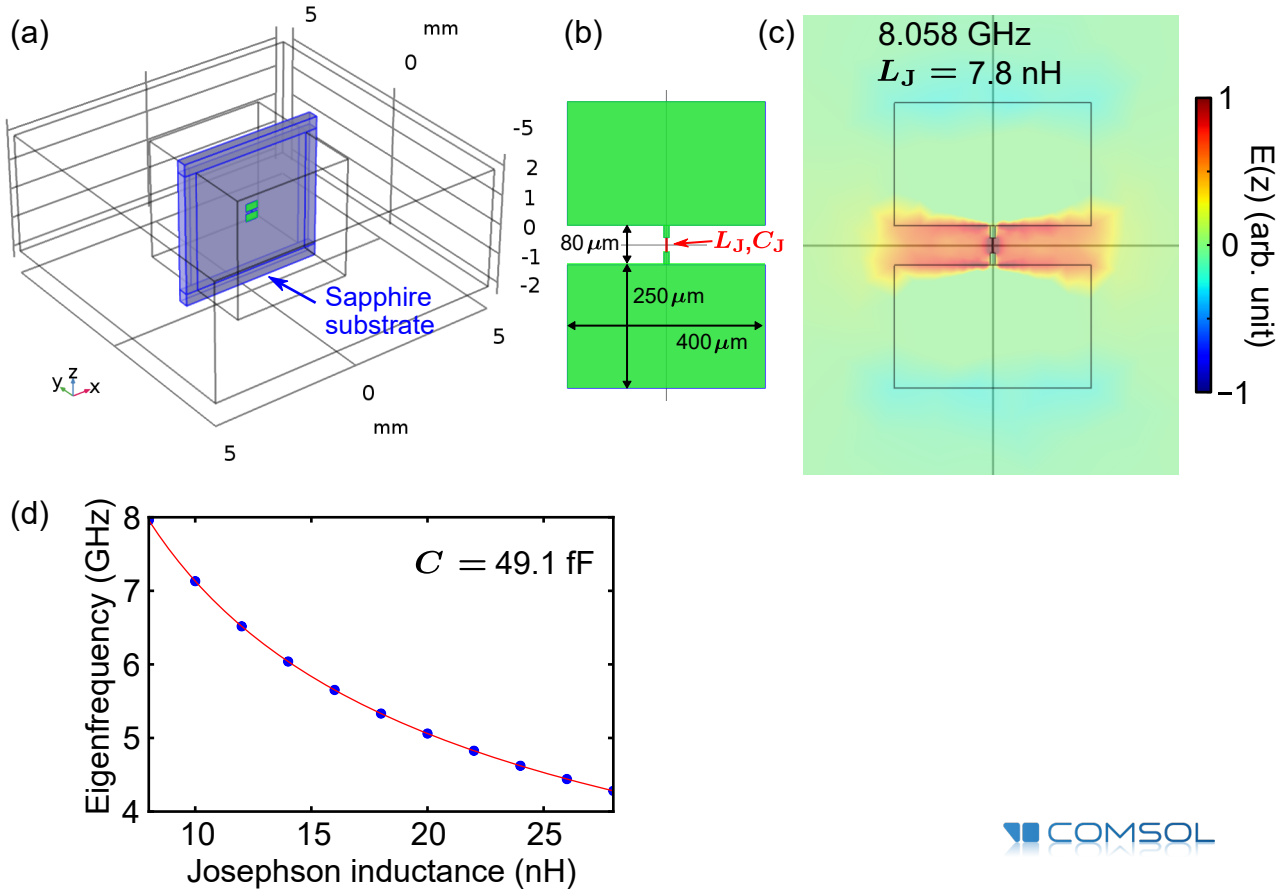


Figure 4.4: Transmon qubit modeled in the simulation. (a) Transmon qubit on the sapphire substrate in the 3D cavity. The outer box depicts the cavity. The inner box is used to make the finner mesh for the qubit mode. The blue box depicts the sapphire substrate. The green pattern is the transmon qubit. (b) Circuit design of the transmon qubit. (c) Electric field modes of the transmon qubit. The normalized electric fields along the $z$-axis are plotted. (d) Linearized qubit frequency as a function of the Josephson inductance. The blue dots are the simulation results and the red line is the theoretical fits.

Here, we roughly estimate the tunneling energy and the capacitive energy quantum to achieve the target ratio and resonance frequency. Given the ratio of $\omega_C/\omega_J$ and the resonance frequency $\omega_q \approx \omega_q^l = \sqrt{\omega_J \omega_C}$, the tunneling energy and the capacitive energy quantum can be roughly determined in frequency units as

$$\begin{aligned} \omega_J &= \sqrt{\frac{\omega_J}{\omega_C}}\,\omega_q^l \approx \sqrt{\frac{\omega_J}{\omega_C}}\,\omega_q \\ \omega_C &= \sqrt{\frac{\omega_C}{\omega_J}}\,\omega_q^l \approx \sqrt{\frac{\omega_C}{\omega_J}}\,\omega_q. \end{aligned} \tag{4.12}$$

For instance, to achieve $\omega_C/\omega_J = 0.1$ and $\omega_q/2\pi = 8$ GHz, $\omega_J/2\pi = 25$ GHz and $\omega_C/2\pi = 2.5$ GHz or $\alpha/2\pi = -\omega_C/8/2\pi = -0.3$ GHz are required. The Josephson inductance and the capacitance can be calculated as $L_J = 6.5$ nH and $C = 62$ fF, respectively.

As for the 3D cavity, the resonance frequency and electromagnetic field of the transmon qubit can be calculated in the classical electromagnetic field simulator. As shown in Fig. 4.4(a), the transmon qubit on the sapphire substrate is placed in the cavity. Note

that the cavity mode frequencies are pushed further away from the qubit frequency, so as not to affect the qubit mode, here. The example of the circuit pattern of the transmon qubit is shown in Fig 4.4(b). The two electrodes, on which the perfect electric conductors are defined, behave as the geometric capacitance. The lumped-element inductor $L_{\rm J}$ is assigned to the bar between the two electrodes, the red bar in Fig. 4.4(b). Furthermore, the junction capacitance can also be defined as the lumped element in the same way. Then, the circuit pattern of the capacitance is designed so that the resonance frequency can be the target one. Once the target resonance frequency is obtained, the target ratio of $\omega_{\rm C}/\omega_{\rm J}$ can be automatically satisfied. The result of the linearized frequency and the electric field of the transmon qubit mode is shown in Fig. 4.4(c). Note that the junction capacitance is set to zero in this simulation.

Then, we consider the nonlinear effect from the Josephson junction perturbatively. From the results in Sec. 2.5, the qubit frequency shifts and the anharmonicity due to the nonlinearity are given by $-\omega_{\rm C}/8$, where $\hbar\omega_{\rm C}/2\pi = (2e)^2/C$ is the capacitive energy quantum. Although it can be calculated as $\omega_{\rm C} = {\omega_{\rm q}^l}^2/\omega_{\rm J}$, it is considered more carefully by calculating the resonance frequency of the qubit mode as a function of the Josephson inductance $L_{\rm J}$, shown in Fig. 4.4(d). Note that the inductance range is determined such that the cavity modes does not affect the qubit frequency. The simulation results are well-fitted by

$$\omega_{\rm q}^l = \sqrt{\omega_{\rm J}\omega_{\rm C}} = \frac{1}{\sqrt{(L_{\rm J}+L_{\rm S})C}}, \tag{4.13}$$

where $C$ is the total capacitance of the transmon qubit and $L_{\rm S}$ is the stray inductance in series with the Josephson junction. With the obtained fitting parameters of $C = 49.1$ fF, $L_{\rm S} = 0.14$ nH, the capacitive energy quantum is calculated in frequency units as $\omega_{\rm C}/2\pi = (2e)^2/C/h = 3.16$ GHz. We confirm that the stray inductance accounts for about ten percent of the total inductance. Thus, we may neglect the stray inductance in determining the capacitance. Nevertheless, the fitting is helpful to confirm that the qubit frequency is not affected by the frequency shift due to the coupling with the cavity modes. Furthermore, we also confirm that the capacitance is not varied within one percent in the case of the different size of the cavity as long as the cavity does not affect the qubit frequency. Now, we can accurately calculate the resonance frequency of the transmon qubit with the Josephson inductance $L_{\rm J} = 7.8$ nH as $\omega_{\rm q} = \omega_{\rm q}^l - \omega_{\rm C}/8 = 7.663$ GHz. Furthermore, the anharmonicity of the transmon qubit is obtained as $\alpha = -\omega_{\rm C}/8 = -395$ MHz.

By comparing the capacitances between the simulation and the experiment, we can evaluate the junction capacitance. The simulation and experimental results are listed in Table 4.4.Here, since the junction capacitance is set to zero in the simulation, the capacitance is composed of only the geometric capacitance from the two electrodes. Thus, the difference of the capacitances gives the actual junction capacitance, which is calculated as 7.5 fF. We find that the junction capacitance is about 15 percent of the total capacitance, which may not be neglected. Therefore, we take into account the junction capacitance in the simulation, hereinafter. Note that the junction capacitance is varied in proportional to the tunneling energy of the Josephson junction as both of them scale with the Junction area.

## 4.3 3D Circuit QED system

We explain how to design the 3D circuit QED system, where the transmon qubit is coupled to the 3D cavity. In the eigenfrequency analysis of the electromagnetic field simulator,

we obtain their diagonalized modes and the resonance frequencies of the coupled system. By comparing the results with the eigenfrequency of the Hamiltonian of two coupled resonators, we can characterize and design the circuit QED system.

### 4.3.1 Coupling strength

Assuming that there are only two modes, or a cavity mode and a transmon qubit mode, the eigenfrequency of the electromagnetic field simulation can be modeled by two capacitively-coupled resonators. The assumption is valid when the other modes are far-detuned in frequency from the circuit QED system. As explained in Sec. 2.2.1, the frequency splitting of the coupled resonators in the resonance condition corresponds to twice the coupling strength. In other words, the minimum of the frequency splitting in terms of the frequency detuning gives us twice the coupling strength. In the simulation, since the qubit frequency can be varied by changing the Josephson inductance while keeping the capacitance structures, the minimum of the frequency splitting can be obtained. One of the good points of this characterization is that the frequency splitting cannot be affected by the coupling with the other far-detuned modes. As shown in Fig. 4.5(a), the 3D circuit QED system is modeled in the simulation. The cavity and qubit frequencies and the frequency splitting as a function of the Josephson inductance are shown in Figs. 4.5(b) and (c). By fitting the frequency splitting with the polynomial function, the minimum of the frequency splitting can be obtained more accurately. Then, the coupling strength is calculated as $g_0/2\pi = 185$ MHz. Note that the coupling strength is valid in the resonance condition.

### 4.3.2 Dispersive regime

The 3D circuit QED system is often used in the dispersive regime, where the frequency detuning is larger than the coupling strength.

#### Resonance frequencies

First of all, since the simulator calculates the eigenfrequencies of the diagonalized modes, we can directly obtain the cavity frequency and the linearized qubit frequency with the Lamb shifts as

$$\begin{aligned} \omega_{\mathrm{c}}' &= \omega_{\mathrm{c}} + \frac{g^2}{\Delta} \\ \omega_{\mathrm{q}}^{l\,\prime} &= \omega_{\mathrm{q}}^{l} - \frac{g^2}{\Delta} \end{aligned} \tag{4.14}$$

where $\Delta = \omega_{\mathrm{c}} - \omega_{\mathrm{q}}^{l}$ is the frequency detuning and $g$ is the coupling strength in the dispersive regime. Here, we use $\omega_{\mathrm{c}}'$ and $\omega_{\mathrm{q}}{}'$ for the characterization.

Table 4.4: Capacitive energy quanta of the transmon qubit. In the simulation, the junction capacitance is not included. Thus, the difference indicates the junction capacitance of $C_{\mathrm{J}}$=7.5 fF.

| Configuration | $\omega_{\mathrm{C}}/2\pi$ (GHz) | $\alpha/2\pi$ (MHz) | $C$ (fF) |
|---|---|---|---|
| Simulation | 3.16 | −395 | 49.1 |
| Experiment | 2.74 | −342 | 56.6 |

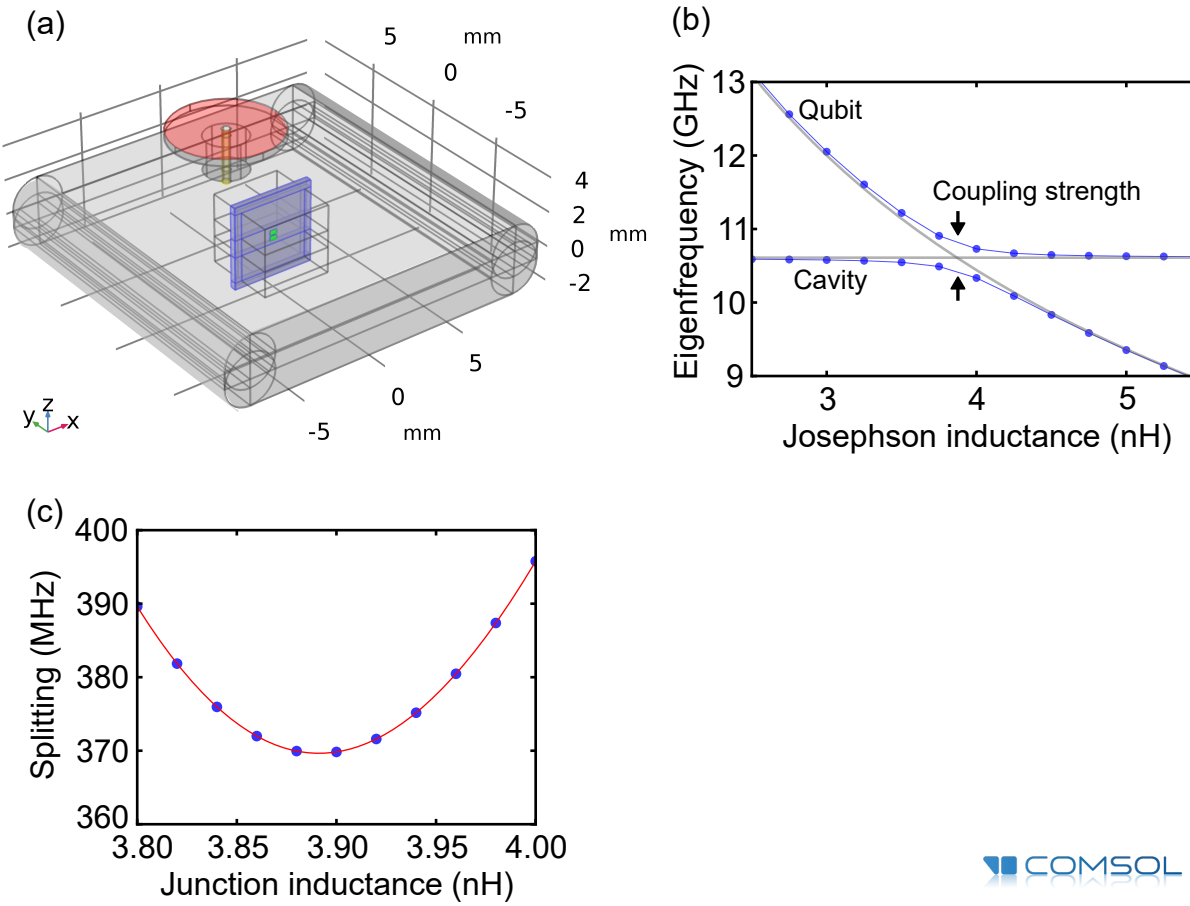


Figure 4.5: 3D circuit QED system modeled in the simulation. (a) 3D cavity simulation with the sapphire substrate and the external coupling pin. The outer box and the blue box depict the cavity and the sapphire substrate, respectively. The green pattern is the transmon qubit. The yellow rod and the red part depict the coupling pin and the lumped element port, respectively. (b) Eigenfrequencies of the qubit and the cavity as a function of the Josephson inductance. The minimum frequency splitting gives twice the coupling strength. (c) Frequency splitting as a function of the Josephson inductance. The blue dots and the red line are the simulation results and the polynomial function fit. The coupling strength in the resonance condition is evaluated to be $g_0/2\pi = 185$ MHz.

Next, the capacitance energy quantum $\omega_C$ is calculated by the qubit frequency as a function of the Josephson inductance, as discussed in Sec. 4.2.2. Note that the qubit frequency should be set to be far detuned from the cavity modes. Using the obtained $\omega_C$, the qubit frequency and the anharmonicity can be calculated as $\omega_q' = \omega_q^{l\,\prime} - \omega_C/8$ and $\alpha = -\omega_C/8$, respectively.

Table 4.5: State-dependent shift. In the simulation, the junction inductance is set to be 6.54 nH so that the qubit frequency can reproduce the experimental results.

| Configuration | $\omega_c'/2\pi$ (GHz) | $\omega_q'/2\pi$ (GHz) | $\alpha/2\pi$ (GHz) | $g/2\pi$ (MHz) | $\chi/2\pi$ (MHz) |
|---|---|---|---|---|---|
| Simulation | 10.62 | 7.87 | $-343$ | 163 | 1.60 |
| Experiment | 10.6267 | 7.8693 | $-342$ | - | 1.50 |

### State-dependent dispersive shift

From Eq. (2.22) in Sec. 2.2, we know that the coupling strength induced by the capacitive coupling has the frequency dependence in terms of the linearized qubit frequency as

$$\frac{2g}{\sqrt{\omega_{\rm c}\omega_{\rm q}^{l}}} = \text{Const.}, \tag{4.15}$$

where the right side is constant in terms of the Josephson inductance, which is determined from the capacitances. Therefore, with the value of $g_0$ which can be obtained from the minimum frequency splitting as in Sec. 4.3.1, the coupling strength in the dispersive regime can be calculated as

$$g = \sqrt{\frac{\omega_{\rm q}^{l}}{\omega_{\rm c}}}\, g_0 \approx \sqrt{\frac{\omega_{\rm q}^{l\,\prime}}{\omega_{\rm c}{}'}}\, g_0. \tag{4.16}$$

The approximation is valid as long as the carrier frequencies of $\omega_{\rm c}$ and $\omega_{\rm q}^{l}$ are much larger than the Lamb shift of $g^2/\Delta$.

The actual frequency detuning $\Delta = \omega_{\rm c} - \omega_{\rm q}^{l}$ is also indispensable for the state-dependent dispersive shift. From Eq. (4.14), the frequency detuning in the diagonalized modes $\Delta' = \omega_{\rm c}' - \omega_{\rm q}^{l\,\prime}$ is described as

$$\Delta' = \Delta + 2\frac{g^2}{\Delta}. \tag{4.17}$$

Then, the actual frequency detuning is calculated approximately in the leading order of $g/\Delta'$ as

$$\Delta \approx \Delta' - 2\frac{g^2}{\Delta'}. \tag{4.18}$$

Finally, the state-dependent dispersive shift can be calculated as

$$\chi = \left(\frac{g}{\Delta}\right)^2 \alpha. \tag{4.19}$$

The state-dependent dispersive shift $\chi$ as a function of the qubit frequency $\omega_{\rm q}'$ is shown in Fig. 4.6(a). The dispersive shift in the 3D circuit QED system is found to be in the order of 1 MHz.

The summary of the simulation and experimental results are listed in Table 4.5.Note that the junction inductance is set to 6.54 nH so that the qubit frequency can reproduce the observed one, since we did not measure the normal-state resistance of the Josephson junction for this sample. The cavity length is also adjusted to reproduce the cavity frequency and to compensate the machining error. The junction capacitance is also determined to reproduce the anharmonicity, as explained in Sec. 4.2.2. The important point is that the state-dependent dispersive shift calculated from the simulation results well reproduces the observed one.

Table 4.6: Comparison of the relaxation times of the qubit.

| | Experiment | All-modes Purcell decay | Single-mode Purcell effect |
|---|---|---|---|
| $T_1$ ($\mu$s) | 32 | 43 | 11 |

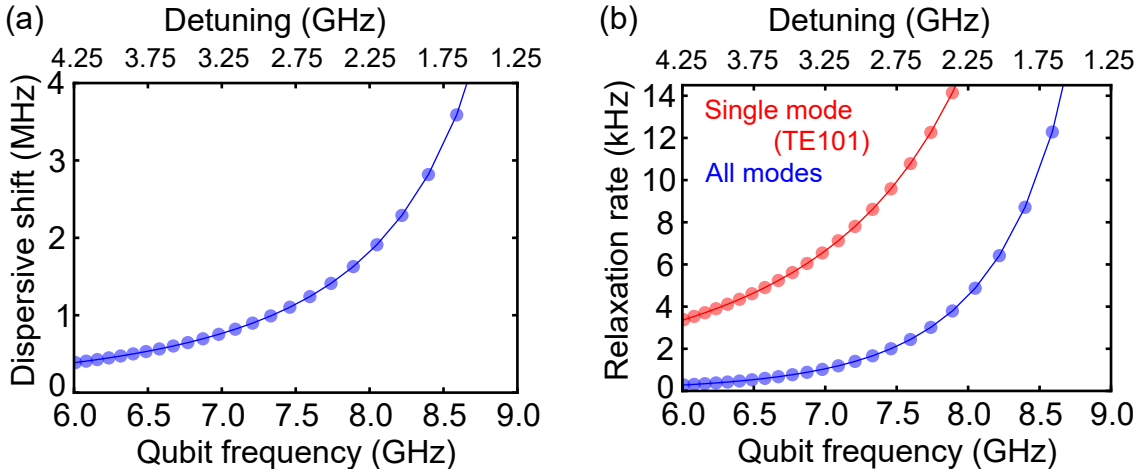


Figure 4.6: Dispersive 3D circuit QED system. (a) State-dependent dispersive shift as a function of the qubit frequency. (b) External relaxation rate of the qubit as a function of the qubit frequency. The horizontal axis on the upper side depicts the frequency detuning between the cavity and the qubit. The blue data are directly obtained from the electromagnetic field simulator. The red data are calculated from the theoretical Purcell decay induced by the fundamental mode $TE_{101}$.

## External coupling rates in the dispersive regime

The external coupling rates in the dispersive regime can be also obtained from the imaginary parts of the eigenfrequencies. First, the cavity external relaxation rate is evaluated, as explained in Sec. 4.1.2. Second, we obtain the qubit external relaxation rate in the same way. As explained in Sec. 2.5.1, the diagonalized qubit mode with the finite mixing of the cavity mode is coupled to the waveguide, which gives the external relaxation rate to the qubit. Since the simulation calculates the eigenfrequencies of the diagonalized modes, including the imaginary parts, the Purcell effect can be naturally included. Therefore, the qubit external relaxation rate can be simply obtained by calculating twice the imaginary part of the eigenfrequency of the qubit mode. Furthermore, we can calculate the qubit relaxation rate by taking into account all the cavity modes which are coupled to the qubit. Thus, the results of the qubit relaxation rate can be more accurate than that obtained from the circuit model in Sec. 2.5.1. The qubit external relaxation rate as a function of the qubit frequency $\omega_q'$ is shown as blue dots in Fig. 4.6(b). The red dots are the external coupling rates, which are calculated based on the Purcell effect via the fundamental mode $TE_{101}$ as $(g/\Delta)^2\,\kappa_{ex}$. Surprisingly, the actual external coupling rate is about five-times smaller than that from the single-mode Purcell effect. In other words, the energy-relaxation time in the Purcell limit is longer in the 3D circuit QED system than a circuit QED system with a single cavity mode. It can be understood that the higher cavity modes play a role of the Purcell filter, where the qubit relaxation is canceled by the relaxation through the higher cavity modes to some extent [67]. The experimental result of the relaxation time and the simulated relaxation times in the Purcell limit are listed in Table 4.6.We find that our qubit relaxation time reaps the benefit of the Purcell filter.

# Chapter 5

# Experimental setup

In this section, we explain the experimental setup. To control a superconducting qubit, it is crucial to make the environment in which our system exists well-cooled down. To measure it, we need to amplify a weak probe microwave signal with high efficiency. Here, we evaluate and modify our experimental setup by measuring the coherence and the thermal excitation of a transmon qubit.

## 5.1 Dilution refrigerator

Since quantum information is encoded in the energy excitations in microwave circuits, it is crucial to use superconductors for the circuit materials in order to hold the energy excitations as long as possible. Therefore, the microwave circuits should be cooled far below the critical temperature of the materials. Moreover, Josephson effects, which are indispensable for the realization of a superconducting qubit, can be observed only in superconductors. Therefore, a refrigerator is indispensable to realize superconducting circuits. The critical temperatures of the materials which are typically used for superconducting circuits are listed in Table 5.1.

To promote superconducting circuits to superconducting "quantum" circuits, it is also important to cool down their environment well. The typical environment of superconducting circuits are electromagnetic modes. From the lindblad master equation in Eq. (2.102) in Sec. 2.5.1, the transition rates of the qubit in the thermal environment can be described as

$$\begin{aligned} \gamma_\downarrow &= (1 + n_{\mathrm{th}})\gamma \\ \gamma_\uparrow &= n_{\mathrm{th}}\gamma, \end{aligned} \tag{5.1}$$

where $\gamma_\downarrow$ is the transition rate from the excited to ground states, $\gamma_\uparrow$ is the transition rate from the ground to excited states, $\gamma$ is the coupling rate of the qubit to the environment, and $n_{\mathrm{th}}$ is the thermal photon number in the environment around the qubit frequency. The transition rates are increased as the thermal photon number is increased. From the detailed balance, the qubit excitation probability at thermal equilibrium can be written as

$$P_{\mathrm{e}} = \frac{n_{\mathrm{th}}}{1 + 2n_{\mathrm{th}}}, \tag{5.2}$$

Table 5.1: Examples superconducting of critical temperatures.

| Al | Nb | TiN | In |
|---|---|---|---|
| 1.2 K | 9.2 K | 3.7 K | 3.4 K |

which corresponds to the initialization error, or the success probability in the conditional experiments. Moreover, the dephasing rate of the qubit, which is coupled to the readout cavity, can be written as

$$\gamma_{\phi,\mathrm{th}} = \frac{4\chi^2\kappa}{\kappa^2 + 4\chi^2} n_{\mathrm{th}}, \tag{5.3}$$

where $\chi$ is the dispersive shift, $\kappa$ is the coupling rate of the cavity to the environment, and $n_{\mathrm{th}}$ is the thermal photon number in the environment around the cavity frequency [68, 7]. The dephasing rate is also increased as the thermal photon number is increased. From these calculations, we find that the thermal photon number in the environment is crucial for quantum control of the qubit.

From Eq. (3.166), the average photon number in the environment is determined as

$$n_{\mathrm{th}} = \frac{1}{e^{\hbar\omega/k_{\mathrm{B}}T} - 1}, \tag{5.4}$$

where $\omega$ is the system frequency and $T$ is the environment temperature. Here, it is useful to convert the system frequency to the corresponding temperature $T_\omega$, which is described as

$$T_\omega = \frac{\hbar\omega}{k_{\mathrm{B}}}. \tag{5.5}$$

Then, Eq. (5.4) can be written as

$$n_{\mathrm{th}} = \frac{1}{e^{T_\omega/T} - 1} \tag{5.6}$$

For superconducting circuits, the typical resonance frequency of 10 GHz can be converted to the corresponding temperature of ∼500 mK. When the temperature of the environment is cooled down to be less than the corresponding temperature, the average photon number can be suppressed exponentially as $n_{\mathrm{th}} \propto e^{-T_\omega/T}$. Using a dilution refrigerator, we can cool down the environment to be tens of mK, which corresponds to the average photon number at 10 GHz of as small as $10^{-22}$. Therefore, we can control superconducting circuits quantum-mechanically in the dilution refrigerator. Note that the effective temperature of the superconducting circuits is not cooled down to the base temperature in most of cases.

The average photon number in the cavity and the thermal excitation probability of the qubit as a function of the temperature are shown in Fig. 5.1.

In Fig. 5.2, we show the inner part of the "Triton 200" dilution refrigerator made by Oxford Instruments. This inner part is covered with an outer vacuum chamber (OVC), which create a vacuum and suppress heat conduction with room temperature environment via the residual gas. We need to pump the OVC for at least half a day before starting the cool-down process. As shown in Fig. 5.2, there are five plates which are at different temperature inside the dilution refrigerator. Radiation shields are connected to each stage to suppress the heat contact mediated by the radiation fields. The dilution refrigerator uses mainly two different cooling mechanisms [69]. First, the pulse tube refrigerator cools down the 60 K and 4 K plates to be at their corresponding temperatures. Since the still and mixing chamber (MC) plates are isolated from the cold parts of the pulse tube refrigerator, they are thermally connected by the mixture of $^3$He and $^4$He gases After the mixing chamber plate becomes below 10 K, the mixture gas is removed from the pre-cool line, and then is compressed and injected through the condensing line. The mixture of gas is condensed in the still pot and the mixing chamber by the Joule-Thomson effect. At about 900 mK, the mixture liquid is separated into two liquid phases, a $^3$He-rich phase (concentrated phase) and a $^3$He-poor phase (dilute phase). By pumping the $^3$He from the dilute phase in the still chamber, the $^3$He in the concentrated phase is evaporated

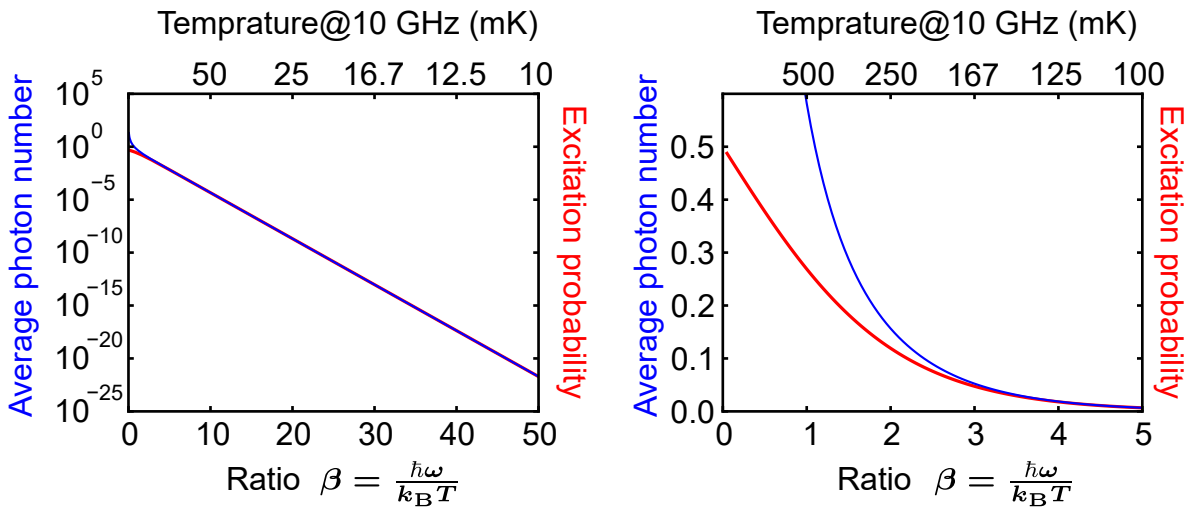


Figure 5.1: Average photon number in the cavity (blue) and thermal excitation probability of the qubit (red) as a function of the temperature. The horizontal axes on the lower and upper sides indicate the ratio $\beta = \hbar\omega/k_B T$ and the temperature at 10 GHz, respectively.

to the dilute phase in the mixing chamber. The evaporation of the $^3$He into the dilute phase is the heart of the cooling of the dilution refrigerator, which cools the mixing chamber plate to tens of mK. Since the lower temperature prevents the liquid He from exchanging heat with the metal, heat exchangers, which have a large contact area, are installed between the still pot and the mixing chamber. As a result, the mixing chamber stage achieves tens of mK within one and a half day after starting the cooling down.

## 5.2 Sample setting

The superconducting circuits should be thermally well-connected to the mixing chamber plates. We made a copper cold finger, as shown in Fig. 5.3(b). There is a space for wiring between the MC plate and the sample plate. Each microwave component, such as a filter and a circulator, should be mounted to the cold finger with enough thermal contact.

A three-dimensional (3D) microwave cavity is simply mounted on a sample holder, as shown in Fig. 5.3(a). The 3D cavity is well connected thermally to the sample holder. A coupling pin for the 3D cavity is connected to a flexible coaxial cable via an SMA connector.

A two-dimensional (2D) microwave circuit, such as a JPA, is mounted on a sample table, as shown in Fig. 5.3(d). The signal and ground electrodes which are fabricated on a silicon substrate are connected to a PCB on the sample table by wire bondings. On the PCB board, there are many vias which connect the top and bottom ground electrodes to remove the spurious modes induced by stray capacitance. Furthermore, SMP connectors are mounted on the PCB board with paste solders for input and output of microwaves. The 2D sample is covered by a copper cap to suppress box modes, which may cause radiation loss of the superconducting circuit. The sample table with the cap is mounted on a sample holder, as shown in Fig. 5.3(c).

Superconductors are easily affected by magnetic fluxes. For instance, magnetic-flux noise causes a jump in the resonance-frequency of superconducting circuit. Therefore, the sample holder is covered by a magnetic shield, as shown in Fig 5.4 (a). The magnetic shield

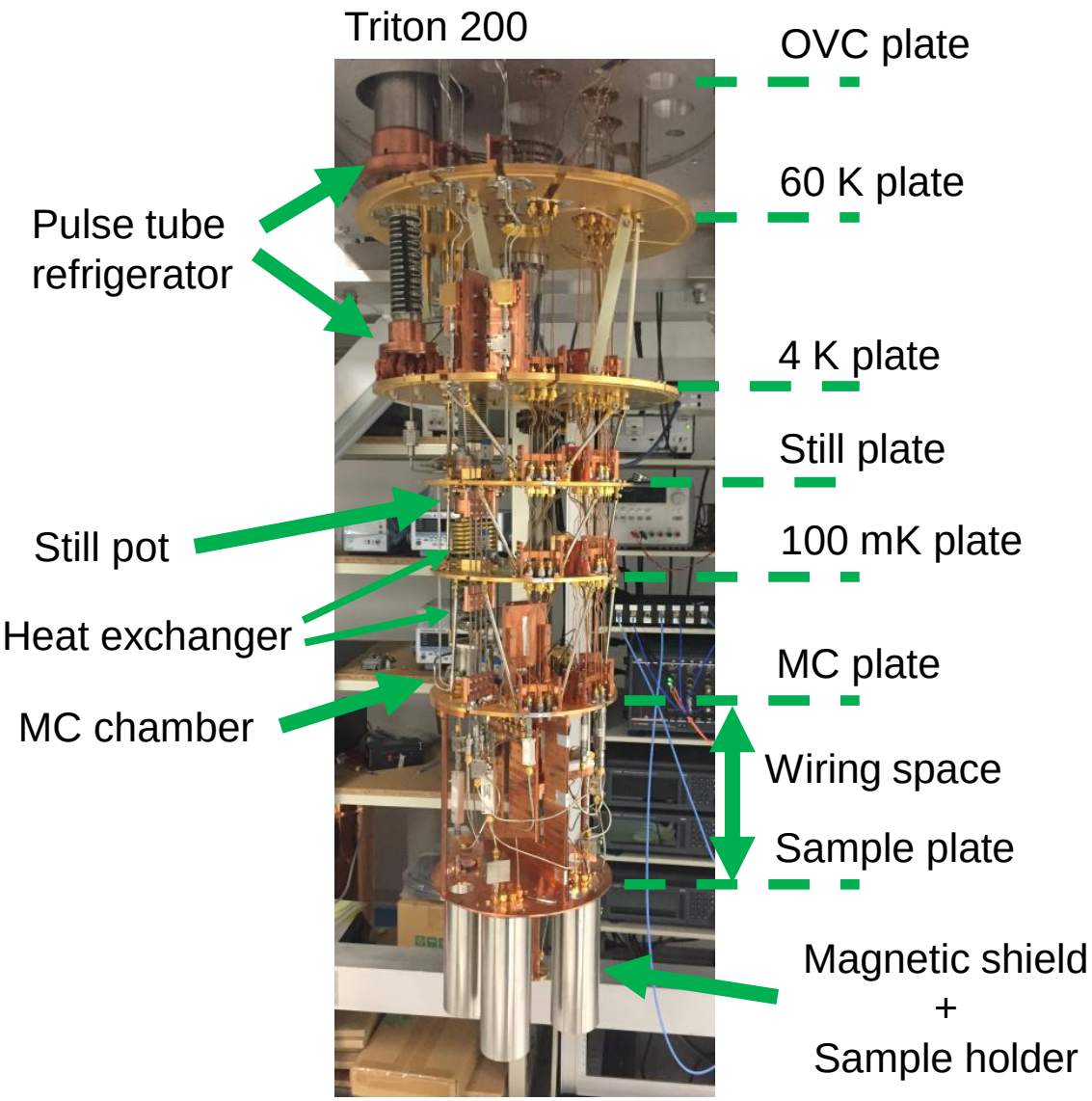


Figure 5.2: Inner part of the dilution refrigerator. There are the five plates at the different temperature stages. The sample plate is thermally well-connected to the mixing chamber (MC) plate. The sample holder covered by the magnetic shield is connected to the sample plate.

is composed of three layers, which is connected thermally to a copper jig, as shown in Fig. 5.4(b). The innermost shield is made of aluminum which becomes superconducting at the base temperature and shields the magnetic-flux noise by the Meissner effect. However, the aluminum shield can trap a residual magnetic flux when it becomes superconducting. Therefore, the two outer shields are installed to suppress the residual magnetic flux. They are made of $\mu$-metal (A4K from Amuneal) with very high permeability and which is magnetically neutral. Note that $\mu$-metal is easy to be magnetized by a physical shock. Our magnetic shield is not completely closed magnetically, and the magnetic flux can penetrate from the open end to the sample. Therefore, the sample is hung from the cold finger by a distance longer than the radius of the shield. The length-to-diameter ratio of the shield is designed to be about 4:1.

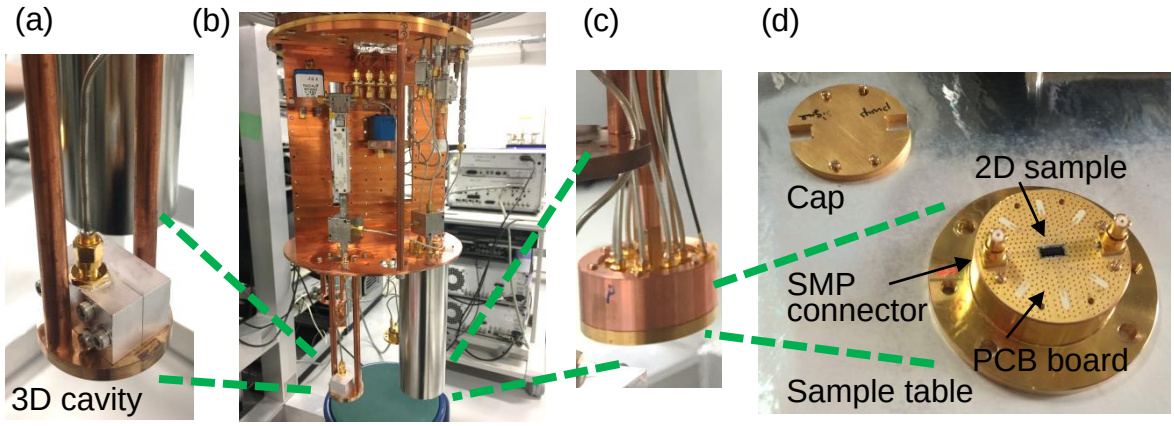


Figure 5.3: Sample setting. (a) Sample holder for the 3D cavity. (b) Cold finger and wiring space. (c) Sample holder for the 2D sample. (d) 2D sample on the sample table. The 2D sample is electrically connected to a PCB board with wire bondings and is covered by a copper-made cap to suppress box modes. SMP connectors are installed on the PCB board for input and output of microwaves.

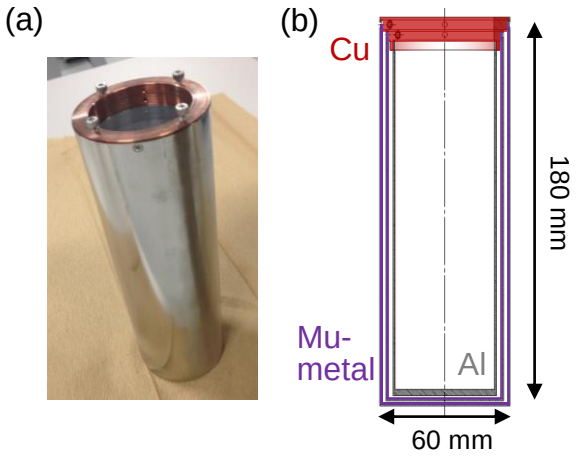


Figure 5.4: Magnetic shield. (a) Image. (b) Design.

## 5.3 Josephson parametric amplifier

We use a flux-driven JPA, which is designed and fabricated in Nakamura group in RIKEN [52]. The $\lambda/4$ coplanar waveguide resonator, which is made of niobium, is patterned on a silicon substrate, as shown in Fig. 5.5(a) and (d). There are many holes in the ground plane to trap magnetic-flux noise. The resonator is over-coupled to a waveguide with an external coupling capacitor, as shown in Fig. 5.5(b). The external Q factor is designed to be about 300. The other end of the resonator is shunted to the ground plane via a SQUID, as shown in Fig. 5.5(c). Therefore, the resonance frequency of the JPA is determined from the resonator length and the shunt inductance of the SQUID, which is designed to be about 10 GHz. The SQUID loop has a mutual inductance with the pump line, which enables us to modulate the SQUID inductance. The area of the SQUID loop is designed to be 100 $\mu$m$^2$. Note that SQUID is made by double-angle evaporation of aluminum, as show in Fig. 5.5(e). The image of the JPA, which is mounted and wire bounded on the sample table is shown in Fig. 5.5(d).

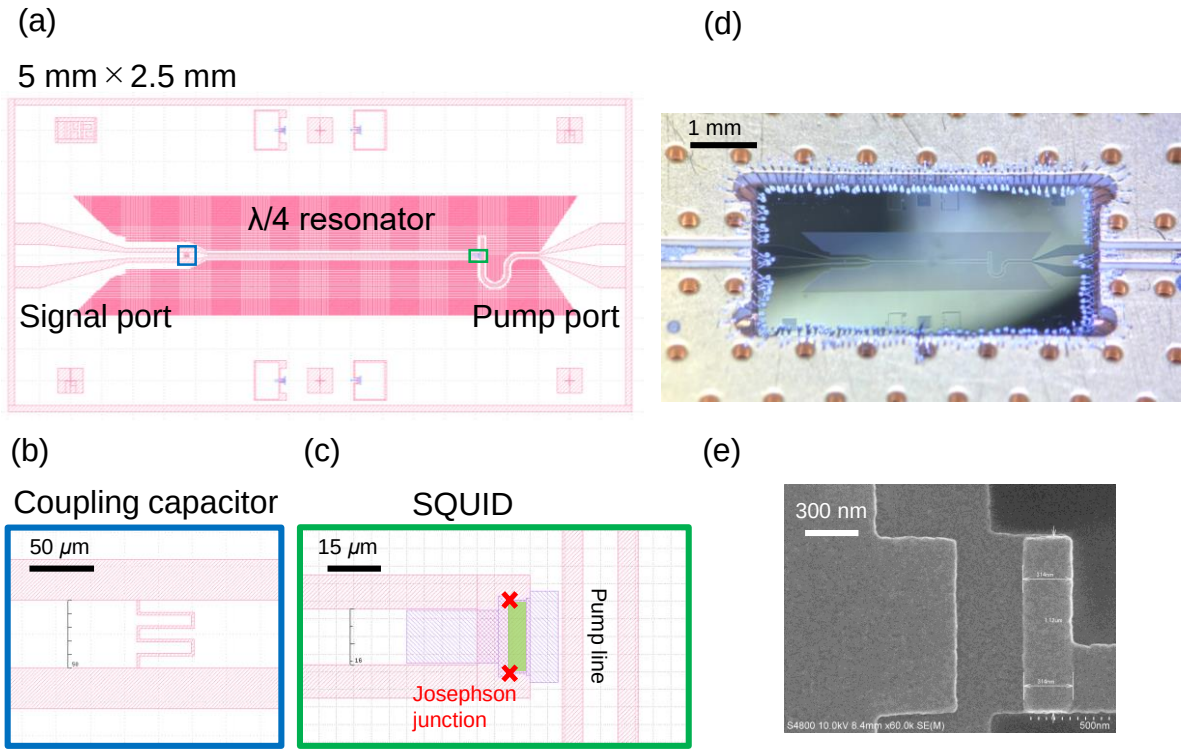


Figure 5.5: Josephson parametric amplifier. (a) Design of the JPA. The blue and green frames depict the regions of an external coupling capacitor and a SQUID, respectively. (b) Design of the external coupling capacitor. (c) Design of the SQUID and a pump line. The SQUID loop has a mutual inductance with the pump line. The green square depicts the SQUID area. (d) Image of the JPA mounted on a sample table. (e) SEM image of one of the Josephson junction in the SQUID.

## 5.4 Cryogenic microwave wirings

The superconducting circuits are connected to microwave lines which extend through the dilution refrigerator to room temperature. Therefore, reducing the thermal noise from room temperature is indispensable for control and readout of a superconducting qubit quantum mechanically. Here, we explain the microwave wirings for input and output, respectively.

Before going into detail, we calculate how much power we need for control and readout of a transmon qubit.

The transmon qubit is controlled by a Rabi oscillation. The Rabi frequency is given by

$$\Omega_{\mathrm{Rabi}} = 2\sqrt{\gamma_{\mathrm{ex}}\dot{n}_{\mathrm{ct}}}, \tag{5.7}$$

where $\gamma_{\mathrm{ex}}$ is the coupling rate to the control line, $\dot{n}_{\mathrm{ct}} = P_{\mathrm{ct}}/\hbar\omega_{\mathrm{q}}$ is the photon flux for the qubit control, $P_{\mathrm{ct}}$ is the control power and $\omega_{\mathrm{q}}$ is the qubit frequency. For trasmon qubit, the Rabi frequency is limited by the anharmonicity. Then, the critical control power for the transmon qubit is defined as the power when the Rabi frequency coincides with the anharmonicity as

$$P_{\mathrm{ct}}^{\mathrm{crit}} = \frac{\alpha^2}{4\gamma_{\mathrm{ex}}}\hbar\omega_{\mathrm{q}}. \tag{5.8}$$

From this, we can roughly estimate how much control power we need. The order of the critical control power can be calculated as $P_{\mathrm{ct}}^{\mathrm{crit}} = -70$ dBm, where we use $\alpha/2\pi =$

$-100$ MHz, $\gamma_{\rm ex}/2\pi = 1$ kHz, and $\omega_{\rm q}/2\pi = 10$ GHz.

Furthermore, the transmon qubit is read out by a dispersive shift of the cavity. As explained in Sec. 2.4.2, the average photon number in the cavity can be calculated as

$$\langle \hat{a}^\dagger \hat{a} \rangle = \frac{4}{\kappa_{\rm ex}} \dot{n}_{\rm ro}, \tag{5.9}$$

where $\kappa_{\rm ex}$ is the coupling rate to the readout line, $\dot{n}_{\rm ro} = P_{\rm ro}/\hbar\omega_{\rm c}$ is the photon flux for the qubit readout, $P_{\rm ro}$ is the readout power and $\omega_{\rm c}$ is the cavity frequency. Note that the internal loss of the cavity is neglected for simplicity. In additon, the critical photon number in the cavity, which is defined in Sec. 2.6.1, is given by

$$n_{\rm crit} = \frac{\Delta^2}{4g^2}, \tag{5.10}$$

where $\Delta$ and $g$ are the detuning and coupling strength between the cavity and the qubit, respectively. Then, the critical readout power is defined as the power when the average photon number reaches the critical photon number:

$$P_{\rm ro}^{\rm crit} = \left(\frac{\Delta}{g}\right)^2 \frac{\kappa_{\rm ex}}{16} \hbar\omega_{\rm c}. \tag{5.11}$$

This is also useful to estimate how much readout power we need. The order of the critical readout power can be calculated as $P_{\rm ro}^{\rm crit} = -126$ dBm, where we use $g/\Delta = 0.1$ and $\kappa_{\rm ex}/2\pi = 1$ MHz. Using these reference powers, we should optimize the attenuation and filtering of the thermal noise at each frequency.

### 5.4.1 Input microwave wiring

For the input microwave wiring, the thermal noise from room temperature should be attenuated and filtered suitably while keeping the transmission for the control and readout of the qubit. The thermal photon number at room temperature at 10 GHz can be calculated as $\sim$600.

First of all, the total attenuation rate should be set to more than at least 40 dB, which roughly corresponds to the ratio of the base temperature to room temperature. However, since the cooling power at the MC plate may not be strong enough to absorb the 300 K noise in the entire frequency range, it is not reasonable to install all the attenuators at the MC plate. Taking into account the fact that an attenuator at a finite temperature also emits a corresponding thermal noise, the attenuation rate at each plate should be determined from the temperature ratio between the plates step by step. In our setup, the attenuators with a total combined attenuation of 42 dB for the input line are installed across separate plates as shown in Fig 5.6. Each attenuator is thermally anchored to each plate. For the input microwave line, we use phosphor-bronze coaxial cables with a diameter of 1.19 mm, "SC-119/50-PCB-PCB", which is manufactured in COAX CO. The cables are bent to release the stress induced during thermal cycles. The total attenuation rate including the cable loss is about 50 dB around 10 GHz. Then, the thermal photon number at base temperature can be calculated as 0.006.

Furthermore, the frequency range which we do not use should be attenuated as much as possible. In this thesis, the control and readout frequencies for the qubit are set to about 8 GHz and 10 GHz, respectively. Therefore, we install a low-pass filter with a cutoff frequency of 12.4 GHz, which is the "F-30-12.4-R" model from RLC Electronics. The stopband frequency range of 60 dB is from 16.74 GHz to 40 GHz. A picture of the low pass filter is shown in Fig. 5.7(a).

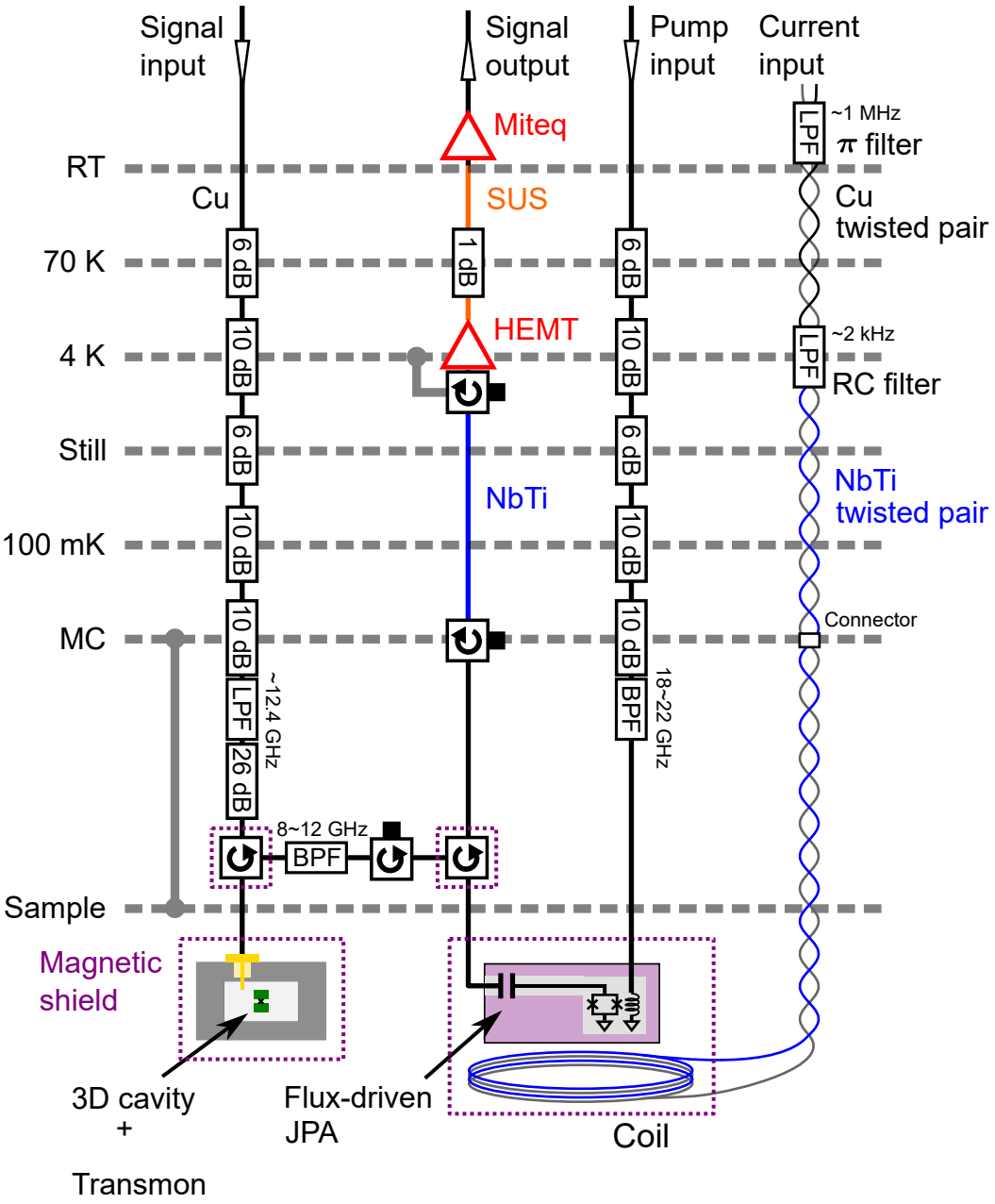


Figure 5.6: Summary of the wirings in the dilution refrigerator.

We consider the attenuation around the qubit frequency in terms of the thermal excitation of the qubit. Taking into account the 50 dB attenuation for the input line, the qubit excitation probability can be calculated as 0.006 from Eq. (5.2). However, the typical qubit excitation probability is measured to be around 0.1 with an effective temperature of 100 mK in a single-shot experiment (see Sec. 6.2.6). We also confirm that the qubit excitation probability cannot be suppressed by installing additional attenuators in the input line and additional circulators in the output line. It shows that the qubit effective temperature is limited by another environment, such as a high-frequency radiation field and quasiparticles [70, 71]. Here, it is important to confirm that the thermal excitation probability is much less than unity, which ensures that the qubit coherence is not limited by the thermal photon number in the environment. As shown in Eq. (5.1), until the

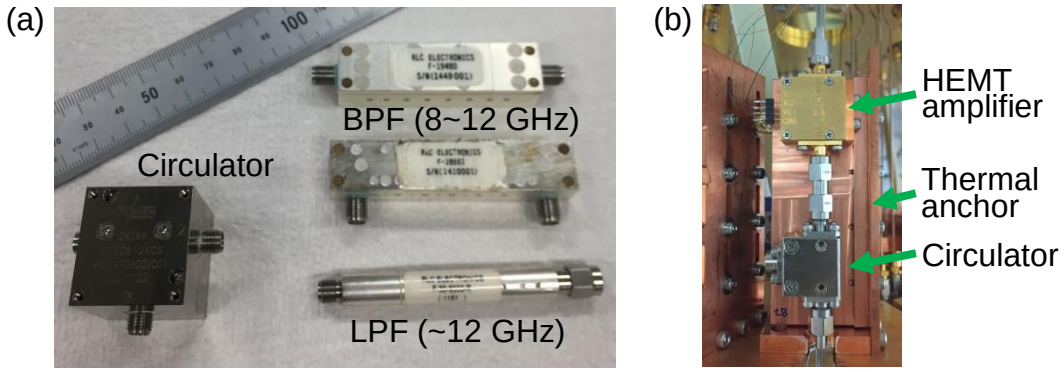


Figure 5.7: Microwave components. (a) Filters and a circulator with the magnetic shield. (b) HEMT amplifier. The amplifier is connected to the thermal anchor together with a circulator.

thermal noise is comparable to the vacuum noise, it does not affect the qubit coherence much. Therefore, as long as the qubit coherence is not limited by the thermal excitation, the initialization error of the thermal excitation is not so critical since it can be corrected by the use of postselection or feedback control.

Next, we consider the attenuation around the cavity frequency from the viewpoint of the qubit dephasing. As shown in Eq. (5.3), since the dephasing rate is proportional to the thermal photon number in the cavity, it may be not enough only to decrease the thermal photon number below unity. For example, the dephasing rate is calculated to be

$$\gamma_\phi/2\pi = \frac{4\chi^2\kappa}{\kappa^2+4\chi^2} n_{\rm th}/2\pi = 0.5\, n_{\rm th}\ \text{MHz} \tag{5.12}$$

where we assume $\kappa/2\pi = 2\chi/2\pi = 1$ MHz. To obtain the thermal-noise-induced dephasing rate of 1 kHz, which does not limit the best dephasing time of a transmon qubit, we should have $n_{\rm th} = 0.001$. Thus, we need to attenuate the thermal noise from room temperature by at least 60 dB.

We find that there is a difference of an order of magnitude for the required attenuation level between the qubit and cavity frequencies, as shown in Eqs. (5.8) and (5.11). Therefore, the frequency-dependent attenuators are needed for the realization of an efficient measurement setup. However, for simplicity, we just install additional attenuators of 26 dB at the MC plate and confirm that the dephasing time of the qubit is saturated.

Thermal noise in the infrared-frequency range, which cannot be cut by structure-type filters, may affect the qubit coherence. This is because the noise with a large photon energy easily excites quasiparticles. An Eccosorb filter, which is composed of a lossy material with a linear-frequency-dependent attenuation, is used to cut the infrared thermal noise [72]. However, we confirm that there is no difference in the qubit coherence with or without the Eccorsorb filter, which indicates the infrared-frequency noise does not limit our qubit coherence.

In this thesis, a flux-driven JPA is used for a single-shot readout of the qubit. Then, we need to pump the JPA at twice the readout frequency using a pump line. The attenuators with a total attenuation rate of 42 dB is installed, as shown in Fig. 5.6. Thanks to the large detuning, we can completely suppress the thermal noise from the pump line for the circuit QED system by using a band-pass filter at the pump frequency. We use the band-pass filter model "F-19799" which is custom made in RLC Electronics.

### 5.4.2 Output microwave wiring

For the output microwave wiring, we need to install a cryogenic amplifier while suppressing the thermal and amplifier noise.

First of all, we use a High-Electron-Mobility Transistor amplifier (HEMT amplifier) at the 4 K plate. Typical gain and noise temperature of a HEMT amplifier are 35-40 dB and 5-10 K, respectively. Note that the noise temperature of 5-10 K corresponds to the thermal photon number of 10-20 at 10 GHz. This is always useful for the average measurement of microwave signals. However, the noise temperature is not low enough to perform a single-shot readout of a superconducting qubit since the readout pulse typically contains only tens of signal photons. This is the critical reason why we use an amplifier based on Josephson junctions for the single-shot readout. As shown in Fig. 5.7(b), we install the HEMT amplifier model "CITCRYO1-12A" which is manufactured by Cosmic Microwave Technology, Inc. (a spin-off from California Institute of Technology). The amplifier is connected to a thermal anchor at the 4 K plate. The gain is about 40 dB, the gain bandwidth is from 1 GHz up to 15 GHz, and the noise temperature is around 5 K. Although the HEMT amplifier itself plays a role in the isolation of the thermal noise, it emits a backward thermal noise. Therefore, the backward thermal noise should also be attenuated in the output line, as well as the 300 K noise.

For the output wiring, we need to pass and amplify microwaves while attenuating the thermal noise. Therefore, it is indispensable to use nonreciprocal devices, such as circulators and isolators. Note that an isolator is realized by terminating one of the ports of a circulator. In general, the circulator has a finite working bandwidth since its nonreciprocity is realized by interference in a magnetic material inside the circulator. Therefore, we should use the circulator together with a band-pass filter to cut the thermal noise out of the circulator bandwidth. We use the circulator model "XTE0812KC" and the isolator model "XTE0812KI" which are made by Quinstar. The isolator is installed at the 4 K plate together with the HEMT amplifier, as shown in Fig. 5.7(b). The circulator with the magnetic shield ("XTE0812KCS"), which is shown in Fig. 5.7(a), is installed directly above the sample plate. The circulation bandwidth is from 8 GHz to 10 GHz. The insertion loss is about 1 dB. Practically, since the isolation of the circulator or the isolator is about 20 dB, at least in a total of three isolators or circulators are needed between the HEMT amplifier and the sample in order to not decrease the qubit dephasing time. Then, together with the circulators and isolators, we use a band-pass filter with a bandwidth from 8 GHz to 10 GHz, which is custom made by RLC electronics. The model number of the band-pass filter is "F-18851". The isolation from DC to 7 GHz and from 13 GHz to 20 GHz is designed to be about 60 dB.

Furthermore, the circulator is indispensable to separate the outgoing signal from the incoming input signal. As shown in Fig. 5.6, we use the circulators for the circuit QED system and the JPA to realize the reflection-type measurements. In this thesis, to suppress the amplifier noise from the JPA (squeezed vacuum leaked from the isolator), we install an additional isolator between the circuit QED system and the JPA. Although the dephasing of the qubit during the single-shot readout is not always a problem, it is very crucial for quantum state tomography of itinerant microwave photons.

From the MC plate to the HEMT amplifier, we use a NbTi superconducting coaxial cable with a diameter of 2.19 mm of "SC-219/50-NbTi-NbTi", which is manufactured by COAX CO. with connectors from Kawashima Manufacturing Co., Ltd. From the HEMT amplifier to the output port at room temperature, we use a stainless steel made coaxial cable with a diameter of 2.19 mm of "TCR-219CG/SUS", which is manufactured by COAX CO. with connectors from Kawashima Manufacturing Co., Ltd. The low thermal conductivity of stainless steel is helpful for thermal isolation. The cables are also bent to

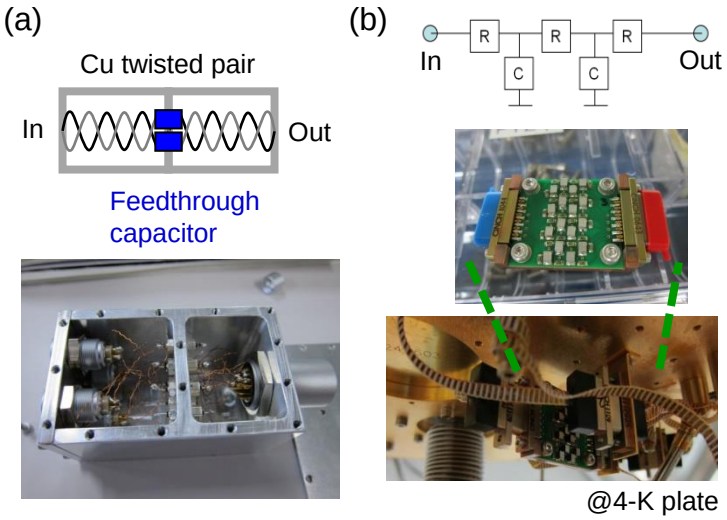


Figure 5.8: Low-pass filters for the DC current lines. (a) Equivalent circuit and image of $\pi$-filters. (b) Equivalent circuit and image of RC filters. The RC filter is installed at 4-K plate.

release the stress induced during thermal cycle.

The microwave power, which is amplified in the dilution refrigerator, is not enough for typical measurement devices, such as a vector network analyzer and an analog-to-digital converter. Therefore, we additionally install a room-temperature microwave amplifier "AFS4-08001200-09-10P-4" which is manufactured by MITEQ Inc. The gain is about 35 dB, the gain bandwidth is from 4 GHz to 12 GHz, and the noise temperature is about 70 K. The 4 K noise temperature with 40 dB gain from the HEMT amplifier exceeds that of the Miteq amplifier. It means that our signal-to-noise ratio is limited by the noise of the HEMT amplifier. When the JPA is used as a preamplifier, the microwave signals can be amplified in the near quantum limit by suppressing the HEMT noise effectively. However, the insertion loss of the circulator needed for the reflection-type JPA often limits the efficiency of the quantum measurement.

## 5.5 Cryogenic current lines

For operating the JPA, we need to apply a DC magnetic flux into the SQUID loop. In our setup, the JPA on the silicon substrate is mounted in the 2D sample holder, which is equipped with a superconducting coil made of NbTi. The superconducting coil of about 4000 turns can apply a uniform magnetic field of 1 Gauss at the sample with a current of 1 mA. Taking into account our SQUID area of about 100 $\mu$m$^2$, a current of about 200 $\mu$A is needed to apply the magnetic flux quantum into the SQUID loop. The estimated magnetic flux penetrating into the SQUID loop may deviate from the coil design due to the screening effect of the superconductors. However, practically, we can estimate the magnetic flux in the SQUID by measuring the periodic behavior of the SQUID inductance. The resistance of the coil at room temperature is about 2.5 k$\Omega$.

As shown in Fig 5.8, to filter out a high-frequency noise, a $\pi$-filter and an RC filter are installed at room temperature and at the 4 K plate, respectively. The $\pi$-filter with a feed-through capacitor is used as a low-pass filter with a cutoff frequency of about 1 MHz and an insertion loss at 100 MHz of about 65 dB. The RC filter with resistors and capacitors is used as a low-pass filter with a cutoff frequency of about 2 kHz and an insertion loss at

100 kHz of about 50 dB. As shown in Fig. 5.6, a twisted pair made of copper is used for the connection between the DC current input and the RC filter. A twisted pair made of NbTi is used for the connection between the RC filter and the connector. The NbTi coil is connected to the connector at the MC plate.

## 5.6 Frequency-domain measurement setup

Here, we explain a frequency-domain measurement setup. First, a vector network analyzer (VNA) is a powerful tool in frequency-domain measurements. The VNA can measure the reflection and transmission coefficients of the circuits as a function of the probe frequency. Second, a microwave source is additionally used for driving the circuits which are being measured by the VNA. Third, a current source is also used to apply a magnetic flux into the SQUID loop of the circuits. Finally, a rubidium atomic clock is an essential tool to decrease the phase noise or to improve the long-term stability of microwave devices. Microwave devices, such as the VNA or the microwave source, should be connected to the rubidium atomic clock. In the following, we explain the measurement devices we use in this thesis; the VNA, the microwave source, the current source, and the rubidium atomic clock.

### 5.6.1 Vector network analyzer

The VNA can modulate and demodulate between the intermediate and probe frequencies using an identical internal local oscillator. Therefore, the VNA can perform a phase sensitive measurement with high long-term stability.

We use the VNA model "N5222A", which is manufactured by Keysight (former Agilent). The picture of the VNA is shown in Fig. 5.9(a). From the specification details of the device, the dynamic range and the noise floor with the IF bandwidth of 10 Hz are 127 dB and $-114$ dBm, respectively. Then, the noise spectral density of the VNA is calculated as $-124$ dBm/Hz. The vacuum noise spectral density is $\hbar\omega/2 = -205$ dBm/Hz at 10 GHz Therefore, if we have ideal amplifiers with the total gain of at least 80 dB, we can measure the probe microwave in the vacuum noise limit by the VNA. Since the sum of the gains of the HEMT and Miteq amplifiers is about 75 dB, the noise spectral density of the VNA is comparable with the amplified vacuum noise. As explained before, without the JPA, the signal-to-noise ratio is limited by the HEMT amplifier. The noise spectral density of the HEMT amplifier with a noise temperature of 5 K is $-191$ dBm/Hz at 10 GHz, which corresponds to $-115$ dBm/Hz with a total gain of 75 dB from the HEMT and Miteq amplifiers. The noise spectral density exceeds the noise floor of the VNA, which means that we can achieve microwave measurement with the noise floor $-191$ dBm/Hz at 10 GHz at the base temperature.

The SSB phase noise is about $-83$ dBc/Hz from 8 GHz to 16 GHz with a frequency offset of 1 kHz, which shows that the linewidth of the probe microwave from the VNA is much narrower than 1 kHz. Therefore, the linewidth of the probe microwave is much less than that of the typical superconducting circuits, which enable us to measure the linewidths of the superconducting circuits accurately.

### 5.6.2 Microwave source

The microwave source is useful to additionally drive the superconducting circuit which is being measured by the VNA.

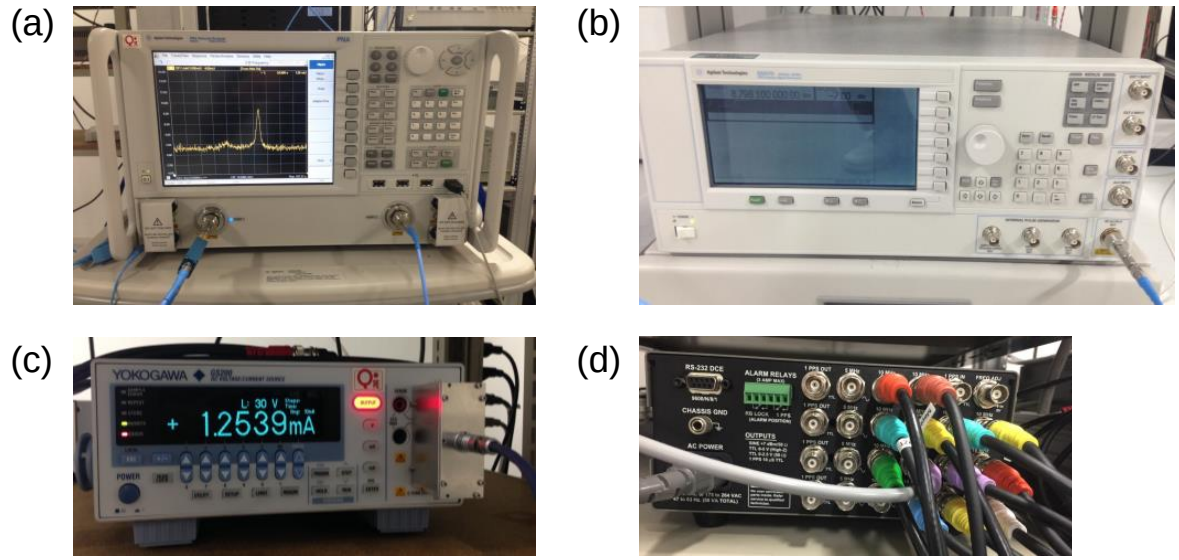


Figure 5.9: Photographs of instruments. (a) Vector network analyzer (VNA). (b) Microwave source. (c) Current source. (d) Rb atomic clock.

In this thesis, we use the microwave source model "E8257D", which is manufactured by Keysight (former Agilent). The microwave source is shown in Fig. 5.9(b). From the device specifications, the microwave source can generate microwaves with a power range from $-20$ dBm to 20 dBm and with a frequency range from 250 kHz to 20 GHz. The dynamic range of the output power can be controlled with suitable attenuators. The SSB phase noise is about $-40$ dBc/Hz at 10 GHz with a frequency offset of 1 Hz, which shows the linewidth of the microwave is much narrower than 1 Hz. Again, it is much less than that of the typical superconducting circuits, which enables us to control or drive the superconducting circuits in the limit of their linewidths.

### 5.6.3 Current source

The current source is used to apply the magnetic flux into the SQUID loop. In this thesis, we use the current source model "GS200", which is manufactured by Yokogawa Electric Corporation. The current source is shown in Fig. 5.9(c). From the device specifications, the current resolution of the 1 mA range is 10 nA. For our superconducting coil, the current of 10 nA corresponds to about 1 $\mu$G. Taking into account the typical area of our SQUID of about 100 $\mu$m$^2$, the magnetic field of 1 $\mu$G applies a magnetic flux of about $1 \times 10^{-19}$ Wb into the SQUID loop, which corresponds to $\Delta\Phi_{\mathrm{ex}}/\Phi_0 = 5 \times 10^{-5}$. The frequency deference of the JPA in terms of the magnetic flux can be rewritten as

$$\frac{\Delta\omega_r}{\omega_r} = \frac{1}{4}\tan\left(\pi\frac{\Phi_{\mathrm{ex}}}{\Phi_0}\right)2\pi\frac{\Delta\Phi_{\mathrm{ex}}}{\Phi_0} \approx 8 \times 10^{-5}, \tag{5.13}$$

where we set $\Phi_{\mathrm{ex}}/\Phi_0 = 1/4$. Typically, the Q factor of the JPA is from $10^2$ to $10^3$. From this, we confirm that $\frac{\Delta\omega_r}{\omega_r} \ll Q^{-1}$, which means that the resolution of the current source is low enough to tune the JPA frequency within its linewidth. The long-term stability of the current is within tens of nanoampere in a day, which does not drift the JPA frequency largely beyond the linewidth. Note that high-frequency current noise is expected to be strongly attenuated by the low-pass filters, the $\pi$-filter at room temperature and the RC filter at the 4 K plate.

### 5.6.4 Rubidium atomic clock

A microwave device generates a frequency-stable microwave using a phase-locked loop (PLL), where an unstable voltage controlled oscillator (VCO), which generates a microwave, is stabilized by a reference signal. The low-frequency signal which is frequency-divided from the microwave of the VCO is compared with the reference signal at a phase comparator to stabilize the VCO. Most of the microwave devices have their own reference signals which are generated from quartz crystal oscillators. However, a more stable reference signal enables the microwave devices to generate more stable microwaves.

It is known that an atomic clock generates a more stable reference signal than a quartz crystal oscillator. Therefore, a caesium atomic clock is used for the definition of the second. However, in laboratories, a rubidium atomic clock is commonly used for the reference signal since it is more compact and inexpensive than that of caesium.

In this thesis, we use a rubidium atomic clock model "FS725", which is manufactured by Stanford Research Systems (SRS). The rubidium atomic clock is shown in Fig. 5.9(d). The clock generates a reference signal at 10 MHz. The relative Allan variance measured in 1 second, which shows the long-term stability, is less than $2.0\times10^{-11}$, which means that the clock is working with an expected error of only 1 second in about ten thousand years. The SSB phase noise is about $-130$ dBc/Hz at 10 MHz with a frequency offset of 10 Hz. Thus, the SSB phase noise of the microwave with the ideal PLL can be estimated as about $-100$ dBc/Hz at 10 GHz with a frequency offset of 10 Hz, which is much better than that of the microwave source we use in this thesis. This shows that the reference signal from the clock may improve the phase noise of the microwave source. Therefore, all microwave devices are connected to an identical rubidium atomic clock. Furthermore, the microwave devices which share identical reference signals can be phase-locked with each other.

## 5.7 Time-domain measurement setup

For the time-domain measurement, we need to control and measure microwave pulses. In the state-of-the-art technology for microwaves, we may directly control and measure microwave pulses using a digital-to-analog converter (DAC) and an analog-to-digital converter (ADC) with ultrafast sampling frequencies. However, in this thesis, we establish a system similar to what is used in radio communications, where low-frequency signals, which can be easily controlled by DACs and ADCs, are up- and down- converted to and from microwave signals. The continuous microwave carrier signal from the microwave source is modulated to a microwave pulse by a low-frequency signal at an IQ mixer. The returning microwave pulse is demodulated to a low-frequency signal at another IQ mixer driven by the continuous microwave carrier signal.

Here, we will explain our system by dividing them into three components; the IQ mixer, the DAC system, and the ADC system.

### 5.7.1 IQ mixer

We use a IQ mixer to up- and down- convert the low-frequency signals to microwave signals. The IQ mixer is a passive device based on diodes, which can multiply incoming signals at different frequencies with each other, performing frequency conversion. The multiplication of the signals is realized by the nonlinearity of the diodes. The spurious frequency signals are cut by the interferences inside the mixer and the filters outside of the mixer.

In this thesis, we use the IQ mixer "IQ-0318L", which is manufactured by Marki Microwave. The possible sideband frequency (IF) is from DC to 500 MHz. The IQ mixer can modulate and demodulate microwaves with a carrier frequency from 3 GHz to 18 GHz. From the device specifications, the conversion loss is 7 dB and the isolation of the continuous microwave carrier signal (LO) from the modulated microwave signal is about 40 dB.

### 5.7.2 Modulation

First of all, we will explain how to up-convert the low-frequency signals into microwave signals. The simplified circuit diagram of the IQ mixer is shown in Fig. 5.10. There are a total of four ports in the IQ mixer. One of the ports is for the input of continuous microwave carrier signal from the microwave source. The other two ports, $I$ and $Q$ ports, are used for up-conversion of the low-frequency signal input. The last port is for the output of the up-converted microwave signals. Inside the IQ mixer, the carrier signal is split into two, one of which is multiplied with the low-frequency signal from the I port, and the other is phase-shifted by $-\pi/2$ and is multiplied with the signal from the Q port. Thus, the output signal can be written as

$$V_{\mathrm{S}}(t) = I(t)\cos\omega_{\mathrm{LO}}t + Q(t)\sin\omega_{\mathrm{LO}}t, \tag{5.14}$$

where the real parts of $I(t)$ and $Q(t)$ are the low-frequency signals which were sent into the I and Q ports, and $\omega_{\mathrm{LO}}$ is the microwave frequency, or the local oscillator (LO) frequency. $I(t)$ and $Q(t)$ are called the in-phase and out-of-phase quadratures at the frequency of $\omega_{\mathrm{LO}}$, respectively. The output signal can be described by a point in the IQ plane in the rotating frame of $\omega_{\mathrm{LO}}$. Therefore, it is obvious that the in-phase and out-of-phase quadratures at the frequency of $\omega_{\mathrm{LO}}$ can be controlled directly by $I(t)$ and $Q(t)$. Note that $I$ and $Q$ correspond to $x$ and $p$, respectively, which are used for the representation of a quantum state of a harmonic oscillator in Sec 3.3.

The output signal of the IQ mixer in Eq. (5.14) can be transferred to the output propagating microwave, which is described as

$$S(t) = [I(t) + iQ(t)]e^{-i\omega_{\mathrm{LO}}t}. \tag{5.15}$$

Note that the output signal corresponds to the real part of the complex amplitude of the output propagating microwave signal as $V_{\mathrm{S}}(t) = \mathrm{Re}[S(t)]$. To sum up, by applying $I(t)$ and $Q(t)$, we can directly control the in-phase and out-of-phase signals with the carrier frequency of $\omega_{\mathrm{LO}}$.

Next, we will explain how to control the in-phase and out-of-phase quadratures with another carrier frequency of $\omega_{\mathrm{LO}} + \omega_{\mathrm{s}}$, where $\omega_{\mathrm{s}}$ is called a sideband frequency. Here, the in-phase and out-of-phase quadratures at $\omega_{\mathrm{LO}} + \omega_{\mathrm{s}}$ are described as $I_{\mathrm{s}}(t)$ and $Q_{\mathrm{s}}(t)$. Then, the output signals should be

$$\begin{aligned} V_{\mathrm{S}}(t) &= I_{\mathrm{s}}(t)\cos(\omega_{\mathrm{LO}} + \omega_{\mathrm{s}})t + Q_{\mathrm{s}}(t)\sin(\omega_{\mathrm{LO}} + \omega_{\mathrm{s}})t \\ &= [I_{\mathrm{s}}(t)\cos\omega_{\mathrm{s}}t + Q_{\mathrm{s}}(t)\sin\omega_{\mathrm{s}}t]\cos\omega_{\mathrm{LO}}t + [-I_{\mathrm{s}}(t)\sin\omega_{\mathrm{s}}t + Q_{\mathrm{s}}(t)\cos\omega_{\mathrm{s}}t]\sin\omega_{\mathrm{LO}}t. \end{aligned} \tag{5.16}$$

Therefore, $I(t)$ and $Q(t)$ can be represented as

$$\begin{pmatrix} I(t) \\ Q(t) \end{pmatrix} = \begin{pmatrix} I_{\mathrm{s}}(t)\cos\omega_{\mathrm{s}}t + Q_{\mathrm{s}}(t)\sin\omega_{\mathrm{s}}t \\ -I_{\mathrm{s}}(t)\sin\omega_{\mathrm{s}}t + Q_{\mathrm{s}}(t)\cos\omega_{\mathrm{s}}t \end{pmatrix}. \tag{5.17}$$

It can be interpreted that $I(t)$ and $Q(t)$, which are rotating at the frequency of $\omega_{\mathrm{s}}$ in the IQ plane in the rotating frame of $\omega_{\mathrm{LO}}$, can generate a signal at the frequency of $\omega_{\mathrm{LO}} + \omega_{\mathrm{s}}$.

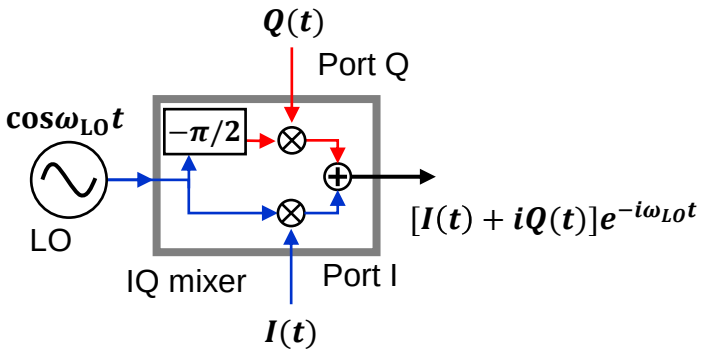


Figure 5.10: Equivalent circuit of the modulation at the IQ mixer.

The output propagating microwave signal can be described as

$$S(t) = [I_{\rm s}(t) + iQ_{\rm s}(t)]e^{-i(\omega_{\rm LO}+\omega_{\rm s})t}. \tag{5.18}$$

Thus, we can control the in-phase and out-of-phase quadratures at $\omega_{\rm LO} + \omega_{\rm s}$ using $I(t)$ and $Q(t)$ which are determined in Eq. (5.17). Note that $I(t)$ and $Q(t)$ can control not only the in-phase and out-of-phase quadratures at $\omega_{\rm LO} + \omega_{\rm s}$ but also the carrier frequency of the output propagating microwave by changing $\omega_{\rm s}$. This frequency control is quite useful since the microwave source cannot change its output frequency very quickly. Moreover, we can generate the output propagating microwaves with the different sideband frequencies simultaneously.

Our purpose here is to generate a microwave pulse with the carrier frequency of $\omega_{\rm LO} + \omega_{\rm s}$. As discussed in Sec. 2.3.4, the pulse mode is defined as

$$m(t) = f(t)e^{-i(\omega_{\rm LO}+\omega_{\rm s})t}, \tag{5.19}$$

where $f(t)$ is a normalized complex function, describing the pulse form. Then, the output microwave pulse is described as

$$S(t) = \alpha m(t) = \alpha f(t)e^{-i(\omega_{\rm LO}+\omega_{\rm s})t}, \tag{5.20}$$

where $\alpha$ is the coherent amplitude of the pulse mode, describing the amplitude and phase. By comparing Eq. (5.20) with Eq. (5.18), $I_{\rm s}(t)$ and $Q_{\rm s}(t)$ should be set to

$$\begin{aligned} I_{\rm s}(t) &= {\rm Re}\,[\alpha f(t)] \\ Q_{\rm s}(t) &= {\rm Im}\,[\alpha f(t)]\,. \end{aligned} \tag{5.21}$$

Using Eq. (5.17), $I(t)$ and $Q(t)$ should be set to

$$\begin{pmatrix} I(t) \\ Q(t) \end{pmatrix} = \begin{pmatrix} {\rm Re}\,[\alpha f(t)]\cos\omega_{\rm s}t + {\rm Im}\,[\alpha f(t)]\sin\omega_{\rm s}t \\ -{\rm Re}\,[\alpha f(t)]\sin\omega_{\rm s}t + {\rm Im}\,[\alpha f(t)]\cos\omega_{\rm s}t \end{pmatrix}. \tag{5.22}$$

Practically, it is useful to obtain $I(t)$ and $Q(t)$ in Eq. (5.22) intuitively from the microwave pulse in Eq. (5.20). First, we define $\tilde{S}(t)$ with the replaced carrier frequency of $\omega_{\rm s}$ as

$$\tilde{S}(t) = \alpha\tilde{m}(t) = \alpha f(t)e^{-i\omega_{\rm s}t}, \tag{5.23}$$

where $\tilde{m}(t) = f(t)e^{-i\omega_{\rm s}t}$ is the pulse mode with the replaced carrier frequency of $\omega_{\rm s}$. Then, we can easily confirm that the real and imaginary parts of $\tilde{S}(t)$ exactly correspond to $I(t)$

and $Q(t)$ in Eq. (5.22) as

$$\begin{pmatrix} I(t) \\ Q(t) \end{pmatrix} = \begin{pmatrix} \mathrm{Re}\left[\tilde{S}(t)\right] \\ \mathrm{Im}\left[\tilde{S}(t)\right] \end{pmatrix}. \tag{5.24}$$

The modulation process is also valid with a sideband frequency less than or equal to zero. However, practically, the signals with a sideband frequency of zero easily contain larger low-frequency noise, such as 1/f noise. Moreover, the continuous leakage noise at the LO frequency from the IQ mixer may affect the system resonantly. Therefore, we do not perform the modulation with a sideband frequency of zero.

### 5.7.3 Demodulation

Demodulation is realized by using the inverse process of modulation. As shown in Fig. 5.11, the IQ mixer and the continuous microwave carrier signal at $\omega_{\mathrm{LO}}$ are used here.

First of all, we will show the output signals from the I and Q ports correspond to the in-phase and out-of-phase quadratures of the input propagating microwave at $\omega_{\mathrm{LO}}$. Generally speaking, the input propagating microwave signal can be described as

$$S(t) = [I(t) + iQ(t)]e^{-i\omega_{\mathrm{LO}}t}, \tag{5.25}$$

where $I(t)$ and $Q(t)$ are the in-phase and out-of-phase quadratures at $\omega_{\mathrm{LO}}$. The input signal at the IQ mixer corresponds to the real part of $S(t)$, which can be calculated as

$$V_{\mathrm{S}}(t) = \mathrm{Re}[S(t)] = I(t)\cos\omega_{\mathrm{LO}}t + Q(t)\sin\omega_{\mathrm{LO}}t. \tag{5.26}$$

As shown in Fig. 5.11, the output signals from the I and Q ports are described as

$$\begin{aligned} \text{Output from I port} &= V_{\mathrm{S}}(t)\cos\omega_{\mathrm{LO}}t = \frac{I(t)}{2} + \cancel{\frac{I(t)}{2}\cos(2\omega_{\mathrm{LO}}t)} + \cancel{\frac{Q(t)}{2}\sin(2\omega_{\mathrm{LO}}t)} \propto I(t) \\ \text{Output from Q port} &= V_{\mathrm{S}}(t)\sin\omega_{\mathrm{LO}}t = \frac{Q(t)}{2} - \cancel{\frac{(t)}{2}\cos(2\omega_{\mathrm{LO}}t)} + \cancel{\frac{I(t)}{2}\sin(2\omega_{\mathrm{LO}}t)} \propto Q(t), \end{aligned} \tag{5.27}$$

where the high-frequency components are cut by suitable low-pass filters. From this calculations, we confirm that the output signals from the I and Q ports exactly correspond to the in-phase and out-of-phase quadratures at $\omega_{\mathrm{LO}}$. This is the inverse process of the modulation in Eq. (5.15).

Here, we consider the input propagating microwave signal, described in the rotating frame of $\omega_{\mathrm{LO}} + \omega_{\mathrm{s}}$ as

$$S(t) = [I_{\mathrm{s}}(t) + iQ_{\mathrm{s}}(t)]e^{-i(\omega_{\mathrm{LO}}+\omega_{\mathrm{s}})t}. \tag{5.28}$$

Similarly to the demodulation, we can obtain the output signals from the I and Q ports as

$$\begin{pmatrix} I(t) \\ Q(t) \end{pmatrix} = \begin{pmatrix} I_{\mathrm{s}}(t)\cos\omega_{\mathrm{s}}t + Q_{\mathrm{s}}(t)\sin\omega_{\mathrm{s}}t \\ -I_{\mathrm{s}}(t)\sin\omega_{\mathrm{s}}t + Q_{\mathrm{s}}(t)\cos\omega_{\mathrm{s}}t \end{pmatrix}. \tag{5.29}$$

Note that this exactly corresponds to Eq. (5.17). Thus, we obtain the inverse relation as

$$\begin{pmatrix} I_{\mathrm{s}}(t) \\ Q_{\mathrm{s}}(t) \end{pmatrix} = \begin{pmatrix} \cos\omega_{\mathrm{s}}t & -\sin\omega_{\mathrm{s}}t \\ \sin\omega_{\mathrm{s}}t & \cos\omega_{\mathrm{s}}t \end{pmatrix} \begin{pmatrix} I(t) \\ Q(t) \end{pmatrix}, \tag{5.30}$$

which shows that we can obtain the in-phase and out-of-phase quadratures at $\omega_{\mathrm{LO}} + \omega_{\mathrm{s}}$ from the output signals of $I(t)$ and $Q(t)$.

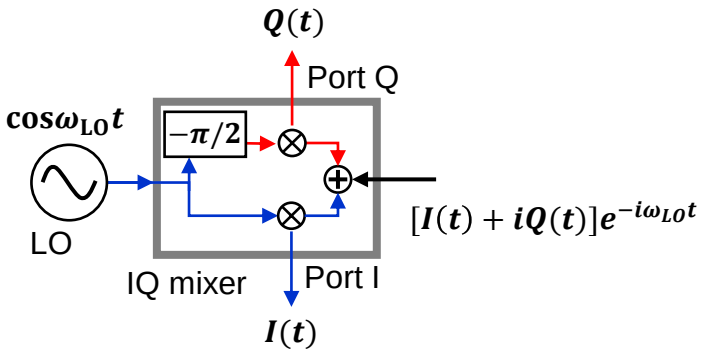


Figure 5.11: Equivalent circuit of the demodulation at the IQ mixer.

### Pulse mode measurement

Here we consider measurement of our system in a a pulse mode, which is defined as

$$m_{\rm w}(t) = f_{\rm w}(t)e^{-i(\omega_{\rm LO}+\omega_{\rm s})t} = [I_{\rm w}(t) + iQ_{\rm w}(t)]e^{-i(\omega_{\rm LO}+\omega_{\rm s})t}, \tag{5.31}$$

where $f_{\rm w}(t) = I_{\rm w}(t) + iQ_{\rm w}(t)$ is a normalized complex function, called a measurement window. Then, the complex amplitude $\alpha_{\rm w}$ measured with $m_{\rm w}(t)$ is given by

$$\alpha_{\rm w} = \int_{-\infty}^{\infty} dt\, m_{\rm w}^*(t)S(t). \tag{5.32}$$

Note that the complex amplitude in the pulse mode orthogonal to $m_{\rm w}(t)$ cannot be measured here. Using Eqs. (5.28), (5.31), and (5.32), the real and imaginary parts of the measured complex amplitude $\alpha_{\rm w}$ are obtained as

$$\begin{aligned} I_{\rm w} = {\rm Re}[\alpha_{\rm w}] &= \int_{-\infty}^{\infty} dt\, [I_{\rm w}(t)I_{\rm s}(t) - Q_{\rm w}(t)Q_{\rm s}(t)] \\ Q_{\rm w} = {\rm Im}[\alpha_{\rm w}] &= \int_{-\infty}^{\infty} dt\, [I_{\rm w}(t)Q_{\rm s}(t) + Q_{\rm w}(t)I_{\rm s}(t)]. \end{aligned} \tag{5.33}$$

In this way, using the output signals $I(t)$ and $Q(t)$ from the I and Q ports, we can obtain the real and imaginary parts in the pulse mode defined by $m_{\rm w}(t)$.

Suppose that the demodulation window is a real-valued function as $f_{\rm w}(t) = I_{\rm w}(t)$, Eq. (5.33) are described as

$$\begin{aligned} I_{\rm w} = {\rm Re}[\alpha_{\rm w}] &= \int_{-\infty}^{\infty} dt\, f_{\rm w}(t)I_{\rm s}(t) \\ Q_{\rm w} = {\rm Im}[\alpha_{\rm w}] &= \int_{-\infty}^{\infty} dt\, f_{\rm w}(t)Q_{\rm s}(t), \end{aligned} \tag{5.34}$$

which can be interpreted as the weighted average of the in-phase and out-of-phase components of signals at $\omega_{\rm LO} + \omega_{\rm s}$, with the real-valued function of $f_{\rm w}(t)$.

To describe Eq. (5.33) more simply, the pulse mode with carrier frequency of $\omega_{\rm s}$ is defined as

$$\tilde{m}_{\rm w}(t) = f_{\rm w}(t)e^{-i\omega_{\rm s}t}, \tag{5.35}$$

which is the pulse mode of $m_{\rm w}(t)$ whose carrier frequency of $\omega_{\rm LO}+\omega_{\rm s}$ is replaced by $\omega_{\rm s}$. Using $\tilde{m}_{\rm w}(t)$, Eq.(5.33) can be described as

$$\begin{aligned} I_{\rm w} = {\rm Re}[\alpha_{\rm w}] &= \int_{-\infty}^{\infty} dt\, {\rm Re}\left[\tilde{m}_{\rm w}(t)\right] I(t) + \int_{-\infty}^{\infty} dt\, {\rm Im}[\tilde{m}_{\rm w}(t)] Q(t) \\ Q_{\rm w} = {\rm Im}[\alpha_{\rm w}] &= -\int_{-\infty}^{\infty} dt\, {\rm Im}[\tilde{m}_{\rm w}(t)] I(t) + \int_{-\infty}^{\infty} dt\, {\rm Re}[\tilde{m}_{\rm w}(t)] Q(t). \end{aligned} \tag{5.36}$$

**Mode mismatch**

The mode mismatch between the signal and measurement pulse modes is critical from the viewpoint of the signal-to-noise ratio. Here, the signal and measurement pulse modes are described as $m(t)$ and $m_{\rm w}(t)$, respectively. As explained in Sec. 2.3.5, using the beam splitter transformation, the measurement pulse mode can be represented with the signal pulse mode without loss of generality as

$$m_{\rm w}(t) = \sqrt{\eta}\, m(t) + \sqrt{1-\eta}\, m_{\perp}(t), \tag{5.37}$$

where $\eta = \left|\int_{-\infty}^{\infty} dt\, m_{\rm w}^*(t) m(t)\right|^2 = \left|\int_{-\infty}^{\infty} dt\, f_{\rm w}^*(t) f(t)\right|^2$ is the mode overlap between $m(t)$ and $m_{\rm w}(t)$, and $m_{\perp}(t)$ is the pulse mode orthogonal to $m(t)$, satisfying $\int_{-\infty}^{\infty} dt m^*(t) m_{\perp}(t) = 0$. $\eta$ is also called the measurement efficiency.

Here, the input propagating microwave signal can be written as

$$S(t) = \alpha m(t) + \alpha_{\perp} m_{\perp}(t) + \sum_i \alpha_i m_i(t), \tag{5.38}$$

where $\alpha$, $\alpha_{\perp}$ and $\alpha_i$ are the complex amplitudes of the orthogonal pulse modes. Note that $m_i(t)$ with $\alpha_i$ are the orthogonal pulse modes which are not related to the measurement with $m_{\rm w}(t)$. From Eq. (5.32), the complex amplitude measured with $m_{\rm w}(t)$ is written as

$$\alpha_{\rm w} = \int_{-\infty}^{\infty} dt\, m_{\rm w}^*(t) S(t) = \sqrt{\eta}\, \alpha + \sqrt{1-\eta}\, \alpha_{\perp}. \tag{5.39}$$

It shows that $\alpha_{\rm w}$ contains not only the complex amplitude from the signal pulse mode but also that from the orthogonal pulse mode.

Usually, the orthogonal pulse mode $m_{\perp}(t)$ contains the same amount of noise as the signal mode $m(t)$, since they may be amplified in the same way. For instance, suppose that the signal-to-noise ratio of the signal mode is $SNR = S/N$, where $S$ and $N$ are the signal and noise powers, respectively, and ,the orthogonal pulse mode can also ocontain the noise power of $N$. Here, we suppose there is no pulse mode which has a finite complex amplitude, except for the signal pulse mode. Therefore, from Eq. (5.39), the signal and noise powers in the measurement are calculated as

$$\begin{aligned} S_{\rm w} &= \eta\, S \\ N_{\rm w} &= \eta\, N + (1-\eta)\, N = N. \end{aligned} \tag{5.40}$$

Then, the signal-to-noise ratio of the measurement can be calculated as

$$SNR_{\rm m} = \frac{\eta\, S}{N} = \eta \times SNR, \tag{5.41}$$

which means that the signal-to-noise ratio is $\eta$ times worse than that of the signal pulse mode due to the mode mismatch. Therefore, if the measurement pulse mode is set to $m_{\rm w}(t) = m(t)$, the measurement efficiency of $\eta$ becomes unity, where the signal-to-noise ratio of the measurement is maximized.

**Pulse mode measurement with single quadrature signal**

In the scheme in Eq. (5.36), to measure the complex amplitude of the pulse mode, we needed to use both of the in-phase and out-of-phase signals from the IQ mixer. However, we can actually measure it by using only one of the quadrature signals.

Suppose we measure the complex amplitude obtained with $m_{\rm w}(t) = f(t)e^{-i(\omega_{\rm LO}+\omega_{\rm s})t}$ by using another measurement pulse mode, which is defined as

$$m_{\rm wR}(t) = \frac{m_{\rm w}(t) + m_{\rm w-}(t)}{\sqrt{2}}, \tag{5.42}$$

where $m_{\rm w-}(t) = f^*(t)e^{-i(\omega_{\rm LO}-\omega_{\rm s})t}$ is defined as a pulse mode with the conjugate demodulation window of $f^*(t)$ and the negative sideband frequency $\omega_{\rm LO} - \omega_{\rm s}$. If the bandwidth of $m_{\rm w}(t)$ is much smaller than the sideband frequency of $\omega_{\rm s}$, the mode overlap between $m_{\rm w}(t)$ and $m_{\rm w-}(t)$ becomes zero, which means that $m_{\rm w}(t)$ and $m_{\rm w-}(t)$ are orthogonal to each other. Therefore, the measurement pulse mode of $m_{\rm w-}$ satisfies the normalization condition as

$$\int_{-\infty}^{\infty} dt\, |m_{\rm wR}(t)|^2 = \frac{1}{2}\int_{-\infty}^{\infty} dt\, |m_{\rm w}(t)|^2 + \frac{1}{2}\int_{-\infty}^{\infty} dt\, |m_{\rm w-}(t)|^2 = 1. \tag{5.43}$$

Thus, the measurement by $m_{\rm wR}(t)$ becomes valid.

According to the definition of $\eta$ in Eq. (5.37), Eq. (5.42) directly shows that the mode overlap between $m_{\rm w}(t)$ and $m_{\rm wR}(t)$ gives $\eta = 1/2$. Thus, using $m_{\rm wR}(t)$, we can perform a measurement of the complex amplitude of $m_{\rm w}(t)$ with a mode overlap of $\eta = 1/2$.

Now, as shown in Eq. (5.35), we can define the measurement pulse modes with sideband frequencies of $\omega_{\rm s}$ as

$$\begin{aligned} \tilde{m}_{\rm w}(t) &= f(t)e^{-i\omega_{\rm s}t} \\ \tilde{m}_{\rm w-}(t) &= f^*(t)e^{+i\omega_{\rm s}t} = \tilde{m}_{\rm w}^*(t) \\ \tilde{m}_{\rm wR}(t) &= \frac{\tilde{m}_{\rm w}(t) + \tilde{m}_{\rm w-}(t)}{\sqrt{2}} = \frac{\tilde{m}_{\rm w}(t) + \tilde{m}_{\rm w}^*(t)}{\sqrt{2}} = \sqrt{2}{\rm Re}[\tilde{m}_{\rm w}(t)]. \end{aligned} \tag{5.44}$$

Then, we can confirm that

$$\begin{aligned} {\rm Re}[\tilde{m}_{\rm wR}(t)] &= \sqrt{2}{\rm Re}[\tilde{m}_{\rm w}(t)] \\ {\rm Im}[\tilde{m}_{\rm wR}(t)] &= 0. \end{aligned} \tag{5.45}$$

Therefore, from Eq. (5.36), we can obtain the real part $I_{\rm wR}$ measured by $\tilde{m}_{\rm wR}(t)$ using only the in-phase signal of $I(t)$, as

$$I_{\rm wR} = \sqrt{2}\int_{-\infty}^{\infty} dt\, {\rm Re}[\tilde{m}_{\rm w}(t)]I(t). \tag{5.46}$$

Suppose $m_{\rm w-}(t)$ contains only noise, then $I_{\rm wR}$ is composed of the half signal power from the target pulse mode $m_{\rm w}(t)$ and the half noise power from $m_{\rm w-}(t)$. Importantly, the carrier frequency of $m_{\rm w-}(t)$ is far from that of $m_{\rm w}(t)$ by twice the sideband frequency $2\omega_{\rm s}$. This frequency detuning enables us to suppress the noise in $m_{\rm w-}(t)$ sufficiently with a band-pass filter for $m_{\rm w}(t)$ before the IQ mixer. Therefore, the real part measured with $m_{\rm w}(t)$ can be obtained using the single quadrature signal $I(t)$ as

$$I_{\rm w} = \sqrt{2} \times I_{\rm wR} = 2\int_{-\infty}^{\infty} dt\, {\rm Re}[\tilde{m}_{\rm w}(t)]I(t). \tag{5.47}$$

In the same way, we can also measure the imaginary part of $\tilde{m}_{\rm w}(t)$ by the definition of another measurement pulse mode as

$$\begin{aligned} m_{\rm wI}(t) &= \frac{m_{\rm w}(t) - m_{\rm w-}(t)}{\sqrt{2}} \\ \tilde{m}_{\rm wI}(t) &= \frac{\tilde{m}_{\rm w}(t) - \tilde{m}_{\rm w-}(t)}{\sqrt{2}} = \frac{\tilde{m}_{\rm w}(t) - \tilde{m}^*_{\rm w}(t)}{\sqrt{2}} = i\sqrt{2}{\rm Im}[\tilde{m}_{\rm w}(t)]. \end{aligned} \tag{5.48}$$

We confirm ${\rm Re}[\tilde{m}_{\rm wI}(t)] = 0$ and ${\rm Im}[\tilde{m}_{\rm wI}(t)] = \sqrt{2}{\rm Im}[\tilde{m}_{\rm w}(t)]$. Then, from Eq. (5.36), we obtain

$$Q_{\rm wI} = -\sqrt{2}\int_{-\infty}^{\infty} dt\, {\rm Im}[m_{\rm w}(t)]I(t), \tag{5.49}$$

where $Q_{\rm wI}$ is the imaginary part measured with $\tilde{m}_{\rm wI}(t)$. By suppressing the noise in $m_{\rm w-}(t)$, we can measure the imaginary part measured with $m_{\rm w}(t)$ by using only the in-phase signal $I(t)$, as

$$Q_{\rm w} = \sqrt{2} \times Q_{\rm wI} = -2\int_{-\infty}^{\infty} dt\, {\rm Im}[\tilde{m}_{\rm w}(t)]I(t). \tag{5.50}$$

Suppose that the demodulation window is the real-valued function as $f_{\rm w}(t) = f^*_{\rm w}(t)$. Then the real part and imaginary part measured with $m_{\rm w}(t) = f_{\rm w}(t)e^{-i(\omega_{\rm LO}-\omega_{\rm s})t}$ in Eqs. (5.47) and (5.50) are described as

$$\begin{aligned} I_{\rm w} &= 2\int_{-\infty}^{\infty} dt\; f_{\rm w}(t)\cos\omega_{\rm s}t\; I(t) \\ Q_{\rm w} &= 2\int_{-\infty}^{\infty} dt\; f_{\rm w}(t)\sin\omega_{\rm s}t\; I(t). \end{aligned} \tag{5.51}$$

In practice, the scale of $I_{\rm w}$ and $Q_{\rm w}$ does not matter, because we can determine it from the reference of the vacuum input, as explained in Chapter 8.

### 5.7.4 DAC system

As explained before, a microwave pulse can be generated by applying low-frequency signals and a continuous microwave carrier signal to a IQ mixer.

We use a FPGA board with DACs to generate the low-frequency signals. The FPGA board, which is called GHzDAC, is designed by the research group of John Martinis in UC Santa Barbara (now in Google). The GHzDAC is a dual-channel 14-bit DAC operating at 1-GHz sampling rate. DACs "AD9736", which are manufactured by Analog Devices, are used at the heart of GHzDAC. The output differential-voltage range with double 50 Ω terminations is from 0 to 1 V. The GHzDACs are phase-locked with a 10-MHz reference signal from the rubidium atomic clock. The GHzDAC is controlled and the waveform data is downloaded through an Ethernet interface. The memory capacity corresponds to the maximum pulse-sequence length of 8 $\mu s$, which is long enough to perform simple protocols. However, it is not enough to measure the energy-relaxation or dephasing times of a superconducting qubit. Then, such a long pulse sequence is performed by pausing the pulse sequence at the point when we need a long interval. The GHzDACs, which are phase-locked with the identical rubidium atomic clock, can be paused synchronously. Note that the minimum time interval of the pausing is 360 ns.

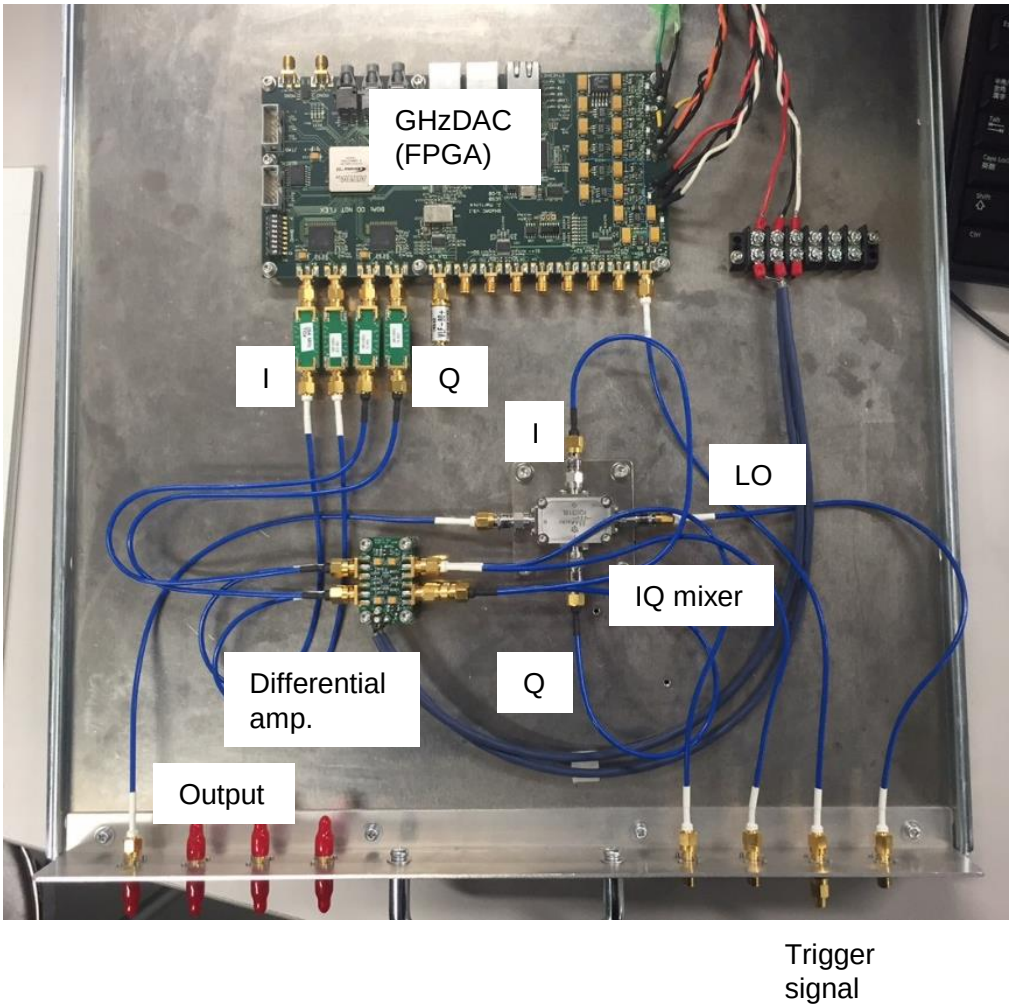


Figure 5.12: Total DAC system.

### Total modulation system

The total modulation system is shown in Fig. 5.12. The output signals from the GHzDAC after the low-pass filters are amplified by a differential amplifier and are applied into the I and Q ports of the IQ mixer. The continuous microwave carrier signal from the microwave source is applied to the LO port of the IQ mixer. We install a 3-dB attenuator to each input port to attenuate the input signals reflected by the IQ mixer. Here, we explain the details one by one.

From the Nyquist-Shannon sampling theorem, with a 1-GHz sampling rate, we can generate low-frequency signals for the sideband modulation up to 500 MHz. However, an ideally-steep low-pass filter with a cutoff frequency of 500 MHz is not easily available. Therefore, according to the cutoff frequency of the low-pass filter, the maximum sideband frequency is determined. Practically, we determine the sideband frequency depending on the bandwidth needed for each purpose. Since the typical bandwidth of the control and readout pulses for a superconducting qubit are about 30 MHz and 10 MHz, the sideband frequencies are set to about 150 MHz and 50 MHz, respectively. Depending on the sideband frequencies required, the Gaussian low-pass filters with a cutoff frequencies of about 300 MHz and 75 MHz are installed at the output ports of the GHzDACs, which

are used for control and readout pulses, respectively. The Gaussian filter is an absorption-type filter used to minimize an reflection of the out-of-band signals.

The differential-voltage signals from the Gaussian filters are amplified by differential amplifiers, which were also designed by the aforementioned group of John Martinis. In the differential amplifier, there are the two output ports, which output the amplified signals with opposite signs. One of the output signals is applied to the IQ mixer. The other is terminated or is used for monitoring the output signals from the GHzDAC directly with a sampling oscilloscope.

#### DAC calibration

The modulation in Eq.(5.14) can be interpreted as the result of the interference between the low-frequency signals of $I(t)$ and $Q(t)$. However, practically, the phase shift and the multiplications at the IQ mixer are not perfect, and the attenuations and the phase shifts between the IQ mixer and the GHzDAC are not identical for each port. This imperfection causes the output of spurious signals at the carrier frequency $\omega_{\rm LO}$ and the image band frequency $\omega_{\rm LO} - \omega_{\rm s}$. Therefore, we correct the imperfection by modifying the low-frequency signals from the GHzDAC. Since the imperfection is considered to be stable in time, it is useful to modify the low-frequency signals in the frequency domain. By measuring the continuously-modulated signals at $\omega_{\rm LO} + \omega_{\rm s}$, $\omega_{\rm LO}$, and $\omega_{\rm LO} - \omega_{\rm s}$ by using a spectrum analyzer, we can determine the additional correction signals necessary for minimizing the spurious outputs at $\omega_{\rm LO}$ and $\omega_{\rm LO} - \omega_{\rm s}$. Concretely, we optimize the offset DC signal and the image sideband frequency signal to cancel the spurious outputs. The measurement of the correction signals is performed at every carrier frequency $\omega_{\rm LO}$ and every sideband frequency $\omega_{\rm s}$ which we are going to use. For a microwave pulse, the corresponding low-frequency signals are Fourier transformed, corrected according to the frequency-domain calibration results, and inverse-transformed again.

An example of the calibration results is shown in Fig. 5.13(a). The output signal from the IQ mixer is shown as a function of the DAC amplitude in arbitrary units. Typically, the suppression ratio of the spurious signals to the target signal is from 30 to 40 dB. We use the results to associate the actual output power with the DAC amplitude. The linearity of the output signal is also important. The output power as a function of the square of the DAC amplitude is shown in Fig. 5.13(b). From this, we confirm that our modulation system can up-convert the low-frequency signals linearly.

### 5.7.5 ADC system

To measure the microwave pulse, the demodulation signals from the IQ mixer are measured by an ADC.

In this thesis, we use the ADC model "Acqiris AP240", which is manufactured by Keysight (former Agilent). The ADC board is plugged directly into the PCI slot in the PC "Precision T7500" from Dell. The ADC can digitize the input signal into 256 levels (8 bits) with dual channels at 1-GHz sampling rate. The measurement range of the input signal in full span can be set to a value from 50 mV to 5 V.

#### Total demodulation system

The total demodulation system is shown in Fig. 5.14. The output microwave pulse, which is amplified by the cryogenic and room temperature amplifiers, arrives at the demodulation system.

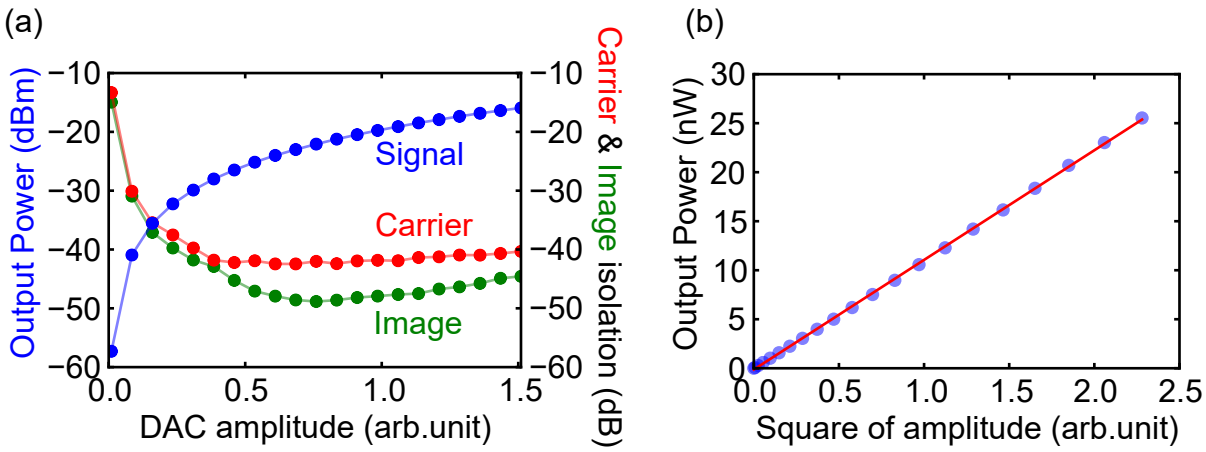


Figure 5.13: DAC calibration results. (a) Output powers as a function of the DAC amplitude. The blue dots are the output power at the target frequency $\omega_{\mathrm{LO}} + \omega_{\mathrm{s}}$. Here, we set $\omega_{\mathrm{LO}}/2\pi = 10.6753$ GHz and $\omega_{\mathrm{s}}/2\pi = -100$ MHz. The red and green dots are the isolation ratio of the carrier and image band frequencies to the target signal, respectively. (b) Output powers as a function of the square of the DAC amplitude.

In this thesis, for simplicity, we only measure one of the demodulated signals from the IQ mixer. As described in Sec. 5.7.1, the noise of the image sideband frequency is crucial from the viewpoint of the signal-to-noise ratio. Therefore, before the IQ mixer, we install the tunable band-pass filter model "507345 10.0-11.0 GHz", which is manufactured by COLEMAN MICROWAVE CO. The microwave pulse after the band-pass filter is applied into the RF port of the IQ mixer. The continuous microwave carrier signal from the microwave source is applied to the LO port of the IQ mixer. Importantly, in order to cancel the slow phase noise, the microwave source for the demodulation should be identical to that for the modulation. In this thesis, the sideband frequency to be measured is always set to 50 MHz. Therefore, we can use the fixed narrow band-pass filter model "SIF-50+", which is manufactured by Mini-Circuits, Inc. The down-converted signals are amplified by the amplifier model "ZFL-500LN+", which is manufactured by Mini-Circuits, Inc. Finally, the signal is amplified by the amplifier of "SR445A", which is manufactured by Stanford Research Systems (SRS), to match the required signal range of the ADC. Then, the signals are applied to the input port of the ADC.

### Phase lock

The phase lock between the GHzDAC and the ADC is crucial for the phase-sensitive measurement.

The 10-MHz reference signal from the identical rubidium atomic clock is applied to both the GHzDAC and the ADC. Therefore, the 1-GHz sampling frequency of the ADC is phase-locked with that of the GHzDAC, which enables us to realize the phase stability of the microwave measurements.

The trigger signal from the GHzDAC is also applied to the ADC. The ADC starts to record the signals after it receives the trigger signal. Therefore, the relative phase of the low frequency signal from the trigger time is also crucial for the phase-sensitive measurement by the ADC.

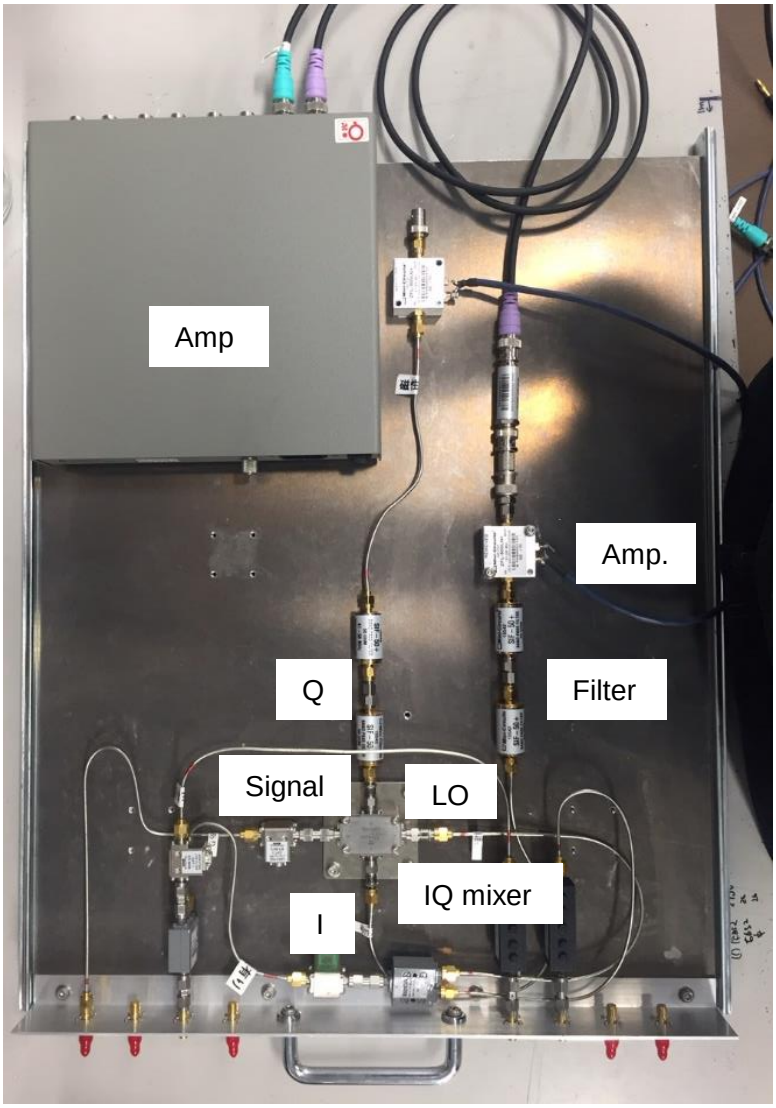


Figure 5.14: Total ADC system.

### Quantization noise

In the measurement using an ADC, the quantization noise has to be evaluated in advance. If the step of the digitization is much smaller than the signal amplitude, the quantization noise can be considered to be uncorrelated with the signal. When the input signal with the full-span amplitude is sinusoidal, the signal-noise-ratio can be approximated as

$$SNR = 1.761 + N \times 6.02\,\mathrm{dB}, \tag{5.52}$$

where $N$ is the bit number of the digitizer. In the case of our 8-bit digitizer, the signal-to-noise ratio can be calculated to be about 50 dB. Therefore, when we set the measurement range of the ADC suitably for the maximum amplitude of the input signal, our signal-to-noise ratio is not limited by quantization noise.

### Time sampling

The ADC measures input signals at 1-GHz sampling rate. Therefore, we also need to consider the effect of the time sampling.

First of all, the measurement outcomes of the ADC can be modeled as the average of the input signals as

$$\begin{aligned}\bar{I}_n &= \frac{1}{\tau}\int_{\tau(n-1/2)}^{\tau(n+1/2)} dt\, I(t) = \frac{1}{\tau}\int_{-\infty}^{\infty} dt\ \sqcap\left(\frac{t-\tau n}{\tau}\right) I(t)\\ \bar{Q}_n &= \frac{1}{\tau}\int_{\tau(n-1/2)}^{\tau(n+1/2)} dt\, Q(t) = \frac{1}{\tau}\int_{-\infty}^{\infty} dt\ \sqcap\left(\frac{t-\tau n}{\tau}\right) Q(t),\end{aligned} \tag{5.53}$$

where, $\sqcap(t)$ is the rectangle function, $I(t)$ and $Q(t)$ are the input signals to the ADC, $\tau$ is the measurement time (the inverse of the sampling frequency) of the ADC, and $n$ is the discrete time. Using the measurement outcomes, the propagating signal can be described with the discrete time as

$$\bar{S}_n = [\bar{I}_n + i\bar{Q}_n]e^{-i\omega_{\rm LO}\tau n}. \tag{5.54}$$

Here, we consider the measurement by the pulse mode with a carrier frequency of $\omega_{\rm LO}+\omega_{\rm s}$, as discussed in Sec. 5.7.1. Without loss of generality, the measurement pulse mode can be described at the rotating frame of $\omega_{\rm LO}$ as

$$m_{\rm w}(t) = f_{\rm w}(t)e^{-i\omega_{\rm LO}t}. \tag{5.55}$$

Then, the time-discrete measurement pulse can be defined as

$$m_{{\rm w},n} = \frac{m_{\rm w}(\tau n)}{\sqrt{\sum_n |m(\tau n)|^2}} = \frac{f_{\rm w}(\tau n)e^{-i\omega_{\rm LO}\tau n}}{\sqrt{\sum_n |f(\tau n)|^2}}. \tag{5.56}$$

Then, the complex amplitude measured by $m_{{\rm w},n}$ can be defined as

$$\begin{aligned}\bar{\alpha}_m &= \sum_n m^*_{{\rm w},n}\bar{S}_n\\ &= \sum_n \frac{f^*_{\rm w}(\tau n)}{\sqrt{\sum_n |f(\tau n)|^2}}[\bar{I}_n + i\bar{Q}_n].\end{aligned} \tag{5.57}$$

Here, we will show the complex amplitude calculated from the ADC outcomes corresponds to that of the pulse mode measurement, which is defined in Eq.(5.32). The complex amplitude in Eq. (5.57) can be represented as

$$\begin{aligned}\bar{\alpha}_m &= \int_{-\infty}^{\infty} dt\, \frac{\sum_n f^*_{\rm w}(\tau n)\sqcap\left(\frac{t-\tau n}{\tau}\right)}{\tau\sqrt{\sum_n |f(\tau n)|^2}}[I(t)+iQ(t)]\\ &= \int_{-\infty}^{\infty} dt\, f^*_{{\rm w}\sqcap}(t)[I(t)+iQ(t)]\\ &= \int_{-\infty}^{\infty} dt\, m^*_{{\rm w}\sqcap}(t)S(t),\end{aligned} \tag{5.58}$$

where $f_{{\rm w}\sqcap}(t) = \frac{\sum_n f_{\rm w}(\tau n)\sqcap\left(\frac{t-\tau n}{\tau}\right)}{\tau\sqrt{\sum_n |f(\tau n)|^2}}$ is the time-discrete measurement window of $f(t)$, and $m_{{\rm w}\sqcap}(t) = f_{{\rm w}\sqcap}(t)e^{-i\omega_{\rm LO}t}$ is the time-discrete measurement pulse mode of $m(t)$. We can confirm that $m_{{\rm w}\sqcap}(t)$ satisfies the normalization condition. Therefore, we find that the complex amplitude calculated from the ADC outcomes corresponds to that measured by the time-discrete pulse mode of $m_{{\rm w}\sqcap}(t)$.

As described in Sec. 5.7.1, the mode mismatch between the time-discrete pulse mode $m_{{\rm w}\sqcap}(t)$ and the ideal pulse mode $m_{\rm w}(t)$ gives the additional noise. The mode overlap can be calculated as

$$\eta = \left|\int_{-\infty}^{\infty} dt\, m^*(t)m_{{\rm w}\sqcap}(t)\right|^2 = \left|\int_{-\infty}^{\infty} dt\, f^*(t)f_{{\rm w}\sqcap}(t)\right|^2. \tag{5.59}$$

Then, as in Eq. (5.37), the time-discrete pulse mode is described as

$$m_{\mathrm{w}\sqcap}(t) = \sqrt{\eta}\, m_{\mathrm{w}}(t) + \sqrt{1-\eta}\, m_{\mathrm{w}\perp}(t), \tag{5.60}$$

where $m_{\mathrm{w}\perp}(t)$ is the compensating pulse mode, which has its frequency component with the detuning of the sampling frequency from the ideal pulse mode $m_{\mathrm{w}}(t)$. When the sampling frequency is sufficiently larger than the sideband frequency, the mode overlap of $\eta$ becomes close to unity. In our measurement, the sampling frequency and the sideband frequency are 1 GHz and 50 MHz, respectively. Moreover, the additional noise in the compensating pulse mode $m_{\mathrm{w}\perp}(t)$ can be easily suppressed by the tunable band-pass filter before the IQ mixer. Therefore, we confirm that the time sampling of the ADC does not affect our measurement.

# Chapter 6

# Characterization

Here, we explain how to characterize a three-dimensional 3D circuit quantum electrodynamical (QED) system. Based on the obtained system parameters, we optimize the control and readout of a superconducting qubit. We also characterize a Josephson parametric amplifier (JPA). Then, we implement single-shot readout of the superconducting qubit using the JPA. Note that the 3D circuit QED system, which we characterize here, is also used in Chapters 8 and 9.

## 6.1 Frequency-domain measurement

In this section, we show results of basic experiments in the frequency domain. By measuring the transmission or reflection of superconducting microwave circuits, we can characterize their resonance frequencies and linewidths. The resonance frequencies tell us not only the transition frequencies between the eigenstates of the qubit and resonator, but also the coupling strengths between different modes, which we obtain by measuring the frequency splittings or frequency shifts. The linewidth of the resonance indicates the energy-relaxation rate and dephasing rate. By measuring the nonlinear effects from Josephson junctions, we characterize the power at the sample in the dilution refrigerator. The basic experimental setup for the frequency-domain measurements is shown in Fig. 6.1. A three-dimensional (3D) circuit QED system and a Josephson parametric amplifier (JPA) are characterized by reflection measurements. Although both of the reflection coefficients are measured in the same output line, they can be measured without any interference and be characterized separately if there is a sufficient frequency detuning between them.

Note that the microwave powers arriving at the sample are represented by taking account of the total attenuation.

### 6.1.1 Cavity spectroscopy

Here, we characterize the 3D cavity coupled dispersively to the transmon qubit.

Firstly, we search for the cavity resonance around the frequency range which we determine by the measurement at room temperature. Note that the resonance frequency at the base temperature is about 50 MHz higher than at room temperature due to thermal contraction (see Sec. 4.1.1). To find the cavity resonance easily, we send as high probe power as we can put into the dilution refrigerator since the cavity is a linear system and the resonance frequency is not largely shifted by the high probe power. Taking into account the external coupling rate we tune at room temperature, we can roughly determine the optimal spectral resolution of the measurement.

### Probe power dependence

After we find the cavity resonance, we measure its probe power dependence. The reflection spectra as a function of the probe power are shown in Fig. 6.2. When the probe power is getting higher, the cavity resonance jumps to a lower frequency at around $-115$ dBm. The jump is due to the nonlinearity of the transmon qubit in the 3D cavity. Therefore, the observation of the jump indicates that the transmon qubit is alive and coupled to the cavity we are measuring. This observation is the first step of the characterization of a circuit QED system. Note that if the Josephson junction is broken, the cavity does not show such a strong probe power dependence.

The probe power dependence of the cavity spectra can be classified into three regimes: (i) dispersive, (ii) critical, and (iii) bare regimes [73, 74]. When the average photon number in the cavity is far below the critical photon number, the perturbative treatment of the dispersive coupling is valid. In the dispersive regime (i), the cavity spectrum shows a linear response, or no probe power dependence. It means that we can treat the cavity as a harmonic oscillator. When the average photon number is close to and above the critical photon number, the perturbative picture collapses. In the critical regime (ii), as the cavity mode is largely mixed with the transmon qubit, the cavity spectrum shows strong nonlinearity induced by the transmon qubit. The dressed system cannot be considered as a harmonic oscillator anymore. When the larger probe power is applied to the cavity, the cavity spectrum shows the linear response again, since the cavity is decoupled to the transmon qubit due to its saturation. The transmon qubit is off-resonantly driven by the cavity probe despite the large detuning. In the bare regime (iii), the bare cavity can be considered as a harmonic oscillator.

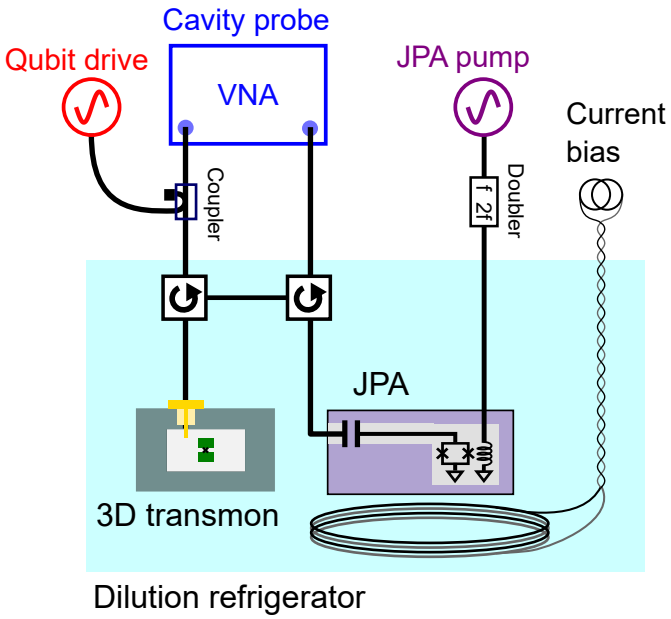


Figure 6.1: Simplified measurement setup for the reflection measurement of the circuit QED system and the JPA in the frequency domain.

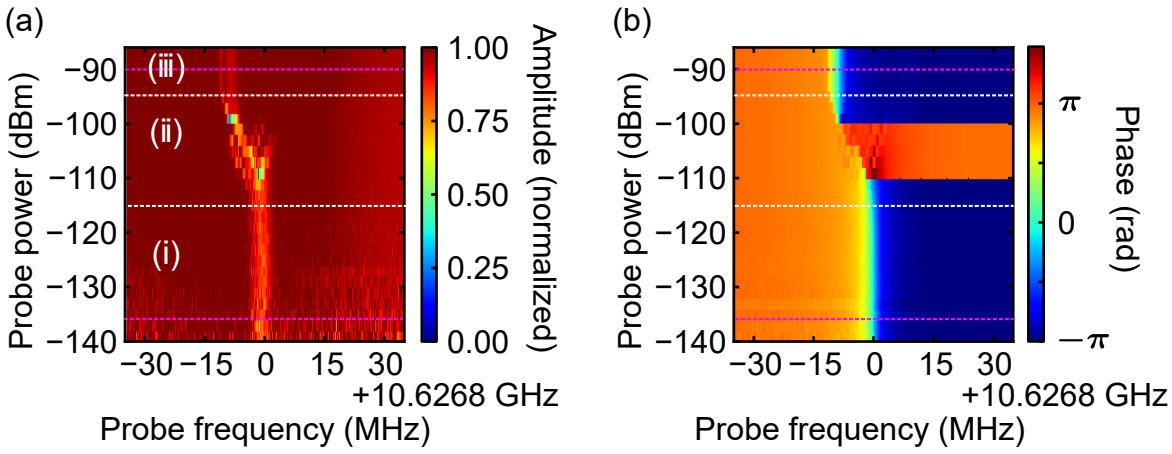


Figure 6.2: Probe power dependence of the cavity spectrum. (a) Normalized amplitude and (b) phase of the reflection coefficients as a function of the probe frequency and power. The white dashed lines separate three regimes: (i) dispersive, (ii) critical, and (iii) bare regimes. The magenta lines depict the probe power for the dispersive cavity and the bare cavity.

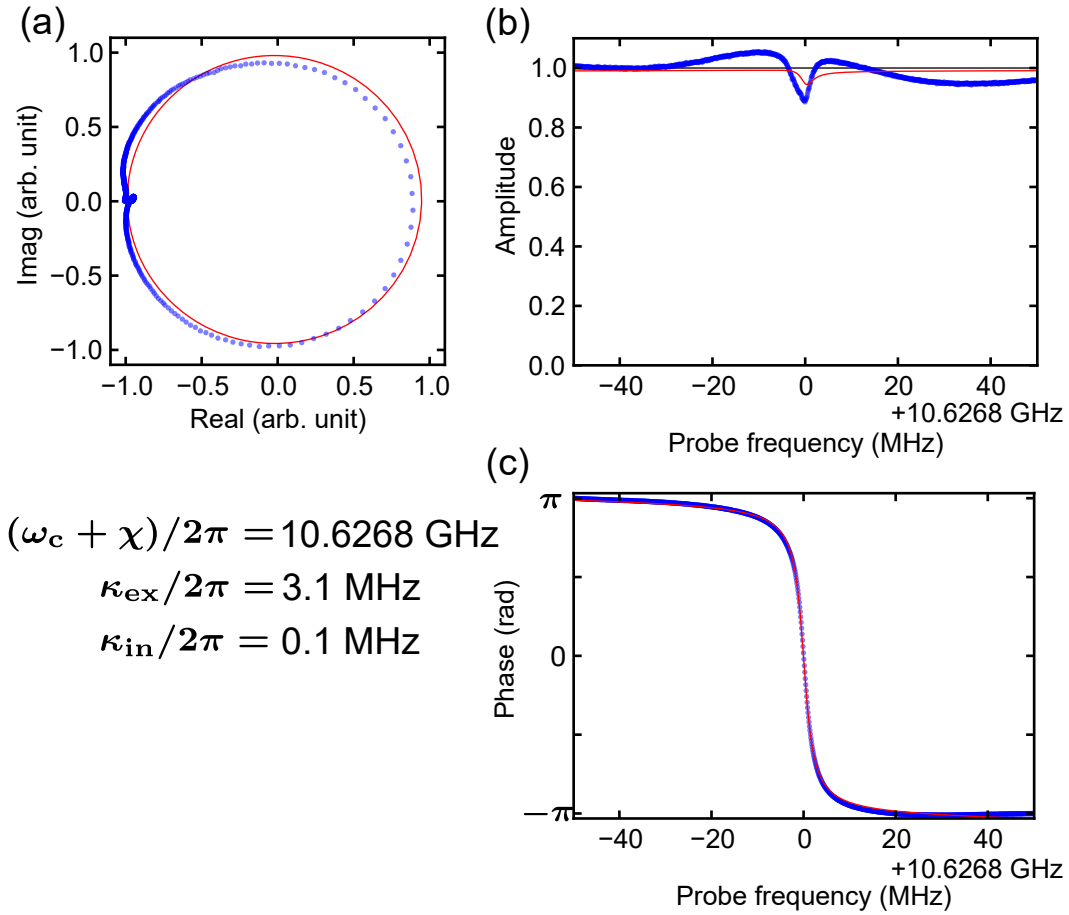


Figure 6.3: Cavity spectroscopy at the single-photon power level (−136 dBm). (a) Reflection coefficient in the complex plane. (b) Normalized amplitude and (c) phase as a function of the probe frequency. The blue dots and the red lines are the experimental results and the fitting results, respectively.

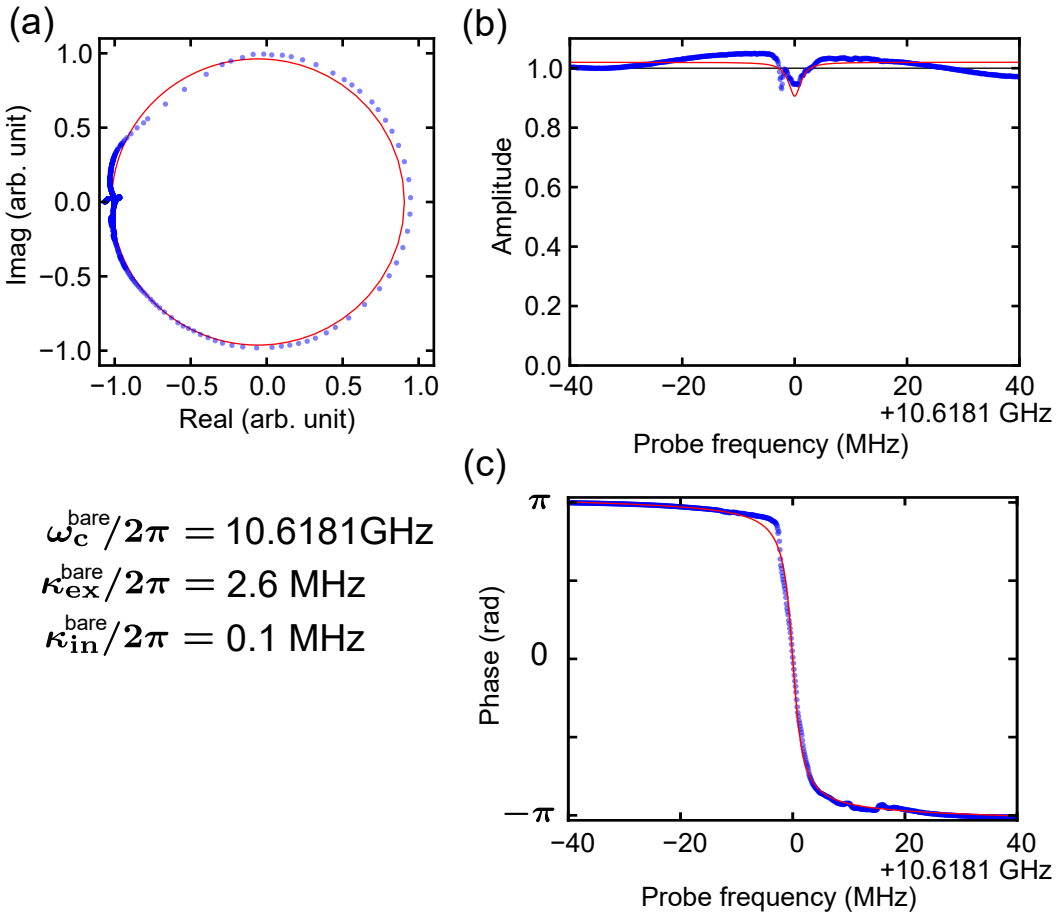


Figure 6.4: Cavity spectroscopy at the high-power level (−90 dBm). (a) Reflection coefficient in the complex plane. (b) Normalized amplitude and (c) phase as a function of the probe frequency. The blue dots and the red lines are the experimental results and the fitting results, respectively.

### Single photon power level

In the dispersive regime, the Hamiltonian of the circuit QED system is described as

$$\mathcal{H} = (\omega_c - \chi\hat{\sigma}_z)\,\hat{a}^\dagger\hat{a} + \frac{\omega_q}{2}\hat{\sigma}_z, \tag{6.1}$$

where $\omega_c$ is the cavity resonance frequency, $\omega_q$ is the qubit resonance frequency, and $\chi$ is the dispersive shift. From the Hamiltonian, the dispersive interaction can be understood as state-dependent frequency shifts. Now, we assume that the transmon qubit inside the cavity is well cooled down to be in the ground state. The resonance frequency corresponds to that of the cavity with the qubit in the ground state $\omega_c + \chi$. The cavity spectrum, which is measured with the probe power of −136 dBm, is shown in Fig. 6.3. By fitting the cavity spectrum, we obtain the cavity parameters: the resonance frequency $\omega_r = \omega_c + \chi$, the external coupling rate $\kappa_{ex}$ and the internal loss rate $\kappa_{in}$. The fitting results are shown in Fig. 6.3. The reflection coefficient is obtained in Sec. 2.4.2. Note that these parameters may not be so reliable for the following reasons. First, there is a frequency dependent background signal due to the impedance mismatching in the measurement line. Next, the obtained spectrum can be a probabilistic mixtures of the two cavity spectra for the qubit in the ground and excited states due to the finite thermal excitation. Typically, the thermal excitation population is about 10 percent in our experimental setup.

It is known that the internal loss of the cavity can be power dependent [75]. When the cavity is coupled to a nonlinear bath, such as a finite number of two-level systems in a dielectric material, many photons in the cavity cannot be linearly absorbed due to the saturation of the bath. Then, the internal loss rate of the cavity may be decreased at the higher probe power. Therefore, it is very important to characterize the cavity with a probe power at the single-photon level. Using the cavity parameters obtained in the dispersive regime, we estimate the average photon number excited by the resonant cavity probe as

$$\langle \hat{a}^\dagger \hat{a} \rangle = \frac{\kappa_{\rm ex}}{\left(\frac{\kappa_{\rm ex}+\kappa_{\rm in}}{2}\right)^2} \langle \hat{a}_{\rm i}^\dagger \hat{a}_{\rm i} \rangle, \tag{6.2}$$

where $\langle \hat{a}^\dagger \hat{a} \rangle$ is the average photon number in the cavity, $\langle \hat{a}_{\rm i}^\dagger \hat{a}_{\rm i} \rangle = P/\hbar\omega_{\rm p}$ is the average photon number per unit time of the probe microwave signal, $P$ is the probe power, and $\omega_{\rm p}$ is the probe frequency. The average photon number in the cavity with the resonant coherent probe is obtained in Sec. 2.4.2. From this, the probe power at the single-photon level, the probe power which corresponds to a single photon in the cavity, is calculated as

$$P(\text{@single photon level}) = \frac{(\kappa_{\rm ex}+\kappa_{\rm in})^2}{4\kappa_{\rm ex}} \hbar\omega_{\rm p} = -134\,(\text{dBm}). \tag{6.3}$$

Therefore, we confirm that the cavity spectrum in Fig. 6.3 is measured at the single photon level.

**High power level**

In the bare regime, the cavity spectrum can be considered as that of a harmonic oscillator. The cavity spectrum, which is obtained with a high probe power of $-90$ dBm is shown in Fig. 6.4. By fitting the spectrum, the cavity parameters are obtained, as shown in Fig. 6.4.

### 6.1.2 Qubit spectroscopy

Here we explain how to characterize the transmon qubit by using frequency-domain measurements. Here, the qubit excitation spectrum, which is the excitation probability of the qubit as a function of the qubit drive frequency, is measured.

In the dispersive circuit QED system, the qubit excitation spectrum can be obtained by measuring the cavity probe with fixed frequency while sweeping the qubit drive frequency. This is called a two-tone spectroscopy measurement [76]. From the Hamiltonian in Eq. (6.1), the cavity frequency is shifted depending on the qubit state. Therefore, the cavity reflection coefficients at the fixed probe frequency are varied depending on the qubit states. Note that the cavity probe power should be set to much below the critical photon number in the cavity not to break the perturbation of the dispersive interaction. Usually, the measurement bandwidth in the frequency domain is much smaller than the energy relaxation and dephasing rates of the qubit. Thus, the measurement outcome of the VNA is the average value of the reflection coefficients for the qubit in the ground and excited states, reflecting the occupation probability in the steady states. By projecting the reflection coefficients in the quadrature plane onto one axis, we evaluate the occupation probability of the excited state of the qubit. The projected amplitude as a function of the qubit drive frequency corresponds to the qubit excitation spectrum. Note that the determination of the projection axis is not critical. Nevertheless, it is important from the viewpoint of the signal-to-noise ratio. To maximize the signal-to-noise ratio of the spectrum, the projection axis should be chosen such that it is parallel with the straight

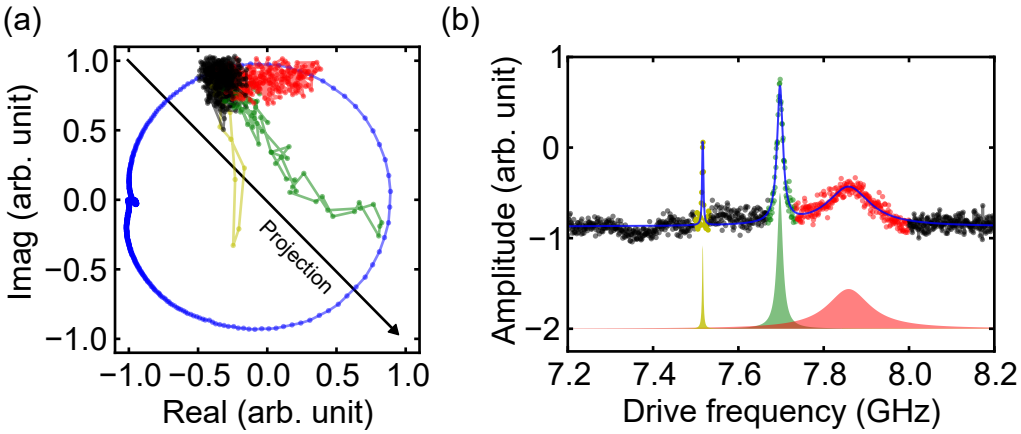


Figure 6.5: Qubit excitation spectrum. (a) Cavity reflection coefficient as a function of the qubit drive frequency in the complex plane. The black, red, green and yellow dots are experimental results. The colors correspond to those in the qubit spectrum in (b). The blue dots are the reflection coefficients of the cavity as a function of the probe frequency. The black arrow depicts the projection axis to obtain the qubit excitation spectrum. (b) Projected amplitude as a function of the drive frequency, which corresponds to the qubit excitation spectrum. The dots are the experimental results. The blue line is the fit of the data to the multiple Lorentzian functions. The color-shaded peaks show the Lorentzian components corresponding to the different transitions.

line connecting the reflection coefficients for the qubit in the ground and excited states (or any other higher excited state you are interested in).

Before searching for the qubit resonance peak, we determine several experimental parameters. First, we choose the qubit drive power and frequency sweep interval. Since we know the order of magnitude of the qubit external coupling rate from the simulation in Sec. 4.3.2, we can roughly estimate the Rabi frequency of the qubit for a given qubit drive power. In the high power limit of the qubit drive, the Rabi frequency determines the linewidth of the qubit excitation spectrum. The qubit resonance peak broadened by the larger drive power can be easily detected. Moreover, we determine the optimal frequency sweep interval by taking into account the linewidth. Note that the Rabi frequency should not exceed the anharmonicity of the transmon qubit. Typically, the Rabi frequency is set to ten times smaller than the anharmonicity in order to avoid additional complexity. Second, we should consider the cavity probe power. In the dispersive circuit QED Hamiltonian in Eq. (6.1), the qubit resonance frequency is shifted depending on the photon number in the readout cavity. Therefore, to observe the qubit excitation spectrum without the photon-number dependent shift, we need to set the cavity probe power to be at or below the single-photon power level. However, due to the small signal-to-noise ratio, it is time-consuming to search for the qubit excitation peak with such a small probe power. Thus, at first, we find the qubit resonance peak using the probe power tens of times larger than the single-photon power level, and then decrease the probe power to obtain the zero-photon qubit frequency.

In Fig. 6.5(a), we show the cavity reflection coefficients as a function of the qubit drive frequency. The probe power is set to $-136$ dBm, which is below the single-photon power level. The qubit excitation spectrum, which corresponds to the projected amplitude along the black arrow as a function of the qubit drive frequency, is shown in Fig. 6.5(b). There are three peaks observed around the drive frequency of 7.8 GHz. The experimental result

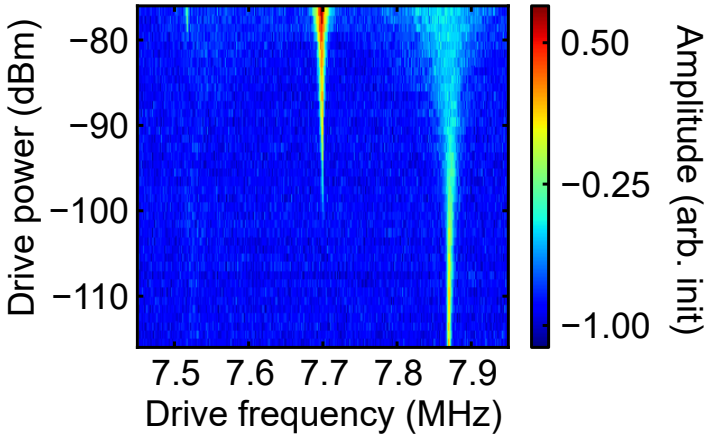


Figure 6.6: Qubit drive power dependence of the qubit excitation spectrum.

is well fitted by the multiple Lorentzian functions. As shown in Fig. 6.5(a), these peaks are derived from the different signal directions in the complex plane, which indicates that each peak corresponds to a different excited state giving a different frequency shift to the readout cavity. Actually, the highest resonance frequency corresponds to the transition frequency between the ground state and the first excited state $\omega_{\mathrm{eg}}$. The center peak is associated with the second excited state, which is excited by the two-photon process from the ground state, as explained in Sec. 2.5.3. Thus, the resonance frequency corresponds to half the transition frequency between the ground state and the second excited state $\omega_{\mathrm{fg}}/2$. Since the two-photon transition is derived by the higher order perturbation, the Rabi frequency (the linewidth) is smaller than that of the first excited state. The lowest frequency peak corresponds to the three-photon excitation of the third excited state, which gives the resonance frequency $\omega_{\mathrm{hg}}/3$.

As discussed in the previous paragraph, the three peaks are associated with the transitions between the states of the transmon qubit. Nevertheless, the experimental result is not direct evidence of detecting the qubit. For example, if harmonic oscillators are dispersively coupled to the probed cavity, we will obtain the same results as shown in Fig. 6.5. However, there is a stark difference between the qubit excitation spectrum and that of the harmonic oscillator. As explained before, the linewidth of the qubit excitation spectrum is broadened as the qubit drive power is increasing. This is called a power broadening of the qubit resonance [77]. The qubit excitation spectrum as a function of the qubit drive power are show in Fig. 6.6. As we expected, the linewidths are broader as the qubit drive power is increased. Therefore, we can confirm that these three peaks correspond to the transitions of the transmon qubit.

### First excited state

Here, we focus on the resonance peak corresponding to the transition between the ground state and the first excited state. The qubit excitation spectrum is shown in Fig 6.7. The probe power is set to $-136$ dBm, which is below the single-photon power level. The experimental results are well fitted by a Lorentzian. Although the resonance frequency of an ideal qubit is not shifted by the qubit drive, the resonance frequency of the transmon qubit can be shifted due to the presence of the second excited state. To obtain the qubit frequency without the qubit-drive induced shift, the qubit drive power should be

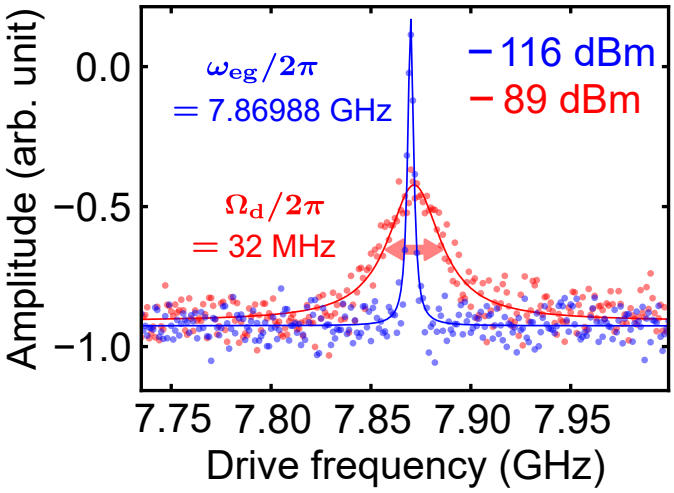


Figure 6.7: Qubit excitation spectra around the transition frequency between the ground and first excited state of the transmon qubit. The dots are the experimental results. The lines are the results of the Lorentzian fits. The blue and red data are measured with the drive powers of −116 dBm and −89 dBm, respectively. The qubit resonance frequency without any microwave-induced shift can be obtained by the qubit excitation spectrum with the lower drive power (blue). The qubit drive power needed for the applicable Rabi frequency of 32 MHz is about −89 dBm.

so low that the corresponding Rabi frequency is much smaller than the anharmonicity of the transmon qubit. The linewidth of the qubit excitation spectrum with the low drive power (blue) is about 3 MHz, which is about one hundred times smaller than the anharmonicity of 342 MHz, as we will obtain. Furthermore, since the cavity probe power is also smaller than the single-photon level, the obtained resonance frequency is close to the qubit frequency without any microwave-induced shift. The transition frequency between the ground state and the first excited state is obtained as $\omega_{eg}/2\pi = 7.86988$ GHz

By measuring the Rabi frequency, we estimate the qubit drive power which is needed for high-fidelity qubit control. The applicable Rabi frequency should be much smaller than the anharmonicity [48, 49]. In Fig. 6.7, we show the qubit excitation spectrum whose Rabi frequency is about ten times smaller than the anharmonicity of 342 MHz. From this measurement, we find the necessary qubit drive power of −89 dBm.

The frequency difference between the qubit resonance frequencies obtained with the lower and higher qubit drive power can be calculated as 7.86988 GHz − 7.8716 GHz = 1.7 MHz. This is consistent within the fitting errors with the theoretical frequency shift due to the second exited state, which is calculated in Sec. 2.5.2 as

$$\frac{|\Omega_d|^2}{2\alpha}/2\pi = 1.5 \text{ MHz}. \tag{6.4}$$

### Second excited state

Here, we focus on the resonance peak corresponding to the two-photon transition between the ground state and the second excited state. As explained in Sec. 2.5.3, the two photon transition is attributed to the transmon qubit. Then, the resonance frequency between

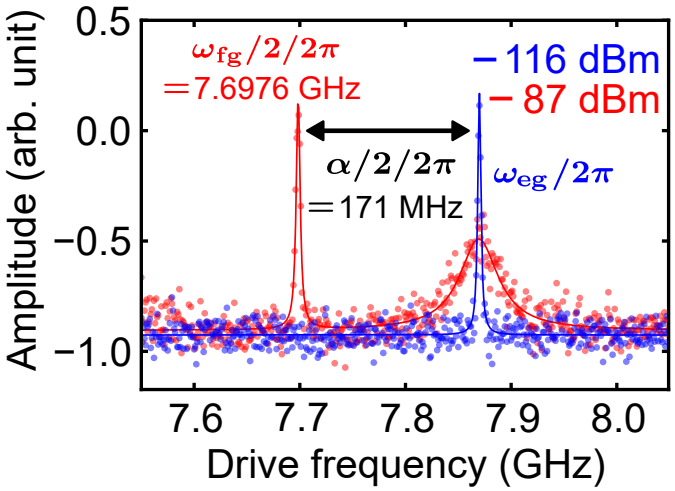


Figure 6.8: Qubit excitation spectra around the transition frequency between the ground and second excited state of the transmon qubit. The dots are the experimental results. The line are the results of the Lorentzian fits. The blue and red data are measured with drive powers of −116 dBm and −87 dBm, respectively. The two-photon resonance frequency without any microwave-induced shift can be obtained from the qubit excitation spectrum (red).

the ground and second excited states are measured, which can be used to characterize the anharmonicity.

The peak at around 7.7 GHz in Fig. 6.8 shows the two photon resonance peak. The spectrum was obtained with a qubit drive power of −87 dBm and a cavity probe power of −116 dBm. Since the two-photon Rabi frequency is about 3 MHz, which is much smaller than the anharmonicity, we obtain the transition frequency $\omega_{fg}/2/2\pi = 7.8694$ GHz with negligible microwave-induced shift. From this, we can calculate the anharmonicity as

$$\alpha/2\pi = (\omega_{fe} - \omega_{eg})/2\pi = 2\left(\frac{\omega_{fg}}{2} - \omega_{eg}\right)/2\pi = -342 \text{ MHz}. \tag{6.5}$$

### Qubit characterization

Now, we know the qubit resonance frequency and the anharmonicity. Therefore, we can characterize the qubit parameters as in Sec. 2.6. The capacitive energy quantum is calculated in frequency units as

$$\omega_C/2\pi = -8\alpha/2\pi = 2.736 \text{ GHz}. \tag{6.6}$$

Thus, the linearized qubit frequency with the Lamb shift is obtained as

$$\omega_q^l/2\pi = \omega_q + \omega_C/8/2\pi = 8.212 \text{ GHz}. \tag{6.7}$$

Then, the tunneling energy of the Josephson junction is calculated as

$$\omega_J/2\pi = \frac{{\omega_q^l}^2}{\omega_C}/2\pi = 24.648 \text{ GHz}. \tag{6.8}$$

Finally, the ratio of the capacitance energy quantum to the tunneling energy can be obtained as

$$\frac{\omega_C}{\omega_J} = 0.111. \tag{6.9}$$

We confirm that the ratio is small enough for the realization of a transmon qubit.

### 6.1.3 JPA spectroscopy

Here we will show how to characterize the flux-driven JPA in the frequency domain. In this thesis, the JPA plays an essential role as a microwave amplifier for single-shot readout of the transmon qubit and efficient measurement of the quadrature amplitude of itinerant microwave photons. Although the JPA works in the near-quantum limit, its gain bandwidth is much smaller than that of commercial cryogenic microwave amplifiers such as a HEMT amplifier. Therefore, the resonance frequency of the JPA should be set to match the signal frequency. Since the tunable inductance from the SQUID participates in the JPA, the JPA frequency can be varied by applying the magnetic flux into the SQUID loop. Here, we explain how to optimize the current for the JPA frequency and how to obtain the gain parameters at the operation point, such as the gain, gain bandwidth, and 1-dB compression point. As shown in Fig 6.1, the JPA is characterized by reflection measurement.

#### Current dependence

First of all, we need to optimize the probe power. Once we find the JPA resonance frequency, we measure its probe power dependence. The JPA frequency becomes lower due to the self-Kerr effect as the probe power is increased. We set the probe power to $-136$ dBm which is small enough to ignore the self-Kerr frequency shift.

Next, the JPA spectrum as a function of the current is measured, as shown in Figs. 6.9(c) and (d). The current flowing through the coil in the sample holder applies a global magnetic field to the JPA chip. The magnetic flux penetrating into the SQUID loop is supposed to be proportional to the applied current. However, the magnetic flux strongly depends on the screening effect of the surrounding superconductors, and thus the coefficient is not easily simulated. In the experiment, since the SQUID inductance shows periodic behavior in terms of the magnetic flux, the actual magnetic flux can be well calibrated. From the current dependence measurement, we find the magnetic flux quantum corresponds to about a current of 16 $\mu$A. At the current of 7.68 $\mu$A, the maximum JPA frequency is obtained as 11.1103 GHz. Normally, a maximum JPA frequency should be obtained at the zero current bias point. In the experimental results, nevertheless, the maximum JPA frequency was shifted by about half the magnetic flux quantum. It is due to the trapped magnetic flux in the surrounding superconducting electrode. However, the static magnetic flux offset is not critical for our measurement.

Typically, the linewidth of a JPA is larger compared to that of a readout cavity. Therefore, the baseline of the JPA spectrum easily shows the frequency dependence, which prevents us from fitting the spectrum with the ideal reflection coefficient of a harmonic oscillator. Moreover, in a typical situation where the JPA is on resonance with the readout cavity, the probe microwave interacts with both of them, as the blue dots show in Figs. 6.9 (a) and (b). However, since the JPA frequency is tunable, we can measure the frequency-dependent baseline separately by placing the JPA resonance far from the measurement range. Around the reduced magnetic flux of $\pi$, the SQUID inductance increases drastically, and the JPA resonance falls out of the measurement range, as the experimental results at the current of $-0.4$ $\mu$A indicate in Figs. 6.9(c) and (d). At this flux bias point, we obtain the baseline of our measurement configuration as the black dots in Figs. 6.9(a) and (b). Therefore, we can correct the frequency-dependent baseline by dividing the complex amplitude of the raw JPA spectrum by that of the baseline. The JPA spectra with the correction of the baseline as a function of the current are shown in

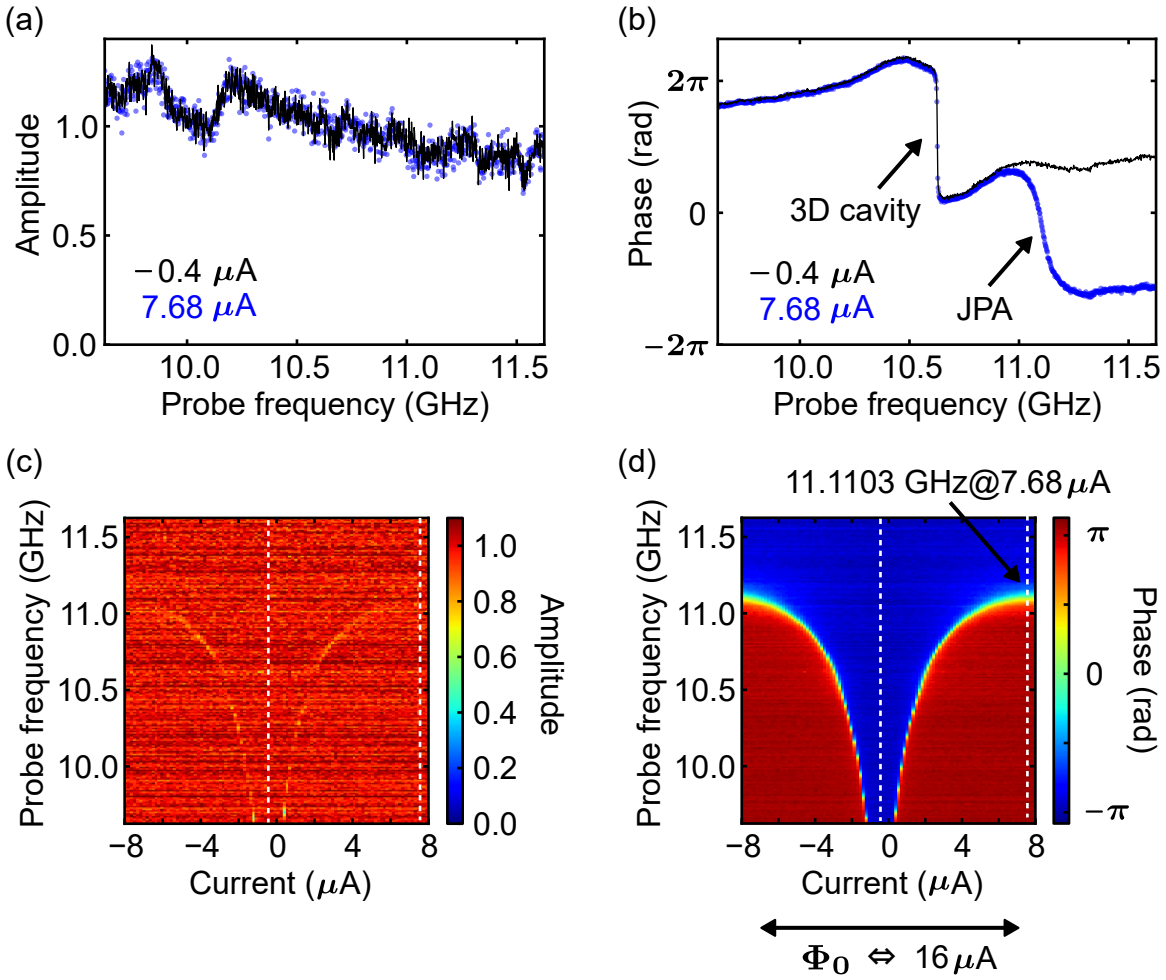


Figure 6.9: Frequency-dependent baseline and current dependence of JPA spectrum. (a) Amplitude and (b) phase as a function of the probe frequency. The black and blue dots are the experimental results measured at the current of $-0.4$ $\mu$A and 7.68 $\mu$A, respectively. The phase shift from both the JPA and the readout cavity (black arrows) are observed at 7.68 $\mu$A. (c) Current dependence of the amplitude of the JPA spectrum. (d) Current dependence of the phase of the JPA spectrum. The maximum JPA frequency of 11.1103 GHz is observed at 7.68 $\mu$A. From the periodicity of the JPA frequency, the magnetic flux quantum penetrating into the SQUID loop corresponds to the current of about 16 $\mu$A.

Figs 6.9(c) and (d). By fitting the experimental reflection coefficients with the analytical ones, we obtain the JPA parameters, as shown in Figs. 6.10(a), (b) and (c).

Here, our purpose is to tune the current so that the JPA frequency is on resonance with the signal frequency. In the flux-driven JPA, since the pump microwave does not cause a frequency shift for the JPA, we optimize the current independently of the pump microwave. This is a stark difference from the current-driven JPA whose resonance frequency depends on the pump power [78]. In Fig. 6.10(d), we show the JPA frequency as a function of the applied current. From the linear fitting, the slope is obtained as $-0.309$ MHz/nA. Since our current resolution is 10 nA, we can set the JPA frequency with a resolution of about 3 MHz, which is much smaller than the linewidth of the JPA. The current which most closely sets the JPA to the target frequency of 10.6253 GHz is determined to be 1.97 $\mu$A. The current is fixed for the amplification of the target frequency

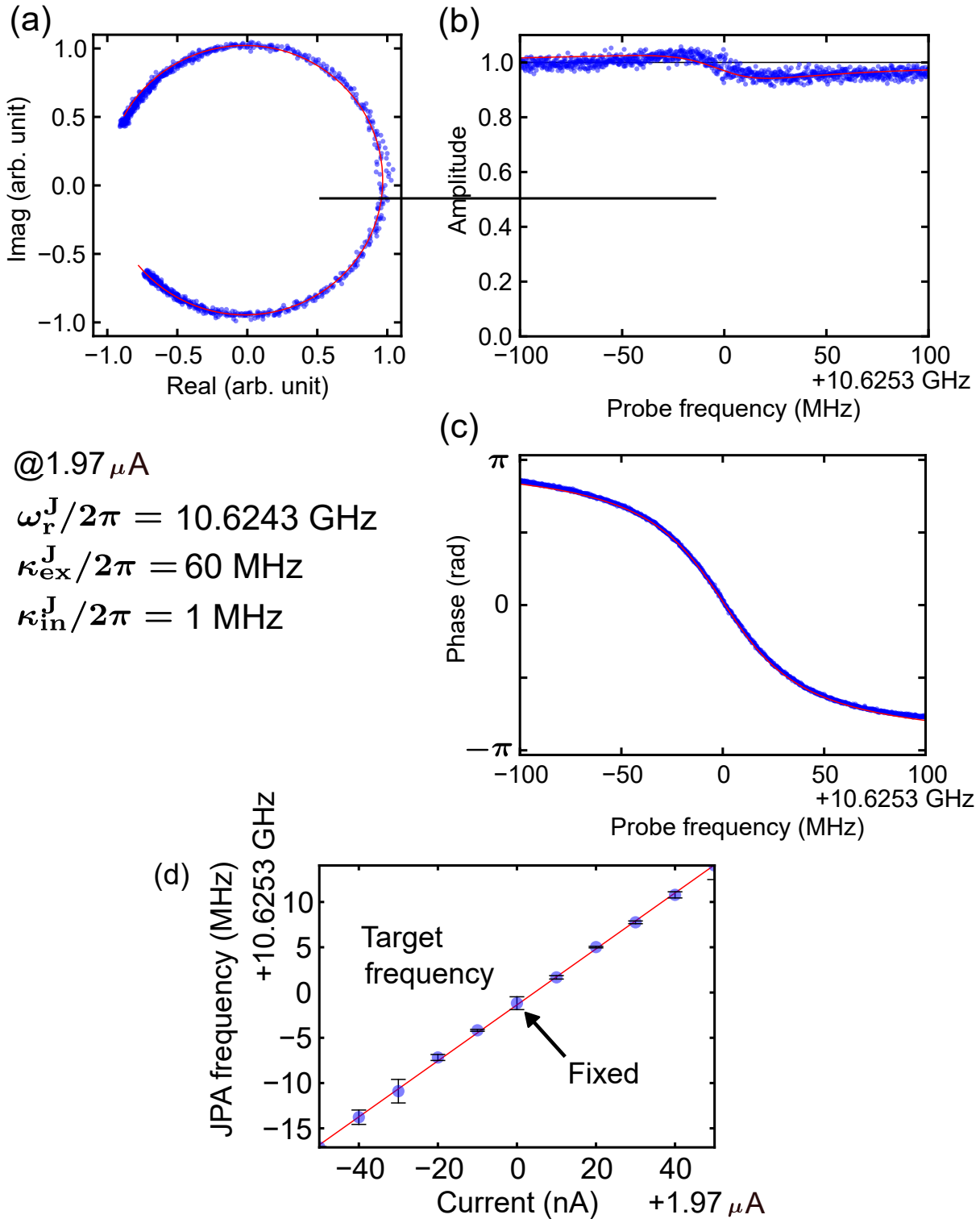


Figure 6.10: Setting of the JPA frequency. (a) Reflection coefficients in the complex plane. (b) Normalized amplitude and (c) phase as a function of the probe frequency. (d) JPA frequency as a function of the current. The blue dots and the red lines are the experimental results and the fitting results, respectively.

signal. The JPA spectrum at the optimal current of 1.97 $\mu$A is shown in Figs. 6.10(a), (b) and (c).

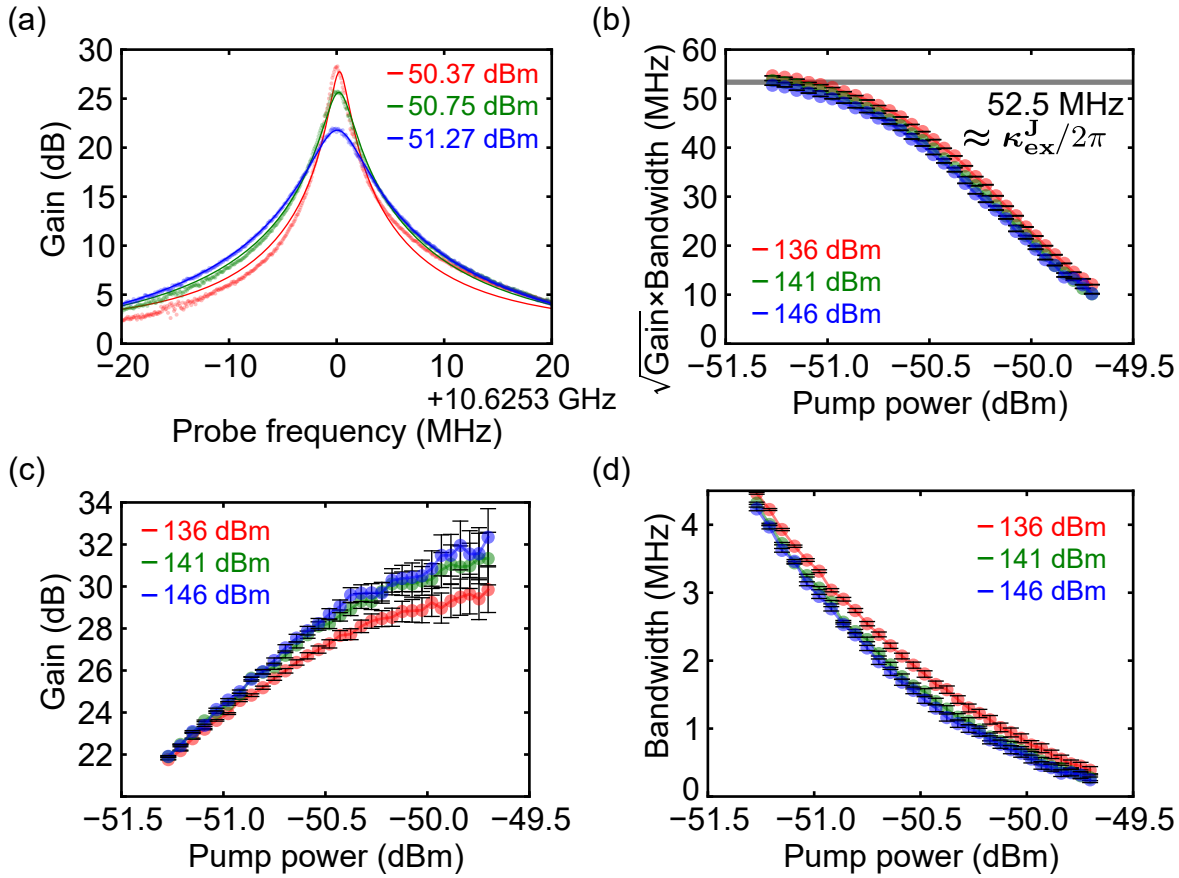


Figure 6.11: Pump power dependence of the gain spectrum. (a) Gain spectrum at the pump powers of −51.27 dBm (blue), −50.75 dBm (green), and −50.37 dBm (red). The dots and the lines are the experimental results and the Lorentzian fits, respectively. The probe power is set to −136 dBm. (b) Root gain bandwidth product, (c) gain, and (d) gain bandwidth as a function of the pump power. The dots are the experimental results measured with the probe powers of −146 dBm (blue), −141 dBm (green), and −136 dBm (red). The root gain product is close to the linewidth of the JPA, $\kappa_{\mathrm{ex}}^{\mathrm{J}}$, for smaller pump powers.

### Pump power dependence

We study the gain properties by measuring the reflection coefficient of the JPA as a function of the probe frequency while pumping it at twice the JPA frequency. Here, we characterize the JPA gain and the bandwidth by measuring the phase-insensitively amplified probe signal. Thus, we set the pump frequency so that the detuning from all the probe frequencies can be more than the IF bandwidth of the VNA.

In our experiment, the pump tone is generated as an output of the doubler. Since the optimal power at the output is fixed by the supplier, it is better to change the pump power by using continuously variable attenuators. However, we change the output power by adjusting the input power, although it deviates a little from the optimal power.

With different pump powers, the gain spectrum, or the gain as a function of the probe frequency, is shown in Fig. 6.11(a). To obtain the gain, the raw amplified amplitude signal is divided by that of the frequency-dependent baseline and is squared. The baseline is obtained as in Fig. 6.9 with a probe power of −136 dBm. By fitting the gain spectrum with a Lorentzian, we determine the gain and the gain bandwidth. With the lower pump power of −51.27 dBm and −50.75 dBm, the spectrum is well-fitted by a Lorentzian.

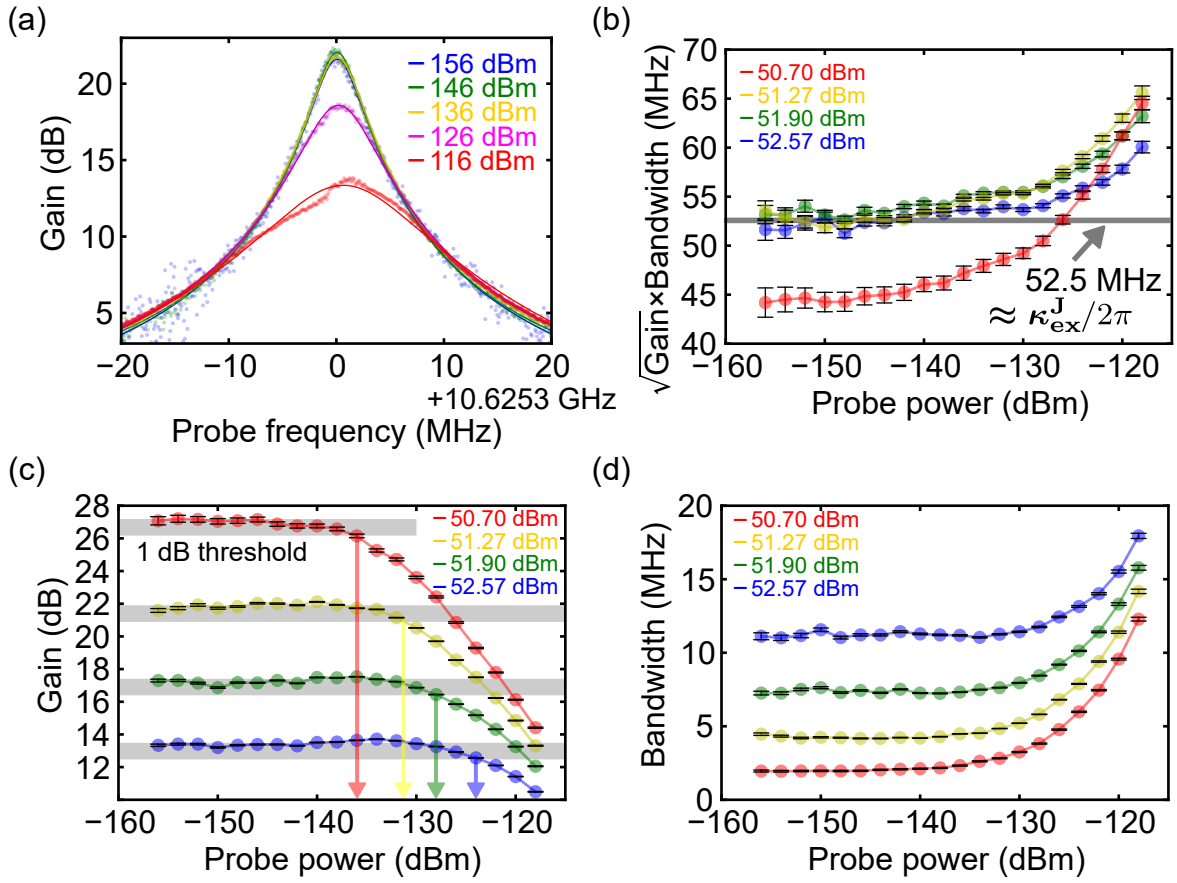


Figure 6.12: Probe power dependence of the gain spectrum. (a) Gain spectrum at the probe powers of −156 dBm (blue), −146 dBm (green), −136 dBm (yellow), −126 dBm (magenta), and −116 dBm (red). The dots and the lines are the experimental results and the Lorentzian fits. The pump power is set to −51.27 dBm. (b) Root gain bandwidth product, (c) gain, and (d) gain bandwidth as a function of the probe power. The dots are the experimental results measured with the pump powers of −52.57 dBm (blue), −51.90 dBm (green), −51.27 dBm (yellow), and −50.70 dBm (red). The root gain bandwidth product is close to the linewidth of the JPA at the small probe power. The gray lines in (c) depict the 1-dB threshold to determine the 1-dB compression point. The top of the gray lines match the gain of the smallest probe power, and the width of the gray lines is 1 dB. Thus, the cross point of the bottom of the gray lines and the gain curve gives the 1-dB compression point (arrow).

However, with the higher pump power of − 50.27 dBm, the spectrum deviates from the Lorentzian and shows the asymmetry due to the saturation by the self-Kerr effect. The asymmetric gain spectrum indicates that the pump or probe power which we use is too large to support the linearity of the gain. We will study the detail of the probe power dependence in Fig. 6.12.

With different probe powers, the gain and the gain bandwidth as a function of the pump power are shown in Figs. 6.11(c) and (d). As the pump power is increased, the gain increases while the bandwidth decreases. The smaller probe powers of −146 dBm and −141 dBm show almost the same gain property.

The larger the gain is, the better it is from the viewpoint of the signal-noise ratio. However, there is a trade-off between the gain and the bandwidth. The bandwidth is crucial for the amplification of qubit readout pulses and itinerant microwave photons

with finite bandwidths. The trade-off is described by the root gain bandwidth product, which is defined as $\sqrt{\text{Gain}} \times \text{Bandwidth}$. The trade-off as a function of the pump power is shown in Fig. 6.11(b). We find that the product is approaching about 52.5 MHz in the small power limit of the pump power. Theoretically, the product corresponds to the linewidth of the JPA $\kappa_{\text{ex}}^{\text{J}}/2\pi = 60$ MHz, which almost agrees with our experimental results [79]. Finally, we determine the pump power according to the bandwidth of the pulse mode to be amplified.

#### Probe power dependence

We study the saturation of the JPA gain in terms of the probe power. The average photon number which can be stored in the JPA is limited by the strength of the self-Kerr effect. Therefore, there is an upper bound on the input probe power which can be amplified linearly.

We plot the gain spectrum with the different probe powers in Fig. 6.12(a). With the probe power lower than $-136$ dBm, the spectra look the same. At the larger probe power, we cannot obtain the same gain due to the saturation. The gain, the bandwidth and the root gain bandwidth product are shown in Figs. 6.12(c), (d), and (b), respectively. As the probe power is increased, the gain is decreased at some point. The gain saturation can be characterized by the 1-dB compression point, which is defined as the probe power at which the gain is 1-dB less than the gain at the small probe power. For instance, from Fig. 6.12(c), the 1 dB compression point is determined as $-132$ dBm at the pump power of $-52.27$ dBm.

## 6.2 Time-domain measurement

Here, we explain the time-domain measurements which are used for characterization of the transmon qubit. As explained before, in the frequency-domain measurement, the probe and drive microwaves are applied to the system simultaneously. Thus, the linewidth of the qubit excitation spectrum is broader than the dephasing rate of the qubit since it includes the measurement-induced dephasing and the power broadening. Furthermore, the energy-relaxation rate of the qubit cannot be derived from the linewidth of the qubit excitation spectrum. Therefore, to measure the natural dephasing rate and the energy relaxation rate of the qubit, the time-domain measurement is indispensable. In Fig. 6.13, we show the simplified time-domain measurement setup for control and readout of the transmon qubit in the 3D cavity. Not that except for single-shot readout of the qubit, the JPA is not operated. For average measurements, the down-converted signals are measured and averaged in the ADC, and then they are sent to the control PC. For single-shot measurements, every signal is stored in the ADC until the memory is fully occupied, then it is sent to the PC.

### 6.2.1 Readout pulse

First of all, the readout pulse is optimized. As in the frequency-domain measurement, the dispersive shift of the cavity frequency is used for the readout of the qubit state. The parameters of the readout pulse can be optimized from the cavity parameters obtained in the frequency-domain measurement. First, the power of the readout pulse is determined to be about tens of times larger than the single photon power level. Here, unlike in the frequency-domain measurement, the readout power can be larger than the single-photon power level, since the timing of the readout can be separated from that of the qubit

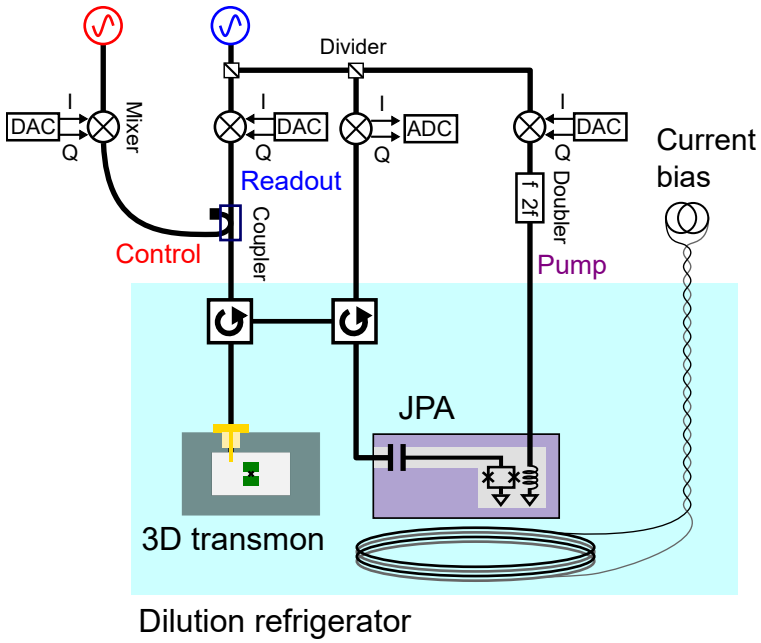


Figure 6.13: Simplified time-domain measurement setup for control and readout of the transmon qubit in the 3D cavity.

dynamics with which we are concerned. Nevertheless, the readout power should be set to below the critical photon number in order to avoid the qubit-state mixing. Second, the carrier frequency of the readout pulse should be determined to maximize the visibility taking into account the cavity linewidth and the dispersive shift. Last, the readout pulse length is optimized with respect to the energy-relaxation times of the readout cavity and the qubit. The pulse length should be longer than the energy-relaxation time of the readout cavity, which corresponds to the inverse of the external coupling rate. However, the longer readout pulse makes the visibility lower due to the state jump of the qubit during the readout, although the signal-noise ratio becomes better. Typically, the qubit jump during the readout is mainly due to the energy relaxation, which is justified by the following reasons. First, the thermal excitation rate is much smaller than the energy-relaxation rate since the qubit environment is well cooled. Second, the qubit-state mixing rate is also much smaller than the energy-relaxation rate since the readout power is set to be weaker than that corresponding to the critical photon number. From the above discussions, the readout pulse length should be set to be longer than the energy-relaxation time of the readout cavity and much shorter than the energy-relaxation time of the qubit.

Here, the readout power is set to $-132$ dBm or $-127$ dBm, which corresponds to twice or three times larger than the single-photon power level. The carrier frequency is set to 10.6253 GHz, which maximizes the visibility. The pulse length is 500 ns, which is about ten times longer than the cavity energy-relaxation time and is about sixty times shorter than the qubit energy-relaxation time, which we will observe later (see Sec. 6.2.7).

The readout pulse reflected by the cavity is measured as shown in Fig. 6.14(a). Here, the in-phase quadrature $I(t)$ is shown. The nominal input readout pulse with an arbitrary amplitude and a phase is also drawn for reference. We can understand the distortion of the reflected readout pulse in three regions. The first one (i) is the time region when the cavity photon number is increasing and approaching a steady state. In this region, the cavity cannot respond to the rising of the pulse which has a large bandwidth, and most of the signal is reflected without entering the cavity. Therefore, the signal in this

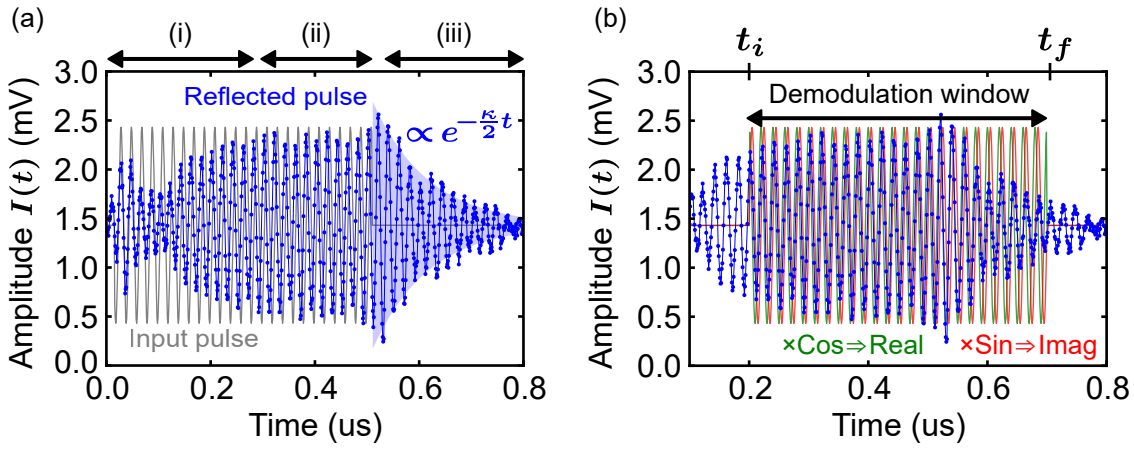


Figure 6.14: (a) Reflected readout pulse. The blue dots are the recorded data in the ADC. The black line depicts the nominal input readout pulse. The reflected pulse mode is divided into three regions: (i) rise-up, (ii) steady-state, and (iii) ring-down. The blue-shaded exponential curve is the theoretical amplitude-decay calculated from the linewidth of the readout cavity in the frequency domain. (b) The same data as in (a) with the demodulation window. The demodulation window is set between 200 ns and 700 ns. The green and red lines depict the cosine and sine functions with the demodulation window to obtain the real and imaginary parts of the readout pulse.

region contains little information on the qubit state. The second one (ii) is the time region when the cavity is in the steady state. Here, the reflected signal originates from the interference of the reflected input signal and the leak-out signal from the cavity in the steady state. The important point is that as long as the qubit does not jump to the other state, the reflected signal exactly corresponds to the cavity reflection coefficient in the frequency-domain measurement. This measurement is useful for characterization of the cavity with the qubit in the ground or excited state. The third one (iii) is the time region when the cavity is ringing down. Since the input signal is now turned off, the output signal corresponds to the decaying cavity state. The signal is called a ring down. As the blue-shaded exponential decay curve shows, the amplitude decay rate of the ring down corresponds to the cavity linewidth which is obtained in the frequency-domain measurement.

Next, we define the measurement pulse mode. As discussed in Sec. 5.7.1, the mismatch between the signal and measurement pulse modes decreases the signal-to-noise ratio. For simplicity, we use a real-valued rectangle function $f_{\rm w}(t) = \frac{1}{\sqrt{t_f - t_i}} \sqcap \left( \frac{t-(t_i+t_f)/2}{t_f - t_i} \right)$ as the demodulation window. Note that the sideband frequency of the demodulation should be the same as that of the modulation. From Eq. (5.51), we obtain the real and imaginary parts of the pulse mode $m_{\rm w}(t) = f_{\rm w}(t) e^{-i(\omega_{\rm LO}+\omega_{\rm s})t}$ as

$$\begin{aligned} I_{\rm w} &\propto \int_{-\infty}^{\infty} dt\, f_{\rm w}(t) \cos\omega_{\rm s} t\, I(t) \propto \int_{t_i}^{t_f} dt\, \cos\omega_{\rm s} t\, I(t) \\ Q_{\rm w} &\propto \int_{-\infty}^{\infty} dt\, f_{\rm w}(t) \sin\omega_{\rm s} t\, I(t) \propto \int_{t_i}^{t_f} dt\, \sin\omega_{\rm s} t\, I(t). \end{aligned} \tag{6.10}$$

As shown in Fig. 6.14(b), the demodulation window is set between $t_i = 200$ ns and $t_f = 700$ ns.

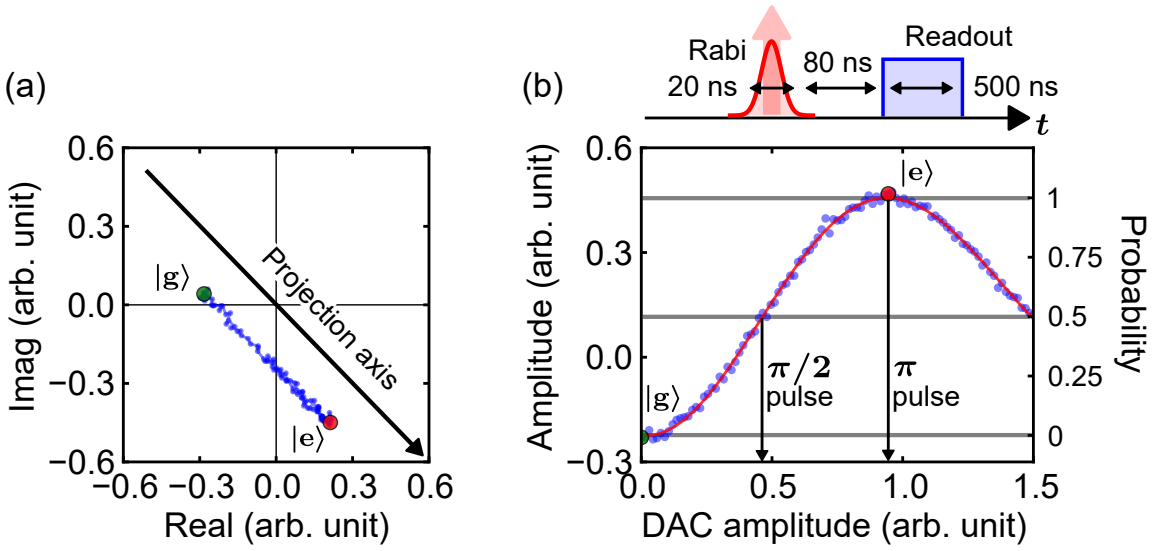


Figure 6.15: (a) Readout signal in the complex plane as a function of the DAC amplitude. The occupation probability of the qubit states can be obtained by projecting the complex amplitude into the projection axis (black arrow). (b) The projected amplitude as a function of the DAC amplitude. The pulse sequence is shown above. The control and readout pulse lengths are 20 ns and 500 ns, respectively. The time interval between the control and the readout is 80 ns. The occupation probability of the qubit states is obtained as the internally dividing point between the horizontal lines corresponding to the ground and excited states (see the vertical axis on the right side). The DAC amplitude of 1.5 corresponds to the control power of about −86 dBm at the sample.

### 6.2.2 Rabi oscillation

A Rabi oscillation is used for quantum control of the superconducting qubit.

First of all, the control frequency is set to the qubit resonance frequency of $\omega_{\rm eg}/2\pi =$ 7.86988 GHz from the frequency-domain measurement in Fig. 6.7. Then, the control frequency is set such that $\omega_{\rm LO} + \omega_{\rm s} = \omega_{\rm eg}$. The sideband frequency of the modulation should be set to negative so that the image band leakage at $\omega_{\rm LO} - \omega_{\rm s}$ does not influence the transition between the first and second excited states at $\omega_{\rm fe} = \omega_{eg} + \alpha$. The sideband frequency is set to −100 MHz. The applicable maximum power of the control pulse can be estimated from the linewidth, or the Rabi frequency, of the qubit excitation spectrum. Typically, the Rabi frequency is set to about ten times smaller than the anharmonicity of −340 MHz. From the qubit excitation spectrum in Fig. 6.7, the Rabi frequency of $\Omega_{\rm d}/2\pi = 32$ MHz corresponds to the control power of −89 dBm. The maximum control power is set to about −86 dBm. The length of a $\pi$ pulse is calculated as $\pi/\Omega_{\rm d} \approx 16$ ns with the Rabi frequency of 32 MHz. Thus, we use a Gaussian pulse with a full width of the half maximum amplitude of 20 ns.

The real and imaginary parts of the demodulated signal as a function of the control amplitude are shown in Fig. 6.15. As shown in Fig. 6.15(a), the complex amplitude is oscillating between two points in the complex plane. The start point corresponds to the ground state, while the farthest point from that of the ground state corresponds to the excited state. However, these complex amplitudes may deviate from the actual ones due to the thermal excitation of the qubit and the imperfect $\pi$ pulse. This deviation affects the visibility, or the distance between the complex amplitudes in average measurements. However, the decrease of the visibility is not critical for optimization of the qubit gates

and the characterization of the qubit coherence, as long as the signal-to-noise ratio is enough. The important point here is that the actual complex amplitudes are located on the same straight line observed in Fig. 6.15(a). Therefore, by projecting the measured complex amplitude onto the line, we obtain the amplitude which gives the qubit occupation probability with the maximized signal-to-noise ratio. More precisely, the projected amplitude corresponds to the occupation probability in the excited state of the qubit. This is valid as long as the qubit is not driven to the second excited state. In this thesis, we will use the projected amplitude to show the occupation probability of the first excited state. The projected amplitude as a function of the control amplitude is shown in Fig. 6.15(b). The experimental results are well fitted with a sinusoidal function, which indicates that we observe the Rabi oscillation of the qubit. From the fitting, we determine the control amplitudes corresponding to the $\pi/2$ and $\pi$ pulses. The Rabi frequency for the $\pi$ pulse is roughly evaluated as $\Omega_{\rm d}/2\pi = 1/(2 \times 20\ {\rm ns}) = 25$ MHz.

### 6.2.3 Gate optimization

So far, we have generated the qubit gates with the qubit frequency obtained from the frequency-domain measurement. If there is a frequency detuning, the rotation axis in the Bloch sphere deviates from the $xy$ plane. Although the finite frequency detuning will be negligible in the limit of a fast Rabi pulse, the detuning between the control and qubit frequencies means that the free time evolution of the qubit is governed by the continuous $z$ rotation. Of course, such an unitary error can be corrected by additional qubit control or frame change. However, the phase correction is cumbersome in most cases. Thus, the control frequency should match the qubit frequency within the detuning much smaller the dephasing rate of the qubit.

Here, we use a Ramsey sequence to measure the detuning more precisely. As the pulse sequence is shown in Fig. 6.16, the qubit prepared in the superposition state in the $x$ axis by $\hat{Y}/2$ is measured in the $X$ basis after the varying time intervals. Here, we assume that the Rabi frequency is much larger than the detuning and that the gate fidelity of the $\pi/2$ pulse is not too small. This assumption is valid if the qubit frequency is obtained with the weak cavity-probe and qubit-drive powers in the frequency-domain measurement (see Fig. 6.7). When there is the detuning between the qubit and control frequencies, the qubit state is rotated about the $z$ axis by $\Delta\tau$, where $\Delta$ is the detuning and $\tau$ is the time interval. Therefore, by measuring the occupation probability of the qubit as a function of the time interval, we obtain the damped oscillations, as shown in Fig 6.16. The results are well fitted by the exponentially-damped sinusoid. From the fitting, we obtain the detuning and the dephasing time of the qubit. Note that the detuning can be obtained more precisely with a longer time interval, although the maximum time interval is limited by the qubit dephasing time. Furthermore, note that we can measure only the absolute value of the detuning by the single Ramsey sequence. To determine the sign of the detuning, we should perform another Ramsey sequence with a different qubit measurement axis or with a different value of detuning. The fitting error of the detuning is about 200 Hz, which is about tens of times smaller than the qubit dephasing rate of $\gamma_\phi/2/\pi = 1/T_2^*/2/\pi = 6$ kHz.

Once the control frequency is optimized from the Ramsey sequence, the Rabi sequence as a function of the control amplitude is performed to reset the control amplitude, as shown in Fig 6.15(b). Through this procedure, we can optimize the $\pi/2$ and $\pi$ pulses with the precise qubit frequency.

As we discussed in Sec. 2.5.2, the transmon qubit is not a pure two-level system. Therefore, the qubit frequency is shifted by the second excited state driven off-resonantly

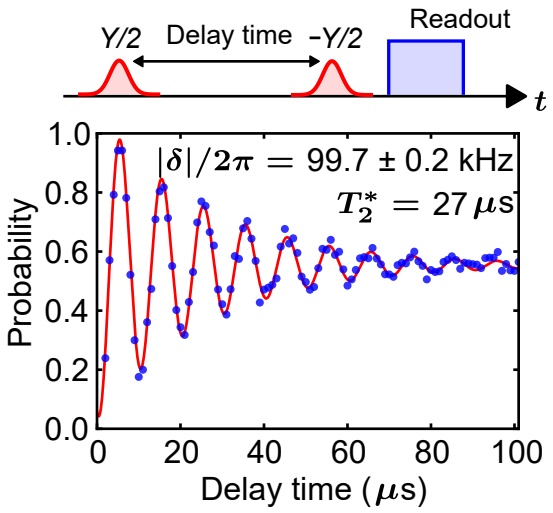


Figure 6.16: Ramsey measurement for the determination of the qubit control frequency. The pulse sequence is shown above. The projected amplitude is converted to the occupation probability in the excited state. The blue dots and red line are the experimental results and the fit to an exponentially-damped sinusoid, respectively.

by the control pulse. If the frequency shift cannot be negligible, the DRAG pulse [48, 49], which can cancel the effect of the second excited state in the perturbation, is useful. Here, the frequency shift induced by our $\pi$ pulse is $\Delta/2\pi = \frac{(\sqrt{2}\Omega_{\rm d})^2}{4\alpha}/2\pi = 0.9$ MHz. Therefore, the error probability, which is characterized as the squared ratio of the frequency shift to the Rabi frequency, can be calculated as $(\Delta/\Omega_{\rm d})^2 = (\Omega_{\rm d}/2\alpha)^2$ =0.001, which is negligible at this stage. From this calculation, in this thesis, we do not use the DRAG pulse.

Note that other gates about different rotation axis on the $xy$ plane in the Bloch sphere are easily realized by choosing the corresponding control phase. Typically, the stability and accuracy of the control phase with our measurement setup is much better than the qubit coherence. Therefore, we do not need to optimize each gate, and we only have to choose the corresponding phase for the optimized gates at one phase.

### 6.2.4 Readout optimization

To decrease the measurement time, we should optimize the readout pulse. In Sec. 6.2.1, we optimized them by measuring the readout pulse reflected by the cavity with the qubit in the ground state. Here, we can optimize them to maximize the visibility between the ground and excited states.

As described in Sec. 6.2.1, the readout error is mainly due to the energy relaxation of the qubit during readout. Therefore, the pulse length for the readout should be much shorter than the energy relaxation time. First of all, we measure the energy-relaxation time by using the sequence shown in Fig. 6.18(a). The qubit which is prepared in the excited state by applying the $\pi$ pulse is measured after the varying time interval. The occupation probability in the excited state as a function of the time interval is shown in Fig. 6.18(a). The results are well fitted by an exponential curve. From the fitting, the energy-relaxation time of the qubit is found to be 32 $\mu$s. Therefore, we confirm that the pulse length of 500 ns is much shorter than the relaxation time of the qubit. Here, we roughly estimate the readout error for the excited state as the ratio of the readout time to the relaxation time: 0.5 $\mu$s/32 $\mu s$=0.016. In Sec. 6.2.6, we will confirm that this

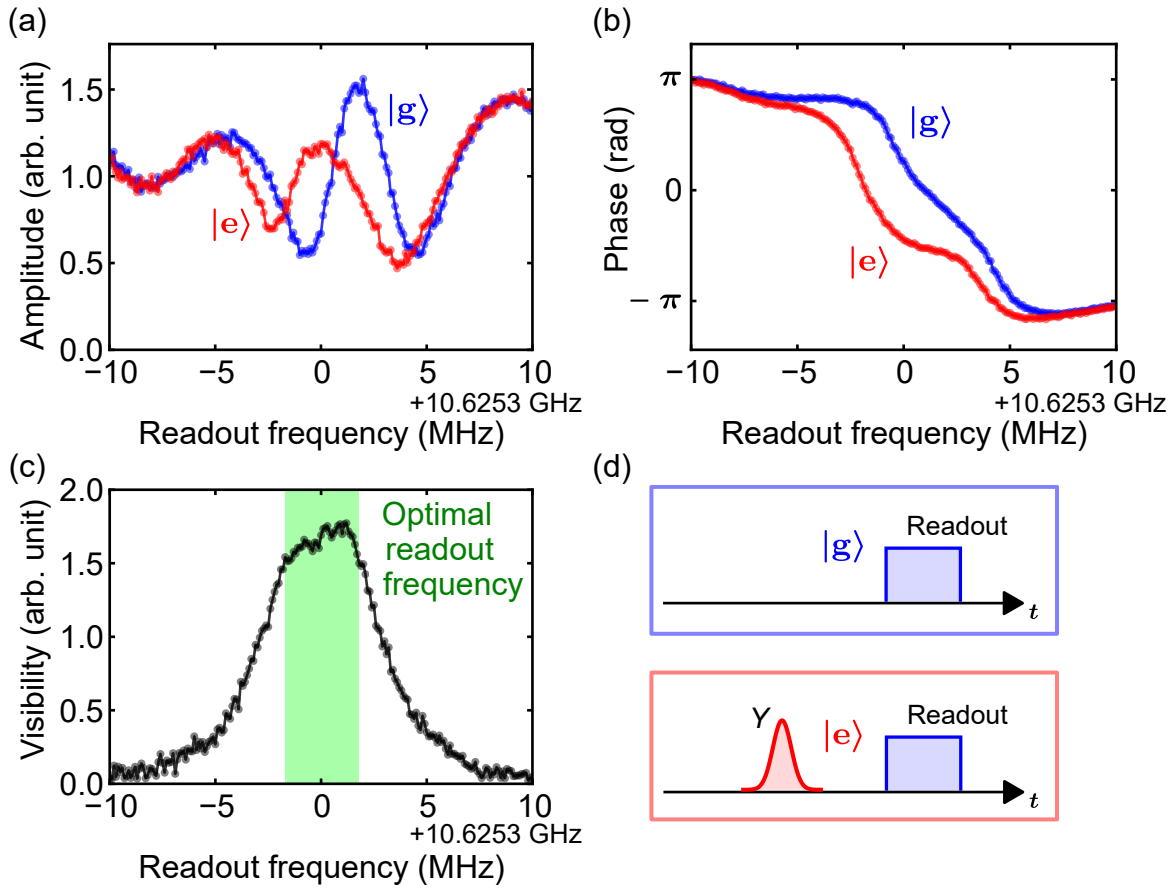


Figure 6.17: (a) Amplitude and (b) phase of the readout signal for the qubit in the ground and excited state as a function of the readout frequency. The dots are the experimental results. (c) Visibility as a function of the readout frequency. The green region shows the optimal readout condition. (d) Pulse sequence to obtain the readout signals depending on the qubit states.

estimation is consistent with the readout-error probability which is obtained from the single-shot readout of the qubit.

Next, we optimize the readout frequency. As explained in Sec. 6.2.1, we use the rectangle demodulation window so that it can cover the reflected pulse almost completely. After the qubit initialization for the ground and excited states, we measure the readout signal which is reflected by the cavity with the qubit in the ground and excited states, as shown in Fig. 6.17(d). The amplitude and the phase of the readout pulse as a function of the readout frequency are shown respectively in Figs. 6.17(a) and (b). We find that the cavity frequency is shifted depending on the qubit state. Note that the complex amplitudes do not exactly correspond to the reflection coefficients of the cavity in the frequency-domain measurement. The visibility or the distance between the complex amplitudes corresponding to the ground and excited states as a function of the readout pulse is shown in Fig. 6.17(c). From this plot, the readout frequency is determined as the frequency which gives us the maximum visibility [green region in Fig. 6.17(c)]. We confirm that the readout frequency which we have used is in the optimized frequency region.

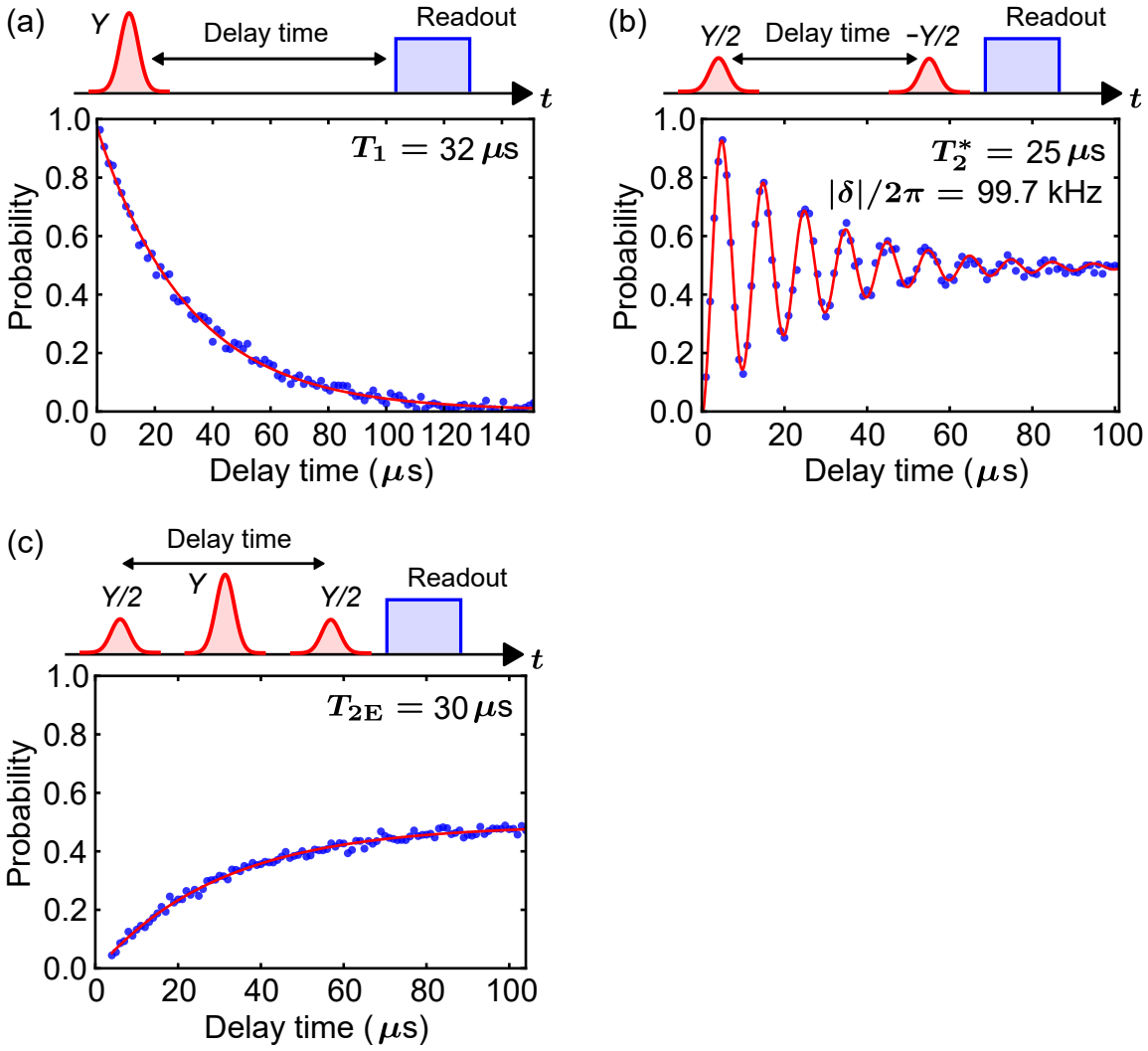


Figure 6.18: (a) Energy-relaxation time measurement. (b) Ramsey measurement. (c) Echo measurement. A corresponding pulse sequence is shown above each plot. The blue dots and red lines are the experimental and fitting results, respectively.

### 6.2.5 Qubit coherence times

Using the optimized control and readout pulses, we characterize the qubit coherence. We use the energy relaxation measurement, Ramsey and Echo sequences, here. These sequences can be implemented using the $\pi/2$ and $\pi$ pulses. The pulse sequence for each measurement is shown in Figs. 6.18(a), (b), and (c).

In the energy relaxation sequence in Fig. 6.18(a), by fitting the results with a exponential curve, we obtain an energy-relaxation time of $T_1 = 32$ $\mu$s.

In the Ramsey sequence in Fig 6.18(b), by fitting the results with an exponentially-decaying sinusoid, we obtain a dephasing time of $T_2^* = 25$ $\mu$s and a detuning of $|\delta|/2\pi = 99.7$ kHz. Here, we set the control frequency with a detuning of 100 kHz.

In the Echo sequence, we add another $\pi$ pulse at the middle between the two $\pi/2$ pulses in the Ramsey sequence. Here, we set the control frequency to the qubit frequency and we apply the $\pi/2$ and $\pi$ pulses with identical control phases so that the qubit comes back to the ground state if there is no dephasing. The $\pi$ pulse can cancel the frequency fluctuation slower than the time scale of the single sequence. In Fig. 6.18(c), by fitting the results with an exponential curve, we obtain a dephasing time with the Echo pulse of

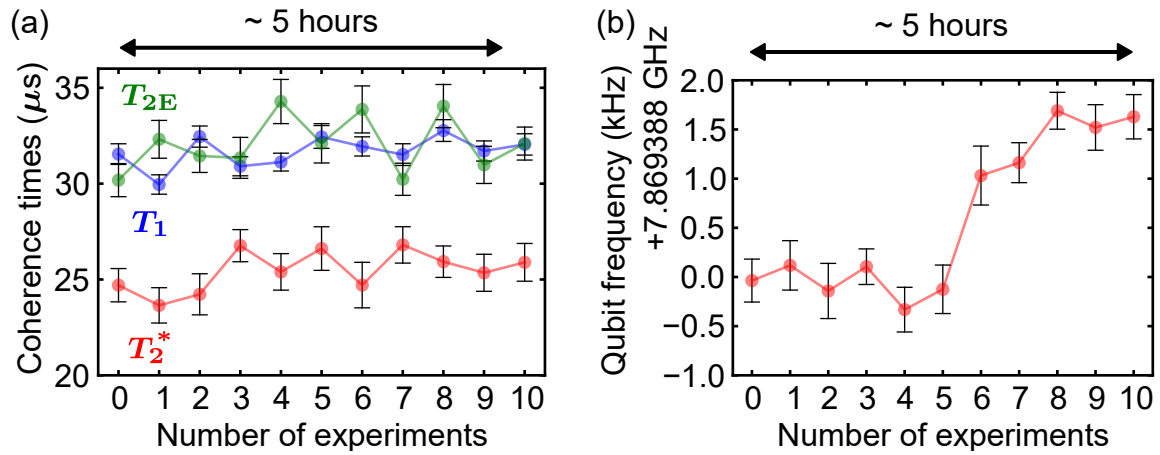


Figure 6.19: (a) Fluctuations of the coherence times of the qubit. The blue, red, and green dots depict the fitting results of $T_1$, $T_2^*$ and $T_{2E}$, respectively. (b) Fluctuation of the qubit resonance frequency measured by the Ramsey sequence. The total measurement time is about 5 hours.

$T_2^E = 30$ $\mu$s. Typically, $T_2^E$ is longer than $T_2^*$

Finally, the qubit coherence times and the detuning, which are obtained by repeating these sequences, are shown in Fig 6.19. The total measurement time is about 5 hours. In this time scale, the coherence times do not fluctuate too much, while the detuning is shifted on the order of a few kHz. However, the slow frequency drift can be corrected by calculating the control frequency between experiments.

### 6.2.6 Single-shot readout of qubit

Here, we explain how to realize a single-shot readout of the qubit. As discussed in Sec. 5.4.2, a JPA is indispensable since the thermal photons from the HEMT amplifier exceed the average photon number of a readout pulse, which is limited by the critical photon number of the readout cavity. Now, the JPA frequency is set to match the readout frequency, as explained in Sec. 6.1.3.

As seen in the frequency-domain measurements, the gain properties of the JPA are very sensitive to the pump power. Therefore, we need to calibrate the pump power again for the time-domain setup. First, we measure the vacuum noise which is amplified in a phase sensitive manner by the JPA. In other words, we pump the JPA at twice the readout frequency without any readout signal and measure the quadratures in a single shot. The demodulation window is set to be the same as for the readout pulse. Note that the vacuum noise, which is amplified in a phase-sensitive manner, can be a squeezed vacuum state. The quadratures, which are measured in a single shot with different DAC amplitudes for the pump, are shown in the complex plane in Fig. 6.20. With the smallest pump amplitude of 0.5, the measured noise is governed by the classical noise, or the HEMT noise. As the DAC amplitude is increased, the shape of the noise distribution becomes more elliptic, which indicates that the amplified (anti-squeezed) vacuum noise exceeds the HEMT noise. At this point, the signal-to-noise ratio in the amplified axis can be limited by the JPA. With a larger pump amplitude, the amplified noise starts to oscillate coherently, which is called a parametric oscillation [80]. From the symmetry breaking, the coherent phase is randomly chosen to 0 or $\pi$ relative to the pump phase. Therefore, the measured quadrature distribution has two local maxima, as shown in Fig. 6.20(f). Here, the pump amplitude should be set to be below the one which causes the parametric oscillation.

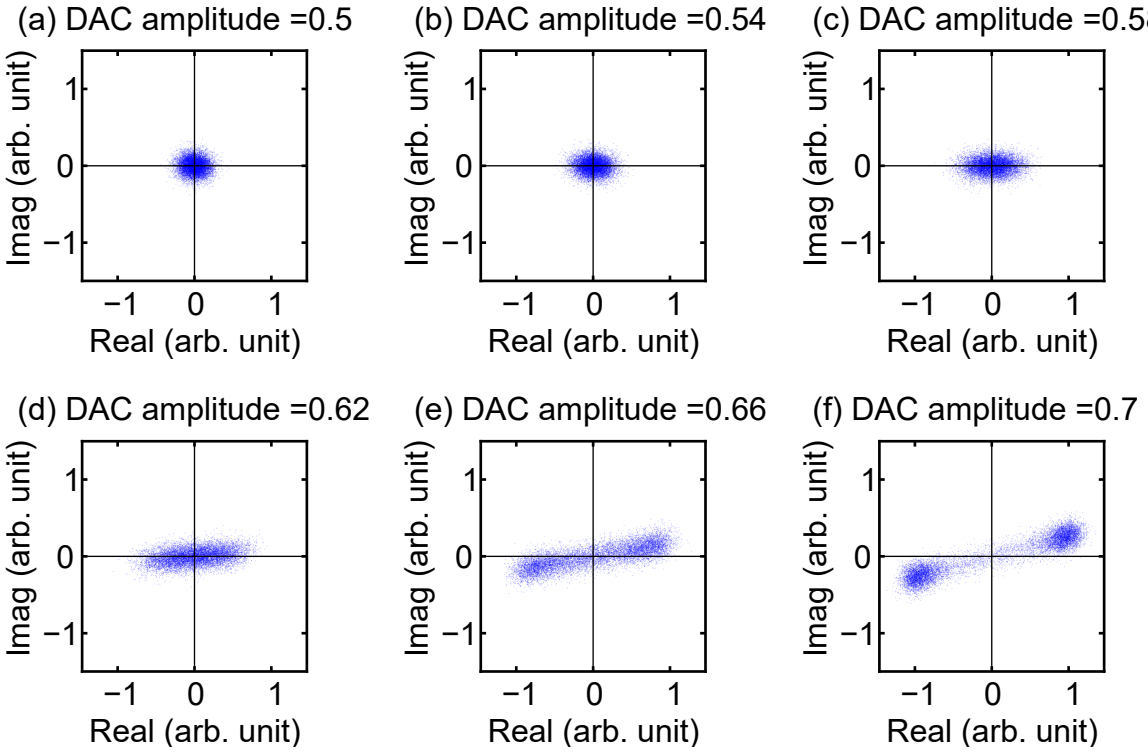


Figure 6.20: Pump amplitude dependence of the quadratures of the vacuum noise, which are measured in a single shot. The pump amplitudes are represented as the DAC amplitudes in arbitrary units. The DAC amplitudes are set to be (a) 0.5, (b) 0.54, (c) 0.62, (e) 0.66, and (f) 0.7, respectively. The DAC amplitude of 0.6 roughly corresponds to −52 dBm at the JPA.

Quantitatively, we determine the upper limit of the pump amplitude by checking if the noise distribution deviates from a Gaussian profile.

Next, we apply a readout pulse together with the pump pulse. The pump pulse with a rectangle shape is applied to cover the readout pulse. Here, we use the same readout pulse which is optimized in the previous section. The averaged demodulated readout signal amplitudes in time with and without the pump pulse are shown in different scale in Fig. 6.21(a). Note that the relative phase between the readout and pump pulses are set to have the maximum gain, as shown in Fig. 6.21(a). We optimize the pump amplitude so that the readout pulse is maximally amplified while roughly maintaining the original pulse form. Here, the small pulse distortion is not a problem for the single-shot readout. Therefore, we just confirm that the readout pulse is not so largely delayed compared to the pulse length. The DAC amplitude for the pump is set to be 0.6. The gain, the square of the ratio of the amplitudes with and without the pump, can be calculated as 24 dB. The gain of the phase-sensitive amplifier corresponds to 18 dB in the phase-insensitive amplifier. From the root gain bandwidth product in Fig. 6.11, the gain bandwidth is calculated as about 6.6 MHz. Thus, we confirm that the bandwidth is much broader than that of the readout pulse. Once the pump amplitude is determined, the visibility, which is discussed in Fig. 6.17, is measured as a function of the relative phase, and then the relative phase is optimized. In our setup, the optimal relative phase corresponds to that which the maximum gain for the readout pulse with the qubit in the ground state [Fig. 6.21(b)].

Then, single-shot readouts for the qubit in the ground and excited states are performed. The excited state is prepared by applying a $\pi$ pulse before the readout. The

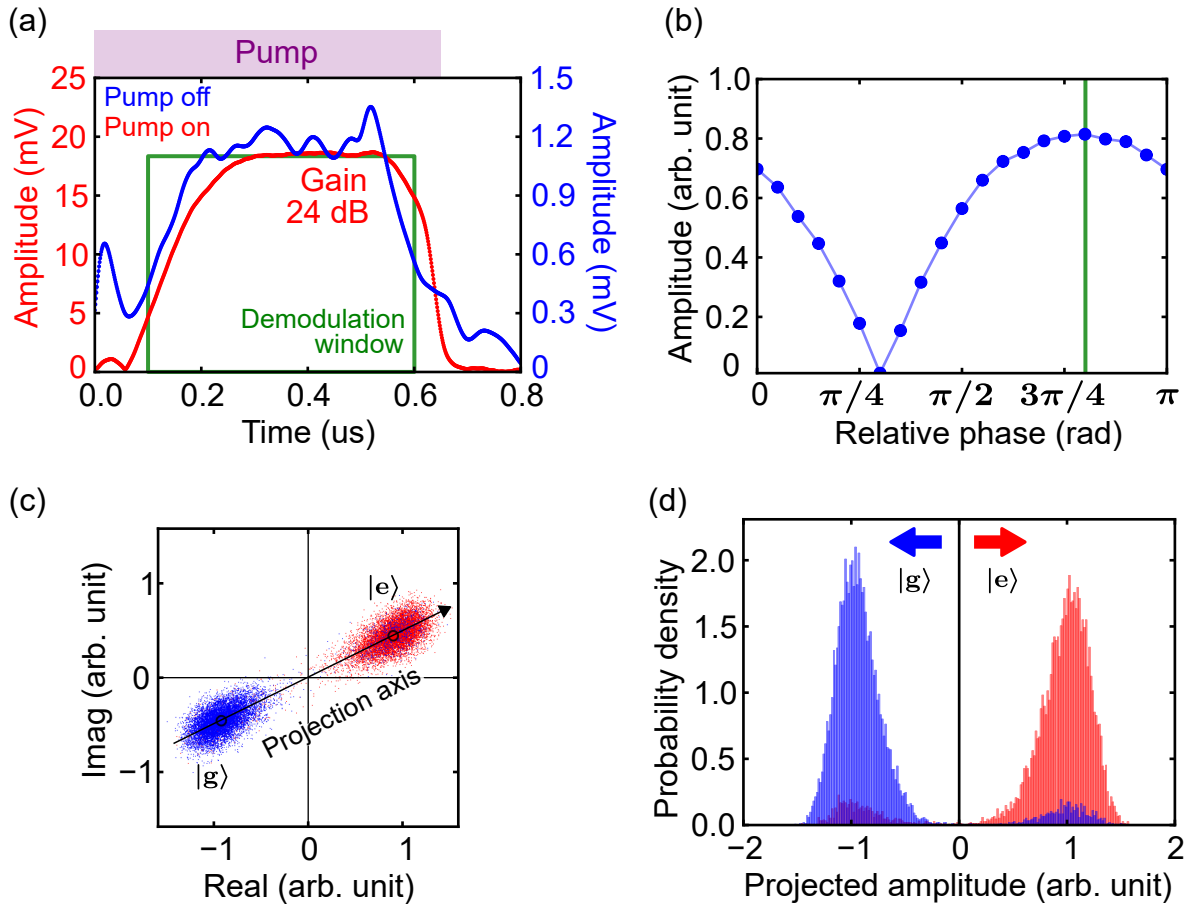


Figure 6.21: Single-shot readout of the qubit. (a) Pulse amplitude of the demodulated readout signal in time. The blue and red dots depict the readout pulse with and without the pump in different scales. The starting time corresponds to the start of the readout pulse. The pump pulse is applied from 0.0 $\mu$s to 0.6 $\mu$s. The demodulation window is set to be 0.1 $\mu$s to 0.6 $\mu$s. (b) Amplitude of the readout pulse as a function of the relative pump phase. The relative phase is set to have a maximum gain, as shown in the green line. (c) Complex amplitudes of the readout pulses in a single shot. The blue and red dots correspond to the complex amplitudes for the qubit which is nominally prepared in the ground and excited states, respectively. The complex amplitudes are projected on to the straight line which maximizes the visibility. (d) Probability density of the projected amplitudes. The blue and red bars correspond to the probability densities for the qubit which is nominally prepared in the ground and excited states, respectively. The middle point between the centers of mass of the two distributions is used for the discrimination.

complex amplitudes of the readout pulse, which are measured in a single shot, are plotted in Fig. 6.21(c). The complex amplitudes corresponding to the ground and excited states are well-separated, which enables us to realize single shot readout of the qubit. To assign the qubit state from the measurement outcome, the complex amplitude of the readout pulse is projected onto the line which passes through the centers of mass of the distributions corresponding to each of the qubit states. Then, the middle point between the corresponding peaks is used for the discrimination of the qubit states. The probability densities of the projected amplitudes for the qubit prepared in the ground and excited states are shown in Fig. 6.21(d). The projected amplitudes corresponding to each qubit state are well separated. Nevertheless, the qubit which may be prepared in the ground or

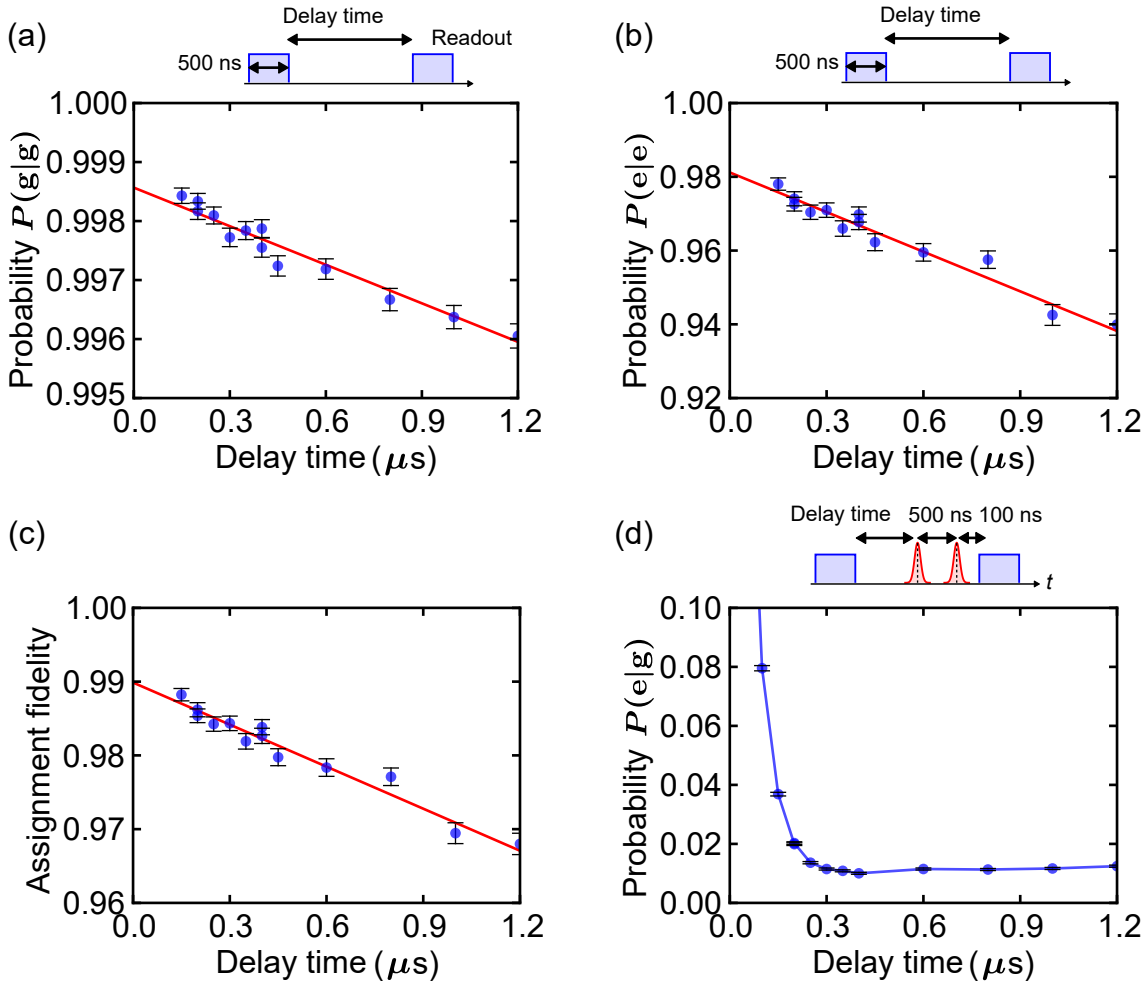


Figure 6.22: Characterization of the single-shot readout of the qubit. The conditional probability $P(p|q)$ in the two successive qubit readouts ($p, q$ = g,e) are shown. The blue dots and the red lines are the experimental results and the linear fits, respectively. (a) Dependence of $P(\mathrm{g}|\mathrm{g})$ on the delay time between the two readouts. (b) The same for $P(\mathrm{e}|\mathrm{e})$. (c) Assignment fidelity $[P(\mathrm{g}|\mathrm{g}) + P(\mathrm{e}|\mathrm{e})]/2$ as a function of the delay time between the two readouts. (d) Dependence of $P(\mathrm{e}|\mathrm{g})$ on the delay time of the Ramsey sequence from the first readout. The error bars on the data points are the standard deviations from the mean.

excited state is measured in the opposite state. This can be explained by the fact that the qubit is in thermal equilibrium to some extent. The excitation probability of the qubit is found to be about 0.067, which corresponds to an effective temperature of 143 mK. The temperature is much higher than the base temperature of the dilution refrigerator, which indicates that the qubit is coupled to the environment at higher temperature.

To initialize the qubit, we read out the qubit and perform postselection according to the readout outcome. Therefore, a correlation of two successive readout outcomes should be characterized. In Figs. 6.22(a) and (b), we show the correlation between the first and second readout outcomes as a function of the delay time between the two. As the delay time increases the correlations decreases due to the thermal excitation and energy relaxation of the qubit. By fitting the slope, the thermal-excitation and energy-relaxation rates can be determined as $\gamma_\uparrow/2\pi = 0.35$ kHz and $\gamma_\downarrow/2\pi = 5.7$ kHz, respectively. The rates may roughly correspond to the state-mixing rates during readout since the readout errors is considered to be limited by the qubit decay. The thermal excitation

probability is calculated as $\gamma_\uparrow/(\gamma_\uparrow+\gamma_\downarrow) = 0.057$, which slightly deviates from the measured one. This can be explained by the readout errors and the state mixing induced by the readout. At a delay time of 150 ns (the end time of the first pump pulse), we evaluate an assignment fidelity [81] of $[P(\mathrm{g}|\mathrm{g})+P(\mathrm{e}|\mathrm{e})]/2 = 0.988\pm0.001$. The assignment fidelity as a function of the delay time is shown in Fig. 6.22(c). Since the assignment fidelity includes both the readout errors and the initialization errors based on the postselection, it is useful for the characterization of qubit readout. In other words, we can optimize readout parameters, such as the amplitude and length of the readout, so that the assignment fidelity is maximized.

Furthermore, the conditional probabilities can be modeled as

$$\begin{aligned} P(\mathrm{g}|\mathrm{g}) &= (1-\varepsilon_\mathrm{i}^\mathrm{g})(1-\varepsilon_\mathrm{r}^\mathrm{g}) + \varepsilon_\mathrm{i}^\mathrm{g}\varepsilon_\mathrm{r}^\mathrm{e} \\ P(\mathrm{e}|\mathrm{e}) &= (1-\varepsilon_\mathrm{i}^\mathrm{e})(1-\varepsilon_\mathrm{r}^\mathrm{e}) + \varepsilon_\mathrm{i}^\mathrm{e}\varepsilon_\mathrm{r}^\mathrm{g}, \end{aligned} \tag{6.11}$$

where $\varepsilon_\mathrm{r}^\mathrm{g}$ and $\varepsilon_\mathrm{r}^\mathrm{e}$ are the readout errors for the ground and excited states, and $\varepsilon_\mathrm{i}^\mathrm{g}$ and $\varepsilon_\mathrm{i}^\mathrm{e}$ are the initialization errors for the ground and excited states with the postselections according to the first readout outcomes. Then, we can determine the upper bound of the readout error of the qubit in the ground state (excited state) to be $\varepsilon_\mathrm{r}^\mathrm{g} \leq 1 - P(\mathrm{g}|\mathrm{g}) = 0.0016$ $[\varepsilon_\mathrm{r}^\mathrm{e} \leq 1 - P(\mathrm{e}|\mathrm{e}) = 0.022]$.

Next, we study the effect of the residual cavity photons after the readout. In Fig. 6.22(d), we plot the conditional probability $P(\mathrm{e}|\mathrm{g})$ as a function of the delay time of the Ramsey pulses, whose interval is fixed to 500 ns. The qubit is initialized in the ground state by postselection on the first outcome. For a delay time shorter than the cavity relaxation time $1/\kappa_\mathrm{tot} \approx 50$ ns, the photons excited by the readout pulse stay inside the cavity, causing dephasing of the qubit. Therefore, the probability of finding the qubit in the excited state, resulting from the dephasing, is larger. The probability takes its minimum at the delay time of 400 ns, when both of the qubit and the cavity are initialized to the ground state. For longer delay times than 400 ns, the excitation probability becomes larger because the initialization infidelity increases due to the thermalization as shown in Fig. 6.22(a). At the delay time of 400 ns, the qubit is initialized to the ground state with a fidelity of 0.998 [Fig. 6.22(a)] and the cavity state is also initialized to the vacuum state to the extent that the residual photons cannot affect the qubit dephasing.

### 6.2.7 Cavity spectrum depending on qubit states

Here, the cavity spectrum with the qubit initialized in the ground and excited states is measured. As shown in Fig. 6.23, after the first readout, the cavity probe pulse is applied, and then the qubit is read out again. When both of the first and second outcomes of the qubit readouts give the same results, the qubit may remain in the corresponding state with a high probability during the cavity probe. Therefore, the cavity spectra, which are conditionally obtained, correspond to the cavity with the qubit in the ground and excited states. This is different from the average measurement, which is affected by the finite thermal excitation probability of the qubit. A rectangle pulse with a pulse length of 700 ns is used for the cavity probe. The steady-state time region of the cavity probe, which is discussed in Sec. , is demodulated to obtain the amplitude and phase. The sideband frequency of the cavity probe is varied while maintaining the readout and pump frequencies. The amplitude and phase of the cavity probe as a function of the probe frequency is shown in Figs. 6.23(b) and (c). The baseline may be frequency-dependent, which prevents us from analyzing the experimental data with the ideal reflection coefficients of a harmonic oscillator.

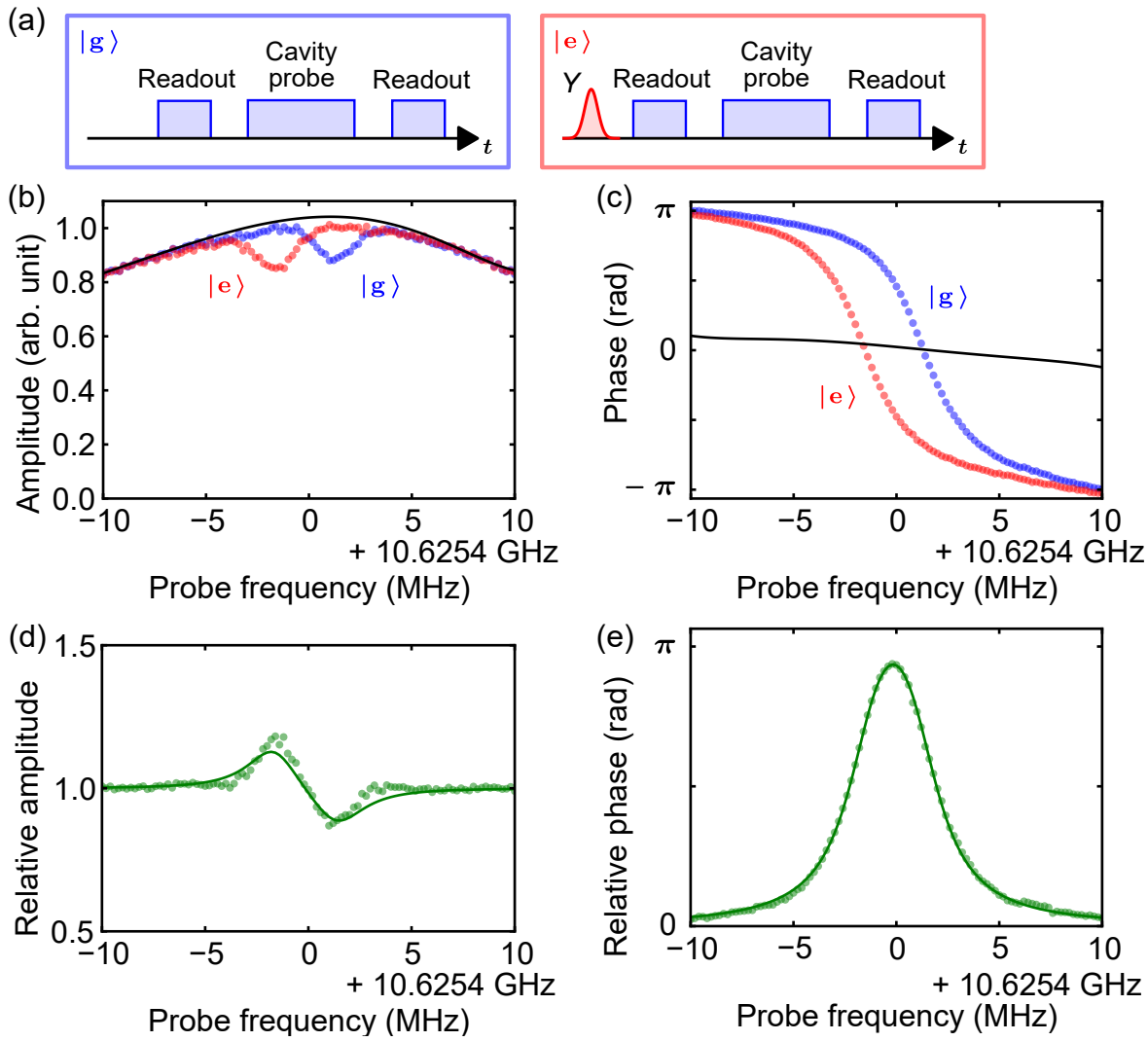


Figure 6.23: Extraction of the frequency-dependent baseline. (a) Pulse sequences for the measurements of the cavity spectra with the qubit in the ground and the excited states. The excited state is prepared by applying a $\pi$ pulse. The qubit state during the cavity probe is conditioned with postselection according to the outcomes of the two readouts before and after. (b), (c) Raw data of the amplitude and phase of the cavity probe as a function of the probe frequency. The blue and red dots depict the data with the qubit conditioned in the ground and excited states, respectively. The black lines are the baselines, which are obtained from the fitting in (d) and (e). (d), (e) Relative amplitude and phase of the complex amplitude with the qubit in the ground state to that in the excited state. The dots are the experimental results and the lines are the theoretical fits.

Here, we explain how to extract the frequency-dependent baseline. First, the complex amplitudes with the qubit in the ground state are divided by those of the excited state. The amplitude and phase of the divided complex amplitudes as a function of the probe frequency are shown in Figs. 6.23(d) and (e). The experimental results of the divided amplitudes are well fitted by ideal reflection coefficients divided by reflection coefficients with a different resonance frequency since the frequency-dependent baseline are canceled out. Then, we extract the baseline by dividing the raw data of the complex amplitudes with the ideal reflection coefficients obtained from the fitting. The baseline [black line in Figs. 6.23(b) and (c)] is obtained by fitting the extracted baseline with a polynomial function to suppress the noise.

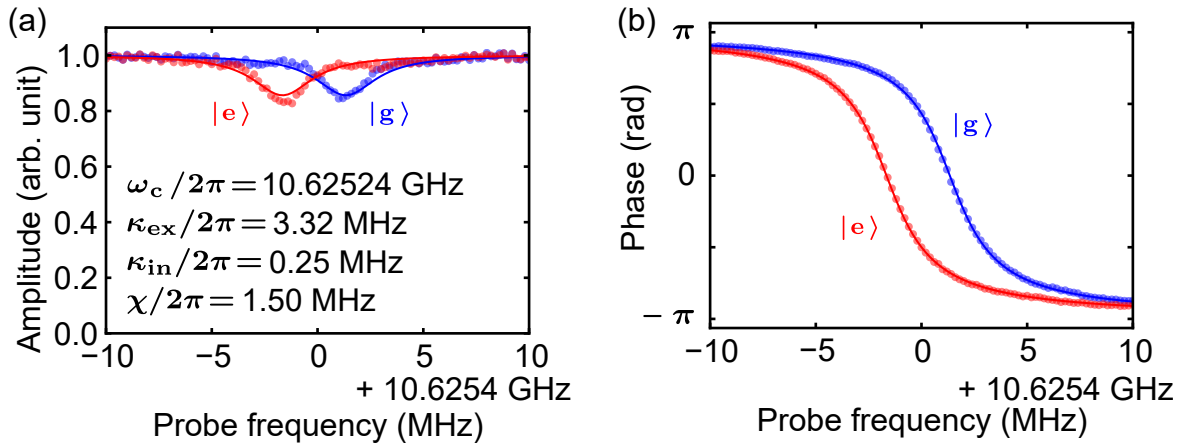


Figure 6.24: Cavity spectra with the qubit in the ground (blue) and excited (red) states. (a) Ampitude and (b) phase as a function of the probe frequency. The dots and lines are the experimental and fitting results, respectively.

The reflection coefficients, which are divided by the baseline, as a function of the probe frequency are shown in Figs. 6.24(a) and (b). The experimental results are well fitted with ideal reflection coefficients of a harmonic oscillator. From this fitting, we obtain the cavity parameters and the dispersive shift without being affected by the frequency-dependent baseline and the thermal excitation probability of the qubit. These parameters are shown in Figs. 6.24(a).

## 6.3 System parameters

Here, the system parameters, which have been obtained in this chapter, are listed in Table. 6.1. The 3D circuit QED system and the JPA are used in the experiments in Chapters 8 and 9.

Table 6.1: System parameters.

| | | |
|---|---|---|
| Cavity resonant frequency | $\omega_c/2\pi$ | 10.62524 GHz |
| Cavity external coupling rate | $\kappa_{ex}/2\pi$ | 3.32 MHz |
| Cavity internal loss rate | $\kappa_{in}/2\pi$ | 0.25 MHz |
| Qubit resonant frequency | $\omega_q/2\pi$ | 7.8693 GHz |
| Qubit anharmonicity | $\alpha/2\pi$ | −0.342 GHz |
| Qubit relaxation time | $T_1$ | 32 $\mu$s |
| Qubit dephasing time | $T_2^*$ | 26 $\mu$s |
| Qubit dephasing time (Echo) | $T_{2E}$ | 33 $\mu$s |
| Qubit thermal population | $p_{th}$ | 0.067 |
| Dispersive shift | $\chi/2\pi$ | 1.50 MHz |
| JPA external coupling rate | $\kappa_{ex}^J/2\pi$ | 60 MHz |
| JPA internal loss rate | $\kappa_{in}^J/2\pi$ | 0.7 MHz |
| JPA gain | $G$ | 24 dB |
| JPA gain bandwidth | $B/2\pi$ | 6.6 MHz |

# Chapter 7

# Nonclassical photon-number distribution

## 7.1 Introduction

The advancement of the superconducting quantum circuit technologies [30] and the advent of circuit quantum electrodynamics (QED) [12] have led to the emergence of the field of microwave quantum optics, enabling us to generate and characterize nonclassical states of electromagnetic fields in the microwave domain.

A squeezed vacuum is one of the most widely studied nonclassical states, and is commonly used as a resource in quantum technologies, such as computation, communication and metrology [82]. In microwave quantum optics, a squeezed vacuum is conveniently generated by degenerated parametric down conversion in a Josephson parametric amplifier (JPA), a device based on the nonlinearity of Josephson junctions and the tunability of SQUIDs [50, 51, 52]. Characterizations of such states propagating in a waveguide have been realized by measuring quadrature amplitudes of reflected signals by using a homodyne technique with the aid of a JPA [83] or a cryogenic HEMT amplifier [59, 84]. JPAs and related circuits are also used to generate and characterize two-mode squeezing in spatially or spectrally separated propagating modes [85, 86, 87, 88, 53]. More recently, it has been shown that a squeezed vacuum injected into a cavity induces nontrivial effects to the relaxations of a qubit [89, 90] and a spin ensemble [91]. In the Fock basis, on the other hand, a squeezed vacuum displays another feature of nonclassicality, i.e., a photon-number distribution composed of only even photon numbers [92]. In the optical domain, direct observations of the photon-number distributions using a photon-number-resolving detector have been previously reported [93, 94]. In the microwave domain, however, due to the much smaller single photon energy compared to the optical domain, photon counting in a propagating mode is still a challenging task. Nonetheless, a few realizations of microwave single-photon detectors have been reported [38, 39, 95]. Note that generation and detection of a photon-number distribution of a microwave squeezed state are theoretically proposed using a circuit QED system [96].

Here, we report the measurement of the photon-number distribution of a squeezed vacuum continuously injected into a cavity containing a superconducting qubit. In the strong dispersive regime of the circuit-QED architecture, the spectrum of a superconducting qubit is split into multiple peaks, with each peak corresponding to a different photon number in the cavity [18, 97]. Furthermore, it is known that the area ratio of the peaks obeys the photon-number distribution in the cavity [17]. In practice, however, we find that the effect of the finite power of the qubit drive field gives rise to a discrepancy between the observed peak area ratio and the actual photon-number distribution. At the

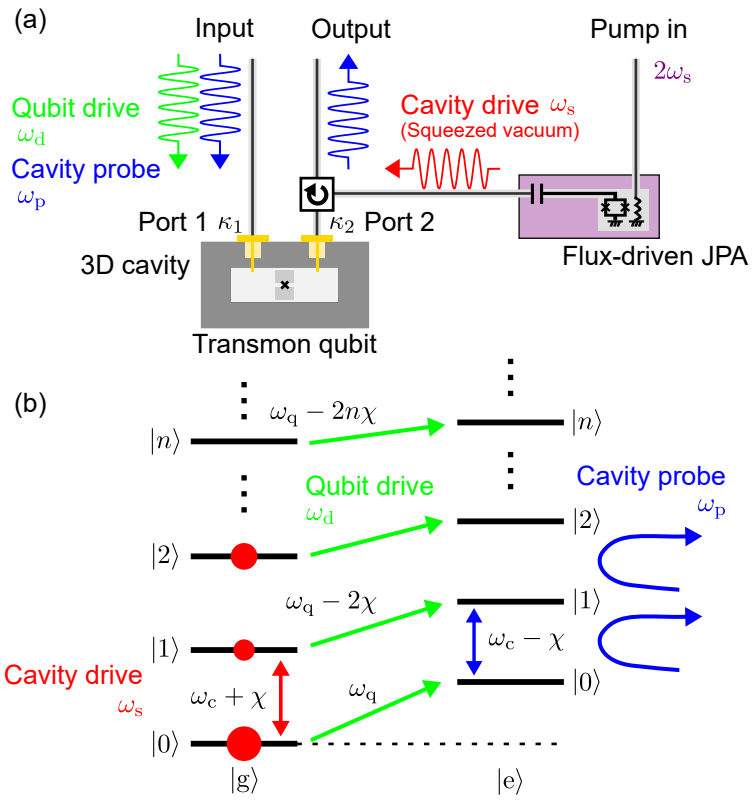


Figure 7.1: (a) Schematic of the experimental setup with squeezed vacuum injection. A squeezed vacuum generated by a flux-driven Josephson parametric amplifier (JPA), as a cavity drive field at $\omega_s$, is injected into the cavity from port 2. The cavity probe field at $\omega_p$ and the qubit drive field at $\omega_d$ are input from port 1, and the transmission of the cavity probe field is measured. For the thermal- and coherent-state injections, the connection to the JPA is switched to a heavily attenuated microwave line connected to their respective sources at room temperature. (b) Energy levels of a dispersively coupled qubit-cavity system. $|g\rangle$ and $|e\rangle$ label the ground and the first exited states of the transmon qubit, and $|n\rangle$ $(n = 0, 1, 2, \cdots)$ indicates the photon number states of the cavity. The cavity drive field generates the steady-state photon-number distribution in the cavity (red dots).

same time, it turns out that the qubit drive actually enhances the signal-to-noise ratio of the photon number peaks in the qubit spectrum. By fitting the obtained spectrum with a model which takes into account this effect, we determine the actual photon-number distribution.

The photon-number distribution confirms its nonclassicality by Klyshko's criterion, quantitatively indicating an even-odd photon number oscillation [98]. This is a steady-state realization and characterization of a nonclassical photon-number distribution in a cavity which is continuously driven by a squeezed vacuum. Owing to the input-output relation [47], the photon-number distribution in the cavity can be interpreted as that of the injected microwave state in a propagating mode. This is in stark contrast with the dynamical generations and characterizations of nonclassical states (e.g., cat states) in a cavity [19, 21].

## 7.2 Measurement scheme

We use a circuit-QED system operating in the strong dispersive regime, where a transmon qubit is mounted at the center of a three-dimensional superconducting cavity as shown schematically in Fig. 7.1(a). The qubit-cavity coupled system is described by the Hamiltonian

$$\hat{\mathcal{H}}/\hbar = \omega_{\rm c}\hat{a}^\dagger\hat{a} + \frac{\omega_{\rm q}}{2}\hat{\sigma}_z - \chi\hat{a}^\dagger\hat{a}\hat{\sigma}_z, \tag{7.1}$$

where $\hat{a}^\dagger(\hat{a})$ is the creation (annihilation) operator of the cavity mode, $\hat{\sigma}_z$ is the Pauli operator of the transmon qubit, $\omega_{\rm c}/2\pi = 10.4005$ GHz is the cavity resonance frequency, $\omega_{\rm q}/2\pi = 8.7941$ GHz is the qubit resonance frequency, and $\chi/2\pi = 3.9$ MHz is the dispersive shift. Note that the Hamiltonian is truncated to the subspace of the ground state $|{\rm g}\rangle$ and the first excited state $|{\rm e}\rangle$ of the transmon qubit; the higher excited states of the qubit are not populated in the experiment below. The total energy-relaxation rate of the cavity is $\kappa/2\pi = 0.5$ MHz, the relaxation time of the qubit is $T_1 = 5.5$ $\mu$s, and the dephasing time of the qubit is $T_2^* = 4.5$ $\mu$s, determined independently from separate measurements (see Sec. 7.7). As shown in Fig. 7.1(b), the dispersive interaction produces both the qubit-state-dependent shift of the cavity resonance frequency and the photon-number-dependent shift of the qubit resonance frequency (discrete ac Stark shift).

In our experiment, three inputs of continuous microwaves are used: a cavity drive, a qubit drive and a cavity probe (see Fig. 7.1). The cavity drive field, whose frequency $\omega_{\rm s}$ is fixed at the cavity resonance frequency for the qubit in the ground state, $\omega_{\rm c}+\chi$, is injected into the cavity to generate a steady-state photon-number distribution. The qubit drive field is applied to the qubit whose excitation probability depends on the photon-number distribution in the cavity. The cavity probe field, whose frequency $\omega_{\rm p}$ is fixed around the cavity resonance frequency, is used to probe the transmission of the cavity depending on the qubit excitation probability. By measuring the cavity transmission as a function of the qubit drive frequency $\omega_{\rm d}$, we can observe a qubit spectra reflecting the photon-number distribution in the cavity. Note that the cavity is designed to have asymmetric external coupling rates of $\kappa_2 \approx 100 \times \kappa_1$ so that the photon-number distribution in the cavity can be determined mainly by the cavity drive field from Port 2.

In the cavity drive field, we use different kinds of states, such as thermal states, coherent states, and squeezed vacuum states. Thermal states are generated by amplifying the thermal noise at room temperature, and coherent states are generated by a microwave source at room temperature. They are led to the cavity through a series of attenuators to suppress the background noise. Squeezed vacuum states are generated by pumping a flux-driven JPA [52] at twice the JPA resonance frequency as shown in Fig. 7.1(a). The correlated photon pairs, generated from individual pump photons, result in an even-odd photon number oscillation in the photon-number distribution. Note that the squeezed vacuum field propagating through the waveguide has a bandwidth broader than that of the cavity, and the photon pairs are generated symmetrically in frequency with respect to the center frequency of the squeezed vacuum in order to conserve energy.

## 7.3 Probe frequency dependence

Here we study the effect of the cavity probe field on qubit spectra. In Fig. 7.2(a), we plot the cavity transmission as a function of the cavity probe frequency $\omega_{\rm p}$ and the qubit drive frequency $\omega_{\rm d}$. The red (blue) dots in Fig. 7.2(b) depict the cross-section at $\omega_{\rm p} = \omega_{\rm c} + \chi$ ($\omega_{\rm p} = \omega_{\rm c} - \chi$) in Fig. 7.2(a). Despite the absence of the cavity drive field at $\omega_{\rm s}$, we observe unexpected dips and peaks corresponding to single or double photon numbers in

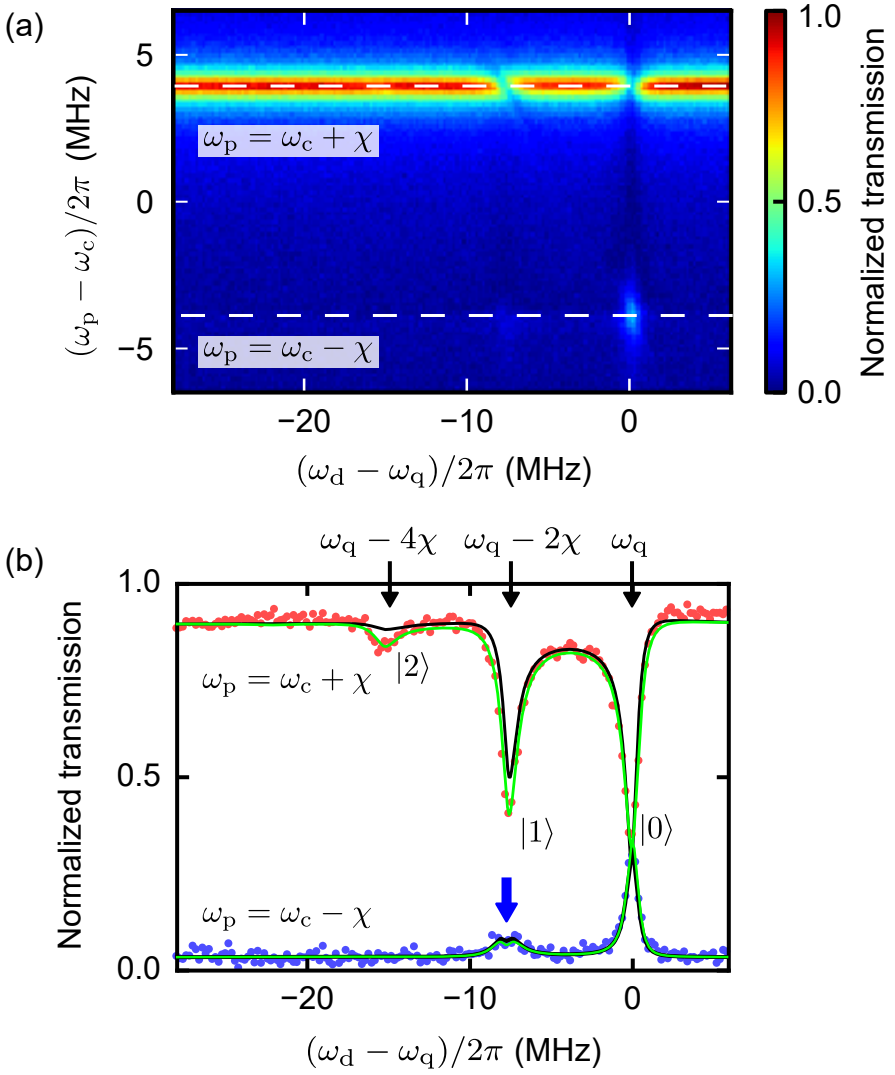


Figure 7.2: (a) Cavity transmission as a function of the qubit drive frequency $\omega_d$ and the cavity probe frequency $\omega_p$. The transmission is normalized by the maximum peak value. White dashed lines indicate $\omega_p = \omega_c \pm \chi$. (b) Cross sections of (a) at $\omega_p = \omega_c \pm \chi$ (red and blue dots, respectively). Green lines represent the rigorous numerical results in which the finite cavity probe power is fully incorporated, whereas the black lines represent the numerical results within the linear response to the cavity probe field, which corresponds to the weak power limit of the cavity probe field. The splitting of the single-photon peak, which is observed for $\omega_p = \omega_c - \chi$ (blue arrow), is understood as the Autler-Townes effect of the qubit, driven strongly at $\omega_d = \omega_q - 2\chi$.

the cavity. Numerical simulations obtained via the Lindblad master equation, taking into account the finite qubit drive and cavity probe power, do nevertheless reproduce these spectra very well (green lines). The details of the Lindblad master equation are explained in Sec. 7.7. The excess dips in the spectrum at $\omega_p = \omega_c + \chi$ (cavity resonance frequency for the qubit in the ground state) are induced by the back-action of the cavity probe field on the cavity transmission which is described in Sec. 7.7. On the other hand, for $\omega_p = \omega_c - \chi$ (cavity resonance frequency for the qubit in the excited state), the back-action is minimal. Note that the small single-photon peak still remains due to the thermal background noise, corresponding to an average photon number $n_{th} = 0.04$ in the cavity.

The black solid lines in Fig. 7.2(b) represent the numerical results for the linear re-

sponse to the cavity probe field, which corresponds to the weak power limit of the probe B. The deviation of the linear response from the observed spectrum is smaller at $\omega_{\rm p} = \omega_{\rm c} - \chi$ than at $\omega_{\rm p} = \omega_{\rm c} + \chi$. For the measurements below, we fix the cavity probe frequency at $\omega_{\rm p} = \omega_{\rm c} - \chi$ which does not influence the qubit spectra significantly and apply linear-response analysis.

Note the splitting at the single-photon peak for $\omega_{\rm p} = \omega_{\rm c} - \chi$ as the blue arrow shows in Fig. 7.2. This can be understood as the Autler-Townes effect of the qubit due to the strong qubit drive at $\omega_{\rm d} = \omega_{\rm q} - 2\chi$, which is explained in Sec. 7.7.

## 7.4 Photon number distribution

Qubit spectra obtained in the cavity driven by different states of microwave fields are shown in Figs. 7.3(a)-(c). We find that each of the qubit spectra apparently reflects the corresponding photon-number distribution. The qubit spectrum induced by the thermal state shows the peaks with their heights monotonically decreasing, which is consistent with the Boltzmann distribution. The qubit spectrum with the coherent drive shows that the peak heights have a single local maximum, which is consistent with the Poisson distribution. More importantly, the qubit spectrum with the squeezed drive shows an even-odd photon number oscillation. We can naively say that the nonclassical feature from a squeezed vacuum is captured in the qubit spectrum.

We determine the actual photon-number distribution in the cavity by fitting the observed qubit spectrum with the corresponding numerical calculations. The details of the theoretical description will be explained in Appendix. B. In the numerical calculations, we use several system parameters which are not associated with the cavity drive field. These system parameters, such as the cavity bandwidth and the qubit drive power, can be independently determined as explained in Sec. 7.7. Then, the characteristic parameters of each cavity drive field are determined as the fitting parameters for the qubit spectrum, as follows. When the cavity is driven by the thermal state, the thermal average photon number in the cavity is used as the fitting parameter. In the case of the coherent input, the coherent amplitude for the cavity is used as the fitting parameter. For the squeezed drive, the pump amplitude and internal loss of the JPA are used as the fitting parameters. As shown in Fig. 7.3, the fitted numerical calculations (black solid lines) agree well with the experimental results (blue dots). Then, using the characteristic parameters obtained from the fitting, the actual photon-number distributions are calculated from the numerical calculations in the absence of the qubit drive and cavity probe fields. The obtained photon-number distributions are shown as dots in Figs. 7.3(d)-(f).

Here, we will discuss what quantum state each photon-number distribution corresponds to. Although we may calculate the corresponding quantum state from the obtained characteristic parameters, it will be complicated due to our redundant model in Appendix. B. Therefore, we compare the obtained photon-number distributions with the expectations based on simple models. The red line in Fig. 7.3(d) is the distribution of the thermal state with an average photon number $n_{\rm th} = 0.20$, which is described as

$$\hat{\rho}_{\rm th} = \frac{1}{n_{\rm th}+1} \sum_{n=0}^{\infty} \left( \frac{n_{\rm th}}{n_{\rm th}+1} \right)^n |n\rangle\langle n|. \tag{7.2}$$

The green line in Fig. 7.3(e) is the distribution of a thermal coherent state with $n_{\rm th} = 0.04$ and a displacement amplitude $|\alpha| = 0.49$, which is described as

$$\hat{\rho}_{{\rm th},\alpha} = \hat{D}(\alpha)\hat{\rho}_{\rm th}\hat{D}^{\dagger}(\alpha), \tag{7.3}$$

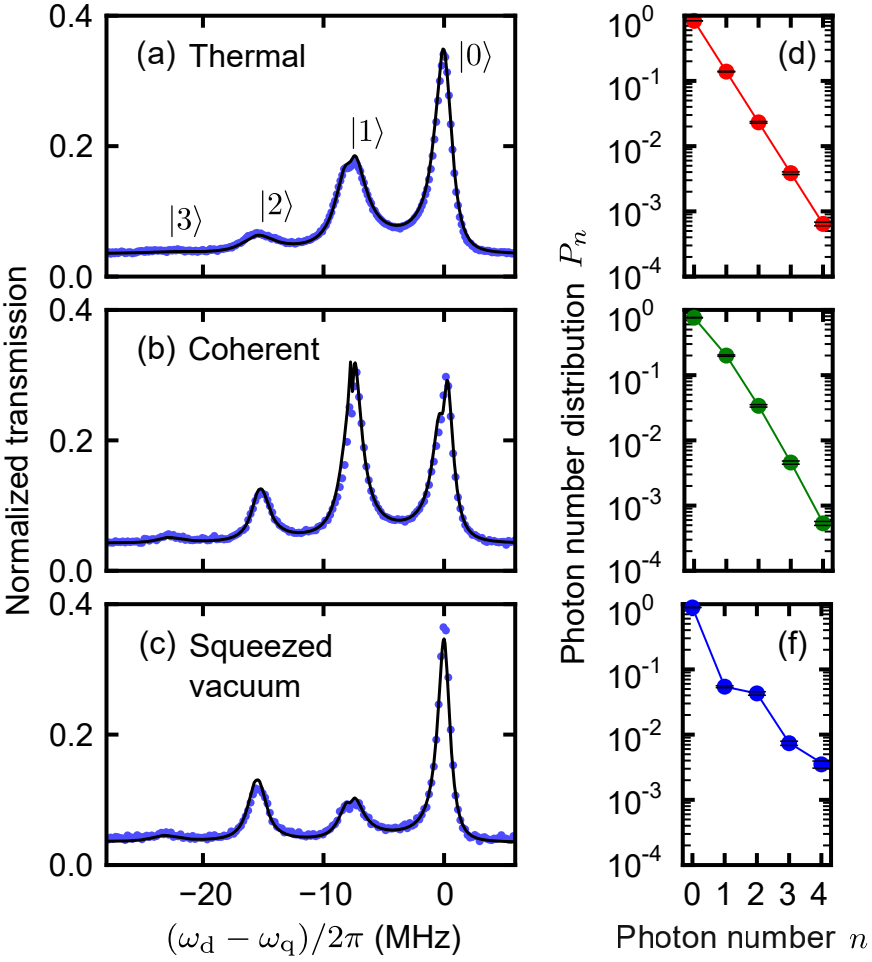


Figure 7.3: (a)-(c) Qubit spectra reflecting the photon-number distributions in the cavity. The cavity drive fields at frequency $\omega_s$ are in (a) thermal, (b) coherent, and (c) squeezed vacuum states, respectively. The average photon number in each state is set to about 0.2. Blue dots are the experimental data, and the black solid lines are the numerically calculated linear responses. (d)-(f) Photon number distributions determined from the fittings (dots). Solid lines are the photon-number distributions calculated from their corresponding models. The error bars are calculated by the fitting errors.

where $\hat{D}(\alpha) = \exp\left(\alpha\,\hat{a}^\dagger - \alpha^*\,\hat{a}\right)$ is the displacement operator. Note that the thermal average photon number corresponds to the thermal background noise in the cavity. The blue line in Fig. 7.3(f) is the distribution of a squeezed vacuum state with a squeezing parameter $r = 0.54$ and a transmittance $\eta = 0.58$, which is described as

$$\hat{\rho}_{r,\eta} = \mathrm{Tr}_{\hat{a}'}\left[\hat{U}_{\mathrm{BS}}(\Theta)\,\rho_r \otimes |0\rangle\langle 0|\,\hat{U}_{\mathrm{BS}}^\dagger(\Theta)\right], \tag{7.4}$$

where $\rho_r = \hat{S}(r)|0\rangle\langle 0|\hat{S}^\dagger(r)$ is a squeezed vacuum state of the cavity mode $\hat{a}$ with a squeezing parameter $r$, $|0\rangle\langle 0|$ is a vacuum state of an ancilla mode $\hat{a}'$, $\hat{U}_{\mathrm{BS}}(\theta) = \exp\left[-\Theta\left(\hat{a}^\dagger\hat{a}' + \hat{a}\hat{a}'^\dagger\right)\right]$ is a unitary operator describing a beam splitter with a transmittance of $\eta = \cos^2\Theta$, and $\mathrm{Tr}_{\hat{a}'}$ is a partial trace for the ancilla mode $\hat{a}'$. Remember that $\hat{S}(r) = \exp\left(\frac{r}{2}(\hat{a}^2 - \hat{a}^{\dagger 2})\right)$ is the squeezing operator. The squeezed vacuum state with finite loss corresponds to a 2.1-dB squeezed state.

Note that the obtained photon-number distributions have much lower weights for larger $n$ than the apparent peak area ratio in the qubit spectra. This is because the qubit

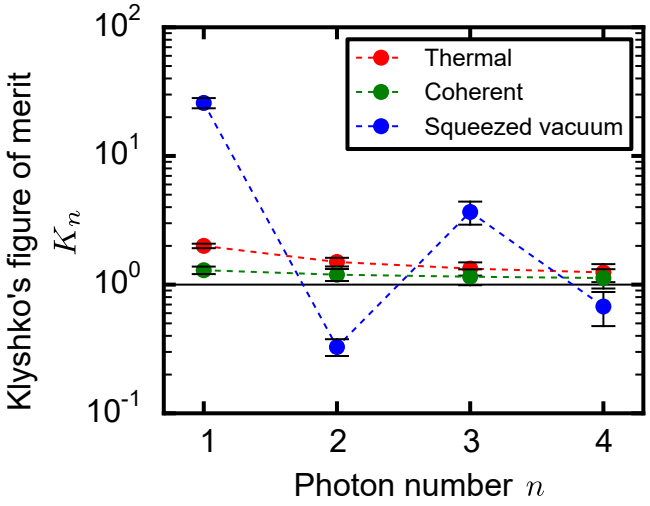


Figure 7.4: Klyshko's figure of merit $K_n$ evaluated for each state of the cavity drive.

excitation rate and the cavity energy-relaxation rate are larger than the qubit energy-relaxation rate. In the steady-state measurement, once the qubit is excited in the presence of the cavity photons ($n \geq 1$), the photons leave the cavity rapidly and the population accumulates in the state $|\mathrm{e}, 0\rangle$. Therefore, the cavity transmission signal conditioned on the qubit excited state is enhanced. The detail of the enhancement effect of the finite qubit drive is discussed in Sec. 7.7.

## 7.5 Klyshko's figure of merit

To verify the nonclassicality of the photon-number distribution under the squeezed drive, we evaluate Klyshko's figure of merit [98], which is described as

$$K_n = \frac{(n+1)P_{n-1}P_{n+1}}{nP_n{}^2} \ (n = 1, 2, \cdots). \tag{7.5}$$

A set of $K_n$ gives a nonclassicality criterion which can be calculated with the photon-number distribution alone. If any of $K_n$ is less than unity, the state is determined to be nonclassical. For instance, the $K_n$ of coherent and thermal states can be described as

$$\begin{aligned} K_n &= 1 && \text{(coherent)}, \\ K_n &= \frac{n+1}{n} \geq 1 && \text{(thermal)}, \end{aligned} \tag{7.6}$$

respectively. As expected, these states are considered as classical states by Klyshko's figure of merit. Moreover, a coherent state represents a boundary between classical and nonclassical.

The Klyshko's figure of merit is calculated from the photon number distributions, obtained from the fitting in Fig. 7.3. The resulting values are shown in Fig. 7.4. $K_n$ is below unity for $n = 2$ and 4 under the squeezed drive. Thus, the photon-number distribution fulfills Klyshko's criterion for nonclassicality. In contrast, all the values of $K_n$ up to 4 are found to be larger than unity for the coherent and the thermal drives.

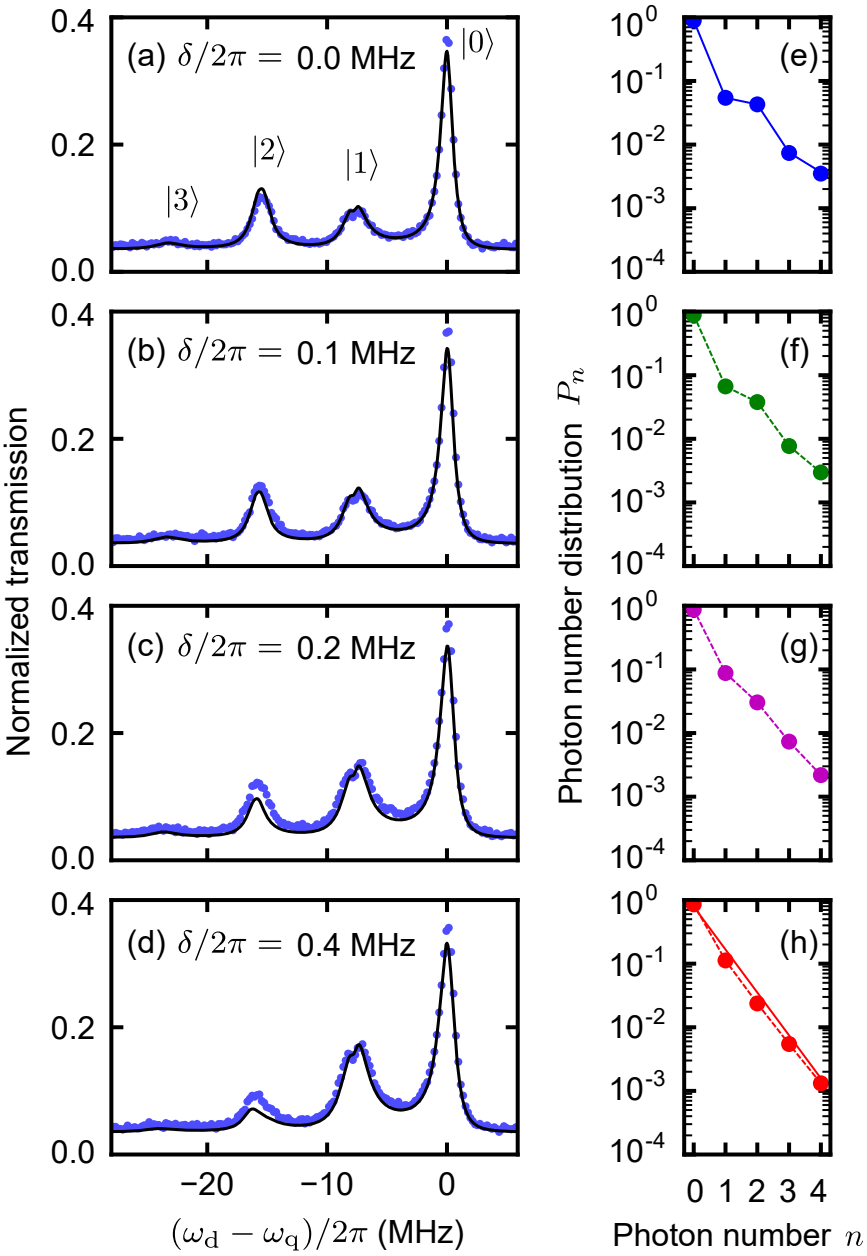


Figure 7.5: (a)-(d) Squeezed-drive-frequency dependence of the qubit spectrum. $\delta = \omega_s - (\omega_c + \chi)$ is the detuning between the center frequency $\omega_s$ of the squeezed vacuum field and the cavity resonance frequency $\omega_c + \chi$. Blue dots are the experimental results, and black solid lines are the numerical calculations. (e)-(h) Photon number distributions determined from the fittings (dots and dashed lines). Solid lines in (e) and (h) are the photon-number distributions calculated from their corresponding models.

## 7.6 Squeezed-drive-frequency dependence

We study the squeezed-drive-frequency dependence of the qubit spectrum as shown in Figs. 7.5(a)-(d). When the detuning $\delta$ between the center frequency $\omega_s$ of the broadband squeezed vacuum and the cavity resonance frequency $\omega_c + \chi$ is zero, both photons in a pair are injected into the cavity with a high and identical probability, so that the even-odd photon number oscillation is conserved. When the detuning is increased, however, the injection probabilities of the photon pairs are asymmetrically biased, and the photon number oscillation is weakened. In the large detuning limit, the cavity state becomes a

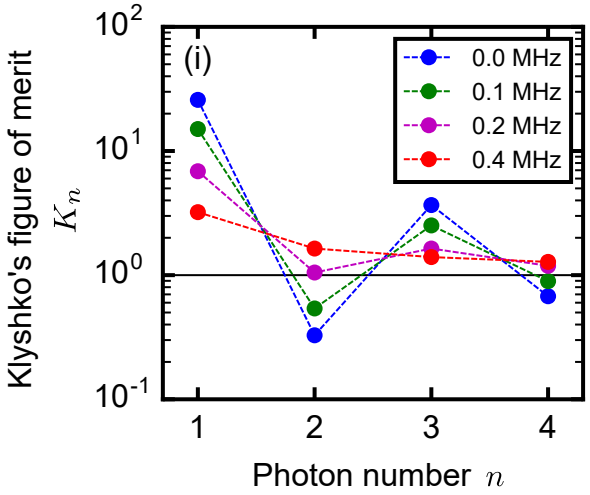


Figure 7.6: Klyshko's figure of merit $K_n$ evaluated for each detuning $\delta$.

thermal state. This can be understood from the fact that a two-mode squeezed vacuum state is reduced to a thermal state after tracing out one of the modes. The qubit spectra with the detuning are calculated using the fitting parameters which are obtained in Fig. 7.3(c). The numerical calculations (black solid lines) agree well with the experimental results (blue dots) once again. Then, the photon-number distributions are determined from the numerical results. In Fig. 7.5, we observe that the photon number oscillation is diminished as the detuning is increased. Eventually, the photon-number distribution approaches the Boltzmann distribution of a thermal state with an average photon number $n_{\rm th} = 0.27$ [red solid line in Fig. 7.5(h)]. These observations indicate that a broadband squeezed vacuum has correlated photon pairs in frequency space. Klyshko's figures of merit plotted in Fig. 7.6 show that the nonclassicality is reduced as the detuning is increased and that the cavity state becomes a classical state, i.e., $K_n > 1$ for any photon number $n$.

## 7.7 Characterization

The actual photon-number distributions are determined by fitting the qubit spectrum with the rigorous numerical calculations. Therefore, our results on the photon-number distributions strongly depend on the system parameters. Thus, here, we explain how the parameters used in the previous sections were determined. Furthermore, we also describe the origins of the unexpected effects in the qubit spectrum, such as the discrepancy between the area ratio of the peaks and the actual photon number states.

### System parameters

First of all, the system parameters to be calibrated are shown in a simplified Lindblad master equation without a cavity drive.

Since the cavity drive field at $\omega_{\rm s}$ is absent here, we can take a rotating frame determined by $\hat{\mathcal{H}}_{\rm A0}/\hbar = \omega_{\rm p}\hat{a}^\dagger\hat{a} + \frac{\omega_{\rm d}}{2}\hat{\sigma}_z$. Then, the Hamiltonian Eq. (B.1) is rewritten as

$$\hat{\mathcal{H}}_{\rm A}/\hbar = (\omega_{\rm c} - \omega_{\rm p})\hat{a}^\dagger\hat{a} + \frac{(\omega_{\rm q} - \omega_{\rm d})}{2}\hat{\sigma}_z - \chi\hat{a}^\dagger\hat{a}\,\hat{\sigma}_z + \frac{\Omega_{\rm d}}{2}(\hat{\sigma}_+ + \hat{\sigma}_-) + \frac{\Omega_{\rm p}}{2}(\hat{a}^\dagger + \hat{a}). \quad (7.7)$$

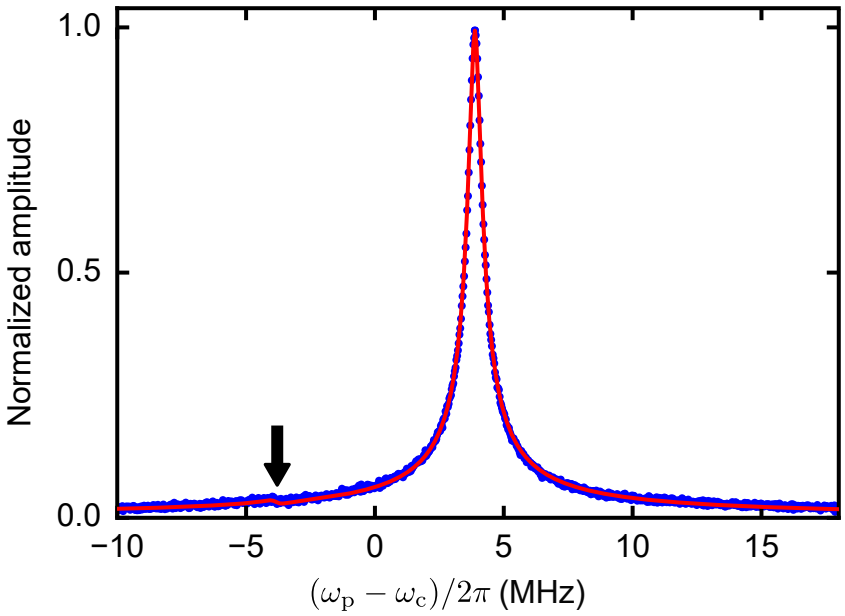


Figure 7.7: Cavity transmission as a function of the cavity probe frequency $\omega_p$. The amplitude is normalized by the maximum peak value. This normalization factor is used throughout this chapter. The main peak at $\omega_p = \omega_c + \chi$ corresponds to the cavity resonance with the qubit in the ground state. The small cavity peak at $\omega_p = \omega_c - \chi$ (arrow), corresponding to the qubit excited state, is also observed due to the thermal excitation of the qubit. Red solid line represents the numerical result.

By using Eq. (B.12) with $S_B = \hat{1}$ and $\kappa_{ex}^J = 0$, we calculate the time-evolutions and the steady-state solutions of System A. They correspond to the solution of the conventional system-bath master equation of System A as

$$\dot{\hat{\rho}}_A = \frac{1}{i\hbar}[\hat{\hat{H}}_A, \hat{\rho}_A] + \mathcal{D}[\sqrt{\kappa(n_{th}+1)}\,\hat{a}]\hat{\rho}_A + \mathcal{D}[\sqrt{\kappa n_{th}}\,\hat{a}^\dagger]\hat{\rho}_A + \mathcal{D}[\sqrt{\gamma(p_{th}+1)}\,\hat{\sigma}_-]\hat{\rho}_A + \mathcal{D}[\sqrt{\gamma p_{th}}\,\hat{\sigma}_+]\hat{\rho}_A, \tag{7.8}$$

where $\hat{\rho}_A$ is th density matrix of System A and $\mathcal{D}[\hat{O}]\hat{\rho}_A = \hat{O}\hat{\rho}_A\hat{O}^\dagger - \frac{1}{2}(\hat{O}^\dagger\hat{O}\hat{\rho}_A + \hat{\rho}_A\hat{O}^\dagger\hat{O})$ is the Lindblad superoperator. Note that since the time-derivative equation of Eq. (7.8) is described in the Schrödinger picture, we replace $i$ with $-i$ in Eq. (B.12). The steady state of $\hat{\rho}_A$ can be obtained with the condition of $\dot{\hat{\rho}}_A = 0$ in Eq. (7.8).

The cavity transmission amplitude, measured as a function of the cavity probe frequency $\omega_p$ in the absence of any drive field, is shown in Fig. 7.7. The cavity resonance is observed at the probe power corresponding to the single photon level. The main peak at $\omega_p = \omega_c + \chi$ is the cavity resonance with the qubit in the ground state. In addition, the small peak corresponding to the cavity resonance with the qubit in the excited state is also observed at $\omega_p = \omega_c - \chi$ due to the finite thermal excitation probability of the qubit, $p_{th}$. The red solid line is calculated from the steady-state solution of $\langle\hat{a}\rangle$ in Eq. (7.8). From this, we find $p_{th} = 0.01$.

Next, time-domain measurements are conducted to evaluate the coherence of the qubit. The results of the qubit energy relaxation and Ramsey measurements are shown in Figs. 7.8(a) and (b). We obtain $T_1 = 5.5\ \mu$s and $T_2^* = 4.5\ \mu$s by fitting the data. The total dephasing rate of the qubit $1/T_2^*$ is described by $\gamma/2 + \gamma_{\phi,n} + \gamma_{th}$, where $\gamma_{th} = \frac{4\kappa\chi^2}{\kappa^2+\chi^2}\,n_{th}$ is the dephasing rate due to the thermal photon fluctuation in the cavity [68]. Assuming

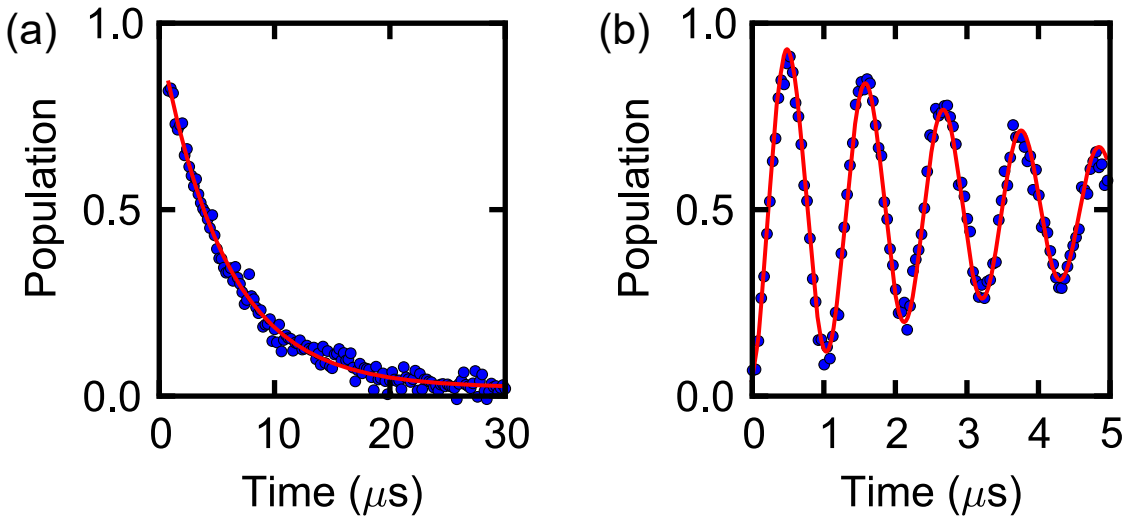


Figure 7.8: Time-domain measurements of the qubit coherence. (a) Relaxation of the qubit. Red solid line is a fit to a exponential curve with $T_1 = 5.5\ \mu s$. (b) Dephasing of the qubit. $T_2^*$ is 4.5 $\mu s$. Red solid line is the numerical result with $n_{\rm th} = 0.04$.

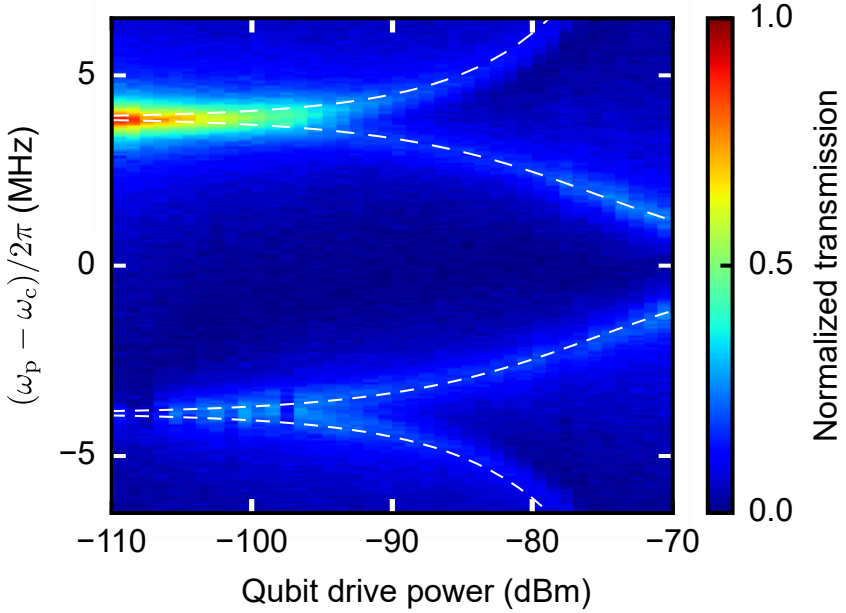


Figure 7.9: Cavity transmission as a function of the cavity probe frequency $\omega_{\rm p}$ and the qubit drive power ($\Omega_{\rm d}$). White dashed lines depict the analytically calculated cavity resonances.

$\gamma_{\phi,{\rm n}} = 0$, the thermal average photon number $n_{\rm th}$ in the cavity is determined to be 0.04 by using the simple formula. The red solid line in Fig. 7.8(b) is the time-evolution solution of $\langle(\hat{\sigma}_z + 1)/2\rangle$ in Eq. (7.8), where $(\omega_{\rm q} - \omega_{\rm d})/2\pi = 0.9$ MHz, $\Omega_{\rm d} = \Omega_{\rm p} = 0$, and $n_{\rm th} = 0.04$ are used. The calculation agrees well with the experimental result.

In order to calibrate the qubit drive power, the cavity transmission is measured as a function of the cavity probe frequency $\omega_{\rm p}$ and the qubit drive amplitude $\Omega_{\rm d}$, which is shown in Fig. 7.9. The qubit drive frequency $\omega_{\rm d}$ is in resonance with the qubit resonance

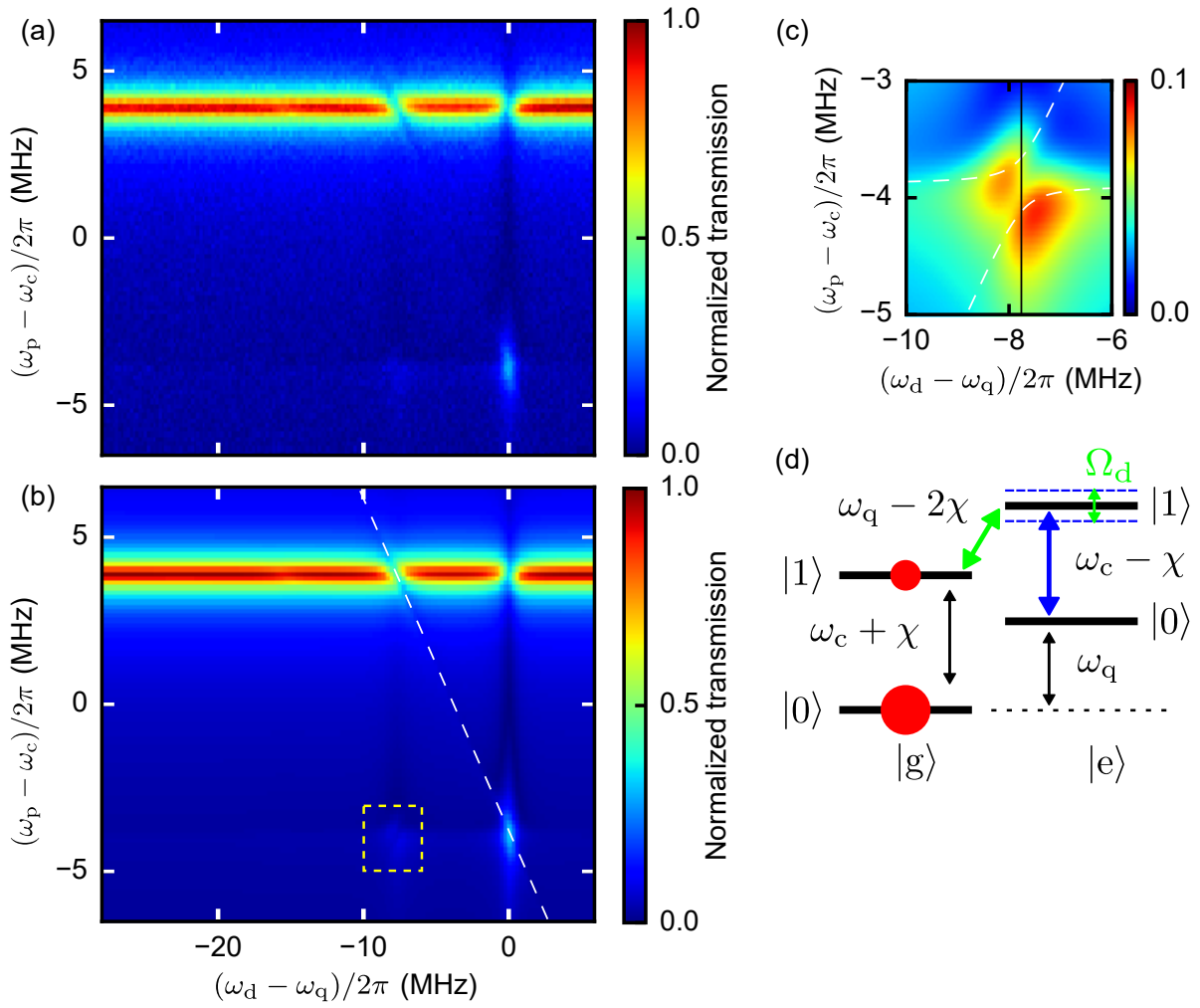


Figure 7.10: Cavity transmission as a function of the qubit drive frequency $\omega_d$ and the cavity probe frequency $\omega_p$. (a) Experimental data. (b) Steady-state solutions of $\langle\hat{a}\rangle$ in Eq. (7.8). Diagonal dashed line corresponds to the resonance condition for the two-photon transition, $\omega_p + \omega_d = \omega_c + \omega_q - \chi$. (c) Magnified plot of the region in the yellow dashed rectangle in (b) at around $\omega_p = \omega_c - \chi$ and $\omega_d = \omega_q - 2\chi$. White dashed lines depict the calculated transition frequencies between $|e, 0\rangle$ and the hybridized states composed of $|e, 1\rangle$ and $|g, 1\rangle$. Black solid line indicates $\omega_d = \omega_q - 2\chi$, corresponding to the qubit transition frequency with the single photon state in the cavity. (d) Energy levels of the dispersively coupled qubit-cavity system with the qubit drive field. $|e, 1\rangle$ and $|g, 1\rangle$ are hybridized by the qubit drive.

frequency $\omega_q$. As the qubit drive power increases, the cavity peak corresponding to the qubit in the excited state appears, and each peak splits in two due to the Rabi splitting of the qubit. In this experiment, the cavity probe power is weak enough to excite at most the single photon state in the cavity. Therefore, the four resonances in Fig. 7.9 correspond to the transitions between the lowest eigenfrequencies: $\omega_{0\pm} = \pm\frac{\Omega_d}{2}$ and $\omega_{1\pm} = \omega_c \pm \sqrt{\chi^2 + \left(\frac{\Omega_d}{2}\right)^2}$, which are calculated from the Hamiltonian Eq. (7.7) with $\omega_d = \omega_q$ and $\omega_p = \Omega_p = 0$. The white dashed lines in Fig. 7.9 depict these transition frequencies and agree with the observed resonance peaks. With this plot, we performed the calibration between the actual qubit drive power and the qubit drive amplitude $\Omega_d$. The qubit drive power of $-97$ dBm at the sample, which is used for the qubit spectroscopy

Table 7.1: System parameters.

| | | |
|---|---|---|
| Cavity resonance frequency | $\omega_c/2\pi$ | 10.4005 GHz |
| Cavity external coupling rate | $\kappa_{ex}/2\pi$ | 0.490 MHz |
| Cavity total energy-relaxation rate | $\kappa/2\pi$ | 0.494 MHz |
| Cavity thermal average photon number | $n_{th}$ | 0.04 |
| Cavity probe amplitude | $\Omega_p/2\pi$ | 0.16 MHz |
| Qubit resonance frequency | $\omega_q/2\pi$ | 8.7941 GHz |
| Qubit energy-relaxation rate | $\gamma = 1/T_1$ | $1/5.5\ \mu s^{-1}$ |
| Qubit natural dephasing rate | $\gamma_{\phi,n}$ | 0 |
| Qubit thermal excitation probability | $p_{th}$ | 0.01 |
| Qubit drive amplitude | $\Omega_d/2\pi$ | 0.46 MHz |
| Effective dispersive shift | $\chi/2\pi$ | 3.9 MHz |
| JPA external (total) coupling rate | $\kappa_{ex}^J/2\pi$ | 40 MHz |

measurement, corresponds to $\Omega_d/2\pi = 0.46$ MHz.

In order to calibrate the cavity probe power, we use the qubit spectra at $\omega_p = \omega_c \pm \chi$, as shown in Fig. 7.2(b). The red (blue) dots plot the cavity transmission as a function of the qubit drive frequency $\omega_d$, fixing the cavity probe frequency $\omega_p = \omega_c + \chi$ ($\omega_p = \omega_c - \chi$). The qubit spectra strongly reflect the cavity probe power $\Omega_p$ and the average thermal photon number $n_{th}$ in the cavity. The green solid lines are the steady-state solutions of $\langle \hat{a} \rangle$ in Eq. (7.8). From the simulations, we find the cavity probe power of $-125$ dBm at sample, that we use for the qubit spectroscopy, corresponds to $\Omega_p/2\pi = 0.16$ MHz. The average thermal photon number $n_{th}$, which is determined from the $T_2^*$ measurement, agrees well with the qubit spectra.

To sum up, the obtained system parameters are lisetd in Table 7.1.

## Autler-Townes effect

Using the parameters, listed in Table 7.1, the cavity transmission as a function of the qubit drive frequency $\omega_d$ and the cavity probe frequency $\omega_p$ are numerically calculated from the steady-state solution of $\langle \hat{a} \rangle$ in Eq. (7.8), as shown in Fig. 7.10. The calculation results agree well with the experimental results, which ensures accuracy in the determination of the parameters.

In the qubit spectrum for $\omega_p = \omega_c - \chi$ [Fig. 7.2(a)], we find a splitting in the peak corresponding to the single photon occupancy. The splitting is understood as the Autler-Townes effect involving the three states: $|e, 0\rangle$, $|e, 1\rangle$ and $|g, 1\rangle$ [99]. In the cavity probe frequency $\omega_p$ dependence of the qubit spectra, an anti-crossing like splitting is observed at around $\omega_p = \omega_c - \chi$ and $\omega_d = \omega_q - 2\chi$, as shown in the yellow rectangle in Fig. 7.10(b) and in Fig. 7.10(c). Due to the thermal photon excitation in the cavity, the population of $|g, 1\rangle$ is finite. In the steady state, the qubit drive field at $\omega_d = \omega_q - 2\chi$ transfers the population of $|g, 1\rangle$ to $|e, 0\rangle$, because the qubit drive amplitude $\Omega_d$ and the cavity energy-relaxation rate $\kappa$ are larger than the qubit energy-relaxation rate $\gamma$. Therefore, the cavity probe field around $\omega_p = \omega_c - \chi$ can excite the photons in the cavity from $|e, 0\rangle$. The qubit drive field couples $|e, 1\rangle$ to $|g, 1\rangle$ and splits the spectrum into the two peaks with the separation of $\Omega_d$ [see fig. 7.10(d)]. The white dashed lines in Fig. 7.10(c) depict the transition frequencies from $|e, 0\rangle$ to the hybridized states composed of $|g, 1\rangle$ and $|e, 1\rangle$, which is calculated from the Hamiltonian Eq. (7.7) with $\omega_p = \Omega_p = 0$.

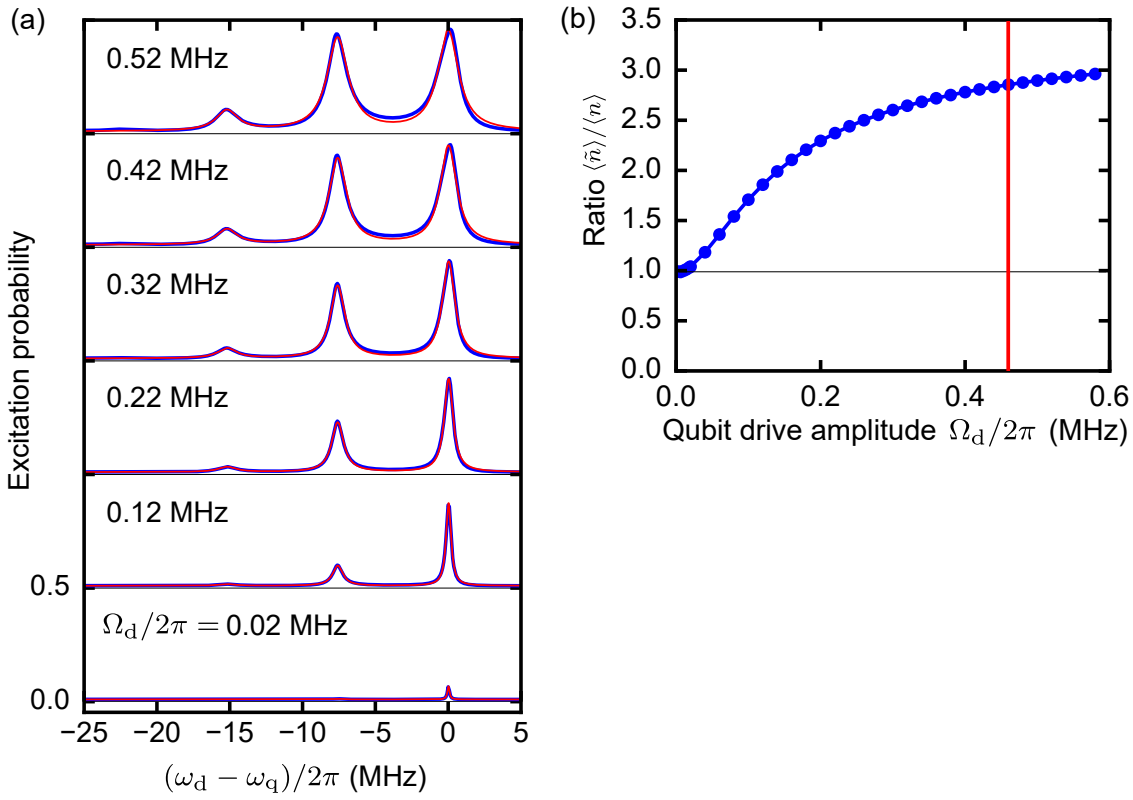


Figure 7.11: (a) Qubit spectrum for each qubit drive amplitude $\Omega_d$. The spectra are offset vertically by 0.5 each. Blue solid lines are the numerical results and red solid lines are the multi-Lorentzian fits. The average photon number in the cavity under a coherent drive is fixed to 0.2. (b) Ratio of the apparent average photon number $\langle\tilde{n}\rangle$ to the actual average photon number $\langle n\rangle$ as a function of the qubit drive amplitude $\Omega_d$. Red solid line indicates the qubit drive amplitude we used in the qubit spectroscopy.

## Effect of qubit drive field

As shown in Figs. 7.3 and 7.5, the peak area ratio in the qubit spectrum does not coincide exactly with the actual photon-number distribution in the cavity due to the finite qubit drive field. This discrepancy can be explained by the accumulation of the population in the state $|e, 0\rangle$ in the relation between the excitation and energy-relaxation rate of the system.

To be more quantitative, we study the effect of the qubit drive amplitude $\Omega_d$ on the qubit spectrum. For simplicity, the steady state solutions of $\langle(\hat{\sigma}_z + 1)/2\rangle$ are calculated using Eq. (7.8). Note that the cavity probe power is so weak that the excitation probability of the qubit is proportional to the cavity transmission, which is measured in the experiment. As an example, the cavity is driven by a coherent state to have a steady-state with an average photon number of 0.2. Therefore, to simulate the coherent drive for the cavity, we can simply replace the cavity probe with $\omega_p$ and $\Omega_p$ with a cavity drive with $\omega_s = \omega_c + \chi$ and $\Omega_s$ in Eq. (7.8), respectively.

In Fig. 7.11(a), we plot the qubit excitation probability $\langle(\hat{\sigma}_z + 1)/2\rangle$ as a function of the qubit drive frequency $\omega_d$ for each drive amplitude $\Omega_d$ (blue solid lines). As the drive amplitude $\Omega_d$ is increased, the peaks in the qubit spectrum are enhanced, which allows us to observe the peaks with a higher signal-to-noise ratio in the experiment. Specifically, this effect makes it easier to characterize a microwave quantum state whose average photon

number is small. The red solid lines are multi-Lorentzian fits to deduce the apparent average photon numbers $\langle\tilde{n}\rangle$ from the peak area ratios. In Fig. 7.11(b), we plot the ratio of $\langle\tilde{n}\rangle$ to the actual average photon number $\langle n\rangle$ as a function of the drive amplitude $\Omega_{\rm d}$. In the small amplitude limit of the qubit drive, $\langle\tilde{n}\rangle$ is identical to $\langle n\rangle$. However, as $\Omega_{\rm d}$ increases, the ratio $\langle\tilde{n}\rangle/\langle n\rangle$ increases, meaning that the populations of the larger photon number states are effectively enhanced.

# Chapter 8

# Wigner quantum state tomography

## 8.1 Introduction

The availability of experiments on microwave quantum optics is highly dependent on controllability and measurability of superconducting qubits [100]. A circuit QED system, where microwave photons confined in a cavity strongly interact with a superconducting qubit [12, 13], is known as a powerful tool to control and measure microwave photons. For example, an arbitrary superposition state of the photon number states and a Schrödinger cat state with large-amplitude coherent states are generated and characterized using a superconducting qubit in a cavity [19, 21]. Furthermore, the superconducting qubit can generate a quantum state not only in the cavity mode but also in a propagating mode. Itinerant microwave photons, which can be carriers of quantum information, have been well studied toward a quantum network between localized quantum processors [31]. So far, the generation of a single photon state and a Schrödinger cat state are demonstrated by using a circuit QED system with the cavity mode over-coupled to the output waveguide [101, 32, 102, 33, 34]. Recently, quantum state transfers have also been demonstrated between two localized circuit QED systems [35, 36, 37]. Nevertheless, the characterization of itinerant microwave photons is still a challenging task, since photon detectors, which are commonly applied for optical photons, are not available in the microwave frequency domain [38, 39, 40]. Moreover, the superconducting qubit, which can be a powerful probe for the cavity photons, cannot be easily applicable for the detection of itinerant microwave photons, since it has been difficult to be coupled to the propagating mode efficiently. Thus, in contrast to that of optical photons [57], the characterization of the itinerant microwave photons is normally realized by using linear amplifiers, such as a HEMT amplifier and a Josephson parametric amplifier (JPA) [83, 59, 32, 33, 34]. Moreover, high efficient measurement of quadratures of itinerant microwave photon based on JPAs enables to demonstrate continuous monitoring and feedback control of a superconducting qubit [103, 104]. However, in the microwave domain, the measurement efficiency of the itinerant microwave photons is largely limited by the amplifier noises or the propagation loss. Therefore, the low measurement efficiency need to be corrected based on a calibrated thermal noise. However, the validity of the loss correction is not always guaranteed. For instance, the cable loss is may be uncertain in some experiments. Furthermore, a vacuum state in the propagating mode, which often determines the scale of the quadratures, is sometimes assumed simply from the base temperature.

Here, we demonstrate a Wigner quantum state tomography of itinerant microwave pulse modes using a phase-sensitive amplifier, or a flux-driven JPA [52]. The quadratures of th microwave pulses are efficiently measured and used to reconstruct the density matrix of the quantum state using the iterative maximum likelihood method with correction of

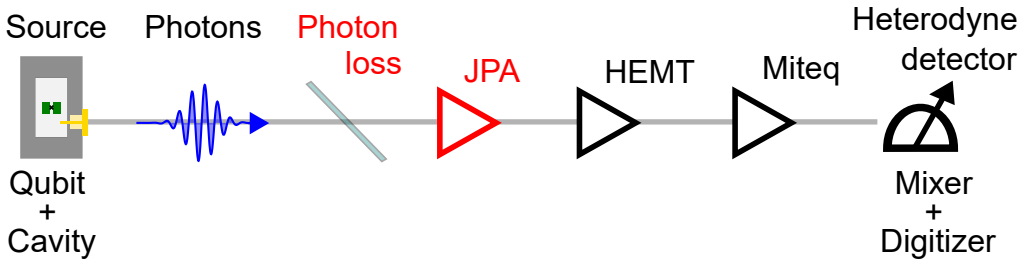


Figure 8.1: Measurement chain for the quadrature. The details are explained in Chapter 4.

the inefficiency in the quadrature measurement [105]. Importantly, the measurement inefficiency is reliably determined by a coherent state which is well-calibrated by the cavity-drive-induced dephasing of the transmon qubit in the cavity [17]. Furthermore, the vacuum state in the propagating mode is guaranteed by the thermal-photon-induced dephasing of the transmon qubit in the cavity [68, 7].

## 8.2 Quadrature measurement

In the microwave domain, the quadrature of itinerant microwave photons can be measured by using linear amplifiers and a digitizer together with a demodulation system. A pre-amplifier is most important for high-efficiency measurement of the quadratures since it can effectively suppress the latter inefficiencies. As discussed in Sec. 3.4.7, adding half a vacuum noise is inevitable with a phase-insensitive amplifier. Therefore, phase-sensitive amplification, which can be realized by a flux-driven JPA, is applied to the pre-amplifier in this thesis.

Here, the Wigner quantum state tomography is applied to itinerant microwave pulse modes emitted from a circuit QED system in the dispersive regime. This can be a typical setup to generate a quantum state in the propagating mode [32, 102, 33, 34]. The microwave pulses are guided to a JPA through several circulators and are amplified at the JPA. Then, the microwave photons are amplified again by the classical amplifiers and are demodulated to the low frequency signal at the IQ mixer and are digitized by the ADC. The schematic of the measurement chain for quadrature is shown in Fig. 8.1.

### Measurement efficiency

In the Wigner quantum state tomography, the probabilistic distributions of the measured quadratures are used to reconstruct the density matrix of the microwave photons. Therefore, we need to consider how the quadrature distributions are transformed in the complicated measurement chain. As discussed in Sec. 3.5, the transformation of the quadrature distribution $P_\theta(x)$ to be measured is characterized by the scaling and the added noise. The typical parameters in the measurement chain are listed in Table. 8.1.Note that the thermal noise added by the demodulation and the heterodyne detection are not listed since we can assume that the noises are well suppressed by the total gains of about 100 dB.

From Eq. (3.129) in Sec. 3.5, the input quadrature distribution $P_\theta(x)$ is cascade-

transformed with the scaling $c_1, c_2, c_3, \cdots$ and the added noises $n_1, n_2, n_3 \cdots$ as,

$$\begin{aligned} P_{\theta,\mathrm{tot}}(x) &= \frac{1}{\sqrt{c_{\mathrm{tot}}}} P_{\theta * N}\left(\frac{x}{\sqrt{c_{\mathrm{tot}}}}, n = n_{\mathrm{tot}}\right) \\ &= \frac{1}{\sqrt{c_{\mathrm{tot}}}} \int_{-\infty}^{\infty} dx_{\mathrm{a}}\, P_\theta\left(x_{\mathrm{a}}\right)\; N\left(\frac{x}{\sqrt{c_{\mathrm{tot}}}} - x_{\mathrm{a}}, n = n_{\mathrm{tot}}\right), \end{aligned} \tag{8.1}$$

where

$$\begin{aligned} c_{\mathrm{tot}} &= c_1 c_2 c_3 \cdots \\ n_{\mathrm{tot}} &= n_1 + \frac{n_2}{c_1} + \frac{n_3}{c_1 c_2} + \cdots, \end{aligned} \tag{8.2}$$

where $N(x,n) = 1/\sqrt{2\pi n}\exp(-x^2/2n)$ is the noise distribution which describes the added noise. The transformed quadrature distribution $P_{\theta,\mathrm{tot}}(x)$ corresponds to the measured one. The added noise is the sum of the modified noises, which are defined as each noise divided by the gain up to that point. The total gain, the total added noise, and the modified noise at each step are also listed in Table 8.1.We find that the added noises in the photon loss and in the HEMT noise can be dominant in the total added noise. From this analysis, the measurement chain with the JPA as a preamplifier enables us to measure the quadrature of microwave photons in the nearly-quantum limit.

Here, we explain how to determine the scaling of the quadrature distribution for the quantum state tomography without knowledge of the actual total scaling $c_{\mathrm{tot}}$. Suppose the input state is a vacuum state. Then, the measured quadrature distribution is obtained as

$$\begin{aligned} P_{0,\mathrm{tot}}(x) &= \frac{1}{\sqrt{c_{\mathrm{tot}}}} \int_{-\infty}^{\infty} dx_{\mathrm{a}}\, P_0\left(x_{\mathrm{a}}\right)\; N\left(\frac{x}{\sqrt{c_{\mathrm{tot}}}} - x_{\mathrm{a}}, n = n_{\mathrm{tot}}\right) \\ &= \frac{1}{\sqrt{c_{\mathrm{tot}}}} \int_{-\infty}^{\infty} dx_{\mathrm{a}}\, N\left(x_{\mathrm{a}}, n = \frac{1}{2}\right)\; N\left(\frac{x}{\sqrt{c_{\mathrm{tot}}}} - x_{\mathrm{a}}, n = n_{\mathrm{tot}}\right) \\ &= \frac{1}{\sqrt{c_{\mathrm{tot}}}} N\left(\frac{x}{\sqrt{c_{\mathrm{tot}}}}, n = \frac{1}{2} + n_{\mathrm{tot}}\right) \\ &= N\left(x, n = c_{\mathrm{tot}}\left(\frac{1}{2} + n_{\mathrm{tot}}\right)\right), \end{aligned} \tag{8.3}$$

where $P_0 = N(x, n = 1/2)$ is the quadrature distribution of the vacuum state. The variance is found to be $c_{\mathrm{tot}}\left(1/2 + n_{\mathrm{tot}}\right)$.

Then, we rescale the quadrature distribution so that the variance becomes that of the vacuum state 1/2. In other words, the quadrature distribution is rescaled by $\sqrt{1/2}/\sqrt{c_{\mathrm{tot}}\left(1/2 + n_{\mathrm{tot}}\right)} =$

Table 8.1: Typical parameters of the scaling and the added noise in the measurement chain. From these parameters, the total scaling and the total added noise, and the measurement efficiency of the measurement chain can be calculated. Here, the added noise in the JPA is assumed to be negligible.

| | Scaling | Added noise | Modified noise |
|---|---|---|---|
| Photon loss to JPA | 0 – −3 dB | 0 – 0.5 (10 mK@10 GHz) | 0 – 0.5 |
| JPA | 25 dB | 0 | 0 |
| HEMT | 40 dB | 10 (5 K@10 GHz) | 0.03 – 0.06 |
| Miteq | 35 dB | 150 (70 K@10 GHz) | $5 – 9\times10^{-5}$ |
| Total | 100 dB – 97 dB | 0.03 – 0.56 ($\eta_{\mathrm{meas}} = 0.94 – 0.47$) | - |

$1/\sqrt{2c_{\mathrm{tot}}\,(1/2+n_{\mathrm{tot}})}$ as

$$\begin{aligned}\bar{P}_{0,\mathrm{out}}(x) &= N\left(x, n=\frac{1}{2}\right)\\ &= P_0(x),\end{aligned} \tag{8.4}$$

which corresponds to that of the vacuum state.

Using the rescaling factor of $1/\sqrt{2c_{\mathrm{tot}}\,(1/2+n_{\mathrm{tot}})}$, the quadrature distribution to be concerned in Eq. (8.1) is also rescaled as

$$\begin{aligned}\bar{P}_{\theta,\mathrm{tot}}(x) &= \sqrt{2c_{\mathrm{tot}}\,(1/2+n_{\mathrm{tot}})}P_{\mathrm{tot}}\left(\sqrt{2c_{\mathrm{tot}}\,(1/2+n_{\mathrm{tot}})}x\right)\\ &= \sqrt{2\,(1/2+n_{\mathrm{tot}})}\int_{-\infty}^{\infty}dx_{\mathrm{a}}\,P\left(x_{\mathrm{a}}\right)\,N\left(\sqrt{2\,(1/2+n_{\mathrm{tot}})}x-x_{\mathrm{a}}, n=n_{\mathrm{tot}}\right)\\ &= \frac{1}{\sqrt{\eta_{\mathrm{meas}}}}\int_{-\infty}^{\infty}dx_{\mathrm{a}}\,P\left(x_{\mathrm{a}}\right)\,N\left(\frac{x}{\sqrt{\eta_{\mathrm{meas}}}}-x_{\mathrm{a}}, n=\frac{1-\eta_{\mathrm{meas}}}{\eta_{\mathrm{meas}}}\times\frac{1}{2}\right)\\ &= \frac{1}{\sqrt{\eta_{\mathrm{meas}}}}P_{*N}\left(\frac{x}{\sqrt{\eta_{\mathrm{meas}}}}, n=\frac{1-\eta_{\mathrm{meas}}}{\eta_{\mathrm{meas}}}\times\frac{1}{2}\right),\end{aligned} \tag{8.5}$$

where the measurement efficiency is defined as

$$\eta_{\mathrm{meas}} = \frac{1/2}{(n_{\mathrm{tot}}+1/2)}. \tag{8.6}$$

Finally, we find that the rescaled quadrature distribution exactly corresponds to the quadrature distribution which is obtained by an ideal quadrature detector after a beam splitter with the transmittance $\eta_{\mathrm{meas}}$. This enables us to characterize the complicated measurement chain as a single parameter of the measurement efficiency $\eta_{\mathrm{meas}}$. From the definition of the measurement efficiency, it can be understood as the occupancy of the vacuum noise in the input mode in the total measured noise. By using the typical parameters in the measurement chain, the measurement efficiency is calculated to be between $\eta_{\mathrm{meas}} = 0.94$ and $\eta_{\mathrm{meas}} = 0.56$. This shows that we are in a parameter region for quantum measurement of the quadrature of microwave photons. In addition, we find the measurement efficiency is mostly limited by the propagation loss between the quantum state emitter and the JPA.

## 8.3 Iterative maximum likelihood method

As explained in Sec. 3.3, the Wigner function can be reconstructed from the set of the quadrature distributions via the inverse Radon transformation. However, the statistical errors may cause unphysical results [57]. One of the good solutions is to use the maximum likelihood method. Since we confirmed that the set of the quadrature distributions contain the necessary information, the density matrix can be reliably reconstructed via the maximum likelihood method. Here, we adopt the iterative maximum likelihood method for the density matrix of a photonic mode [105]. Note that the maximum likelihood method always gives physical results, which prevents us from getting an artifact.

First of all, we explain the basic algorithms for the iterative maximum likelihood method. Suppose the density matrix $\hat{\rho}$ will be reconstructed from a set of the measurement outcomes $x_i$. The corresponding projection operator of $x_i$ is defined as $\hat{\Pi}_{x_i}$. $N$ and $f_i$ are the total number of measurements and the frequency of occurrences for $x_i$, respectively. Since the measurement probability of $x_i$ with a density matrix $\hat{\rho}_k$ can be obtained as

$P_{\hat{\rho}_k}(x_i) = \mathrm{Tr}\left[\hat{\Pi}_{x_i}\hat{\rho}_k\right]$, the likelihood function is defined as

$$\mathcal{L}(\hat{\rho}_k) = \prod_i P_{\hat{\rho}}(x_i)^{f_i} = \prod_i \mathrm{Tr}\left[\hat{\Pi}_{x_i}\hat{\rho}_k\right]^{f_i}. \tag{8.7}$$

Then, the density matrix which maximizes the likelihood function will be determined.

Given a density matrix of $\hat{\rho}_k$, a semi-positive definite matrix is defined as

$$\hat{R}(\hat{\rho}_k) = \frac{1}{N}\sum_i \frac{f_i}{P_{\hat{\rho}_k}(x_i)}\hat{\Pi}_{x_i}. \tag{8.8}$$

It is known that the density matrix $\hat{\rho}_\mathrm{m}$ which maximizes the likelihood function fulfills

$$\hat{R}(\hat{\rho}_\mathrm{m})\,\hat{\rho}_\mathrm{m}\,\hat{R}(\hat{\rho}_\mathrm{m}) \approx \hat{\rho}_\mathrm{m}. \tag{8.9}$$

This is because $\hat{\rho}_\mathrm{m}$ gives the closest measurement probability as $P_{\hat{\rho}_\mathrm{m}}(x_i) \approx f_i/N$, and then $\hat{R}(\hat{\rho}_m) \approx \sum_i \hat{\Pi}_{x_i} = \hat{1}$.

Based on this, the density matrix $\hat{\rho}_\mathrm{m}$ can be obtained as follows.

1. The maximally mixed state $\hat{\rho}_k = \mathcal{N}\left[\hat{1}\right]$ is prepared as an initial guess ($k = 0$).
2. The semi-positive definite matrix $R_k(\hat{\rho}_k)$ is calculated using the measurement outcomes and $\hat{\rho}_k$.
3. $\hat{\rho}_{k+1}$ is determined as $\hat{\rho}_{k+1} = \mathcal{N}\left[\hat{R}(\hat{\rho}_k)\,\hat{\rho}_k\,\hat{R}(\hat{\rho}_k)\right]$, where $\mathcal{N}$ describes the normalization.
4. Repeat the steps 2 and 3 until $\hat{\rho}_k$ converges to $\hat{\rho}_\mathrm{m}$.

In this way, we can obtain the density matrix which maximizes the likelihood function.

Here, the quadratures are measured for quantum state tomography of the microwave pulse modes. Although the projection operator can also be defined in the continuous variable basis, it is defined in the Fock basis for simplicity. Note that the cutoff photon number $n_c$ should be set to be large enough to describe the quantum state. Then, the quantum state can be described in the Fock basis as

$$\hat{\rho} = \sum_{n,m}^{n_\mathrm{c}} \langle n|\hat{\rho}|m\rangle\ |n\rangle\langle m| = \sum_{n,m}^{n_\mathrm{c}} \hat{\rho}_{nm}\ |n\rangle\langle m|, \tag{8.10}$$

where $|n\rangle$ is the Fock state and $\rho_{nm} = \langle n|\hat{\rho}|m\rangle$ is the element of the density matrix. The measurement outcomes of the quadrature can be labeled with the measured amplitude $x$ and the measurement phase $\theta$ as ($x$, $\theta$). The projection operator $\hat{\Pi}(x,\theta) = |x,\theta\rangle\langle x,\theta|$ is described in the Fock basis as

$$\begin{aligned}
\hat{\Pi}(x,\theta) &= \sum_{n,m}^{n_\mathrm{c}} \langle n|x,\theta\rangle\langle x,\theta|m\rangle\ |n\rangle\langle m| \\
&= \sum_{n,m}^{n_\mathrm{c}} \frac{e^{i(n-m)\theta}}{\sqrt{2^{n+m}n!m!\pi}} H_n(x)H_m(x)e^{-x^2}\ |n\rangle\langle m| \\
&= \sum_{n,m}^{n_\mathrm{c}} \Pi_{nm}(x,\theta)\ |n\rangle\langle m|,
\end{aligned} \tag{8.11}$$

where we use $\langle x,\theta|m\rangle = \langle x|\hat{R}(\theta)|m\rangle = \left(\frac{1}{\pi}\right)^{\frac{1}{4}} \frac{e^{-im\theta}}{\sqrt{2^m m!}} H_m(x) e^{-\frac{x^2}{2}}$. Moreover, the element of the projection operator is defined as $\Pi_{nm}(x,\theta) = \frac{e^{i(n-m)\theta}}{\sqrt{2^{n+m}n!m!\pi}} H_n(x)H_m(x)e^{-x^2}$. Thus, $\hat{R}(\hat{\rho})$ is simply obtained as

$$\hat{R}(\hat{\rho}) = \frac{1}{N}\sum_{(x,\,\theta)} \frac{1}{P_{\hat{\rho}_k}(x,\theta)} \hat{\Pi}(x,\theta), \tag{8.12}$$

where $P_{\hat{\rho}_k}(x,\theta) = \mathrm{Tr}[\hat{\Pi}(x,\theta)\,\hat{\rho}_k]$. Thus, we can perform the iterative algorithm in the Fock basis.

Furthermore, we can apply the maximum likelihood method for a quantum state in the presence of photon loss. As explained in Sec. 3.4.4, the photon loss can be characterized by the transmittance $\eta$ of the beam splitter transformation. When the transmittance $\eta$ is reliably determined, we can estimate the quantum state before the photon loss. According to the reference [106], the quantum state $\hat{\rho}$ is transformed by the photon loss as

$$\hat{\rho}' = \sum_{k=0}^{n_c} \hat{A}_k\,\hat{\rho}\,\hat{A}_k^\dagger, \tag{8.13}$$

where the Kraus operators describing the photon loss are defined as

$$\hat{A}_k = \sum_{n=k}^{n_c} \sqrt{\begin{pmatrix} n \\ k \end{pmatrix}} \sqrt{\eta}^{\,n-k} \sqrt{1-\eta}^{\,k} \,|n-k\rangle\langle n|. \tag{8.14}$$

Then, the measurement probability of $x$ is described as

$$\begin{aligned} P'_{\hat{\rho}}(x,\theta) &= \mathrm{Tr}\left[\hat{\Pi}(x,\theta)\hat{\rho}'\right] \\ &= \mathrm{Tr}\left[\hat{\Pi}(x,\theta)\left(\sum_{k=0}^{n_c}\hat{A}_k\,\hat{\rho}\,\hat{A}_k^\dagger\right)\right] \\ &= \mathrm{Tr}\left[\left(\sum_{k=0}^{n_c}\hat{A}_k^\dagger\,\hat{\Pi}(x,\theta)\,\hat{A}_k\right)\,\hat{\rho}\right] \\ &= \mathrm{Tr}\left[\hat{\Pi}'(x,\theta)\,\hat{\rho}\right], \end{aligned} \tag{8.15}$$

where a projection operator of $x$ for the density matrix with photon loss is defined as

$$\hat{\Pi}'(x,\theta) = \sum_{k=0}^{n_c} \hat{A}_k^\dagger\,\hat{\Pi}(x,\theta)\,\hat{A}_k. \tag{8.16}$$

Then, we can apply the maximum likelihood method in the presence of photon loss just by replacing $\hat{\Pi}(x,\theta)$ by $\hat{\Pi}'(x,\theta)$ in the iterative algorithm. As explained in Sec. 8.2, the measurement inefficiency can be modeled as photon loss. Therefore, using the iterative maximum likelihood method taking into account the photon loss, we can determine the density matrix with the correction of the measurement inefficiency.

## 8.4 Phase-sensitive linear amplification

Here, we explain how to measure quadratures of a pulse mode in the nearly quantum limit using a phase-sensitive amplifier, or, the JPA. The simplified measurement setup is shown in Fig. 8.2, and the sample is identical to that characterized in Chapter 6. Basically,

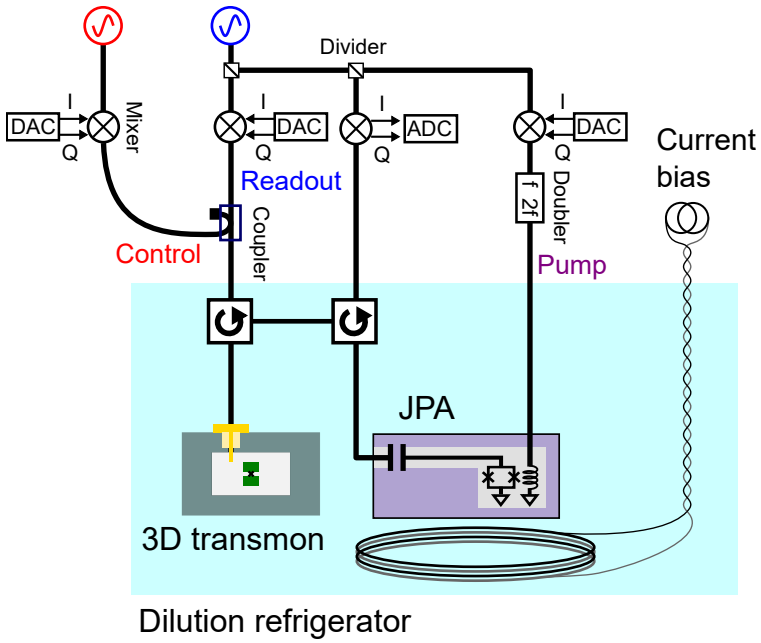


Figure 8.2: Simplified measurement setup for the quantum state tomography.

the way to amplify the pulse mode is the same as for the readout pulse, as explained in Sec. 6.2.1. However, we need to treat the amplification for the quadrature measurement more seriously. Note that the pulse distortion and the linearity of the gain are not critical for discrimination of the qubit state. Here, we focus on the amplification of a pulse mode of a Gaussian with a full width at half maximum amplitude of 500 ns.

First of all, we characterize the phase-sensitive amplifier using a coherent state as the input. A coherent state in a pulse mode can be generated by heavily attenuating a classical microwave pulse in the same temporal mode. After the optimization of the relative phase between the input coherent pulse and the pump pulse, the amplified coherent pulse is measured in time, as shown in Fig. 8.3(a). The pump amplitude is maximized to the extent that pulse distortion does not occur. We will confirm if the gain bandwidth is large enough to amplify the input pulse mode, later.

As explained in Sec. 5.7.1, the mode matching between the target pulse mode and a measurement pulse mode is critical. We use an identical pulse mode with the input as the measurement pulse mode. Now, since we have confirmed that the amplification does not cause the pulse distortion, the mode matching should be perfect. However, the pulse delay may be difficult to estimate from the experimental setup, thus, we optimize the relative time of the measurement pulse mode to maximize the measured amplitude, as shown in Fig. 8.3(b).

Next, we check the linearity of the phase-sensitive gain. We use a coherent state as the input again. We plot the measured amplitude of the pulse mode without the pump, as a function of the square root of the average photon number in the input pulse mode. Here, the average photon number is well calibrated from the cavity-drive-induced dephasing as discussed in Sec. 8.6.2. Note that the calibration is not so critical when the input average photon number is roughly within the range of that of the target state. Then, the signal which is amplified in a phase-sensitive manner is shown as a function of the relative pump phase, as shown in Fig. 8.4(b). The relative pump phase is chosen so that the signal can be amplified maximally. With the optimal pump phase, the amplified signal as a function of the square root of the average photon number is shown in Fig. 8.4(c). The

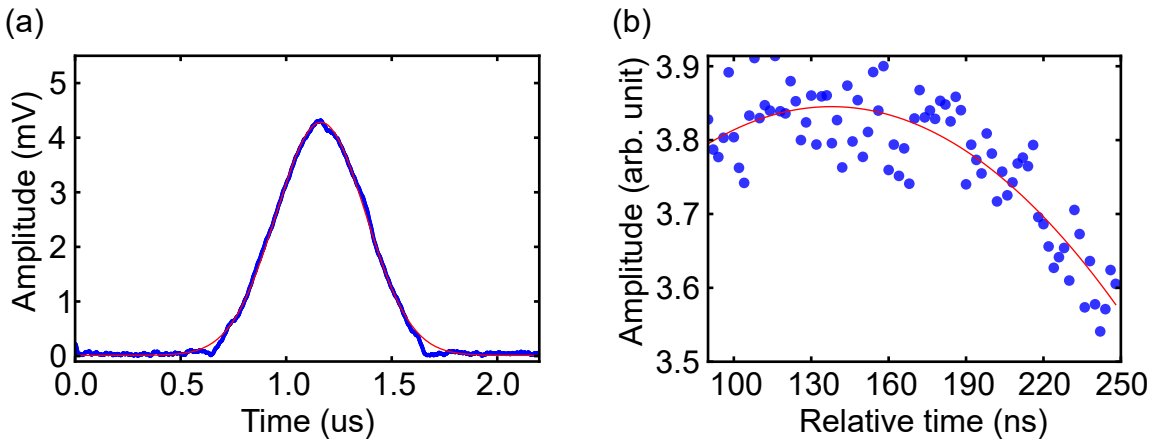


Figure 8.3: Amplified coherent pulse. (a) Amplified amplitude of a coherent pulse in time. The blue dots are the experimental results and the red line is the input pulse mode of a Gaussian with a full width at half maximum amplitude of 500 ns. (b) Amplitude as a function of the relative time between the signal and the measurement pulse mode. The blue dots and the red line are the experimental results and the polynomial function fit. The measurement pulse mode is set to be the same as the input.

magenta line is the linear fit in the weak amplitude limit. From this plot, we confirm that the JPA can linearly amplify the quadratures in this range. By calculating the square of the ratio of the amplitude with and without the pump, we obtain a gain of about 25 dB, as shown in Fig. 8.4(d). The gain of the phase-sensitive amplifier corresponds to 19 dB in the phase-insensitive amplifier. From the square root gain bandwidth product in Fig. 6.11 in Sec. 6.1.3, the gain bandwidth is calculated as about 5.9 MHz. On the other hand, the bandwidth of the input Gaussian pulse mode with a full width at half maximum amplitude of 500 ns is calculated as 1.25 MHz. Therefore, we confirm that the gain bandwidth is much broader than that of the input pulse mode.

Finally, we measure a vacuum noise to determine the scale of the quadratures. Here, the input state is set to be a vacuum, or no input of a coherent pulse. The complex amplitudes of the amplified vacuum noise, which are measured in a single shot with the identical gain and measurement pulse mode to be used for the Wigner tomography, are plotted in Fig. 8.5(a). The amplitude which is projected onto the axis of the phase-sensitive amplification corresponds to the quadrature of the pulse mode. The projection axis is determined so that the variance of the projected amplitudes is maximized. The projected amplitudes with the different pump phase are shown in Fig. 8.5(b). The complex amplitudes are measured $10^4$ times for each pump phase, which is swept from $-\pi$ to $\pi$, divided into 101 points. The probability density of the projected amplitudes with a pump phase of 0, shown in the right side of Fig. 8.5(b), is well fitted by a Gaussian, which shows that the vacuum noise is linearly amplified by the JPA. Therefore, we can determine the scale of the quadratures so that the variance can be the vacuum noise of 1/2, as explained in Sec. 8.2.

The average and variance of the projected amplitudes as a function of the pump phase are shown in Figs. 8.5(c) and (d). There is a finite offset in the average, which may be due to the leakage of a coherent tone. Moreover, the variance is drifting in time. This may be explained by the fact that the pump amplitude is varied in time due to a temperature drift. Therefore, we can correct the offset and the scaling of the quadrature by measuring the average and variance of the vacuum input as a reference at each pump phase of the

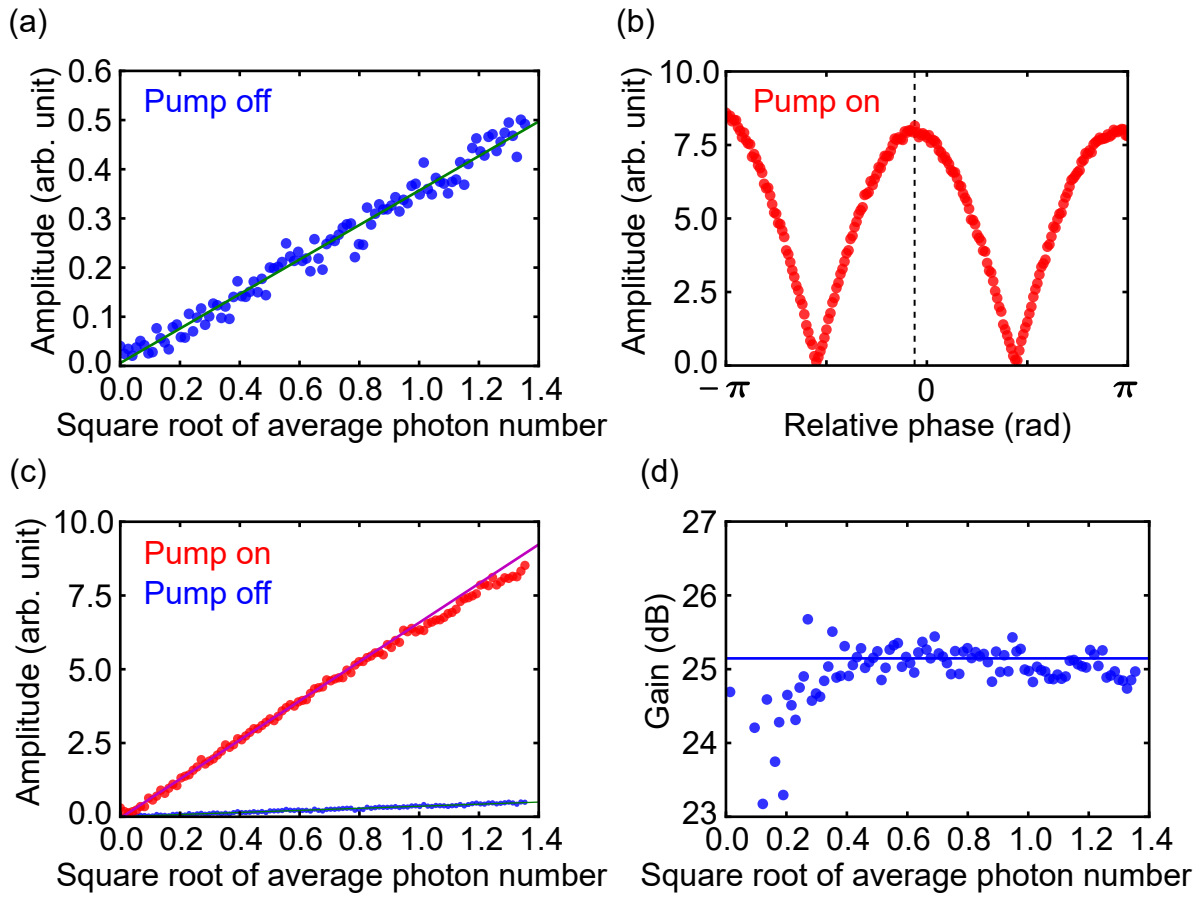


Figure 8.4: Linearity of the phase-sensitive gain by the JPA. (a) Signal without the pump as a function of the square root of the average photon number. The blue dots and the green line are the experimental results and the linear fit, respectively. (b) Amplified signal as a function of the relative pump phase. The black dotted line depicts the relative phase which gives the maximum gain. (c) Amplified signal as a function of the square root of the average photon number. The JPA amplifies the coherent pulse in a phase-sensitive manner. The blue and red dots are the experimental results with and without the pump, respectively. The lines are their corresponding linear fits. (d) Gain as a function of the square root of the average photon number. The horizontal line dipict the average of the gain.

quadrature measurement.

## 8.5 Wigner tomography

Here, we show a result of the iterative maximum-likelihood method based on the quadrature measurements. For the input state, we use a coherent state in a Gaussian pulse mode with a full width at half maximum amplitude of 500 ns. In our setup, shown in Fig. 8.2, the coherent state is reflected by the 3D cavity dispersively coupled to the transmon qubit. As a result, the coherent state can suffer dephasing due to thermal excitation of the qubit. Therefore, the qubit is initialized in the ground state by the non-destructive readout and the postselection, as explained in Sec. 6.2.6. The complex amplitudes of the target state and the vacuum state are measured in a single shot at each pump phase. The data of the vacuum state is used as the reference to obtain the quadrature of the target

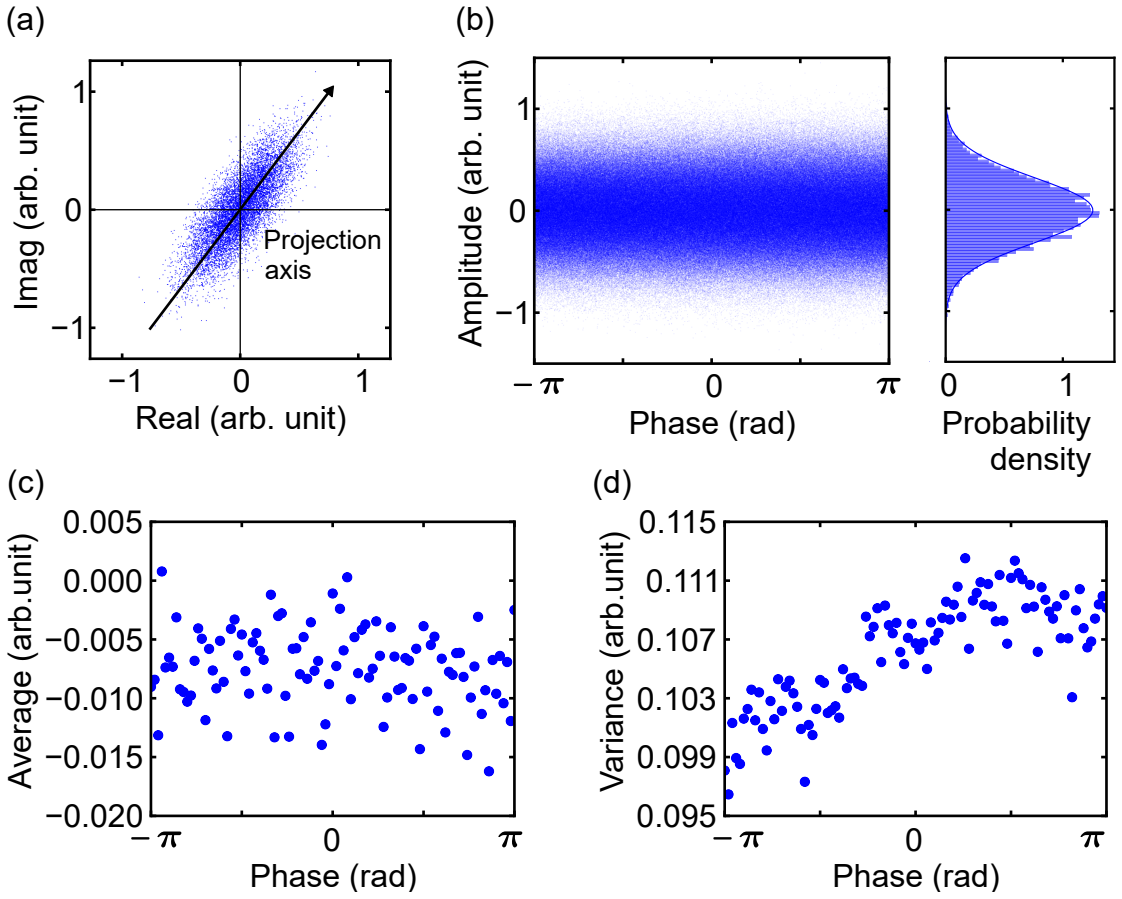


Figure 8.5: Phase-sensitively amplified vacuum noise. (a) Complex amplitudes of the vacuum noise which are amplified in a phase-sensitive manner by the JPA and are measured in a single shot. The complex amplitudes are projected onto the axis (arrow) of the phase-sensitive amplification. (b) Projected amplitudes measured at the various pump phases. The right plot shows the probability density of the projected amplitudes obtained with a pump phase of 0. The distribution is well fitted by a Gaussian (blue line). The variance is used to determine the scaling of the quadrature. (c) Average and (d) variance of the projected amplitude as a function of the pump phase. The average has an offset from zero and the variance is drifting in time. By measuring the average and the variance for each pump phase, the offset and the drifting variance are corrected for the quadrature measurement.

state as follows: The quadratures of the target pulse mode are obtained by projecting the corresponding complex amplitude onto the axis of the phase-sensitive amplification, subtracting the reference offset, and normalizing by the square root of the reference variance. The obtained quadratures are shown as a function of the pump phase in Fig. 8.6(a). The results can be intuitively interpreted as a coherent state or a vacuum state with a coherent displacement.

Using the quadratures at the various pump phases, the iterative maximum likelihood method to reconstruct a Wigner function is performed as explained in Sec. 8.3. The iterative algorithm is repeated $10^5$ times. There, we confirm that the density matrix in the iteration converged. The reconstructed Wigner function and photon-number distribution are shown in Figs. 8.6(b) and (c). The determined quantum state is found to be a coherent state with the average photon number of 0.058, with the fidelity of 0.998.

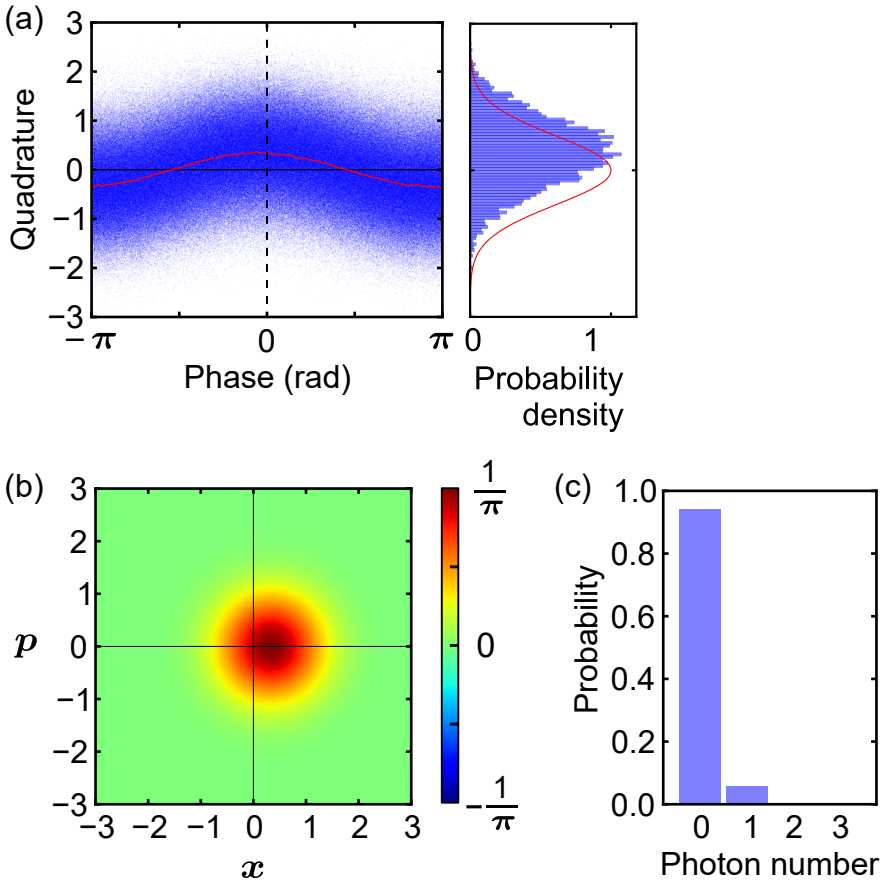


Figure 8.6: Wigner tomography of a coherent state. (a) Quadratures which are measured at each pump phase in a single shot. The blue dots are the experimental results. The red line is the average of the quadratures as a function of the pump phase. The blue bars in the right side shows a probability density of the quadrature at a pump phase of 0. The red line is the probability density of a vacuum state. The measured distribution is found to be a vacuum state with a displacement. (b) Wigner function which is reconstructed from the quadratures using the iterative maximum-likelihood method. (c) Photon number distribution of the reconstructed quantum state.

## 8.6 Calibration

As we will see later, the reconstructed quantum state undergoes photon loss in the measurement chain. When we intend to characterize the quantum state unaffected by the photon loss in the measurement chain, the maximum likelihood method with the correction of the measurement infidelity is useful. However, to determine the measurement inefficiency is very crucial to avoid the unfaithful estimation of a quantum state.

### 8.6.1 Validity of vacuum

If we suppose that the propagating mode in a thermal state is in the vacuum state by mistake, the maximum likelihood method with correction of the measurement inefficiency gives a wrong estimation of the quantum state. Therefore, it is crucial to confirm if the propagating mode is a vacuum state. Assuming that the propagating mode is in thermal equilibrium with the base temperature of the dilution refrigerator, it gives a vacuum state. However, it is not necessarily the case in the experimental setup since the propagating

mode is connected to devices at room temperature. Therefore, we experimentally determine the thermal average photon number in the propagating mode by measuring the thermal-photon-induced dephasing of the qubit.

The thermal photons in the cavity, which are coupled to the qubit dispersively, cause qubit dephasing. The thermal-photon-induced qubit depahsing rate can be described as

$$\gamma_{\phi,\mathrm{th}} = \frac{4\chi^2\kappa}{\kappa^2 + 4\chi^2} n_{\mathrm{th}}, \tag{8.17}$$

where $\chi$ is the dispersive shift, $\kappa = \kappa_{\mathrm{ex}} + \kappa_{\mathrm{in}}$ is the total relaxation rate of the cavity, $\kappa_{\mathrm{ex}}$ is the external coupling rate to the propagating mode which we are concerned with, $\kappa_{\mathrm{in}}$ is the internal loss rate, and $n_{\mathrm{th}}$ is the thermal average photon number in the cavity [68, 7]. The cavity parameters, which are experimentally obtained as in Sec. 6.2.6, are shown in Table 8.2.Furthermore, the thermal average photon number can be calculated as

$$n_{\mathrm{th}} = \frac{\kappa_{\mathrm{ex}}\, n_{\mathrm{th,ex}} + \kappa_{\mathrm{in}}\, n_{\mathrm{th,in}}}{\kappa_{\mathrm{ex}} + \kappa_{\mathrm{in}}}, \tag{8.18}$$

where $n_{\mathrm{th,ex}}$ and $n_{\mathrm{th,in}}$ are the thermal average photon number in the propagating mode and the internal loss mode, respectively.

Then, the total qubit dephasing rate can be represented as

$$\gamma_\phi = \frac{\gamma}{2} + \gamma_{\phi,\mathrm{n}} + \gamma_{\phi,\mathrm{th}} \tag{8.19}$$

where $\gamma_{\phi,\mathrm{n}}$ is the natural dephasing rate, and $\gamma$ is the energy-relaxation rate. The total dephasing rate and the energy-relaxation rate can be experimentally obtained and are displayed in Table 8.2.Here, we obtain the total dephasing rate using the echo sequence, which enables us to minimize the natural dephasing rate $\gamma_{\phi,\mathrm{n}}$.

Thus, we can determine the upper bound on the thermal average photon number of the propagating mode. Using Eqs. (8.17), (8.18), and (8.19), the thermal photon number can be described as

$$n_{\mathrm{th,ex}} = \frac{\kappa^2 + 4\chi^2}{4\chi^2\kappa_{\mathrm{ex}}} \left[ \left( \gamma_\phi - \frac{\gamma}{2} \right) - \gamma_{\phi,\mathrm{n}} \right] - \frac{\kappa_{\mathrm{in}}}{\kappa_{\mathrm{ex}}} n_{\mathrm{th,in}} \;\leq\; \frac{\kappa^2 + 4\chi^2}{4\chi^2\kappa_{\mathrm{ex}}} \left( \gamma_\phi - \frac{\gamma}{2} \right), \tag{8.20}$$

where we obtain the upper bound with $\gamma_{\phi,\mathrm{n}} = n_{\mathrm{th,in}} = 0$. Using the experimentally obtained parameters, shown in Table 8.2, the upper bound of $n_{\mathrm{th,ex}}$ can be calculated as $\max\left[n_{\mathrm{th,ex}}\right] = 0.0017$. Then, we confirm that the thermal average photon in the propagating mode can be negligible compared with the error bar of the efficiency of the quadrature measurement ($\eta_{\mathrm{meas}} = 0.43 \pm 0.01$).

### 8.6.2 Calibration of coherent state

As explained in Sec. 8.2, the inefficiency of the quadrature measurement can be modeled by a transmittance of $\eta_{\mathrm{meas}}$ of a beam splitter in front of an ideal quadrature detector [54].

Table 8.2: Cavity and qubit parameters.

| | | |
|---|---|---|
| Cavity external coupling rate | $\kappa_{\mathrm{ex}}/2\pi$ | 3.32 MHz |
| Cavity internal loss rate | $\kappa_{\mathrm{in}}/2\pi$ | 0.25 MHz |
| Cavity-qubit dispersive shift | $\chi/2\pi$ | 1.50 MHz |
| Qubit energy-relaxation rate | $\gamma/2\pi$ $(= 1/T_1\,/2\pi)$ | 5.0 kHz |
| Qubit total dephasing rate | $\gamma_\phi/2\pi$ $(= 1/T_{2\mathrm{E}}\,/2\pi)$ | 4.8 kHz |

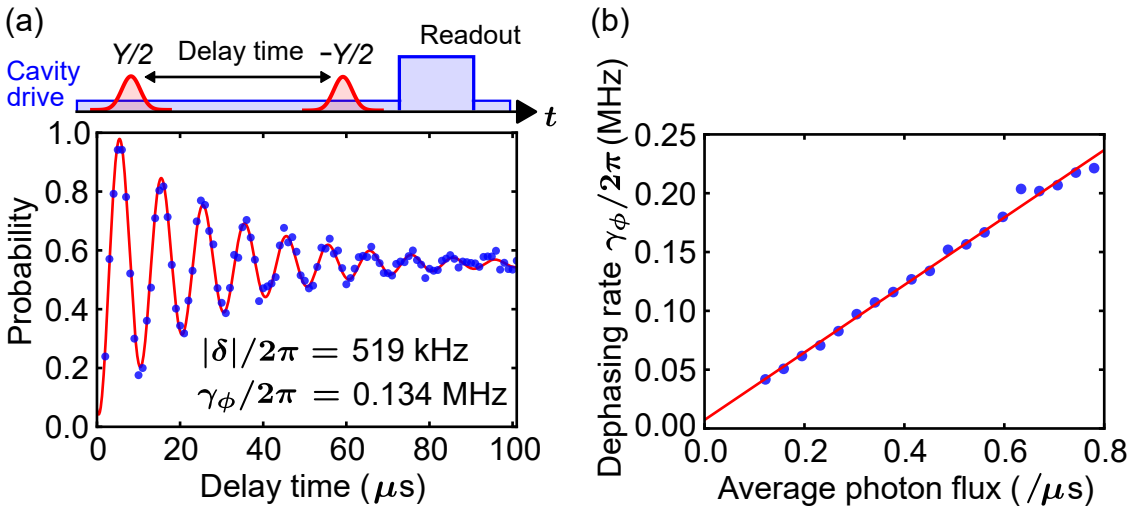


Figure 8.7: Cavity-drive-induced dephasing of the qubit. (a) Ramsey sequence with the cavity drive. (b) Qubit dephasing rate as a function of the flux of average photon number in the cavity drive. The blue dots and red lines are the experimental and fitting results, respectively. The offset is attributed to the pure dephasing of the qubit.

Suppose we have a coherent state of $|\alpha\rangle$ as an input for Wigner tomography. Then the quantum state reconstructed from the inefficient quadrature measurement can be described as $|\alpha'\rangle = \left|\sqrt{\eta_{\rm meas}}\alpha\right\rangle$. Therefore, the measurement efficiency can be simply obtained by calculating the ratio of the average photon number of the reconstructed coherent state to that of the input as

$$\eta_{\rm meas} = \frac{|\alpha'|^2}{|\alpha|^2}. \tag{8.21}$$

In other words, it is imperative to calibrate the coherent state in the input pulse mode in order to determine the measurement efficiency. Here, we calibrate the flux of the average photon number in a coherent drive for the 3D cavity by measuring the cavity-drive-induced qubit dephasing.

A coherent drive for the cavity is characterized by a photon flux $\dot{n}_{\rm d}$, which is defined as the average photon number of the continuous coherent drive passing through per unit time. To determine the photon flux $\dot{n}_{\rm d}$ reaching the cavity, we measure the dephasing rate of the qubit in a cavity that is driven continuously with the coherent microwaves. As shown in Fig. 8.7(a), a Ramsey sequence under the continuous cavity drive is performed to measure the cavity-drive-induced dephasing rate of the qubit. The dephasing rate as a function of the photon flux $\dot{n}_{\rm d}$ of the continuous coherent drive is shown in Fig. 8.7(b), where the cavity-drive frequency $\omega_{\rm d}$ is fixed closely to the cavity frequency $\omega_{\rm c}$. Here, we just confirm that the dephasing rate is proportional to the square of the input amplitude, and obtain the slope by fitting the experimental results with a linear function. Theoretically, the cavity-drive-induced dephasing rate is described as

$$\gamma_{\phi,{\rm d}} = \frac{\kappa\,\chi^2}{\kappa^2/4+\chi^2+\Delta_{\rm d}^2}(\overline{n}_+ + \overline{n}_-), \tag{8.22}$$

where $\Delta_{\rm d} = \omega_{\rm d} - \omega_{\rm c} = 0.16$ MHz is the detuning, and $\overline{n}_\pm = \frac{\kappa_{\rm ex}}{\kappa^2/4+(\Delta_{\rm d}\pm\chi)^2}\,\dot{n}_{\rm d}$ is the average photon number in the cavity with the qubit in the ground state or in the excited state [17]. By comparing the slope [red line in Fig. 8.7(b)] of the experimental results with that of

Eq. (8.22), we calibrate the photon flux $\dot{n}_{\rm d}$ at the cavity. Then, we determine a coherent state $|\alpha\rangle$ in an input pulse mode by integrating the photon flux $\dot{n}_{\rm d}$ with the temporal mode function as

$$|\alpha|^2 = \int dt\, |m(t)|^2\, \dot{n}_{\rm d} = \int dt\, |f(t)|^2\, \dot{n}_{\rm d}, \tag{8.23}$$

where $m(t) = f(t)e^{-i\omega_{\rm d}t}$ is a pulse mode with a carrier frequency of $\omega_{\rm d}$ and $f(t)$ is the temporal mode function.

### 8.6.3 Measurement efficiency

Here, we calibrate the efficiency of the quadrature measurement based on the phase-sensitive amplification.

To calibrate $\eta_{\rm meas}$, we measure a coherent state in the pulse mode reflected by the cavity with the qubit being in the ground state. An input coherent state $|\alpha_{\rm in}\rangle$ before the reflection is calibrated by the qubit dephasing induced by a coherent drive (see Sec. 8.6.2). We denote the average photon number in the input coherent pulse as $|\alpha_{\rm in}|^2 = \int d\omega\, |\alpha_{\rm in}\, m_{\rm in}(\omega)|^2$, where $m_{\rm in}(\omega)$ is the input pulse mode in the frequency space, or the Fourier transform of the input pulse mode in time. Furthermore, the cavity parameters are determined from independent measurements. Thus, the output coherent state in the reflected pulse mode can also be characterized. Denoting the average photon number in the reflected pulse as $|\alpha_{\rm out}|^2$, we derive from the input-output theory

$$|\alpha_{\rm out}|^2 = \int d\omega\, \frac{\frac{(\kappa_{\rm ex}-\kappa_{\rm in})^2}{4} + [\omega - (\omega_{\rm c}+\chi)]^2}{\frac{(\kappa_{\rm ex}+\kappa_{\rm in})^2}{4} + [\omega - (\omega_{\rm c}+\chi)]^2}\, |\alpha_{\rm in}\, m_{\rm in}(\omega)|^2. \tag{8.24}$$

In the experiment, we use an input coherent pulse with $|\alpha_{\rm in}|^2 = 0.165 \pm 0.003$. Note that the pulse mode is a Gaussian with a full width at half maximum amplitude of 500 ns. From Eq. (8.24), we obtain $|\alpha_{\rm out}|^2 = 0.137 \pm 0.003$. The well-calibrated coherent state in the reflected pulse mode can be an input state for the quadrature measurement chain. Therefore, we perform Wigner tomography for this input state to calibrate the efficiency of the quadrature measurement, as explained in Sec. 8.3. The Wigner function and the photon-number distribution of the determined quantum state are shown in Fig. 8.6. The reflected pulse mode is in a coherent state with an average photon number $|\alpha'_{\rm out}|^2 = 0.058$, with an fidelity of 0.998. Following Eq. 8.21, we can determine the measurement efficiency by comparing the average photon numbers between the ideal and measured ones as $\eta_{\rm meas} = |\alpha'_{\rm out}|^2/|\alpha_{\rm out}|^2 = 0.43 \pm 0.01$.

## 8.7 Wigner tomography with loss correction

Here, we perform the iterative maximum likelihood method with correction of measurement inefficiency. For simplicity, the input state is also a coherent state with a Gaussian pulse mode. Therefore, for the Wigner tomography with correction of the measurement inefficiency, we use the same experimental results of the quadrature measurement, which are shown in Fig. 8.6. Using a measurement efficiency of 0.43, a quantum state is obtained through the procedure which is explained in Sec. 8.3, as shown in Fig. 8.8. It corresponds to a coherent state with an average photon number of 0.137, with a fidelity of 0.995. We confirm that the correction process is accurately performed by comparing the average photon numbers of the coherent states reconstructed with and without the loss correction.

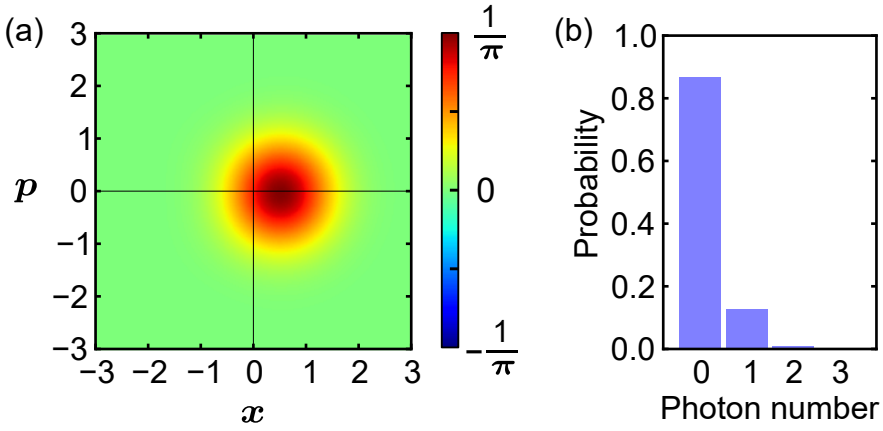


Figure 8.8: Wigner tomography of a coherent state with correction of the measurement inefficiency. (a) Reconstructed Wigner function. (b) Reconstructed photon-number distribution.

# Chapter 9

# Quantum non-demolition (QND) detection

## 9.1 Introduction

Photon detectors are elementary tools used to measure electromagnetic waves at the quantum limit [56, 41] and are heavily demanded in emerging quantum technologies such as communication [31], sensing [107], and computing [108]. Of particular interest is a quantum non-demolition (QND) type detector, which projects an electromagnetic wave onto the photon-number basis [109, 110, 111, 112, 113]. This is in stark contrast to conventional photon detectors [111] which absorb a photon to trigger a 'click'. The long-sought QND detection of a flying photon was recently demonstrated in the optical domain using a single atom in a cavity [114, 115]. However, the counterpart for microwaves has been elusive despite the recent progress in microwave quantum optics using superconducting circuits [19, 21, 116, 102, 34, 117, 95]. Here, we implement a deterministic entangling gate between a superconducting qubit and an itinerant microwave photon reflected by a cavity containing the qubit. Using the entanglement and a high-fidelity qubit readout, we demonstrate QND detection of a single photon with a quantum efficiency of 0.84 and a photon survival probability of 0.87. Our scheme can be a building block for quantum networks connecting distant qubit modules as well as a microwave photon counting device for multiple-photon signals.

Microwave quantum optics in superconducting circuits enables us to investigate unprecedented regimes of quantum optics. The strong nonlinearity brought by Josephson junctions together with the strong coupling of the qubits with resonators/waveguides reveals rich physics not seen in the optical domain before. It has also been applied in demonstrations of the generation and characterization of non-classical states in cavity modes [19, 21, 116] and propagating modes [102, 34] as well as the remote entanglement of localized superconducting qubits [117, 95]. However, single-photon detection in the microwave domain is still a challenging task because microwave photon energy is four to five orders of magnitude smaller than in optics. The sensitivities of conventional incoherent detectors such as avalanche photodiodes, bolometers, and superconducting nanowires are not sufficient for single microwave photons [41]. Therefore, resonant absorption of a microwave photon with a superconducting qubit was exploited for single-photon detection [38, 39, 40]. Note also that QND measurements of cavity-confined microwave photons have been realized by using a Rydberg atom or a superconducting qubit as a probe [118, 22]. Recently, a QND detection of an itinerant microwave photon have been demonstrated using a circuit QED system with the same kind of interaction [119], as used in the scheme in the optical frequency domain [114].

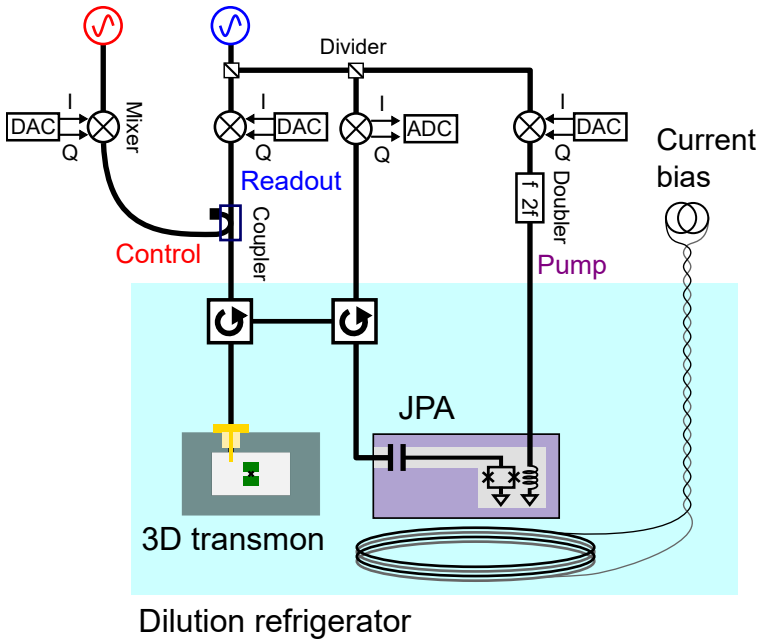


Figure 9.1: Simplified measurement setup for the QND detection of an itinerant microwave photon. A transmon qubit is mounted in a 3D superconducting cavity that is over-coupled to a 1D transmission line composed of a coaxial cable. An input pulse mode is injected into the cavity through the cable, and the reflected pulse mode is guided via circulators to a JPA and a heterodyne detector. Qubit control and readout pulses follow the same path.

## 9.2 Detection scheme

For QND detection of an itinerant microwave photon, we use a circuit QED architecture with a transmon qubit in a far detuned 3D cavity [23]. An input pulse mode through a 1D transmission line to the cavity is entangled with the qubit upon reflection [120] and is projected to a number state by the subsequent qubit readout without destroying the photon.

In our setup, the qubit-cavity interaction is described with the dispersive Hamiltonian

$$\mathcal{H}/\hbar = \omega_{\rm c}\hat{a}^\dagger\hat{a} + \frac{\omega_{\rm q}}{2}\hat{\sigma}_z - \chi\hat{a}^\dagger\hat{a}\,\hat{\sigma}_z, \tag{9.1}$$

where $\hat{a}^\dagger(\hat{a})$ is the creation (annihilation) operator of the cavity mode, $\hat{\sigma}_z$ the Pauli operator of the transmon qubit, $\omega_{\rm c}$ the cavity resonance frequency, $\omega_{\rm q}$ the qubit resonance frequency, and $\chi$ the dispersive shift due to the interaction. As explained in Chapter 6, the system parameters are determined from independent measurements as follows: the cavity resonance frequency $\omega_{\rm c}/2\pi = 10.62524$ GHz, the qubit resonance frequency $\omega_{\rm q}/2\pi = 7.8693$ GHz, the dispersive shift $\chi/2\pi = 1.50$ MHz, the cavity external coupling rate $\kappa_{\rm ex}/2\pi = 3.32$ MHz, the cavity internal loss rate $\kappa_{\rm in}/2\pi = 0.25$ MHz, the qubit relaxation time $T_1 = 32$ $\mu$s, the qubit dephasing time $T_2^* = 26$ $\mu$s, and the echo dephasing time $T_{2\rm E} = 33$ $\mu$s. We control the qubit state with a Rabi oscillation driven by a resonant pulse and read out the qubit nondestructively by observing the dispersive shift of the cavity frequency. A readout pulse reflected by the cavity is led to a flux-driven Josephson parametric amplifier (JPA) [52] and is measured in the quadrature by a heterodyne detector. The nearly quantum-limited amplifier enables us to read out the qubit state in a single shot. The qubit readout fidelity of the ground state (excited state) is better than

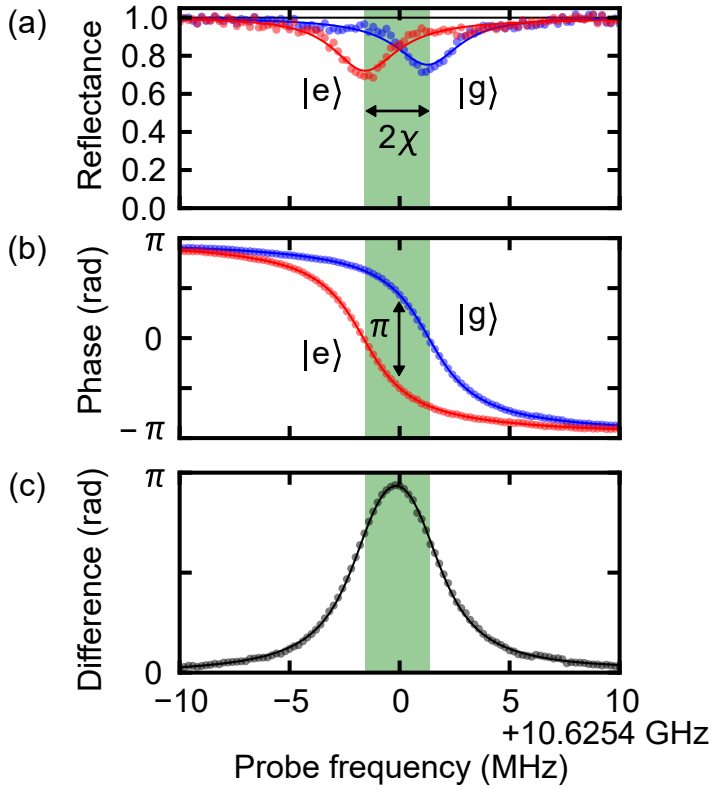


Figure 9.2: Cavity spectrum depending on the qubit state. (a) Reflectance (squared amplitude) and (b) phase shift of the cavity reflection coefficient as a function of the probe frequency, with the qubit being in the ground state (blue) or the excited state (red). The qubit is prepared in each state by postselection according to the outcomes of the single-shot readouts before and after the cavity probe. (c) Phase difference between the cavity with the qubit in the ground and excited states. The phase difference at the cavity frequency $\omega_c/2\pi = 10.62524$ GHz is found to be close to $\pi$. The dots are the experimental results and the lines are the theoretical fits.

0.998 (0.978). The assignment fidelity of $0.988 \pm 0.001$ is calculated as the average of the two [81]. Since there is a finite excitation probability of the qubit of 0.067 in thermal equilibrium, the qubit is initialized via the qubit readout and postselection with a fidelity better than 0.998.

The interaction between an itinerant microwave field and the superconducting qubit through the cavity is first characterized by the cavity reflection of weak continuous microwaves. Figure 9.2(a) shows the cavity spectra, with the qubit being in the ground state $|\mathrm{g}\rangle$ (blue) or the excited state $|\mathrm{e}\rangle$ (red). The cavity spectrum is measured by conditioning the qubit state with postselection according to the outcomes of the qubit readouts before and after the cavity probe pulse (see Sec. 6.2.6). The dispersive shift of the cavity frequency is observed in accordance with Eq. (9.1). The reflected field obtains a phase shift depending on the qubit state. The conditional phase shift is described as the phase difference of the reflection coefficients, as shown in Fig. 9.2(c). This interaction has been conventionally used for nondestructive readout of a transmon qubit.

The phase-shift condition also holds for a pulse mode as long as its spectral bandwidth fits inside the cavity bandwidth. In other words, when the phase difference within the spectral bandwidth of the pulse mode can be constant, the pulse mode can obtain the qubit-dependent phase shift without pulse distortion. Here, we are interested in the

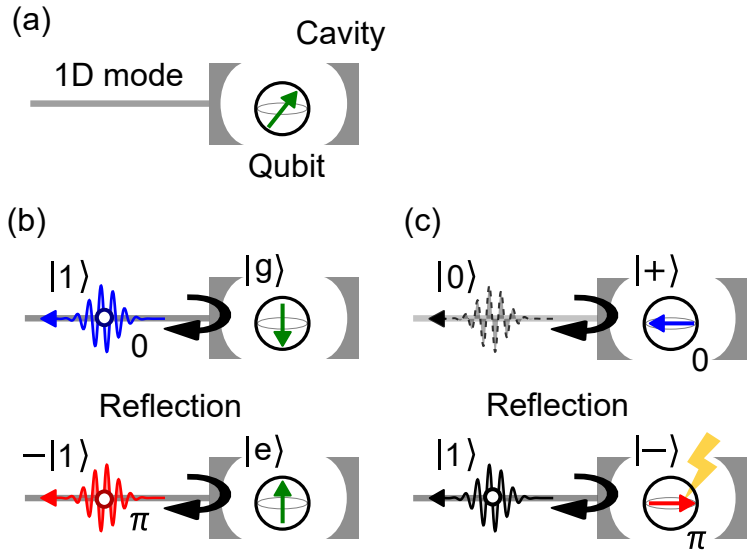


Figure 9.3: Interaction between the qubit and an itinerant microwave photon. (a) Schematic of the circuit QED system which is connected to a one-dimensional transmission line mode. (b) Phase flip (no flip) of the reflected single photon caused by the qubit in the excited state (ground state). (c) Phase flip (no flip) of the qubit caused by the reflection of the single photon (zero photon). Here, $|\mathrm{g}\rangle$ and $|\mathrm{e}\rangle$ label the ground and exited states of the qubit, and $|\pm\rangle$ is the superposition state $\frac{1}{\sqrt{2}}(|\mathrm{g}\rangle \pm |\mathrm{e}\rangle)$. $|0\rangle$ and $|1\rangle$ indicate the photon-number states in the pulse mode.

conditional phase shift of $\pi$ with as an interaction bandwidth as large as possible. With the optimal configuration where the external coupling rate of the cavity $\kappa_{\mathrm{ex}}$ is adjusted to twice the dispersive shift, $2\chi$, the qubit-dependent phase shift [phase difference in Fig. 9.2(c)] of the reflected field is close to $\pi$ within the larger bandwidth centered at the cavity frequency $\omega_{\mathrm{c}}$ (green region in Fig. 9.2). We achieve the optimal condition by adjusting the external coupling rate of the 3D cavity at room temperature to twice the dispersive shift, which has been measured at the base temperature of the dilution refrigerator.

Next, we explain how an itinerant photon interacts with the qubit through the cavity mode. The circuit QED system connected to a 1D transmission line is schematically shown in Fig. 9.3(a). A single photon in the reflected pulse mode acquires a $\pi$-phase shift conditioned on the excited state of the qubit [Fig. 9.3(b)], while maintaining the temporal and spatial mode shapes. It corresponds to a controlled-$Z$ gate between the superconducting qubit and the pulse mode. Because of the symmetry between the control and target qubits in a controlled-$Z$ gate, the interaction can also be interpreted as a phase-flip gate of the qubit induced by the reflection of the single photon [Fig. 9.3(c)]. There is a trade-off between the quantum efficiency of the single-photon detection (the fidelity of the controlled-$Z$ gate) and the detection (interaction) bandwidth. A longer single-photon pulse acquires a more ideal phase flip at the cost of increased qubit decoherence. We optimize the input pulse length in terms of the quantum efficiency (see Sec. 9.3).

The protocol for the QND detection of an itinerant photon is shown in Figs. 9.4(a) and (b).

(i) The qubit is initialized to the ground state $|\mathrm{g}\rangle$ via nondestructive readout and postselection. The input state of the microwave pulse mode is a coherent state in the weak power limit with the single-photon occupancy $p_1$, which well approximates

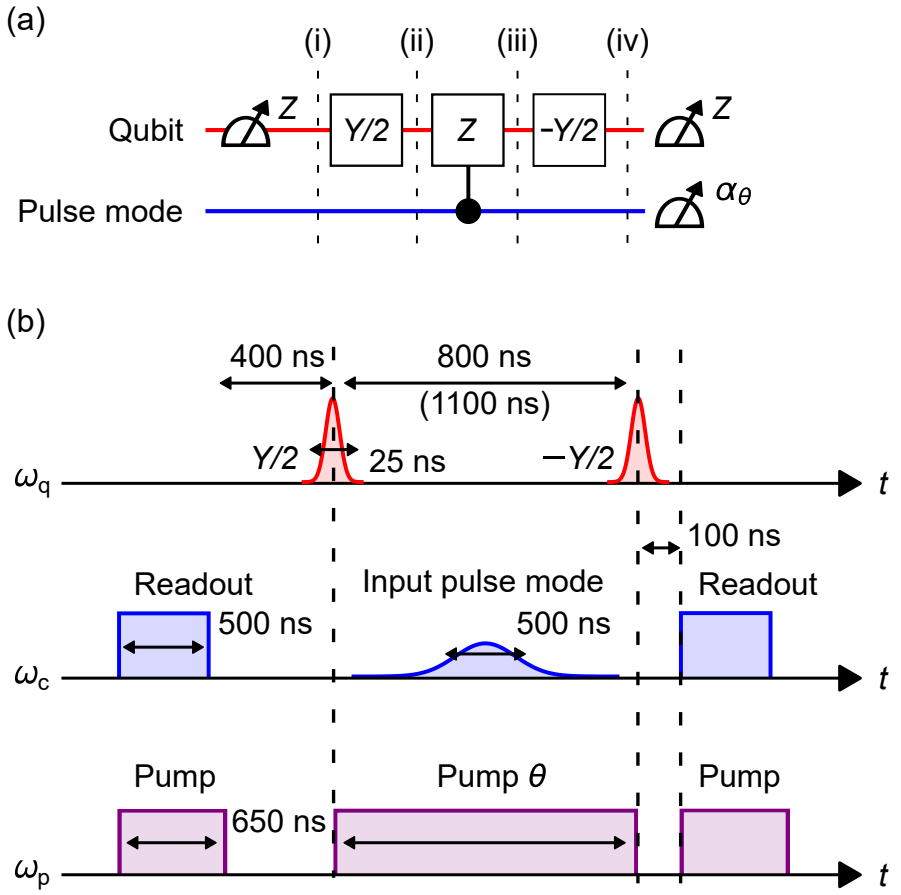


Figure 9.4: QND detection of an itinerant microwave photon. (a) Quantum circuit diagram of the protocol. The qubit is first read out for the initialization with postselection. Then, a Ramsey sequence, consisting of $Y/2$ and $-Y/2$ rotations and a $Z$-basis readout, is applied to detect the phase flip of the qubit induced by a single photon. For the quantum state tomography of the pulse mode, the quadrature $\alpha_\theta$ of the reflected pulse mode is measured with various phases $\theta$. (b) Corresponding pulse sequences at the qubit, cavity, and JPA pump frequencies, $\omega_\mathrm{q}$, $\omega_\mathrm{c}$, and $\omega_\mathrm{p}$, respectively. The pulse lengths for the qubit control and readout are 25 ns and 500 ns, respectively. The length of the JPA pump pulse accompanying the qubit readout pulse is 650 ns. The amplitude envelope of the input pulse mode is defined to be a Gaussian with a full width at half maximum of 500 ns. The gate intervals of the Ramsey sequence are set to 800 ns for the evaluation of the quantum efficiency, and to 1100 ns for the quantum state tomography of the reflected pulse mode in order to avoid overlap with the readout pulse.

a superposition of the vacuum and single-photon states, $\sqrt{p_0}|0\rangle + \sqrt{p_1}|1\rangle$.

(ii) The qubit state is rotated by $\pi/2$ about the $Y$-axis and the composite system becomes $|+\rangle(\sqrt{p_0}|0\rangle + \sqrt{p_1}|1\rangle)$.

(iii) The pulse mode is reflected by the cavity, and the state after the controlled-$Z$ gate becomes entangled, $\sqrt{p_0}|+\rangle|0\rangle + \sqrt{p_1}|-\rangle|1\rangle$.

(iv) The qubit is rotated by $-\pi/2$ about the $Y$-axis to obtain $\sqrt{p_0}|\mathrm{g}\rangle|0\rangle + \sqrt{p_1}|\mathrm{e}\rangle|1\rangle$ and is then measured in the $Z$ basis. The presence of a single photon in the pulse mode is correlated with the excited state of the qubit and is detectable.

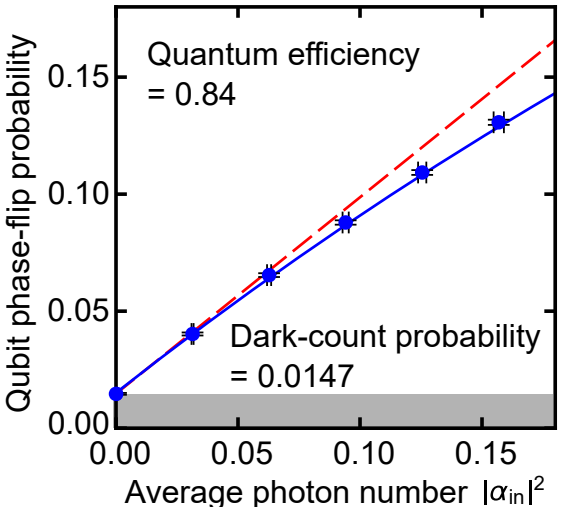


Figure 9.5: Phase-flip probability of the qubit as a function of the average photon number $|\alpha_{in}|^2$ in the input pulse. The blue dots represent the experimental data, while the blue solid line is the numerical calculation using independently obtained parameters (see Appendix. C). The red dashed line is the linear fit in the weak power limit. The error bars on the data points are the standard deviations from the mean.

To achieve a high quantum efficiency for the QND detection, there are two required conditions. First, the cavity should be over-coupled to the 1D transmission line, or the internal loss rate of the cavity should be much smaller than the external coupling rate as $\kappa_{in} \ll \kappa_{ex}$. In the optimal condition, the itinerant photon reflected by the cavity can obtain the maximum conditional phase shift $\pi$, while the photon absorbed in the cavity aquires a different conditional phase shift smaller than $\pi$, which causes an incomplete phase-flip of the qubit. In our sample, $\kappa_{in}/\kappa_{ex} = 0.075$ is achieved. Second, the qubit dephasing rate should be much smaller than the detection bandwidth as $\gamma_\phi \ll \kappa_{ex} = 2\chi$. For QND detection, the qubit should keep its coherence during the interaction with the itinerant photon. The qubit dephasing causes dark counts, as well as a drop in the quantum efficiency because of the reduced visibility. We achieve $\gamma_\phi/\kappa_{ex} = 0.0018$.

## 9.3 Quantum efficiency of QND detection

The calibration of the average photon number in the input pulse mode reaching the detector or the circuit QED system is crucial to evaluate the quantum efficiency. We calibrate the photon flux of a continuous cavity drive by measuring the cavity-drive-induced dephasing rate of the qubit [17], from which we calculate the average photon number $|\alpha_{in}|^2$ by integrating the photon flux within the input temporal mode (see Sec. 8.6.2).

The phase-flip probability of the qubit as a function of the average photon number $|\alpha_{in}|^2$ in the input pulse is shown in Fig. 9.5. To obtain the probability, the sequence is repeated $10^5$ times for each input average photon number. The phase-flip probability is increased as the input average photon number increases, which apparently shows that the qubit detects itinerant photons. The slight deviation from the linear relationship is due to the two-photon occupation in the pulse mode since a coherent state is used for the input. Since the quantum efficiency corresponds to the slope in the weak average photon number limit, it is determined by fitting the experimental results with a quadratic function and evaluating the differential coefficient at $|\alpha_{in}|^2 = 0$. Then, the quantum efficiency is found

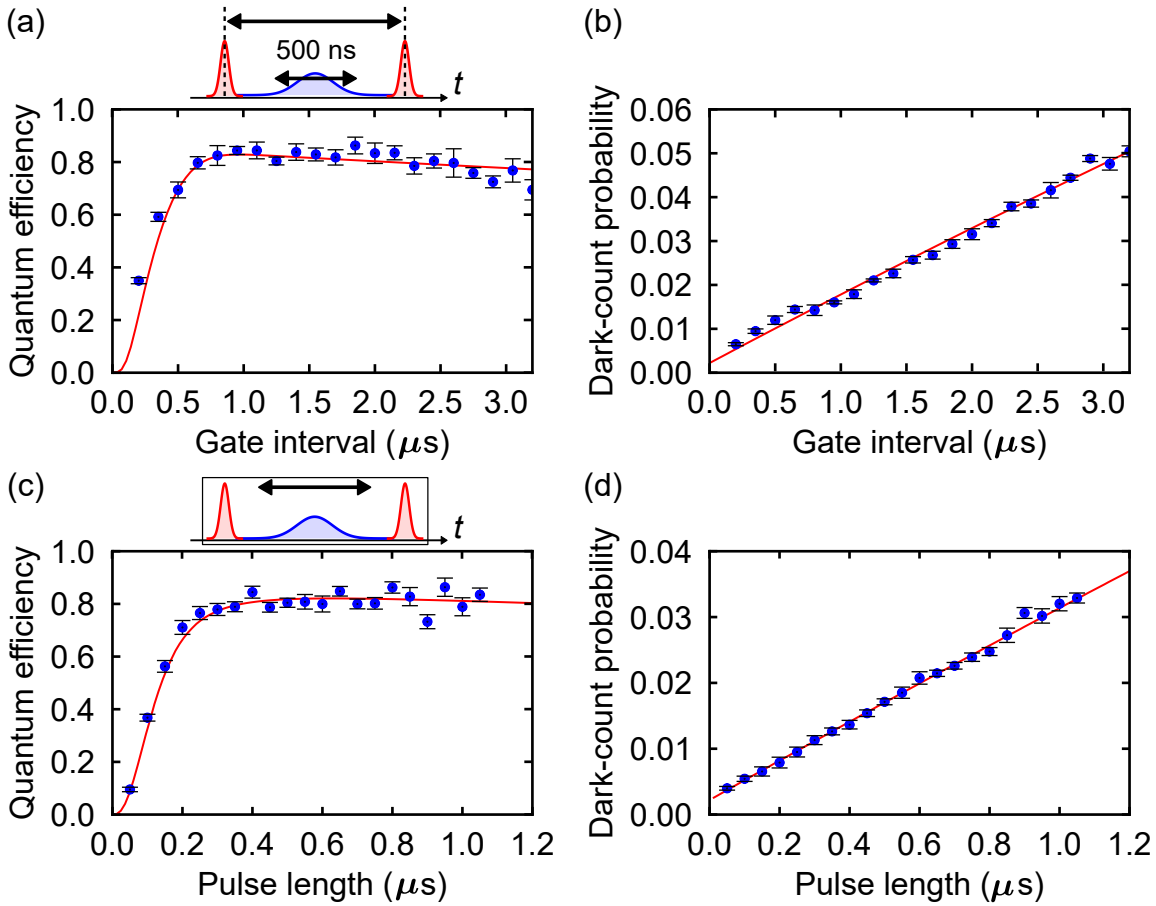


Figure 9.6: Dependence of gate interval and input pulse length on QND detection. (a) Gate interval dependence of the quantum efficiency and (b) the dark-count probability. (c) Pulse length (FWHM in amplitude) dependence of the quantum efficiency and (d) the dark-count probability. The blue dots are the experimental results and the red lines are the numerical calculations without free parameters. The error bars on the data points include the fitting error and the uncertainty of the input average photon number. We determine the qubit natural dephasing rate $\gamma_{\phi,\mathrm{n}}$ by fitting the dark-count probability. The value of $\gamma_{\phi,\mathrm{n}}$ slowly fluctuates by $\sim 10\%$ on the time scale of a few days.

to be $0.84 \pm 0.02$.

The reduction of the efficiency from unity is attributed to a few mechanisms. The quantum efficiencies reduced by each factor, which are obtained from the numerical calculations, are listed in Table 9.1. First, an input photon is probabilistically absorbed in the cavity due to the finite internal loss rate, which gives rise to an incomplete phase flip. Second, the qubit dephasing during the gate interval results in an erroneous phase

Table 9.1: Quantum efficiencies decreased by each factor.

| | |
|---|---|
| Internal loss of the cavity | 0.93 |
| Qubit dephasing | 0.96 |
| Initialization and readout errors | 0.98 |
| Mismatch of $\kappa_{\mathrm{ex}}$ and $2\chi$ | 0.99 |
| Detection bandwidth | 0.99 |

flip of the qubit. Third, the initialization and readout errors also result in a state flip of the qubit. Fourth, the external coupling rate is not perfectly adjusted to twice the dispersive shift ($\kappa_{\rm ex}/2\chi = 1.1$), which causes the incomplete phase flip of the qubit. Last, the finite bandwidth of the detection results in the incomplete phase flip of the qubit. In our sample, the internal loss of the cavity limits the quantum efficiency dominantly.

Furthermore, the dark count is also one of the characteristic parameters for photon detection. Here, the dark-count probability corresponds to the phase-flip probability in the absence of any input signal, which is found to be $0.0147 \pm 0.0005$. The dark count is caused by the qubit dephasing during the detection.

Here, we study the dependencies of the gate interval and the input pulse length on the quantum efficiency and the dark-count probability of QND detection.

First, the $\pi/2$-gate interval is varied as shown in Figs. 9.6(a) and (b), where a coherent Gaussian pulse with a pulse length (a full width at half maximum amplitude) of 500 ns is used as an input. The bandwidth of the input pulse is set to be narrow enough to be reflected by the cavity without noticeable temporal/spectral mode distortion. When the gate interval is shorter than the input-pulse length, the quantum efficiency is reduced since the qubit can interact with the itinerant photons only when it is in the superposition state. The quantum efficiency increases up to the gate interval comparable with the pulse length, and then decreases for a gate interval longer than the pulse length. The longer the gate interval, the more phase-flip errors due to the dephasing occur, resulting in a decrease of the quantum efficiency. From the experiment, we determine an optimized gate interval of 800 ns for the input-pulse length of 500 ns. Namely, the gate interval should be set to be 8/5 times longer than the input pulse length.

Next, we study the input-pulse length dependence on the quantum efficiency and the dark-count probability, as shown in Figs. 9.6(c) and (d). The gate interval is set to be 8/5 times longer than the input pulse length, as discussed in Figs. 9.6(a) and (b). Since the bandwidth in which the reflected pulse mode acquires the phase flip without pulse distortion corresponds to that of the cavity, the qubit cannot efficiently detect a single photon with a larger bandwidth. The quantum efficiency rises up at about 50 ns, which corresponds to the cavity relaxation time of $1/\kappa$. A single photon with a narrow bandwidth interacts with the qubit ideally, while the longer gate interval causes the dephasing of the qubit, resulting in a decrease of the quantum efficiency again. To sum up, the QND detection can detect an itinerant photon regardless of pulse form, as long as the bandwidth is smaller than the cavity bandwidth.

## 9.4 Wigner tomography of reflected pulse mode

To verify the QND property of the photon detector, we analyze the reflected pulse mode by using Wigner tomography via quadrature measurements. We measure the quadrature $\alpha_\theta$ of the reflected pulse mode, which is amplified by the phase-sensitive amplifier (JPA) with various pump phases $\theta$. The large gain and small added noise by the JPA in the quadrature measurement suppress the effect of the imperfections in the measurement chain following the JPA [33], which enables us to realize the quadrature measurement in the near quantum limit. As explained in Chapter 8, the remaining propagation loss and Gaussian noise can be modeled with the insertion of a beam splitter with a transmittance $\eta_{\rm meas}$ in front of an ideal quadrature detector [54]. From the calibration with a weak coherent pulse (see Sec. 8.6.2), the measurement efficiency is found to be $\eta_{\rm meas} = 0.43 \pm 0.01$. Using the outcomes of the quadrature measurement, we reconstruct the quantum state with the iterative maximum likelihood method [105]. Here, we show the quantum states which are reconstructed without or with correction for the inefficiency of the quadrature

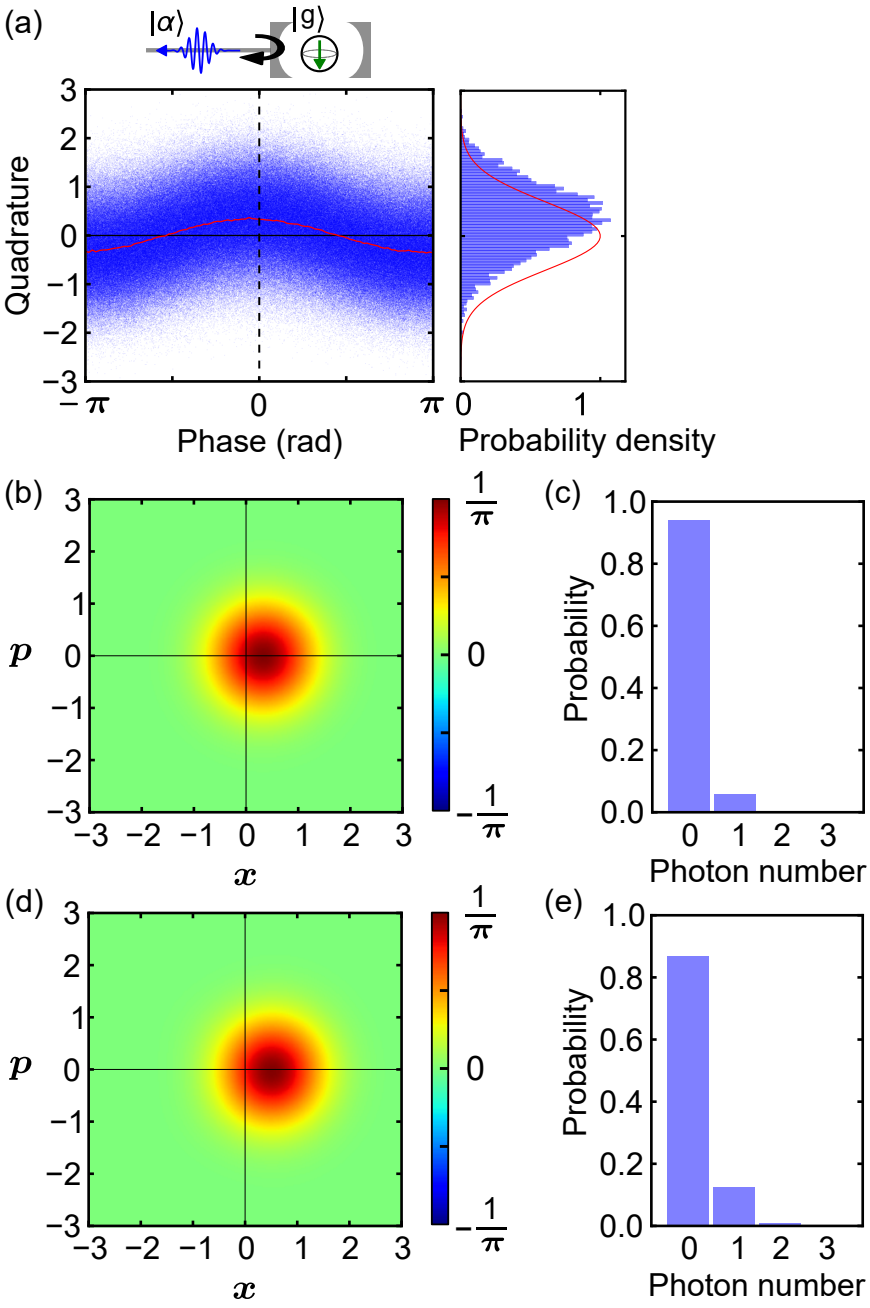


Figure 9.7: Wigner tomography of the pulse mode, which is reflected by the cavity with the qubit in the ground state. (a) Quadratures which are measured with the various pump phases. The red line depicts the average of the quadratures. The blue bars and red line in the right plot are the probability density of the measured quadratures at a pump phase of 0 and the theoretical one of a vacuum state, respectively. (b) Reconstructed Wigner function and (c) photon-number distribution without the loss correction. (d), (e) The same with the correction of the measurement inefficiency. Note that the data is the same as in Figs. 8.6 and 8.8.

measurements. For the input signal, we use a coherent pulse with an average photon number of $|\alpha_{\rm in}|^2 = 0.165 \pm 0.003$.

First of all, we characterize a coherent state for the input, as shown in Fig. 9.7. The quadratures of the coherent state, which is reflected by the cavity with the qubit initialized in the ground state, are measured with the various pump phases in a single shot. The

pump phase is swept from 0 to $2\pi$ with a step of $\pi/101$. The sequence is repeated $10^4$ times for each phase. As shown in Fig. 9.7(a), the outcomes of the quadrature measurement give the pump phase dependence, which intuitively indicates the reflected pulse mode retains the coherence. In other words, the preservation of the coherence shows the reflected pulse mode is not entangled with the qubit and is not measured in the Fock basis by the qubit. We find that the reconstructed quantum states without and with the correction of the measurement inefficiency correspond to coherent states with average photon numbers of 0.058 and 0.137, respectively. Note that the reflected coherent state undergoes the internal loss of the cavity.

Next, the quadratures of the pulse mode, which is reflected by the cavity with the qubit prepared in the superposition state $|+\rangle$, are measured with the various pump phases. The pump phase is swept from 0 to $\pi$ with a step of $\pi/101$. The sequence is repeated $10^4$ times for each phase. An input state is set to be the same as in Fig. 9.7. The unconditional quadratures are shown in Fig. 9.8(a). The important point, here, is that the quadratures do not give the pump phase dependence, which intuitively shows the coherent pulse may be entangled with the qubit, resulting in the dephasing. The quadratures conditioned on the absence and presence of the qubit phase flip are shown in Figs. 9.8(b) and (c), respectively. We find that the quadratures are apparently correlated with the qubit phase flip.

Then, using each set of the quadratures, we reconstruct each Wigner function and photon-number distribution of the reflected pulse mode. The results, which are reconstructed without or with the correction of the inefficiency of the quadrature measurement, are shown in Figs. 9.9 and 9.10, respectively. Even when we do not use the correction, we clearly see the correlation between the photon number in the reflected pulse mode and the presence of the qubit phase flip.

From now on, to characterize the QND detection more quantitatively, we focus on the quantum states which are reconstructed through the maximum likelihood method with the correction of the measurement inefficiency.

Without being conditioned on the outcome of the qubit readout, the obtained state is an incoherent mixture of the coherent states which are reflected by the cavity with the qubit in the ground and excited states. Importantly, the interaction for the photon detection retains the photon-number distribution with a survival probability of $0.87\pm0.03$, which is calculated from the ratio of the average photon number of the reflected pulse mode to that of the input. From the results of Figs. 9.5 and 9.10(b), we confirm that the qubit detects an itinerant microwave photon without destroying the photon. Nevertheless, we also need to confirm the correlation beween the itinerant photon and the presence of the qubit phase flip, since a QND detection is characterized by successive correlation measurements, such as an assignment fidelity [81].

Figures 9.10(c)–(f) show the conditioned results. In the case without a qubit phase flip, the reflected pulse mode is in the vacuum state with a fidelity of $0.9844 \pm 0.0002$ (theory: 0.9894), as shown in Figs. 9.10(c) and (d). The weak squeezing seen in the Wigner function is due to the finite probability of two-photon occupation ($\sim 0.007$) in the pulse mode and the coherence between the vacuum and the two-photon state. On the other hand, for the case with a qubit phase flip [Figs. 9.10(e) and (f)], the reflected pulse mode is in the single-photon state with a fidelity of $0.84 \pm 0.02$ (theory: 0.82). The infidelity is mainly due to the internal loss of the cavity and dark counts. The small anisotropy in the observed Wigner function is attributed to the incomplete phase flip of the qubit, which does not erase the coherence completely. Those results prove that the outcome of the qubit readout is strongly correlated to the photon-number state of the reflected pulse mode and constitutes a QND single-photon detection. The system also works as a

heralded single-photon generator. Since the QND detection maintains the pulse mode as long as the pulse bandwidth is within the cavity bandwidth, we can control the temporal mode shape of the heralded single photon by tuning the envelope of the input coherent pulse.

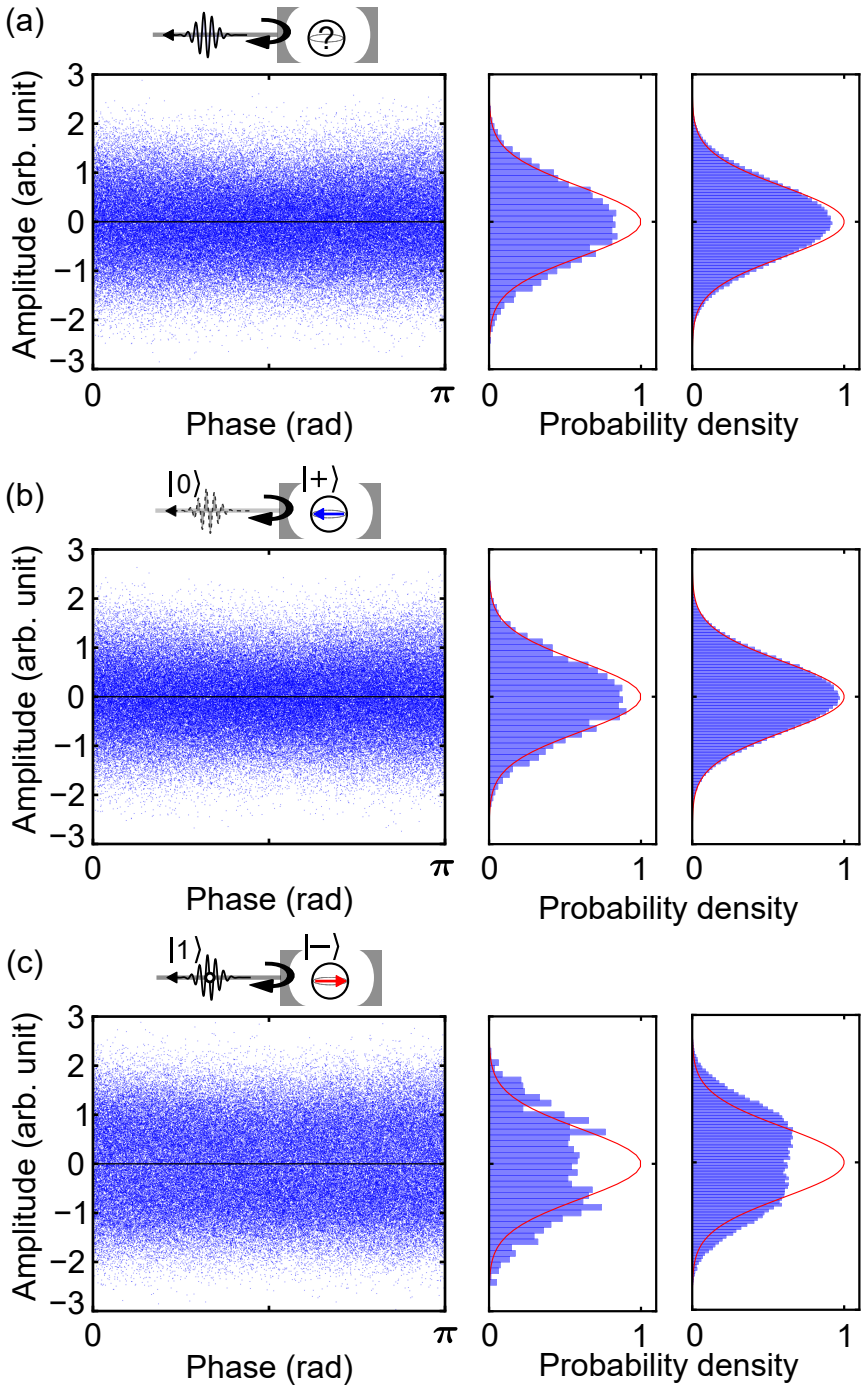


Figure 9.8: Quadratures of the pulse mode, which is reflected by the cavity with the qubit prepared in the superposition state $|+\rangle$. (a) Unconditional quadratures of the reflected pulse mode as a function of the pump phase. (b) The same conditioned on the absence of the qubit phase flip. (c) The same conditioned on the detection of the qubit phase flip. The middle plots are the probability densities of the quadratures measured with the pump phase of 0. The right plots are the probability densities of the quadratures with all the pump phases. The red lines depict the theoretical ones of a vacuum state.

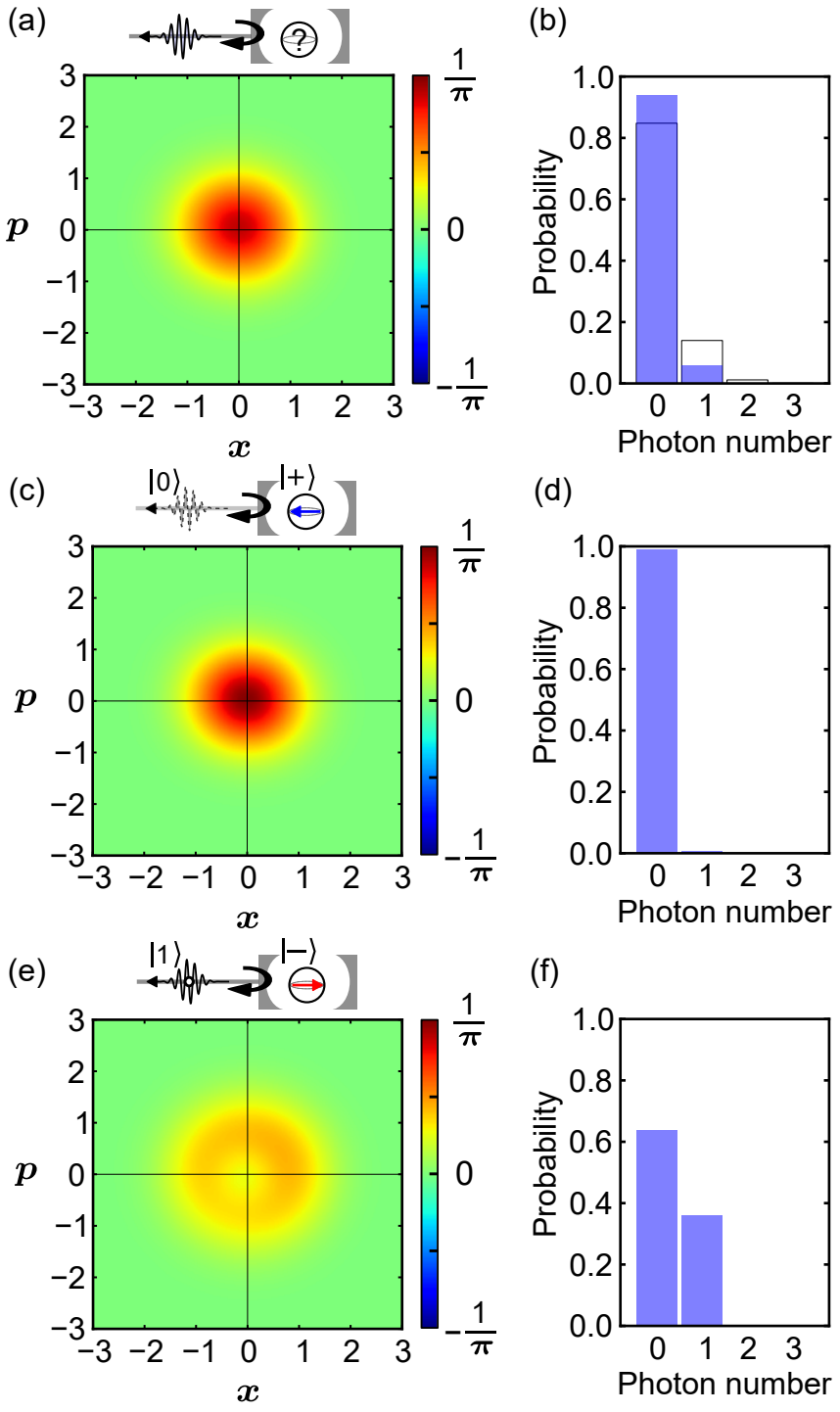


Figure 9.9: Quantum state tomography of the reflected pulse mode without loss correction. (a) Unconditional Wigner function and (b) photon-number distribution after interaction with the qubit prepared in the state $|+\rangle$. The blue bars in (b) show the distribution in the reflected pulse, while the thin black frames depict that in the input pulse. (c), (d) The same conditioned on the absence of the qubit phase flip. (e), (f) The same conditioned on the detection of the qubit phase flip.

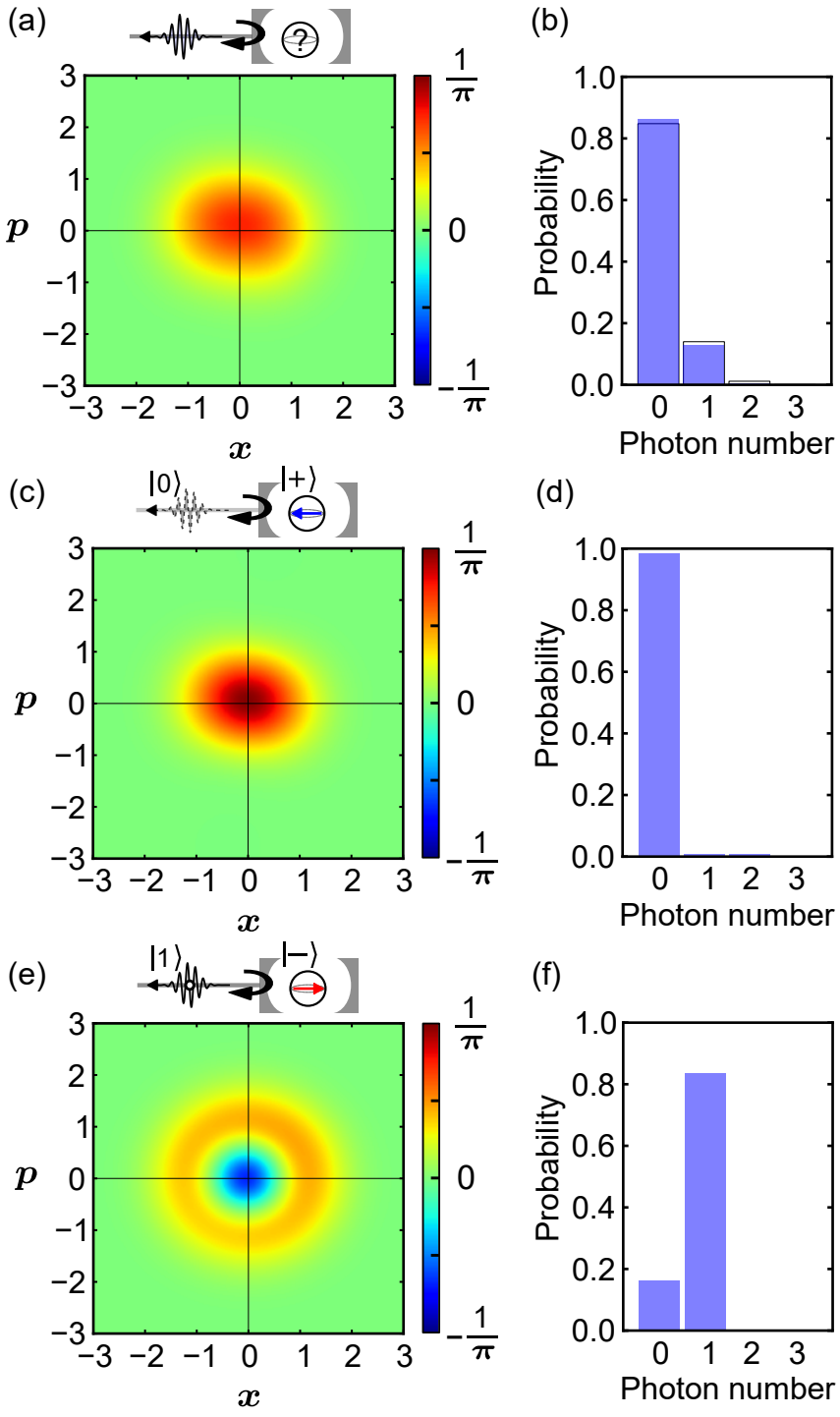


Figure 9.10: Quantum state tomography of the reflected pulse mode with loss correction. (a) Unconditional Wigner function and (b) photon-number distribution in the pulse mode reflected by the cavity with the qubit in the state $|+\rangle$. The blue bars in (b) show the distribution in the reflected pulse, while the thin black frames depict that in the input pulse. (c), (d) The same conditioned on the absence of the qubit phase flip. (e), (f) The same conditioned on the detection of the qubit phase flip.

## 9.5 Qubit-photon entanglement

Here, we study the entanglement between the qubit and the reflected pulse mode. As explained before, the qubit can be entangled with the itinerant photon upon reflection as $|\Psi\rangle = \sqrt{p_0}|+\rangle|0\rangle + \sqrt{p_1}|-\rangle|1\rangle$.

One of the interesting features of an entangled state is that a composite system in an entanglement gives a correlation in the readout outcomes regardless of the measurements basis. For example, when the qubit in the entangled state $|\Psi\rangle$ is projected onto the $x$ basis, the composite system is projected in $\mathcal{N}|+\rangle\langle+|\Psi\rangle = |+\rangle|0\rangle$ or $\mathcal{N}|-\rangle\langle-|\Psi\rangle = |-\rangle|1\rangle$, depending on the qubit readout outcome, where $\mathcal{N}$ describes the normalization. Moreover, when the qubit is projected in the $y$ basis, the system is projected onto $\mathcal{N}|+i\rangle\langle+i|\Psi\rangle = |+i\rangle(\sqrt{p_0}|0\rangle + i\sqrt{p_1}|1\rangle)$ or $\mathcal{N}|-i\rangle\langle-i|\Psi\rangle = |-i\rangle(\sqrt{p_0}|0\rangle - i\sqrt{p_1}|1\rangle)$, where $|\pm i\rangle = \frac{1}{\sqrt{2}}(|\mathrm{g}\rangle \pm i|\mathrm{e}\rangle)$. Then, when the qubit is projected in the $z$ basis, the system is projected onto $\mathcal{N}|\mathrm{g}\rangle\langle\mathrm{g}|\Psi\rangle = |\mathrm{g}\rangle(\sqrt{p_0}|0\rangle + \sqrt{p_1}|1\rangle)$ or $\mathcal{N}|\mathrm{e}\rangle\langle\mathrm{e}|\Psi\rangle = |\mathrm{e}\rangle(\sqrt{p_0}|0\rangle - \sqrt{p_1}|1\rangle)$. To observe these correlations, we characterize the quantum states in the reflected pulse mode, together with the qubit readouts in the three orthogonal bases. The conditional Wigner functions, reconstructed without and with the correction of the measurement inefficiency, are shown in Figs. 9.11 and 9.12, respectively. In both cases, the outcomes of the qubit readout in the $x$ basis shows the correlation in the Fock basis of the reflected pulse mode. Furthermore, the outcomes of the qubit readout in the $y$ and $z$ bases shows the correlations in the $p$ and $x$ axes in the quadrature space, respectively. These results qualitatively indicate that the composite system of the qubit and the reflected pulse mode are entangled.

Then, to verify the entanglement quantitatively, we perform a full quantum state tomography of the composite system of the qubit and the reflected pulse mode. Generally speaking, to perform quantum state tomography of a composite system, we need to measure the system with the tensor product of the complete orthogonal measurement basis of each subspace. Here, we should measure the qubit-photon system in the three Pauli bases of the qubit and in the quadrature basis of the photonic mode. Thus, the experimental data which are used in Figs. 9.11 and 9.12 include the necessary information for the quantum state tomography of the composite system.

Furthermore, we apply the iterative maximum likelihood method to the composite system. Now, the projection operator of the quadrature $\hat{\Pi}(x,\phi)$ is replaced by the tensor product of the projection operators as

$$\hat{\Pi}(\pm,\hat{\sigma}:x,\phi) = |\pm,\hat{\sigma}\rangle\langle\pm,\hat{\sigma}| \otimes \hat{\Pi}(x,\phi), \tag{9.2}$$

where $\pm$ depicts the readout outcome of the qubit, $\hat{\sigma}$ depicts the Pauli basis of $\hat{\sigma}_x$, $\hat{\sigma}_y$, and $\hat{\sigma}_z$, $|\pm,\hat{\sigma}\rangle$ is an eigenstate with the eigenvalue of $\pm$ in the basis of $\hat{\sigma}$. In other words, $|\pm,\hat{\sigma}_x\rangle = |\pm\rangle$, $|\pm,\hat{\sigma}_y\rangle = |\pm i\rangle$, and $|\pm,\hat{\sigma}_z\rangle = |\mathrm{g}\rangle$ or $|\mathrm{e}\rangle$. When the inefficiency of the quadrature measurement of the photonic mode is corrected, the projection operator can be rewrriten as

$$\hat{\Pi}'(\pm,\hat{\sigma}:x,\phi) = |\pm,\hat{\sigma}\rangle\langle\pm,\hat{\sigma}| \otimes \hat{\Pi}'(x,\phi), \tag{9.3}$$

where $\hat{\Pi}'(x,\phi) = \sum_{k=0}^{n_c} \hat{A}_k^\dagger\, \hat{\Pi}(x,\phi)\, \hat{A}_k$ and $\hat{A}_k$ is the Kraus operator describing the photon loss, and $n_c$ is a cutoff photon number (see Sec. 8.3). Here, $n_c$ is set to 2.

The density matrix of the composite system, which is reconstructed without or with the loss correction, is shown in Fig. 9.13 (a) or (b), respectively. The correlation in the diagonal elements enables the QND detection of an itinerant photon. Moreover, the off-diagonal elements indicate the presence of entanglement. Here, we are interested in the quantum state without the photon loss in the quadrature measurement, and then quantitatively evaluate the entanglement of the density matrix reconstructed with the

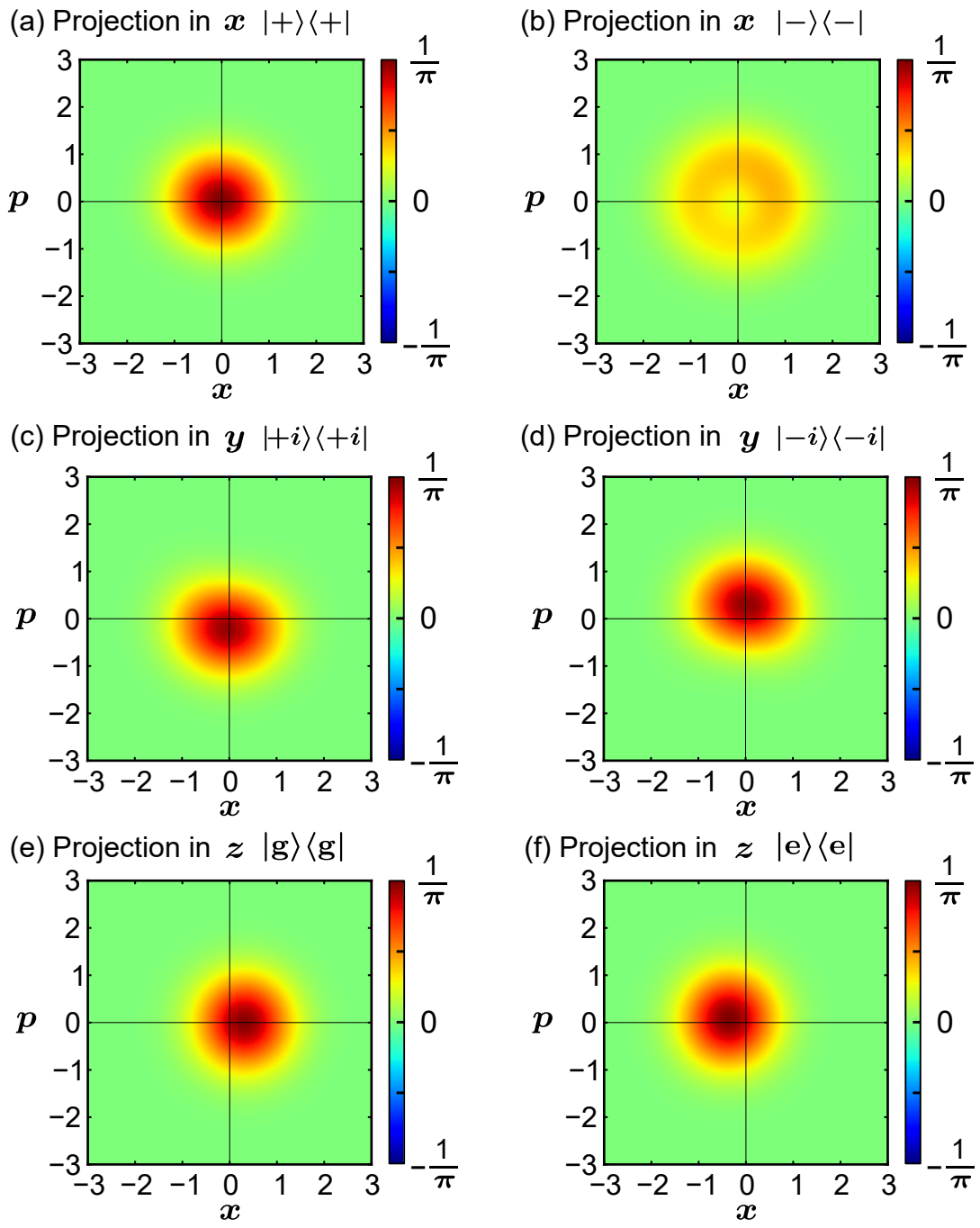


Figure 9.11: Conditional Wigner tomography of the reflected pulse mode with the qubit projected onto the three orthogonal measurement bases, without loss correction. (a), (b) Wigner function conditioned on the qubit readout outcomes in the $x$ measurement basis. (c), (d) The same with the qubit readout in the $y$ measurement basis. (e), (f) The same with the qubit readout the $z$ measurement basis.

correction of the measurement inefficiency. We calculate the negativity $\mathcal{N}(\rho)$ of the composite system from the density matrix and obtain $\mathcal{N}(\rho) = 0.296 \pm 0.005 > 0$, quantifying the entanglement [121]. Note that for the given value of the average photon number $|\alpha_{\mathrm{in}}|^2$, the maximum possible value of the negativity in the composite system is 0.346. The fidelity of the experimentally obtained density matrix to the one with the ideal controls and measurements is found to be $0.957 \pm 0.003$. The high state fidelity indicates that the interaction between the qubit and the itinerant microwave photon can be used as a two

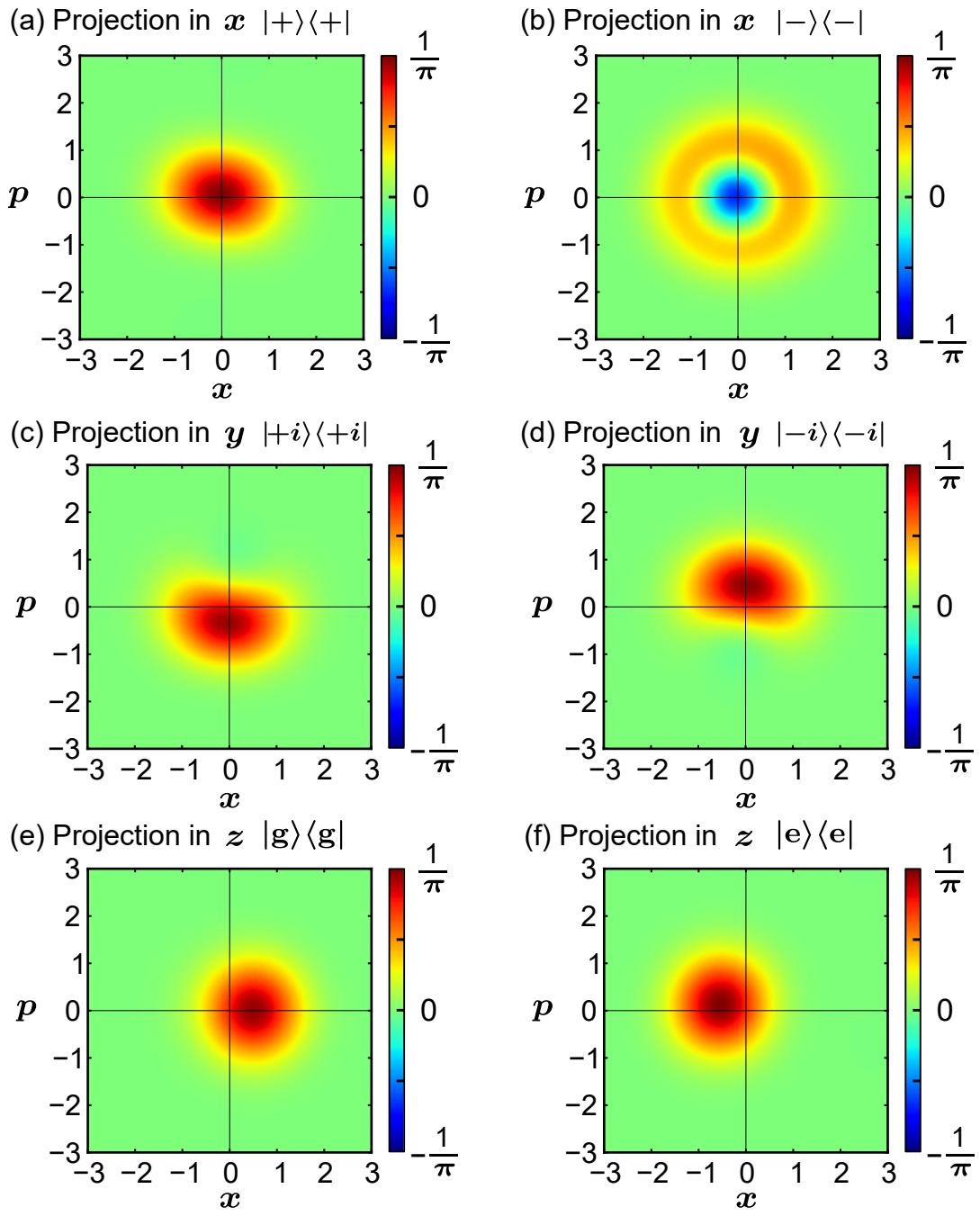


Figure 9.12: Conditional Wigner tomography of the reflected pulse mode with the qubit projected onto the three orthogonal measurement bases, with loss correction. (a), (b) Wigner function conditioned on the qubit readout outcomes in the $x$ measurement basis. (c), (d) The same with the qubit readout in the $y$ measurement basis. (e), (f) The same with the qubit readout the $z$ measurement basis.

qubit gate.

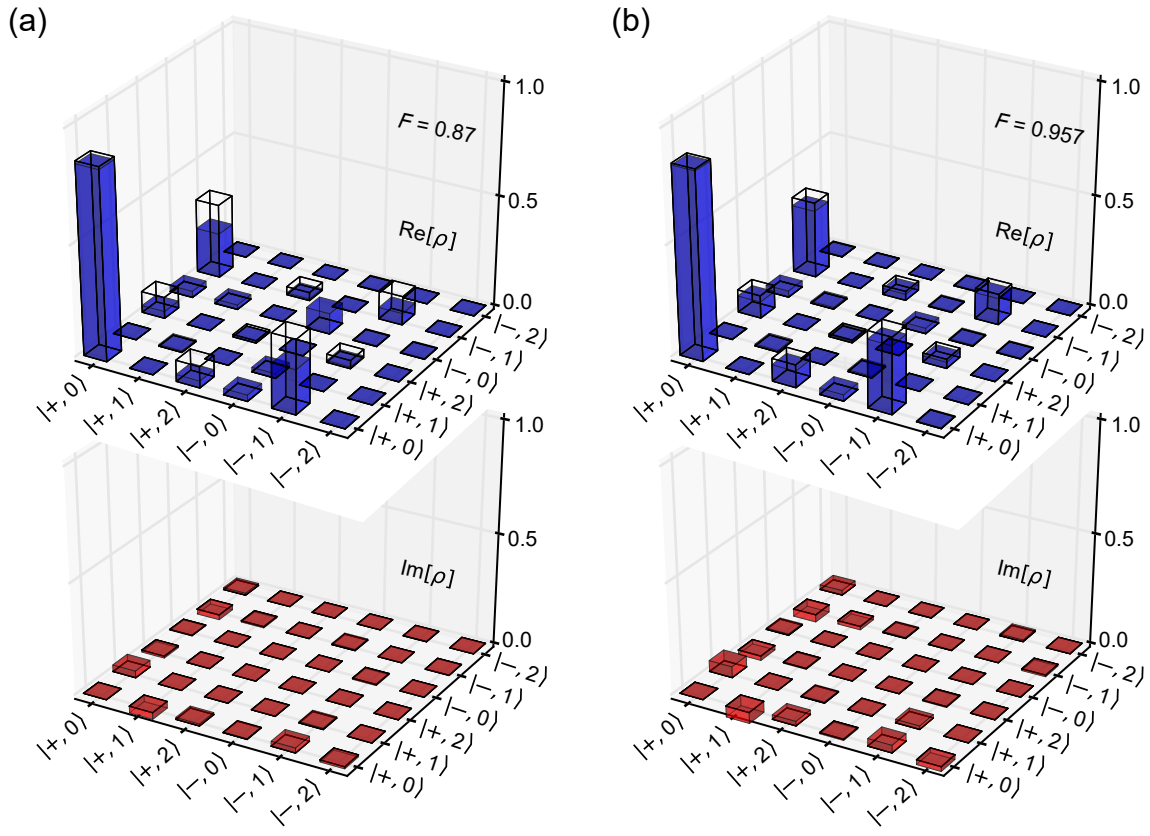


Figure 9.13: Qubit-photon entanglement. (a) The density matrix of the system consisting of the qubit and the reflected pulse mode, which is reconstructed without the correction of the inefficiency in the quadrature measurement of the pulse mode. (b) The same with the loss correction. The blue and red bars respectively show the real and imaginary parts of the experimentally obtained density matrix. The black wireframes are the density matrix in the ideal case. The qubit state is represented in the $X$ basis ($|+\rangle$, $|-\rangle$), and the state in the reflected pulse mode is represented in the photon-number basis ($|n\rangle$; $n$=0,1,2).

# Chapter 10

# Conclusion and prospects

## 10.1 Nonclassical photon-number distribution

We developed a circuit-QED scheme to characterize a microwave squeezed vacuum in the Fock basis. By analyzing the qubit excitation spectrum in a cavity driven continuously by the squeezed vacuum, we determined the photon-number distribution, which is associated with the squeezed vacuum in a propagating mode according to the input-output relation. Most importantly, the distribution fulfilled Klyshko's criterion for nonclassicality. It shows that the qubit excitation spectrum with photon-number splitting can distinguish a nonclassical state from classical states, such as a thermal state and a coherent state.

We adopted the weak probe power not to disturb the cavity state. However, the finite qubit drive power not only improved the signal-to-noise ratio but also distorted the peak ratio in the qubit excitation spectrum from the actual photon-number distribution in the cavity. This distortion forced us to fit the experimental data with a numerical simulation to obtain the actual photon-number distribution. However, we also confirmed that the peak ratio corresponds to the actual photon-number distribution in the weak qubit drive limit. It shows that the actual photon-number distribution can be obtained from the qubit spectrum by improving the signal-to-noise ratio of the cavity probe with amplification by a JPA.

Our scheme can apply to various other quantum states propagating through a waveguide. Moreover, in combination with displacement operations, it allows acquiring the necessary information about an arbitrary quantum state in a propagating mode, i.e., to implement quantum-state tomography [19].

## 10.2 Wigner quantum state tomography

We demonstrated Wigner quantum state tomography for itinerant microwave photons. We measured the quadratures of the microwave photons in the nearly-quantum limit using a JPA as a phase-sensitive amplifier. A coherent state in a pulse mode was reconstructed from the quadrature measurements using an iterative maximum likelihood method.

Then, we also performed Wigner tomography with loss correction. To avoid underestimation or overestimation of a quantum state, we verified a vacuum state in the propagating mode in which a target quantum state was generated. Using the thermal-photon-induced qubit dephasing, we confirmed that the thermal photon in the propagating mode was well suppressed within the error of the measurement efficiency. Moreover, the efficiency of the quadrature measurement was also calibrated to be $0.43 \pm 0.01$ using a coherent state which was calibrated by the cavity-drive-induced qubit dephasing.

For simplicity, we performed the Wigner quantum state tomography for a coherent state in a pulse mode. However, this scheme can be applied to an arbitrary quantum state from a circuit QED system in the dispersive regime, which can be a basic component for a quantum state emitter [32, 102, 33, 34]. Note that the average photon number of the input state should be small enough not to saturate the JPA gain.

High-efficiency Wigner quantum state tomography without loss correction can be a more reliable tool for characterizing microwave itinerant photons. Furthermore, for experiments on continuous monitoring and real-time feedback, the improvement of the quadrature measurement efficiency is indispensable [104, 103]. In our current experimental setup, the measurement efficiency can be limited by the propagation loss between the circuit QED system and the JPA. The propagation loss is mostly due to the circulators, which are necessary for reflection-type interactions. To improve the measurement efficiency, we need to use transmission-type interactions, such as a device based on chiral quantum optics [122] and directional amplifiers [53, 123].

## 10.3 QND detection

We demonstrated a QND detection of an itinerant microwave photon by utilizing an entangling gate with a transmon qubit in a far-detuned three-dimensional cavity. We experimentally confirmed that the input single photon induced a phase-flip of the qubit upon reflection by the cavity. By using a well-calibrated coherent pulse as an input, the quantum efficiency and the dark-count probability were found to be 0.84 and 0.0147, respectively. Then, the quantum state in the reflected pulse mode was reconstructed using the iterative maximum likelihood method with correction of the inefficiency of the quadrature measurement. We found a strong correlation between the presence of the single photon and the qubit phase flip, indicating that we have achieved high-efficiency QND detection of an itinerant microwave photon. Finally, we also confirm that the composite system of the qubit and the reflected pulse mode was an entangled state, which shows the interaction between the qubit and the itinerant photon via the cavity mode can be applied as a two-qubit gate between them.

The quantum efficiency or the fidelity of the entangling gate was mainly limited by the internal loss of the cavity. If a state-of-the-art microwave cavity [24] were used in our scheme, the fidelity could reach almost unity. The high-efficiency entangling gate between a localized qubit and a flying qubit can stimulate a new architecture in a quantum network [124]. In this direction, the insertion loss of circulators is critical. Thus, we need to consider implementing a lossless superconducting circulator [125, 126] or to realize a chiral or directional interaction between an itinerant photon and a localized mode [122].

Here, we applied the QND detection for a single-photon state in a pulse mode. However, the detection scheme can be readily applied to many-photon states, where the qubit detects the even/odd parity of the photon number in the pulse mode. This can be applied to Wigner quantum state tomography of multi-photon states [21] as well as to heralded generation of a Schrödinger cat state in an itinerant mode [127, 128]. Moreover, by cascading the QND detectors with different conditional phases, we can realize a number-resolved photon counter for a microwave pulse mode [11].

# Publication list

1. S. Kono, Y. Masuyama, T. Ishikawa, Y. Tabuchi, R. Yamazaki, K. Usami, K. Koshino, and Y. Nakamura. Nonclassical photon number distribution in a superconducting cavity under a squeezed drive. *Phys. Rev. Lett.*, 119:023602, 2017.

2. Y. Masuyama, K. Funo, Y. Murashita, A. Noguchi, S. Kono, Y. Tabuchi, R. Yamazaki, M. Ueda, and Y. Nakamura. Information-to-work conversion by maxwell's demon in a superconducting circuit quantum electrodynamical system. *Nature Commun.*, 9:1291, 2018.

3. S. Kono, K. Koshino, Y. Tabuchi, A. Noguchi, and Y. Nakamura. Quantum nondemolition detection of an itinerant microwave photon. *Nature Phys.*, 14:546–549, 2018.

4. J. Joo, C.-W Lee, S. Kono, and J. Kim. Logical measurement-based quantum computation in circuit-QED. *arXiv*:1808.07638, 2018.

5. S. Masuda, S. Kono, K. Suzuki, Y. Tokunaga, Y. Nakamura, and K. Koshino. Nonreciprocal microwave transmission based on Gebhard-Ruckenstein hopping. *Phys. Rev. A*, 99:013816, 2019.

# Appendix A

# Quantization of circuits

Here, we explain how to quantize superconducting circuits. In this thesis, we consider two-terminal electrical elements, such as capacitors, inductors, and Josephson junctions.

Before proceeding to an explanation of each element, a generalized magnetic flux and electric charge of a two-terminal element are defined as

$$\Phi = \int_{-\infty}^{t} dt\, V, \tag{A.1}$$

$$Q = \int_{-\infty}^{t} dt\, I, \tag{A.2}$$

where $V$ is the relative voltage between the nodes and $I$ is the current through the branch. As we will see later, each electrical element is characterized by a relation between the generalized magnetic flux $\Phi$ and the generalized electric charge $Q$.

## A.1 Capacitor

A capacitor is an element which can store an electric charge om the two electrodes. The accumulation of charges of opposite sign on the electrodes creates an electric field in the capacitor, in a direction from the positive to the negative electrodes. With the line integral of the electric field, we can derive the relative voltage between the two electrodes:

$$V = \int_{\text{beginning}}^{\text{end}} \vec{dl} \cdot \vec{E}. \tag{A.3}$$

From Gauss's law, the electric field which the electrodes generates is proportional to the total electric charge. From this, we can obtain a linear relationship between the relative voltage $V$ and the electric charge $Q$:

$$Q = CV, \tag{A.4}$$

where $C$ is a capacitance, a coefficient which relates the electric charge stored in a capacitor to the voltage produced across it. With the generalized magnetic flux expressed as an integral over time with respect to the voltage, we obtain a relationship between the time derivative of the magnetic flux and the electric charge:

$$Q = C\dot{\Phi}. \tag{A.5}$$

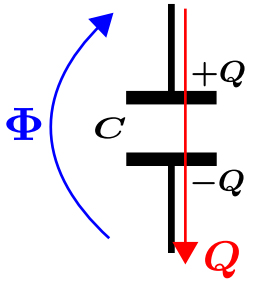


Figure A.1: Relation of the generalized magnetic flux and electric charge of a capacitor.

Consider an electric charge $Q$ stored by a capacitor at time $t$. Then the energy stored inside the capacitor is calculated by

$$\begin{aligned}\mathcal{E}_{\mathrm{K}} &= \int_{-\infty}^{t} dt\, IV \\ &= \int_{-\infty}^{t} dQ \frac{dt}{dQ}\, IV \\ &= \int_{-\infty}^{t} dQ\, \frac{Q}{C} \\ &= \frac{Q^2}{2C} \\ &= \frac{C\dot{\Phi}^2}{2},\end{aligned} \tag{A.6}$$

where the energy is represented in terms of the magnetic flux. When we proceed to the node flux representation, we will find that this energy corresponds to the kinetic energy.

## A.2 Inductor

An inductor is an element which can store a magnetic flux around a wire. The current $I$ flowing in the inductor is associated with the magnetic field $\vec{B}$ from Ampère's law:

$$I = \frac{1}{\mu_0} \oint_{\text{around}} \vec{dl} \cdot \vec{B}, \tag{A.7}$$

where $\mu_0$ is the vacuum permeability. With the surface integral of the magnetic field, we can calculate the magnetic flux $\Phi$ and then obtain the linear relationship between $\Phi$ and the current $I$ as

$$\Phi = LI, \tag{A.8}$$

where $L$ is the inductance, a coefficient which relates the current flowing in an inductor to the magnetic flux stored in it. From Lenz's law, we obtain

$$V = \frac{d\Phi}{dt}, \tag{A.9}$$

where $V$ is the relative voltage between the two ends of the inductor. In comparison with the definition of the generalized magnetic flux as written in Eq. (A.1), we confirm that the generalized magnetic flux exactly corresponds to the magnetic flux stored in the inductor.

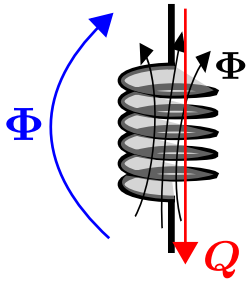


Figure A.2: Relation of the generalized magnetic flux and electric charge of an inductor.

Finally, we can derive the relationship between the magnetic flux and the electric charge from Eqs. (A.2), (A.8) as

$$\dot{Q} = \frac{\Phi}{L}. \tag{A.10}$$

If a magnetic flux $\Phi$ is stored at time $t$, the stored energy in the inductor is calculated as

$$\begin{aligned} \mathcal{E}_{\mathrm{U}} &= \int_{-\infty}^{t} dt\, IV \\ &= \int_{0}^{\Phi} d\Phi \frac{dt}{d\Phi}\, IV \\ &= \int_{0}^{\Phi} d\Phi\, \frac{\Phi}{L} \\ &= \frac{\Phi^2}{2L}, \end{aligned} \tag{A.11}$$

where the energy is represented in terms of the magnetic flux. When we proceed to the node flux representation, we will find that this energy corresponds to the potential energy.

## A.3 Josephson junction

A Josephson junction is an element which is made by a thin insulator sandwiched between two superconductors. In a Josephson junction, a Cooper pair can tunnel quantum-mechanically through the insulating barrier, producing a Josephson current. Here, we explain how to treat the Josephson current in a circuit.

From the dc Josephson effect, we have

$$I = I_{\mathrm{c}} \sin \phi, \tag{A.12}$$

where $I_{\mathrm{c}}$ is the critical current of the Josephson junction, and $\phi$ is the gauge-invariant phase difference between the two superconductors.

From the ac Josephson effect, we have

$$V = \frac{\hbar}{2e} \frac{d\phi}{dt}, \tag{A.13}$$

where $\hbar = h/2\pi$ is the reduced Planck constant, and $e$ is the elementary electric charge.

Here, we can associate the phase difference across the junction with the generalized magnetic flux:

$$\Phi = \phi_0 \phi, \tag{A.14}$$

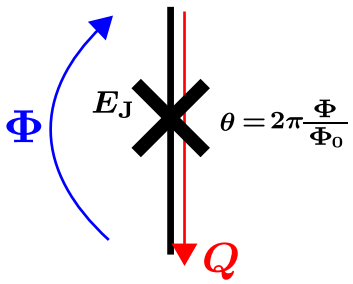


Figure A.3: Relation of the generalized magnetic flux and electric charge of a Josephson junction.

where $\phi_0 = \frac{\hbar}{2e}$ is the reduced magnetic flux quantum. We confirm that $\Phi$ in the ac Josephson effect in Eq. (A.13) satisfies the definition of the generalized magnetic flux in Eq. (A.1):

$$V = \frac{d\Phi}{dt}. \tag{A.15}$$

The ac Josephson effect is therefore analogous to Lenz's law. The dc Josephson effect can be rewritten with the generalized magnetic flux as

$$I = I_c \sin\left(\frac{\Phi}{\phi_0}\right). \tag{A.16}$$

From the above relation between the current and magnetic flux, together with the electric charge of Eq. (A.2), we derive the relation between the magnetic flux and the electric charge:

$$\dot{Q} = I_c \sin\left(\frac{\Phi}{\phi_0}\right). \tag{A.17}$$

Comparing this with Eq. (A.10), we may find that the only difference is whether the relation between $\dot{Q}$ and $\Phi$ is linear or not. Therefore, we can understand the behavior of a Josephson junction as a kind of nonlinear inductor to some extent. However, a Josephson junction does not exactly correspond to a nonlinear inductor due to the periodic condition of the generalized magnetic flux $\Phi$, given that the magnetic flux is defined by the phase difference which is itself of a periodic nature. As we will discuss later in the quantization procedure of the transmon qubit, when the potential energy (tunneling energy of the Josephson junction) is much larger than the corresponding Kinetic energy (capacitive energy), the dynamic range of the magnetic flux is limited around the potential minimum, which makes the periodic condition irrelevant. In that case, we can consider the generalized magnetic flux in a Josephson junction to be the same as in linear elements, such as a capacitor and an inductor.

If the generalized magnetic flux $\Phi$ is stored at time $t$, the stored energy in the Josephson

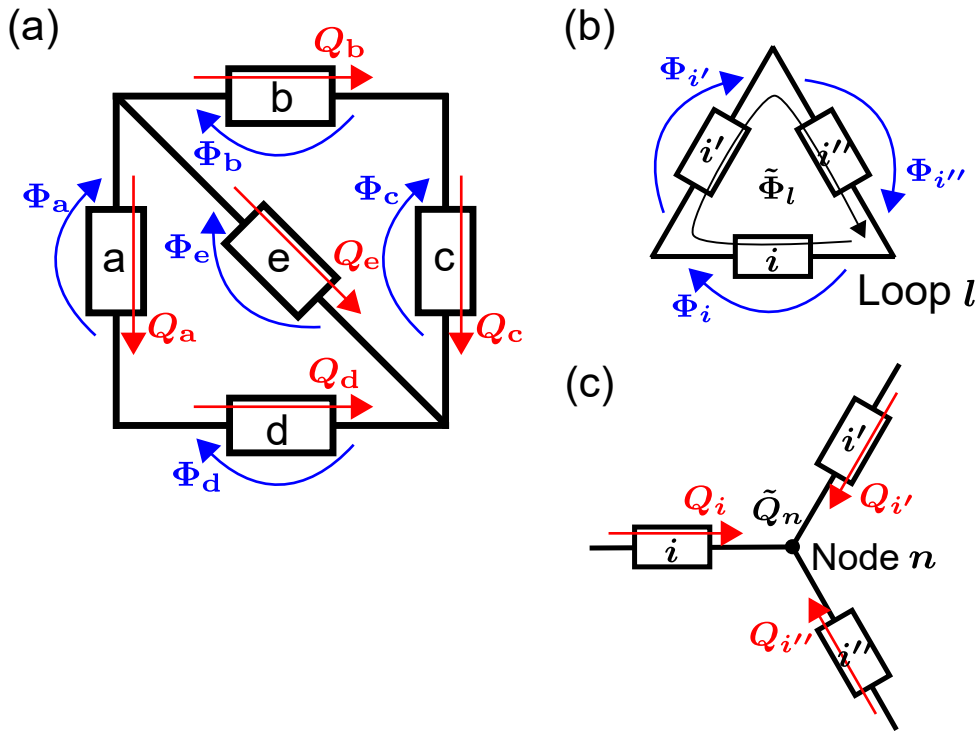


Figure A.4: (a) Example of a closed loop circuit. (b) Schematic of Kirchhoff's law described in Eq. (A.20). (c) Schematic of Kirchhoff's law described in Eq. (A.21).

junction $\mathcal{E}_\mathrm{U}$ is calculated as

$$\begin{aligned}\mathcal{E}_\mathrm{U} &= \int_{-\infty}^{t} dt\, IV \\ &= \int_0^{\Phi} d\Phi \frac{dt}{d\Phi}\, IV \\ &= \int_0^{\Phi} d\Phi\, I_\mathrm{c} \sin\left(\frac{\Phi}{\phi_0}\right) \\ &= E_\mathrm{J}\left[1-\cos\left(\frac{\Phi}{\phi_0}\right)\right],\end{aligned} \tag{A.18}$$

where we define the tunneling (Josephson) energy as $E_\mathrm{J} = I_\mathrm{c}\phi_0$. Neglecting the constant energy term since it does not affect the dynamics of our system, we set

$$\mathcal{E}_\mathrm{U} = -E_\mathrm{J}\cos\left(\frac{\Phi}{\phi_0}\right). \tag{A.19}$$

We will find that this energy corresponds to the potential energy in the node flux representation

From the structure of the separated electrodes in the Josephson junction, a capacitor is formed in parallel. However, when the Josephson junction is used for a transmon qubit or a Josephson parametric amplifier, the junction capacitance is relatively small and is sometimes neglected. Or, the capacitance can be included in a capacitance which is placed in parallel with the Josephson junction.

## A.4 Equations of motion

As shown in Fig. A.4(a), for the closed-loop circuit, we have twice as many degrees of freedom as the number of elements ($\Phi_i$, $Q_i$ for $i = a, b, \cdots$), where $i$ is the label for each element, and $\Phi_i$, $Q_i$ are the generalized magnetic flux and electric charge of element $i$, respectively. However, the degrees of freedom are not independent due to two types of constraints. The first one is the relation between $\Phi_i$ and $Q_i$, as previously discussed. The second constraint is imposed by Kirchhoff's laws, written as

$$\sum_{\text{all } i \text{ in loop } l} \Phi_i = \tilde{\Phi}_l \tag{A.20}$$

$$\sum_{\text{all } i \text{ arriving at node } n} Q_i = \tilde{Q}_n, \tag{A.21}$$

where $\tilde{\Phi}_l$, $\tilde{Q}_n$ are the constant magnetic flux in the loop $l$ and the constant electric charge at the node $n$, respectively. As schematically shown in Fig. A.4(b), Kirchhoff's law of Eq. (A.20) gives the path-independent uniqueness condition of the electric potential energy. As schematically represented in Fig. A.4(c), Kirchhoff's law of Eq. (A.21) means the conservation of electric charge.

Therefore, we can derive the equations of motion for the circuit from these two kinds of constraints. However, by taking into account only one of the equations in Kirchhoff laws, we can still sufficiently define the degrees of freedom and derive the equations of motion of the circuit. If we proceed with only Eq. (A.20), we enter "node flux representation" and if we proceed with only Eq. (A.21), we find "loop charge representation".

### A.4.1 Node flux representation

As shown in Fig. A.5(a), in the node flux representation, the absolute generalized magnetic flux $\Phi_n$ assigned at each node $n$ is the independent degree of freedom describing the equations of motion. Note that the absolute generalized magnetic flux is defined by the time integral of the relative voltage from the ground. In this representation, one can easily confirm that Eq. (A.20) is automatically satisfied. For simplicity, we can determine the ground at one of the nodes as $\Phi_{\rm g} = 0$, as shown in Fig. A.5(a). Then, the final task is to satisfy the Kirchhoff law of Eq. (A.21) by considering the relation between the magnetic flux and the electric charge. Here, we use the time derivative of Eq. (A.21) for convenience.

To satisfy the constraint of Eq. (A.21), we need to calculate the total electric charge at node $n$. The electric charge $Q_i^{(n)}$ at node $n$ through element $i$ can be calculated by using the absolute magnetic fluxes at nodes $n$ and $m$ according to the element $i$, where node $m$ is the node on the opposite side of element $i$, with respect to node $n$.

When element $i$ is a capacitor of capacitance $C_i$, the electric charge $Q_i^{(n)}$ arriving at node $n$ from node $m$ is characterized by

$$\dot{Q}_i^{(n)} = C_i(\ddot{\Phi}_n - \ddot{\Phi}_m), \tag{A.22}$$

which is determined from the time derivative of Eq. (A.5).

When element $i$ is an inductor of inductance $L_i$, the electric charge $Q_i^{(n)}$ arriving at node $n$ from node $m$ is characterized by

$$\dot{Q}_i^{(n)} = \frac{\Phi_n - \Phi_m}{L_i}, \tag{A.23}$$

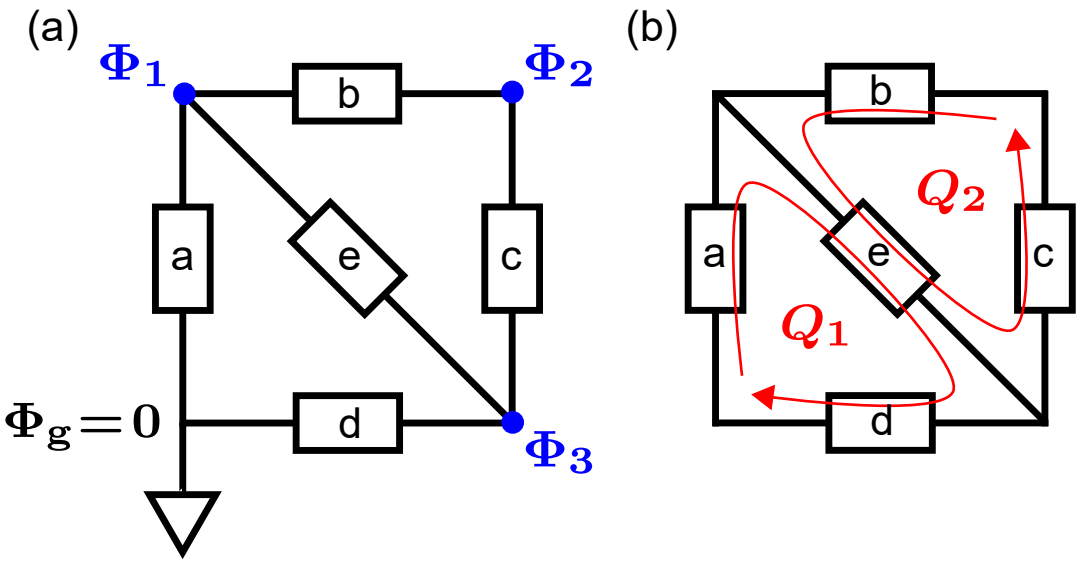


Figure A.5: (a) Example of the node flux representation. (b) Example of the loop charge representation.

which is directly derived from Eq. (A.10).

When element $i$ is a Josephson junction of critical current $I_{c,i}$, the electric charge $Q_i^{(n)}$ arriving at node $n$ from node $m$ is characterized by

$$\dot{Q}_i^{(n)} = I_{c,i} \sin\left(\frac{\Phi_n - \Phi_m}{\phi_0}\right), \tag{A.24}$$

which is directly derived from Eq. (A.17).

The time derivative of Eq. (A.21) is used to satisfy the constraints of Eq. (A.21) and to obtain the equations of motion:

$$\sum_{i \text{ at } n} \dot{Q}_i^{(n)} = 0, \tag{A.25}$$

where $i$ labels the element which is connected to node $n$. Furthermore, we can derive as many equations of motion as the number of nodes which have an independent degree of freedom $\Phi_n$. Now, the number of the degrees of freedom corresponds to the number of independent equations of motion we have. Therefore, the equations of motion for the set of $\Phi_n$ can be solved. Note that the equations are second-order differential equations for $\Phi_n$.

### A.4.2 Loop charge representation

In the loop charge representation, each independent loop has a degree of freedom; an electric charge $Q_l$ which flows in the loop. Note that Eq. (A.21) is automatically satisfied in this representation. As shown in Fig. A.5(b), from the definition of $Q_l$, we can calculate the total electric charge at each element using the principle of superposition, and then calculate the relative magnetic flux from the relation between the magnetic flux and the electric charge. The equations of motion are obtained from the time derivative of the constraints imposed by Eq. (A.20):

$$\sum_{i \text{ in } l} \dot{\Phi}_i^{(l)} = 0, \tag{A.26}$$

where $i$ labels the element in loop $l$. Since the equations of motion can be derived from the constraint for each independent loop, we can obtain as many equations of motion as the number of the degrees of freedom $Q_l$ in the loop. Then, the equations of motion for the set of $Q_l$ can be solved. Note that the equations are also second-order differential equations for $Q_l$.

However, the definition of the independent loop is not unique. Moreover, the relation between the generalized magnetic flux and electric charge in a Josephson junction is not linear, and the relative magnetic flux which is calculated from the electric charge is nontrivial [See Eq. (A.17)]. Therefore, the loop charge representation is considered to be more complicated than the node flux representation. In this thesis, the node flux representation will be used hereinafter.

## A.5 Lagrangian formalism

Now, we understand how to describe a closed-loop circuit and how to derive its equations of motion. Here, we study the Lagrangian formalism as a preparation for the quantization of circuits.

Using the absolute generalized magnetic fluxes, the equation of motion Eq. (A.25) is represented more specifically as

$$\sum_{i \text{ at } n} \left[ C_i(\dot{\Phi}_n - \dot{\Phi}_m) \text{ or } \frac{\Phi_n - \Phi_m}{L_i} \text{ or } I_{\mathrm{c},i} \sin\left(\frac{\Phi_n - \Phi_m}{\phi_0}\right) \right] = 0, \tag{A.27}$$

where $i$ labels the capacitor, the inductor or the Josephson junction which is connected to node $n$. To make Eq. (A.27) consistent with the Euler-Lagrange equation

$$\frac{d}{dt}\frac{\partial \mathcal{L}_n}{\partial \dot{\Phi}_n} - \frac{\partial \mathcal{L}_n}{\partial \Phi_n} = 0, \tag{A.28}$$

we can define the Lagrangian $\mathcal{L}_n$ at node $n$ as

$$\mathcal{L}_n = \sum_{i \text{ at } n} \left[ \frac{C_i}{2}(\dot{\Phi}_n - \dot{\Phi}_m)^2 \text{ or } -\frac{1}{2L_i}(\Phi_n - \Phi_m)^2 \text{ or } E_{\mathrm{J},i} \cos\left(\frac{\Phi_n - \Phi_m}{\phi_0}\right) \right], \tag{A.29}$$

where $E_{\mathrm{J},i} = I_{\mathrm{c},i}\phi_0$ is the Josephson energy in Josephson junction $i$. Note that the Lagrangian has dimensions of energy.

Moreover, by considering all the nodes in the circuit, we obtain the total Lagrangian of the circuit:

$$\mathcal{L} = \sum_{\text{all } i} \left[ \frac{C_i}{2}(\dot{\Phi}_n - \dot{\Phi}_m)^2 \text{ or } -\frac{1}{2L_i}(\Phi_n - \Phi_m)^2 \text{ or } E_{\mathrm{J},i} \cos\left(\frac{\Phi_n - \Phi_m}{\phi_0}\right) \right], \tag{A.30}$$

where $i$ labels all the elements, and $n$, $m$ label both of the nodes adjacent to the element. We confirm that the total Lagrangian also gives the equation of motion Eq. (A.27) by the Euler-Lagrange equation:

$$\frac{d}{dt}\frac{\partial \mathcal{L}}{\partial \dot{\Phi}_n} - \frac{\partial \mathcal{L}}{\partial \Phi_n} = 0. \tag{A.31}$$

We can understand the total Lagrangian as the subtraction of the total potential energy for the generalized magnetic fluxes $\mathcal{E}_{\mathrm{U}}$ from the total kinetic energy $\mathcal{E}_{\mathrm{K}}$. In electrical circuits, the kinetic energy corresponds to a capacitive energy and the potential energy corresponds to an inductive or Josephson energy.

In summary, we define the absolute magnetic flux $\Phi_n$ at each node with the ground at one of the nodes. We construct the Lagrangian which is defined by the subtraction of the potential energy from the kinetic energy:

$$\mathcal{L} = \mathcal{E}_{\mathrm{K}} - \mathcal{E}_{\mathrm{U}}, \tag{A.32}$$

where

$$\mathcal{E}_{\mathrm{K}} = \sum_{\text{all } i} \frac{C_i}{2}(\dot{\Phi}_n - \dot{\Phi}_m)^2, \tag{A.33}$$

and

$$\mathcal{E}_{\mathrm{U}} = \sum_{\text{all } i} \left[ \frac{1}{2L_i}(\Phi_n - \Phi_m)^2 \quad \text{or} \quad -E_{\mathrm{J},i} \cos\left(\frac{\Phi_n - \Phi_m}{\phi_0}\right) \right], \tag{A.34}$$

where $i$ labels all the capacitors, inductors and Josephson junctions in the closed-loop circuit. Then, the equations of motion are derived for each magnetic flux $\Phi_n$ from Eq. (A.31).

## A.6 Hamiltonian formalism

While the Lagrangian is described by $\Phi_n$ and $\dot{\Phi}_n$, the Hamiltonian is described by $\Phi_n$ and $Q_n$, where $Q_n$ is the conjugate momentum of $\Phi_n$ and is calculated by

$$Q_n = \frac{\partial \mathcal{L}}{\partial \dot{\Phi}_n}. \tag{A.35}$$

Note that $Q_n$ does not exactly correspond to the electric charge at the element $i$, although $Q_n$ has units of electric charge. Rather, the electric charge in element $i$ can be calculated from the difference of the absolute magnetic fluxes $\Phi_n$ in the Hamiltonian formalism and by the relation between the relative magnetic flux and the electric charge in the element $i$.

Then, we obtain the Hamiltonian through a Legendre transformation:

$$\mathcal{H} = \sum_n Q_n \dot{\Phi}_n - \mathcal{L}. \tag{A.36}$$

Note that the Hamiltonian should be represented by $\Phi_n$ and $Q_n$ without including any $\dot{\Phi}_n$. To represent the Hamiltonian with the set of $\Phi_n$ and $Q_n$, we need to describe $\dot{\Phi}_n$ with $Q_n$ from Eq. (A.35). At this point, it is useful to describe the relation between $\dot{\Phi}_n$ and $Q_n$ using linear algebra. First, we define the magnetic flux vector as

$$\boldsymbol{\Phi} = \begin{pmatrix} \Phi_0 \\ \Phi_1 \\ \cdots \\ \Phi_n \\ \cdots \end{pmatrix}, \tag{A.37}$$

which is a one-dimensional column vector. The capacitive energy in the Lagrangian of Eq. (A.33) can be described by the magnetic flux vector $\boldsymbol{\Phi}$ and the capacitance matrix $\boldsymbol{C}$ since the Lagrangian is in the quadratic form of $\dot{\boldsymbol{\Phi}} = \frac{d\boldsymbol{\Phi}}{dt}$:

$$\mathcal{E}_{\mathrm{K}} = \frac{1}{2}\dot{\boldsymbol{\Phi}}^{\mathrm{T}} \boldsymbol{C} \dot{\boldsymbol{\Phi}}. \tag{A.38}$$

Then, the Lagrangian can be written as

$$\mathcal{L} = \frac{1}{2}\dot{\boldsymbol{\Phi}}^{\mathrm{T}} \boldsymbol{C} \dot{\boldsymbol{\Phi}} - \mathcal{E}_{\mathrm{U}}. \tag{A.39}$$

Note that the capacitance matrix is a symmetric matrix since the Lagrangian is symmetric under the exchange of magnetic flux at the nodes of each capacitor: $\boldsymbol{C} = \boldsymbol{C}^{\mathrm{T}}$. We can also write a conjugate momentum vector $\boldsymbol{Q}$ as

$$\begin{aligned}\boldsymbol{Q} &= \begin{pmatrix} Q_0 \\ Q_1 \\ \cdots \\ Q_n \\ \cdots \end{pmatrix} \\ &= \begin{pmatrix} \frac{\partial \mathcal{L}}{\partial \dot{\Phi}_0} \\ \frac{\partial \mathcal{L}}{\partial \dot{\Phi}_1} \\ \cdots \\ \frac{\partial \mathcal{L}}{\partial \dot{\Phi}_n} \\ \cdots \end{pmatrix} \\ &= \frac{\partial \mathcal{L}}{\partial \dot{\boldsymbol{\Phi}}} \\ &= \boldsymbol{C}\dot{\boldsymbol{\Phi}}.\end{aligned} \tag{A.40}$$

This corresponds to Eq. (A.35). Then, we obtain

$$\dot{\boldsymbol{\Phi}} = \boldsymbol{C}^{-1}\boldsymbol{Q}, \tag{A.41}$$

where $\boldsymbol{C}^{-1}$ is the inverse matrix of $\boldsymbol{C}$ and is also a symmetric matrix. We represent $\mathcal{E}_{\mathrm{K}}$ and $\boldsymbol{Q}^{\mathrm{T}}\dot{\boldsymbol{\Phi}}$ using the following formula:

$$\begin{aligned}\mathcal{E}_{\mathrm{K}} &= \frac{1}{2}\dot{\boldsymbol{\Phi}}^{\mathrm{T}}\boldsymbol{C}\dot{\boldsymbol{\Phi}} \\ &= \frac{1}{2}\boldsymbol{Q}^{\mathrm{T}}\boldsymbol{C}^{-1^{\mathrm{T}}}\boldsymbol{C}\boldsymbol{C}^{-1}\boldsymbol{Q} \\ &= \frac{1}{2}\boldsymbol{Q}^{\mathrm{T}}\boldsymbol{C}^{-1}\boldsymbol{Q},\end{aligned} \tag{A.42}$$

and

$$\boldsymbol{Q}^{\mathrm{T}}\dot{\boldsymbol{\Phi}} = \boldsymbol{Q}^{\mathrm{T}}\boldsymbol{C}^{-1}\dot{\boldsymbol{Q}}, \tag{A.43}$$

where we use $\boldsymbol{C}^{-1^{\mathrm{T}}} = \boldsymbol{C}^{-1}$. The Hamiltonian is described with the set of $\Phi_n$ and $Q_n$:

$$\begin{aligned}\mathcal{H} &= \sum_n Q_n\dot{\Phi}_n - \mathcal{L} \\ &= \boldsymbol{Q}^{\mathrm{T}}\dot{\boldsymbol{\Phi}} - \mathcal{E}_{\mathrm{K}} + \mathcal{E}_{\mathrm{U}} \\ &= \boldsymbol{Q}^{\mathrm{T}}\boldsymbol{C}^{-1}\boldsymbol{Q} - \frac{1}{2}\boldsymbol{Q}^{\mathrm{T}}\boldsymbol{C}^{-1}\boldsymbol{Q} + \mathcal{E}_{\mathrm{U}} \\ &= \frac{1}{2}\boldsymbol{Q}^{\mathrm{T}}\boldsymbol{C}^{-1}\boldsymbol{Q} + \mathcal{E}_{\mathrm{U}}.\end{aligned} \tag{A.44}$$

Finally, the equations of motion for the set of $\Phi_n$ and $Q_n$ are calculated by

$$\begin{aligned}\dot{\Phi}_n &= \frac{\partial \mathcal{H}}{\partial Q_n} \\ \dot{Q}_n &= -\frac{\partial \mathcal{H}}{\partial \Phi_n},\end{aligned} \tag{A.45}$$

which correspond to the Euler-Lagrange equations in the Lagrangian formalism.

## A.7 Quantization

In quantum mechanics, classical variables are replaced by their corresponding operators:

$$\begin{aligned} \Phi_n &\to \hat{\Phi}_n \\ Q_n &\to \hat{Q}_n \\ \mathcal{H} &\to \hat{\mathcal{H}}. \end{aligned} \tag{A.46}$$

Furthermore, the canonical commutation relations are imposed on the pairs of conjugate operators:

$$[\hat{\Phi}_n,\, \hat{Q}_n] = i\hbar. \tag{A.47}$$

In the Schrödinger picture, the dynamics of the state of the circuit are described by the wave function $|\Psi\rangle$ which evolves in time as

$$i\hbar\frac{\partial}{\partial t}|\Psi\rangle = \hat{\mathcal{H}}|\Psi\rangle. \tag{A.48}$$

The time evolution of the expectation value of an observable is calculated by the corresponding operator and the wave function.

In the Heisenberg picture, the observable $\hat{O}$ evolves according to

$$\frac{d}{dt}\hat{O} = \frac{1}{i\hbar}\left[\hat{O}, \hat{\mathcal{H}}\right]. \tag{A.49}$$

The time evolution of the expectation value of the observable is calculated by the operator and the initial wave function.

# Appendix B

# Simulation on nonclassical photon-number distribution

In this section, we present the formula used in the numerical calculations.

## B.1 Hamiltonian

In the setup considered (Fig. B.1), a qubit-cavity system (System A) is subject to a continuous squeezed vacuum field generated by a JPA (System B). The Hamiltonian of System A, including the qubit drive and the cavity probe fields, is described by

$$\hat{\mathcal{H}}_{\rm A}/\hbar = \omega_{\rm c}\hat{a}^\dagger\hat{a} + \frac{\omega_{\rm q}}{2}\hat{\sigma}_z - \chi\hat{a}^\dagger\hat{a}\,\hat{\sigma}_z + \frac{\Omega_{\rm d}}{2}(e^{-i\omega_{\rm d}t}\hat{\sigma}_+ + e^{i\omega_{\rm d}t}\hat{\sigma}_-) + \frac{\Omega_{\rm p}}{2}(e^{-i\omega_{\rm p}t}\hat{a}^\dagger + e^{i\omega_{\rm p}t}\hat{a}), \quad \text{(B.1)}$$

where $\hat{a}$ and $\hat{\sigma}_-$ respectively denote the annihilation operators of the cavity mode and the qubit, $\hat{\sigma}_z = \hat{\sigma}_+\hat{\sigma}_- - \hat{\sigma}_-\hat{\sigma}_+$, $\omega_{\rm c}$ is the cavity resonance frequency, $\omega_{\rm q}$ is the qubit resonance frequency, $\omega_{\rm d}$ is the qibit drive frequency, $\omega_{\rm p}$ is the cavity probe frequency, $\chi$ is the dispersive shift, and $\Omega_{\rm d}$ and $\Omega_{\rm p}$ are the amplitudes of the qubit drive and the cavity probe, respectively. The Hamiltonian of System B is given by

$$\hat{\mathcal{H}}_{\rm B}/\hbar = \omega_{\rm s}\hat{b}^\dagger\hat{b} + \frac{\Omega_{\rm s}}{2}(e^{-2i\omega_{\rm s}t}\hat{b}^{\dagger 2} + e^{2i\omega_{\rm s}t}\hat{b}^2), \quad \text{(B.2)}$$

where $\hat{b}$ is the annihilation operator of the JPA mode, and $\omega_{\rm s}$ is its frequency. We apply a pump field with frequency $2\omega_{\rm s}$ and amplitude $\Omega_{\rm s}$ to the JPA to generate a squeezed vacuum.

By taking the free Hamiltonian $\hat{\mathcal{H}}_{\rm A0}/\hbar = \omega_{\rm s}(\hat{a}^\dagger\hat{a}+\hat{b}^\dagger\hat{b}) + \frac{\omega_{\rm d}}{2}\hat{\sigma}_z$, we switch to the rotating frame. In this frame, $\hat{\mathcal{H}}_{\rm A}$ and $\hat{\mathcal{H}}_{\rm B}$ are rewritten as

$$\hat{\mathcal{H}}_{\rm A}/\hbar = (\omega_{\rm c}-\omega_{\rm s})\hat{a}^\dagger\hat{a} + \frac{(\omega_{\rm q}-\omega_{\rm d})}{2}\hat{\sigma}_z - \chi\hat{a}^\dagger\hat{a}\hat{\sigma}_z + \frac{\Omega_{\rm d}}{2}(\hat{\sigma}_+ + \hat{\sigma}_-) + \frac{\Omega_{\rm p}}{2}(e^{-i(\omega_{\rm p}-\omega_{\rm s})t}\hat{a}^\dagger + e^{i(\omega_{\rm p}-\omega_{\rm s})t}\hat{a}), \quad \text{(B.3)}$$

$$\hat{\mathcal{H}}_{\rm B}/\hbar = \frac{\Omega_{\rm s}}{2}(\hat{b}^{\dagger 2} + \hat{b}^2). \quad \text{(B.4)}$$

The squeezed vacuum field generated by System B is guided to System A through a waveguide. We define a spatial coordinate $r$ along the direction of propagation of the waveguide field (see Fig. B.1). The waveguide field interacts with System A at $r_a$ and System B at $r_b$. Setting the microwave velocity in the waveguide to unity, the overall Hamiltonian is written as

$$\hat{\mathcal{H}}_{\rm total}/\hbar = \hat{\mathcal{H}}_{\rm A}/\hbar + \hat{\mathcal{H}}_{\rm B}/\hbar + \int dk\; k\hat{c}_k^\dagger\hat{c}_k + \sqrt{\kappa_{\rm ex}^{\rm J}}\left(\hat{b}^\dagger\widetilde{c}_{r_b} + \widetilde{c}_{r_b}^\dagger\hat{b}\right) + \sqrt{\kappa_{\rm ex}}\left(\hat{a}^\dagger\widetilde{c}_{r_a} + \widetilde{c}_{r_a}^\dagger\hat{a}\right), \quad \text{(B.5)}$$

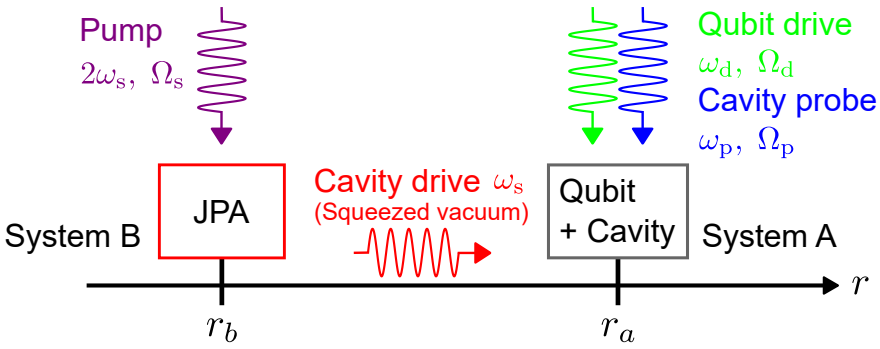


Figure B.1: Schematic of the model. The output field from System B (JPA) is used as the input for System A (qubit and cavity). The coordinate $r$ is defined along the propagation direction of the waveguide field.

where $\hat{c}_k$ is the waveguide-field operator with wave number $k$, and $\kappa_{\rm ex}$ ($\kappa_{\rm ex}^{\rm J}$) represents the external coupling of System A (B) to the waveguide field. $\widetilde{c}_r$ is the spatial representation of the waveguide-field operator, as given by $\widetilde{c}_r = (2\pi)^{-1/2}\int dk e^{ikr}\hat{c}_k$. Note that the photon frequency should be measured relative to $\omega_{\rm s}$, since we are in the rotating frame.

## B.2 Time evolution

We denote an arbitrary operator belonging to System A (B) by $S_{\rm A}$ ($S_{\rm B}$) and investigate its time evolution at $t$ $(t-l)$, where $l = r_a - r_b (> 0)$ is the distance between the two systems. Note that $S_{\rm A}(t)$ and $S_{\rm B}(t-l)$ are on the same light cone and are therefore relativistically simultaneous. From Eq. (B.5), we can derive the following Heisenberg equations,

$$\frac{d}{dt}S_{\rm A} = \frac{i}{\hbar}[\hat{\mathcal{H}}_{\rm A}, S_{\rm A}] + i\sqrt{\kappa_{\rm ex}}\,[\hat{a}^\dagger, S_{\rm A}]\widetilde{c}_{r_a}(t) + i\sqrt{\kappa_{\rm ex}}\,\widetilde{c}^\dagger_{r_a}(t)[\hat{a}, S_{\rm A}], \tag{B.6}$$

$$\frac{d}{dt}S_{\rm B} = \frac{i}{\hbar}[\hat{\mathcal{H}}_{\rm B}, S_{\rm B}] + i\sqrt{\kappa_{\rm ex}^{\rm J}}\,[\hat{b}^\dagger, S_{\rm B}]\widetilde{c}_{r_b}(t-l) + i\sqrt{\kappa_{\rm ex}^{\rm J}}\,\widetilde{c}^\dagger_{r_b}(t-l)[\hat{b}, S_{\rm B}], \tag{B.7}$$

and the input-output relation,

$$\begin{aligned}\widetilde{c}_r(t) \;=\; & \widetilde{c}_{r-t}(0) - i\sqrt{\kappa_{\rm ex}^{\rm J}}\,\theta(r-r_b)\theta(t-r+r_b)\hat{b}(t-r+r_b) \\ & - i\sqrt{\kappa_{\rm ex}}\,\theta(r-r_a)\theta(t-r+r_a)\hat{a}(t-r+r_a),\end{aligned} \tag{B.8}$$

where $\theta(t)$ is the step function. Since we analyze the stationary response, we assume that $t$ is sufficiently large. Therefore, $\widetilde{c}_{r_b}(t-l) = \widetilde{c}_{r_a-t}(0) - i\sqrt{\kappa_{\rm ex}^{\rm J}}\,\hat{b}(t-l)/2$ and $\widetilde{c}_{r_a}(t) = \widetilde{c}_{r_a-t}(0) - i\sqrt{\kappa_{\rm ex}}\,\hat{a}(t)/2 - i\sqrt{\kappa_{\rm ex}^{\rm J}}\,\hat{b}(t-l)$. From these equations, Eqs. (B.6) and (B.7) are

rewritten as

$$\begin{aligned}\frac{d}{dt}S_{\rm A} &= \frac{i}{\hbar}[\hat{\mathcal{H}}_{\rm A}, S_{\rm A}] + \frac{\kappa_{\rm ex}}{2}\mathcal{L}_a[S_{\rm A}] \\ &\quad + \sqrt{\kappa_{\rm ex}\kappa_{\rm ex}^{\rm J}}\,[\hat{a}^\dagger, S_{\rm A}]\hat{b} + \sqrt{\kappa_{\rm ex}\kappa_{\rm ex}^{\rm J}}\,\hat{b}^\dagger[S_{\rm A}, \hat{a}] \\ &\quad + i\sqrt{\kappa_{\rm ex}}\,[\hat{a}^\dagger, S_{\rm A}]\widetilde{c}_{r_a-t}(0) + i\sqrt{\kappa_{\rm ex}}\,\widetilde{c}_{r_a-t}^\dagger(0)[\hat{a}, S_{\rm A}],\end{aligned} \tag{B.9}$$

$$\begin{aligned}\frac{d}{dt}S_{\rm B} &= \frac{i}{\hbar}[\hat{\mathcal{H}}_{\rm B}, S_{\rm B}] + \frac{\kappa_{\rm ex}^{\rm J}}{2}\mathcal{L}_b[S_{\rm B}] \\ &\quad + i\sqrt{\kappa_{\rm ex}^{\rm J}}\,[\hat{b}^\dagger, S_{\rm B}]\widetilde{c}_{r_a-t}(0) + i\sqrt{\kappa_{\rm ex}^{\rm J}}\,\widetilde{c}_{r_a-t}^\dagger(0)[\hat{b}, S_{\rm B}],\end{aligned} \tag{B.10}$$

where $\mathcal{L}_a[S_{\rm A}] = [\hat{a}^\dagger, S_{\rm A}]\hat{a} + \hat{a}^\dagger[S_{\rm A}, \hat{a}]$. The Heisenberg equation for the product operator $S_{\rm B}S_{\rm A}$ can be derived from Eqs. (B.9) and (B.10). Care should be taken that $[\widetilde{c}_{r_a-t}(0), S_{\rm B}(t-l)] = i\sqrt{\kappa_{\rm ex}^{\rm J}}[\hat{b}(t-l), S_{\rm B}(t-l)]/2$ and $[\widetilde{c}_{r_a-t}(0), S_{\rm A}(t)] = i\sqrt{\kappa_{\rm ex}}[\hat{a}(t), S_{\rm A}(t)]/2$, both of which result from Eq. (B.8).

In the considered setup, we do not apply an input field to System A through the waveguide. Therefore, denoting the initial state vector of the overall system by $|\psi_{\rm i}\rangle$, we can rigorously take $\widetilde{c}_r(0)|\psi_{\rm i}\rangle = 0$. Then, the equation of motion for $\langle S_{\rm A}S_{\rm B}\rangle = \langle\psi_{\rm i}|S_{\rm A}S_{\rm B}|\psi_{\rm i}\rangle$ is written as

$$\begin{aligned}\frac{d}{dt}\langle S_{\rm A}S_{\rm B}\rangle &= \frac{i}{\hbar}\langle[\hat{\mathcal{H}}_{\rm A}, S_{\rm A}]S_{\rm B}\rangle + \frac{i}{\hbar}\langle S_{\rm A}[\hat{\mathcal{H}}_{\rm B}, S_{\rm B}]\rangle \\ &\quad + \sqrt{\kappa_{\rm ex}\kappa_{\rm ex}^{\rm J}}\,\langle[S_{\rm A}, \hat{a}]\hat{b}^\dagger S_{\rm B}\rangle + \sqrt{\kappa_{\rm ex}\kappa_{\rm ex}^{\rm J}}\,\langle[\hat{a}^\dagger, S_{\rm A}]S_{\rm B}\hat{b}\rangle \\ &\quad + \frac{\kappa_{\rm ex}}{2}\langle\mathcal{L}_a[S_{\rm A}]S_{\rm B}\rangle + \frac{\kappa_{\rm ex}^{\rm J}}{2}\langle S_{\rm A}\mathcal{L}_b[S_{\rm B}]\rangle.\end{aligned} \tag{B.11}$$

Up to here, we assumed for simplicity that Systems A and B damp only through the radiative coupling to waveguide field. Here, we include other dissipation channels, such as the energy relaxation of cavities A and B into other environments, and the energy relaxation and pure dephasing of the qubit in System A. Furthermore, we take account of the thermal excitation of the systems through the environment. Then, Eq. (B.11) should be replaced with the following one,

$$\begin{aligned}\frac{d}{dt}\langle S_{\rm A}S_{\rm B}\rangle &= \frac{i}{\hbar}\langle[\hat{\mathcal{H}}_{\rm A}, S_{\rm A}]S_{\rm B}\rangle + \frac{i}{\hbar}\langle S_{\rm A}[\hat{\mathcal{H}}_{\rm B}, S_{\rm B}]\rangle \\ &\quad + \sqrt{\kappa_{\rm ex}\kappa_{\rm ex}^{\rm J}}\,\langle[S_{\rm A}, \hat{a}]\hat{b}^\dagger S_{\rm B}\rangle + \sqrt{\kappa_{\rm ex}\kappa_{\rm ex}^{\rm J}}\,\langle[\hat{a}^\dagger, S_{\rm A}]S_{\rm B}\hat{b}\rangle \\ &\quad + \frac{\kappa_{\rm ex}^{\rm J}}{2}\langle S_{\rm A}\mathcal{L}_b[S_{\rm B}]\rangle + \frac{\kappa(1+n_{\rm th})}{2}\langle\mathcal{L}_a[S_{\rm A}]S_{\rm B}\rangle \\ &\quad + \frac{\kappa n_{\rm th}}{2}\langle\mathcal{L}_{a^\dagger}[S_{\rm A}]S_{\rm B}\rangle + \frac{\gamma(1+p_{\rm th})}{2}\langle\mathcal{L}_\sigma[S_{\rm A}]S_{\rm B}\rangle \\ &\quad + \frac{\gamma p_{\rm th}}{2}\langle\mathcal{L}_{\sigma^\dagger}[S_{\rm A}]S_{\rm B}\rangle + \frac{\gamma_\phi}{2}\langle\mathcal{L}_{\sigma^\dagger\sigma}[S_{\rm A}]S_{\rm B}\rangle.\end{aligned} \tag{B.12}$$

where $\kappa$ is the total cavity energy-relaxation rate, $n_{\rm th}$ is the average thermal photon number in the cavity, $\gamma = 1/T_1$ is the qubit energy-relaxation rate, $p_{\rm th}$ is the thermal excitation probability of the qubit, and $\gamma_\phi$ is the qubit pure dephasing rate. Note that the internal loss and the thermal photon excitation of the JPA mode are neglected in Eq. (B.12).

## B.3 Linear response

In the Fock-state basis, an arbitrary state of the composite system is written as a superposition of $|q, n, m\rangle$, where $q(= \mathrm{g}, \mathrm{e})$ denotes the qubit state in System A, and $n$ and $m(= 0, 1, \cdots)$ denote the cavity photon numbers in Systems A and B, respectively. The density matrix of the composite system is obtained by setting $S_{\mathrm{A}}S_{\mathrm{B}} = S_{qnm,q'n'm'} = |q, n, m\rangle\langle q', n', m'|$ in Eq. (B.12). Since the probe field is weak, we solve this equation perturbatively in $\Omega_{\mathrm{p}}$. For this purpose, we first determine the steady-state solution $\langle S_{qnm,q'n'm'}\rangle^{(0)}$ by setting $\Omega_{\mathrm{p}} = 0$ in Eq. (B.12). Then, we determine the linear response $\langle S_{qnm,q'n'm'}\rangle^{(1)}$, which is proportional to $\Omega_{\mathrm{p}}e^{-i(\omega_{\mathrm{p}}-\omega_{\mathrm{d}})t}$. Since the output probe field is measured at a different port (Port 2 in Fig. 7.1) from the input probe field (Port 1 in Fig. 7.1), the probe transmission coefficient is proportional to the cavity amplitude of System A, $\langle \hat{a}\rangle^{(1)} = \sum_{q,n,m}\sqrt{n+1}\langle S_{qnm,q(n+1)m}\rangle^{(1)}$. The parameters used in the numerical calculations, which are independently determined in Sec. 7.7, are shown in Table 7.1.

The parameters characterizing the cavity drive fields (thermal, coherent, and squeezed vacuum states) are determined by fitting the qubit spectrum with numerical results from Eq. (B.12). Then, the photon-number distribution is determined from Eq. (B.12) in the absence of the qubit drive and cavity probe fields ($\Omega_{\mathrm{d}} = \Omega_{\mathrm{p}} = 0$). When a thermal state is applied as the cavity drive field, the thermal average photon number $n_{\mathrm{th}}$ is used as the fitting parameter. When a coherent state is used as the cavity drive, the Hamiltonian of System B is replaced with

$$\hat{\mathcal{H}}_{\mathrm{B}}/\hbar = \frac{\Omega_{\mathrm{s}}}{2}(\hat{b}^{\dagger} + \hat{b}). \tag{B.13}$$

Then, the output field from System B becomes a coherent state. The amplitude $\Omega_{\mathrm{s}}$, corresponding to the strength of the coherent drive to the cavity, is used as an additional fitting parameter. For the case of a squeezed vacuum drive, we need to incorporate the loss of the waveguide between the JPA and the cavity, since the squeezed vacuum state is degraded considerably by the loss in the waveguide. Theoretically, such waveguide loss is taken into account by decreasing the coupling $\kappa_{\mathrm{ex}}$ between the waveguide and the cavity of System A while keeping its total energy-relaxation rate $\kappa$. Accordingly, the pump amplitude for the JPA, $\Omega_{\mathrm{s}}$, and the external coupling rate of the cavity, $\kappa_{\mathrm{ex}}$, are used as the fitting parameters.

In the numerical simulations in Fig. 7.3, we employed the following parameters: $n_{\mathrm{th}} = 0.20$ in Fig. 7.3(a), $\Omega_{\mathrm{s}}/2\pi = 1.3$ MHz in Fig. 7.3(b), and $\Omega_{\mathrm{s}}/2\pi = 4.0$ MHz and $\kappa_{\mathrm{ex}}/2\pi = 0.42$ MHz in Fig. 7.3(c).

# Appendix C

# Simulation on QND detection

We explain a theoretical description of the QND detection of an itinerant photon based on the circuit QED system in the dispersive regime.

## C.1 Hamiltonian

The Hamiltonian describing the considered setup consists of three parts as

$$\hat{\mathcal{H}} = \hat{\mathcal{H}}_{\rm sys} + \hat{\mathcal{H}}_{\rm field} + \hat{\mathcal{H}}_{\rm env}, \tag{C.1}$$

where $\hat{\mathcal{H}}_{\rm sys}$, $\hat{\mathcal{H}}_{\rm field}$, and $\hat{\mathcal{H}}_{\rm env}$ respectively describe the qubit-cavity system, the interaction between the system and the pulse mode in the 1D transmission line, and the environmental degrees of freedom. Using the qubit operator $\hat{\sigma}_{pq} = |p\rangle\langle q|$ $(p, q = {\rm g,e})$, $\hat{\mathcal{H}}_{\rm sys}$ is given by

$$\hat{\mathcal{H}}_{\rm sys}/\hbar = (\omega_{\rm c} + \chi)\hat{a}^\dagger\hat{a}\hat{\sigma}_{\rm gg} + [\omega_{\rm q} + (\omega_{\rm c} - \chi)\hat{a}^\dagger\hat{a}]\hat{\sigma}_{\rm ee}, \tag{C.2}$$

which is identical to Eq. (9.1). The input/output port of the photon field is a semi-infinite transmission line field interacting with the cavity in reflection geometry. Setting the microwave velocity in the transmission line to unity, $\hat{\mathcal{H}}_{\rm field}$ is given by

$$\hat{\mathcal{H}}_{\rm field}/\hbar = \int dk \left[ k\hat{a}_k^\dagger\hat{a}_k + \sqrt{\kappa_{\rm ex}/2\pi}(\hat{a}_k^\dagger\hat{a} + \hat{a}^\dagger\hat{a}_k) \right], \tag{C.3}$$

where $\hat{a}_k$ is the field annihilation operator with wave number $k$ and $\kappa_{\rm ex}$ is the cavity external coupling rate to this port. The field operator in the real-space representation is defined by $\widetilde{a}_r = (2\pi)^{-1/2}\int dk e^{ikr}\hat{a}_k$. The environmental Hamiltonian $\mathcal{H}_{\rm env}$ involves other relaxation channels of the qubit and the cavity. The relevant parameters are $\kappa_{\rm in}$ (cavity internal loss rate), $n_{\rm B} = \frac{p_{\rm th}}{1+2p_{\rm th}}$ (average thermal quantum number of the qubit bath), $\gamma = \frac{1}{(1+2n_{\rm B})T_1}$ (qubit relaxation rate), and $\gamma_{\phi,{\rm n}} = \frac{1}{T_2^*} - \frac{1}{2T_1}$ (qubit pure dephasing rate).

We model these dampings by the interaction with fictitious continuous fields similar to Eq. (C.3). We omit their explicit forms here.

## C.2 Initial state

The input pulse mode has a Gaussian envelope with pulse length (full width at half maximum in amplitude) $l$ and carrier frequency $\omega_{\rm c}$. Its mode function $f_{\rm in}(r)$ is given, in the real-space representation, by

$$f_{\rm in}(r) = \left(\frac{8\ln 2}{\pi l^2}\right)^{1/4} 2^{-(2r/l)^2} e^{-i\omega_{\rm c} r}, \tag{C.4}$$

which is normalized as $\int dr|f_{\rm in}(r)|^2 = 1$. We write the mode function in the time representation as $f_{\rm in}(-t)$, by setting the speed of light $c = 1$. The origin of the time coordinate $t$ is chosen so that the photon amplitude entering the cavity reaches a maximum at $t = 0$. Since the quantum state in the input pulse mode is a weak coherent state, its state vector $|\psi_{\rm i}\rangle$ at the initial moment $t = t_{\rm i}$ is written as

$$|\psi_{\rm i}\rangle = \mathcal{N} \exp\left(\alpha_{\rm in} \int dr f_{\rm in}^*(r - t_{\rm i}) \widetilde{a}_r^\dagger\right) |{\rm vac}\rangle, \tag{C.5}$$

where $\alpha_{\rm in}$ is the amplitude of the input coherent state (average photon number $= |\alpha_{\rm in}|^2$), $|{\rm vac}\rangle$ is the vacuum state of the waveguide field, and $\mathcal{N} = e^{-|\alpha_{\rm in}|^2/2}$ is a normalization factor. The initial state of the qubit-cavity system at the initial moment $t = t_{\rm i}$ is $|{\rm g}, 0\rangle$. The initialization error of the qubit state is taken into account as a part of the readout errors ($\varepsilon_{\rm r}^{\rm g}$, $\varepsilon_{\rm r}^{\rm e}$). Therefore, the initial density matrix of the overall system is written as

$$\rho(t_{\rm i}) = |{\rm g}, 0\rangle\langle {\rm g}, 0| \otimes |\psi_{\rm i}\rangle\langle\psi_{\rm i}|. \tag{C.6}$$

## C.3 Time evolution

Throughout this study, we analyze the interaction between the input pulse mode and the qubit-cavity system in the Heisenberg picture. The Heisenberg equations for the system operators are obtained from Eq. (C.1). For example, $a$, $\sigma_{\rm ge}$ and $\sigma_{\rm ee}$ evolve as

$$\frac{d}{dt}\hat{a} = [-i(\omega_{\rm c} + \chi) - \kappa/2]\hat{a} + 2i\chi\hat{a}\hat{\sigma}_{\rm ee} - i\sqrt{\kappa_{\rm ex}}\,\widetilde{a}_{-t+t_{\rm i}}(t_{\rm i}) + \cdots, \tag{C.7}$$

$$\frac{d}{dt}\hat{\sigma}_{\rm ge} = (-i\omega_{\rm q} - \gamma_\phi)\hat{\sigma}_{\rm ge} + 2i\chi\hat{a}^\dagger\hat{a}\hat{\sigma}_{\rm ge} + \cdots, \tag{C.8}$$

$$\frac{d}{dt}\hat{\sigma}_{\rm ee} = -\gamma_1\hat{\sigma}_{\rm ee} + \gamma_2\hat{\sigma}_{\rm gg} + \cdots, \tag{C.9}$$

where $\kappa = \kappa_{\rm ex} + \kappa_{\rm in}$, $\gamma_1 = \gamma(1 + n_{\rm B})$, $\gamma_2 = \gamma n_{\rm B}$, $\gamma_\phi = \gamma_{\phi,{\rm n}} + (\gamma_1 + \gamma_2)/2$, and the dots represent the contributions from the environmental vacuum fluctuations. We denote the expectation value of an operator $A(t)$ by $\langle A\rangle = {\rm Tr}\{A(t)\rho(t_{\rm i})\}$, where the initial density matrix is defined in Eq. (C.6). From the property that a coherent state is an eigenstate of a field operator, we can rigorously replace $\widetilde{a}_r(t_{\rm i})$ with $\alpha_{\rm in} f_{\rm in}^*(r - t_{\rm i})$. Then, the operator equations (C.7)–(C.9) are recast into the following $c$-number ones,

$$\frac{d}{dt}\langle\hat{a}\rangle = [-i(\omega_{\rm c} + \chi) - \kappa/2]\langle\hat{a}\rangle + 2i\chi\langle\hat{a}\hat{\sigma}_{\rm ee}\rangle - i\sqrt{\kappa_{\rm ex}}\,\alpha_{\rm in} f_{\rm in}^*(-t), \tag{C.10}$$

$$\frac{d}{dt}\langle\hat{\sigma}_{\rm ge}\rangle = (-i\omega_{\rm q} - \gamma_\phi)\langle\hat{\sigma}_{\rm ge}\rangle + 2i\chi\langle\hat{a}^\dagger\hat{a}\hat{\sigma}_{\rm ge}\rangle, \tag{C.11}$$

$$\frac{d}{dt}\langle\hat{\sigma}_{\rm ee}\rangle = -\gamma_1\langle\hat{\sigma}_{\rm ee}\rangle + \gamma_2\langle\hat{\sigma}_{\rm gg}\rangle. \tag{C.12}$$

Besides the above time evolution, the $Y/2$ and $-Y/2$ gates are applied to the qubit. We treat these gates simply as instantaneous unitary transformations on the qubit operators. The $Y/2$ gate at $t = t_{\rm i}$ is written as

$$\begin{pmatrix} \sigma_{\rm gg} & \sigma_{\rm ge} \\ \sigma_{\rm eg} & \sigma_{\rm ee} \end{pmatrix} \to \frac{1}{2}\begin{pmatrix} \sigma_{\rm gg} + \sigma_{\rm eg} + \sigma_{\rm ge} + \sigma_{\rm ee} & -\sigma_{\rm gg} - \sigma_{\rm eg} + \sigma_{\rm ge} + \sigma_{\rm ee} \\ -\sigma_{\rm gg} + \sigma_{\rm eg} - \sigma_{\rm ge} + \sigma_{\rm ee} & \sigma_{\rm gg} - \sigma_{\rm eg} - \sigma_{\rm ge} + \sigma_{\rm ee} \end{pmatrix}, \tag{C.13}$$

and the $-Y/2$ gate at $t = t_{\rm g}$ is written as

$$\begin{pmatrix} \sigma_{\rm gg} & \sigma_{\rm ge} \\ \sigma_{\rm eg} & \sigma_{\rm ee} \end{pmatrix} \to \frac{1}{2}\begin{pmatrix} \sigma_{\rm gg} - \sigma_{\rm eg} - \sigma_{\rm ge} + \sigma_{\rm ee} & \sigma_{\rm gg} - \sigma_{\rm eg} + \sigma_{\rm ge} - \sigma_{\rm ee} \\ \sigma_{\rm gg} + \sigma_{\rm eg} - \sigma_{\rm ge} - \sigma_{\rm ee} & \sigma_{\rm gg} + \sigma_{\rm eg} + \sigma_{\rm ge} + \sigma_{\rm ee} \end{pmatrix}. \tag{C.14}$$

At the final moment $t = t_{\rm f}$, the qubit state is measured in the $Z$ axis with readout errors ($\varepsilon_{\rm r}^{\rm g}$, $\varepsilon_{\rm r}^{\rm e}$).

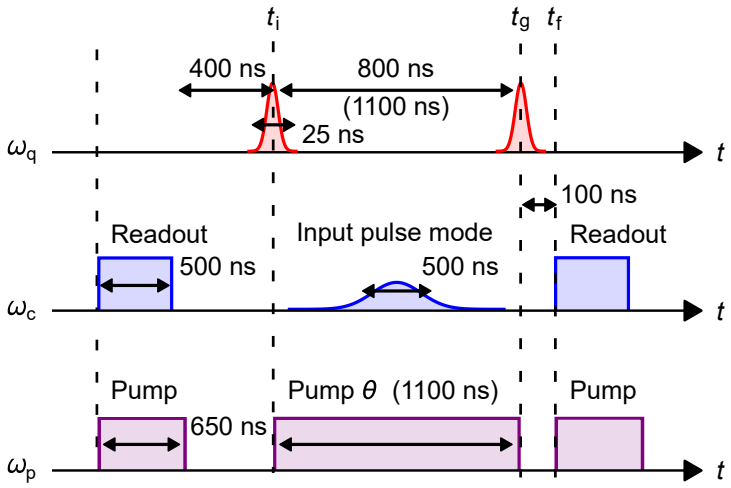


Figure C.1: Pulse sequence for the QND detection of an itinerant single photon. The interval between the $\pi/2$-gates are 800 ns for the evaluation of the quantum efficiency and 1100 ns for the quantum state tomography of the reflected pulse mode. $t_i$ is the initial time, $t_g$ is the second gate time, and $t_f$ is the measurement time in the numerical calculation.

## C.4 Quantum efficiency

By solving Eqs. (C.10)–(C.12) and similar equations for the terms such as $\langle a\sigma_{ee}\rangle$ and $\langle a^\dagger a\sigma_{ge}\rangle$, together with the qubit rotations of Eqs. (C.13) and (C.14), we calculate $P_e = \langle\sigma_{ee}(t_f)\rangle$ at the final moment $t_f$. Taking account of the readout errors, we obtain the qubit excitation probability as $\widetilde{P}_e = \varepsilon_r^g + \langle\sigma_{ee}(t_f)\rangle(1-\varepsilon_r^g-\varepsilon_r^e)$. In Fig. C.1, we set $l = 500$ ns, $t_i = -400$ ns, $t_g = 400$ ns, and $t_f = 500$ ns.

The quantum efficiency of the single-photon detection and the dark-count probability are accessible by varying the average photon number $|\alpha_{in}|^2$ in the input pulse mode. (Theoretically, this is automatically done by solving the evolution equations perturbatively in $\alpha_{in}$ and calculating the components of $\widetilde{P}_e$ proportional to $|\alpha_{in}|^0$ and $|\alpha_{in}|^2$.)

In Fig. C.2, we show the dependence of the quantum efficiency on the system parameters, $\kappa_{ex}$, $\kappa_{in}$, $\gamma$, and $\gamma_\phi$. The following parameters are fixed here: $\chi/2\pi = 1.5$ MHz, $n_B = 0$, $l = 500$ ns, and $\varepsilon_r^g = \varepsilon_r^e = 0$. Considering the experimentally achieved values of $\kappa_{ex}/2\chi = 1.1$, $\kappa_{in}/2\chi = 0.083$, $\gamma/2\chi = 0.0014$, and $\gamma_{\phi,n}/2\chi = 0.0012$, we conclude that the quantum efficiency in the experiment is limited by the internal loss of the cavity.

## C.5 Density matrix of reflected pulse mode

Here, we outline the theoretical evaluation of the conditional/unconditional density matrix of the reflected pulse mode. We first introduce the mode function $f_{out}(r)$ of the reflected pulse mode. For a long input pulse ($l \gg \kappa_{ex}^{-1}$), the pulse envelope is almost unchanged after reflection except for the slight delay due to absorption and re-emission by the cavity. We therefore set $f_{out}(r) = f_{in}(r+\tau_d)$, where $\tau_d$ is the delay time of the order of $\kappa_{ex}^{-1}$. Using this wavepacket, we define the creation operator $\hat{A}^\dagger$ of the output photon (in the Heisenberg picture at time $t$) by

$$\hat{A}^\dagger(t) = \int_0^{t-t_i} dr\ f_{out}^*(r-t)\tilde{a}_r^\dagger(t). \tag{C.15}$$

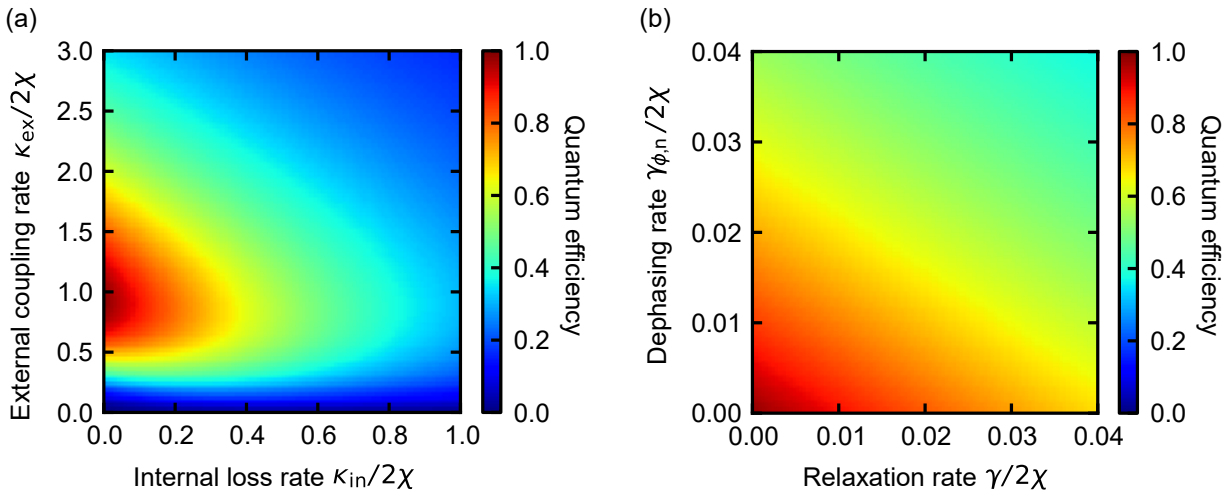


Figure C.2: Dependence of the quantum efficiency on the system parameters. (a) Quantum efficiency as a function of $\kappa_{\rm ex}$ and $\kappa_{\rm in}$. An ideal qubit ($\gamma = \gamma_{\phi,{\rm n}} = 0$) is assumed here. (b) Quantum efficiency as a function of $\gamma$ and $\gamma_{\phi,{\rm n}}$. The optimal cavity parameters $\kappa_{\rm ex} = 2\chi$ and $\kappa_{\rm in} = 0$ are used in accordance with the result in (a).

This operator satisfies the bosonic commutation relation of $[\hat{A}, \hat{A}^\dagger] = 1$.

For concreteness, we hereafter focus on the density matrix conditioned on the outcome of the qubit state ($q$ = g,e) at the final moment $t_{\rm f}$. This density matrix is determined from the moments of the field operators, $\langle \sigma_{qq}(t_{\rm f}) \hat{A}^{\dagger m}(t_{\rm f}) \hat{A}^n(t_{\rm f}) \rangle$ $(m, n = 0, 1, \cdots)$ [129]. In particular, when the reflected pulse mode contains up to one photon as in the current case, we need only three quantities, $P_q = \langle \hat{\sigma}_{qq} \rangle$, $A_q = \langle \hat{\sigma}_{qq} \hat{A} \rangle$, and $N_q = \langle \hat{\sigma}_{qq} \hat{A}^\dagger \hat{A} \rangle$. $P_q$ can be calculated with the prescription presented in Section C.3. For calculation of $A_q$ and $N_q$, which contain the output field operator ($\widetilde{a}_r$ with $r > 0$), we use the input-output relation,

$$\widetilde{a}_r(t) = \widetilde{a}_{r-t+t_{\rm i}}(t_{\rm i}) - i\sqrt{\kappa_{\rm ex}} \hat{a}(t-r)\theta(r)\theta(t - t_{\rm i} - r), \tag{C.16}$$

where $\theta$ is the Heaviside step function. $A_q$ is recast into the following form,

$$A_q = \langle \hat{\sigma}_{qq}(t) \rangle \times \alpha \int_{t_{\rm i}}^{t_{\rm f}} dt\ f_{\rm out}(-t) f_{\rm in}^*(-t) - i\sqrt{\kappa_{\rm ex}} \int_{t_{\rm i}}^{t_{\rm f}} dt\ f_{\rm out}(-t) \langle \hat{\sigma}_{qq}(t_{\rm f}) \hat{a}(t) \rangle. \tag{C.17}$$

Similarly, up to the three-time correlation function is required for calculation of $N_q$. The elements of the conditional density matrix $\rho^{\rm q}$ are determined from $P_q$, $A_q$, and $N_q$ by

$$\rho^q_{00} = \frac{P_q - N_q}{P_q}, \tag{C.18}$$

$$\rho^q_{01} = \frac{A_q}{P_q}, \tag{C.19}$$

$$\rho^q_{11} = \frac{N_q}{P_q}. \tag{C.20}$$

Taking account of the readout errors, the conditional density matrices $\widetilde{\rho}^q$ are determined by

$$\widetilde{\rho}^{\rm g} = \frac{P_{\rm e}(1 - \varepsilon_{\rm r}^{\rm e})\, \rho^{\rm e} + P_{\rm g} \varepsilon_{\rm r}^{\rm g}\, \rho^{\rm g}}{P_{\rm e}(1 - \varepsilon_{\rm r}^{\rm e}) + P_{\rm g} \varepsilon_{\rm r}^{\rm g}}, \tag{C.21}$$

$$\widetilde{\rho}^{\rm e} = \frac{P_{\rm g}(1 - \varepsilon_{\rm r}^{\rm g})\, \rho^{\rm g} + P_{\rm e} \varepsilon_{\rm r}^{\rm e}\, \rho^{\rm e}}{P_{\rm g}(1 - \varepsilon_{\rm r}^{\rm g}) + P_{\rm e} \varepsilon_{\rm r}^{\rm e}}. \tag{C.22}$$

We confirm that the numerical results well reproduce the experimental results.

# Bibliography


[1] M. A. Nielsen and I. L. Chuang. *Quantum computation and quantum information*. Cambridge university press, Cambridge, 2010.

[2] Y. Nakamura, Y. A. Pashkin, and J. S. Tsai. Coherent control of macroscopic quantum states in a single-cooper-pair box. *Nature*, 398:786, 1999.

[3] A. J. Leggett. Macroscopic quantum systems and the quantum theory of measurement. *Progress of Theoretical Physics Supplement*, 69:80–100, 1980.

[4] J. M. Martinis, M. H. Devoret, and J. Clarke. Experimental tests for the quantum behavior of a macroscopic degree of freedom: The phase difference across a Josephson junction. *Phys. Rev. B*, 35:4682–4698, 1987.

[5] R. Barends, J. Kelly, A. Megrant, D. Sank, E. Jeffrey, Y. Chen, Y. Yin, B. Chiaro, J. Mutus, C. Neill, P. O'Malley, P. Roushan, J. Wenner, T. C. White, A. N. Cleland, and John M. Martinis. Coherent Josephson qubit suitable for scalable quantum integrated circuits. *Phys. Rev. Lett.*, 111:080502, 2013.

[6] C. Wang, C. Axline, Y. Y. Gao, T. Brecht, Y. Chu, L. Frunzio, M. H. Devoret, and R. J. Schoelkopf. Surface participation and dielectric loss in superconducting qubits. *Applied Physics Letters*, 107:162601, 2015.

[7] F. Yan, S. Gustavsson, A. Kamal, J. Birenbaum, A. P. Sears, D. Hover, T. J. Gudmundsen, D. Rosenberg, G. Samach, S. Weber, J. L. Yoder, T. P. Orlando, J. Clarke, A. J. Kerman, and W. D. Oliver. The flux qubit revisited to enhance coherence and reproducibility. *Nature Commun.*, 7:12964, 2016.

[8] L. B. Nguyen, Y.-H. Lin, A. Somoroff, R. Mencia, N. Grabon, and V. E. Manucharyan. The high-coherence fluxonium qubit. *arXiv:1810.11006*, 2018.

[9] J. Koch, T. M. Yu, J. Gambetta, A. A. Houck, D. I. Schuster, J. Majer, A. Blais, M. H. Devoret, S. M. Girvin, and R. J. Schoelkopf. Charge-insensitive qubit design derived from the cooper pair box. *Phys. Rev. A*, 76:042319, 2007.

[10] J. A. Schreier, A. A. Houck, Jens Koch, D. I. Schuster, B. R. Johnson, J. M. Chow, J. M. Gambetta, J. Majer, L. Frunzio, M. H. Devoret, S. M. Girvin, and R. J. Schoelkopf. Suppressing charge noise decoherence in superconducting charge qubits. *Phys. Rev. B*, 77:180502, 2008.

[11] J. M. Raimond, M. Brune, and S. Haroche. Manipulating quantum entanglement with atoms and photons in a cavity. *Rev. Mod. Phys.*, 73:565–582, 2001.

[12] A. Blais, R.-S. Huang, A. Wallraff, S. M. Girvin, and R. J. Schoelkopf. Cavity quantum electrodynamics for superconducting electrical circuits: An architecture for quantum computation. *Phys. Rev. A*, 69:062320, 2004.

[13] A. Wallraff, D. I. Schuster, A. Blais, L. Frunzio, R-S Huang, J. Majer, S. Kumar, S. M. Girvin, and R. J. Schoelkopf. Strong coupling of a single photon to a superconducting qubit using circuit quantum electrodynamics. *Nature*, 431:162, 2004.

[14] A. Blais, J. Gambetta, A. Wallraff, D. I. Schuster, S. M. Girvin, M. H. Devoret, and R. J. Schoelkopf. Quantum-information processing with circuit quantum electrodynamics. *Phys. Rev. A*, 75:032329, 2007.

[15] R. Barends, J. Kelly, A. Megrant, A. Veitia, D. Sank, E. Jeffrey, T. C. White, J. Mutus, A. G. Fowler, B. Campbell, Y. Chen, Z. Chen, B. Chiaro, A. Dunsworth, C. Neill, P. O'Malley, P. Roushan, A. Vainsencher, J. Wenner, A. N. Korotkov, A. N. Cleland, and J. M. Martinis. Superconducting quantum circuits at the surface code threshold for fault tolerance. *Nature*, 508:500, 2014.

[16] M. H. Devoret, S. M. Girvin, and R. J. Schoelkopf. Circuit-QED: How strong can the coupling between a Josephson junction atom and a transmission line resonator be? *Ann. Phys.*, 16:767–779, 2007.

[17] J. Gambetta, A. Blais, D. I. Schuster, A. Wallraff, L. Frunzio, J. Majer, M. H. Devoret, S. M. Girvin, and R. J. Schoelkopf. Qubit-photon interactions in a cavity: Measurement-induced dephasing and number splitting. *Phys. Rev. A*, 74:042318, 2006.

[18] D. I. Schuster, A. A. Houck, J. A. Schreier, A. Wallraff, J. M. Gambetta, A. Blais, L. Frunzio, J. Majer, B. Johnson, M. H. Devoret, S. H. Girvin, and R. J. Schoelkopf. Resolving photon number states in a superconducting circuit. *Nature*, 445:515, 2007.

[19] M. Hofheinz, H. Wang, M. Ansmann, R. C. Bialczak, E. Lucero, M. Neeley, A. D. O'Connell, D. Sank, J. Wenner, J. M. Martinis, and A. N. Cleland. Synthesizing arbitrary quantum states in a superconducting resonator. *Nature*, 459:546–549, 2009.

[20] R. W. Heeres, P. Reinhold, N. Ofek, L. Frunzio, L. Jiang, M. H. Devoret, and R. J. Schoelkopf. Implementing a universal gate set on a logical qubit encoded in an oscillator. *Nature Commun.*, 8:94, 2017.

[21] B. Vlastakis, G. Kirchmair, Z. Leghtas, S. E. Nigg, L. Frunzio, Steven M. Girvin, M. Mirrahimi, M. H. Devoret, and R. J. Schoelkopf. Deterministically encoding quantum information using 100-photon Schrödinger cat states. *Science*, 342:607–610, 2013.

[22] B. R. Johnson, M. D. Reed, A. A. Houck, D. I. Schuster, L. S. Bishop, E. Ginossar, J. M. Gambetta, L. DiCarlo, L. Frunzio, S. M. Girvin, and R. J. Schoelkopf. Quantum non-demolition detection of single microwave photons in a circuit. *Nature Phys.*, 6:663–667, 2010.

[23] H. Paik, D. I. Schuster, Lev S. Bishop, G. Kirchmair, G. Catelani, A. P. Sears, B. R. Johnson, M. J. Reagor, L. Frunzio, L. I. Glazman, S. M. Girvin, M. H. Devoret, and R. J. Schoelkopf. Observation of high coherence in Josephson junction qubits measured in a three-dimensional circuit QED architecture. *Phys. Rev. Lett.*, 107:240501, 2011.

[24] M. Reagor, H. Paik, G. Catelani, L. Sun, C. Axline, E. Holland, I. M. Pop, N. A. Masluk, T. Brecht, L. Frunzio, M. H. Devoret, L. Glazman, and R. J.) View Affiliations Schoelkopf. Reaching 10 ms single photon lifetimes for superconducting aluminum cavities. *Applied Physics Letters*, 102:192604, 2013.

[25] N. Ofek, A. Petrenko, R. Heeres, P. Reinhold, Z. Leghtas, B. Vlastakis, Y. Liu, L. Frunzio, S. M. Girvin, L. Jiang, M. Mirrahimi, M. H. Devoret, and R. J. Schoelkopf. Extending the lifetime of a quantum bit with error correction in superconducting circuits. *Nature*, 536:441, 2016.

[26] K. S. Chou, J. Z. Blumoff, C. S. Wang, P. C. Reinhold, C. J. Axline, Y. Y. Gao, L. Frunzio, M. H. Devoret, L. Jiang, and R. J. Schoelkopf. Deterministic teleportation of a quantum gate between two logical qubits. *Nature*, 561:368, 2018.

[27] R. Barends, A. Shabani, L. Lamata, J. Kelly, A. Mezzacapo, U. Las Heras, R. Babbush, A. G. Fowler, B. Campbell, Y. Chen, Z. Chen, B. Chiaro, A. Dunsworth, E. Jeffrey, E. Lucero, A. Megrant, J. Y. Mutus, M. Neeley, C. Neill, P. J. J. O'Malley, C. Quintana, P. Roushan, D. Sank, A. Vainsencher, J. Wenner, T. C. White, E. Solano, H. Neven, and J. M. Martinis. Digitized adiabatic quantum computing with a superconducting circuit. *Nature*, 534:222, 2016.

[28] J. S. Otterbach, R. Manenti, N. Alidoust, A. Bestwick, M. Block, B. Bloom, S. Caldwell, N. Didier, E. S. Fried, S. Hong, P. Karalekas, C. B. Osborn, A. Papageorge, E. C. Peterson, G. Prawiroatmodjo, N. Rubin, C. A. Ryan, D. Scarabelli, M. Scheer, E. A. Sete, P. Sivarajah, R. S. Smith, A. Staley, N. Tezak, W. J. Zeng, A. Hudson, B. R. Johnson, M. Reagor, M. P. da Silva, and C. Rigetti. Unsupervised machine learning on a hybrid quantum computer. *arXiv:1712.05771*, 2017.

[29] J. Preskill. Quantum Computing in the NISQ era and beyond. *Quantum*, 2:79, 2018.

[30] M. H. Devoret and R. J. Schoelkopf. Superconducting circuits for quantum information: an outlook. *Science*, 339:1169–1174, 2013.

[31] H. J. Kimble. The quantum internet. *Nature*, 453:1023–1030, 2008.

[32] C. Eichler, D. Bozyigit, C. Lang, L. Steffen, J. Fink, and A. Wallraff. Experimental state tomography of itinerant single microwave photons. *Phys. Rev. Lett.*, 106:220503, 2011.

[33] W. F. Kindel, M. D. Schroer, and K. W. Lehnert. Generation and efficient measurement of single photons from fixed-frequency superconducting qubits. *Phys. Rev. A*, 93:033817, 2016.

[34] W. Pfaff, C. J. Axline, L. D. Burkhart, U. Vool, P. Reinhold, L. Frunzio, Liang Jiang, M. H. Devoret, and R. J. Schoelkopf. Controlled release of multiphoton quantum states from a microwave cavity memory. *Nature Phys.*, 13:882–887, 2017.

[35] P. Kurpiers, P. Magnard, T. Walter, B. Royer, M. Pechal, J. Heinsoo, Y. Salathé, A. Akin, S. Storz, J-C Besse, S. Gasparinetti, A. Blais, and A. Wallraff. Deterministic quantum state transfer and remote entanglement using microwave photons. *Nature*, 558:264, 2018.

[36] C. J. Axline, L. D. Burkhart, W. Pfaff, M. Zhang, K. Chou, P. Campagne-Ibarcq, P. Reinhold, L. Frunzio, S. M. Girvin, Liang Jiang, M. H. Devoret, and R. J. Schoelkopf. On-demand quantum state transfer and entanglement between remote microwave cavity memories. *Nature Phys.*, 14:705–710, 2018.

[37] P. Campagne-Ibarcq, E. Zalys-Geller, A. Narla, S. Shankar, P. Reinhold, L. Burkhart, C. Axline, W. Pfaff, L. Frunzio, R. J. Schoelkopf, and M. H. Devoret. Deterministic remote entanglement of superconducting circuits through microwave two-photon transitions. *Phys. Rev. Lett.*, 120:200501, 2018.

[38] Y.-F. Chen, D. Hover, S. Sendelbach, L. Maurer, S. T. Merkel, E. J. Pritchett, F. K. Wilhelm, and R. McDermott. Microwave photon counter based on Josephson junctions. *Phys. Rev. Lett.*, 107:217401, 2011.

[39] K. Inomata, Z. R. Lin, K. Koshino, W. D. Oliver, J. S. Tsai, T. Yamamoto, and Y. Nakamura. Single microwave-photon detector using an artificial $\Lambda$-type three-level system. *Nature Commun.*, 7:12303, 2016.

[40] G. Oelsner, C. K. Andersen, M. Rehák, M. Schmelz, S. Anders, M. Grajcar, U. Hübner, K. Mølmer, and E. Il'ichev. Detection of weak microwave fields with an underdamped Josephson junction. *Phys. Rev. Applied*, 7:014012, 2017.

[41] R. H. Hadfield. Single-photon detectors for optical quantum information applications. *Nature Photon.*, 3:696–705, 2009.

[42] S. Kono, Y. Masuyama, T. Ishikawa, Y. Tabuchi, R. Yamazaki, K. Usami, K. Koshino, and Y. Nakamura. Nonclassical photon number distribution in a superconducting cavity under a squeezed drive. *Phys. Rev. Lett.*, 119:023602, 2017.

[43] S. Kono, K. Koshino, Y. Tabuchi, A. Noguchi, and Y. Nakamura. Quantum non-demolition detection of an itinerant microwave photon. *Nature Phys.*, 14:546–549, 2018.

[44] M. H Devoret. Quantum fluctuations in electrical circuits. *Les Houches, Session LXIII*, 7, 1995.

[45] N. Imoto. Quantum effects of spatial/temporal modulation of the optical field. *Materials Science and Engineering: B*, 48:34–38, 1997.

[46] C. W. Gardiner and P. Zoller. *Quantum Noise*. Springer-Verlag, Berlin, 1999.

[47] A. A. Clerk, M. H. Devoret, S. M. Girvin, F. Marquardt, and R. J. Schoelkopf. Introduction to quantum noise, measurement, and amplification. *Rev. Mod. Phys.*, 82:1155, 2010.

[48] F. Motzoi, J. M. Gambetta, P. Rebentrost, and F. K. Wilhelm. Simple pulses for elimination of leakage in weakly nonlinear qubits. *Phys. Rev. Lett.*, 103:110501, 2009.

[49] E. Lucero, J. Kelly, R. C. Bialczak, M. Lenander, M. Mariantoni, M. Neeley, A. D. O'Connell, D. Sank, H. Wang, M. Weides, J. Wenner, T. Yamamoto, A. N. Cleland, and J. M. Martinis. Reduced phase error through optimized control of a superconducting qubit. *Phys. Rev. A*, 82:042339, 2010.

[50] R. Movshovich, B. Yurke, P. G. Kaminsky, A. D. Smith, A. H. Silver, R. W. Simon, and M. V. Schneider. Observation of zero-point noise squeezing via a Josephson-parametric amplifier. *Phys. Rev. Lett.*, 65:1419–1422, 1990.

[51] M. A. Castellanos-Beltran, K. D. Irwin, G. C. Hilton, L. R. Vale, and K. W. Lehnert. Amplification and squeezing of quantum noise with a tunable Josephson metamaterial. *Nature Phys.*, 4:929–931, 2008.

[52] T. Yamamoto, K. Inomata, M. Watanabe, K. Matsuba, T. Miyazaki, W. D. Oliver, Y. Nakamura, and J. S. Tsai. Flux-driven Josephson parametric amplifier. *Appl. Phys. Lett.*, 93:042510, 2008.

[53] C. Macklin, K. O'Brien, D. Hover, M. E. Schwartz, V. Bolkhovsky, X. Zhang, W. D. Oliver, and I. Siddiqi. A near–quantum-limited Josephson traveling-wave parametric amplifier. *Science*, 350:307–310, 2015.

[54] U. Leonhardt. *Measuring the Quantum State of Light.* Cambridge University Press, Cambridge, 1997.

[55] H. J. Carmichael. *Statistical Methods in Quantum Optics 1.* Springer-Verlag, Berlin, 1999.

[56] D. F. Walls and G. J. Milburn. *Quantum optics.* Springer-Verlag, Berlin, 2008.

[57] A. I. Lvovsky and M. G. Raymer. Continuous-variable optical quantum-state tomography. *Rev. Mod. Phys.*, 81:299, 2009.

[58] D. Gottesman, A. Kitaev, and J. Preskill. Encoding a qubit in an oscillator. *Phys. Rev. A*, 64:012310, Jun 2001.

[59] E. P. Menzel, R. Di Candia, F. Deppe, P. Eder, L. Zhong, M. Ihmig, M. Haeberlein, A. Baust, E. Hoffmann, D. Ballester, K. Inomata, T. Yamamoto, Y. Nakamura, E. Solano, A. Marx, and R. Gross. Path entanglement of continuous-variable quantum microwaves. *Phys. Rev. Lett.*, 109:250502, 2012.

[60] COMSOL Multiphysics® v.5.2. www.comsol.com. COMSOL AB, Stockholm, Sweden.

[61] S. E. Nigg, H. Paik, B. Vlastakis, G. Kirchmair, S. Shankar, L. Frunzio, M. H. Devoret, R. J. Schoelkopf, and S. M. Girvin. Black-box superconducting circuit quantization. *Phys. Rev. Lett.*, 108:240502, 2012.

[62] M. Reagor. *Superconducting Cavities for Circuit Quantum Electrodynamics.* 2015.

[63] E. Jeffrey, D. Sank, J. Y. Mutus, T. C. White, J. Kelly, R. Barends, Y. Chen, Z. Chen, B. Chiaro, A. Dunsworth, A. Megrant, P. J. J. O'Malley, C. Neill, P. Roushan, A. Vainsencher, J. Wenner, A. N. Cleland, and J. M. Martinis. Fast accurate state measurement with superconducting qubits. *Phys. Rev. Lett.*, 112:190504, 2014.

[64] E. A. Sete, J. M. Martinis, and A. N. Korotkov. Quantum theory of a bandpass purcell filter for qubit readout. *Phys. Rev. A*, 92:012325, 2015.

[65] V. Ambegaokar and A. Baratoff. Tunneling between superconductors. *Phys. Rev. Lett.*, 10:486, 1963.

[66] D. H. Douglass and R. Meservey. Energy gap measurements by tunneling between superconducting films. i. temperature dependence. *Phys. Rev.*, 135:A19–A23, 1964.

[67] A. A. Houck, J. A. Schreier, B. R. Johnson, J. M. Chow, Jens Koch, J. M. Gambetta, D. I. Schuster, L. Frunzio, M. H. Devoret, S. M. Girvin, and R. J. Schoelkopf. Controlling the spontaneous emission of a superconducting transmon qubit. *Phys. Rev. Lett.*, 101:080502, 2008.

[68] A. A. Clerk and D. W. Utami. Using a qubit to measure photon-number statistics of a driven thermal oscillator. *Phys. Rev. A*, 75:042302, 2007.

[69] D. O. Edwards and M. S. Pettersen. Lectures on the properties of liquid and solid 3he-4he mixtures at low temperatures. *Journal of Low Temperature Physics*, 87:473–523, 1992.

[70] X. Y. Jin, A. Kamal, A. P. Sears, T. Gudmundsen, D. Hover, J. Miloshi, R. Slattery, F. Yan, J. Yoder, T. P. Orlando, S. Gustavsson, and W. D. Oliver. Thermal and residual excited-state population in a 3D transmon qubit. *Phys. Rev. Lett.*, 114:240501, 2015.

[71] K. Serniak, M. Hays, G. de Lange, S. Diamond, S. Shankar, L. D. Burkhart, L. Frunzio, M. Houzet, and M. H. Devoret. Hot nonequilibrium quasiparticles in transmon qubits. *Phys. Rev. Lett.*, 121:157701, 2018.

[72] K. Geerlings. *Improving Coherence of Superconducting Qubits and Resonators*. 2013.

[73] Lev S. Bishop and S. M. Ginossar, E.and Girvin. Response of the strongly driven jaynes-cummings oscillator. *Phys. Rev. Lett.*, 105:100505, 2010.

[74] M. D. Reed, L. DiCarlo, B. R. Johnson, L. Sun, D. I. Schuster, L. Frunzio, and R. J. Schoelkopf. High-fidelity readout in circuit quantum electrodynamics using the jaynes-cummings nonlinearity. *Phys. Rev. Lett.*, 105:173601, 2010.

[75] G. Calusine, A. Melville, W. Woods, R. Das, C. Stull, V. Bolkhovsky, D. Braje, D. Hover, D. K. Kim, X. Miloshi, D. Rosenberg, A. Sevi, J. L. Yoder, E. A. Dauler, and W. D. Oliver. Analysis and mitigation of interface losses in trenched superconducting coplanar waveguide resonators. *Appl. Phys. Lett.*, 112:062601, 2018.

[76] D. I. Schuster, A. Wallraff, A. Blais, L. Frunzio, R.-S. Huang, J. Majer, S. M. Girvin, and R. J. Schoelkopf. ac stark shift and dephasing of a superconducting qubit strongly coupled to a cavity field. *Phys. Rev. Lett.*, 94:123602, 2005.

[77] R. W. Boyd. *Nonlinear Optics*. Academic Press, 2008.

[78] M. A. Castellanos-Beltran and K. W. Lehnert. Widely tunable parametric amplifier based on a superconducting quantum interference device array resonator. *Appl. Phys. Lett.*, 91:083509, 2007.

[79] C. Eichler and A. Wallraff. Controlling the dynamic range of a josephson parametric amplifier. *EPJ Quantum Technology*, 1:2, 2014.

[80] Z. R. Lin, K. Inomata, K. Koshino, W. D. Oliver, Y. Nakamura, J.-S. Tsai, and T. Yamamoto. Josephson parametric phase-locked oscillator and its application to dispersive readout of superconducting qubits. *Nature communications*, 5:4480, 2014.

[81] E. Magesan, J. M. Gambetta, A. D. Corcoles, and J. M. Chow. Machine learning for discriminating quantum measurement trajectories and improving readout. *Phys. Rev. Lett.*, 114:200501, 2015.

[82] P. D. Drummond and Z. Ficek. *Quantum Squeezing*, volume 27. Springer Science & Business Media, 2013.

[83] F. Mallet, M. A. Castellanos-Beltran, H. S. Ku, S. Glancy, E. Knill, K. D. Irwin, G. C. Hilton, L. R. Vale, and K. W. Lehnert. Quantum state tomography of an itinerant squeezed microwave field. *Phys. Rev. Lett.*, 106:220502, 2011.

[84] L. Zhong, E. P. Menzel, R. Di Candia, P. Eder, M. Ihmig, A. Baust, M. Haeberlein, E. Hoffmann, K. Inomata, T. Yamamoto, Y. Nakamura, E. Solano, F. Deppe, A. Marx, and R. Gross. Squeezing with a flux-driven Josephson parametric amplifier. *New J. Phys.*, 15:125013, 2013.

[85] C. M. Wilson, G. Johansson, A. Pourkabirian, M. Simoen, J. R. Johansson, T. Duty, F. Nori, and P. Delsing. Observation of the dynamical Casimir effect in a superconducting circuit. *Nature*, 479:376–379, 2011.

[86] C. Eichler, D. Bozyigit, C. Lang, M. Baur, L. Steffen, J. M. Fink, S. Filipp, and A. Wallraff. Observation of two-mode squeezing in the microwave frequency domain. *Phys. Rev. Lett.*, 107:113601, 2011.

[87] N. Bergeal, F. Schackert, L. Frunzio, and M. H. Devoret. Two-mode correlation of microwave quantum noise generated by parametric down-conversion. *Phys. Rev. Lett.*, 108:123902, 2012.

[88] E. Flurin, N. Roch, F. Mallet, M. H. Devoret, and B. Huard. Generating entangled microwave radiation over two transmission lines. *Phys. Rev. Lett.*, 109:183901, 2012.

[89] K. W. Murch, S. J. Weber, K. M. Beck, E. Ginossar, and I. Siddiqi. Reduction of the radiative decay of atomic coherence in squeezed vacuum. *Nature*, 499:62–65, 2013.

[90] D. M. Toyli, A. W. Eddins, S. Boutin, S. Puri, D. Hover, V. Bolkhovsky, W. D. Oliver, A. Blais, and I. Siddiqi. Resonance fluorescence from an artificial atom in squeezed vacuum. *Phys. Rev. X*, 6:031004, 2016.

[91] A. Bienfait, P. Campagne-Ibarcq, A. H. Kiilerich, X. Zhou, S. Probst, J. J. Pla, T. Schenkel, D. Vion, D. Esteve, J. J. L. Morton, K. Moelmer, and P. Bertet. Magnetic resonance with squeezed microwaves. *Phys. Rev. X*, 7:041011, 2017.

[92] W. Schleich and J. A. Wheeler. Oscillations in photon distribution of squeezed states and interference in phase space. *Nature*, 326:574–577, 1987.

[93] E. Waks, B. C. Sanders, E. Diamanti, and Y. Yamamoto. Highly nonclassical photon statistics in parametric down-conversion. *Phys. Rev. A*, 73:033814, 2006.

[94] K. Wakui, Y. Eto, H. Benichi, S. Izumi, T. Yanagida, K. Ema, T. Numata, D. Fukuda, M. Takeoka, and M. Sasaki. Ultrabroadband direct detection of nonclassical photon statistics at telecom wavelength. *Sci. Rep.*, 4:4535, 2014.

[95] A. Narla, S. Shankar, M. Hatridge, Z. Leghtas, K. M. Sliwa, E. Zalys-Geller, S. O. Mundhada, W. Pfaff, L. Frunzio, R. J. Schoelkopf, and M. H. Devoret. Robust concurrent remote entanglement between two superconducting qubits. *Phys. Rev. X*, 6:031036, 2016.

[96] K. Moon. Photon-number splitting of squeezed light by a single qubit in circuit QED. *Phys. Rev. A*, 88:043830, 2013.

[97] B. Suri, Z. K. Keane, Lev S. Bishop, S. Novikov, F. C. Wellstood, and B. S. Palmer. Nonlinear microwave photon occupancy of a driven resonator strongly coupled to a transmon qubit. *Phys. Rev. A*, 92:063801, 2015.

[98] D. N. Klyshko. Observable signs of nonclassical light. *Phys. Lett. A*, 213:7–15, 1996.

[99] B. Suri, Z. K. Keane, R. Ruskov, Lev S. Bishop, C. Tahan, S. Novikov, J. E. Robinson, F. C. Wellstood, and B. S. Palmer. Observation of autler–townes effect in a dispersively dressed Jaynes–Cummings system. *New J. of Phys.*, 15:125007, 2013.

[100] X. Gu, A. F. Kockum, A. Miranowicz, Y. X. Liu, and F. Nori. Microwave photonics with superconducting quantum circuits. *Physics Reports*, 718:1–102, 2017.

[101] A. A. Houck, D. I. Schuster, J. M. Gambetta, J. A. Schreier, B. R. Johnson, J. M. Chow, L. Frunzio, J. Majer, M. H. Devoret, S. M. Girvin, and R. J. Schoelkopf. Generating single microwave photons in a circuit. *Nature*, 449:328, 2007.

[102] M. Pechal, L. Huthmacher, C. Eichler, S. Zeytinoğlu, A. A.. Abdumalikov Jr, S. Berger, A. Wallraff, and S. Filipp. Microwave-controlled generation of shaped single photons in circuit quantum electrodynamics. *Phys. Rev. X*, 4:041010, 2014.

[103] S. Hacohen-Gourgy, L. S. Martin, E. Flurin, V. V. Ramasesh, K. B. Whaley, and I. Siddiqi. Dynamics of simultaneously measured non-commuting observables. *Nature*, 538:491–494, 2016.

[104] P. Campagne-Ibarcq, S. Jezouin, N. Cottet, P. Six, L. Bretheau, F. Mallet, A. Sarlette, P. Rouchon, and B. Huard. Using spontaneous emission of a qubit as a resource for feedback control. *Phys. Rev. Lett.*, 117:060502, 2016.

[105] A. I. Lvovsky. Iterative maximum-likelihood reconstruction in quantum homodyne tomography. *Journal of Optics B: Quantum and Semiclassical Optics*, 6:S556–S559, 2004.

[106] Y. X. Liu, Ş. K. Özdemir, A. Miranowicz, and N. Imoto. Kraus representation of a damped harmonic oscillator and its application. *Phys. Rev. A*, 70:042308, 2004.

[107] C. L. Degen, F. Reinhard, and P. Cappellaro. Quantum sensing. *Rev. Mod. Phys.*, 89:035002, 2017.

[108] E. Knill, R. Laflamme, and G. J. Milburn. A scheme for efficient quantum computation with linear optics. *Nature*, 409:46–52, 2000.

[109] N. Imoto, H. A. Haus, and Y. Yamamoto. Quantum nondemolition measurement of the photon number via the optical Kerr effect. *Phys. Rev. A*, 32:2287–2292, 1985.

[110] P. Grangier, J. A. Levenson, and J.-P. Poizat. Quantum non-demolition measurements in optics. *Nature*, 396:537–542, 1998.

[111] F. Helmer, M. Mariantoni, E. Solano, and F. Marquardt. Quantum nondemolition photon detection in circuit QED and the quantum Zeno effect. *Phys. Rev. A*, 79:052115, 2009.

[112] S. R. Sathyamoorthy, L. Tornberg, A. F. Kockum, B. Q. Baragiola, J. Combes, C. M. Wilson, T. M. Stace, and G. Johansson. Quantum nondemolition detection of a propagating microwave photon. *Phys. Rev. Lett.*, 112:093601, 2014.

[113] B. Royer, A. L. Grimsmo, A. Choquette-Poitevin, and A. Blais. Itinerant microwave photon detector. *Phys. Rev. Lett.*, 120:203602, 2018.

[114] A. Reiserer, S. Ritter, and G. Rempe. Nondestructive detection of an optical photon. *Science*, 342:1349–1351, 2013.

[115] A. Reiserer and G. Rempe. Cavity-based quantum networks with single atoms and optical photons. *Rev. Mod. Phys.*, 87:1379–1418, 2015.

[116] L. Bretheau, P. Campagne-Ibarcq, E. Flurin, F. Mallet, and B. Huard. Quantum dynamics of an electromagnetic mode that cannot contain $N$ photons. *Science*, 348:776–779, 2015.

[117] N. Roch, M. E. Schwartz, F. Motzoi, C. Macklin, R. Vijay, A. W. Eddins, A. N. Korotkov, K. B. Whaley, M. Sarovar, and I. Siddiqi. Observation of measurement-induced entanglement and quantum trajectories of remote superconducting qubits. *Phys. Rev. Lett.*, 112:170501, 2014.

[118] G. Nogues, A. Rauschenbeutel, S. Osnaghi, M. Brune, J. M. Raimond, and S. Haroche. Seeing a single photon without destroying it. *Nature*, 400:239–242, 1999.

[119] J.-C. Besse, S. Gasparinetti, M. C. Collodo, T. Walter, P. Kurpiers, M. Pechal, C. Eichler, and A. Wallraff. Single-shot quantum nondemolition detection of individual itinerant microwave photons. *Phys. Rev. X*, 8:021003, 2018.

[120] L.-M. Duan and H. J. Kimble. Scalable photonic quantum computation through cavity-assisted interactions. *Phys. Rev. Lett.*, 92:127902, 2004.

[121] G. Vidal and R. F. Werner. Computable measure of entanglement. *Phys. Rev. A*, 65:032314, 2002.

[122] P. Lodahl, S. Mahmoodian, S. Stobbe, A. Rauschenbeutel, P. Schneeweiss, J. Volz, H. Pichler, and P. Zoller. Chiral quantum optics. *Nature*, 541:473, 2017.

[123] K. M. Sliwa, M. Hatridge, A. Narla, S. Shankar, L. Frunzio, R. J. Schoelkopf, and M. H. Devoret. Reconfigurable Josephson circulator/directional amplifier. *Phys. Rev. X*, 5:041020, 2015.

[124] K. Koshino, K. Inomata, Z. R. Lin, Y. Tokunaga, T. Yamamoto, and Y. Nakamura. Theory of deterministic entanglement generation between remote superconducting atoms. *Phys. Rev. Applied*, 7:064006, 2017.

[125] A. Kamal, J. Clarke, and M. H. Devoret. Noiseless non-reciprocity in a parametric active device. *Nature Phys.*, 7:311, 2011.

[126] S. Masuda, S. Kono, K. Suzuki, Y. Tokunaga, Y. Nakamura, and K. Koshino. Non-reciprocal microwave transmission based on Gebhard-Ruckenstein hopping. *Phys. Rev. A*, 99:013816, 2019.

[127] M. Brune, S. Haroche, J. M. Raimond, L. Davidovich, and N. Zagury. Manipulation of photons in a cavity by dispersive atom-field coupling: Quantum-nondemolition measurements and generation of "Schrödinger cat" states. *Phys. Rev. A*, 45:5193–5214, 1992.

[128] B. Hacker, S. Welte, S. Daiss, A. Shaukat, S. Ritter, L. Li, and G. Rempe. Deterministic creation of entangled atom-light Schrödinger-cat odinger-cat states. *arXiv:1812.09604*, 2018.

[129] V. Bužek, G. Adam, and G. Drobnỳ. Quantum state reconstruction and detection of quantum coherences on different observation levels. *Phys. Rev. A*, 54:804, 1996.